Dissertation

submitted to the

Combined Faculties for the Natural Science and for Mathematics

of the Ruperto-Carola University of Heidelberg, Germany

for the degree of

Doctor of Natural Sciences

presented by

Diplom-Physiker Hansjörg Veitel

born in Eppingen

Oral examination: 17 July 2002

VERTICAL PROFILES OF NO_2 AND HONO *IN THE BOUNDARY LAYER*

Referees: Prof. Dr. Ulrich Platt

Prof. Dr. Ulrich Schurath

Vertikalprofile von NO_2 und HONO in der planetaren Grenzschicht

Zusammenfassung

Diese Arbeit stellt die Weiterentwicklung eines kommerziellen Langpfad - DOAS (Differentielle Optische Absorptions-Spektroskopie) Systems zur vollen Marktreife, sowie die Charakterisierung seiner optischen und mechanischen Komponenten vor. Das Gerät wurde für Dauermessungen (über 13 Monate) der Vertikalprofile von NO_2 und HONO über dem Stadtzentrum von Heidelberg genutzt. Beide Spurengase zeigten mit zunehmender Höhe fallende Konzentrationen unter fast allen atmosphärischen Bedingungen. Außerdem wurde – im Vergleich mit NO_2 – eine stärkere Abnahme des HONO - Mischungsverhältnisses mit der Höhe beobachtet. Dies bestärkt die Annahme, dass HONO primär heterogen an Oberflächen am Boden bzw. in Bodenhöhe gebildet wird. Während der Messungen in Heidelberg konnten, selbst an klaren Tagen, HONO – Konzentrationen am Nachmittag von mehr als 100 ppt nachgewiesen werden. Diese Werte sind deutlich höher als bisher beobachtet und verlangen Korrekturen im Verständnis der HONO - Tagchemie.

Außerdem wurde das LP-DOAS System weiterentwickelt, um Messungen zu Reflektoren an einem Fesselballon zu ermöglichen. Dazu wurden sowohl neue Gerätekomponenten entwickelt (allem voran eine Quarzfaser, die das Sichtfeld des Empfangsteleskops erweitert) als auch die Software zur Steuerung des Geräts erweitert. Mit dem weiterentwickelten Gerät wurden erstmals LP-DOAS - Vertikalprofilmessungen zu beweglichen Reflektoren durchgeführt: Experimente am Forschungszentrum Karlsruhe dienten der Messung von NO_2-Vertikalprofilen.

Vertical profiles of NO_2 and HONO in the boundary layer

Abstract

Within this dissertation, a commercial active Long Path Differential Optical Absorption Spectroscopy (LP-DOAS) instrument has been advanced to fully operational status and its optical and mechanical parameters were characterised. This system was used for long-term measurements (13 months) of vertical profiles of NO_2 and HONO on three light paths above the city of Heidelberg, Germany. Both trace gasses were observed to feature concentrations that decrease with increasing altitude under virtually all atmospheric conditions. It was also found that the vertical gradient of HONO is always steeper than the NO_2 gradient. These findings give a further indication that heterogeneous formation of nitrous acid proceeds primarily at or near to the ground. During the Heidelberg measurements, daytime HONO mixing ratios exceeding 100 ppt were observed regularly, even in bright sunshine. These values are substantially higher than previously reported and require a rethinking of the importance of HONO for the oxidation capacity of the polluted atmosphere.

Additionally, the LP-DOAS instrument was adapted to enable measurements to a set of reflectors fixed to a tethered balloon. This task required the development and the integration of additional hardware and software. For instance, a major re-design of the quartz fibre connected to the receiving telescope was carried out to widen the field of view of the instrument. The improved instrument allowed the first ever DOAS measurements on a light path to moving reflectors on a balloon: NO_2 vertical profiles were studied in a campaign at the Forschungszentrum (FZ) Karlsruhe.

Table of Contents

1 Introduction

First studies on the chemical composition of the atmosphere date back to the 18th century and concentrated on the identification of the major constituents of the atmosphere, being nitrogen, oxygen, water, carbon dioxide and the noble gasses. As more sophisticated instruments were available in the late 19th century, the focus changed to the so-called trace gasses, species present in at less than 1 molecule per million air molecules (1 part per million, ppm). This relation is now widely used as the unit for atmospheric compounds: 1 µmol per mole is defined as an mixing ratio of 1 ppm, further refinements for species being present at lower mixing ratios are 1 ppb ($1 \cdot 10^{-9}$ mol per mole) and 1 ppt ($1 \cdot 10^{-12}$ mol per mole). It is now known that myriads of trace species are present in the atmosphere often measurable in the lower ppt range and even below. The reason for the growing interest of atmospheric research in the exact quantification of trace gasses is obvious: the beginning industrialisation in the 19th century lead to an dramatic increase of anthropogenic emissions of various species into the atmosphere. The effects of these pollutants on the biosphere were dramatic.

First reports on the so-called "London Smog" caused by the widespread use of high-sulphur coal for domestic heating even date back to the 17th century. However, these studies were largely phenomenological and the actual pollutants or combination of pollutants responsible for the "London smog" were not identified at that time. a major treatise on air pollution published by John Evelyn describes the effect of air pollution and acidic rain on buildings, but also on public health [*Finlayson-Pitts and Pitts*, 2000]:

"...it is evident to every one who looks on the yearly Bill of Mortality, that near half the children are born and bred in London die under two years of age";

And, contrastingly:

"A child born in a Country Village has even a chance of living near 40 years..."

In the following years, episodes of air pollution were reported regularly. In all cases, the combination of increased levels of SO_2 and particles and strong meteorological inversions concentrated the pollutants in a relatively small volume in the lowermost 50-100 m of the Boundary Layer. As the particles were observed as smoke and the strong inversions lead to fog, the resultant phenomenon was described as smog. The evaluation of several heavy smog events yielded the result that public health was badly affected, leading to more than 4000 excess deaths during distinct smog episodes [*Finlayson-Pitts and Pitts*, 2000].

Another remarkable air pollution phenomenon was first reported in the late 1940s: while London smog occurred in winter at low temperatures and high humidity, the so-called "Los Angeles smog" was observed during hot summer days in bright sunshine. The effects on the environment were also different: under these conditions, ambient air contained pollutants that caused plants to die off and irritated the respiratory tract and the eyes of animals and humans [*Middleton et al.*, 1950]. These effects could be reproduced in the laboratory by irradiating plants with strong sunlight and exposing them to high amounts of NO_2 and alkenes [*Hagen-Smit et al.*, 1952]. A number of successive papers by Hagen-Smit and co-workers revealed that the damage to plants and humans was caused by the strongly oxidising ozone. The physical and chemical mechanisms in the atmosphere causing Los Angeles smog have been the focus of atmospheric research ever since. The basic cycles leading to this phenomenon will be discussed in chapter 2.1.

The impact of nitrogen oxides on photosmog was known from the very beginning, but it was only discovered in the late 1970 that other nitrogen compounds such as nitrous acid also have a huge impact on ozone formation in the polluted Planetary Boundary Layer (PBL). Shortly after Differential Optical Absorption Spectroscopy (DOAS) was introduced for the detection and quantification of atmospheric trace gasses, nitrous acid (HONO) was detected in the atmosphere for the first time [*Perner and Platt*, 1979; *Platt and Perner*, 1980]. Subsequent

studies under Los Angeles conditions revealed that the presence of HONO in the night-time atmosphere caused strongly enhanced levels of O_3 at noon [*Harris et al.*, 1982]. More than 20 years later, the sources and the atmospheric fate of HONO are still subject of intense research. The current knowledge of the chemistry of nitrogen oxides and HONO will be presented in chapters 2.2 and 2.3, respectively.

Vertical trace gas profiles have been used to identify and quantify source and sink processes of atmospheric compounds from the very start: [*Götz*, 1931] published first ground-based measurements of ozone profiles, which were the fundament for the description of the steady-state of O_3 by [*Chapman*, 1930]. [*Regener and Regener*, 1935] performed direct measurements using in-situ ozone monitors carried by meteorological balloons and verified the assumptions of Chapman and Götz. Meteorological and tethered balloons have been used since then in various configurations for the measurement of trace gas profiles in the atmosphere (see e.g. [*Baumbach and Vogt*, 1995; *Bösch*, 2001] and references therein)

First measurements of vertical trace gas profiles in the PBL using active Long-Path-DOAS were published as early as 1978 [*Platt*, 1978]. Even though recent scientific publications have stressed the importance of vertical profile measurements in the PBL, the DOAS technique has since only seen few applications in this context. Especially for HONO and the quantification of its source and sink processes, profile measurements can be expected to yield valuable information. The most recent – and de facto the first published – measurements of HONO vertical profiles by DOAS were performed by [*Stutz et al.*, 2001]. However, these experiments, as previous DENUDER measurements by [*Harrison and Peak*, 1997], spanned only a limited height interval of some metres above ground (see chapter 2.3.4).

For the interpretation of vertical trace gas profiles measured in the PBL, the transport processes in the lower atmosphere have to be understood. Therefore chapter 3 presents a brief overview on this subject. The DOAS measurement technique, the evaluation algorithm and resulting errors are discussed in chapter 4. Additionally, this chapter presents the retrieval algorithm for vertical trace gas profiles from LP-DOAS measurements.

The aims of this thesis have been:

- To advance a semi-commercial DOAS system to make it suitable for long-term measurements of trace gas gradients on fixed light paths.
- To perform long-term measurements of vertical profiles of HONO and NO_2 (as its most prominent precursor) using light paths to retro reflectors installed at several heights of a mountain side.
- The evaluation of the measured data to gain further knowledge about the seasonal and diurnal variation of HONO in a low to medium polluted environment, as well as on its source processes.
- The improvement of the LP-DOAS system to allow gradient measurements using a variable light path to reflectors fixed on a tethered balloon. As a proof-of-concept, first measurements of trace gas profiles using the LP-Balloon-DOAS have been intended.

For the long-term measurements of vertical profiles, a compact and easy-to-use LP-DOAS system has been developed by the Institut für Umweltphysik, Universität Heidelberg, in a joint project with Hoffmann Messtechnik, Rauenberg, as an industrial partner. The improvement of the existing prototype and the characterisation of the improved system has been one of the main focal points of this PhD thesis. This system was tested during long-term vertical profile measurements of NO_2 and HONO above the city of Heidelberg lasting 13 months (see chapter 5). Experience gained during this campaign was continuously used to upgrade the instrument. Chapter 5.2 presents a detailed characterisation of the hardware and the achieved stability of its optical and mechanical components.

The spectra evaluation algorithm for HONO and NO_2 was adapted to the instrument characteristics and its reliability was tested by extensive simulations presented in chapter 5.3.

The evaluation and analysis of the data measured at Heidelberg is the focus of chapter 6, while Annex A presents an overview of all data recorded during the 13-month campaign. Special emphasis was placed on the statistical analysis of the data to obtain the seasonal and diurnal cycles of the NO_2 and HONO profiles, while the ratio HONO/NO_2 and the relative gradients of both compounds were used to obtain information on the efficiency of possible HONO source processes. A major goal has been to estimate the contributions of surfaces at the ground and of aerosol surfaces for the HONO formation. Therefore, distinct meteorological situations, characterised by stable and instable stratification of the PBL, were separated and evaluated.

Surprisingly, the HONO measurements at Heidelberg provided the opportunity to quantify HONO daytime concentrations in bright sunlight. Chapter 7 and Annex B present the results of these studies and show possible implications for our understanding of the oxidation capacity of the atmosphere in daytime.

The measurements employing a DOAS light path to a reflector fixed on a tethered balloon required further modifications of the optical and mechanical set-up of the instrument. Chapter 8 deals with the improvements applied to the system to allow such measurements. Especially the characteristics of quartz fibres and the design of a sophisticated quartz fibre assembly emerged to be critical for the LP-DOAS-Balloon measurements. After all hardware and software improvements had been applied, first successful gradient measurements with a DOAS long path system in conjunction with a tethered balloon could be performed in January 2001. The processing of the measurements and the resulting data will be presented in chapter 9.

Finally, a summary and conclusion of the thesis will be presented in chapter 10.

2 Nitrogen oxides in the boundary layer

Scientific publications on atmospheric chemistry show that most of the major focal points of atmospheric research are linked – directly or indirectly – to nitrogen oxides. The most prominent examples are the “Ozone Hole” in the stratosphere, “Acidic Rain” in the lee of industrial centres and the “Summer Smog” in urban areas.

The importance of nitrogen compounds in the stratosphere is mainly linked to their effect on ozone (for an overview see e.g. [*Finlayson-Pitts and Pitts*, 2000]). [*Crutzen*, 1970] suggested that ozone can be destroyed by NO and NO_2 formed by reactions of N_2O while [*Johnston*, 1971] suggested that NO_X emitted directly into the stratosphere could decrease the steady-state concentration of ozone. In the polar stratosphere, nitrogen compounds act as a reservoir for ozone-destroying halogenic compounds [*Farman et al.*, 1985]. The break-up of these compounds on the surfaces of polar stratospheric clouds and the subsequent photolysis of halogenic compounds like Cl_2 triggers the huge total ozone losses occurring in polar spring known as the “Ozone Hole”.

In the troposphere, acid deposition is one of the popular topics related to nitrogen oxides. Here, directly emitted NO and - to a lesser extent - NO_2 are oxidised further to form nitric acid (HNO_3), which is subsequently transported to the ground by dry or wet deposition. Other forms of acidic rain are due to sulphuric acid generated from SO_2 in urban areas and organic acids, which can be found both in rural and urban areas.

In the planetary boundary layer (PBL), the most simple nitrogen oxides NO and NO_2 (NO_X) play a major role in the genesis of the so-called “Los Angeles smog” or photosmog [*Middleton et al.*, 1950]. This phenomenon occurs in urban areas but also spreads to more rural zones by transport of polluted air masses. In the early 1950´s laboratory experiments could duplicate the effects of photosmog on the biosphere by irradiating polluted air containing a mix of alkenes and nitrogen oxides with sunlight. This yielded, besides other products, high ozone concentrations, which characterise this phenomenon. Similar effects were observed with sunlight-irradiated diluted auto exhaust, which contains NO_x and a variety of hydrocarbons (HC). So the nitrogen oxides play a key role in the formation of tropospheric ozone.

Of further interest is the contribution of nitrogen oxides to the formation of other atmospheric oxidants. Especially nitrous acid has recently been recognised as an important precursor of the hydroxyl radical [*Alicke et al.*, 2001a; *Alicke et al.*, 2001b], which is the most important oxidizing species in the daytime atmosphere (see e.g. review by [*Crutzen and Zimmermann*, 1991; *Logan*, 1983; *Logan et al.*, 1981]).

As the thesis presented here concentrates on gradient measurements in the planetary boundary layer or - more accurately - in the height interval ranging from ground level to 450 m height over ground, the following sections concentrate on chemistry and dynamics in the boundary layer and lower troposphere.

2.1 Photosmog

Since the first observations of photochemical smog events in Los Angeles in the 1940s, high ozone levels have been measured throughout the world with ozone concentrations of up to 400 ppb e.g. in Athens (Greece), Sydney (Australia), and Mexico City. Photochemical air pollution is now recognized to be a worldwide problem in areas where volatile organic compounds (VOC) and NO_x emissions from major mobile and stationary sources are "trapped" by thermal inversions and irradiated by sunlight during transport to downwind regions. In the following, the genesis of photosmog will be discussed in detail.

2.1.1 The photostationary steady state system NO – NO_2 –O_3

In an atmosphere containing only NO, NO_2 and air without organic compounds, the reactions controlling the concentrations of NO and NO_2 are given as:

$$NO_2 + h\nu \xrightarrow{\lambda<420nm} NO + O(^3P) \qquad \text{R. 1}$$

$$O(^3P) + O_2 \xrightarrow{M} O_3 \qquad \text{R. 2}$$

$$O_3 + NO \longrightarrow NO_2 + O_2 \qquad \text{R. 3}$$

Then, the Leighton relationship, named after Philip Leighton, who wrote the first definitive monograph on air pollution in 1961 [*Leighton*, 1961], is given by

$$\frac{[O_3]\cdot[NO_2]}{[NO]} = \frac{k_3}{J_1} \quad \text{or} \quad \frac{[NO_2]}{[NO]} = [O_3]\cdot\frac{k_3}{J_1} \qquad \text{R. 4.}$$

According to this relationship, frequently referred to as the "photostationary state" of NO_x, the concentration ratio of O_3, NO and NO_2 should be a constant. It is defined by the ratio of the rate constant for the reaction of NO with O_3 and for photolysis of NO_2. Since $k_{R.\,1}$ changes with the solar zenith angle, the ratio of concentrations can also be expected to change during the day. In general, the Leighton relationship is valid when reactions R. 1 and R. 3 are the major loss processes for NO_2 and O_3, respectively (reaction R. 2 is essentially always the loss process for $O(^3P)$). Then, the reactions R. 1, R. 2 and R. 3 act as a zero cycle without forming or consuming any species (see Figure 1) and consequently the O_3 net production within this cycle is zero. Thus, if NO_2 and O_3 are measured at the same time and location, deviations from the zero cycle can be identified using the sum

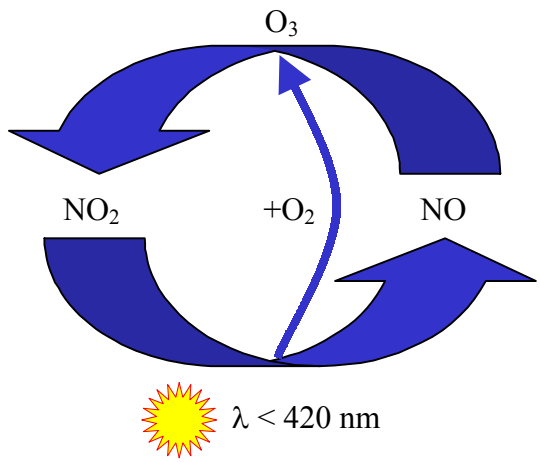

Figure 1: The photostationary state without hydrocarbons. In total no ozone is produced or destroyed ("zero cycle").

$$Ox = [NO_2] + [O_3].$$

Ox should be constant as long as the Leighton ratio correctly describes the relation of NO, NO_2 and O_3. Periods of enhanced photochemistry leading to the photosmog phenomenon are identified by an increase in *Ox*.

2.1.2 Deviations from the steady state yielding ozone

In the presence of volatile organic compounds (VOCs), NO can be converted to NO_2 by reactions other than R. 3. Consequently, the steady state is no longer sustained as *Ox* increases. However, the organic compounds have to be oxidised first to disturb the zero cycle: the most likely oxidant is the OH radical that is formed by ozone photolysis:

$$O_3 + h\nu \xrightarrow{\lambda>320nm} O(^1D) + O_2 \qquad \text{R. 5}$$

$$O(^1D) + H_2O \longrightarrow 2OH \qquad \text{R. 6}$$

The efficiency of this reaction is about 5 to 20 % [*Alicke et al.*, 2001a]. The same author states that nitrous acid must also be considered as a prominent source of OH radicals, especially in the morning hours (see chapter 0). Now, the common scheme of the oxidation of one hydrocarbon (RH) in the troposphere can now be described as:

$$RH + OH \longrightarrow R + H_2O \qquad \text{R. 7}$$

$$R + O_2 \xrightarrow{M} RO_2 \qquad \text{R. 8}$$

Peroxyradicals (RO_2) and hydroxyradicals (HO_2) formed by R. 10 convert NO into NO_2:

$$RO_2 + NO \longrightarrow NO_2 + RO \qquad \text{R. 9}$$

$$RO + O_2 \longrightarrow R'CHO + HO_2 \qquad \text{R. 10}$$

$$HO_2 + NO \longrightarrow OH + NO_2 \qquad \text{R. 11}$$

The overall scheme for reactions R. 7 to R. 11 is expressed by:

$$RH + 2O_2 + 2NO \longrightarrow R'CHO + H_2O + 2NO_2 \qquad \text{R. 12}$$

This scheme can be applied until the initial VOC is transformed to CO_2 (or CO and H_2O). Thus, in the presence of NO_X and O_3 and considering the reactions R. 1 and R. 2, the total ozone-producing cycle from VOCs is simplified to

$$RH + 4O_2 + 2h\nu \xrightarrow{\lambda<420nm} R'CHO + H_2O + 2O_3 \qquad \text{R. 13}$$

Consequently, the reactions R. 9 and R. 11 of NO with RO_2 and HO_2 producing NO_2 have to be taken into account for the description of the balance of NO, NO_2 and O_3 in the presence of VOCs [*Carroll and Thompson*, 1995; *Parrish et al.*, 1986]. The photolysis of the NO_2 molecule gained by these reactions yields the net production of an O_3 molecule. Considering this, R. 4 becomes

$$\frac{[NO_2]}{[NO]} = \frac{1}{J_{(R.1)}} \cdot \left\{ k_{(R.3)} \cdot [O_3] + k_{(R.11)} \cdot [HO_2] + \sum_{RO_2} k_{(R.9)} \cdot [RO_2] \right\} \qquad \text{R. 14}$$

Other deviations from the Leighton ratio can be caused by the following processes:

- At sunset and sunrise, the rate of photolysis of NO_2 via R. 1 is sufficiently small. Under these circumstances, steady-state assumptions are not valid.
- Significant sinks of O_3 other than reaction R. 3 disturb the steady state of O_3. These additional loss processes may include photolysis of O_3 as well as reactions with NO_2, alkenes and the radicals HO_2 and OH.
- Non-chemical loss processes as fluxes of NO from the surface and micrometeorological effects also perturb the Leighton ratio [*Carroll and Thompson*, 1995]. Especially in summer, with high solar radiation and a simultaneous ground inversion, a self-amplification of the system can occur, yielding high concentrations of ozone and other pollutants.

Figure 2 shows the scheme of the formation of photosmog in the polluted atmosphere: the lower cycle depicts the undisturbed stationary state without O_3 net production. In the presence of RO_X radicals, the complete cycle forms a net O_3 source. RO_x radicals can be formed by several formation pathways (see also Figure 2). A detailed description and quantification of the different RO_X sources is presented by [*Alicke*, 2000] and references therein. Here, only the OH source by photolysis of nitrous acid is of major interest, as this thesis concentrates on the

source reactions and vertical profiles of HONO. The source and sink reactions of HONO and their impact on atmospheric chemistry will be discussed below.

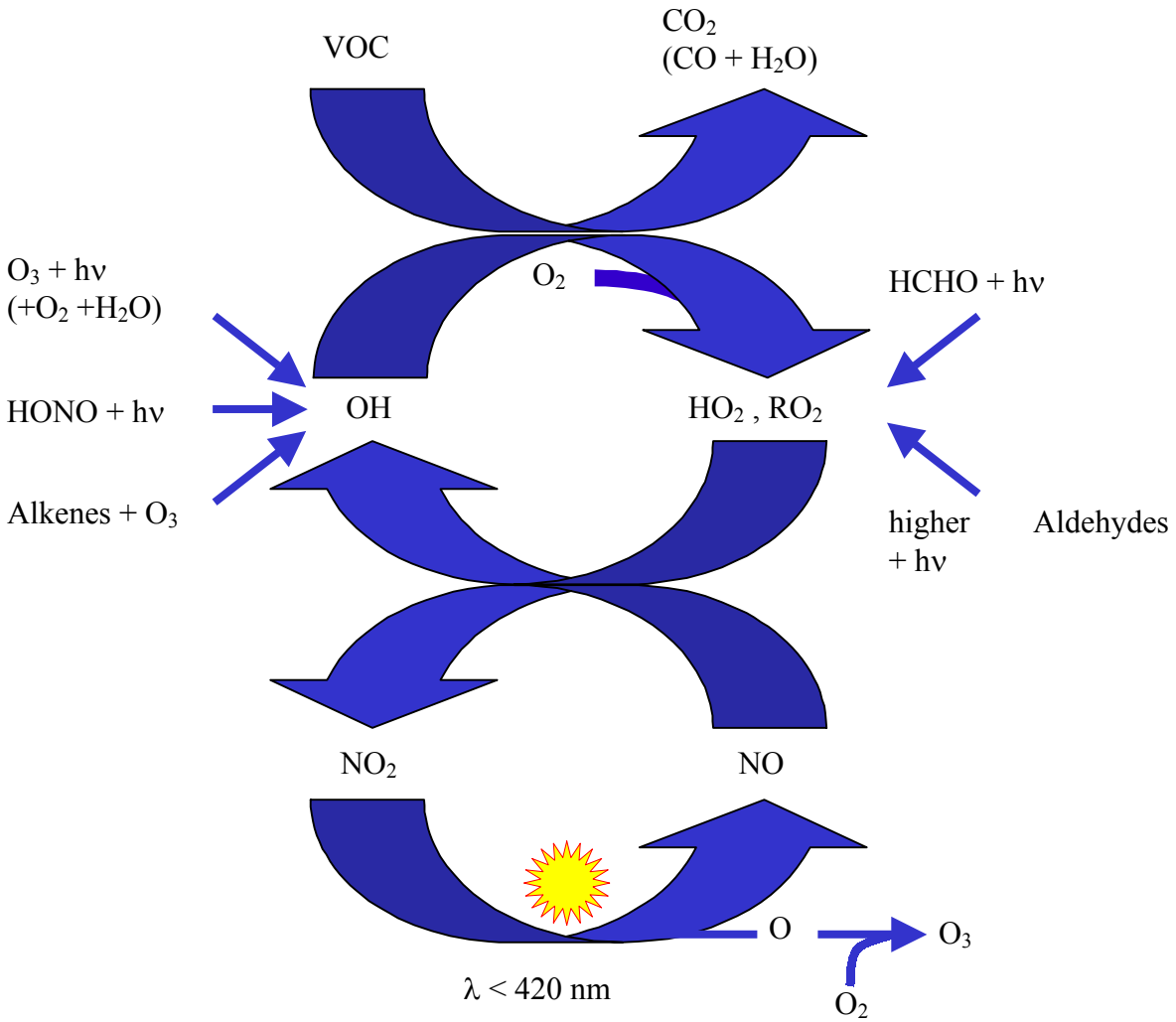

Figure 2: Reaction cycles of tropospheric nitrogen oxides and ozone with the impact of RO_x. Ozone is formed in the presence of RO_X, NO_X and sunlight. Note that HONO photolysis is one of the pathways forming OH and thereby O_3.

2.2 Tropospheric nitrogen oxides

The group of the oxides of nitrogen consists of all molecules with the universal formula N_aO_b. The most important tropospheric species NO and NO_2 are summarized to NO_x:

$$NO_x = NO + NO_2$$

The reactive nitrogen-containing species altogether are called NO_y and are often referred to as nitrogen oxides:

$$NO_y = (NO + NO_2 + HNO_3 + PAN^1 + HONO + NO_3 + N_2O_5 + \text{organic nitrates etc.})$$

NO_y are primarily emitted in the form of NO from biogenic and anthropogenic sources. NO is then converted to higher oxidized nitrogen oxides by different chemical processes in the troposphere. It can be recycled by photolytical cleavage of the higher oxides (e.g. NO_2) during the day. As already stated in chapter 2.1, a photostationary steady state between NO, NO_2 and ozone can be formed quickly during daytime. This steady state is influenced by the oxidation of VOCs, by free radicals (mainly the hydroxyl radical OH) the solar zenith angle (SZA) and non-chemical processes.

2.2.1 Sources of tropospheric nitrogen oxides

The discussion of atmospheric nitrogen oxide chemistry needs to include factors such as location, magnitude and type of emission of the nitrogen oxides. Several reviews have been published on the balancing of sources and sinks of tropospheric NO_x (see e.g. [*Logan*, 1983]). More recent investigations show a strong increase of the anthropogenic sources for some species. For example, nitrogen oxides have risen about 350 % since 1983 [*Hammeed and Dignon*, 1992].

As can be seen in Table 1, about three-quarters of the tropospheric nitrogen oxides are generated anthropogenically, mainly by fossil fuel burning. Figure 3 quantifies the different anthropogenic NO_x sources: the largest sources are road traffic and electrical utility fuel combustion, each with a contribution to the total anthropogenic NO_x in the atmosphere of nearly one third. It is noteworthy in this context that heavy trucks and vehicles without a catalytic converter have the strongest influence on traffic emissions [*Kessler*, 1984].

The largest contribution of anthropogenic NO_x (typically > 90 %) is emitted as NO from combustion by the following reaction scheme:

$$\begin{aligned} &O_2 \xleftrightarrow{M} 2O \qquad\qquad M = N_2, O_2 \\ &O + N_2 \xleftrightarrow{M} NO + N \\ &N + O_2 \longleftrightarrow NO + O \end{aligned} \qquad \text{R. 15}$$

The subsequent oxidation of NO produces small amounts of NO_2. The direct contribution of NO_2 can vary between 1 and 30 % [*Lenner*, 1987].

There are also significant other sources of nitrogen oxides (see Table 1), in particular nitric oxide, which is produced by biomass burning (e.g. in the tropics) as well as by soils, where nitrification, denitrification and the decomposition of nitrite (NO_2^-) contribute to NO production [*EPA*, 1997]. Another important natural source is NO_x produced by lightning, with recent estimates in the range of 10 – 33 Tg/yr [*Flatoy and Hov*, 1997; *Price et al.*, 1997a; *Price et al.*, 1997b]. The production of NO_x by some bacteria in the ground is also a significant source for nitrogen oxides in the troposphere with a contribution of 18 % to the total NO_x emissions. As yet, this source has not been well quantified. The oxidation of NH_3 by photochemical processes in oceans and by some terrestrial plants yields also small

[1] PAN = peroxyacetyl nitrate = $CH_3C(O)OONO_2$

amounts of NO [*Wild et al.*, 1997].
Another nitrogen oxide, which is not produced from NO and also not included by NO_X is Nitrous oxide (N_2O, "laughing gas"). Its main sources are biological and, to a lesser extent, anthropogenic processes. While biomass burning is the major anthropogenic source, there are a variety of smaller sources, including motor vehicles. Interestingly, N_2O emissions from current catalyst cars appear to be higher than from vehicles that are not equipped with a catalyst [*Berges et al.*, 1993], while total NO_x emissions of catalyst-equipped cars are much lower. N_2O is inert in the troposphere and is ultimately transported to the stratosphere.
Model calculations from [*Levy et al.*, 1980], including the stratosphere-troposphere exchange, showed that this source contributes to only about 0.5 % of the total tropospheric NO source strength, but it is nevertheless the most important NO source for the stratosphere.

Table 1: Global Emission estimates from both anthropogenic and natural sources (in Tg/yr) [*Müller*, 1992]**. The anthropogenic sources consist of different combustion processes (see Figure 3). Biomass burning includes both natural and anthropogenic sources. NO formation out of lightening and emission from the stratosphere are not included in this table, but their contribution to the total NO_x is less than 10%, and therefore only important for the atmosphere of remote regions.**

species	anthropogenic sources	biomass burning	continental biogenic sources [a]	oceans	total
CO	383	730	165	165	1440
NO_x [b]	72	18	22	0.01	122
CH_4	132	54	310	10	506
VOC	98	51	500	30 – 300	750

[a] Includes animal, microbial and foliage emissions
[b] Expressed as NO_2

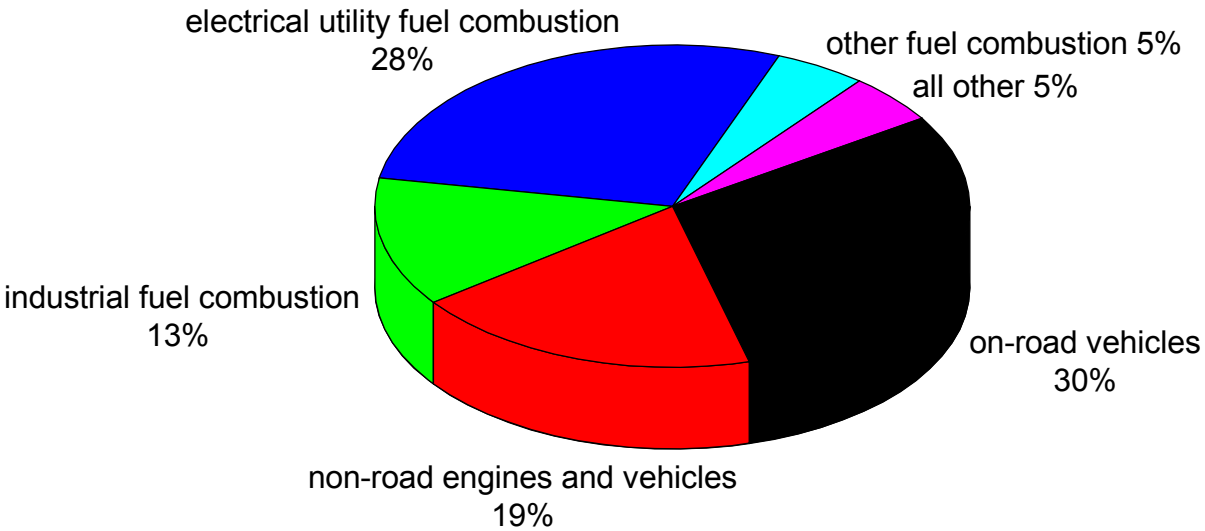

Figure 3: Contribution of various sources to total anthropogenic NO_x emissions in the United States in 1996 [*EPA*, 1997]**.**

2.2.2 Sinks of tropospheric nitrogen oxides

The sinks of nitrogen are primarily dry or wet deposition of nitric acid (HNO_3). As a consequence of several chemical reactions in the atmosphere, NO_x is transformed to water-soluble species like nitric acid or nitrous acid (HONO), which are washed out of the atmosphere by rain (wet deposition) and are therefore a major constituent of acid rain. Dry deposition of the very "sticky" HNO_3 molecule by adsorption on aerosols and the ground has been quantified to be responsible for 16 % to up to 40 % of the total nitrogen flux to the surface by [*Russell et al.*, 1993] and [*Nielsen et al.*, 1996], respectively.

One of the main reactions leading to the formation of nitric acid is the reaction of nitrogen dioxide with the hydroxyl radical:

$$NO_2 + OH \longrightarrow HNO_3 \qquad \text{R. 16}$$

The anhydride of nitric acid, N_2O_5 is believed to play a significant role in tropospheric chemistry [*Finlayson-Pitts and Pitts*, 2000], but has never been directly measured in the troposphere. However, using the measured concentrations of NO_2 and NO_3 and the equilibrium constant for the N_2O_5 source reaction,

$$NO_3 + NO_2 \xleftrightarrow{M} N_2O_5 \qquad \text{R. 17}$$

peak concentrations of N_2O_5 up to about 10 – 15 ppb in a polluted atmosphere have been calculated [*Atkinson et al.*, 1986]. The major loss process of N_2O_5 in the troposphere appears to be hydrolysis and subsequent dry or wet deposition [*Mentel et al.*, 1996]:

$$N_2O_{5(g)} + H_2O_{(g)} \longrightarrow 2HNO_{3(g)} \qquad \text{R. 18}$$

$$N_2O_{5(g)} + H_2O_{(l)} \longrightarrow 2HNO_{3(aq)} \qquad \text{R. 19}$$

[*Dentener and Crutzen*, 1993] predicted that in the northern hemisphere, more than a half and up to 90 % of the HNO_3 formation occurs by reaction R. 19 and the adsorption of NO_3 on wet surfaces. Therefore, N_2O_5 has to be seen as a major sink of nitrogen oxides in the polluted troposphere.

In this context, the formation of NO_3 from NO_2 and O_3 should be introduced as another possible NO_2 (and thereby NO_x) sink :

$$NO_2 + O_3 \longrightarrow NO_3 + O_2 \qquad \text{R. 20}$$

$k_{\text{R. 20}} = 3.2 \cdot 10^{-17}$ cm^{3}molec^{-1}s^{-1} [*DeMore et al.*, 1997]

Even though the rate constant of this reaction at 298K is relatively small, R. 20 cannot be neglected in areas featuring high O_3 concentrations in the evening hours and at night: assuming 100ppb of O_3, which is still near or below the air quality standards of most countries, the lifetime of NO_2 with respect to O_3 is only 3.5 h [*Finlayson-Pitts and Pitts*, 2000].

2.2.3 Overview of the tropospheric NO_y – Chemistry

Prior to the more intensive discussion of the sources and sinks of nitrous acid, Figure 4 presents a brief overview of NO_y-chemistry in the troposphere. This graph summarises the most important reactions discussed above:

The central role is played by NO_x, which is primarily emitted in the form of NO (see chapter 2.2.1), and represents the "basic material" for most other nitrogen oxides. Nitrogen monoxide is directly linked with NO_2 via ozone (see chapter 2.1). A small part of NO_y is directly emitted as nitrous acid, which is mainly formed by the reaction of NO_2 with liquid water (see chapter 2.3.1). HONO is photolysed during the day to form NO and the hydroxyl radical OH, which is part of virtually all reactions in daytime chemistry of polluted air masses.

NO_3 is widely accepted to be the most important radical during the night, (see [*Geyer et al.*, 2000b]). The nitrate radical forms N_2O_5 in the presence of NO_2 very quickly. N_2O_5 reacts subsequently on wet surfaces to form HNO_3. Almost 90 % of the nitrogen oxides are deposited from the troposphere by these production pathways (see chapter 2.2.2). Wet deposition of nitric acid is the most important sink for NO_x and is part of the acidic rain phenomenon.

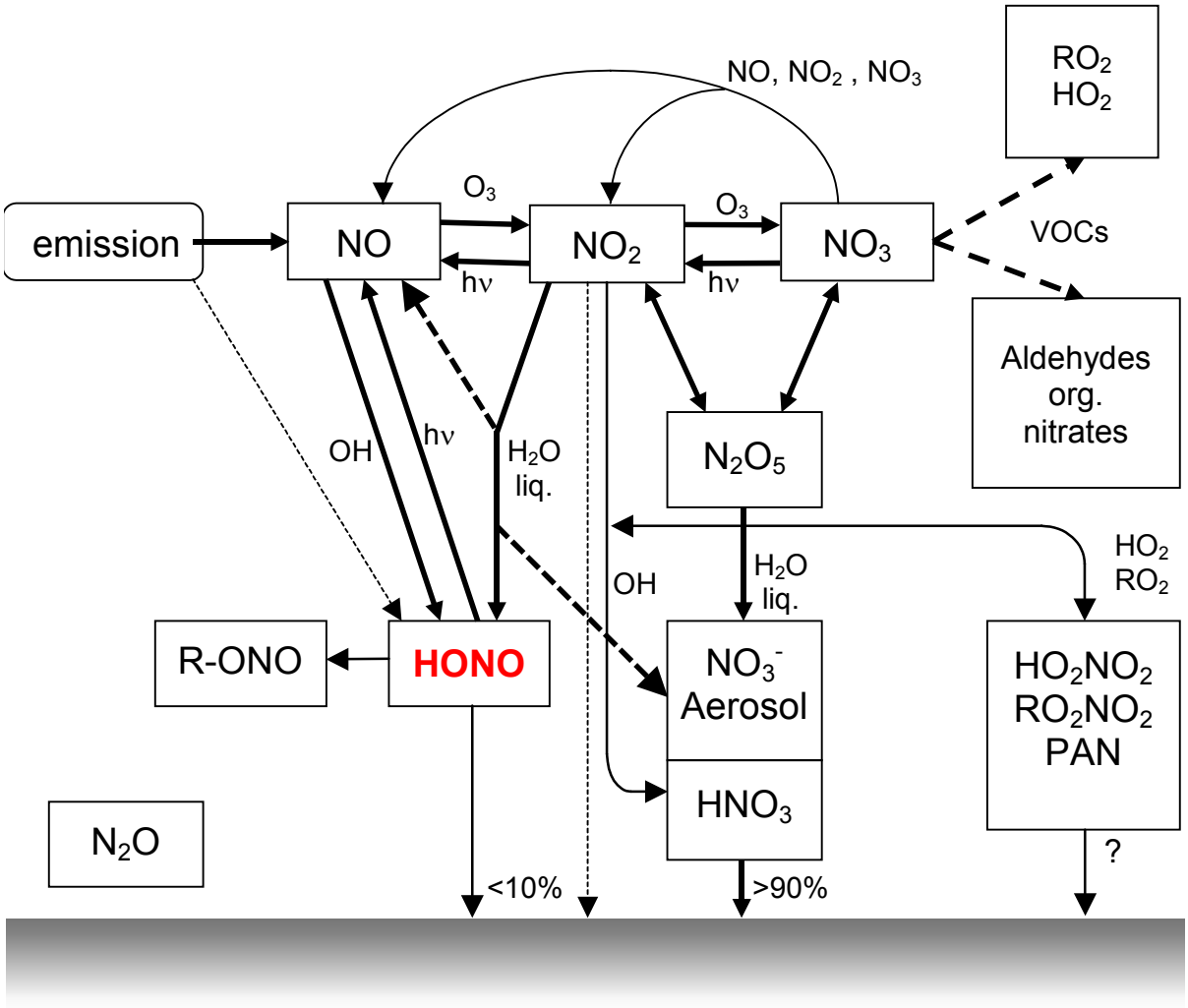

Figure 4: Overview of the tropospheric nitrogen oxides chemistry.

2.3 Nitrous Acid

The role of nitrous acid in atmospheric chemistry has been underestimated for a long time and has therefore been neglected in many models. However, HONO is of major significance in tropospheric chemistry: when irradiated with light in the wavelength range of 300 nm to 405 nm, its photolysis yields an OH radical and NO:

$$HONO + h\nu \xrightarrow{300nm<\lambda<405nm} OH + NO \qquad \text{R. 21}$$

This reaction has been well known since the mid-1970`s [*Cox*, 1974; *Nash*, 1974]. Nitrous acid was first identified in the atmosphere by [*Perner and Platt*, 1979; *Platt et al.*, 1980]. Since then many atmospheric measurements have been reported (see [*Alicke*, 2000] for an overview of published measurements). Maximum mixing ratios reported were up to 15 ppb [*Winer and Biermann*, 1994] in Los Angeles or 10 ppb in Milan, Italy [*Febo et al.*, 1996]. Generally, nitrous acid concentrations were found to scale with NO_2 concentrations and therefore with the degree of pollution.

The diurnal variation of the mixing ratio of HONO is dominated by its photolysis. Daytime values are typically found to be very low, with mixing ratios below 100 ppt in rural and medium polluted areas (see e.g. [*Alicke et al.*, 2001a] and [*Reisinger*, 2000], respectively). In polluted areas, recent measurements using multiple measurement techniques show HONO daytime mixing ratios of about 200 ppt [*Geyer and Trick*, 2002]. During the night the concentration increases until midnight. The time series in the second half of the night seems to depend as much on NO_2 mixing ratios as on meteorological parameters: a further increase of HONO until sunrise [*Alicke et al.*, 2001a; *Harrison et al.*, 1996; *Notholt et al.*, 1992] has been observed as well as a nearly constant value [*Alicke*, 2000], a decrease [*Notholt et al.*, 1992; *Reisinger*, 2000] or slight decrease with a second HONO maximum just before dawn [*Alicke*, 2000; *Trick and Geyer*, 2002]. The influence of the boundary layer height on nitrous acid concentrations, which should be of major importance for these effects, is still not well investigated. Under all circumstances, HONO is quickly photolysed within 2 hours after dusk. The time derivative of the HONO mixing ratio during sunrise depends on the intensity of solar radiation (e.g. on latitude and degree of cloud cover).

The quantification of the OH production by HONO photolysis is difficult, because it requires fast and precise measurements of the HONO mixing ratio, especially during sunrise. Most published measurements were performed with instruments achieving a 0.5 - 24-hour time resolution (e.g. [*Appel et al.*, 1990; *Febo et al.*, 1993; *Harrison et al.*, 1996; *Sjödin and Ferm*, 1985]), which is too slow to follow the decrease of HONO at sunrise. More recent measurements – featuring a better time resolution of about 10 minutes – show that up to 30 % of the total OH is produced by HONO photolysis in a 24-hour period [*Alicke et al.*, 2001a; *Alicke et al.*, 2001b; *Stutz et al.*, 2001].

Contrasting its underestimation as an OH source, the role of HONO as a precursor of different carcinogenic species was published shortly after its first detection in the atmosphere [*Hanst*, 1978; *Pitts et al.*, 1978]. HONO reacts in the dark with secondary amines (DMA and DEA)[2] yielding carcinogenic nitrosamines and water:

$$R_2NH + HONO \longrightarrow R_2NNO + H_2O \qquad \text{R. 22}$$

This reaction proceeds in the atmosphere as well as in the human lung. Amines are emitted in the air as a result of a wide variety of sources (see e.g. [*Fine*, 1980]). Although little is known about the concentrations of amines in urban air, the levels to which the general public is exposed are presumably quite low [*Pitts et al.*, 1978].

[2] DMA: Dimethylamine; DEA: Diethylamine

2.3.1 Sources of Nitrous Acid

The formation of nitrous acid can proceed via three different types of reactions (see Figure 5). One has to distinguish between gas-phase reactions (homogeneous reactions), formation in a thin layer of water on a surface (heterogeneous reactions) and direct emission. The exact formation pathway of nitrous acid is still unknown. Especially the effectiveness of different surfaces for HONO formation and the adsorption processes of the HONO precursors on these surfaces are currently under investigation (e.g. [*Trick et al.*, 2002]). Additionally, the share of direct emission to the total HONO production is not well quantified.

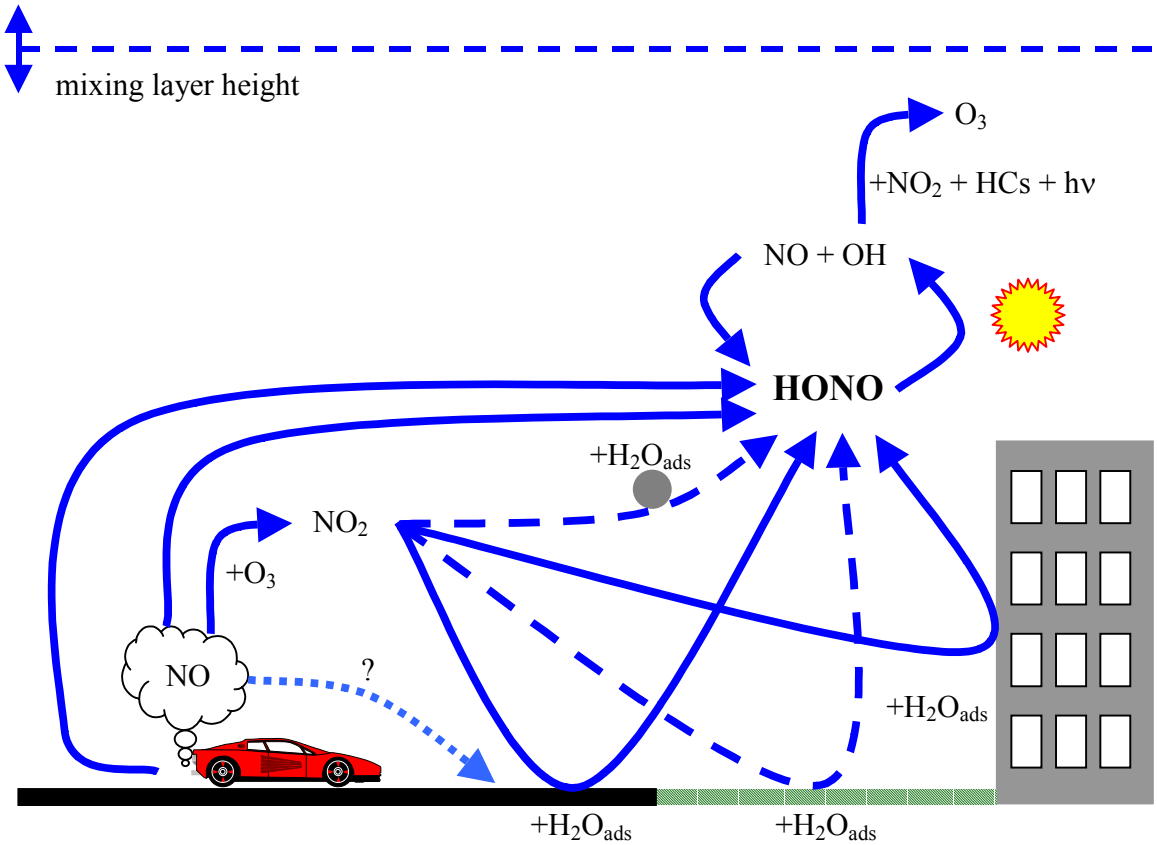

Figure 5: Schematic overview of HONO chemistry: NO_2 reacts with the water of wet surfaces to HONO. Asphalt roads and concrete structures seem to be more effective for this process than grassland or aerosol surfaces (see e.g. [*Harrison and Peak*, 1997; *Stutz et al.*, 2001; *Trick et al.*, 2002]). Therefore the height of the inversion layer is directly linked to HONO concentrations, as the most effective sources are located near the ground. In daylight, HONO is photolysed to NO and OH and plays a key role for the O_3 production in the polluted troposphere.

Direct Emission

Due to the fact that nitrous acid is very closely linked to NO_x chemistry, sources of NO_x are potential sources for HONO as well. However, the thermodynamics and kinetics of combustion processes, which form the most prominent NO_X source, are unfavourable for HONO formation. Nevertheless, HONO may be formed as combustion gases cool down immediately after exiting from the combustion chamber, for example in a car tailpipe. Several studies have been carried out to estimate the source strength of nitrous acid from direct emissions such as combustion engines [*Kessler and Platt*, 1984; *Pitts et al.*, 1984a; *Winer and Biermann*, 1994]. These studies found that up to 1.8% of the total NO_x is emitted as nitrous

acid, making this source important especially in heavily polluted areas with high amounts of traffic. Table 2 shows a comparison for the ratio of nitrous acid versus total NO_x for different engine types: [*Kessler and Platt*, 1984] found that HONO / NO_x is lower for cars without catalytic converters compared to cars or heavy trucks with diesel engines. The reason for the higher amount of HONO emitted from diesel engines is most probably the high aerosol concentration in diesel exhaust and the fast formation of nitrous acid on particles in the exhaust pipe (see chapter 2.3.1). Additionally, the concentration of NO_X is much larger in diesel exhaust compared to normal engines. However, [*Kurtenbach et al.*, 2001] observed virtually the same ratios of HONO / NO_2 for diesel and gasoline engines in automobiles. As the car used for their study was a rather quite old, the same authors state that the ratio for the gasoline engine is not representative for the total fleet. To obtain a value for the direct HONO emission by traffic that is representative for the total (German) car fleet, [*Kurtenbach et al.*, 2001] suggest using the HONO / NO_2 ratio measured during a road tunnel experiment discussed in the same publication.
It is noteworthy in this context that the state of engine operation also influences the amount of HONO directly emitted by traffic (the engines of all cars and trucks passing the tunnel used for the study by [*Kurtenbach et al.*, 2001] had been running for some 15 minutes at least and were therefore "warm"): [*Pitts et al.*, 1984a] indicated that cold engine operation as well as bad maintenance or the age of the catalyst increase HONO tailpipe emissions. This is in agreement with the measurements by [*Calvert et al.*, 1994], who found very low HONO / NO_2 ratios for catalyst-equipped, well-maintained gasoline automobile engines. In Figure 6 the mixing ratios for different nitrogen oxides are shown depending on the engine rotary speed and torque. For the diesel engine, HONO emissions have a maximum at low engine rotary speed.

Table 2: HONO emitted as a fraction of vehicle exhaust NO_x.

System	$\frac{HONO}{NO_x}$ [%]	Reference
Diesel engine	1.0	[*Kessler and Platt*, 1984]
Gasoline engine (rich operation conditions)	< 0.01	[*Kessler and Platt*, 1984]
Gasoline engine (lean operation conditions)	0.15	[*Kessler and Platt*, 1984]
Highway	0.5	[*Kessler and Platt*, 1984]
Variety of vehicles (gasoline engine)	0.1 –1.8	[*Pitts et al.*, 1984a]
Gasoline engine (catalyst-equipped)	< 0.1	[*Calvert et al.*, 1994]
Ambient air	0.8	[*Winer and Biermann*, 1994]
Traffic tube	0.29 ± 0.05	[*Kirchstetter et al.*, 1996]
Traffic tube	0.8 ± 0.1	[*Kurtenbach et al.*, 2001]
Diesel engine (truck)	0.53 ± 0.08	[*Kurtenbach et al.*, 2001]
Diesel engine (car)	0.66 ± 0.2	[*Kurtenbach et al.*, 2001]
Gasoline engine (car, catalyst-equipped)	0.65 ± 0.24	[*Kurtenbach et al.*, 2001]

A report from [*Winer and Biermann*, 1989] showed further evidence for the possible significance of HONO direct emission: time series of HONO and NO_2 between sunset and midnight during six periods in fall 1987 at Los Angeles showed no correlation between HONO and NO_2 concentrations or the square of the NO_2 concentration. However, nitrous acid correlated well with CO and NO during these periods. Since both CO and NO are primary combustion emissions, direct HONO emission from combustion processes can be deduced. A HONO emission rate of about 0.8 % of the total NO_x emissions was derived. In addition, a NO_2 conversion to HONO of about 1 % per hour was interpreted. This is in agreement with the HONO production rate from heterogeneous NO_2 reactions analogous to those observed in smog chambers.
The interpretation of ambient measurements to establish the extent of direct HONO emissions is difficult, however, as some fraction of the NO_x released may undergo a rapid conversion to HONO at the relatively high NO_x concentrations close to the tailpipe.

Measurements inside houses showed elevated levels of nitrous acid as well [*Brauer et al.*, 1990; *Febo and Perrino*, 1991]. Peak levels (15 min) of up to 100 ppb of HONO and 24 h averages as high as 40 ppb were measured [*Brauer et al.*, 1990]. The HONO concentrations increased shortly after combustion (gas heating and gas cooking) started.
Studies inside cars also indicated elevated levels of nitrous acid [*Febo and Perrino*, 1995] with concentrations of up to 30 ppb of HONO (outside concentration: 1.4 ppb) during transit through polluted areas (urban sites). The study showed that high concentrations persist for many hours even when the cars are moved to an unpolluted site.

Additional to these anthropogenic sources, [*Rondon and Sanhueza*, 1988] suggested that HONO generation in fires was important in the Venezuelan savannah during the biomass-burning season.

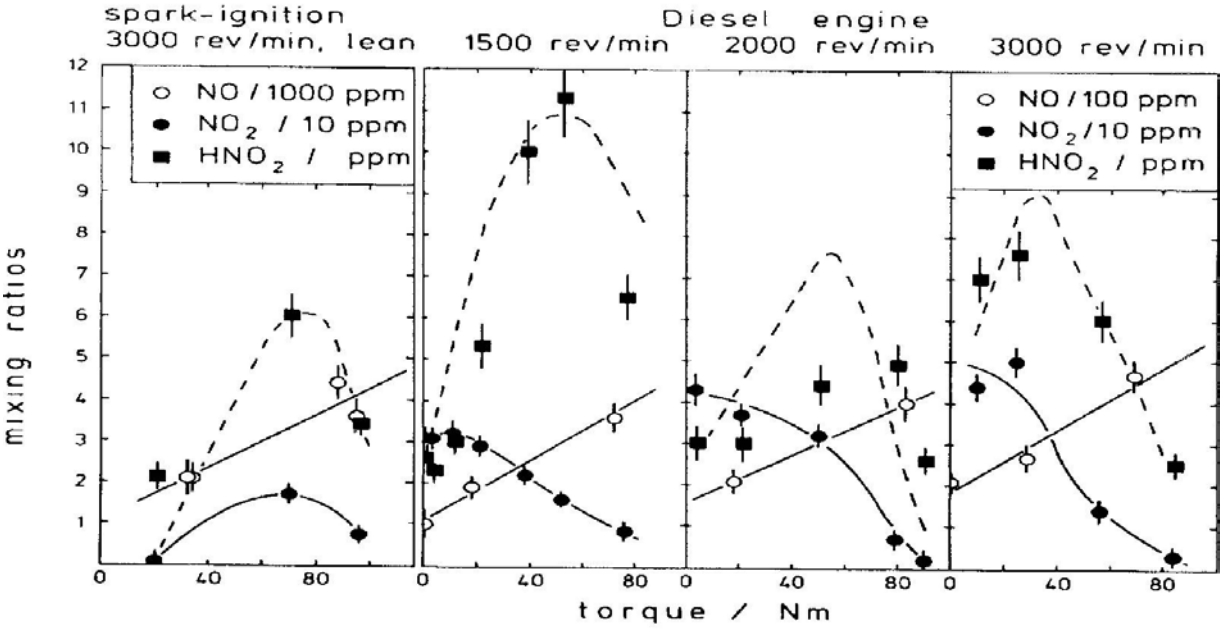

Figure 6: The dependency of HONO, NO_2 and NO in diesel and gasoline exhaust on the engine rotary speed and torque [*Perner et al.*, 1985].

Homogeneous formation

Several homogeneous pathways forming HONO exist among the various chemical reactions that occur in the atmosphere. As this section will show, it is unlikely that any of these processes are significant net sources of tropospheric HONO.

Nitrous acid is known to be produced by the reaction of hydroxyl radicals with nitrogen monoxide [*Nguyen et al.*, 1998; *Pagsberg et al.*, 1997; *Stuhl and Niki*, 1972; *Westenberg and DeHaas*, 1972; *Zabarnick*, 1993]:

$$OH + NO \xrightarrow{M} HONO \qquad \text{R. 23}$$

M represents a third molecule for the three-body collision (e.g. oxygen O_2 or nitrogen N_2), which is necessary to reduce the excess energy of the molecules to form a stable product. The reaction constant for the low and high-pressure limit and a specified temperature [*DeMore et al.*, 1997] can be calculated by:

$$k_0(T) = k_0^{300}(T/300)^{-n} \text{ and } \quad k_\infty(T) = k_\infty^{300}(T/300)^{-m} \qquad \text{R. 24}$$

with $k_0(T) = (7 \pm 1)\cdot 10^{-31}$; $k_\infty(t) = (3.6 \pm 1.0)\cdot 10^{-11}$, n = (2.6 ± 0.3), m = (0.1 ± 0.5). Combining both constants and using the number of reaction partners, the formation rate for a given pressure is defined by:

$$k(M,T) = \left(\frac{k_0(T)[M]}{1 + (k_0(T)[M]/k_\infty(T))}\right) \cdot 0.6^{\left\{1+[\log_{10}(k_0(T)[M]/k_\infty(T))]^2\right\}^{-1}} \qquad \text{R. 25}$$

Including the efficiency of the reaction partners, which is 70 % for O_2 and 30 % for N_2 [*Ahmed et al.*, 1997], a rate constant of

$k_{R.\,23} = 3.89\cdot 10^{-12}$ $cm^3 molec^{-1} s^{-1}$.

is achieved. This reaction may only become important near congested highways with high amounts of OH and NO. Assuming a night-time hydroxyl radical concentration of $1\cdot 10^5$ molec/cm^3 and typical NO night-time mixing ratios of 15 ppb for Heidelberg (see chapter 6), only 21 ppt/h of nitrous acid are formed by reaction R. 23. In daytime, R. 23 is balanced by HONO photolysis (R. 21) and can therefore not be assumed as a net HONO source (see also chapter 7).

It is known that the bulk of urban HONO is formed via other pathways suggested e.g. by [*Kessler and Platt*, 1984; *Perner*, 1980; *Platt*, 1986]. These reactions involve only NO_x and water vapour

$$NO + NO_2 + H_2O \longrightarrow 2HONO \qquad \text{R. 26}$$

$$2NO_2 + H_2O \longrightarrow HONO + HNO_3 \qquad \text{R. 27}$$

and therefore the photolysis of HONO formed via R. 26 and R. 27 represents a net OH source that is important for the genesis of photosmog. But these reactions are rather ineffective for HONO production in the homogeneous phase, as they proceed with a second order reaction constant in NO_x. The rate coefficients for reaction R. 26 were determined as early as 1951 by [*Wayne and Yost*, 1951], who reported $k_{R.\,26} = 1.2\cdot 10^{-34}$ $cm^6 molec^{-2} s^{-1}$. Publications by [*Chan et al.*, 1976] and [*Kaiser and Wu*, 1977a] report reaction constants on the order of 10^{-34} to 10^{-40} for these homogeneous reactions.

[*Stockwell and Calvert*, 1983] suggested that HONO formation in the urban atmosphere may also be initiated by reactions of the NO_3 radical, i.e. predominantly night time chemistry. According to this hypothesis, the HONO and NO_3 chemistry is linked by the HO_2 radical:

reactions of NO_3 with e.g. formaldehyde or acetaldehyde are widely considered as the major night time sources of HO_2 radicals. These radicals react with NO_2 producing HONO and O_2:

$$HO_2 + NO_2 \longrightarrow HONO + O_2 \qquad \text{R. 28}$$

Assuming that reaction R. 28 occurs at the upper limit value for the rate coefficient observed by [*Howard*, 1977] ($k_{R.\,28} < 3\cdot10^{-15}$ $cm^3molec^{-1}s^{-1}$), they found that the time dependency of ambient NO_3, O_3 and NO_2 data from [*Harris et al.*, 1982] could be fitted reasonably well. Contrastingly, [*Pitts et al.*, 1984c] measured NO_3, NO_2 and O_3 in the same air mass and concluded that the [*Stockwell and Calvert*, 1983] mechanism could not explain the results. [*Killus and Whitten*, 1985] were also not able to explain satisfactorily the observations of [*Harris et al.*, 1982] by using this mechanism. Recent measurements of [*Tyndall et al.*, 1995] have further reduced the upper limit for the rate coefficient to $k_{R.\,28} < 5\cdot10^{-16}$ $cm^3molec^{-1}s^{-1}$, Additionally, the primary product (> 99%) of the reaction of HO_2 and NO_2 seems to be HNO_4 via the equilibrium reaction

$$HO_2 + NO_2 \xleftrightarrow{M} HNO_4 \qquad \text{R. 29,}$$

which was found to proceed much faster than R. 28. HNO_4 is not stable under atmospheric conditions and decomposes within seconds via -R. 29. Subsequently, the HO_2 self reaction forms H_2O_2, which reacts in the gas-phase mainly with OH, dissolves in water or on wet surfaces or is photolysed. Thus, R. 28 cannot be a significant source of HONO in the atmosphere.

The similar reaction of alkoxyradicals R. 30 leads to the formation of aldehydes and nitrous acid:

$$R - CH_2O + NO_2 \longrightarrow R - CHO + HONO \qquad \text{R. 30}$$

$$k_{R.\,30} \approx 2.1\cdot10^{-27}\ cm^3molec^{-1}s^{-1}$$

Looking at $k_{R.\,30}$ however, it can be stated that this reaction is too slow to explain the observed night time HONO mixing ratios as well.

Multiphase generation of HONO

None of the homogeneous reactions described above can explain the concentrations of nitrous acid measured in the atmosphere. But the assumption that some of these reactions proceed heterogeneously, for example on wet surfaces like aerosol, buildings or the ground, has been confirmed by several authors [*Ammann et al.*, 1998; *Calvert et al.*, 1994; *Goodman et al.*, 1999; *Junkermann and Ibusuki*, 1992; *Kalberer et al.*, 1999; *Lammel and Perner*, 1988; *Longfellow et al.*, 1998; *Notholt et al.*, 1991; *Notholt et al.*, 1992; *Sakamaki et al.*, 1983]. The reactions R. 26 and R. 27 of NO_x with water are considered as the most likely heterogeneous HONO sources by most authors.

An increase of HONO production proportional to the gas phase water concentration was observed by [*Svensson et al.*, 1987]. However, [*Kleffmann et al.*, 1998] found HONO production being independent from gas phase water concentration, and explained this by the uniform water coverage of the walls of the reaction vessel. It is currently not clear if the reaction depends on gas-phase water concentrations, but most proposed mechanisms assume that an adsorbed water molecule is involved in the formation of HONO. This indicates that water adsorbed on a surface is more important than gas-phase water. This is particularly true for atmospheric situations in which relative humidity is high and virtually all surfaces are covered with water.

The formation rate of HONO is still one of the most uncertain properties of R. 26 and R. 27, since it is apparent that its formation not only depends on the available surface area but also

on the composition of the surface. In the following sections, the different heterogeneous pathways of HONO formation will be discussed in detail.

Aqueous phase chemistry of the NO_x species

[*Schwartz and White*, 1981] reviewed the multiphase chemistry of the nitrogen oxides and considered the possible role of the following equilibriums:

$$NO_{(gas)} + NO_{2(gas)} + H_2O_{(liq)} \longleftrightarrow 2H^+_{(aq)} + 2NO^-_{2(aq)} \qquad \text{R. 31}$$

$$2NO_{2(gas)} + H_2O_{(liq)} \longleftrightarrow 2H^+_{(aq)} + NO^-_{3(aq)} + NO^-_{2(aq)} \qquad \text{R. 32}$$

They have shown that the formation rates of HONO and HNO_3 in cloud water through these reactions are a strong function of the partial pressures of the reactants, thus reflecting higher-order rate expressions. At high NO_x partial pressures (ppm region), these rates may become substantial. But at the lower pressures, which are characteristic of the moderately polluted atmosphere, these rates become slow, even in the presence of 1g of H_2O (liq.) per m^3 of air. Thus, Schwartz concluded that reactions R. 31 and R. 32 cannot represent a significant source of HONO unless high partial pressures (> 0.1 ppm) of NO_x are maintained in contact with liquid water for substantial periods of time (tens of hours).

As all known homogeneous and aqueous reactions which form HONO appear to be too slow to account for a major atmospheric source of this compound, consideration of other sources is required (see as well [*Mertes and Wahner*, 1995]).

Heterogeneous formation on the ground or on aerosols

[*Svensson et al.*, 1987] and [*Kleffmann et al.*, 1998] proved that the reactions R. 26 and R. 27 proceeding heterogeneously with water adsorbed on surfaces form a major HONO source: both authors observed an increase of the reactivity with the surface-to-volume ratio in their reactors. However, the reaction of NO and NO_2 with water on a wet surface

$$NO_{(gas)} + NO_{2(gas)} + H_2O_{(liq)} \xrightarrow{surface} 2HONO_{(gas)} \qquad \text{R. 26}$$

is widely considered to be negligible as a HONO source, as most laboratory studies find the formation of HONO to be independent from NO (e.g. [*Jenkin et al.*, 1988; *Pitts et al.*, 1984b; *Sakamaki et al.*, 1983; *Svensson et al.*, 1987]). Most field observations confirm these laboratory studies, but were carried out in the presence of high ozone concentrations at night, which excluded NO, or low NO levels were directly documented [*Harrison and Kitto*, 1994; *Kessler and Platt*, 1984]. Contrastingly, [*Notholt et al.*, 1992] find substantial HONO formation in episodes of high NO, NO_2 and aerosol concentrations. So reaction R. 26 may become important in polluted air masses containing huge amounts of NO.

It is currently believed that the primary production pathway to form nitrous acid is the reaction of nitrogen dioxide with water on a surface:

$$NO_{2(gas)} + NO_{2(gas)} + H_2O_{(liq)} \xrightarrow{surface} HONO_{(g)} + HNO_{3(g)} \qquad \text{R. 27}$$

The exact mechanism of the heterogeneous formation of HONO summarised in reaction R. 27 is unknown, but several studies (e.g. [*Jenkin et al.*, 1988; *Kleffmann et al.*, 1998; *Svensson et al.*, 1987]) yielded the result that it is first order in NO_2, and that around 50% of the adsorbed NO_2 is released as HONO. Other authors, however, have reported a reaction order between one and two [*Mertes and Wahner*, 1995]. Additionally, [*Stutz et al.*, 2001] found that only one HONO molecule is released from a grass surface for every 33 NO_2 molecules deposited, which sharply contrasts the 50% yield found before. The proposed mechanisms of HONO formation via R. 26 and R. 27 will be discussed in detail in chapter 2.3.2.

Finally, [*Svensson et al.*, 1987] reported evidence for atmospheric production of nitrous acid from reactions of NO_x with sulphuric compounds, namely the reaction with H_2SO_4:

$$NO + NO_2 + 2H_2SO_4 \longrightarrow 2HSO_4NO + H_2O \qquad \text{R. 33}$$

$$HSO_4NO + H_2O \longrightarrow H_2SO_4 + HONO \qquad \text{R. 34}$$

However, [*Kleffmann*, 1998; *Kleffmann et al.*, 1998] have shown that the formation rate is much too slow to play an important role in the troposphere, even in highly polluted air.

Heterogeneous reduction of NO_2 on fresh soot particles

[*Ammann et al.*, 1998] reported that the heterogeneous production of nitrous acid from NO_2 suspended on a reducing soot surface proceeds 10^5 to 10^7 times faster than on other surfaces:

$$NO_2 + red_{surface} \xrightarrow{H_2O} HONO + ox_{surface} \qquad \text{R. 35}$$

For fresh soot particles, reaction R. 35 shows a high reaction probability, whereby only a very small fraction part of the surface acts reducing: the fraction of active surface places is of a few per cent of a monolayer. The same authors found a HONO production of $3.3 \cdot 10^{13}$ molecules per s per cm^2 aerosol surface within the first seconds. The rate constantly decreases afterwards towards zero within a total measurement time of 155 seconds.

A study by [*Kalberer et al.*, 1999] also investigated the formation of nitrous acid on soot particles. As a production of HNO_3 corresponding to reaction R. 27 was not found, the direct reduction of NO_2 to HONO on the soot particle surface according to R. 35 was postulated. A very fast termination of the reaction at a few ppb NO_2 was observed, caused by the limited amount of reactants on the particle surface. The HONO formation potential of the soot used during this experiment was found to be about $1 \cdot 10^{15}$ HONO molecules per cm^{-2} particle surface at 30 % relative humidity (rh).

The HONO production showed a non-linear behaviour as a function of the rh: starting at low rh, the amount of HONO increases with rh increasing up to 30 % rh. This suggests that H_2O is either directly involved in the chemical reaction of NO_2 to HONO or builds up a precursor (e.g. by hydrolysis) which acts as the reaction partner for NO_2. Above 40 % rh the amount of HONO decreases again, and at 70 % rh it is as low as at 2 % rh. At high humidity, the increasing amount of adsorbed water makes the reactive surface less accessible or less reactive to NO_2. [*Kalberer et al.*, 1999] found as well that the strong oxidant O_3 may influence the formation of HONO by aging the soot aerosol surface resulting in a lower HONO formation potential. After exposing the surface to an ozone dose of 105 ppb min, 10 % less HONO was formed on the particle surface, compared to a fresh aerosol surface. It can be concluded that the reaction of NO_2 to HONO on soot particles saturates and is not the main source of HONO in the polluted boundary layer. In addition, modelling studies show that general consequences for the NO_x chemistry in the troposphere are small [*Aumont et al.*, 1999], especially due to the fast saturation of the surface within less than one minute. However, if mechanisms exist in the atmosphere that renew the particle surface reactivity with respect to the NO_2/HONO reaction, a substantial amount of HONO could be build up by soot aerosol particles. [*Aumont et al.*, 1999]. [*Gerecke et al.*, 1998] found evidence for such a recycling mechanism by irradiating soot particles with light.

2.3.2 Mechanistic sequence of HONO formation

Several authors have made assumptions on the sequence of heterogeneous HONO formation and the correlated rate coefficients for the most prominent HONO sources R. 26 and R. 27. But up to now, the full mechanistic sequence of HONO formations via these reactions has not been not understood. In the following chapter, a brief overview on the current state of knowledge and the questions that still remain open will be given.

Heterogeneous reactions on ideal and aerosol surfaces

Resulting from thermodynamics, nitrous acid formation via R. 27 from two NO_2 molecules plus water has to process by a law of reaction rate of second order for NO_2 [*Cheung et al.*, 2000]. But all observations, especially the measurements of NO_2 and HONO concentration time series, concluded that R. 27 proceeds with a first order reaction rate for NO_2.

However, measurements in smog chambers[3] and the atmosphere show a remarkably linear correlation between the HONO formation rate and the NO_2 concentration [*Ackermann*, 2000; *Jenkin et al.*, 1988; *Kessler and Platt*, 1984; *Kleffmann et al.*, 1998; *Pitts et al.*, 1984b; *Svensson et al.*, 1987].

The linear dependency was explained by [*Jenkin et al.*, 1988], considering the effect of the reaction being catalysed at a surface:

$$H_2O_{(gas)} \longrightarrow H_2O_{(ads)} \qquad \text{R. 36}$$

$$2NO_{2(gas)} \longrightarrow 2NO_{2(ads)} \qquad \text{R. 37}$$

$$NO_{2(ads)} + H_2O_{(ads)} \longrightarrow H_2ONO_{2(ads)} \qquad \text{R. 38}$$

$$NO_{2(ads)} + H_2ONO_{2(ads)} \longrightarrow HNO_{3(ads)} + HONO_{(gas)} \qquad \text{R. 39}$$

Net: $$2NO_2 + H_2O \xrightarrow{surface} HONO + HNO_3 \qquad \text{R. 27}$$

Reaction R. 38, which determines the overall reaction rate, takes place in the absorbed phase and would be of first order. The corresponding reverse reaction of nitrous acid

$$HONO_{(gas)} + HNO_{3(ads)} \xrightarrow{surface} 2NO_{2(gas)} + H_2O_{(gas)} \qquad \text{R. 40}$$

was reported to be unimportant, because H_2O and NO_2 have nearly no binding affinity [*Ahmed et al.*, 1997].

However, the results published by [*Ahmed et al.*, 1997] also imply that adsorption of NO_2 on water seems unlikely. Thus, [*Schurath*, 2000] suggests that R. 27 proceeds on wet atmospheric aerosols or surfaces by the following intermediates:

$$NO_{2(gas)} + NO_{2(gas)} \longrightarrow N_2O_{4(g)} \qquad \text{R. 41}$$

$$N_2O_{4(g)} + H_2O_{(liq)} \longrightarrow (HONO + HNO_3)_{(liq)} \qquad \text{R. 42}$$

Subsequently the nitrous acid escapes from the liquid phase to the gaseous phase [*Barney and Finlayson-Pitts*, 2000].

[3] Measurements in smog chambers show generally lower production rates compared to the atmosphere, whereas experiments in a smog chamber by [*Kleffmann*, 1998] showed a parallel formation of NO and N_2O as well.

According to [*Schurath*, 2000], R. 42 would yield an heterogeneous HONO formation rate on aerosols described by:

$$\frac{d[HONO]}{dt} = \gamma \cdot [N_2O_4] \cdot \frac{\bar{v}}{4} \cdot S_{Aerosol} \qquad \text{R. 43}$$

with γ probability for the reaction,
$S_{Aerosol}$ specific surface of the atmospheric aerosol [cm^{-1}],
$\bar{v}$: average speed of the NO_2 molecules.

Still assuming that gas-phase formation of N_2O_4 is more efficient than the adsorption of NO_2 on water, R. 43 is re-written as

$$\frac{d[HONO]}{dt} = \gamma \cdot K_{\dim} \cdot [NO_2]^2 \cdot Z_{surf} \qquad \text{R. 44}$$

with $Z_{surf} = \frac{\bar{v}}{4} \cdot S_{Aerosol}$ collision frequency of N_2O_4 with the particle,

$K_{\dim} = \frac{[N_2O_4]}{[NO_2]^2}$ equilibrium constant for the $NO_2 - N_2O_4$ ratio.

However, R. 44 results again in a HONO production rate which is of second order for NO_2, contrasting the first order law of reaction rate observed in most measurements (see above). Additionally, typical values for the collision frequency and the equilibrium constant are

$Z_{surf} \leq 1\ s^{-1}$ (for typical aerosol surfaces of 1000 $\mu m^2\ cm^{-3}$) and

$K_{dim} = 10^{-18}\ cm^3$ (at a temperature of 283 K),

respectively (see [*Schurath*, 2000]). Consequently, a HONO production rate of

$$\frac{d[HONO]}{dt} = \gamma \cdot 10^{-18}\,cm^3 \cdot [NO_2]^2 \cdot 1\,s^{-1} \qquad \text{R. 45}$$

is computed. Even for a small production rate of 0.05 ppb HONO/h at a NO_2 mixing ratio of 20 ppb, the probability of the reaction γ has to be larger than unity. This leads to the result that adsorption of NO_2 on the water surface of aerosols has to be assumed [*Schurath*, 2000], which contrasts the initial assumption made by [*Ahmed et al.*, 1997].

A different explanation for the HONO formation was given by [*Mertes and Wahner*, 1995; *Schurath*, 2000], who suggest the formation of anhydrides as an important intermediate:

$$NO + NO_2 \longrightarrow N_2O_3 \qquad \text{R. 46}$$

$$NO_2 + NO_2 \longrightarrow N_2O_4 \qquad \text{R. 47}$$

The anhydrides show a moderate solubility in water, so the rate-limiting step proceeds in the condensed phase:

$$[N_2O_3 + N_2O_4 + 2H_2O] \longrightarrow [3HONO + HNO_3] \qquad \text{R. 48}$$

Afterwards, the pH dependent Henry-equilibrium[4] adjusts for HONO and HNO_3. With this mechanism, a much higher nitrous acid formation efficiency is reached compared to the

[4] Henry's law coefficients are a quantitative measure to describe the reaction X (gas) → X (aq). It is calculated by H_x [mol l^{-1} atm^{-1}] = [X (aq)]/P_x, with the partial pressure P_x of [X] in the gas phase. Some Henry's law coefficients for NO_2 can be found in [*Cheung et al.*, 2000].

formation via reaction R. 27. But this reaction scheme includes NO, which was thought to play only a minor role in the formation process of nitrous acid.

Heterogeneous reactions on macroscopic surfaces

The formation of nitrous acid on macroscopic surfaces like the ground might play a significant role because the surface area of these "compounds" (tarmac, grass) is much higher than of aerosols. The total surface of spherical aerosol particles over a ground surface of 1 cm^2 can be estimated by a simple calculation: assuming an aerosol surface of 1000 $\mu m^2 cm^{-3}$, which is comparably large[5], and a boundary layer height of 200 m, the total aerosol surface is only 0.2 cm^2 (excluding the ground).

As this calculation includes only a spherical aerosol surface, whereas the "real" surface is much rougher, soot particles can have a very high HONO reactive uptake coefficient (see e.g. [*Ammann et al.*, 1998; *Kalberer et al.*, 1999; *Notholt et al.*, 1992]).
However, even a larger reactive aerosol surface is comparably small to the real surface of the ground. This does not consider that the reactive uptake coefficient on the ground may differ from the aerosol.

A reaction rate expression for nitrous acid production that includes the surface to volume ratio has been found empirically from smog chamber data [*Kessler*, 1984; *Svensson et al.*, 1987; *Winer and Biermann*, 1994]:

$$\frac{d[HONO]}{dt} = [H_2O] \cdot \frac{S}{V} \cdot k \cdot [NO_2] \qquad \text{R. 49}$$

with: $[H_2O]$ in ppm
S: surface of the reaction chamber
V: volume of the reaction chamber

The different values for k, which can be found in literature (see Table 3), emphasize the strong dependence of k on the nature of the surface. In particular, the measurements by [*Ackermann*, 2000] show that high HONO production rates may be due to high aerosol concentrations and the strongly enlarged[6] surfaces of a road tunnel.

Table 3: Selected values for HONO production rates on different surfaces.

publication	k [s^{-1} ppm^{-1} m]	surface studied
[*Pitts et al.*, 1984b]	$4.2 \cdot 10^{-11}$	Teflon
[*Svensson et al.*, 1987]	$4.6 \cdot 10^{-11}$	Teflon/glass
[*Kleffmann*, 1998]	$3.7 \cdot 10^{-10}$	quartz glass
[*Ackermann*, 2000]	$3.2 \cdot 10^{-9}$	traffic tube (coated metal plates, tarmac)
[*Trick et al.*, 2002]	$6.0 \cdot 10^{-9}$	tarmac

[5] An average aerosol surface at a highly-polluted area was found to be 366 $\mu m^2 cm^{-3}$ [*Streit et al.*, 2000].

[6] Due to the agglomeration of dust and dirt on all surfaces caused by the traffic in the tunnel.

[*Kleffmann*, 1998] supposes a modified expression for the reaction rate of HONO formation: assuming that the rate-limiting step of heterogeneous reactions is the uptake of the gaseous molecule into the liquid phase. This uptake involves several, partly reversible, processes that are illustrated in Figure 7.
The net uptake of a gas molecule into a fluid can be described by the uptake coefficient γ, which can be measured in the laboratory. γ_{exp} can be written as the inverse sum of the different single steps, the gas (Γ_{gas}) and liquid diffusion (Γ_{liq}), and the reaction in the liquid phase (Γ_r):

$$\frac{1}{\gamma_{\exp}} = \frac{1}{\Gamma_{gas}} + \frac{1}{\alpha} + \frac{1}{\Gamma_{liq} + \Gamma_r} \qquad \text{R. 50}$$

The accommodation coefficient α describes the actual transition into the boundary layer. α can be studied by different laboratory techniques and is defined as:

$$\alpha = \frac{\text{number of molecules lost to the surface}}{\text{number of gas - surface collisions}} \qquad \text{R. 51}$$

Now the total flux into the liquid phase J can be calculated with the average speed of the molecules of the gas $(\bar{v})$ and its concentration:

$$J = \frac{\gamma_{\exp} \cdot [gas] \cdot \bar{v}}{4} \qquad \text{R. 52}$$

The slowest law of reaction rate of the total process, comprising chemical reactions and kinetics, limits the total reaction speed. For the adoption of this mechanism on atmospheric conditions, all characteristic constants for the processes participating in the overall process have to be known, which is often not possible.

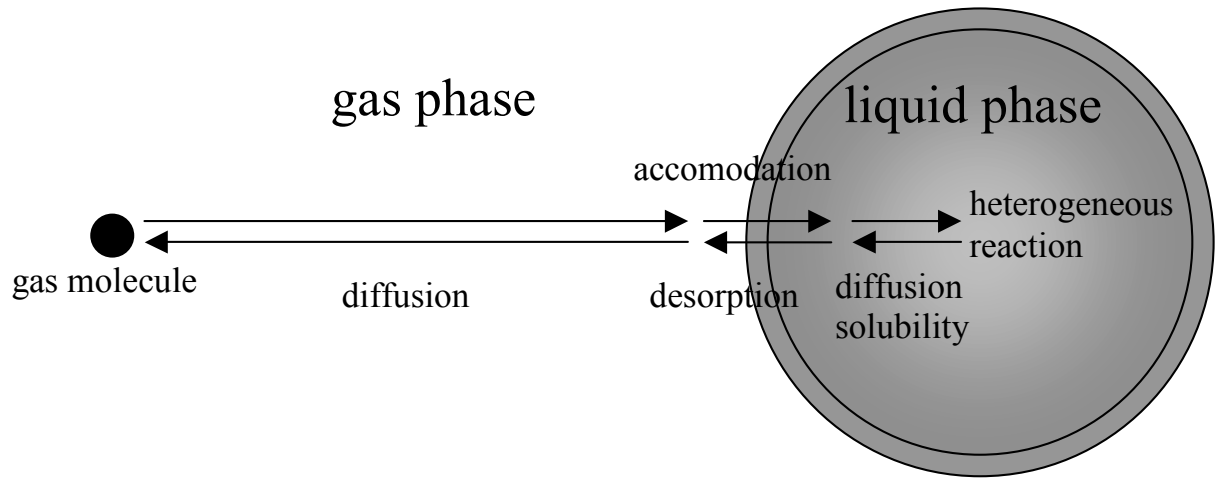

Figure 7: Schematic view of the different processes which are important for the uptake of a species in the liquid phase of an aerosol particle [*Kleffmann*, 1998]**.**

For the calculation of the nitrous acid production in the troposphere, the following assumptions have been made:

- The uptake coefficient γ can vary between $3 \cdot 10^{-7}$ for a sulphuric acid / water solution with more than 60 weight% H_2SO_4 and 10^{-6} for pure H_2O [*Kleffmann et al.*, 1998]). In the case of such a small uptake coefficient, a possible limitation by gas-phase diffusion can be neglected for atmospheric conditions [*Lee and Tang*, 1988].
- Most aerosols are only weakly acidic, so for the accommodation coefficient for pure water ($\alpha = 10^{-6}$) can be used.
- For the aerosol surface two different scenarios are considered:
  1. normally polluted: S/V = 900 $\mu m^2/cm^3$
  2. heavily polluted: S/V = 30000 $\mu m^2/cm^3$
  3. grass meadow[7]: S/V = 100000 $\mu m^2/cm^3$

Taking this into account, [*Kleffmann*, 1998] suggests an expression for the calculation of the NO_2 conversion rate:

$$\frac{\%NO_2}{h} = \frac{1}{4} \cdot \bar{v}_{NO_2} \cdot \frac{S}{V} \cdot \alpha \cdot 3600 \cdot 100 \qquad \text{R. 53}$$

Considering the stoichiometry of reaction R. 27, the calculated values have to be divided by a factor of 2 to obtain the HONO formation rate:

$$\frac{\%HONO}{h} = \frac{1}{8} \cdot \bar{v}_{NO_2} \cdot \frac{S}{V} \cdot \alpha \cdot 3600 \cdot 100 \qquad \text{R. 54}$$

For the examples given above the following formation rates were calculated:

1. normally polluted: %HONO/h = 0.015 %/h
2. heavily polluted: %HONO/h = 0.5 %/h
3. grass meadow: %HONO/h = 1.6 %/h

Tropospheric measurements show nitrous acid formation rates between 0.5 %/h and 1.5 %/h (e.g. [*Kessler and Platt*, 1984; *Stutz et al.*, 2001; *Winer and Biermann*, 1994]). Accordingly, in the case of the high aerosol load or meadow surfaces (scenario b) and c)) a significant amount of the observed HONO formation can be explained by the heterogeneous reaction of NO_2 on wet surfaces.

Since the S/V value for the normally polluted area is calculated with the assumption of a spherical shape of the aerosol, it is most likely to be underestimated: the real surface area can be much larger if one takes into account a possible irregular shape of the aerosol with pores. [*Keyser et al.*, 1991] have shown that molecules can diffuse deeply into porous surfaces, especially for small uptake coefficients. Additionally, under normally polluted conditions a significant amount of atmospheric HONO formation can occur on cloud droplets and fog [*Lammel and Cape*, 1996] and on the ground [*Harrison and Kitto*, 1994].

A strong indication for the thesis that heterogeneous reactions at porous or rough ground surfaces produce HONO very effectively in the "real world" is provided by the measurements of [*Trick et al.*, 2002]. Their experiment using a multi reflection cell [*White*, 1942; *White*, 1976] in a mini-smog-chamber realised by a tent made from PE foil and set up over a plane asphalt street yielded HONO formation rates on asphalt which are about a factor of 16 higher than previously reported by [*Kleffmann et al.*, 1998] and still nearly a factor of 2 higher than determined by [*Ackermann*, 2000]. These formation rates may well explain the HONO concentration rates observed in urban areas.

[7] Assumptions: Mixing height during the night 100 m; 10 times bigger surface with grass compared to a flat even ground.

2.3.3 Sinks for Nitrous Acid

The most important process for the removal of HONO from the atmosphere is photolysis, yielding a typical HONO lifetime of about 10 minutes at noon:

$$HONO + h\nu \xrightarrow{300nm<\lambda<405nm} OH + NO \qquad \text{R. 21}$$

This reaction is the dominating sink reaction for the HONO steady state in daytime, resulting in the observed HONO daytime mixing ratios given above. However, a few percent of HONO is expected to be destroyed by OH radicals:

$$HONO + OH \longrightarrow H_2O + NO_2 \qquad \text{R. 55}$$

$k_{R.\,55} = 4.5 \cdot 10^{-12}$ $cm^3 molec^{-1} s^{-1}$ [*DeMore et al.*, 1997]

But this mechanism is only expected to be important at very high OH concentrations during the day. For typical night OH concentrations ranging from 1 to $7 \cdot 10^5$ molec. cm^{-3}, the lifetime of nitrous acid is thereby 610 – 88 hours [*Holland et al.*, 2000].

The self-reaction of HONO [*Chan et al.*, 1976; *Mebel et al.*, 1998] or the reaction of HONO with nitric acid [*Kaiser and Wu*, 1977b] seem to be too slow to be significant in the atmosphere:

$$2HONO \longrightarrow NO + NO_2 + H_2O \qquad \text{R. 56}$$

$k_{R.\,56}$ (300K) = $1.4 \cdot 10^{-24} - 1.2 \cdot 10^{-27}$ $cm^3 molec^{-1} s^{-1}$ [*Mebel et al.*, 1998]

$$HONO + HNO_3 \longrightarrow 2NO_2 + H_2O \qquad \text{R. 40}$$

$k_{R.\,40}$ (300K) = $1.55 \cdot 10^{-17}$ $cm^3 molec^{-1} s^{-1}$ [*Kaiser and Wu*, 1977b]

It is currently unclear whether these reactions, if proceeding heterogeneously, can become important.

Several authors have reported that reaction R. 56 occurs heterogeneously on surfaces in their reaction vessels. [*Svensson et al.*, 1987], for example, assumed a second order rate of reaction for the HONO loss to model their laboratory results. Changes in the HONO removal rate after treatment of the reactor surface indicated that the HONO sink reactions proceed heterogeneously. A rate constant of 10^{-22} $cm^3 molec^{-1} s^{-1}$ for a passivated surface was derived in this thesis.

In a similar study [*TenBrink and Spoelstra*, 1998] determined a heterogeneous second order loss of HONO with a rate constant of $1.5 \cdot 10^{-19}$ $cm^3 molec^{-1} s^{-1}$. With this rate, a destruction of HONO in the atmosphere is also too slow to be significant.

However, a combined equilibrium via the formation reactions R. 26, R. 27 and the different loss processes for nitrous acid R. 55 and R. 40 is likely establish during the night [*Schurath*, 2000]. [*Trick et al.*, 2002] found evidence for such an equilibrium by experiments in a "smog-tent" set up above an asphalt surface. These experiments saw a rate of reaction law for HONO decomposition changing from an order of 2 to an order of 1 with decreasing HONO concentrations in their chamber.

[*Kleffmann et al.*, 1998; *Kleffmann et al.*, 1994] observed the formation of nitrous oxide during the decay of HONO in a laboratory system, which seems to occur on the reactor surface. The overall reaction is suggested to be

$$4HONO \longrightarrow N_2O + HNO_3 + H_2O \qquad \text{R. 57}$$

but the exact mechanism remains still unclear.

Further chemical sink reactions of HONO occur especially at temperatures below 0°C on freezing cloud or fog droplets or ice surfaces. These reactions include the oxidation of nitrous acid / nitrite in the aqueous solutions of these particles yielding NO_3^- or OH^- ions. But this

HONO sink is not well quantified and thought to be of importance in polar regions, the upper troposphere and lower stratosphere only (see [*Finlayson-Pitts and Pitts*, 2000]).

Finally, nitrous acid can be removed from the atmosphere via wash out by rain (wet deposition), where it contributes to acid rain (for an overview see also [*Finlayson-Pitts and Pitts*, 2000]), or dry deposition by adsorption at aerosols and on the ground [*Stutz et al.*, 2001]. According to this publication, deposition of HONO on rough surfaces plays a key role for the HONO gradient measured in the lower PBL. They also observed that HONO formation and deposition on the ground balance each other. The highest HONO values can be found at the compensation point between both processes accordingly. For a grass meadow surface, this compensation point was found at a HONO / NO_2 ratio of 3 ± 1 %.

2.3.4 Vertical concentration gradients of HONO in the atmosphere

The preceding paragraphs illustrate that the atmospheric chemistry of HONO is strongly coupled to the area and nature of the surface involved. Therefore, the identification and subsequent characterisation of the surfaces most effective for HONO formation is one of the most important open questions on HONO chemistry. As already discussed in chapter 2.3, not only the sources of the suspected HONO predecessors NO and NO_2 are mostly located in the PBL, but also the most effective surfaces are located at or near the ground: at night the ground seems to be the surface with largest surface-to-volume ratios, but aerosols can also be important if they feature a higher reactive uptake coefficient. During the day the aerosol surface to volume ratio can increase to a value comparable to the S/V ratio of the ground. Laboratory measurements can help to understand the nature of the mechanistic sequence of HONO formation, but are of limited use with respect to the composition of surfaces in the real atmosphere and their impact on HONO formation. So the measurement of the HONO gradient in the PBL can be used to draw conclusions on the HONO flux to or from the ground as well as to analyse the impact of aerosol surfaces on HONO formation.

A field study by [*Harrison and Kitto*, 1994; *Harrison et al.*, 1996] gave evidence for formation of nitrous acid on grass surface under certain circumstances. The sample inlets for determining the mixing ratio of HONO and NO_2 were between 0.25 and 2 m above ground. Measurements of the HONO surface exchange showed both upward and downward fluxes at different times. When the magnitude and direction of the flux was plotted against the ambient concentration of NO_2, for nitrogen dioxide concentrations below 10 ppb fluxes of HONO were found to point downwards. When NO_2 exceeded 10 ppb, the net flux was upward. This was interpreted as the net effect of two processes: on the one hand, formation of HONO from NO_2 on the ground surface and, on the other hand, dry deposition of HONO at the ground. In a subsequent paper, the same group presented a model explaining these observations assuming a NO_2-to-HONO conversion rate of $5.6 \cdot 10^{-6} \cdot$ mixing height (m) s^{-1} as the HONO source and a HONO dry deposition rate of 0.02 / mixing height (m) s^{-1} representing the HONO sink [*Harrison et al.*, 1996].

It should be noted that the measurements by [*Harrison and Kitto*, 1994] were performed primarily during daytime with maximum nitrous acid concentrations of 1 ppb around noon. These daytime concentrations are substantially higher than reported by other authors. However, the Denuder technique used for these measurements seems to be troubled at least: nitrite produced by artefacts in the second Denuder was found to be up to 30 % of the production in the first denuder. Thus, it seems questionable that the nitrite formation can be corrected for precisely enough to obtain reliable flux measurements. A comparison of the Denuder system used by [*Harrison and Kitto*, 1994] with a long path DOAS instrument showed no agreement for HONO (see [*Stutz*, 1996]). Hence, the precision of the annular denuder systems used by [*Harrison and Kitto*, 1994] may not have been sufficiently accurate to determine HONO fluxes and correct daytime concentrations.

Measurements over grassland performed with two – more advanced – wet-annular Denuder

systems (WEDD) by [*Spindler et al.*, 2000] showed that HONO concentrations at a height of 4.5 m were generally higher compared to the concentrations measured at a height of 0.8 m. The NO_2 concentration was constantly below 10 ppb, so no inconsistency to the publication by [*Harrison and Kitto*, 1994] could be found, but no clear ratification was found either.

Other gradient measurements over grassland from [*Neftel et al.*, 1996] on a comparable scale gave no evidence for a negative gradient of HONO at NO_2 levels exceeding 10 ppb: the WEDD system at 3.20 m height saw almost the same, sometimes even higher HONO concentrations compared to the system located at a height of 1.60 m.
The most recent HONO gradient measurements were presented by [*Alicke*, 2000; *Stutz et al.*, 2001]. This study took place in Milan on the height interval between 0.5 and 4 m over a grass meadow surface. The data collected during this campaign showed mostly a homogeneous HONO concentration over the whole height interval. Significant HONO gradients were measured only on a few occasions, yielding a net HONO flux towards the ground. As these gradients were measured at high NO_2 concentrations well above 10 ppb, the measurements also disagree with the [*Harrison and Kitto*, 1994] publication.
[*Stutz et al.*, 2001] explain their findings by postulating a steady state between HONO production and deposition on the ground. The gradients measured in this study can only be explained, if less efficient NO_2-to-HONO conversion rate coefficients than found in the laboratory on artificial surfaces are assumed. The authors state that the effectiveness of a grass meadow surface – even in a polluted environment – for HONO formation is about a factor of 10 lower than found in the lab. Interestingly, in this study no evidence for significant production on aerosols was found, even under medium to heavily polluted conditions.

To conclude, gradient measurements in the field have been performed up to now only over grass surfaces yielding lower NO_2 to HONO conversion efficiencies than found on Teflon or glass surfaces in laboratory experiments. Accordingly, these measurements find, if significant, gradients pointing upwards, i.e. HONO increasing with altitude. Most authors find only a weak dependency of the HONO formation rate on atmospheric aerosols, excluding soot aerosol in or near exhaust pipes. So HONO formation has to proceed mainly on other surfaces to yield the typical mixing ratios observed in medium to heavily polluted areas, especially at night.

This thesis presents long-term gradient measurements of HONO and its most important predecessor NO_2 over the city of Heidelberg in the height interval of 10 to 450 m above ground. The set-up of the light paths guaranteed that the measurements took place above a typical mix of urban surfaces (asphalt, concrete and other artificial materials as well as grass- and woodland of parks). Therefore, the HONO and NO_2 gradients measured on these light paths should be representative for most medium-polluted urban areas. It will be shown in chapter 6 that HONO – as well as the ratio HONO / NO_2 – was found to decrease with altitude under virtually all atmospheric circumstances by day and night.

3 Dynamics of the Planetary Boundary Layer

The following chapter presents an overview of the physical cycles and transport processes in the Planetary Boundary Layer (PBL). The PBL is defined as the zone of transition between the stationary air masses right at the Earth's surface and the free troposphere dominated by the geostrophic wind system. [*Stull*, 1988] defines the PBL as "the part of the troposphere that is directly influenced by the Earth's surface and responds to surface forcings with a timescale of about an hour or less". The PBL extends typically over the lowest 300 to 1000 m of the atmosphere. The height of the PBL is influenced by various factors that will be discussed briefly below. [*Roedel*, 1994; *Seinfeld and Pandis*, 1998; *Stull*, 1988] present a more comprehensive description of the structure and the dynamics of the lower troposphere.

3.1 Basics of the theoretical description

3.1.1 Structure of the PBL

Within the PBL, friction between the air masses moving with the geostrophic flow in the free troposphere increases monotonously with increasing proximity to the ground. The steepness of the resulting logarithmic wind profile in the PBL is anti-correlated to the roughness of the ground.

The mathematical description of the vertical wind field in the PBL is based on the theory of friction occurring between two layers of air moving with different velocities along each other: this process can be described as an exchange of impulse between both layers.

If two layers of air move along each other with different velocities, the resulting shear force between the two layers is described by the turbulent and viscous stress tensor τ_{ij}, which is defined as

$$\tau_{xz} = -(K + \nu) \cdot \rho \cdot \frac{dv_x}{dz} \qquad \text{Equ. 1.}$$

In Equ. 1, K and ν characterise the constants for turbulent and laminar diffusion, respectively. ρ labels the density of the air mass and v_x the velocity of the horizontal air stream.

Considering this relation, the PBL is divided into three sub-layers, defined by the dominating transport regime. Starting from the surface, the lower 10^{-3} to 10^{-2} m are called the laminar surface layer, as this layer is dominated by the laminar viscosities. Thus, the transport of trace gasses to and from the surface is limited by laminar diffusion, which is significantly less effective than turbulent diffusion in the boundary layer and the free atmosphere.

The following layer comprises the height range from some 10^{-2} to some 10^{2} m and is commonly called the surface layer. Within this layer, the major components of the viscous stress tensor τ_{ij} feature absolute values of about 0.1 – 0.3 N m^{-1}. This compares to a variation of τ_{ij} with height z of $d\tau/dz \approx 10^{-3}$ N m^{-1} in the same height range. Even though the gradient $d\tau/dz$ is at a maximum within this layer, the absolute value of $d\tau/dz$ is still at least two orders of magnitude smaller than τ_{ij}. (see e.g. [*Roedel*, 1994]). Thus, the surface layer is characterised by τ = const, and therefore by constant turbulent fluxes of momentum, heat and trace gasses.

In the layer extending from some 10^{1} to about 10^{3} m, the absolute value of the wind vector increases to the free tropospheric wind velocities as the friction decreases constantly. The wind direction in this layer is forced by the balance of the friction, the Coriolis and the pressure gradient force. As friction decreases with height over ground, the wind direction turns constantly towards the wind direction in the free troposphere, which is dominated only

by the Coriolis and the pressure gradient force. The movement of the tip of the wind vector[8] is called Ekman spiral, and, consequently, this layer is named the Ekman layer.

The vertical extension of the PBL depends on two major factors: the stability of the thermal stratification and the surface roughness:

Thermal stratification is stable, when warmer and therefore less dense air masses are situated above colder and more dense air masses. Labile stratification is characterised by warmer air situated below colder air, yielding a more effective vertical mixing. In a labile stratified PBL, warmer air climbs adiabatically to higher altitudes, while colder air masses descend adiabatically towards the ground until both air parcels have the same potential energy (including latent and inner heat energy) as the surrounding air. Consequently, the PBL extends to higher altitudes at labile conditions due to more effective vertical mixing, the opposite being the case for stable conditions. In case any air parcel can be shifted adiabatically to any altitude and features always the same potential energy as the surrounding air mass, the stratification is called thermally neutral.

Rough surfaces (such as tall buildings or trees) cause a more effective vertical mixing and hence extend the height of the PBL, while flat surfaces (such as silent water) cause a thinner PBL. Notably, very rough surfaces can inhibit the establishment of a laminar sub-layer.

Depending on both factors, the PBL reaches from below 100 m height at night above flat surfaces to more than 1000 m by day and over a strongly structured surface.

3.1.2 Transport processes in the PBL

Since transport processes in the atmosphere apply to transport of impulse and trace gasses, the laws governing the changes of wind speed and direction also specify the mixing velocities for trace gasses. Assuming thermally neutral stratification, and turbulent mixing surpassing laminar mixing, which is well justified in the surface and Ekman layers, only two factors contribute to the wind profile: the stress tensor τ_{ij} i.e. the friction velocity u^* defined by

$$\tau_{xz} = -\rho \cdot (u^*)^2 \qquad \text{Equ. 2,}$$

and the height over ground z. To derive the vertical wind profile dv_x/dz, the consideration of the physical units yields only one possible relation between both factors [*Roedel*, 1994]:

$$\frac{dv_x}{dz} = \frac{1}{\kappa} \cdot \frac{u^*}{z} \qquad \text{Equ. 3}$$

with the Karman-constant $\kappa \approx 0.4$. This equation, in combination with Equ. 1 and Equ. 2 yields the turbulent diffusion constant K:

$$K(z) = u^* \cdot \kappa \cdot z \qquad \text{Equ. 4}$$

As friction velocity is almost constant in the surface layer (see above), K only depends on the height over ground z. Thus, the flux can be described by diffusive transport according to Fick's law:

$$J = -K(z) \cdot \frac{dc(z)}{dz} \qquad \text{Equ. 5}$$

Based on this relation for vertical transport, the vertical profile of an atmospheric compound can be computed: the difference between the concentrations in two different heights $z_1 > z_2$ is expressed by

[8] Clockwise and counter-clockwise with increasing height in the northern and southern hemisphere, respectively.

$$c(z_2) - c(z_1) = \int_{z_1}^{z_2} \frac{dc(z)}{dz} \cdot dz \qquad \text{Equ. 6}$$

Implementing Equ. 4 and Equ. 5 into this relation yields the logarithmic profile for atmospheric trace gasses :

$$c(z_2) - c(z_1) = -J \cdot \int_{z_1}^{z_2} \frac{1}{K(z)} \cdot dz = -\frac{J}{u^* \cdot \kappa} \cdot \int_{z_1}^{z_2} \frac{1}{z} \cdot dz = -\frac{J}{u^* \cdot \kappa} \cdot \ln\left(\frac{z_2}{z_1}\right) \qquad \text{Equ. 7}$$

To obtain typical mixing times for atmospheric trace gasses, the transfer resistance $R_{i,j}$ is defined, characterising the transport time between the heights i and j:

$$R_{1,2} = \frac{c(z_2) - c(z_1)}{J} = -\frac{1}{u^* \cdot \kappa} \cdot \ln\left(\frac{z_2}{z_1}\right) \qquad \text{Equ. 8}$$

On the other hand, the mean flux of trace gasses between two layers can be derived from measured concentration gradients by changing Equ. 7 to:

$$J = -\frac{c(z_2) - c(z_1)}{\ln(z_2/z_1)} \cdot u^* \cdot \kappa \qquad \text{Equ. 9}$$

To solve both equations, the friction or shear velocity is needed. The next section presents the most common ways of measuring or computing this characteristic physical value of the atmosphere.

3.2 Evaluation of the transport processes

3.2.1 Evaluation of friction velocity

For the calculation of friction velocity, two distinctly different approaches are possible for neutral and non-neutral conditions. Under neutral conditions some approximations can be made to compute the absolute value of friction velocity. For non-neutral stratification however, it is absolutely necessary to measure the vertical profiles of wind speed and heat flux to obtain friction velocity.

Neutral stratification

For neutral conditions in the surface layer, the assumption of friction velocity being constant with increasing height over ground is well-justified [*Roedel*, 1994]. The same author supposes the following approximation for the friction velocity, obtained by the integration of Equ. 3:

$$u^* = v_r \cdot \frac{\kappa}{\ln(z_r/z_0)} \qquad \text{Equ. 10}$$

with v_r labelling a typical wind speed at the reference height h_r and z_0 being a measure for the roughness of the surface. This leads, together with Equ. 4, to the turbulent diffusion constant

$$K(z) = \frac{v_r \cdot \kappa^2}{\ln(z_r/z_0)} \cdot z \qquad \text{Equ. 11,}$$

that increases with height over ground due to the larger eddies that are more effective for the mixing of the PBL and also increase with surface roughness.

Non-neutral stratification

For non-neutral conditions, the heat flux has a strong effect on the efficiency of turbulent transport processes. For a labile stratification of the PBL, a more effective mixing of the lower atmosphere and hence larger values for the diffusion coefficients are expected. For stable conditions, however, the mixing of the lower atmosphere is significantly reduced, which is evident at ground inversion situations in polluted areas. Under these circumstances, the vertical extension of the eddies is limited, thus limiting the effectiveness of turbulent mixing. A detailed derivation considering the effect of heat flux for turbulent mixing can be found e.g. in [*Roedel*, 1994; *Seinfeld and Pandis*, 1998]. The vertical trace gas gradient is commonly described by the relation published by [*Businger*, 1986]:

$$\frac{dC}{dz} = \frac{J}{\kappa \cdot u^* \cdot z} \cdot \Theta\left(\frac{z}{L_{MO}}\right) \qquad \text{Equ. 12}$$

Here, the "stability function" $\Theta(z/L_{MO})$ describes the ratio between the actual wind speed gradient and the wind speed gradient for neutral stratification [*Roedel*, 1994]. The Monin-Obukhov length L_{MO} is used as a scale length that is nearly independent from height, but only depends on factors characterising the stability of the stratification: L_{MO} is positive for stable stratification, and negative for labile stratification. According to its definition, L_{MO} is useless for neutral stratification, as in this case the heat flux H is zero.

Equ. 12 has been applied for the evaluation of various field measurements including gradient measurements by active LP-DOAS: [*Platt*, 1978] measured SO_2 vertical fluxes by measuring the actual wind speed and temperatures at different heights of a meteorological mast. A different approach was chosen by [*Stutz et al.*, 2001], who measured the 3D wind field (*u,v,w*) and the temperature at a single spot using a Gill research anemometer. From the data of this instrument, the friction velocity u^* and the sensible heat flux *H* can be computed as:

$$u^* = \frac{1}{n} \cdot \sum_{i=1}^{n} (v_i - \overline{v}) \cdot (w_i - \overline{w}) = \sqrt{-\overline{vw}} \qquad \text{Equ. 13}$$

and

$$H = -\sqrt{-\overline{wT}} \qquad \text{Equ. 14.}$$

This yields L_{MO} using the Karman-constant $\kappa \approx 0.4$ and $g = 9.81\ m^2s^{-1}$:

$$L_{MO} = -\frac{T \cdot (u^*)^3}{\kappa \cdot g \cdot H} \qquad \text{Equ. 15.}$$

The stability function used by these authors is defined as

$$\Theta\left(z/L_{MO}\right) = \left(1 - 16 \cdot (z-d)/L_{MO}\right)^{-0.5} \text{ for unstable conditions } \left(\frac{z}{L_{MO}} < 0\right)$$

or Equ. 16

$$\Theta\left(z/L_{MO}\right) = \left(1 + 5 \cdot (z-d)/L_{MO}\right) \qquad \text{for stable conditions } \left(\frac{z}{L_{MO}} > 0\right)$$

Now the turbulent exchange coefficient *K* is determined as

$$K(z) = \frac{u^* \cdot \kappa \cdot (z-d)}{\Theta(z/L_{MO})} \qquad \text{Equ. 17,}$$

where *d* specifies a shift of the point of origin necessary for rough ground structures.

However, information on the 3D wind field and the heat fluxes needed for the computation of *K(z)* under non-neutral conditions was not available for the gradient measurements presented in this thesis. So only the propositions for a neutral stratification can be used for the evaluation of the gradients.

3.2.2 Typical diffusion constants and transfer resistances in the PBL

To compute mean mixing times of trace gasses in the PBL, the constants for diffusive transport mechanisms that dominate the mixing under most circumstances[9] have to be known.

Laminar diffusion coefficients

Laminar diffusion dominates the transport of impulse, heat and trace gasses in the laminar sublayer of the PBL. The diffusion constant ν for impulse is defined by

$$\nu = \tfrac{1}{3} \cdot \mathrm{v} \cdot l \qquad (\nu \approx 0.15\,\mathrm{cm^2 s^{-1}} \quad \text{for ambient air at 20°C}) \qquad \text{Equ. 18}$$

with the thermal velocity v and the mean free path length *l*. ν is directly linked to the diffusion constant for trace gasses by Schmidt's number:

$$Sc = \frac{\nu}{D} \qquad (Sc \approx 0.85 \quad \text{for } CO_2 \text{ in ambient air at 20°C}) \qquad \text{Equ. 19}$$

For further details of laminar transport phenomena see e.g. [*Roedel*, 1994].

Turbulent diffusion coefficients

To compute typical turbulent diffusion coefficients, a neutral stratification is assumed. Then, Equ. 11 yields the turbulent diffusion coefficient using a typical wind speed of $v_r = 3\ \mathrm{m\,s^{-1}}$ at a height of $z_r = 30$ m and a surface roughness parameter $z_0 = 0.5$ m:

$$K(z) = \frac{v_r \cdot \kappa^2}{\ln(z_r / z_0)} \cdot z = 0.141\ \mathrm{m\,s^{-1}} \cdot z \qquad \text{Equ. 20,}$$

a value that is substantially higher than the laminar diffusion constant (see e.g. [*Stull*, 1988]).

Transfer resistances in the PBL

In order to obtain mean mixing times, the assumption of a neutrally stratified PBL is used again. The laminar sublayer is neglected; an approximation that is valid for the rough surfaces found in cities [*Roedel*, 1994]. Then Equ. 10 can be implemented in Equ. 8, yielding the transfer resistance for the height interval [z_1 ; z_2]:

$$R_{1,2} = -\frac{\ln(z_r / z_0)}{v_r \cdot \kappa^2} \cdot \ln\left(\frac{z_2}{z_1}\right) \qquad \text{Equ. 21}$$

Using the same constants as for the calculation of the mean turbulent diffusion coefficient (Equ. 20), but varying the mean wind speed, results in the values given in Table 4. It is evident that turbulent mixing under neutral conditions is very effective as trace gasses are transported from the lower to the upper border of the layers assumed in Table 4 within a timescale of some minutes.

[9] Except for hot summer days with no or very even winds, where convective transport in the surface and Ekman layer is more effective than turbulent diffusion.

Table 4: Transfer resistances for a neutrally stratified PBL at different height intervals analogous to those of the Heidelberg long-term measurements (see chapter 5.1)

Height interval	Transfer resistance [s m^{-1}] at a typical wind speed of			
	v_r = 1 m s^{-1}	v_r = 3 m s^{-1}	v_r = 5 m s^{-1}	v_r = 10 m s^{-1}
1 – 30 m	72.3	24.1	14.5	7.23
30 – 150 m	34.2	11.4	6.84	3.42
150 – 480 m	24.7	8.24	4.95	2.47

3.3 Diurnal variations of the PBL

3.3.1 Meteorological description

As already stated in chapter 3.2.1, the efficiency of all mixing processes is closely linked to the temperature gradient in the PBL. The troposphere is, by definition, characterised by a negative temperature gradient, i.e. temperatures decreasing with increasing height over ground. This temperature gradient is due to the warming of the Earth's surface by solar radiation by day and subsequent heat exchange with the air masses close to the surface. Therefore, one might suspect that this gradient would generally yield an effective mixing, as warmer (i.e. less dense) air is situated below colder (i.e. more dense) air. However, the potential energy of the air parcels also has to be considered. An air parcel descending from higher altitudes transforms its potential energy to heat energy while being compressed to the increased pressure of the lower altitude (a process taking place vice versa for the ascending air parcel). To consider this, the potential temperature Θ is introduced, which combines both the potential and the thermal energy of the observed air mass:

$$\Theta = T \cdot \left(\frac{p_0}{p} \right)^{\frac{\chi - 1}{\chi}} \qquad \text{with} \qquad \chi = \frac{c_p}{c_p} \qquad \text{Equ. 22}$$

p_0 labels the normal pressure, T the actual temperature, c_p and c_v the specific heat of air at a constant pressure and volume, respectively. The virtual potential temperature additionally considers the content of water vapour and liquid water in the air mass (see e.g. [*Stull*, 1988]). As the diurnal cycle of solar radiation directly affects the heat fluxes from the surface and within the lower atmosphere, it can be expected that vertical mixing is also strongly influenced by solar radiation. This causes a diurnal change of stratification within the PBL, which is shown in Figure 8. In daytime, the PBL is assumed as a well mixed layer due to strong turbulences driven by wind shear and convection. At nightfall, turbulences in the PBL decrease as only wind shear remains as the driving force: a residual layer is formed containing the air masses of the former mixing layer. Below, a stable boundary layer of sporadic turbulence establishes. Solar radiation increasing after sunrise initiates the well-mixed daytime PBL again .

Figure 9 presents the vertical profile of virtual potential temperature during a 24-hour period at specific times marked S1-S6 in Figure 8. This graph directly indicates the dependency of the mixing efficiency on the potential temperature. Layers that feature constant potential temperatures over their height range are generally well-mixed. Contrastingly, mixing is hampered when the potential temperatures increase with height. Especially in the morning hours, this effect is strong enough to inhibit mixing between air cooled down at night by the surface and warmer air above. Such ground inversions also occur in basins or valleys that fall under the influence of an atmospheric subsidence zone (see e.g. [*Roedel*, 1994]).

Thus, the stratification of the PBL changes its shape not only within the day but that it is also influenced by local topography and large-scale atmospheric phenomena such as cyclones. Thus, an in-depth analysis of transport mechanisms is only possible knowing the 3D wind field and the heat flux in the PBL – if possible, even at different elevations. However, the assumption of a neutrally stratified PBL is justified to gain an impression of the diffusion constants if detailed meteorological information is not available.

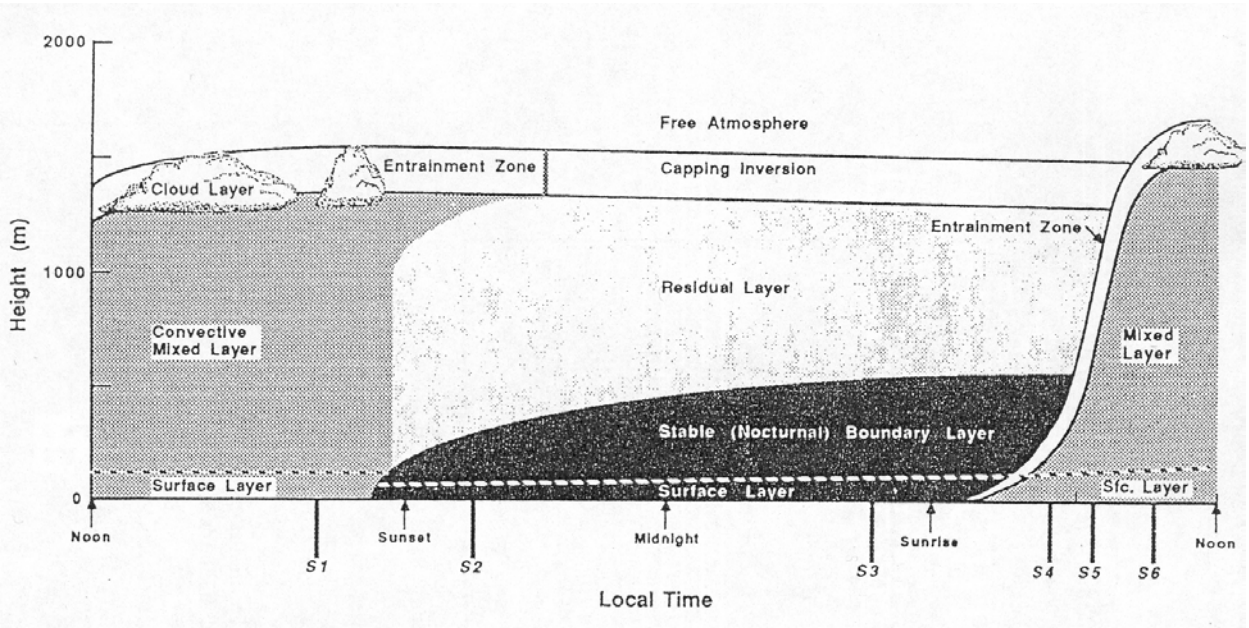

Figure 8: Typical diurnal variation of the stratification of the PBL in high pressure regions over land [*Stull*, 1988]. The time markers indicated by S1-S6 will be used in Figure 9.

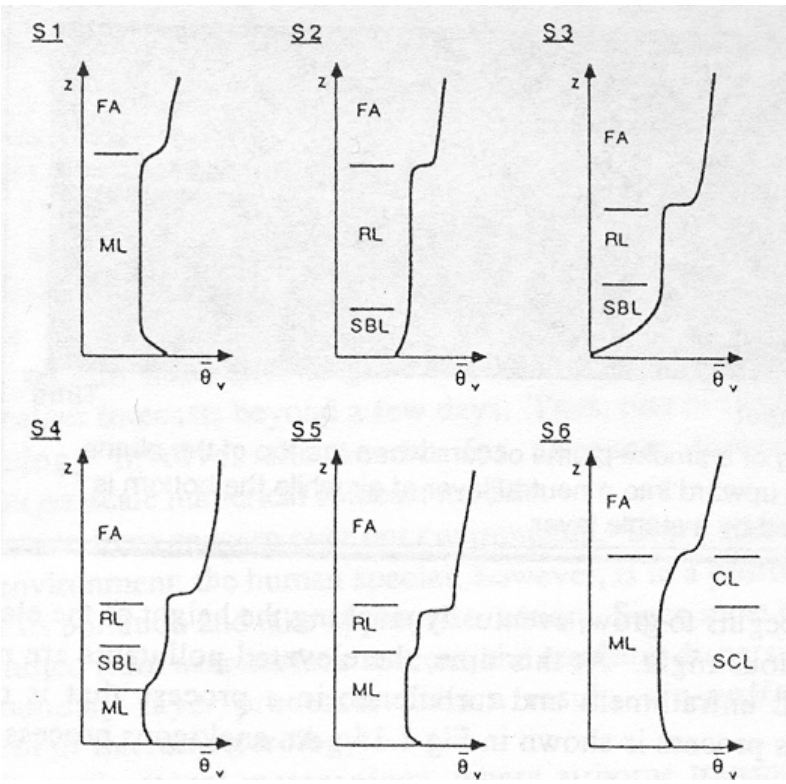

Figure 9: Profiles of mean virtual temperature showing the PBL evolution during a diurnal cycle at the time markers indicated in Figure 8 [*Stull*, 1988]. The labels also correspond to the sublayer names introduced in Figure 8.

3.3.2 The general equation for trace gasses in the atmosphere

To describe the time series of all atmospheric trace gasses, the general differential equation for atmospheric compounds can be used:

$$\frac{\partial C}{\partial t} = \frac{1}{h_{BL}}\left[\Phi_P + \Phi_S\right] - K(z)\cdot\frac{\partial C}{\partial z} + \sum_i P_i - \sum_j L_j - L_S\left[\frac{1}{h_{BL}}; K(z)\cdot\frac{\partial C}{\partial z}\right] + Adv \quad \text{Equ. 23}$$

with
- C = mixing ratio near the ground
- h_{BL} = height of the PBL
- Φ_P = primary emission flux
- Φ_S = surface emission flux
- $K(z)$ = vertical mass exchange due to eddy diffusion and convection
- P_i = chemical production rate from the ith pathway
- L_j = chemical removal rate from the jth pathway
- L_S = removal rate from deposition
- Adv = advection term forced by horizontal transport

For the evaluation of the HONO and NO_2 vertical profiles measured at Heidelberg, it will not be possible to solve Equ. 23 completely: especially, no direct measurements of the vertical diffusion coefficient *K(z)* and the boundary layer height are available. This information however, would be needed to characterise the impact of primary and surface emissions as well as chemical production and removal of HONO and NO_2 in the PBL. Still, the equation can be used – in conjunction with some tracer data and basic assumptions on atmospheric parameters – to analyse the results of the Heidelberg measurements presented in chapters 6 and 0.

Adaptation of the general equation to the Radon activity

Radon is emitted continuously by the ground, with an emission rate depending on the soil type. Thereby, 80-90% of the emission rates are measured in the range of ± 3 times the mean value [*Nazaroff*, 1992]. In the same publication, a detailed discussion on the effect of soil and meteorological parameters can be found. After Radon is emitted by the soil, turbulent diffusion spreads it out into the atmosphere (see chapter 3.2). Radon is inert to almost any chemical reaction. Thus its radioactive decay can be considered as the main Radon sink. The radon decay products being isotopes of heavy metals become readily attached to aerosol particles and precipitation elements [*Jacobi and André*, 1963]. Thus, Radon is a prominent tracer for atmospheric mixing processes, especially, if its activity is compared to the mixing ratio of other trace gasses. The measurement of Radon vertical profiles also allows to deduce the dependency of the turbulent diffusion constant with altitude [*Jacobi and André*, 1963]. As Radon activity data in Heidelberg was only available at a single height, Radon is mainly used as a tracer for the build-up and break-up of ground inversions: if a ground inversion builds up, vertical transport in the PBL is strongly limited (see chapter 3.3.1) and Radon activity increases constantly as long as the inversion layer is stable. If the ground inversion breaks up, Radon activity decreases as mixing becomes more efficient. The variations of Radon activity are also linked to the mixing volume, as the activity increases more quickly when the mixing volume is smaller, i.e. when the inversion height is closer to the ground.
Thus, radon activity can be used as a tracer for the boundary layer height and the efficiency of vertical mixing: Radon is emitted at a nearly constant rate by the ground

$$\Rightarrow \Phi_S = \Phi_{Rn}\ .$$

Direct emissions and chemical reactions of Radon are not known. For first order approximations, advection can be neglected [*Febo et al.*, 1999].

$$\Rightarrow \Phi_P = P_i = L_j = L_S = Adv = 0.$$

This yields the general equation for Radon :

$$\frac{\partial Rn}{\partial t} = \frac{1}{h_{BL}}\left[\Phi_{Rn}\right] - K(z)\cdot\frac{\partial Rn}{\partial z} \qquad \text{Equ. 24.}$$

Generally, the advection term has to be taken into account, especially near the sea (as no Radon is emitted from oceans), but also in continental air masses because the exhalation of Radon depends on the soil type [*Levin et al.*, 2002]. Thus, omitting the advection term is only a first-order approach. This is nevertheless suitable, as the variation of the NO_2 and HONO mixing ratio proceeds on a much shorter timescale. Consequently, the time series of radon described by Equ. 24 can be used as a combined tracer for atmospheric stability and the height of the PBL even without any knowledge of the vertical diffusion coefficient *K(z)*.

4 Experimental techniques

4.1 Overview on Differential Optical Absorption Spectroscopy

The method of "Differential Optical Absorption Spectroscopy" or DOAS, which is applied in this thesis, was introduced to measure trace-gas concentrations in the atmosphere by [*Platt et al.*, 1979]. The basic principle of Active Long-Path DOAS (LP-DOAS), as it is used here, is to send a beam of light – typically in the visible and / or near UV wavelength range – generated by an artificial source on a well-defined light path through the atmosphere. The light is then collected by suitable optics and sent to a spectrograph-detector system. Here, the spectrum is analysed to gain information on the structure and amount of absorption by molecules that took place along the light path. As each molecule has a characteristic absorption structure , the DOAS technique is suitable to measure the concentrations of different trace gasses at the same time. Several trace gasses of particular importance for atmospheric chemistry were measured for the first time using this technique (for an overview see [*Platt*, 1994]). Of special interest for this thesis are the compounds NO_2, HCHO and O_3 [*Platt et al.*, 1979], nitrous acid [*Perner and Platt*, 1979; *Platt et al.*, 1980] and the OH radical [*Perner et al.*, 1976].

Active DOAS has been used for measurements of trace gas profiles in the boundary layer from the very beginning: [*Platt*, 1978] used this technique on folded light paths to mirrors mounted at different heights on a meteorological mast. The same authors suggested the retrieval algorithm for vertical profiles from such measurements used in this thesis. The measurement of vertical profiles, however, has seen only few applications since these first SO_2 flux measurements. So far, only short term DOAS measurements of vertical profiles in the PBL have been published by [*Alicke*, 2000; *Stutz et al.*, 2001].

Another well-established application of DOAS is Passive DOAS, which uses the sun, the moon or stars as light sources. The measurement geometry of Passive DOAS sees either the direct light path from the source to the spectrograph as the absorption pathway or – mostly with the sun acting as the light source – stray light coming from one or multiple (MAX-DOAS) distinct zenith and azimuth angle. These techniques are primarily used for measurements of trace gas concentrations in the upper troposphere and stratosphere with instruments located on the ground (e.g. [*Hönninger*, 2001]) or attached to stratospheric balloons (e.g. [*Bösch*, 2001]).

Most recent DOAS developments are DOAS-Tomography by LP-DOAS and MAX-DOAS to resolve the spatial distribution of trace gasses in the atmosphere.

The following section presents the basic principles of DOAS and the retrieval process that were used for the measurement of trace gas concentration height profiles in the PBL.

4.2 Absorption spectroscopy in the atmosphere

Absorption spectroscopy uses the fact that every molecule, when irradiated by electromagnetic radiation, absorbs at distinct wavelengths. These are directly linked to electronic, vibrational and rotational states of the molecule that can be exited and therefore absorb radiation energy. This process is described by the Lambert – Beer law:

$$I(\lambda) = I_0(\lambda) \cdot \exp\left(-\int_0^L \left(\varepsilon_R(\lambda, l) + \varepsilon_M(\lambda, l) + \sum_i \sigma_i(\lambda, P, T) \cdot c_i(l) \right) \cdot dl \right) \qquad \text{Equ. 25}$$

with	$I(\lambda)$:	light intensity after passing through the atmosphere
	$I_0(\lambda)$:	intensity of the light source
	λ:	wavelength
	$\varepsilon_R(\lambda,l)$:	Rayleigh-scattering coefficient
	$\varepsilon_M(\lambda,l)$:	Mie-scattering coefficient
	$\sigma_i(\lambda,P,T)$:	absorption cross section of absorber i
	$c_i(l)$:	concentration of absorber i
	L:	total light path length

Some characteristics of the contributing processes are of special significance for the analysis of atmospheric absorption spectra:

The scattering coefficients ε_R and ε_M depend mainly on two factors: the location l along the light path and the wavelength. Of crucial importance is the fact that both coefficients depend on the wavelength in a monotonous manner: the Mie-scattering coefficient ε_M, which describes the scattering on particles larger than the wavelength, shows a dependence on $\approx\lambda^{-1.3}$ (see e.g. [*Hulst*, 1957]). The scattering on particles or molecules smaller than the actual wavelength is described by the Rayleigh-coefficient ε_R and depends on λ^{-4} (also [*Hulst*, 1957]).

As every molecule is characterised by the composition and arrangement of the elements it consists of, its electronic and ro-vibronic states also generate a characteristic absorption cross section. The cross sections of all absorbers σ_i therefore form a basis – in the mathematical sense – from which each absorption spectrum can be composed as a unique linear combination. So the concentrations of all compounds that absorb in the observed wavelength range can be measured simultaneously.

But the basic Lambert – Beer Law cannot be applied to trace gas concentration measurements in the atmosphere for several reasons:

1. As extinction processes feature a broad-band spectral response (see above), it is nearly impossible to distinguish between the contributions of the different scattering processes in the atmosphere and broad-band absorption of the continuum bands of the absorbers.
2. The continuum band absorption of the different absorbers is equally hard to describe, as these absorption structures feature no characteristic structures.
3. Stray light from other light sources, which is scattered along the DOAS light path and sent to spectrograph and detector, has to be corrected for. In the case of an Active LP-DOAS system, the main contribution to stray light is made by sunlight scattered along the light path.
4. Artificial light sources used by Active DOAS typically feature not only the broad-band spectral shape defined by the Plank law, but also spectral structures of the same bandwidth than the characteristic trace gas absorptions. Especially Xenon arc lamps, that are widely used, show prominent emission lines that change both in intensity and spectral shape during the lamp lifetime.

5. The spectral response of the spectrograph and detector as well as the sensitivity of the detector, which might also be wavelength-dependant, have to be corrected for. Both effects contribute to the so-called instrument function, which limits not only the spectral resolution, but also causes a dependency of the signal detected at a specific wavelength on the signal of the neighbouring wavelengths.
6. Photon statistics and detector noise add up to a noise spectrum which limits the sensitivity of the DOAS system and therefore the minimum trace gas concentration which is detectable.

So it is impossible to quantify all extinction processes from an absorption spectrum measured on a light path in the real atmosphere, even if all instrument-specific spectral structures were known. Additionally, the knowledge of the trace gas concentrations gained from the characteristic absorption structures would still leave the problem of the quantification of extinction by scattering processes.
One possible solution for this dilemma is provided by the DOAS technique which is discussed in the following section.

4.3 Active Long Path DOAS

4.3.1 Basic principle

To overcome the problem that atmospheric scattering by molecules and particles and broad-band absorption can hardly be quantified, the DOAS technique divides the absorption cross section of trace gasses in two parts:

$$\sigma(\lambda) = \sigma_{broad}(\lambda) + \sigma'(\lambda) \qquad \text{Equ. 26.}$$

σ', which is often referred to as the differential absorption cross section, describes only the characteristic narrow-band absorption structures of the different trace gasses. The broad band structures caused by scattering and broad-band absorption are characterised by σ_{broad}. This is the key principle of DOAS, as it allows to split the exponent of the Lambert-Beer-Law in two parts: the first varying only ”slowly” with the wavelength and containing scattering processes and broad-band absorption. The second part characterises the variations in transmitted intensity featuring a strong dependency on the wavelength due to narrow-band trace gas absorption. Applying this, the Lambert- Beer-Law can be expressed as:

$$I(\lambda) = I_0(\lambda) \cdot \exp\left(-\int_0^L \left(\varepsilon_R(\lambda, l) + \varepsilon_M(\lambda, l) + \sum_i \sigma_{i,broad}(\lambda) \cdot c_i(l) \right) \cdot dl \right) \cdot \exp\left(-\int_0^L \left(\sum_i \sigma'_i(\lambda) \cdot c_i(l) \right) \cdot dl \right) \qquad \text{Equ. 27.}$$

The pressure und temperature dependency can be omitted for most absorbers in the boundary layer and is no longer labelled for the sake of simplicity.
Merging the initial light intensity $I_0(\lambda)$and the extinction varying slowly with wavelength to the new “differential baseline intensity” $I'_0(\lambda)$, the Lambert-Beer-Law for DOAS simplifies to

$$\ln\left(\frac{I(\lambda)}{I'_0(\lambda)} \right) = -\int_0^L \left(\sum_i \sigma'_i(\lambda) \cdot c_i(l) \right) \cdot dl \qquad \text{Equ. 28.}$$

$I'_0(\lambda)$ is computed from the measured spectrum $I(\lambda)$ by applying a low-pass filter, which first removes all narrow-band structures by triangular smoothing or Savitzky – Golay smoothing

and subsequently divides the original spectrum by the smoothed spectrum. A different approach for low-pass filtering is a polynomial regression analysis[10]. The differential absorption cross section σ'_i for all trace gasses that feature characteristic structures in the observed wavelength range have to be computed by the same high pass filter algorithm.
Now the only missing variable, apart from the desired trace gas concentration c_i, is the total light path length L. For a LP-DOAS set-up, the light path length can be measured easily and very accurately e.g. by a laser range finder.

4.3.2 Mathematical description of DOAS spectra

To obtain the trace gas concentrations from the measured spectra, the retrieval process has to account not only for the basic atmospheric spectrum, but also for instrument-specific spectral structures not discussed in the previous section. These corrections depend on the set-up of the DOAS system and the characteristics of its optical components.
Figure 10 shows a simplified set-up of an active LP-DOAS system for the measurement of tropospheric trace gasses. The light emitted by a suitable broad-band source with an initial intensity $I_0(\lambda)$ is focused by a telescope to a light beam that passes trough the atmosphere on the absorption path length L. Extinction by scattering and absorption reduces the initial intensity to $I(\lambda,L)$ as expressed by Equ. 25. The light is then collected by a telescope and sent to the entrance slit of a spectrograph via a quartz glass fibre. Inset a) of Figure 10 features the spectrum at this point, assuming an atmosphere containing only formaldehyde (HCHO). As we are interested in the total signal reaching the detector, Equ. 25 has to be enhanced by the photon noise $N(\lambda)$, which depends directly on $I(\lambda,L)$ and the stray light signal $M(\lambda)$:

$$I(\lambda) = I_0(\lambda)\cdot \exp\left(-\int_0^L \varepsilon_R(\lambda,l) + \varepsilon_M(\lambda,l) + \sum_i \sigma_i(\lambda)\cdot c_i(l)\cdot dl\right) + N(\lambda) + M(\lambda)$$

When the atmospheric spectrum passes the spectrograph, the resolution degrades to a value of $\Delta\lambda / \lambda$ that is defined by the entrance slit width and the number of grooves per millimetre on the grating. Thus, the spectrum at the detector no longer features the very fine structures of the ro-vibronic absorption bands. The mathematical description of this process is the convolution of the initial spectrum with the instrument function H of the spectrograph.

$$I^*(\lambda,L) = I(\lambda,L) * H = \int I(\lambda-\lambda',L)\cdot H(\lambda')\cdot d\lambda' \qquad \text{Equ. 29.}$$

For the evaluation, the cross sections of all absorbers of interest have to be treated in the same way, resulting in cross sections S_i of the same resolution as the measured spectra:

$$S_i(\lambda) = H * \sigma(\lambda) = \int \sigma_i(\lambda-\lambda',L)\cdot H(\lambda')\cdot d\lambda' \qquad \text{Equ. 30.}$$

Inset b) presents the spectrum $I^*(\lambda,L)$ projected on the detector after passing the spectrograph.
The multi-channel detector maps a wavelength range with a width of, typically, some tens of nanometres into n = 1024 discrete pixels numbered j, each integrating the light in the wavelength interval from $\lambda(j-½)$ to $\lambda(j+½)$. This discretisation is defined by:

$$I^+(j) = \int_{\lambda-½}^{\lambda+½} I^*(\lambda',L)\cdot d\lambda' \qquad \text{Equ. 31.}$$

[10] For details and an analysis of the filter behaviour of the different algorithms refer e.g. to [*Geyer*, 1997; *Stutz and Platt*, 1997; *Volkamer*, 1996].

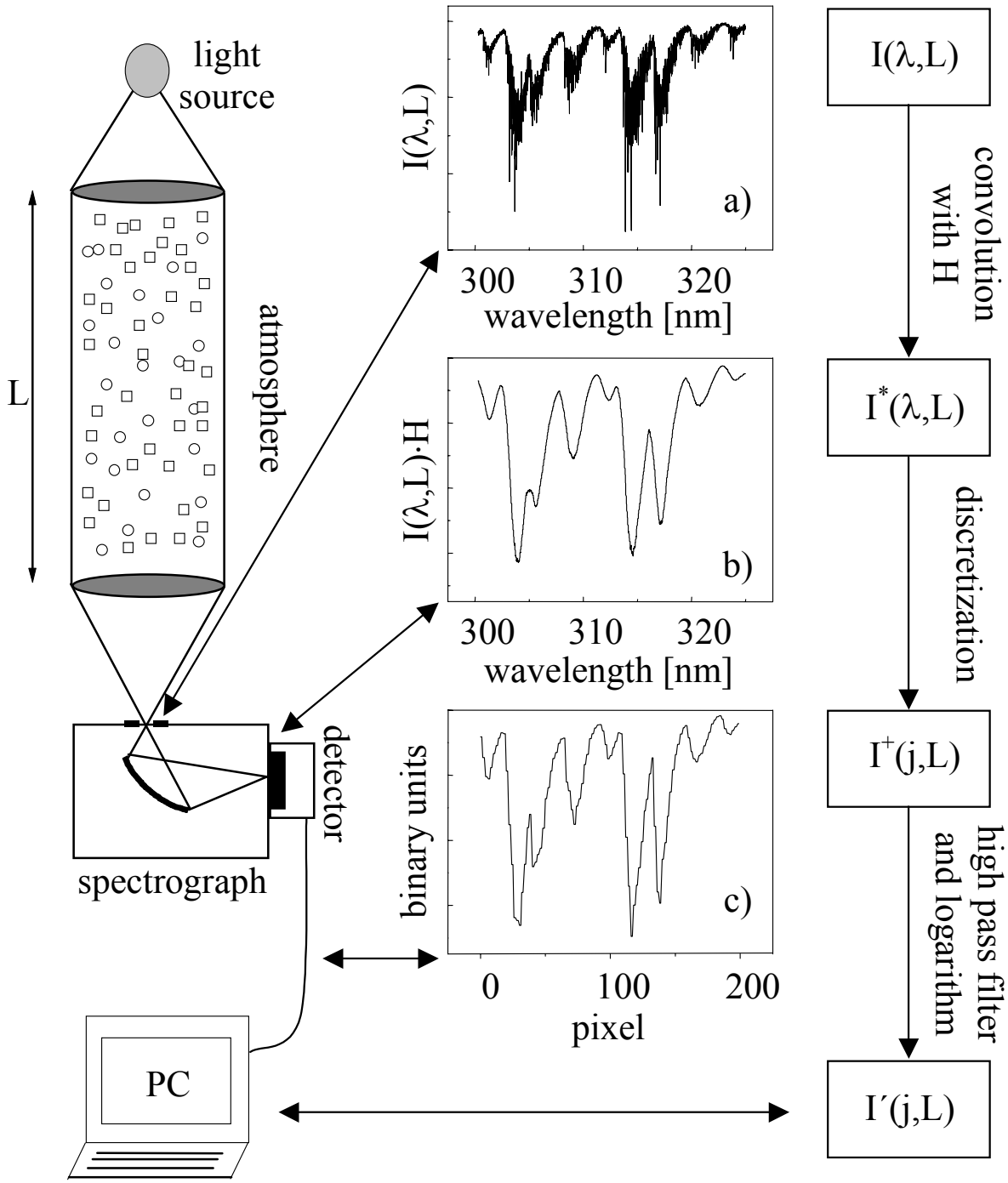

Figure 10: Overview of the components and the spectra processing of a simplified DOAS system

The wavelength interval is defined by the wavelength-to-pixel mapping function Γ_I of the instrument. Usually, the spectral width of a pixel is not a constant, because the mapping function (or dispersion function) is described by a polynomial of degree q:

$$\Gamma_I : \lambda(j) = \sum_{k=0}^{q} \gamma_k \cdot j^k \qquad \text{Equ. 32.}$$

The parameter vector γ_k determines the mapping of pixel j to wavelength $\lambda(j)$. Changes in the parameter γ_0, that defines the "starting wavelength" λ_0 of the spectrum on the detector, describe a linear wavelength shift of the spectrum, often caused by temperature drifts in the

optical alignment of the spectrograph. This effect can partly be suppressed by temperature isolation and thermal stabilisation by heating, but must nevertheless be accounted for in the retrieval process. Changes in the optical alignment can also affect the parameter γ_1 characterising the linear slope of the dispersion relation. The effect of the spectrum being stretched or squeezed with respect to the original dispersion relation must also be accounted for in spectra analysis. The square dependency of the dispersion relation characterised by γ_2 is due to systematic reproduction errors of the spectrograph. As the factor b defining this dependency is usually some orders of magnitude smaller than the linear slope γ_1, it is usually omitted. In this thesis, however, a polynomial of 2nd order is assumed for the dispersion relation as this guarantees better fit results (see chapter 5.3). Changes of this parameter are too small to cause significant effects and are therefore neglected in the evaluation.
Inset c) of Figure 10 presents the spectrum as it is sent to the computer after being mapped on the PDA and digitised by the electronics.

The electronics that detect, amplify and digitise the signal also affect the spectrum as it is seen on the computer screen. The photo diode array (PDA) is not completely homogenous in its specifications, which causes different quantum yields, dark current and electronic noise signals of the individual diodes. The variations of the spectral sensitivity will be summarised by the term $A^+(i)$. All noise effects are summarised to $N^+(i)$ as it is impossible to discriminate them from a single spectrum.

Some last assumptions are necessary for a summary of the mathematical description of the measured spectra : to ease the evaluation of the spectra, the integral over the light path length is separated in the convoluted cross section S^+_I and the concentration of the absorber i integrated on the light path L:

$$\int_0^L S_i^+(j)\cdot c_i(l)\cdot dl = S_i^+(j)\cdot\int_0^L c_i(l)\cdot dl = S_i^+(j)\cdot a_i \qquad \text{Equ. 33}$$

The factor a_i is often referred to as the “column density” of the absorber i.

To depict the influx of all processes contributing to the spectrum measured by an active LP-DOAS system, the logarithm of Equ. 28 can now be re-written as

$$I^+(j) = I_0^+(j)\cdot\exp\left(-R^+(j) - B^+(j) - \sum_i S_i^+(j)\cdot a_i\right) + N^+(j) + M^+(j) + A^+(j).$$

The high-pass filter algorithm as presented in chapter 4.3.1 combines the terms of I_o^+, R^+, B^+ and all instrument-specific broad-band spectral structures in the new I_o'. The logarithm applied to both sides of the equation yields:

$$J(j) = \ln\left(\frac{I'(j)}{I_0'(j)}\right) = -\sum_i S_i'(j)\cdot a_i(j) + N'(j) + M'(j) + A'(j) \qquad \text{Equ. 34}$$

To extract the column densities a_i of all trace gasses absorbing in the observed wavelength range, this equation has to be reproduced by the retrieval algorithm.

4.3.3 Analysis procedure

The evaluation procedure is based on a model that describes the physical behaviour of the measured DOAS spectra according to equation Equ. 34. The logarithm of the smoothed discrete intensity is modelled by a function F(j):

$$F(j) = P_r(j) + \sum_{i=1}^{m} a_i \cdot S'_i(d_{i,0}, d_{i,1}, \ldots)(j) \qquad \text{Equ. 35.}$$

The absorption structures of the trace gasses S'_i, measured in the laboratory or calculated by convolution of high-resolution literature cross sections with the instrument function H, are input data to the procedure. The polynomial $P_r(j)$ describes the broad spectral structures which could not be filtered out completely due to changes in the characteristics of the lamp, the scattering processes and the broad-band absorption by trace gases. It is expressed as

$$P_r(j) = \sum_{h=0}^{r} c_h \times (j - j_c)^h \qquad \text{Equ. 36.}$$

The parameter $j_c = int(n/2)$ represents the centre pixel of the spectral region used for the evaluation. The polynomial refers to j_C to maximize the influence of the non-linear terms.

The scaling parameters a_i and the polynomial coefficients c_h of Equ. 35 and Equ. 36 , respectively, can be found from a linear fit of F represented by Equ. 35 to the measured $J(j)$ described by Equ. 34. Subsequently, the mean trace gas concentrations $\bar{c}_i$ can easily be calculated from the scaling factors by using Equ. 33:

$$S'_i \cdot a_i = S'_i \cdot \int_0^L c_i(l) \cdot dl \quad \Rightarrow \qquad \bar{c}_i = \frac{a_i}{L} \qquad \text{Equ. 37.}$$

Additional to the linear fit, the analysis procedure has to align the reference spectra $S'_i(j)$ with a fixed wavelength-pixel-mapping Γ_j to the measured spectra J(j) with a wavelength-pixel-mapping Γ_J^* varying due to environmental conditions. Therefore the retrieval algorithm has to calculate the reference spectrum $S'_i(j^*)$ used in the linear fit by adopting the wavelength-pixel-mapping Γ_J^* to $S'_i(j)$. This can be approximated by 'shifting and stretching/squeezing' the reference spectrum in wavelength. It is important in this context that Γ_j is a strongly monotonous function defined by Equ. 32. Its inverse can also be described by a polynomial:

$$\Gamma_j^{-1} : x(\lambda) = \sum_{k=0}^{q} \beta_k \times \lambda^k \qquad \text{Equ. 38.}$$

Now $x(\lambda)$ represents the non-integer 'pixel number' that results from the inverse transformation.

To calculate the reference spectrum $S'_i(j^*)$ for the linear fit, the following scheme is used:

$$S'_i(j) \xrightarrow{\text{interpolation}} S'_i(x) \xrightarrow{\Gamma_j^{-1}} S'_i(\lambda) \xrightarrow{\Gamma_J} S'_i(j^*) \qquad \text{Equ. 39.}$$

First, a cubic spline interpolation on the discrete spectrum $S'_i(j)$ yields a continuous spectrum $S'_i(x)$. Now $S'_i(j^*)$ with the wavelength-pixel-mapping Γ_J can be calculated by deriving $S'_i(\lambda)$ with Γ_j^{-1} from $S'_i(x)$, and then applying Γ_J.

It is possible to refrain from calculating $S'_i(\lambda)$ by combining Γ_j^{-1} and Γ_J to one formula, which links i to x using a polynomial with parameters δ_k:

$$x(j)=x(\lambda(j)) = \sum_{k=0}^{q_s \times q_I} \delta_k \times j^k \qquad \text{Equ. 40.}$$

In the analysis procedure, a slightly modified equation equivalent to Equ. 40 is used, which has the advantage that here the spectral alignment parameters $d_{j,k}$, determining the transformation are zero if the wavelength-pixel-mappings of J and $S'_i(j)$ are equal:

$$x=j+f_i(j) \text{ with } f_i(j) = \sum_{k=0}^{p_i} d_{i,k} \times (j - j_c)^k \qquad \text{Equ. 41.}$$

The spectrum $S'_i(d_{i,0},d_{i,1},...)(j) = S'_i(j^*)$ now has the wavelength-pixel-mapping Γ_J , which was calculated with the parameters $d_{i,k}$ following equations Equ. 39 and Equ. 41 and a cubic spline interpolation on $S'_i(j)$.

The parameters $d_{i,k}$ are derived by performing a non-linear fit of the model F to the spectrum J with fixed parameters a_i and c_h. If $p_i = 0$, the spectrum S'_i is shifted by $d_{i,0}$ pixels if $p_i = 1$ the spectrum is additionally linearly squeezed or stretched according to parameter $d_{i,1}$. Higher values of p_i represent a squeeze or stretch of higher order. To optimise the fit results by reducing the number of degrees of freedom, it is possible to select the degree of the squeeze process p_i for every reference spectrum S'_i. It is also possible to use one set of parameters $d_{i,k}$ for two or more reference spectra if the wavelength calibration is identical for these spectra.

The analysis procedure is a combination of the well-known non-linear Levenberg-Marquardt-Method [*Levenberg*, 1944; *Marquardt*, 1963] determining $d_{i,k}$ and a standard linear least-squares fit [*Albritton et al.*, 1976; *Bevington*, 1969] to derive the a_i and the c_k. Both methods minimize χ^2 between F and J.

$$\chi^2 = \sum_{j=0}^{n} \left(J(j)-F(j)\right)^2 \qquad \text{Equ. 42.}$$

The procedure starts with the calculation of the linear fit with starting values $d_{i,k}$. The parameters a_i and c_k resulting from this fit are used as input data for the following call of the non-linear Levenberg-Marquardt fit. Only one step of this non-linear iterative method is then performed, yielding the parameters $d_{i,k}$ that are used in the next call of the linear fit. The procedure continuously alternates between the two methods, always using the result of the last call of one method as starting values for the other fit method. This procedure is repeated until one of several stopping conditions for the non-linear fit is fulfilled. Normally, the fit is aborted when the relative changes of χ^2 in the last step are smaller than a given value (usually 10^{-6}) and thus the fit has converged. The fit also stops if a number of repetitions of the iteration determined by the user is exceeded, or if the non-linear method becomes unstable [*Gomer et al.*, 1996; *Stutz and Platt*, 1996].

4.3.4 Error estimation

A linear least-squares fit will yield the best result and the correct errors only if several assumptions are valid:

1. The errors of the pixel intensity must have a finite variance [*Albritton et al.*, 1976].
2. The normal least-squares fit as discussed in [*Albritton et al.*, 1976; *Bevington*, 1969] and used in most analysis procedures assumes that the intensity errors of the individual pixels are independent.
3. The systematic error of the pixel intensity is zero [*Albritton et al.*, 1976].

As the error of J(j) is dominated by photonic noise, variation of the intensity would be Poisson-distributed. At the high count rates encountered when using an artificial light source, however, the Poisson distribution is approximated by a Gauss distribution Therefore the intensity error is characterised by the standard deviation σ of the Gauss distribution, which fulfils assumption 1). Still, assumptions 2) and 3) are not fulfilled: as the spectra are generally smoothed (see chapter 5.3.1) to minimise noise effects and the diodes of the PDA show cross-dependencies to the neighbouring diodes on both sides of several per cent [*Stutz*, 1996]. Additionally, endowment errors in the diodes cause systematic errors of the pixel intensity. These errors, which are known as "PDA structures", can be corrected for (see also chapter 0 and [*Stutz and Platt*, 1996]), but as the measurements conditions change with time (especially at longer periods without special care to the instrument), the compensation is constantly harder to realise.

To account for these systematic errors of the fit, a correction factor for the "pure" statistic fitting error was introduced by [*Stutz*, 1996]. This factor has to be computed in dependency of spectral resolution, the width of the absorption structures observed and the degrees of freedom for the shifting and squeezing/stretching during the non-linear fit. For the evaluation used here, a correction factor of $3 \cdot \Delta_{Statistics}$ is found. For a more detailed description of the error calculation see also [*Stutz and Platt*, 1996].

The effects of residual structures

A common problem in the analysis of DOAS spectra is the occurrence of structures other than noise in the residuum $R(j) = J(j) - F(j)$ of the fit. These structures may indicate an unknown absorber or can be caused by the instrument itself and will then occur randomly in most cases. Stable residual structures cause systematic errors in the analysis which cannot be described by statistical methods.

Thus, a precise identification and description of the residual structure is required. In a pure noise spectrum, the width of any structure is usually only one pixel, thus indicating the independence of the pixel intensities. In residuals, groups of neighbouring pixel intensities appear to change simultaneously in a random way. Therefore it must be suspected that the errors of these pixel intensities are not independent from each other. A way of simulating this would be smoothing a pure noise spectrum, e.g. by a running mean. In a running mean, every pixel intensity is replaced by the average of its neighbouring pixel intensities. Therefore the errors of the individual pixel intensities are no longer independent from each other. Smoothed noise spectra look similar to residuals normally found in the analysis of atmospheric spectra. This finding confirms that the single pixel errors are not independent from each other (see above and [*Stutz and Platt*, 1996]). Residual structures due to unknown absorbers – often called X-absorbers – generally show a strong diurnal or seasonal variations and therefore can be separated from other systematic errors (see e.g. [*Hönninger*, 2001]).

Residual spectra also have an effect on the detection limits: a first approach would be to assume that only absorbers that cause spectral structures comparable or larger to these of the

residual can be identified positively in DOAS spectra. To quantify DOAS residuals, the following expression is commonly used:

$$\Delta_{\mathrm{Res}} = 1000 \cdot \exp\left(\frac{\max - \min}{\mathrm{avg}}\right) \qquad \text{Equ. 43}$$

with Δ_{Res}: residual in per mille
max: maximum value of J -F in the fitting range
min: minimum value of J -F in the fitting range
avg: average value of J -F in the fitting range

To compute the minimum detection limits which correspond with the residuals gained from Equ. 43, the following approximation can be used to calculate the optical density τ_{Res} of the residual structures:

$$\tau_{\mathrm{Res}} = \ln\left(\frac{I_{\mathrm{Res}}}{I_{0,\mathrm{Res}}}\right) \approx \ln\left(\frac{1 - \frac{1}{2}\Delta_{\mathrm{Res}}}{1 + \frac{1}{2}\Delta_{\mathrm{Res}}}\right) \qquad \text{Equ. 44.}$$

This can be compared to the differential optical density computed from the differential cross sections of the absorbers of interest by

$$\tau_{Abs} = \ln\left(\frac{I_{\min}}{I_{0,\max}}\right) = \delta(\sigma) \cdot c \cdot L = (\sigma_{\max} - \sigma_{\min}) \cdot c \cdot L \qquad \text{Equ. 45.}$$

The minimum concentration that would be detectable for a given Δ_{Res} is obtained by combining Equ. 44 and Equ. 45:

$$c_{\min} = \frac{\tau_{\mathrm{Res}}}{\delta(\sigma) \cdot L} \qquad \text{Equ. 46.}$$

Table 5 presents an overview of typical detection limits and the resulting detection limits for the trace gasses observed during this work. It is obvious from these values that either the detection limits computed by the algorithm of [*Stutz and Platt*, 1996] are underestimated, or the detection limits approximated from the residual structure by Equ. 46 are overestimated by a factor 2 – 5, depending on the absorption structure. This dependency already hints on the fact that the simple approximation given above overly simplifies the problem, and that a more detailed study that comprises the shape of the absorption structure and specifics of the instrument must be done to compute the correct detection limits for DOAS. Apart from the algorithm used by [*Stutz and Platt*, 1996], [*Hausmann et al.*, 1999] supposed a Monte-Carlo algorithm to compute the detection limits with respect to the fitting algorithm and the residuals.

However, systematic errors due to X-absorbers or stable residuals can be partially corrected for by fitting a typical residual or the mean residual of a series of spectra to the single spectra (see chapter 0) If this technique is applied with care, it partially corrects the systematic errors discussed above and therefore decreases the detection limits. A more in-depth analysis of the residuals can be done by a principal components analysis algorithm applied to the DOAS retrieval by [*Ferlemann*, 1998].

As the more sophisticated algorithms both require lots of computation time, they seem unsuitable for the huge amounts of data that accumulate during long-term measurements. Therefore, the method of [*Stutz and Platt*, 1996] has been applied to compute the systematic and statistical 1σ-error of the fit and the resulting detection limits by multiplying the 1σ-error by a factor of 2.

Table 5: Comparison of typical residual structures and resulting detection limits for the instrument and trace gasses discussed in this thesis. The detection limits are computed using the δ of the differential cross section (see above) and a total light path length of 4210 m, to be comparable to the data measured on the shortest light path of the Heidelberg long-term measurements. For the observations, the mean values for the full measurement period of 14 months are displayed.

	δ(differential cross section) [cm^2]			
	NO_2	HONO	HCHO	O_3
	$9.41 \cdot 10^{-20}$	$1.77 \cdot 10^{-19}$	$3.3 \cdot 10^{-20}$	$1.53 \cdot 10^{-21}$
residual [‰]	Theoretical detection limits [ppb]			
	NO_2	HONO	HCHO	O_3
0.1	0.10	0.05	0.29	6.2
0.5	0.50	0.27	1.45	31.0
1.0	1.01	0.54	2.98	62.1
1.5	1.51	0.80	4.35	93.1
2.0	2.02	1.07	5.79	124
Observations				
1.95	0.36	0.20	0.55	55.50

4.3.5 Differential cross sections

An integral part of the spectra evaluation is represented by the trace gas references fitted to the measured spectra. As already discussed above, these references are generated by convolution with the instrument function from high-resolution cross section spectra. Table 6 presents the literature cross sections that were used for the trace gas concentration retrieval within this thesis. The spectral resolution, both for the literature cross sections and the convolution algorithm, is of crucial importance for the quality of the reference spectra: the highest resolution of the literature spectra and of the wavelength grid used for the convolution guarantee that under-sampling effects are effectively suspended and that the Lambert-Beer-Law is also valid for the lower resolutions. For the convolution, all reference spectra were interpolated to a wavelength grid of 0.001 nm, and subsequently processed using the normalised instrument function. The instrument function was derived by normalising the area below a measured spectrum of the Mercury emission line at 366.33 nm. This line is well isolated from other lines and therefore ideally suited for the determination of the instrument function.

After the convolution, all spectra were high-pass filtered to remove all broad-band spectral structures: a triangular smoothing algorithm provided by the MFC software (see [*Gomer et al.*, 1996]) was applied to a copy of the original spectrum 800 times successively. Subsequently, the retained original spectrum was divided by the smoothed spectrum, yielding a high-pass filtered spectrum. These spectra, which contained only the narrow-band absorption structures, were used for the DOAS evaluation.

Figure 11 clarifies this process by the example of the NO_2 cross section in the wavelength range of roughly 334 - 375 nm used for the evaluation of the long-term measurements at Heidelberg.

A variety of differential cross sections used for LP-DOAS measurements is shown in Figure 12. Of special interest for this study are the cross sections of NO_2, HONO, HCHO, O_3 and O_4. These cross sections are already convoluted to the typical resolution of a LP-DOAS instrument (see chapter 5.2) and high-pass filtered by the algorithm specified above.

For further details of the retrieval process used for the long-term and balloon measurements, refer to sections 5.3 and 9, respectively.

Table 6: Specifications and references for the trace gas absorption cross sections used within this work.

species	source	rel. error	resolution	reference
NO_2	FTIR	± 3.5%	0.5 – 1 cm^{-1}	[*Voigt et al.*, 2001b]
HONO	GRAT	± 5 %	0.1 nm	[*Stutz et al.*, 2000]
HCHO	GRAT	± 5 %	0.01 nm	[*Meller and Moortgat*, 2000]
O_3	FTIR	± 3-7 %	5 cm^{-1}	[*Voigt et al.*, 2001a]
O_4	FTIR	n/a	1 cm^{-1}	[*Hermans et al.*, 1999]

FTIR: Fourier transform spectrometer
GRAT: Grating spectrometer

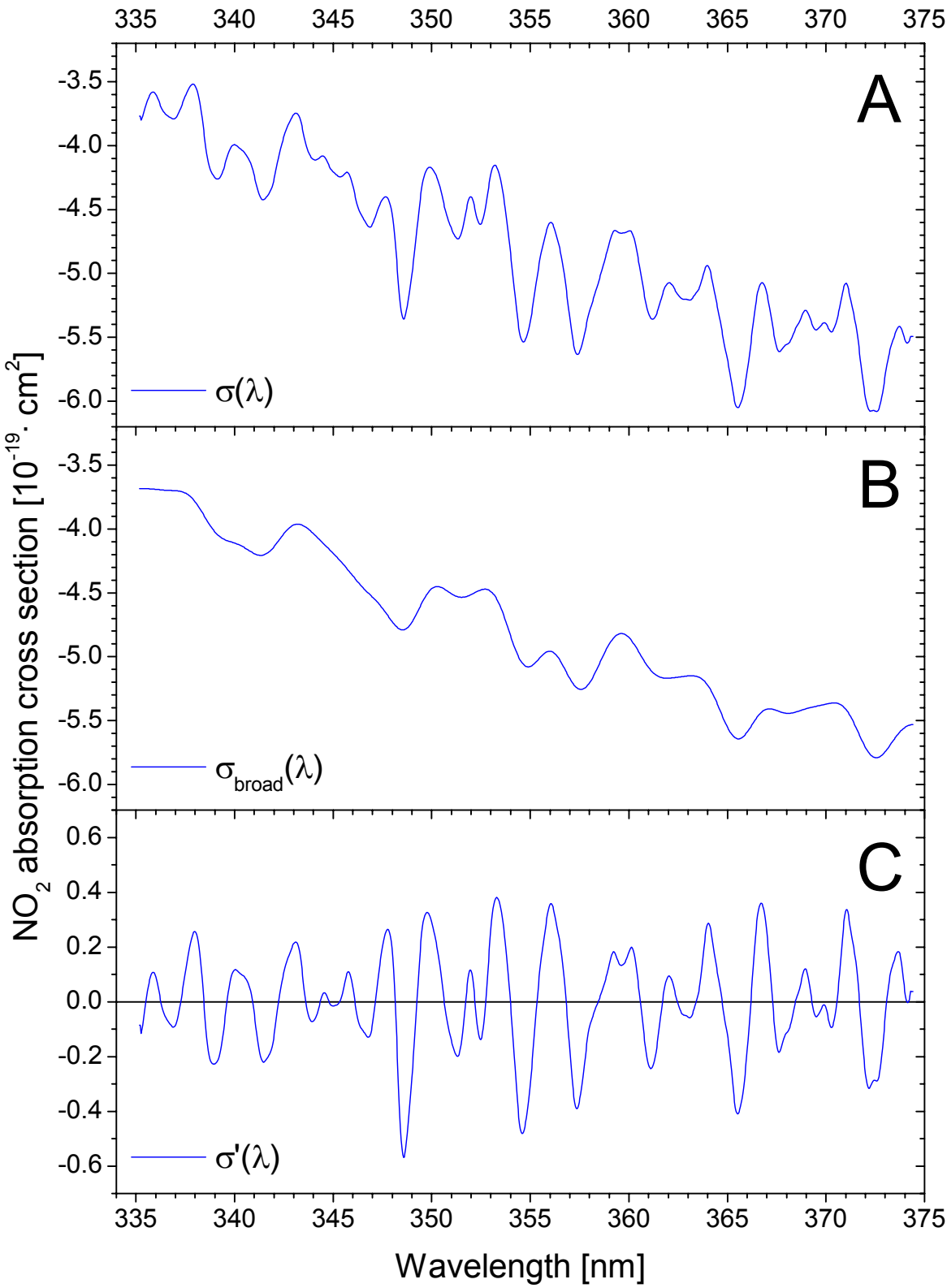

Figure 11: Effect of the high-pass algorithm on the total absorption cross section (panel A), exemplified by the NO_2 cross section. The smoothed cross section (panel B) contains only the broad-band structures. The narrow-band differential absorption cross section σ'(λ) (plotted in row C) is obtained by dividing the original by the smoothed spectrum (i.e. row A / B).

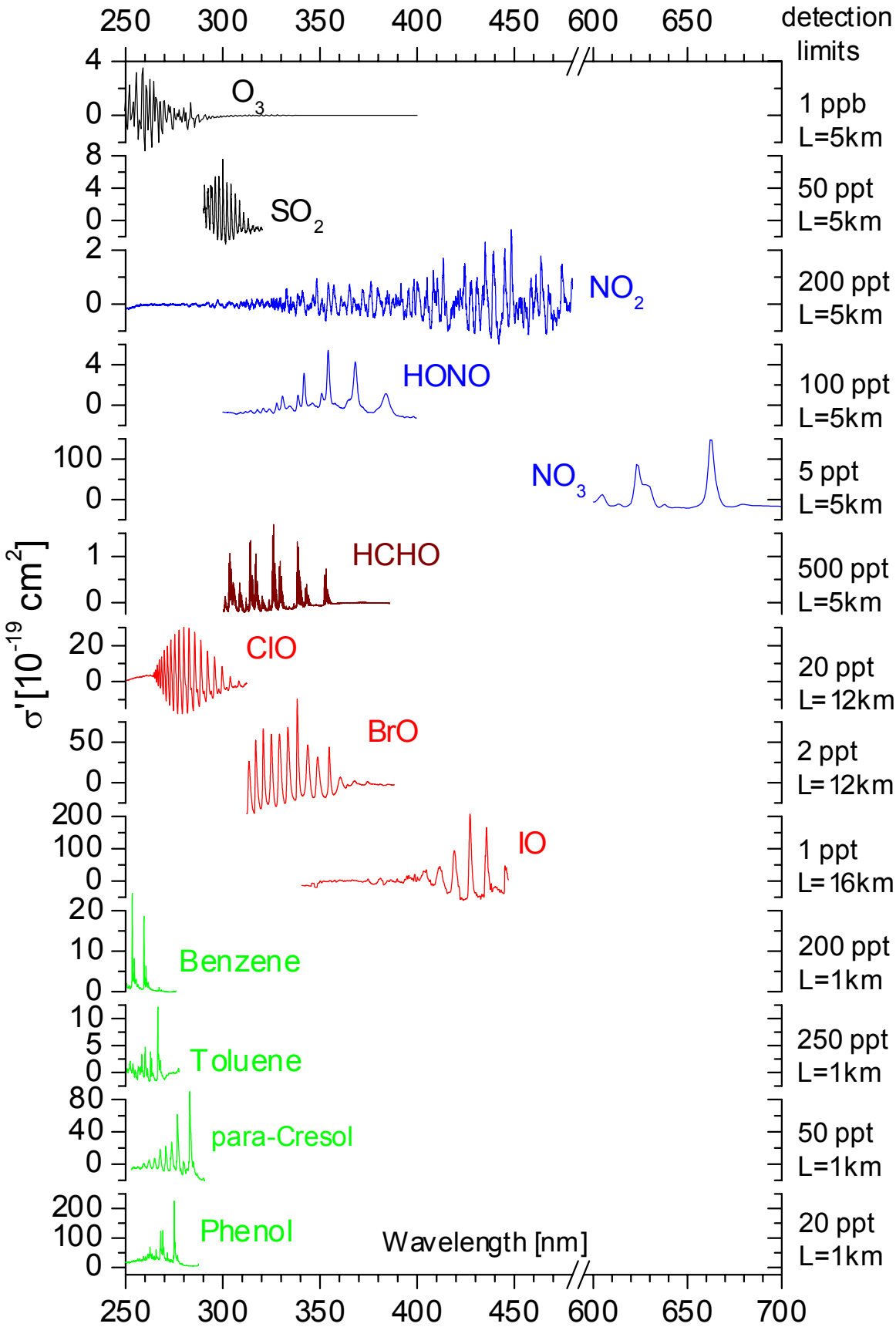

Figure 12: Differential absorption cross sections σ'(λ) of selected atmospheric trace gases measurable by the DOAS technique. For the calculation of the detection limits on the right side a minimum detectable optical density of 10^{-3} and the indicated light path lengths were assumed.

4.4 Retrieval of trace gas profiles from LP-DOAS data

4.4.1 Plane-parallel model with fixed layer heights

As LP-DOAS measurements yield only the mean concentrations integrated over the three light paths (see Equ. 28), a simple model can be used to compute vertical profiles from LP-DOAS measurements to reflectors mounted on different heights (see Figure 13). The boundary layer is divided into layers with upper / lower limits defined by the reflector heights. Assuming the vertical concentration gradient is constant or linearly decreasing or increasing in each layer, the mean concentrations c_i in the layers can be calculated from the mean concentrations $\bar{c}_i$ measured over the light paths. The concentration in the lowermost layer is measured directly:

$$c_1 = \bar{c}_1 \qquad \text{Equ. 47.}$$

For the following light paths, the measured concentrations are assumed to be composed of the mean concentrations in the layers passed en route to / from the respective reflector. The concentrations are summarised and weighted by the height of the respective layer:

$$\bar{c}_i = \frac{1}{h_i} \cdot \sum_{i=1}^{m} c_i \cdot (h_i - h_{i-1}) \qquad \text{(for a set-up of } m \text{ light paths / layers)} \qquad \text{Equ. 48.}$$

If this system of equations is solved to yield the mean concentrations in the layers, it is obvious that the concentrations in the layers can be calculated using only the measured mean concentration and the reflector heights of the current and the previous light path:

$$c_i = \frac{\bar{c}_i \cdot h_i - \bar{c}_{i-1} \cdot h_{i-1}}{h_i - h_{i-1}} \qquad \text{Equ. 49.}$$

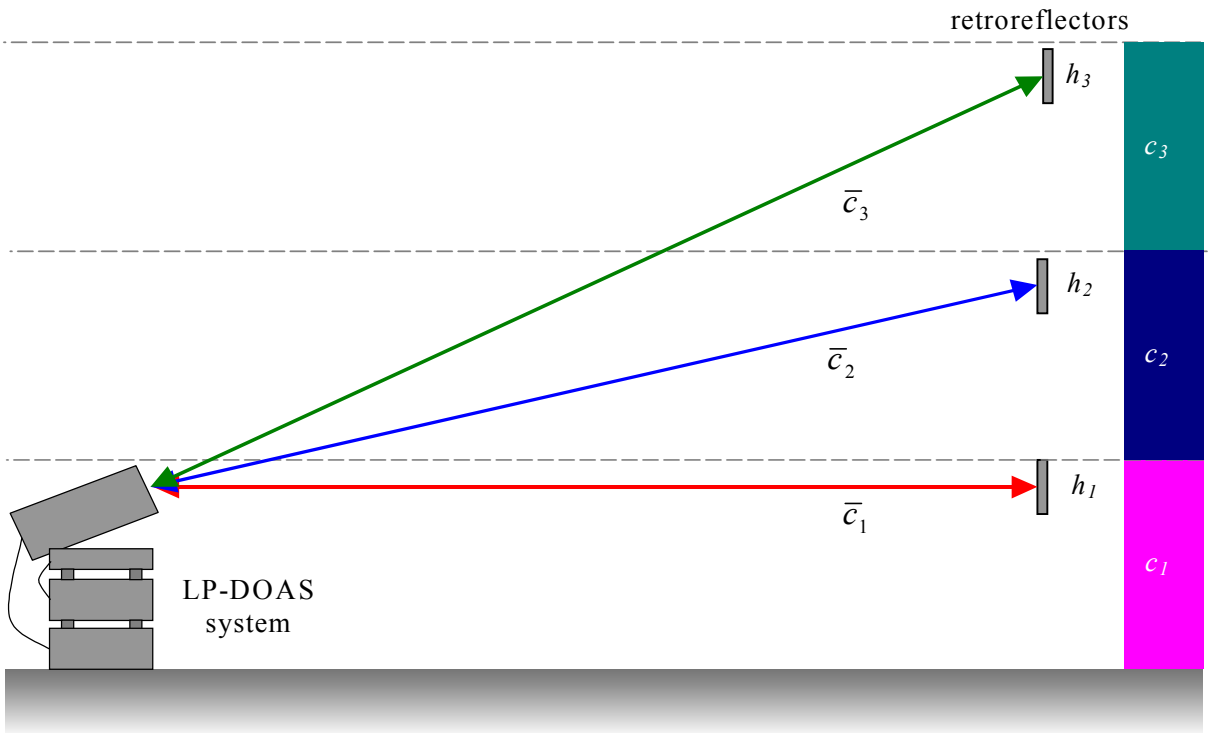

Figure 13: Retrieval of vertical profiles from LP-DOAS measurements on multiple light paths: the mean concentrations $\bar{c}_1, \bar{c}_2, \bar{c}_3$ measured subsequently are computed into the mean concentrations c_1, c_2, c_3 in the layers defined by the reflector heights h_1, h_2, h_3.

The errors of the mean concentrations c_i can be calculated neglecting the errors of the reflector heights, as these can be measured with high precision:

$$\Delta c_i = \sqrt{\left(\frac{\Delta \bar{c}_i \cdot h_i}{h_i - h_{i-1}}\right)^2 + \left(\frac{\Delta \bar{c}_{i-1} \cdot h_{i-1}}{h_i - h_{i-1}}\right)^2} \qquad \text{Equ. 50.}$$

This algorithm yields not only the maximum height resolution that can be obtained from the measurements, it can also be adapted to the measurement geometry very easily, which is important especially for the balloon experiments.

4.4.2 Effects of temporal and spatial variations in the observed air mass

Horizontal means over temporal and spatial concentration changes

DOAS measurements are performed on a light path of several hundred to several thousand meters with time resolutions of 1 to 10 min. This contrasts with the classical approach for measurements of trace gas concentrations at a single point with averaging times of about 5 – 60 minutes. Consequently, trace gas concentrations measured by DOAS always represent an average value over a large air mass in time and space. However, point measurements also yield an average over time and space, as the horizontal wind system transports an usually inhomogeneous air mass past the sampling inlet of the measurement device during its sampling time.

For a typical set-up of a LP-DOAS system with a distance between telescope and reflector of 2 km and a very low tropospheric wind speed of 1 m/s, the horizontal averaging time for the observed air mass will be about 30 minutes along the light path. As the integration times for a DOAS system are in the range of 1 – 10 minutes, this value adds up to the averaging time. Additionally, the measurement indicates not only a temporal mean of the observed air mass, but also a spatial mean over the area which is defined by the light path length and the horizontal wind velocity times the integration time. The averaging over both temporal and spatial variations of the concentration is an advantage in situations when strong local variations would distort the overall picture of the atmospheric processes. This is particularly important as a time resolution of some minutes is sufficient to describe most processes taking place in the atmosphere from the measurements. (see also [*Stutz et al.*, 2001])

Computation of the temporal means

When the concentrations on the light paths are carried out consecutively, there is a temporal spacing between the measurements which inhibits the direct calculation of vertical profiles and the evaluation and distinction of chemical and physical processes in the PBL. Therefore the measured data were brought to a common timeline with a constant spacing between the measured concentrations. This was realised by a linear interpolation between the measured values. The errors caused by this interpolation are dominated by the errors of the single measurements, which were used to compute the error for the interpolated concentrations by Gauss error propagation.

5 Set-up for the measurements in Heidelberg

The major field campaign carried out within this work was the measurement of vertical profiles on fixed light paths above the city of Heidelberg over a time period of about 1½ years. The measurements were performed with a semi-commercial LP-DOAS system, which was constantly upgraded to improve its reliability and data quality. This chapter presents the characteristics of the instrument, the evaluation algorithm used for the evaluation of the spectra and a detailed estimation of the errors for the measured trace gas concentrations. Finally, the sources and quality of the additional meteorological and trace gas data will be are discussed, as these data-sets have been used for the interpretation of the LP-DOAS measurements.

5.1 Set-up of the light paths

For the long-term measurements of vertical trace gas gradients, three light paths were established, all running over the city of Heidelberg. A schematic picture of the measurement set-up is given in Figure 14. The DOAS instrument was situated at the Institut für Umweltphysik (IUP) in the north-west of the city. Retro reflectors were set up on a steeple in the old town (1), at a hotel halfway up (2) and on the radio tower on top of the Königsstuhl mountain (3). Total light path lengths ranged between 4.2 km to the steeple and 8.4 km to the radio tower. The reflectors were situated at heights between 10 m and 470 m above ground level (see Table 7). The orientation of the light paths allowed measurements over the city with its main roads.

Measurements started in late December 1999 and lasted until early March 2000 with interruptions totalling approximately 15 weeks for maintenance work, tests of improved components and the balloon campaigns, which were performed with the same instrument. Other short-term interruptions of the measurements, especially in autumn and winter, were caused by bad weather conditions. Particularly the upper reflector on the Königsstuhl was frequently concealed by clouds. Measured species were NO_2, HONO and HCHO. The detection limits of NO_2 and HONO, which are of particular interest in this thesis, are given in Table 7.

Table 7: Characteristics of the three light paths established in Heidelberg. The light path lengths are given as the double distances to the reflector, which is the actual absorption path in the atmosphere. The reflector locations are listed as height above ground and as height interval Δ_{height} between the DOAS instrument and the reflector. The detection limits are the mean values for a period of 5 weeks.

reflector	light path length	reflector		detection limit [ppb]	
	[m]	height [m]	Δ_{height} [m]	NO_2	HONO
steeple (1)	4210	10	-11 m	0.41	0.22
hotel (2)	6090	180	159 m	0.26	0.14
radio tower (3)	8424	469	448 m	0.18	0.09

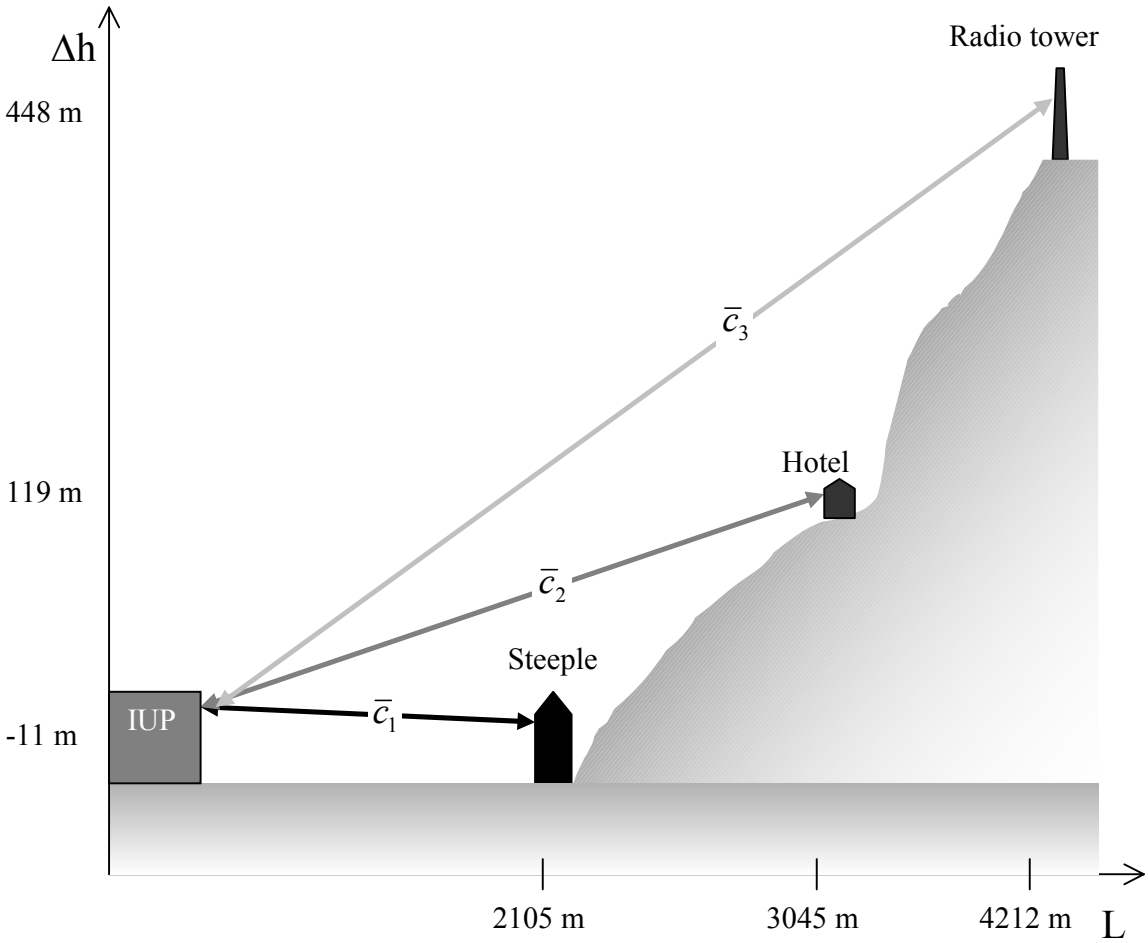

Figure 14: Light paths for the vertical profile measurements in Heidelberg: given here are distances to the reflectors and their heights with respect to the DOAS instrument. The measured concentrations are labelled $\bar{c}_1, \bar{c}_2, \bar{c}_3$.

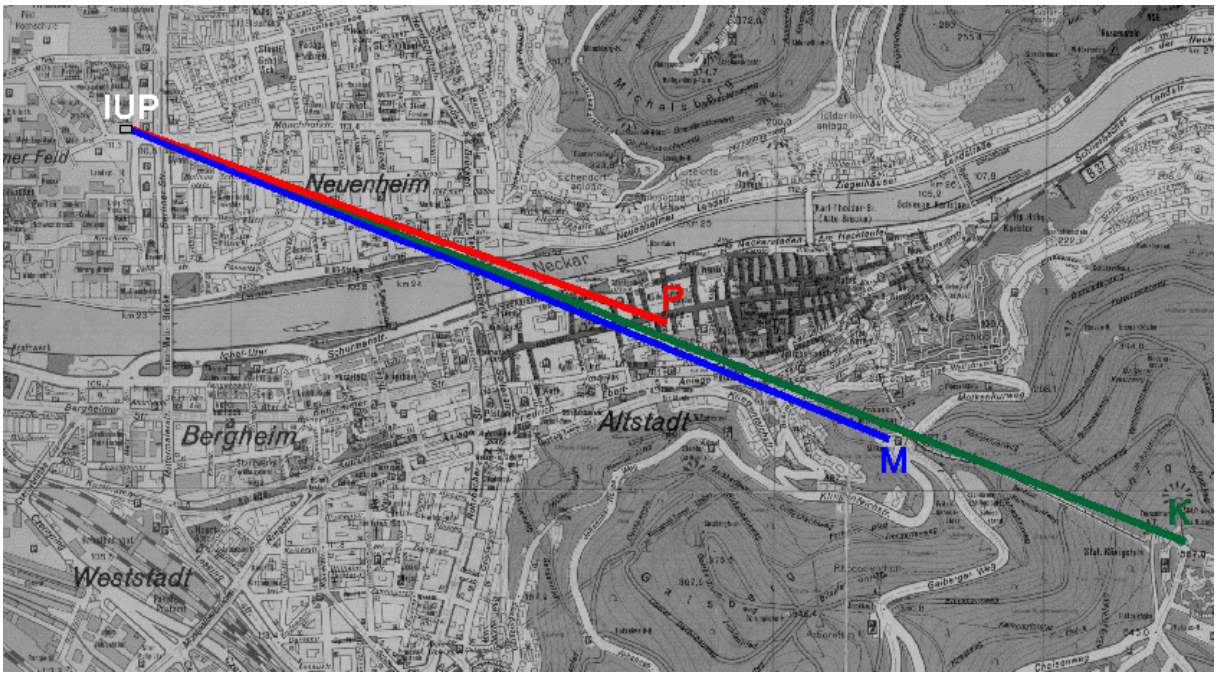

Figure 15: Geographical overview of the light paths starting form the institute building (IUP) to the Providenz church (P), the Hotel Molkenkur (M) and the radio tower on the Königsstuhl (K).

5.2 The HMT-DOAS

The DOAS system presented here was developed in close cooperation with Hoffmann Meßtechnik (HMT), Rauenberg / Germany, and will therefore be referred to as HMT-DOAS. In the following, the components of this system will be discussed in detail.

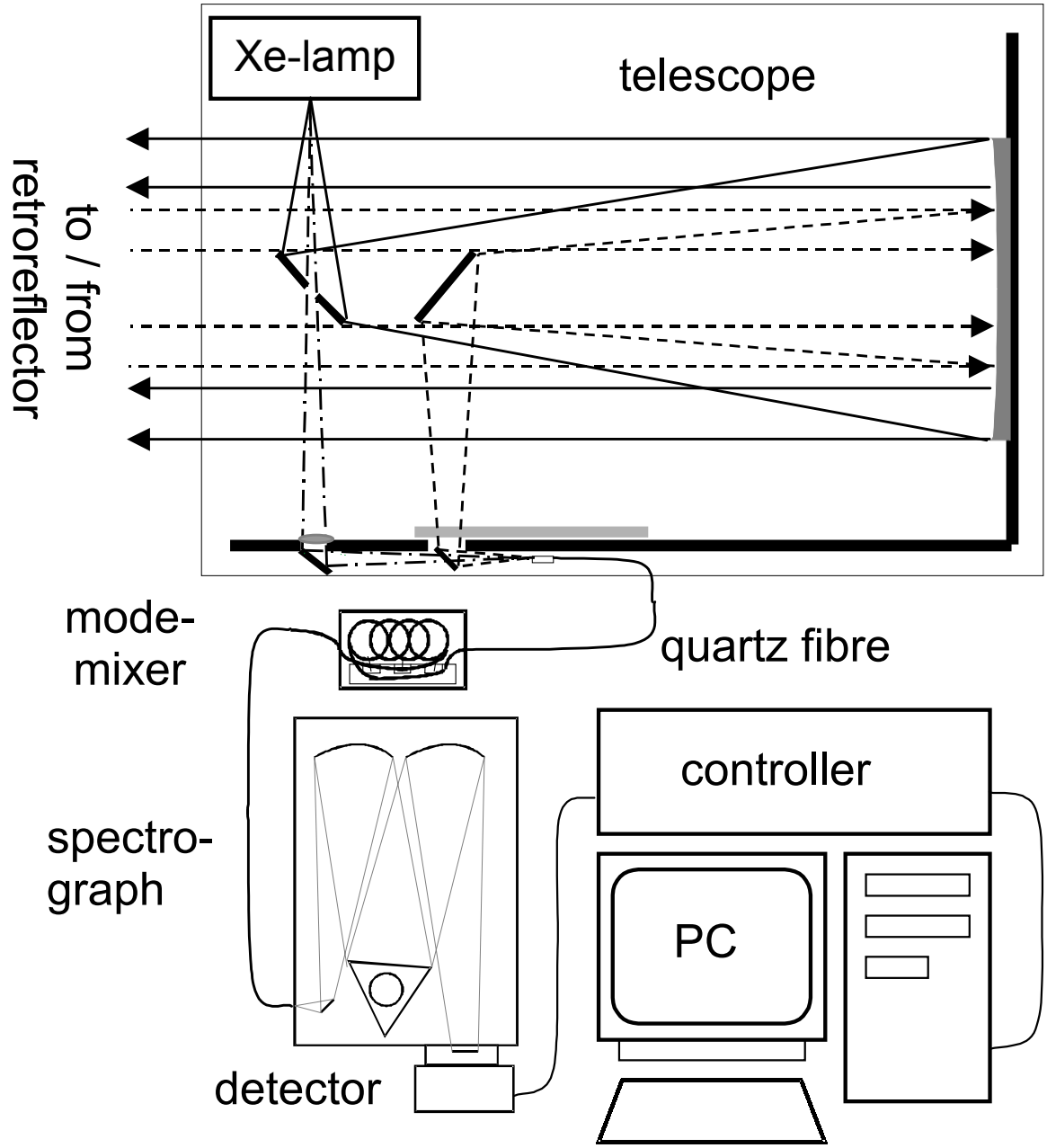

Figure 16: Schematic set-up of the HMT-DOAS instrument: drawn lines represent the light emitted by the lamp and sent to the retro reflectors. The dashed lines show the backscattered light focused on the quartz fibre by the receiving section of the telescope. The light rays used for the shortcut system are plotted in dash/dotted lines.

5.2.1 Telescope and light source

The optical set-up has been kept relatively simple, allowing adjustments only in the essential parameters of the telescope and the spectrograph/detector unit. This results in a reliable and stable instrument which needs only a minimum of maintenance and readjustment.

Light source

The light artificial light source that was used for the measurements were Xenon high pressure short arc lamps. Within these lamps, a light arc of less than one millimetre diameter between anode and cathode is produced from a high voltage ignition discharge which plasmasises the Xenon gas. Therefore, the spectrum of such a Xe arc lamp is the sum of thermal emission according to Planck's law and single Xe emission lines, which are broadened by pressure and temperature. The distance of the electrodes is generally kept small to generate a small arc length and therefore increasing the luminous density. The pressure inside the lamp is very high (up to 100 bar under operation conditions) yielding a high local light intensity. The colour temperature of the Xe lamps used is about 6000 K, which is similar to that of the sun. The flask of a Xe lamp consists of a quartz glass, and therefore extremely resistant to high pressures and temperatures. The electrodes are made from tungsten with endowments depending on the lamp type. The cathode has an edged peak to enhance the electron emission whereas the anode is round-shaped and made from a massive material to absorb the kinetic energy of the incoming electrons.
For the measurements made within this thesis, Xenon arc lamps with a 300 W power uptake of the type XBO 301 B produced by Narva, Gesellschaft für lichttechnische Erzeugnisse mbH, Berlin/Germany, were used. These lamps feature some distinct properties such as a very small "hot spot" of the arc that emits a very high light intensity coupled with a relatively specified long lifetime of 500 hours. Table 8 presents a brief overview of the characteristics of three lamp types used at the IUP. A detailed comparison with other lamp types used for LP-DOAS measurements was performed by [*Hermes*, 1999]. The variability of the emission features caused by flaring lamp plasma was also studied: Xe emission lines were found at several wavelengths from the near UV to the red spectral region. The emission strength and pressure broadening of the Xe lines changes over time, which makes it difficult to remove the lamp structures are difficult to remove from a spectrum. To allow the direct measurement of these structures, a short cut system was implemented in the telescope, which is presented in the next section. The treatment of lamp structures in the spectra evaluation process is discussed in chapter 0.

Table 8: Specifications of different Xe arc lamps [*Hermes*, 1999].

lamp type	Narva XBO 301 B	Osram XBO 450W	Hanovia 959C-1980
power uptake [W]	300	450	500
typ. voltage [V]	17.5	17	17
typ. current [A]	17	25	29
lifetime [h]	500	2000	200
light arc size [mm]	0.3 × 0.2	2.7 × 0.9	0.3 × 0.3

Optical set-up and kinematics of the telescope

The kinematics of the HMT-DOAS-telescope includes four stepper motors that are installed in the telescope:

- Two motors are used to align the telescope on the different retro arrays (or to follow the reflectors mounted on the balloon) in horizontal and vertical direction.
- The third motor drives the lamp shortcut system (see below).
- One stepper motor carries a filter wheel that is attached to the telescope hull on the other side of the shortcut system. For the measurements presented here, the filter wheel was not used.

The steppers are connected to the HMT-controller and steered by the measurement software MFC (see [*Gomer et al.*, 1996]) or DOASIS (formerly WINDOAS, see [*Kraus*, 2001]). It is noteworthy in this context that the controller enables only the movement of one motor at a time, which restricts the flexibility of operation (especially for the balloon operations discussed in chapters 8 and 9).

The long path telescope consists of two coaxial Newtonian telescopes with transmitting and receiving optics combined in one device: in the optical axis[11] of the telescope two elliptical plane mirrors are mounted that reflect the light by + / – 90 degrees from the optical axis for the outgoing and incoming beams, respectively. The parabolic main mirror has a diameter of 200 mm and a focal length of 600 mm. A special feature of the HMT-DOAS is the adjustable mounting of the main mirror, which allows moving the main mirror forward and backward along the optical axis by about ± 10 mm. This enables the partial correction of the beam divergence generated by the transmitting telescope: as the light source is placed in one focal point of the main mirror, the outgoing light beam would be parallel, if the light source were point sized. The arc size of the Xe lamps used, however, has a diameter of 0.2 to 0.3 mm, causing a divergent beam. This divergence can be minimised by focusing the image of the lamp arc in the plane of the reflectors, which is done by adjusting the main mirror along the optical axis of the telescope. The resulting beam profile is significant for the light throughput of the system: an ill-aligned transmitting telescope yields a loss of signal intensity of several magnitudes. However, the difference in the main mirror position for the optimum adjustment between two light paths to reflectors in a distance of about 2000 m and 400 m was in the range of below one millimetre. It is important to notice at this point that the beam sent to the reflectors is not a full circle, but is shaped as a ring due to the Newton mirrors in the optical axis. The shape and size of the transmitted beam changes constantly on the way to the reflectors, not only due to beam divergence caused by the finite lamp spot size, but also to turbulence in the atmosphere. A detailed description and a mathematical approximation of the beam divergence can be found in [*Rudolf*, 1993; *Stutz*, 1996].

The specifications of the retro reflectors positioned at a distance of several hundred meters to several kilometres from the telescope guarantee a maximum deviation of the returned beam from the original below 2’’. For measurements on fixed light paths, the reflectors are aligned to meet the optical axis of the beam by hand once when setting up the reflectors. Effects of changing orientation of the reflectors to the beam axis generally occur only using a flexible light path and will be discussed in detail in chapter 8. The returning beam is also divergent, which is caused by atmospheric turbulence, but also by interference at the opening of the reflectors and inaccuracies of the reflectors causing deviations in the directions of received and backscattered light. An exact mathematical description of these processes is not possible, but a resulting Gauss-shaped beam profile enlarged by a factor of two could be measured at the receiving telescope (see also chapter 8.5.3 and [*Stutz*, 1996]).

[11] Defined as being perpendicular to the centre of the parabolic main mirror.

In the second focal point of the telescope unit, the light reflected from the retro reflectors is sent through a quartz fibre by the slightly smaller elliptic mirror nearer to the main mirror The optical layout both of the receiving telescope and of the quartz fibre connecting it to the spectrograph is optimised for the numerical aperture NA = 0.12 of the spectrograph to minimise the loss of light intensity.
A thorough evaluation of the light throughput of the telescope and a comparison to other systems used at the IUP can be found in [*Kah*, 1998].

Shortcut system

As Xenon arc lamps are known to feature significant spectral structures varying in a time scale below 5 min, the telescope is equipped with an optical arrangement to measure lamp spectra directly. A new optical layout for this "shortcut system" has been developed within this work, using a circular opening in the Newton mirror in front of the lamp, a quartz lens and a plane mirror transmitting the lamp light on the quartz fibre (see Figure 16).
The shortcut system uses a sledge driven by a stepper motor that is mounted on the side of the telescope hull. Moving the sledge upwards and downwards generates different beam geometries for the measurement of atmospheric, direct lamp light and reference gas cell spectra, respectively. Figure 18 depicts the shortcut system in the operating mode used for the measurement of atmospheric spectra: the light from the reflectors is focused on the quartz fibre by the receiving Newtonian mirror and the mirror mounted on the lowermost position of the shortcut sledge. In this position, the latter mirror also blocks the direct lamplight which is sent through the lens tube in the other hull opening and another mirror. In Figure 19, the set-up for the measurement of lamp spectra is shown: now the shortcut sledge has moved down, the light from the lamp is focused by the opening in the sending Newtonian mirror, the quartz lens and the 45° mirror on the quartz fibre. For reference cell measurements, the same geometry is used, but the sledge moves further downwards to let the direct lamp light through gas cells 1 or 2. It is also possible to mount an mercury emission lamp on one of these positions to determine the spectral resolution and wavelength calibration at several times during the measurements
The advantage of this system is that it is insensible to optical de-adjustment, as the sledge moves perpendicularly to the optical axis. Additionally, an end switch is used to control whether the sledge is in the position for the measurement of atmospheric spectra. This is also the reference position for all other beam geometries used during the measurement cycle.
The shortcut system has proved to be of crucial importance for the quality of the measured data: especially sensitive HONO measurements were only possible if a lamp reference spectrum was available for every atmospheric spectrum (or was at least taken within an hour before or after the atmospheric spectrum).

Quartz fibre and mode mixer

The light from the telescope is transmitted to the spectrograph by a quartz fibre to ensure a stable illumination of the grating and the PDA independent from the telescope orientation. The standard quartz fibre installed in the HMT-DOAS is a multi mode step-index fibre with a numerical aperture of 0.12. A general problem of the use of quartz fibres for light transmission in LP-DOAS instruments are interference fringes produced by the total reflections within the fibre: as the light leaves the fibre, interference patterns in the shape of concentric circles and rings featuring different light intensities can be observed. [*Stutz and Platt*, 1997] found that heterogeneous illumination of the grating and the *PDA* leads to a higher residual noise compared to a uniform illumination. To compensate this effect, a quartz fibre mode mixer described in [*Stutz and Platt*, 1997] was installed to the system in April 1999.

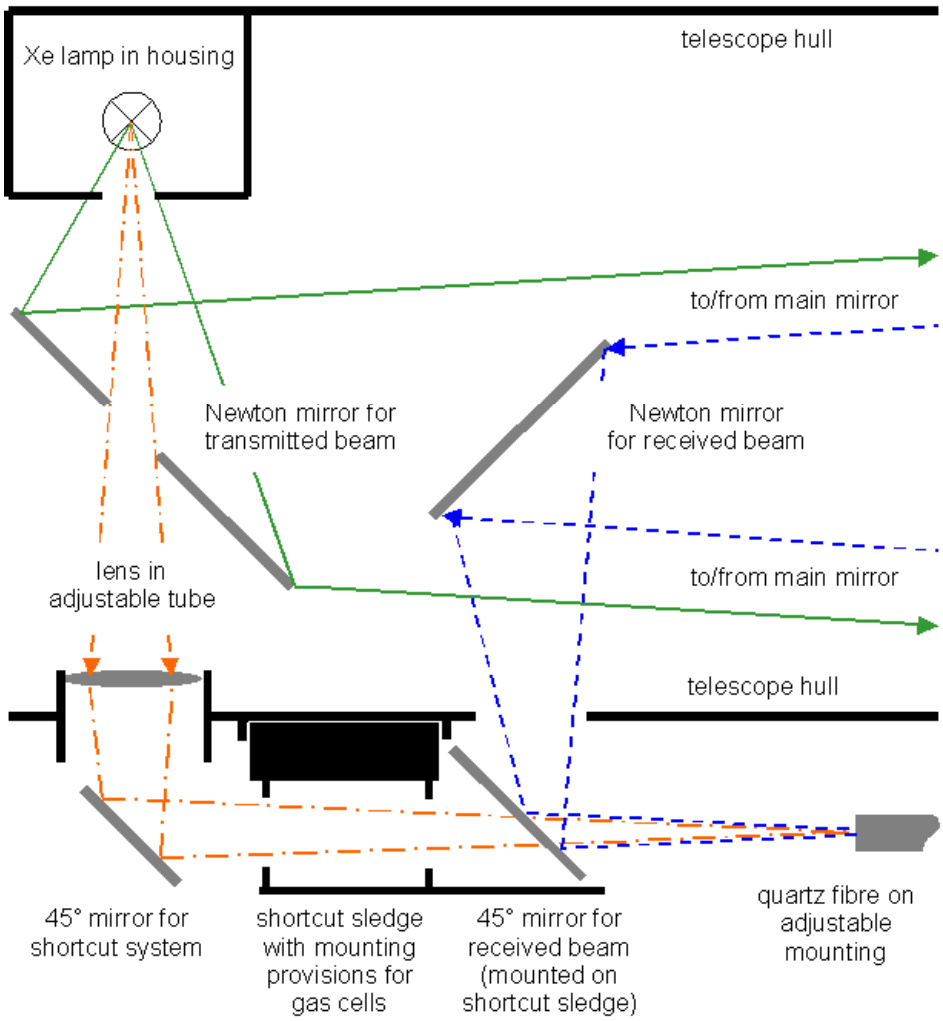

Figure 17: Schematic set-up of the shortcut system of the HMT-DOAS: optical elements are shown in grey. The light rays used for the shortcut system are plotted in colour. The "shortcut sledge" moves up and down perpendicularly to the plotting plane from the top-view perspective shown here.

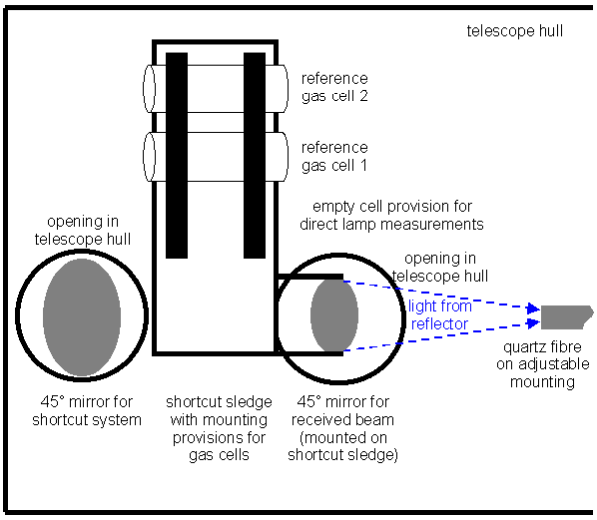

Figure 18: Side view of the shortcut system while measuring atmospheric spectra

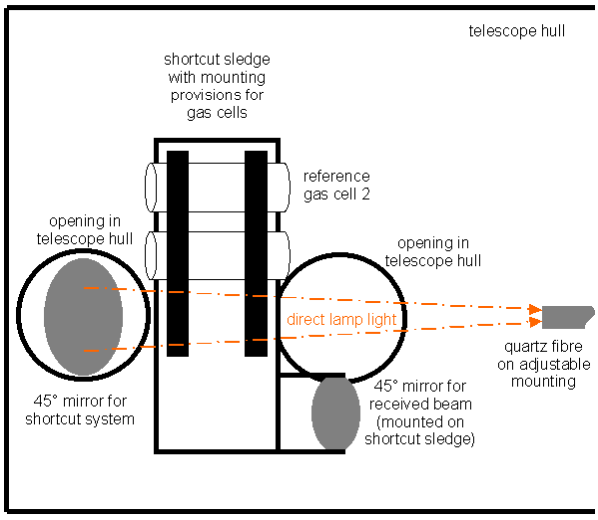

Figure 19: Side view of the shortcut system while measuring lamp spectra

5.2.2 Spectrograph

The spectrograph used for the measurements in this work was an *ACTON Spectra Pro 300i*. This device is based on a set-up originally developed by Czerny and Turner in the year 1930 [*Czerny and Turner*, 1930]: as the fibre itself forms a pinhole of 200 µm diameter, no entrance slit was used for the measurements. Instead, the quartz fibre was mounted fixed directly at the spectrograph entrance, in the focal plane of the first convex mirror. Paralleled by the spherical mirror, the light is reflected to a plane diffraction grating. A second convex spherical mirror focuses the dispersed light onto the detector.
The focal length of the spectrograph is 300 mm, its aperture is 1:4 (i.e. NA = 0.12). The dispersion of the grating (1800 grooves/mm) used is 1.54 nm/mm corresponding to 0.038 nm/channel on the photo diode array (see following section). The centre wavelength of a spectrum can be changed automatically by a computer controlled stepper motor.
The spectrograph is isolated and its temperature stabilised by electrical heating (typically at 30°C) to minimise optical errors due to temperature changes.

Table 9: Characterization of the spectrograph-detector unit used for the vertical profile measurements.

offset [cts./scan]	dark current [cts./sec]	electronic noise [cts./$\sqrt{\text{scans}}$]	1σ-residual noise [arb. units]	diode structures [arb. units]	resolution at 362 nm
584	1.3 – 2.4	3.23	$4 \cdot 10^{-5}$	$(2.9 - 7.7) \cdot 10^{-2}$	$0{,}93 \cdot 10^{-3}$

5.2.3 PDA detector unit

The detector unit is mounted in the focal plane of the spectrograph. The principal component of the unit is a photo diode array (PDA) produced by Hamamatsu (type S3904-1024) consisting of 1024 Si photo diodes (CMOS) of 25 µm width and a height of 2.5 mm. The PDA is placed in an evacuated housing filled with 1.2 bar Argon 5.0. A Peltier cascade is used to cool the PDA down to temperatures of -30 °C. The capacity of a diode is 10 pF, the full well depth corresponds to 1.286 x 10^8 photo electrons. A detailed discussion of the usage of photo diode arrays as DOAS detectors is given by [*Stutz*, 1991; *Stutz and Platt*, 1992]. For a brief overview, the key data that characterise the spectrograph-detector unit is presented in Table 9.

Mode of operation

Every photo diode consists of a n-p semiconductor junction: prior every measurement, an inverse voltage of 2.06 V is applied to the diode inducing a depletion layer which is almost as large as the whole diode area.
At the beginning of the measurement, the PDA is disconnected from the power supply. Subsequently, the incoming light excites a number of electrons proportional to the light intensity into the conducting layer of the semi conductor. These mobile charge carriers reduce the applied inverse voltage. However, the same mechanism works also via thermally activated electrons transiting into the conducting layer. This effect is called dark current and must be considered in the evaluation procedure, especially at low light intensities. In order to reduce the dark current, the PDA was cooled down to a temperature of -15 the Peltier cascade. Thereby the dark current decreases exponentially regarding the Stefan-Boltzmann-law. In addition to its temperature dependence, the dark current is known to depend on integration time, and on signal operation of the diode array (see e.g. [*Stutz*, 1996]).
As soon as the intended integration time is over, the PDA is read out by reconnecting it to the

power supply and measuring the current caused by the rechargement of the PDA. The resulting signal of a scan is amplified electronically within the detector unit. An offset signal is added to every PDA signal to exclude negative signals under low light conditions. This offset signal is proportional to the number of scans added up to a spectrum and must be corrected for in the evaluation process. The signal is digitised by a 16 bit analogue-digital converter (ADC, full saturation corresponds to 2^{16} = 65536 counts) and then transferred to the computer.

A thin protective silicon oxide layer on the diodes leads to a Fabry - Perot etalon structure in the spectra (see [*Stutz*, 1991]). This structure is caused by the interference of multi reflected light beams inside this surface layer. Additionally, water vapour can freeze on the PDA due to the cooling of the detector unit and can also cause an etalon structure . To minimise this effect, the detector is evacuated and filled with dry argon.

Another effect of PDAs is the so-called memory effect: intense spectral structures can appear in the spectra recorded afterwards for some time (some seconds to some minutes, depending on the PDA temperature [*Veitel*, 1997]). This effect was also discussed in detail by [*Stutz*, 1996]. Its origin is still unclear . T he memory effect can usually be reduced significantly by multiple scans without light (or with very short integration times) or just by waiting for a short while.

Spectral resolution of the instrument

To compute the spectral resolution and the dependency between diode number of the PDA and the wavelengths, emission spectra of Ne and Hg high pressure lamps are recorded. Fitting a polynomial of second order to the central wavelengths plotted against the corresponding diode numbers of the line centres, yields the dispersion relation

$$\lambda(j) = 374.41\,\text{nm} - (0.0375\,\text{nm} \cdot j) - (8{,}3 \cdot 10^{-7}\,\text{nm} \cdot j^2) \qquad \text{Equ. 51,}$$

which slightly changes with time in shift and squeeze i.e. in the zero and first order constants due to thermal expansion and compression of the spectrograph-detector unit. The width of a single emission line yields the width of the instrument function and therefore the minimal spectral distance between two absorption/emission lines that can be positively distinguished from each other with the instrument. Now, the spectral resolution can be computed using the FWHM of such a line (in nm) as $\Delta\lambda$: the detector – in combination with the holographic grating of 1800 grooves / mm installed in the spectrograph– features a spectral resolution ($\Delta\lambda/\lambda$) of $0{,}93 \cdot 10^{-3}$ at 362 nm and a spectral window ranging from 336.0 to 374.4 nm.

Offset

The mean offset was determined by adding up 1000 scans taken at the minimum integration time (100 ms) at dark conditions. This spectrum contains the signal of 1000 offsets and a dark current of 100 s. As stated below, the ratio of both signals is larger than $1{:}10^4$. Thus dark current can be neglected in this spectrum.

The mean offset signal averaged over all 1024 diodes for the whole measurement campaign in Heidelberg from January 1999 until February 2000 was 584 counts/scan. The offset signal was measured routinely, at least once in the lifetime of a lamp. The maximum value for the average was found in January 1999 at 596 counts/scan, the minimum value in February 2000 (see Figure 20). Neither a clear trend of the mean offset signal with time nor a dependence of the residuals or detection limits of the evaluation procedure on the offset level or structure could be found (see chapter 0).

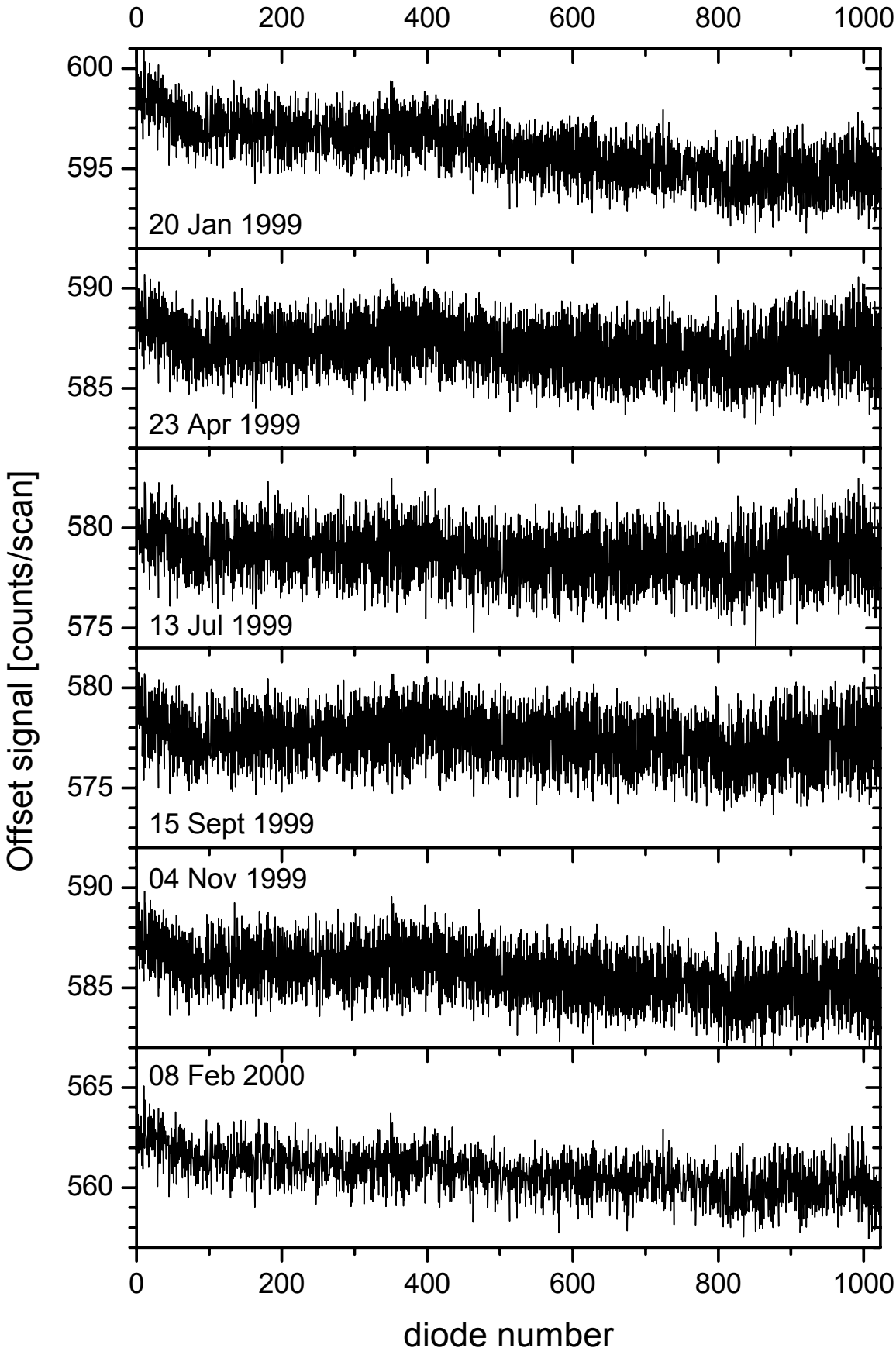

Figure 20: Selected offset spectra measured during the long-term campaign in Heidelberg.

Dark current

The dark current was determined by the measurement of a spectrum with an integration time of 300 sec with a single scan in dark conditions. Subsequently, the offset signal was corrected for. The resulting dark current spectrum contains only the signal generated by thermal transitions of electrons in the conducting layer. The mean dark current signal averaged over all diodes was 1.35 counts/scan immediately after evacuation and re-filling of the detector with argon and rised to 2.41 counts/scan 7 months later. These two spectra are displayed in Figure 21. Obviously, several diodes feature a peak dark current signal, which can be attributed most likely to endowment errors of these diodes, because these peaks do not change with time after evacuation and re-filling of the detector. Additional to the increase of the mean dark current, the spectrum taken 7 months later also shows distinct structures that feature a width of 5 to 20 diodes. These structures are due to a thin layer of water and dirt that remains after the evacuation or leaks into the detector by leakages and thenfreezes on the surface of the PDA. Besides their effect on the dark current, structures due to dirt in the PDA have a strong influence on residuals of the fitting algorithm, which will be discussed later.
The dark current was also found to decrease slightly with increasing saturation of the PDA (see e.g. [*Alicke*, 2000; *Stutz*, 1996]). But this can be neglected in the evaluation procedure as the resulting error is generally smaller than the errors of the fit.

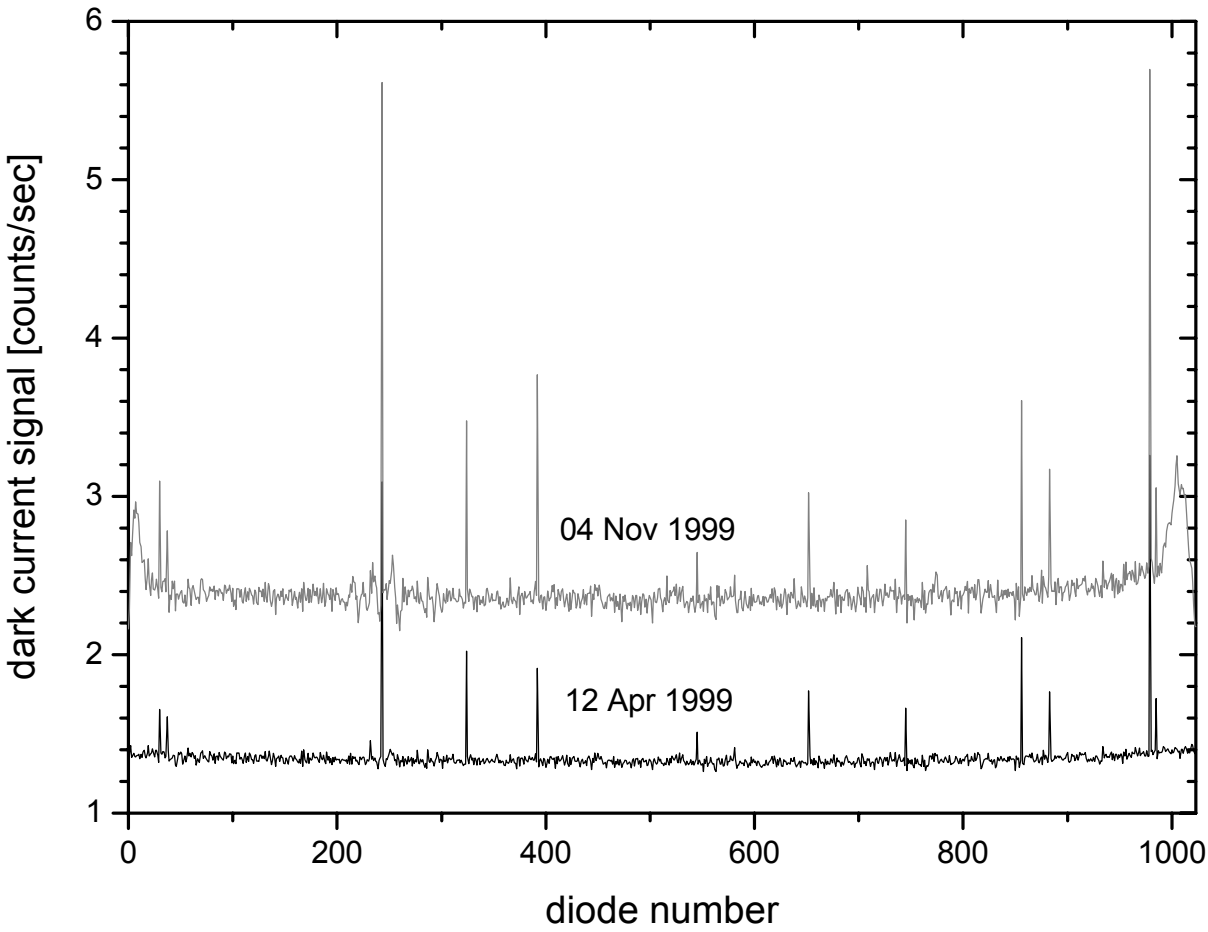

Figure 21: Dark current spectra measured immediately after (black line) and 7 months after (grey line) detector evacuation and refilling. Both spectra are plotted on the same y-axis to demonstrate the increase of dark current with time.

Residual Noise

The residual noise of one spectrum consists of two different noise signals:

- Electronic noise due to the resolution of the digitalisation, the noise of the ADC, and of other electronic components; The electronic noise level can be determined by subtraction of two offset spectra (see above) from each other. Subsequently, the root mean square (RMS) of the difference spectrum is calculated, which corresponds to the 1σ noise. It is remarkable that the peak to peak residual structure is generally found to be 6 - 7 times higher than the RMS of the spectrum. In order to obtain the electronic noise of one scan, the RMS is divided by the square root of the total number of scans.
  For this instrument, an electronic noise signal of 3.23 counts per scan was detected, which is well in the range measured with other detector and controller systems of the same type.
- Photon noise is another source of noise in a measured spectrum: According to Poisson statistics, the mean photon noise signal equals the square root of the number of photons. Considering the well depth of the single diodes of the PDA (1 count = 1962 photo electrons), the photon noise (1σ) of a spectrum with 10^4 or 10^6 counts would be $2.3 \cdot 10^{-4}$ or $2.3 \cdot 10^{-5}$, respectively.

Photon noise and electronic noise must be added up in order to establish the total residual noise, which can be determined experimentally by the division of two (offset-corrected) spectra scanned one after the other with the same integration time. A very stable halogen lamp was used as the light source for these measurements. The lamp light was transmitted into the spectrograph by the standard quartz fibre, including the mode mixer. It should be noted here that the use of a quartz fibre (even if a mode mixer is included) to transmit the light to the spectrograph generally increases the residual noise. This might be caused by the partial illumination of the PDA (200 µm quartz fibre diameter compared to 2.5 mm *PDA* height) [*Stutz*, 1996]. In order to remove broad-band lamp structures from the resulting spectrum a high pass filter (800 times binomial smoothing) was applied. Subsequently, the residual structure (1σ) can be calculated for this spectrum. Figure 22 shows the resulting variation of residual noise with the number of counts for the detector. As expected from the Poisson theory presented above, the noise decreases with the square root of the number of counts.

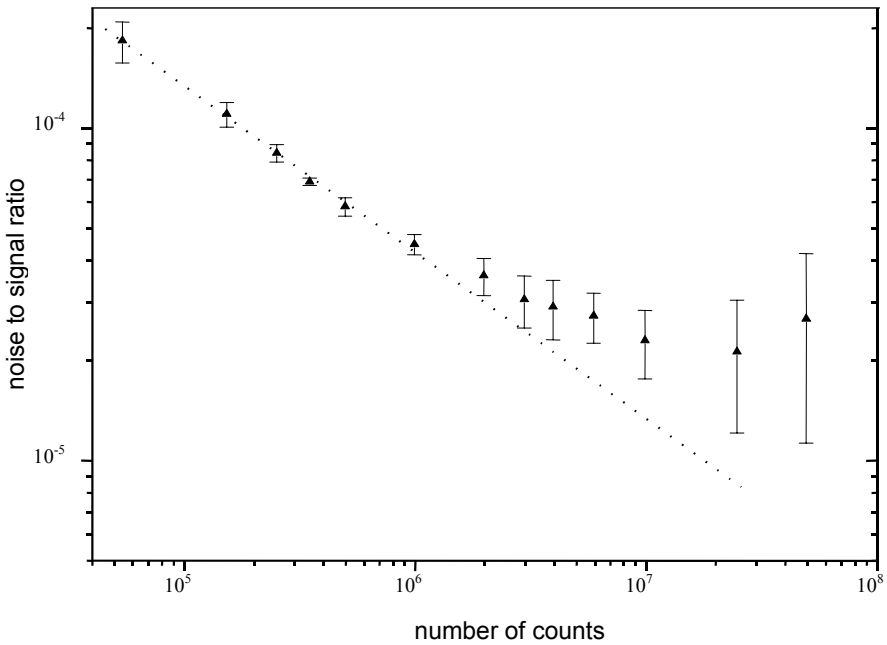

Figure 22: Variation of the ratio between residual noise and measured intensity with the number of counts [*Kah*, 1998].

Linearity

The linearity of the detector is characterised by the dependency of the obtained signal on the integration time. At constant external conditions – especially for the light source – a doubling of the integration time should yield a doubling of the signal detected by the PDA and processed to the computer. For the PDA type used within this work, the linearity is well tested (see e.g. [*Alicke*, 2000; *Geyer*, 2000]) and is therefore not discussed here in detail. The detector implemented in the HMT-DOAS was tested by [*Kah*, 1998] and found to be linear within 0.3 % of the initial intensity.

Fixed structures of the PDA

A major problem occurring when using diode arrays as detectors for DOAS is the high variability of the sensitivity from diode to diode. The diode sensitivity depends on the wavelength of the incoming light and can vary up to some per cent between the single diodes of the array [*Stutz*, 1996]. Additionally, spectral structures fixed on distinct diodes can be caused by dirt or ice on the PDA (see above). Since DOAS is intended to observe optical densities down to less than 10^{-3} , it is necessary to remove the diode structures from atmospheric spectra.

For active LP-DOAS, up to now two different methods for the correction of these diode-fixed structures have been used at the IUP:

- The simplest way is to record Xe-lamp spectra using the shortcut system after each measurement to divide the atmospheric spectrum by the associated lamp spectrum and thereby correcting for the fixed diode structures. But this method can cause increasing residuals of the fitbecause the Xe-lamp also shows structures that are of the same spectral width as the fixed diode structures, but depend only on time (sometimes with variations below some tens of seconds) and on the observed area of the arc. As shortcut systems generally "look" at a lamp arc area that differs from the area used for the atmospheric measurements, the lamp structures also differ in the lamp shortcut and atmospheric spectra. Consequently, the division of atmospheric spectra by the associated Xe-lamp spectra removes fixed diode structures only partially and adds structures related to the variation of the Xe-lamp spectrum with time. So this method does not allow to correct lamp structures and fixed diode structure independently from each other.
- The other common method to eliminate diode sensitivity structures in LP-DOAS spectra is the 'Multi Channel Scanning Technique' (MCST*)* introduced by [*Knoll et al.*, 1990]. The basic idea of the MCST is the combination of a multi channel detection system (PDA) with the scanning technique generally used to cover a larger spectral region with a single channel detection system. Every spectrum is separated in several (e.g. nine) single spectra with slightly different centre wavelengths. These single spectra are recorded in sequence. The spectral shift is performed automatically by the controller of the spectrograph. When adding up all single spectra to one spectrum, the diode resident structures remain at each channel but the spectral information changes depending on the step width of the MCST. The sum spectrum compares to the application of a smoothing algorithm to the original spectrum, because spectral structures are broadened by the shift. Note that the step width must be smaller than any spectral structure that should be analysed later. Otherwise, these structures would not only remain in the sum spectra but would also be duplicated in close proximity to themselves. Every single spectrum subsequently is divided by the summarised spectrum, and this is how the diode resident structures are removed from the single spectra. Afterwards the single spectra are re-shifted to the correct wavelength calibration (usually by additional spectra of a Hg lamp) and added up.

  Yet, the MCST technique has a major drawback: as every spectrum consists of at least

nine single spectra that should all feature a good signal-to-noise ratio, the integration time required for a complete atmospheric spectrum substantially increases . For most LP-DOAS instruments that feature telescopes with larger main mirrors (> 300 mm) and focal lengths of typically 1500 mm, this problem can be neglected: the light throughput of these instruments is about 50 to 100 times higher than of the HMT-DOAS [*Kah*, 1998]. For the desired time resolution of the profile measurements recorded with the HMT-DOAS, however, the MCST technique is not suitable.

The method of correcting for the fixed diode structures used within this was to measure halogen lamp spectra as an additional reference spectrum every time gas cell references, offset and dark current spectra were recorded. As halogen lamps show a remarkably smooth spectrum lacking any narrow-band structures in the 300 to 400 nm region, all structures that remain after the high-pass filtering algorithm must be caused by variations of the diode sensitivity or by dirt or ice frozen on the PDA surface. Figure 23 depicts the variation of the fixed diode structures with time: immediately after the detector was evacuated and refilled with argon, the structures are rather small, but increase considerably with time after evacuation. It is obvious that these structures have to be taken into account for the evaluation and fitting procedure Additionally, such structures must be corrected for independently from the Xe-lamp structures. The treatment of the diode structure spectra as an additional reference within the fitting algorithm will be discussed in chapter 0.

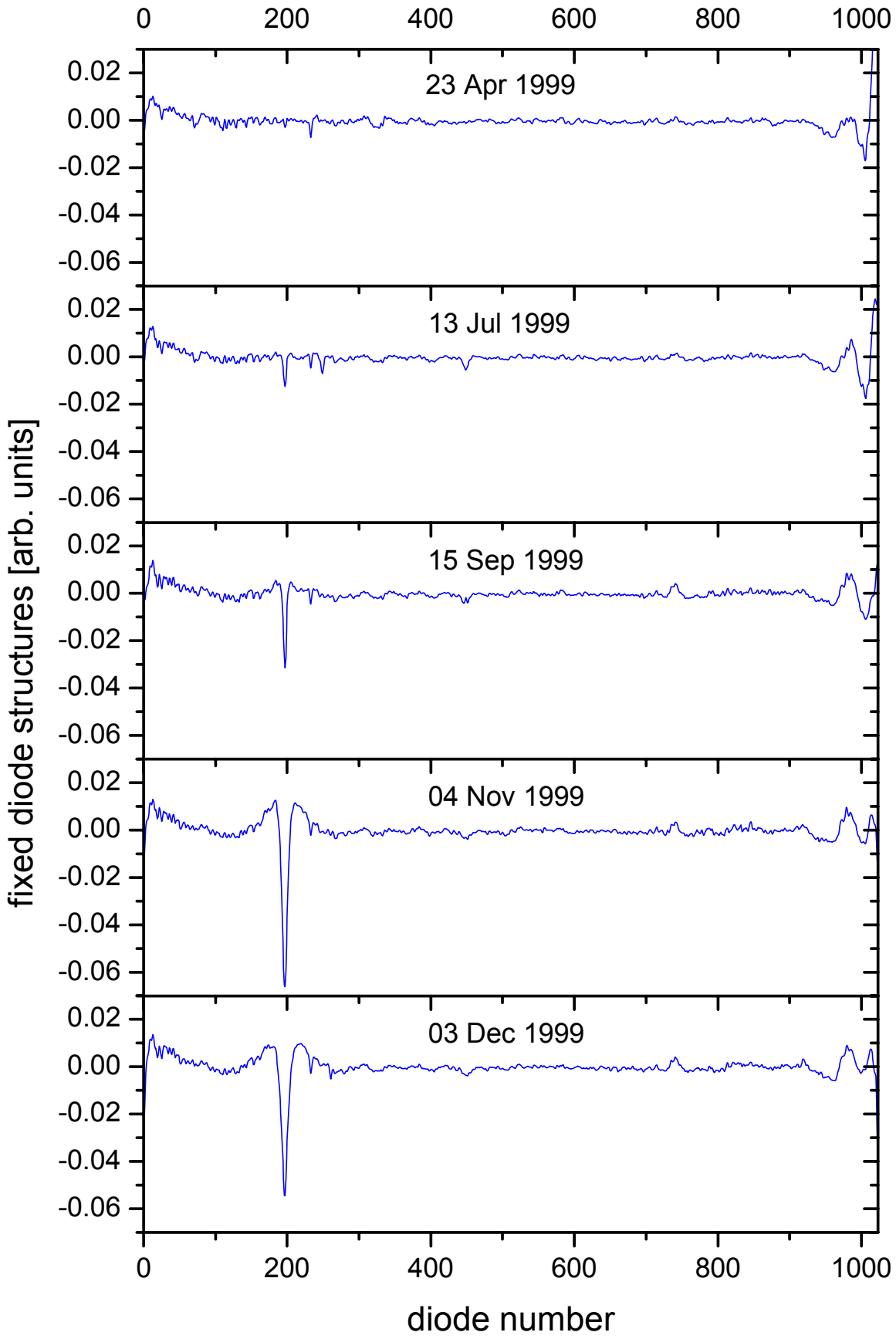

Figure 23: Fixed diode structure spectra derived from high-pass filtered halogen lamp spectra. The increase of the optical density of these structures with time is clearly visible from this graph.

5.2.4 Measurement algorithm for long-term profile measurements

All components of the HMT-DOAS system, including telescope stepper motors, grating control of the spectrograph and the detector and associated electronics, are directly connected to the controller that also handles the temperature control for spectrograph heating and detector cooling. Therefore, all features of the system can be controlled directly by the measurement software on a single personal computer. For the measurements presented in the following, the DOASIS (formerly WINDOAS) software [*Kraus*, 2001] was used to operate the system. All measurements were performed in the wavelength interval of 336 to 375 nm, including three prominent HONO absorption bands, but only weaker absorption structures of HCHO and O_3. The desired time resolution for a full profile (including all three light paths) was set to 15 minutes, which is sufficient to observe the variation of HONO and NO_2 with time (see chapter 6). To stay within this timeframe, additional measurements in a spectral window shifted about 20 to lower wavelengths to obtain better detection limits for HCHO and O_3 were dropped.

In a nutshell, the measurement algorithm proceeded like this:

1. Initialisation of the light path (positioning of the main mirror's position along the optical axis to optimise the beam geometry, moving on pre-set positions of the horizontal and vertical axis of the telescope for the desired light path)
2. Intensity check to decide whether the reflector is concealed by mist or clouds: if light path o.k. proceed at 3), else go to next light path and begin at 1)
3. Adjustment of the horizontal and vertical telescope position to optimise the light intensity returned from the reflector
4. Measurement of the atmospheric absorption spectrum (desired intensity 6·105 ADC counts, max. integration time 600 sec)
5. Moving the telescope by some steps to "miss" the reflector and subsequent measurement of an atmospheric stray light spectrum (with half the integration time of the atmospheric absorption spectrum)
6. Measurement of a lamp spectrum using the short cut system
7. Saving of all spectra and proceeding at 1) with next light path

The measurement routine was started on the lowermost light path to the steeple, proceeding to the middle light path to the hotel and further to the uppermost reflector on the radio tower and finally returning to the lowermost light path. An intensity check prior to every measurement reassured that a light path concealed permanently by clouds was left aside for one hour. If all reflectors showed a reflected intensity below a fixed value, the algorithm returned to the lowermost light path, which was the shortest and therefore the most probable to become operational again. After every measured spectrum, dummy readouts took place to suppress the memory effect. The routine proved to be stable as soon as the teething troubles were remedied. Even after longer mist or cloud periods, all light paths could be reinstated. A detailed description of the measurement control routine written in 16bit Delphi can be found in [*Mößner*, 1999].

The reference spectra required for the determination of instrument-specific parameters such as offset, dark current, fixed diode structures, instrument function and spectral dispersion / resolution were recorded at least once in the lifetime of a lamp, but whenever possible, every two weeks. In the course of these reference measurements, gas cells of NO_2 and HCHO were placed in the shortcut system to allow a comparison between the convoluted literature trace gas references and the trace gas absorption as measured with the real instrument.

5.3 Evaluation algorithm and achieved data quality

The main focus of the long-term profile measurements in Heidelberg was the precise measurement of the profiles of HONO and its most prominent precursor NO_2 (see chapter 2.3). Therefore the spectral window was chosen to include three prominent HONO absorption bands at 341.68, 354.13 and 368.15 nm, respectively. As NO_2 also shows prominent - or de facto the dominant - absorption structures within this spectral range, it was possible to evaluate the spectra in the same spectral window for the concentration of both absorbers. It was not possible, however, to evaluate the concentrations of HCHO and O_3 with a cutting-edge detection limit. The absorption structures of both absorbers, but especially for ozone, are too weak in the chosen spectral range to guarantee a satisfying signal-to-noise ratio. In the following, the evaluation procedure will be presented, and the stability of the algorithm and the errors due to changes in the exterior conditions, as well as due to systematic and statistic errors of the evaluation algorithm will be discussed.

5.3.1 Evaluation procedure

The evaluation was performed with the software MFC [*Gomer et al.*, 1996], which uses the spectra simulation and analysis model presented in chapter 4.3.2 and 4.3.3, respectively. Briefly, the fitting algorithm processed like this:

1. Correction of offset and dark current in the lamp reference spectrum.
2. High pass filtering, application of the logarithm and smoothing of the lamp spectrum.
3. Linear fit of the diode structure reference spectrum and a polynomial of 5th order to the lamp spectrum. Extraction of the residual structure of this fit for use as a lamp reference.
4. Correction of offset and stray light (by offset-corrected atmospheric stray light spectrum) in the atmospheric absorption spectrum.
5. High pass filtering, application of the logarithm and smoothing of the atmospheric absorption spectrum.
6. Non-linear fit of all references and a polynomial of 5th order to the atmospheric absorption spectrum. Extraction of the fitting parameters of all references and of the peak-to-peak maximum of the residual structure in a file.

The evaluation algorithm automatically filtered out all measurement spectra that showed over- or under-range signal-to-noise ratios (resulting in errors within the fit) and assured that all spectra were corrected for the lamp structure, even if no lamp spectrum directly associated to the actual measurement spectrum was available (e.g. due to problems with the shortcut system). A detailed description of the single steps can be found below.

Offset and dark current / stray light correction

Prior to evaluation, all spectra were corrected for the offset by subtracting an offset spectrum recorded within one or to weeks prior or after the measurement spectra, weightened by the numbers of scans in the measured and offset spectrum. The dark current was only corrected for in the lamp shortcut spectra and the atmospheric absorption spectra were corrected for dark current and atmospheric stray light within one step by the integration-time weightened subtraction of the atmospheric stray light spectrum.

High-pass filter

To remove the broad-band structures due to scattering processes and broad-band absorption, a low pass filter was applied: the spectra were smoothed by performing a triangular smoothing, for all 1024 channels simultaneously, 800 times. The original spectrum was subsequently divided by its smoothed equivalent, leaving only the narrow-band spectral structures. After

applying the logarithm to prepare the spectra for the fit, the corrected and filtered spectra were smoothed by the same triangular smoothing algorithm, but only performed two times to even out noise structures. This mechanism was used for both the corrected atmospheric and the lamp spectra as well as for all reference spectra.

Correction of fixed diode and Xe-Lamp structures

The fixed diode structures that proved to be highly variable (see chapter 5.2.3) were corrected by generating a reference spectrum for these structures: a halogen lamp spectrum recorded together with the other reference spectra was high-pass filtered by the algorithm described above (including the logarithm and smoothing). The resulting spectrum was used as the reference for the fixed diode structures.

For the correction of the Xe-lamp spectra, a linear fit[12] of the diode structure reference spectrum and a polynomial of 5th order to the lamp spectrum was performed. The residual of this fit represents a lamp reference spectrum that contains only the Xe-lamp structure and is independent from fixed diode structures.

Correction of Fraunhofer structures

An evaluation of the atmospheric stray light spectra yielded the result, that significant Fraunhofer structures could be identified, especially on the upper light path in broad daylight. These structures are caused by sunlight being scattered in the light path of the LP-DOAS system and collected by the receiving telescope. Under constant atmospheric conditions, these structures are expected to remain constant over integration time: thus, the stray light correction would remove these structures, too. In episodes with changing cloud cover, however, the optical density of these structures might change substantially. Therefore, the division of the atmospheric absorption spectrum by its associated stray light spectrum would leave differential Fraunhofer structures that cause increased residuals of the fit.

To overcome this problem, a Fraunhofer reference spectrum was generated and included in every set of references: adding up 10 to 20 stray light spectra measured on the upper light path in broad daylight (if possible within one or two hours), applying the high pass filter, logarithm and smoothing leaves only the narrow-band Fraunhofer structures that would disturb the fit.

Fitting procedure

For the determination of the trace gas column densities from the atmospheric absorption spectra, the non-linear fitting algorithm discussed in chapter 4.3.3 was used. The following references were fitted to the measured spectra:

1. NO_2 cross section convoluted from [*Voigt et al.*, 2001b]
2. HONO cross section convoluted from [*Stutz et al.*, 2000]
3. HCHO cross section convoluted from [*Meller and Moortgat*, 2000]
4. O_3 cross section convoluted from [*Voigt et al.*, 2001a]
5. O_4 cross section interpolated from [*Hermans et al.*, 1999]
6. Fraunhofer spectrum (see above)
7. corrected lamp structure spectrum (see above)
8. fixed diode structure spectrum (see above)

The references 2, 3, 5 and 6 were linked to the shift and squeeze parameters obtained from the non-linear NO_2 fit to exclude arbitrary shifting and squeezing due to small absorption

[12] Allowing no shift or squeeze of the reference spectra in the course of the fit.

structures (see [*Stutz*, 1996]). For the O_3 reference, permitting a shift or squeeze decreased the quality of the fit and was therefore denied. The correct wavelength scale calibration for the NO_2 and HCHO references was deduced from reference cell measurements. This was not possible for HONO and O_3 due to the lack of suitable reference gas cells, but for both trace gasses no significant shift versus the NO_2 reference could be observed (see chapter 5.3.2). The diode structures were fitted without permitting a shift or squeeze, because no shift or squeeze is expected due to the nature of these structures (see above).
For each evaluated spectrum, the residual was saved to disk and added to the residuals of the spectra evaluated before. After a first run of the evaluation algorithm, residuals featuring a delta above 5 ‰ (which hints on the occurrence of an error within the fit) were removed from the sum of all residuals. The resulting spectrum is used as an additional ninth reference for a second run of the evaluation. The justification for this process is the fact that atmospheric spectra often feature absorption structures that are not explained by the mathematical description. Such structures might be caused by unknown absorbers or absorption structures ("X-absorbers" discussed in several DOAS-related publications e.g. [*Hönninger*, 2001]) in the atmosphere or by structures caused within the instrument due to optical faults (non-homogeneous illumination of the grating and/or the PDA). All mixing ratios presented in the following are computed from the trace gas column densities obtained in the second evaluation run including the residual reference.
Two examples for the evaluation of atmospheric spectra are shown in Figure 24 for an HONO concentration of 1.64 ppb and in Figure 25 for HONO below the detection limit of 0.11 ppb. In both diagrams, the fourth row from the top shows the atmospheric spectrum from which all structures that were identified by the fit have been removed, excluding the HONO absorption structure. Additionally, the HONO absorption cross section scaled by the column density found by the fit is plotted, to allow a direct comparison between the fit result and the atmospheric spectrum. While in Figure 24 the HONO absorption structure can be identified in the atmospheric spectrum with the naked eye, it is impossible to identify HONO in Figure 25. It will become apparent later that the HONO fitting coefficients obtained from such spectra can be of significance when being evaluated by statistical means over a longer period (see chapter 6.2.1).
To illustrate the significance of a positive identification and correction of the fixed diode structures, the spectra displayed below are taken from a set of spectra recorded at the end of the measurement campaign that feature strong diode structures. At the beginning of the measurements in January 1999, the fixed diode structures are of the same order of magnitude as the residuals (i.e. 1-2 per mille), thus being not that significant in the spectra.

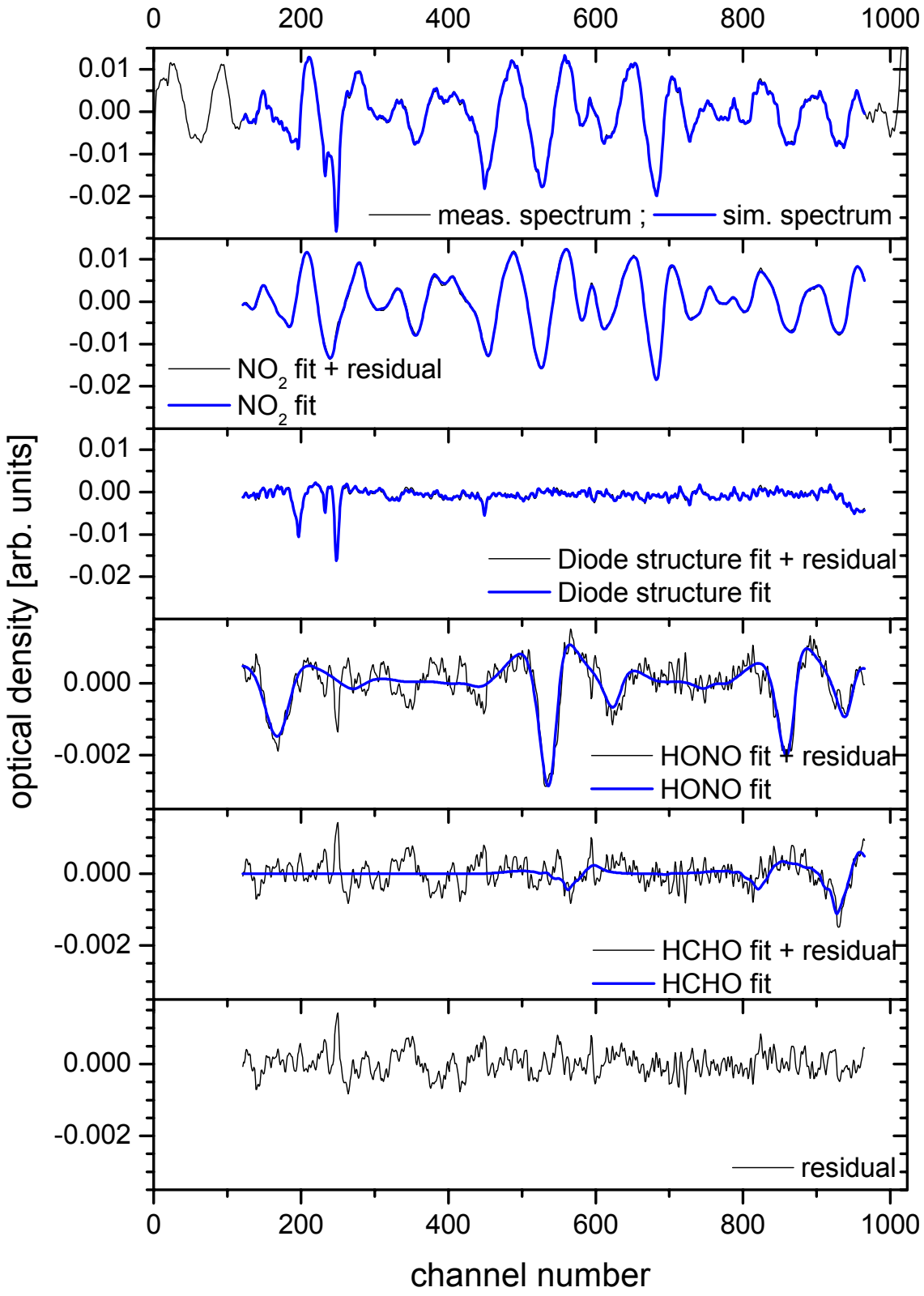

Figure 24: Sample evaluation of an atmospheric spectrum recorded on 27 Feb 2000 at 8:00 local time, containing the absorption structure of 31.0 ± 0.2 ppb NO_2, 1.64 ± 0.08 ppb HONO and 4.5 ± 0.9 ppb HCHO. Note that the scale of the y-axis changes between the upper tree and lower three rows of the graph changes by roughly a factor of 10. The most prominent structures in this spectrum are the NO_2 absorption structures and the fixed diode structures, but the absorption structures of HONO and HCHO are also clearly visible.

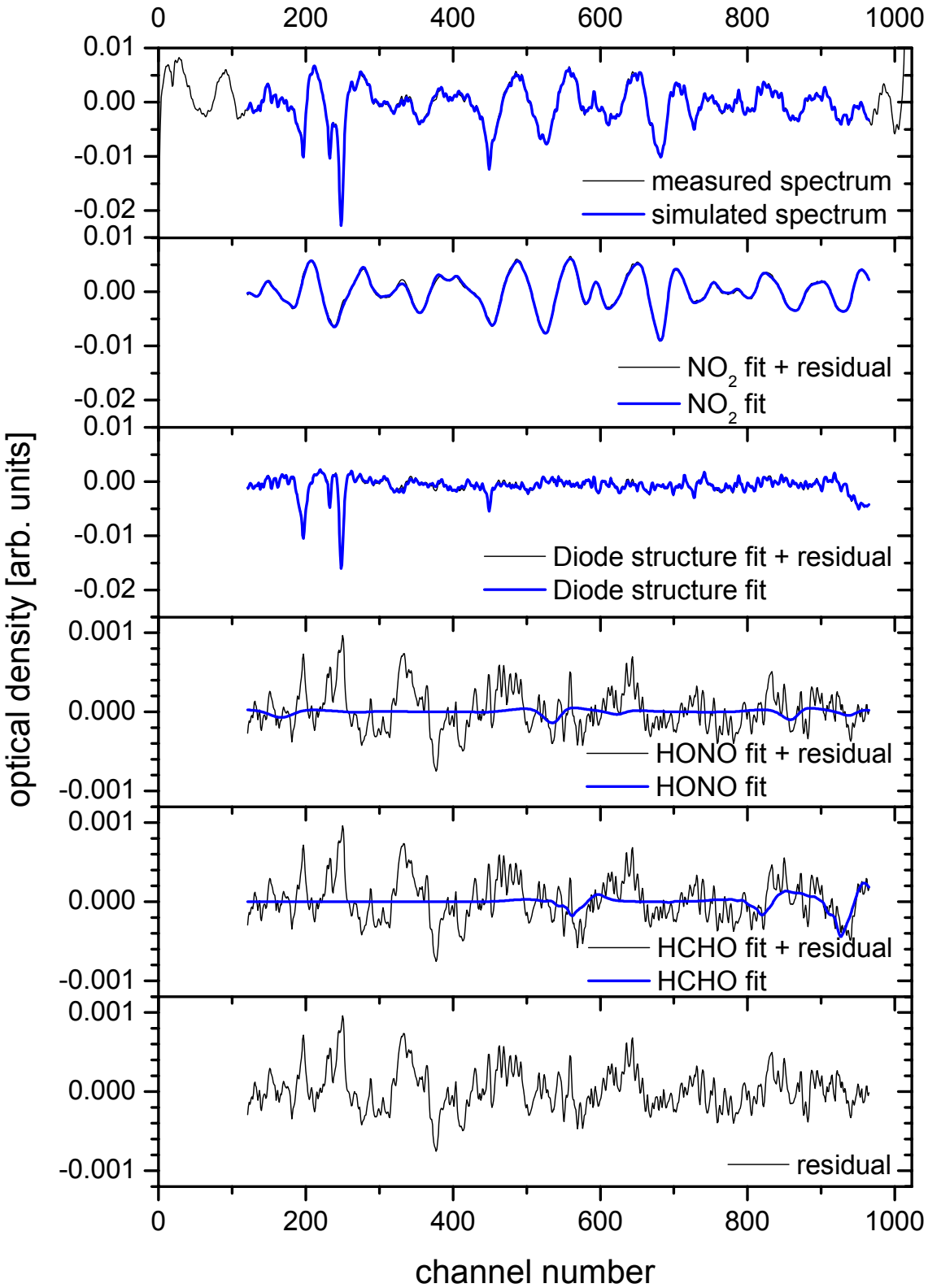

Figure 25: Sample evaluation of an atmospheric spectrum recorded on 16 Feb 2000 at 12:00 local time, containing the absorption structure of 15.1 ± 0.1 ppb NO_2, 0.08 ± 0.05 ppb HONO and 1.7 ± 0.5 ppb HCHO. Note that the scale of the y-axis changes between the upper tree and lower three rows of the graph changes by roughly a factor of 10. Neither HONO nor HCHO can be positively identified in this spectrum with the naked eye.

5.3.2 Error estimations

The total error of trace gas measurements performed by LP-DOAS consists not only of the error of the fitting algorithm: other possible error sources are systematic errors in the reference spectra used by the fit. This includes not only the trace gas cross sections, but also instrument-related references such as the fixed diode structures and narrow-band lamp structures, to mention the most prominent examples.

Systematic DOAS errors

The systematic error of the DOAS spectrometer was determined by [*Stutz*, 1996] as being below 3 %. This error estimation includes the errors of the offset, the dark current, the memory effect and the error due to stray light in the spectrograph-detector unit, the latter being the dominant error source.
Systematic errors within the fitting algorithm were also discussed by [*Stutz*, 1996] and by [*Stutz and Platt*, 1996]. Both publications mainly concentrate on systematic errors caused by the shifting and squeezing of the reference spectra by the non-linear fit, and conclude that the resulting systematic error is described by a factor of 3 (in some cases up to 6, see also [*Stutz*, 1996]), by which the statistical error of the fit must be multiplied.

Systematic errors due to instrument-related spectral structures

The long term measurements provided an ideal opportunity to validate the error estimations made by [*Stutz*, 1996], especially for the offset structure: as the instrument operated more or less constantly for 14 months at the same site, the offset and dark current are not expected to change due to variations of the exterior conditions[13]. The change of the offset structure with time is depicted in Figure 20. Neither the small changes in the mean offset signal nor the changes in the shape of the offset structure show a clear correlation to the mean residual or detection limit. These findings confirm the results obtained by [*Stutz*, 1996], who reported a systematic error due to offset changes of below 0.1 % .
The same author stated that dark current variations do not (about -0.15 %) affect the systematic error of LP-DOAS significantly. The evaluation of the long-term measurements confirmed that dark current variations are negligible as a source for systematic errors.

The systematic errors due to the memory effect and spectrograph stray light were discussed by [*Kah*, 1998] and found to be consistent with the findings of [*Stutz*, 1996]. As these structures do not change with time, these errors are not discussed within this thesis.

The impact on other instrument-related spectral structures on the systematic error of the evaluation will be discussed below. For these structures, the systematic error depends strongly on the associated references used within the fitting algorithm and on the fitting algorithm itself.

Systematic errors of the trace gas references

The systematic errors, i.e. the uncertainties of the trace gas reference spectra, are given as ± 5 % for HONO by [*Stutz et al.*, 2000] and ± 3.5 % for NO_2 by [*Voigt et al.*, 2001b]. For DOAS applications, however, the uncertainty of the absolute value is not the only systematic error related to the cross section: other possible error sources are inconsistent wavelength calibrations of the cross sections for the different trace gasses. In case of the HONO evaluation, errors can also occur by NO_2 cross sections that are contaminated by HONO: this

[13] Except for possible dark current changes due to variations of the PDA temperature, which are corrected for by the thermostatic temperature control (see chapter 5.2.3). However, changes in the dark current are dominated by other PDA structures due to icing (see also chapter 5.2.3).

contamination can easily occur when the NO_2 reference gas and the gas cell used for the measurement of the cross section are not absolutely free from water, the reaction of NO_2 with water adsorbed on surfaces produces HONO very effectively (see chapter 2.3.1).

Extensive sensitivity tests were performed to check whether the wavelength calibration of the references linked to the NO_2 cross section in the fit process are consistent. For every trace gas (i.e. HONO, HCHO and O_3), 200 spectra featuring mixing ratios well above the detection limit for this species were selected among all spectra measured during the Heidelberg long-term campaign. These spectra were evaluated by the same fitting algorithm, but without the linking the respective cross section to the NO_2 reference.

The result of the evaluation for the HONO reference by [*Stutz et al.*, 2000] and the NO_2 reference by [*Voigt et al.*, 2001b] is shown in Figure 26. For this study, 201 atmospheric spectra were chosen that feature HONO mixing ratios above 0.5 ppb with an error of less than 0.2 ppb. To exclude possible errors due to a faulty XBO structure correction, only atmospheric spectra were used for which a valid lamp spectrum was available. To these spectra, the standard evaluation algorithm (described in chapter 5.3.1 above) was applied, but with one major discrepancy: shift and squeeze for the HONO reference were left free and not linked to the NO_2 reference as done in the standard evaluation. The resulting HONO shifts for the spectra were corrected for the associated NO_2 shift to obtain the net HONO shift in each spectrum. Subsequently, a Gauss distribution was fitted to the corrected HONO shift (see also Figure 26). The result is rather inaccurate: a mean shift of 0.39 ± 0.24 channels was found for HONO, with large excursions from the mean (up to 5 channels). If this mean shift of the HONO versus the NO_2 reference was applied to the HONO reference used in the standard evaluation, the residuals and HONO detection limits could not be reduced.

For the remaining trace gasses, a significant shift versus the NO_2 cross section was also not observed. Therefore, all trace gas references were used without additional shifts in the standard evaluation described above.

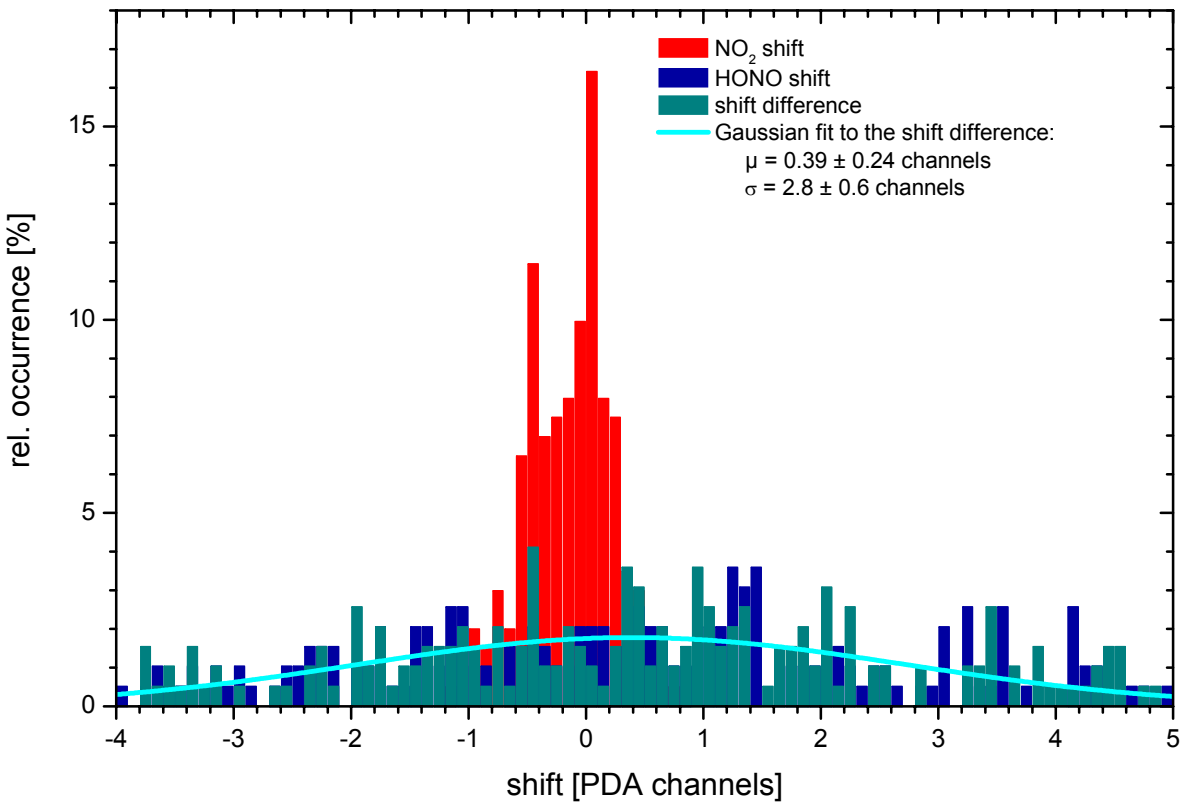

Figure 26: Shift of the HONO and NO_2 references as found by the non-linear shift for 201 spectra containing more than 0.5 ppb of HONO.

The second problem of HONO absorption structures contaminating the NO_2 cross section was examined by another series of test evaluations: the reference cell spectra as well as two different NO_2 absorption cross sections that were used for the HONO evaluation were evaluated against each other with respect to a possible HONO contamination.

In recent publications on HONO measurements by DOAS, most authors (e.g. [*Alicke*, 2000] and references therein) used the NO_2 absorption cross section published by [*Harder et al.*, 1997] to deduce the NO_2 concentrations in the reference cells. First evaluations of the Heidelberg data with this cross section, however, showed larger residuals and detection limits for NO_2 and HONO and contrastingly lower mean HONO mixing ratios than evaluations performed with the cross section by [*Voigt et al.*, 2001b].

To clarify this finding, the cross sections of [*Voigt et al.*, 2001b] and [*Harder et al.*, 1997] were evaluated against each other. Spectra with column densities of NO_2 that are typical for atmospheric spectra measured above Heidelberg were generated by multiplying the cross section of [*Harder et al.*, 1997] with a factor ranging from 10^{15} to $5 \cdot 10^{17}$. 500 of these spectra were generated, each differing from the others by a slant column density of 10^{15} . The cross sections of NO_2 and HONO of [*Voigt et al.*, 2001b] and [*Stutz et al.*, 2000], respectively, were fitted to these spectra, together with a polynomial of 5th degree to compensate for broad-band spectral structures. Figure 27 shows the results of the evaluation of all 500 spectra. The difference between original values and the DOAS fit results increase linearly by 4% from the expected slope of unity. However, this deviation is smaller than the error of 8 % given for the NO_2 cross section by [*Harder et al.*, 1997], but larger than the systematic error of the NO_2 cross section of 3.5 % of [*Voigt et al.*, 2001b].

The results from the HONO fit show that the HONO column density also increases linearly with the NO_2 column density in the original spectra, while the ratio HONO versus NO_2 remains constant. The frequency analysis of the HONO/NO_2 ratios, plotted in the lowermost row of Figure 27, clearly indicates that HONO can be positively found in the cross section of [*Harder et al.*, 1997]: a Gauss fit to the occurrence of the different ratios yields a mean of 0.46 % HONO per NO_2 in the original spectrum. Consequently, HONO would be underestimated by 46 ppt at an ambient NO_2 mixing ratio of 10 ppb. Both values are typical for the HONO and NO_2 mixing ratios expected in a medium polluted area like the city of Heidelberg in bright daylight. Therefore LP-DOAS measurements evaluated with the cross section of [*Harder et al.*, 1997] would not only underestimate the real HONO mixing ratios in the atmosphere, but also yield in the wrong result that HONO can hardly be detected during periods of strong solar radiation (see chapter 0 for the discussion of daytime HONO concentrations).

So for the evaluation of all atmospheric spectra and the gas cell reference spectra, the cross section of [*Voigt et al.*, 2001b] was used, assuming that it contains no significant HONO absorption structures.

Traditionally, trace gas reference spectra recorded with the instrument that performs the measurements in the atmosphere are preferred for the evaluation of LP-DOAS spectra (see e.g. [*Ackermann*, 2000; *Alicke*, 2000]). Only for absorbers such as HONO or OH, for which no suitable and easy-to-use reference gas cells are available, convoluted literature reference cross sections are used for the fitting algorithm. However, a comparative evaluation of the atmospheric spectra with NO_2 and HCHO references from cell measurements and from convoluted literature cross sections showed that the residuals and detection limits for all absorbers were some per cent higher when using the gas cell references. Thus, for the evaluation of the Heidelberg long-term measurements, the NO_2 and HCHO literature references were used for the fitting algorithm.

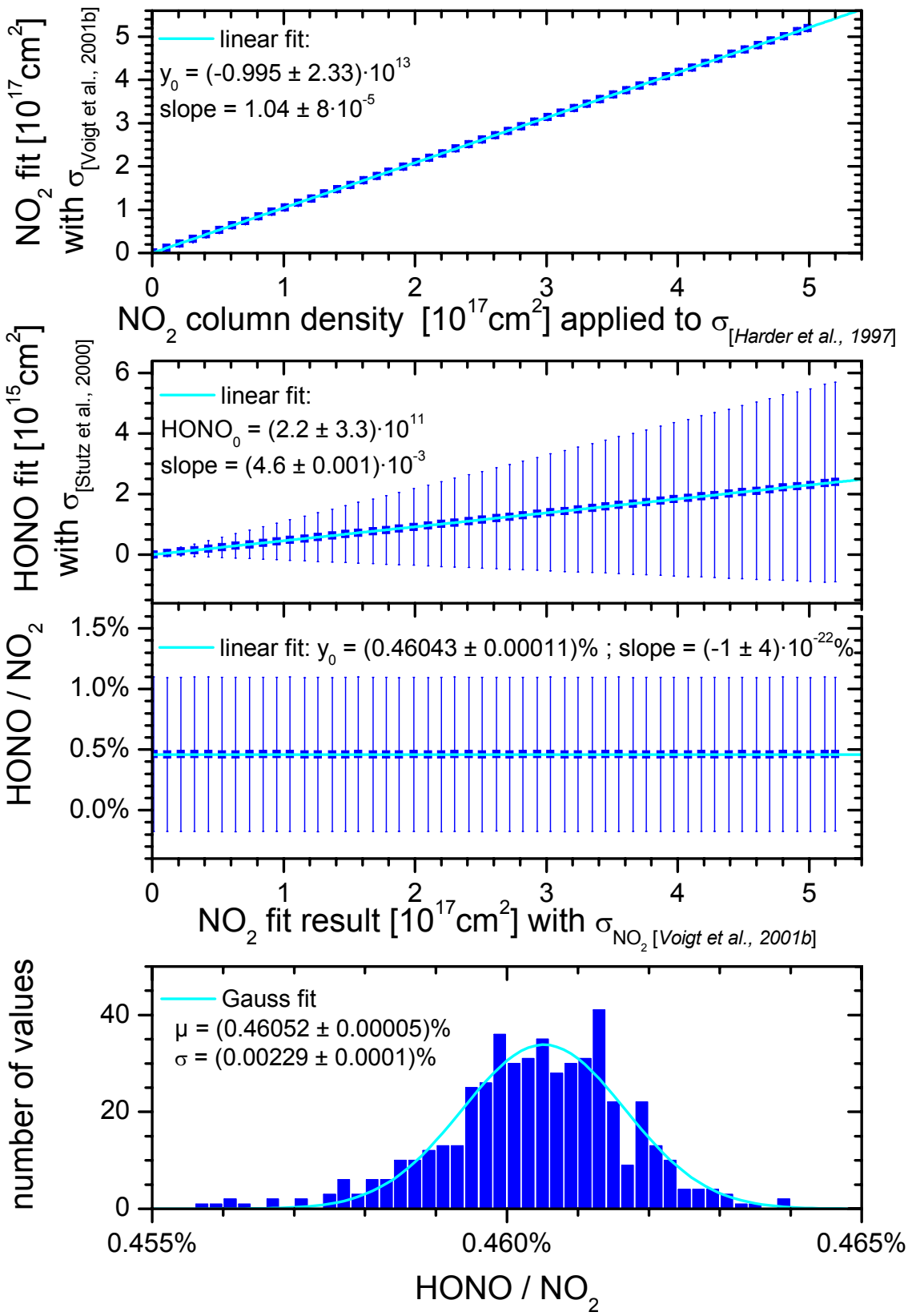

Figure 27: Results from the evaluation of the possible HONO contamination of NO_2 literature cross sections (only every tenth data point is shown for clarity). References for NO_2 [*Voigt et al.*, 2001b] and for HONO [*Stutz et al.*, 2000]) were fitted to spectra generated from the cross section of [*Harder et al.*, 1997]. It is obvious that the NO_2 reference by so[*Harder et al.*, 1997] not only differs in the absolute value from [*Voigt et al.*, 2001b] (upper row), but also seems to be contaminated by HONO (lower three rows).

Artificial HONO "generated" by the fitting algorithm

Systematic errors of the HONO fit are of special interest here, as such errors would significantly hamper the analysis of the very low HONO concentrations expected in the upper layer and by day. Therefore, a series of test evaluations was performed to deduce the impact of different trace gas concentrations and instrument-related structures on the HONO evaluation algorithm.

For the sensitivity check of the evaluation without the PDA reference, a set of test spectra was generated: reference spectra for NO_2, HCHO, O_3, O_4, the XBO structure and the Fraunhofer structure were each multiplied by five typical column densities found in atmospheric spectra (see chapter 6). From these 30 initial spectra, 19530 test spectra were generated by adding up the initial spectra in the following way:

5 spec.:	with 5 different NO_2 column densities
25 spec.:	combining each HCHO spectrum with each of the previous 5
125 spec.:	combining each O_3 spectrum with each of the previous 25
625 spec.:	combining each O_4 spectrum with each of the previous 125
3125 spec.:	combining each XBO spectrum with each of the previous 625
15625 spec.:	combining each Fraunhofer spectrum with each of the previous 3125

These test spectra, which could be assumed to be free of HONO absorption structures, were evaluated by the evaluation algorithm including references for NO_2, HCHO, O_3, O_4, the XBO structure and the Fraunhofer structure plus the HONO reference. The XBO shift and squeeze parameter was left free, while all other references were linked to the NO_2 reference. The results of the first test are displayed in Figure 28 as a frequency analysis plotting the occurrence of different HONO column densities versus the HONO column density. It is obvious that the evaluation algorithm is flawed, as HONO column densities ranging from $-3.8 \cdot 10^{13}$ to $4.6 \cdot 10^{11}$ are found in spectra. Most notably, distinct "modes" of the HONO column density appear in the spectra containing XBO and Fraunhofer structures. This finding arouses the suspicion that these two references account for the erroneous evaluation. The first assumption that the independent shift and squeeze of the XBO structure is responsible for the artificial HONO column densities proved to be wrong: similar modes – albeit with slightly smaller absolute column densities – are found by the same evaluation as before, but with the XBO reference linked to NO_2.

A comparison of the spectra recorded immediately after the evacuation / re-filling of the detector housing with argon and the spectra recorded six months later unveiled the reason for the artificial HONO absorption structures: the fixed structures caused by icing on the PDA surface (see chapter 5.2.3) could be found in both XBO and Fraunhofer spectra. This implies that these two references are no longer orthogonal to each other, contrasting the original requirement of the DOAS evaluation process (see chapter 4.3.3). The resulting effect is that the fitting algorithm generates structures that have no counterpart in the atmospheric spectra, and compensates these by inflating or diminishing the fitting coefficients other references. Thus, the measured values are systematically smaller or larger than the real atmospheric absorptions.

To get an impression of the net effect in the measured HONO column density, a second evaluation run with the test spectra as given above was performed, adding a random noise spectrum to each test spectrum prior to the fit. The peak-to-peak *delta* of the random noise spectra, which is defined as

$$delta = \frac{max.\ intensity - min.\ intensity}{average\ intensity}$$

was chosen to be about 1.7 ‰, a value which is comparable to the residual structure of an atmospheric spectrum recorded with a good signal-to-noise level.

Figure 29 depicts the result of this evaluation: of particular interest is the lower panel of this graph, where the frequency analysis of the evaluation of spectra containing all other spectral structures apart from HONO is plotted: the shape of the resulting curve is the one of a Gauss distribution, featuring a mean HONO value of $\mu = 1.4 \cdot 10^{13}$ and a standard deviation of $\sigma = 5.7 \cdot 10^{14}$. For a light path length comparable to the lower light path in Heidelberg (4210 m), this yields an offset in the HONO mixing ratios of 1.3 ppt. The HONO detection limit for this evaluation, which is equivalent to the 2σ value, would be about 110 ppt for the same light path. It is obvious that the systematic error is rather small compared to the detection limit, but also to the mean HONO daytime mixing ratios of 30 to 100 ppt (see chapter 0). However, an offset of up to 30 ppt HONO at daytime could be found by the evaluation algorithm that neglects the correction of fixed PDA structures under certain circumstances, such as very low HONO levels or strongly varying XBO structures.

Another set of test spectra was generated to allow a comparison between the evaluation with and without an additional reference for the PDA structure. The same spectra for NO_2, HCHO, O_3 and O_4 were used, but new spectra for the XBO and Fraunhofer structures (now corrected for the fixed PDA structure). This yielded a total of 97655 spectra:

5 spec.:	with 5 different NO_2 column densities
25 spec.:	combining each HCHO spectrum with each of the previous 5
125 spec.:	combining each O_3 spectrum with each of the previous 25
625 spec.:	combining each O_4 spectrum with each of the previous 125
3125 spec.:	combining each Fraunhofer spectrum with each of the previous 625
15625 spec.:	combining each XBO spectrum with each of the previous 3125
78125 spec.:	combining each PDA spectrum with each of the previous15625

The result of the frequency analysis for the occurrence of HONO is given in Figure 30: the main modes in the occurrence of HONO column densities are located much more closely to each other and the maximum deviation from zero is significantly smaller than found by the evaluation without PDA structure correction ($-6.2 \cdot 10^{9}$ compared to $4.6 \cdot 10^{11}$).
Adding a random noise spectrum to each test spectrum in the same way as above and repeating the evaluation of the second set of spectra yields the result depicted in Figure 31: the mean of the Gauss distribution is located at a HONO column density of $-7.8 \cdot 10^{11}$ cm^{-2}, yielding an offset in the HONO mixing ratio of -0.074 ppt on a light path length of 4210 m. Thus, a HONO offset generated from erroneous or non-orthogonal trace gas references can be excluded for the improved evaluation using an additional the PDA structure reference.

Interestingly, the average HONO detection limit found for the Heidelberg long-term measurements is about a factor of two larger than the theoretical value: the mean detection limit derived from the measurements on the lowermost light path is 200 ppt, while the final sensitivity test yields a detection limit of $2\sigma = 108$ ppt for the same light path length (see Figure 31).
This leads to the assumption that the residuals of the atmospheric spectra contain systematic structures and are not dominated by the photon noise. This finding is confirmed by the fact that the use of a summarised residual as an additional reference for the evaluation reduces the detection limits and residuals (see chapter 5.3.1). The main sources of the systematic structures within the residuals are thought to be unknown absorbers and Xenon lamp structures varying quickly with time. Unfortunately, the absorption structure of unknown absorbers can only be corrected for by the summarised residual if the residual is dominated by the spectral structure of a single absorber. However, the residual showed a strong dependency on the lamp used (even if all lamps were of the same type), as the lamps proved to be instable in the spatial location of the hot spot. Therefore, it is most likely that the residual is dominated by strongly varying structures of the Xenon arc lamps.

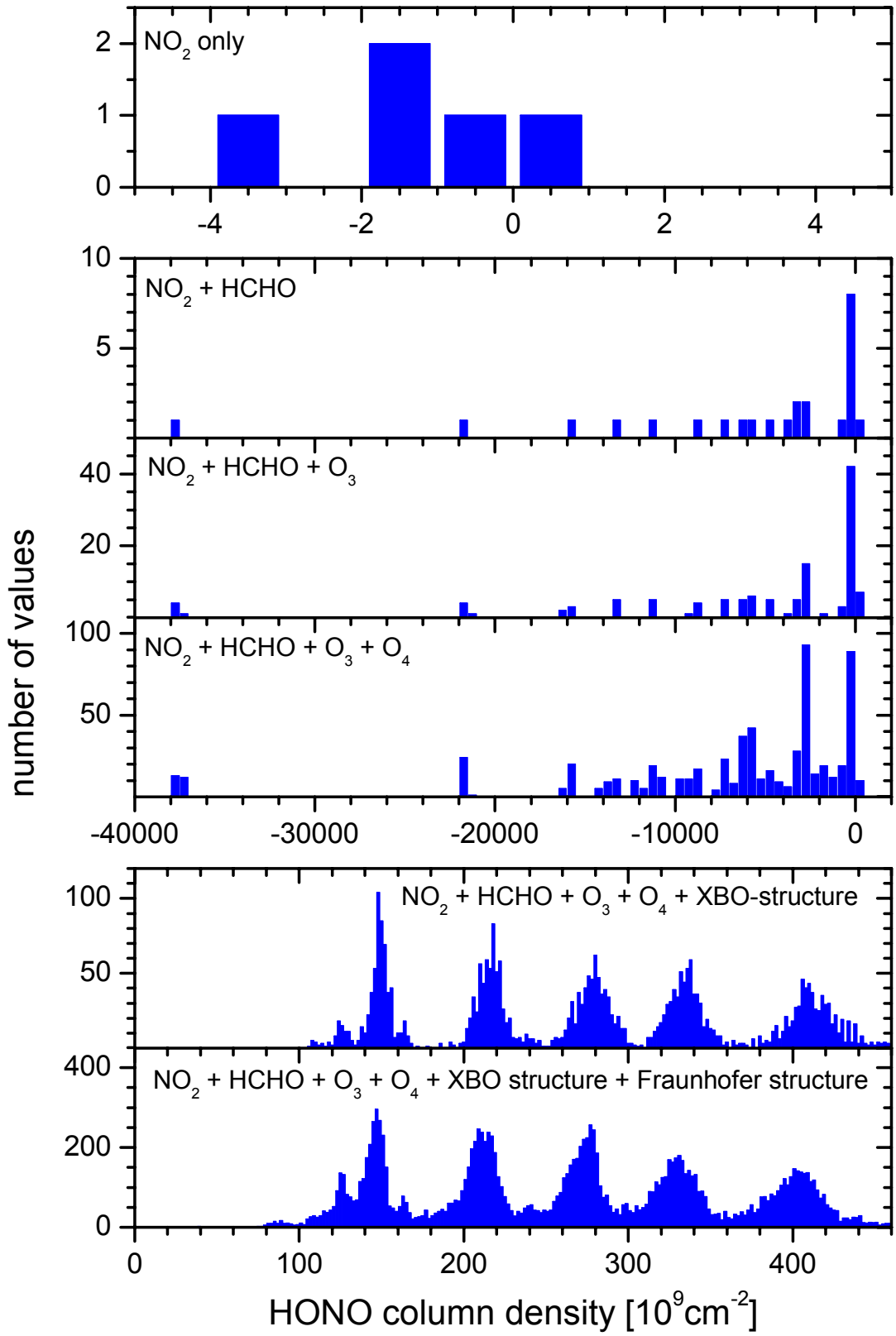

Figure 28: Results of the sensitivity test for artificial HONO generated by the evaluation algorithm without correction for the PDA structure.

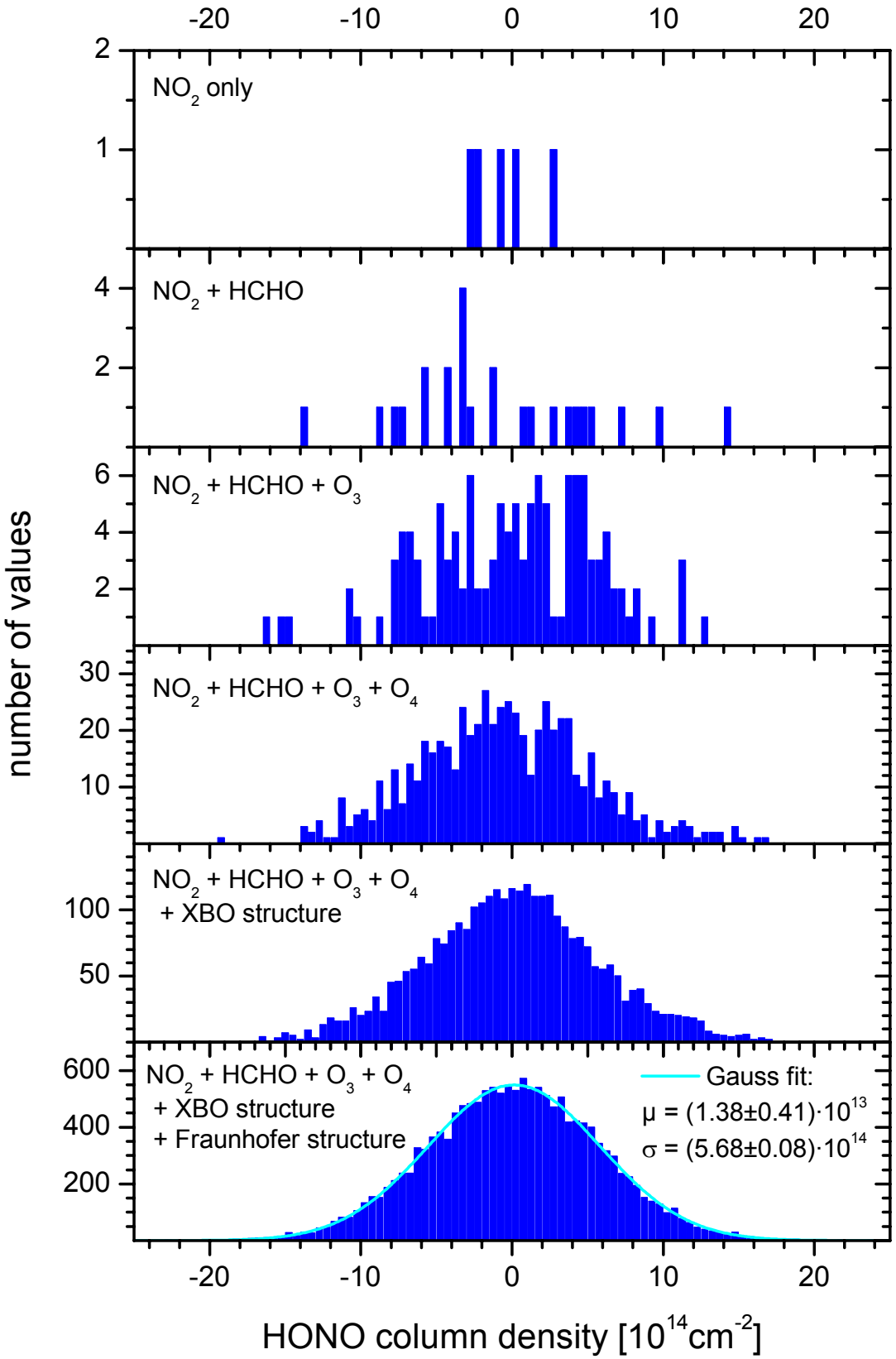

Figure 29: Results of the sensitivity test for artificial HONO generated by the evaluation algorithm without correction for the PDA structure, including a random noise structure comparable to a residual of 1.7 ‰.

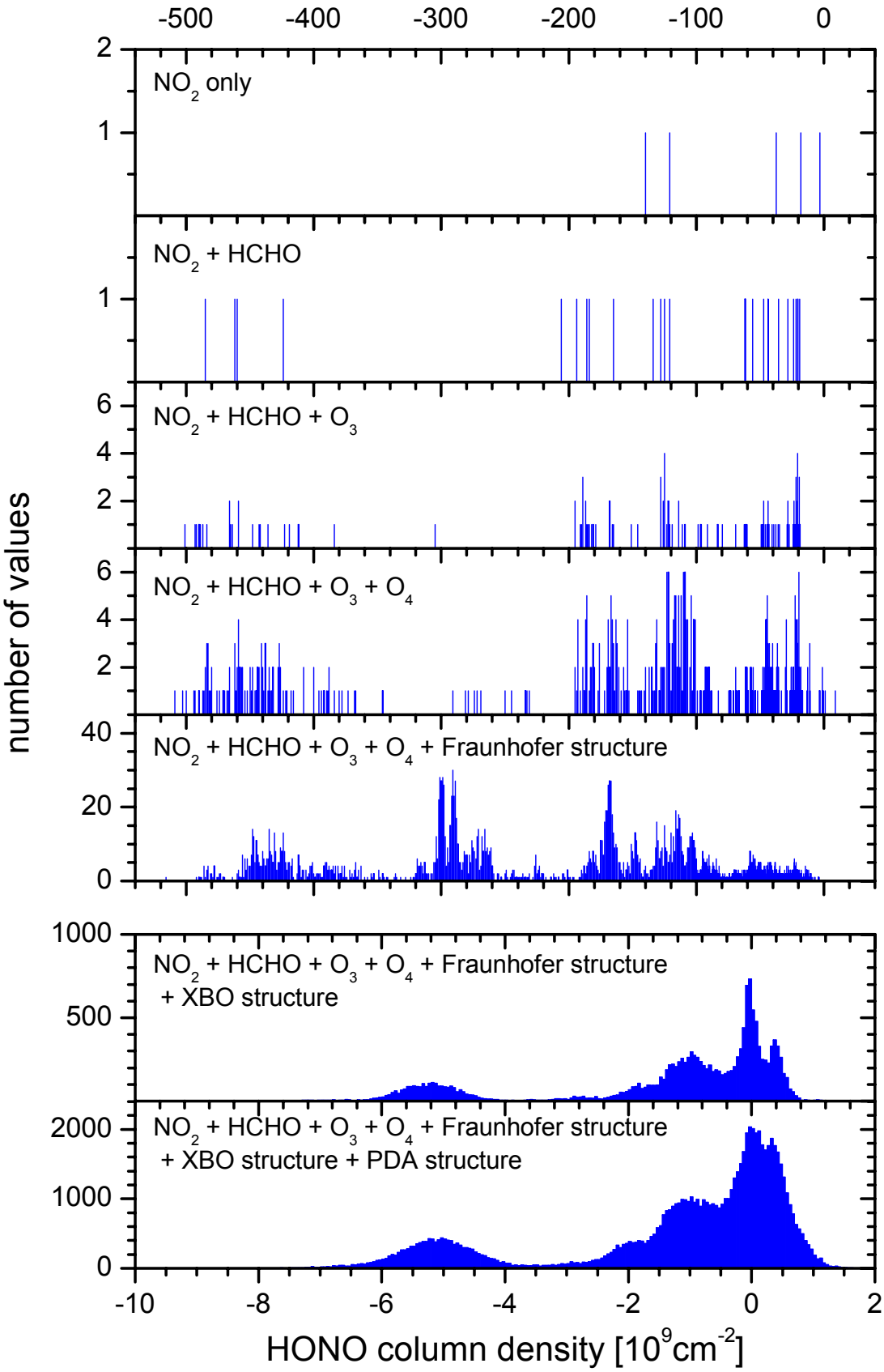

Figure 30: Results of the sensitivity test for artificial HONO generated by the evaluation algorithm including the correction for the PDA structure.

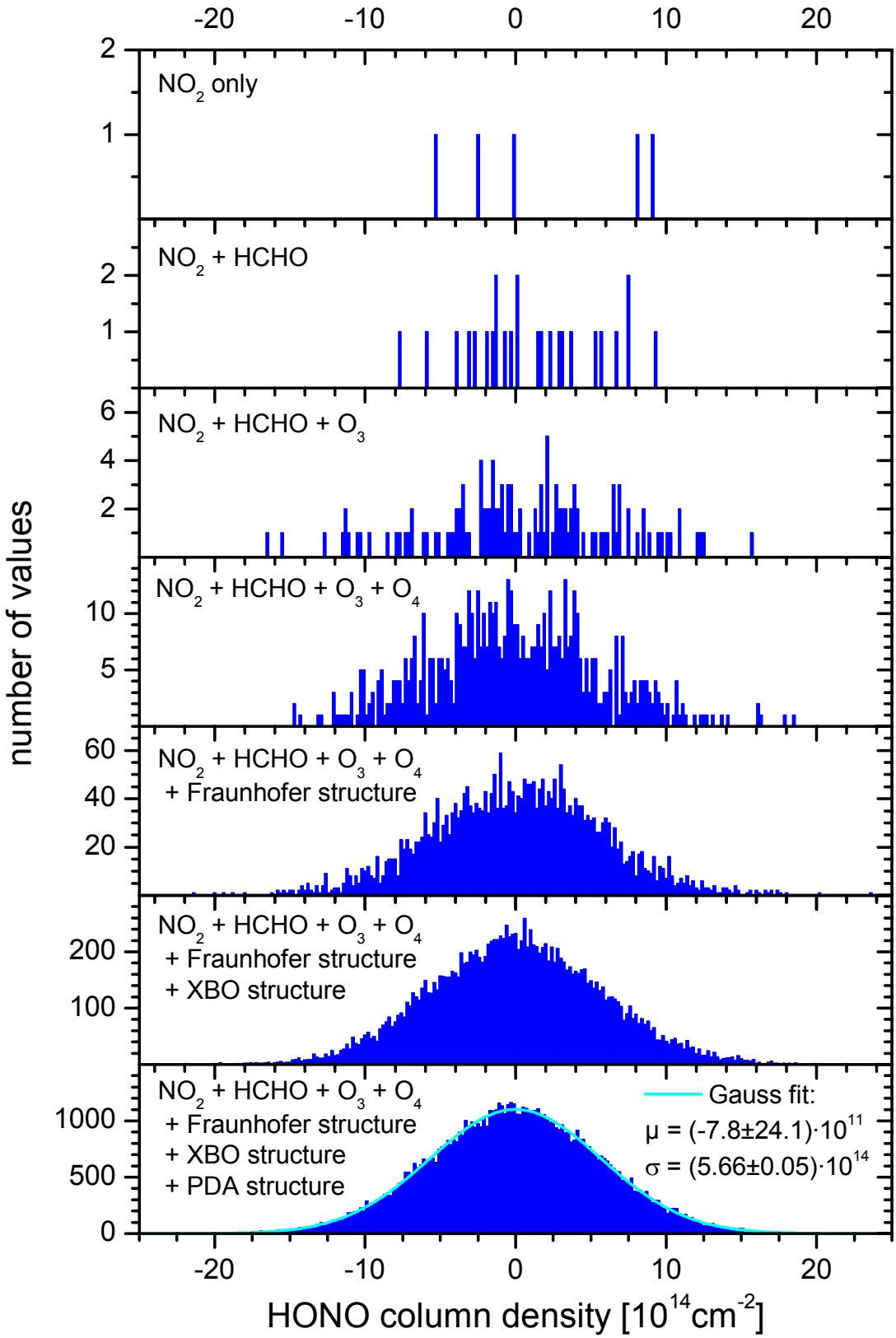

Figure 31: Results of the sensitivity test for artificial HONO generated by the evaluation algorithm including the correction for the PDA structure and a random noise structure comparable to a residual of 1.7 ‰.

Summary and comparison of the different systematic error sources

To summarise the error discussion above, it can be stated that the systematic errors of the DOAS instrument, i.e. errors due to variations in the electronic offset, dark current, memory effect and stray light, are found be in agreement with the values given by [*Stutz*, 1996]. Here, the systematic error of a DOAS system was rated to be about 3 % of the mixing ratio evaluated by the fitting algorithm.

The error of the trace gas references are typically in the range of a few per cent (see Table 6), resulting in a total systematic error of 3.5 to about 7 %. The systematic fitting errors were also discussed by [*Stutz*, 1996], but limited to the error due to systematic errors of additional noise as well as the shift and squeeze of the non-linear fit. [*Stutz*, 1996] states that multiplying the statistical error computed by the fit should be multiplied by a correction factor that depends mainly on the spectral width of the observed absorption structures, being a factor of three in the case of the HONO evaluation presented above.

For the quality assurance of the HONO fit, especially regarding HONO daytime values, another systematic error source was studied within this thesis: the effect of non-orthogonal reference spectra (which are often instrument-related, such as XBO and PDA structures). The extensive sensitivity tests yielded the result that no significant HONO offset could be detected within the fitting algorithm comprising the correction of the PDA structures. The typical offset was found to be less than 1 ppt. The theoretical detection limit from these tests was about a factor of 2 smaller than the actual detection limit, confirming that the residuals are not dominated by (photon) noise but contain strongly varying systematic structures presumably caused by the Xenon lamp.

Table 10: Comparison of the systematic errors of the LP-DOAS system and the evaluation algorithm. All error values given as per cent are relative errors.

	Error	Remarks
DOAS-system		
offset	0.1 %	see [*Stutz*, 1996]
dark current	-0.15 %	see [*Stutz*, 1996]
memory effect	0.4 %	see [*Stutz*, 1996]
stray light	2-3 %	see [*Stutz*, 1996]
fit algorithm		
trace gas references	3.5-5 %	see references in Table 6
shift and squeeze within non-linear fit	factor 3 times statistical fit error	correction yields total fit error see [*Stutz*, 1996] and [*Stutz and Platt*, 1996]
artificial HONO offset	< 1 ppt	can occur due to non-orthogonal reference spectra and must be considered for values near or below the detection limit (see chapter 0)
total (except last two)	≈ 3.5-7 %	usually dominated by the total fit error including the statistical and systematic errors

5.3.3 Stability of the HMT-DOAS instrument

The reliability of the HMT-DOAS instrument was of special importance for the long-term measurements at Heidelberg. Its simplicity, compared with other DOAS instruments in scientific use (as described by [*Geyer et al.*, 1999; *Stutz*, 1996]), can be an important advantage as long as it does not affect the possibilities of adjusting the instrument to optimise the light throughput. The long-term measurements in Heidelberg provided the opportunity to study both the optical and mechanical stability of the system under field conditions as well as the potential of the instrument with respect to time resolution and detection limits. The benchmark for the characteristics of the instrument is defined by other, more complex DOAS systems in use at the IUP.

For the characterisation of hardware and software stability, the mean time between failures and the loss of signal intensity over a period of time without any readjustment of the optical parts was monitored. As soon as the required development work was completed, the hard- and software of the instrument proved to be stable. Under the conditions of the Heidelberg measurements, a readjustment of about 20 min was needed only once or twice every two weeks. Lamp changes, which require a full adjustment of the instrument, were performed every four to six weeks (equalling about 700-1000 hours of lamp life time) and took about an hour to complete. Compared to the operating expenses of more complex systems, this is a major improvement and enables the operator of the HMT-DOAS to perform long-term monitoring of atmospheric trace gasses with good detection limits and low maintenance costs.

The influence of environmental parameters such as changing visibility in the atmosphere, temperature variations and changes in the characteristics of the Xenon arc lamp were also studied. Figure 32 shows the data used for the characterisation of the optical parameters and the quality of spectra evaluation with respect to trace gas absorption. As it can be clearly seen, the peak-to-peak residual structure is in the range of only a few times 10^{-3}. This signifies that the measured spectra can be almost fully understood by simulating the absorber concentrations observed and the spectral structures generated by the instrument. Of particular importance in this context is the fact that the residual is not affected by increasing spectral structures of the lamp, especially at the end of a lamp life cycle. So the correction of lamp structures by spectra taken with the newly designed shortcut system is very effective to even out the spectral characteristics of the lamp. The small variations in spectral shift and squeeze of the reference spectra are due to diurnal temperature variations, which could not be compensated by the temperature stabilisation of the spectrograph. Their effect on data quality is negligible, because they can be corrected easily by the fit algorithm.

In summary, the mechanical and optical stability of the HMT-DOAS is suitable for long-term measurements of atmospheric trace gas profiles. The light throughput and therefore the time resolution is significantly (about a factor of four) smaller compared to the more complex instruments used at the IUP, mainly due to the more compact design. But this does not affect the detection limits of the HMT-DOAS significantly.

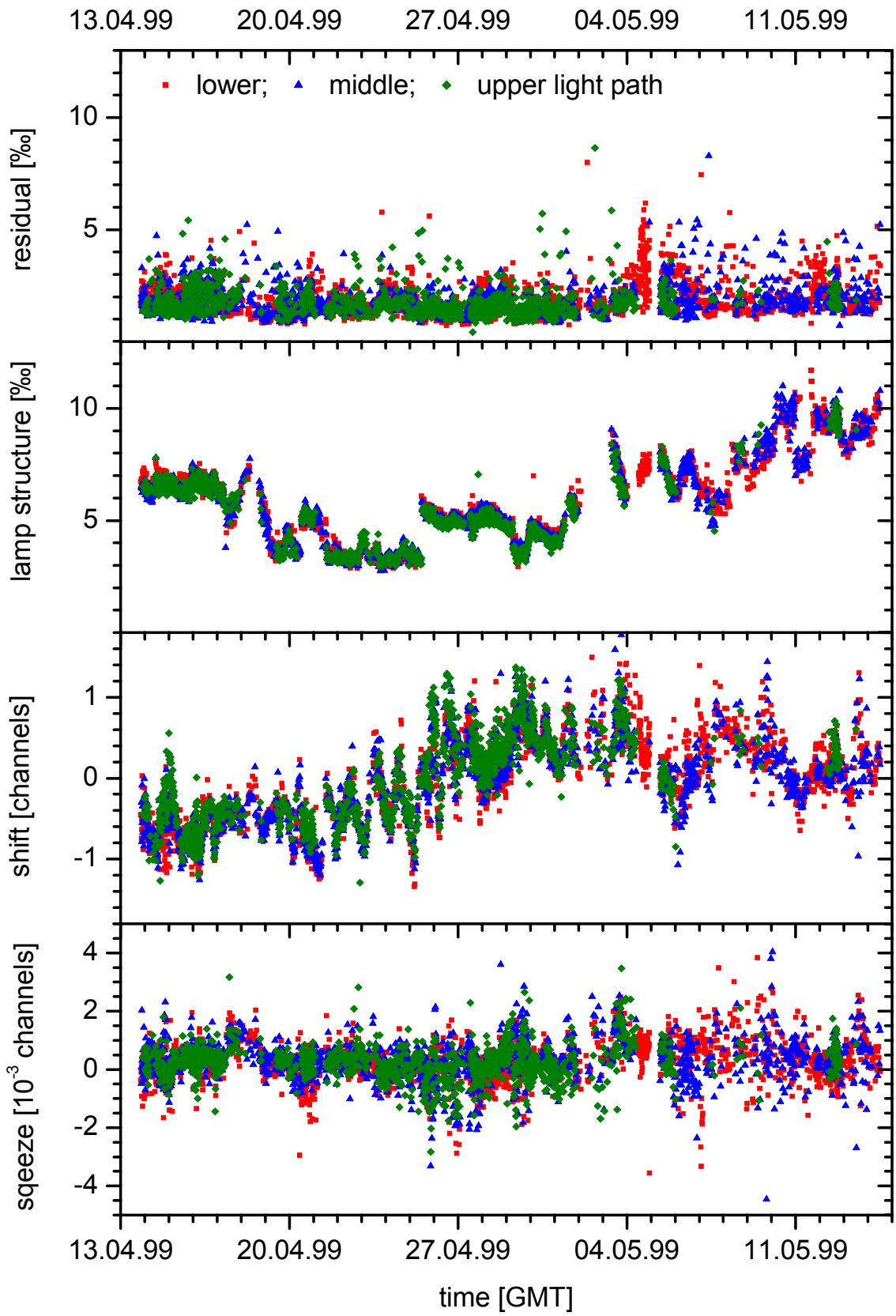

Figure 32: Parameters obtained by the fit algorithm: the residual is the difference between measured and simulated intensity. The lamp structure characterises narrow-band emission structures of the Xenon arc lamp. Shift and squeeze describe the changes in the dispersion of the reference spectra (calculated by the fit algorithm to optimise the residual).

5.4 Meteorological data

Additional data for the evaluation of the measurements were provided by our Institute, namely radon activity as a tracer for the inversion layer height [*Levin et al.*, 2002] and meteorological data. Further meteorological data were obtained from two permanent measurement sites of the state air-monitoring network [*UMEG*, 1999-2001]. An overview over the all meteorological and trace gas data is given in Table 11.

Radon activity

Radon activity in the atmosphere is measured routinely at the Institut für Umweltphysik (IUP, Department of Environmental Physics) through the aerosol attached progeny of ^{222}Ra collected on a filter and subsequently analysed online by α-spectroscopy. The measurement technique and the Rn-monitor developed and used at the IUP is discussed in detail by [*Levin et al.*, 2002].

Meteorological station of the IUP

The meteorological station of the IUP is located on top of the building, beneath the laboratory where the LP-DOAS was set up. Meteorological data was available over most of the measurement period, excluding late spring / early summer 1999, when the IUP moved to a different building. All data were measured with standard of-the-shelf equipment (see Table 11).

Additional meteorological and trace gas data

As a back-up for the meteorological station at the IUP, additional meteorological data has been provided by the state-founded air monitoring network operated by the UMEG[14] (see Table 11). Within this network, the trace gasses NO, NO_2, O_3 and non-methane VOCs as well as soot and dirt are monitored routinely . NO_x data is measured by chemiluminiscence (CL, type Bendix 8101), ozone by UV-absorption spectroscopy (UV, type Bendix 8001) and VOC data are measured as total hydrocarbon concentration using flame ionisation and gas chromatography (FID, Horiba type APHA350E). Soot and suspended dirt (as the PM 10 fraction) are detected by a gravimetric high volume sampler (GVS, Digitel high volume sampler) and integrated over a 24-hour period. The measurement mode is switched from PM10 detection to soot detection every day. The UMEG monitoring site in Heidelberg is located some 200 metres north-west of the new IUP building, near a main road. All additional trace gas data and the soot/dirt data, as well as wind speed and direction, solar irradiance and rainfall were measured there. Temperature and dew point data provided by the UMEG network were measured at the site Mannheim-Süd, located at Rheinau, a south-eastern suburb of Mannheim, about 20 kilometres north-west of Heidelberg. For an overview of the measurement methods and detection limits of the data provided by the UMEG, please refer to Table 11. Detailed information is presented by [*UMEG*, 1999].

[14] Gesellschaft für Umweltmessungen und Umwelterhebungen mbH, Karlsruhe, Germany (www.umeg.de).

Table 11: Additional meteorological and trace gas data used for the interpretation of the long-term profile measurements in Heidelberg.

dataset	site	method	time resolution	detection limit
Radon activity	IUP [(a)]	α-spectroscopy	30 min	error < ± 20%
wind speed and direction	IUP,	VDI 3786	5 min	n/a
	UMEG HD [(b)],		30 min	0.3 m/s or 2.5 deg.
	UMEG MAS [(c)]		30 min	0.3 m/s or 2.5 deg.
pressure	IUP	VDI 3786	5 min	< 0.1%
temperature	IUP,	VDI 3786	5 min	< 0.1%
	UMEG MAS [(c)]		30 min	0.2°C
rel. humidity	IUP	VDI 3786	5 min	1 %
dew point	UMEG MAS	VDI 3786	30 min	n/a
irradiance	IUP	VDI 3786	5 min	1 %
	UMEG HD		30 min	n/a
rainfall	IUP	VDI 3786	5 min	n/a
	UMEG HD		30 min	0.005 mm
NO	UMEG HD	CL	30 min	2.5 µg/m^3
NO_2	UMEG HD	CL	30 min	2.5 µg/m^3
O_3	UMEG HD	UV	30 min	2.0 µg/m^3
VOCs	UMEG HD	FID	24 hours	0.5 µg/m^3
dust / soot	UMEG HD	GVS	24 hours [(d)]	0.4 µg/m^3

[(a)] Institut für Umweltphysik
[(b)] UMEG site Heidelberg
[(c)] UMEG site Mannheim-Süd
[(d)] alternating daily

6 Long-term gradient measurements of NO_2 and HONO

6.1 Introduction

The long term gradient measurements which will be discussed in this chapter were performed with the light path set-up described in chapter 5.1. Routine measurements of NO_2 and HONO profiles started in January 1999 and lasted until February 2000. All NO_2 and HONO data were recorded with the HMT-DOAS instrument (see chapter 5.2), using the measurement algorithm that executed measurements successively along the three light paths (chapter 5.2.4). The DOAS spectra were evaluated with the algorithm described in chapter 5.3, for the mean detection limits during the Heidelberg campaign refer to Table 34 (Annex A). All LP-DOAS data were evaluated with the 3-layer box model to obtain vertical trace gas profiles (see chapter 4.4.1). Detailed information on the measurement sites and references for the additionally trace gas, Radon and meteorological data used for the evaluation and discussion of the profile data can be found in chapter 5.4.

The baseline of knowledge on vertical profiles of NO_2 and HONO and the number of publications dealing with the measurement of such profiles is quite diverse:
In the case of NO_2, the vertical profile is already well understood (see chapter 2.2.1). The main sources of NO, which is the most important predecessor for NO_2 in the atmosphere, are located near the ground. Successively, NO_2 can be formed by oxidation of NO, the most prominent example is reaction R. 3 with O_3. Since these reactions are usually rather fast (see also chapter 2.2.1), the bulk of NO_2 is formed in close proximity to the ground. A smaller fraction of NO_2 is emitted from combustion processes, also mainly at ground level. Dilution of NO_2 within the volume of the PBL generally causes an NO_2 decrease with increasing height (see e.g. [*Alicke*, 2000; *Baumbach and Vogt*, 1995]).
But for the understanding of the HONO vertical profiles, the theory that NO_2 is converted to HONO via reaction R. 27 needs to be refined: the efficiency of different surfaces for HONO formation is still not known (see chapter 2.3). The efficiency of aerosol surfaces, which would be the only explanation for a HONO production within the PBL volume is also not quantified yet. The only recent publication on HONO profile measurements in the lower 4 m of the PBL performed by [*Stutz et al.*, 2001] at Milan, Italy, yielded no clear indication for a pronounced HONO gradient. HONO profiles measured at Nashville, USA on two light paths spanning over height ranges from 0 to 36 m and 36 to 72 m above ground level, showed HONO mixing ratios on the lower light path up to 2.5 ppb, while concentrations on the upper light path hardly exceeded the detection limit of 0.2 ppb [*Alicke*, 2000]. Other publications on HONO gradients measured on a height range comparable to the set-up at Heidelberg do not exist.

A typical 24-hour period of the Heidelberg profile data with all available meteorological information measured in April 1999 is presented in Figure 33: the three lower panels show the mean concentrations of NO_2 and HONO as well as the ratio HONO/NO_2. Meteorological information measured at the IUP and the UMEG site nearby is presented in the three upper panels. The key question that is dealt with in this chapter on the base of such data, is how the observed HONO gradients can be explained: first an overview of the variability of NO_2, HONO and the ratio HONO/NO_2 will be presented in chapters 6.1.1, 6.1.2and 6.1.3, respectively. Chapter 6.1.4 deals with the evaluation of the gradients of NO_2 and HONO in the PBL. The seasonal variation of all quantities by day and night will be discussed in chapter 6.2. The hourly means of all data will be computed and discussed in chapter 6.3 to obtain an impression of the mean diurnal variation of the trace gas time series in the different layers. Finally, chapter 6.4 will present some distinct cases studies representative of typical meteorological situations. For a full overview of all data measured during the Heidelberg long-term campaign please refer to Annex A.

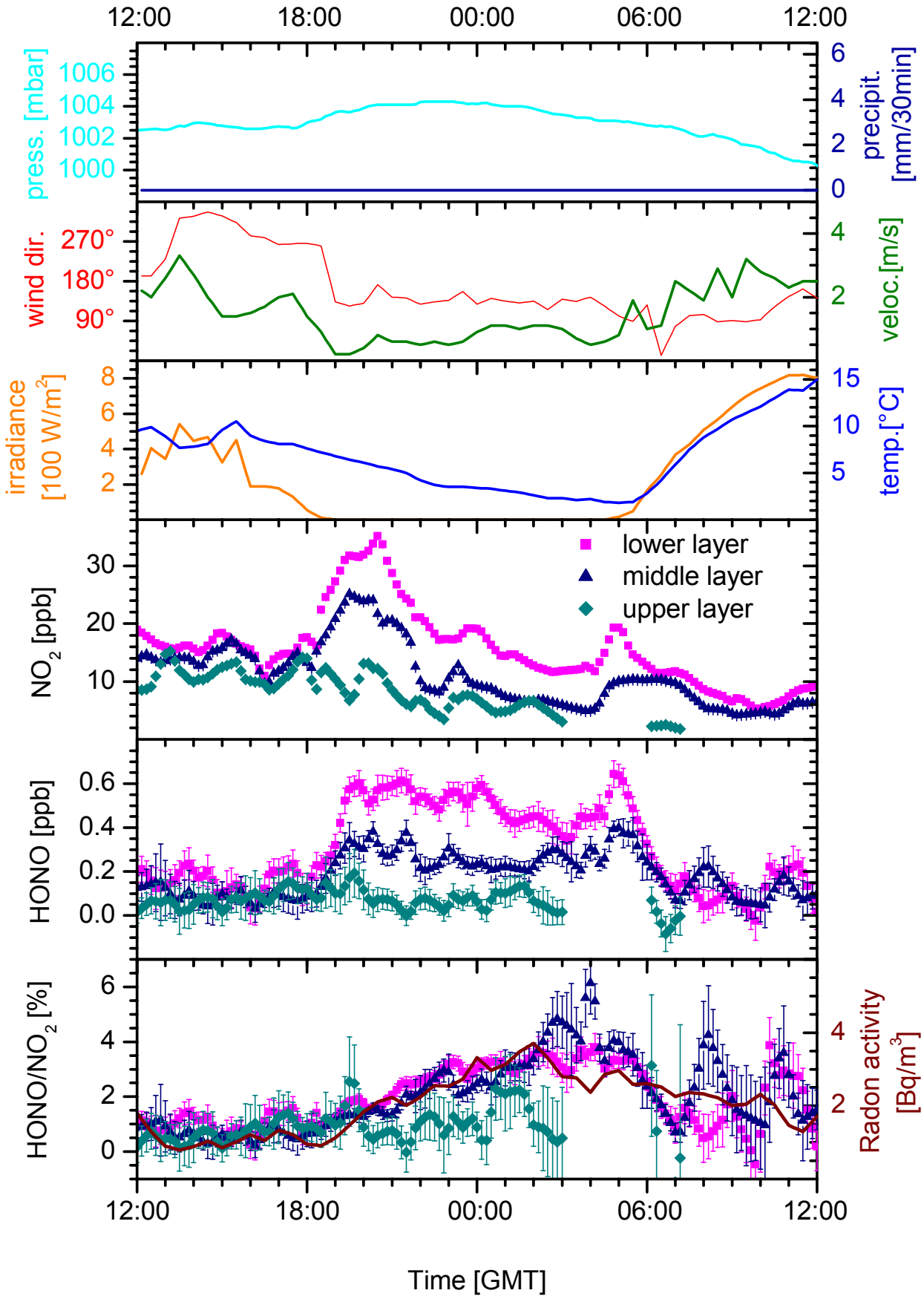

Figure 33: A typical 24-hour period of the data obtained from the long-time measurements in Heidelberg, recorded on 19/20 April 1999.

6.1.1 NO_2 time series

The NO_2 time series of a 5-week period in April/May 1999 is plotted in Figure 34 to give an impression of the variability of the data acquired during the long-term profile measurements at Heidelberg. This period was chosen because all sensitivity studies (see chapter 5.3) used this data set: the maximum NO_2 mixing ratios were up to 40 ppb in the lower layer and 25 ppb in the upper layer. The minimum values at night were found below 1.25 and 0.25 ppb, respectively. The strong diurnal variation NO_2 time series in all three layers has three likely main reasons:

- The diurnal variation of NO_x emissions by traffic causes rush-hour peaks in the morning and in the evening (see also Figure 33). Sometimes, increased traffic at noon , which is routinely observed in Heidelberg, is also visible in the diurnal variation of NO_2.
- Photochemistry forces a diurnal trend anti-correlated to solar irradiation: at daytime, the photostationary steady state between NO, NO_2 and O_3 leads to a higher fraction of NO and O_3, while at night NO_2 is preferred.
- The stability of atmospheric stratification has also an impact on the NO_2 concentrations: the ground inversion usually building up at night inhibits (to a certain degree) vertical transport and therefore causes higher NO_2 concentrations in the lower PBL.

The maximum NO_2 concentration found in the lowermost layer within the whole 13-month measurement period was recorded in January 1999 at 54.0 ppb. In the upper layer, the maximum value of 44.8 ppb was measured in March 1999 (see also chapter 6.2.2).

6.1.2 HONO time series

The HONO time series within the same 5-week period in April/May 1999 plotted in Figure 35 shows the typical variation with solar radiation [*Alicke et al.*, 2001b; *Platt et al.*, 1980]: in daytime, HONO was typically measured at or below the detection limits of 0.22 and 0.09 ppb on the lower and upper light path, respectively. Higher HONO daytime mixing ratios are typically correlated with weak solar radiation due to cloud cover, when values up to 0.6 ppb can be found. With decreasing solar radiation in the evening, the HONO mixing ratio increases to highest values at night up to 1.25 ppb. With rising solar radiation in the morning, HONO is quickly destroyed within 20 min to 2 hours by photolysis and the mixing ratio falls below the detection limit.

Within the whole measurement period, the highest HONO mixing ratio in the lowermost layer was recorded in January 1999 at 2.36 ppb, while the maximum for the uppermost layer was found at 0.78 ppb in March 1999, both at the same time when the maximum NO_2 values were measured (see chapter 6.2.3).

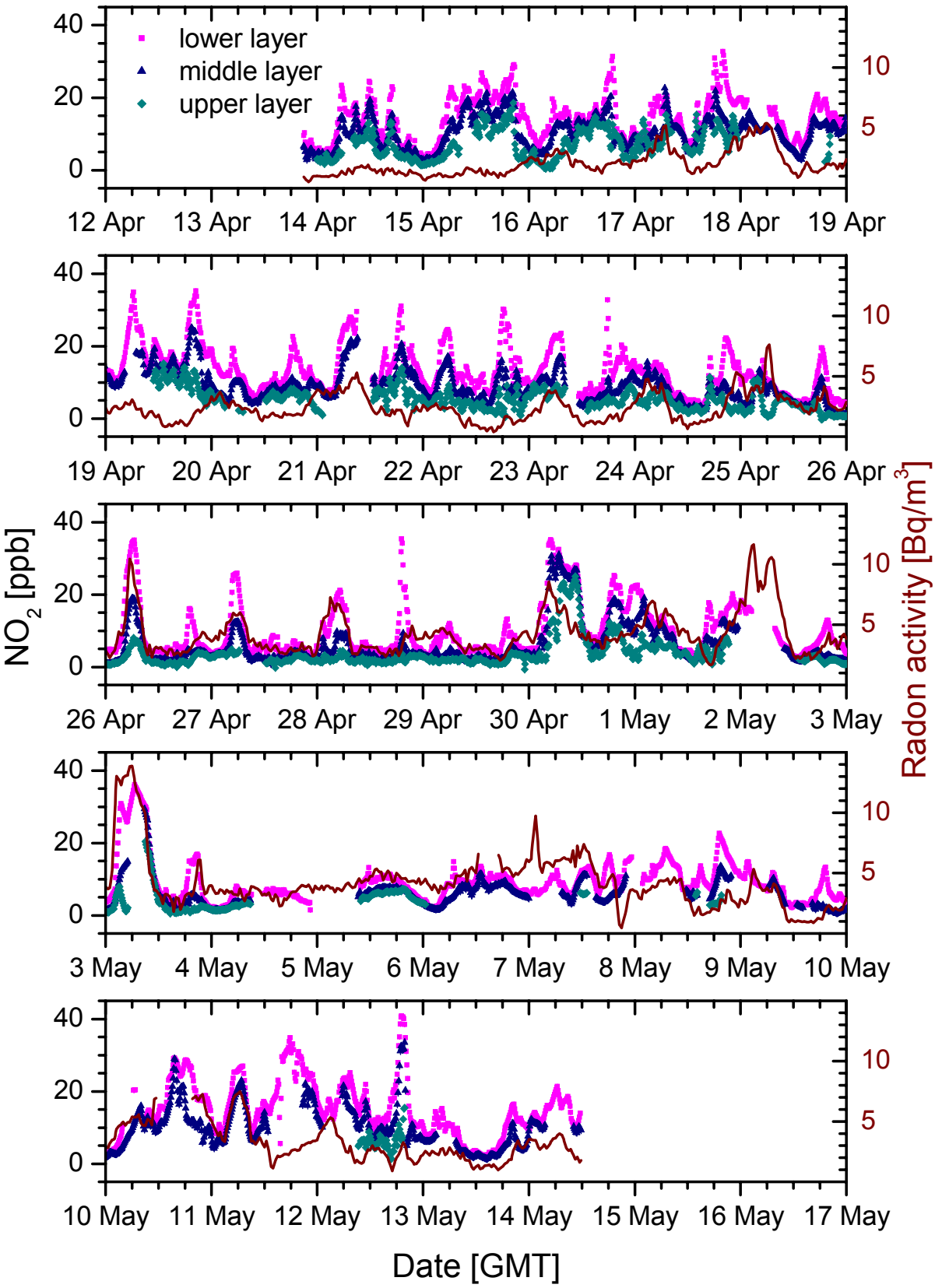

Figure 34: Overview of the NO_2 time series in the three layers evaluated by the three-layer model for 5 weeks in April/May 1999. The ticks mark 0:00 hours GMT of the respective day. Missing data are mainly caused by limited visibility in the atmosphere (especially clouds lead to missing data on the upper light path).

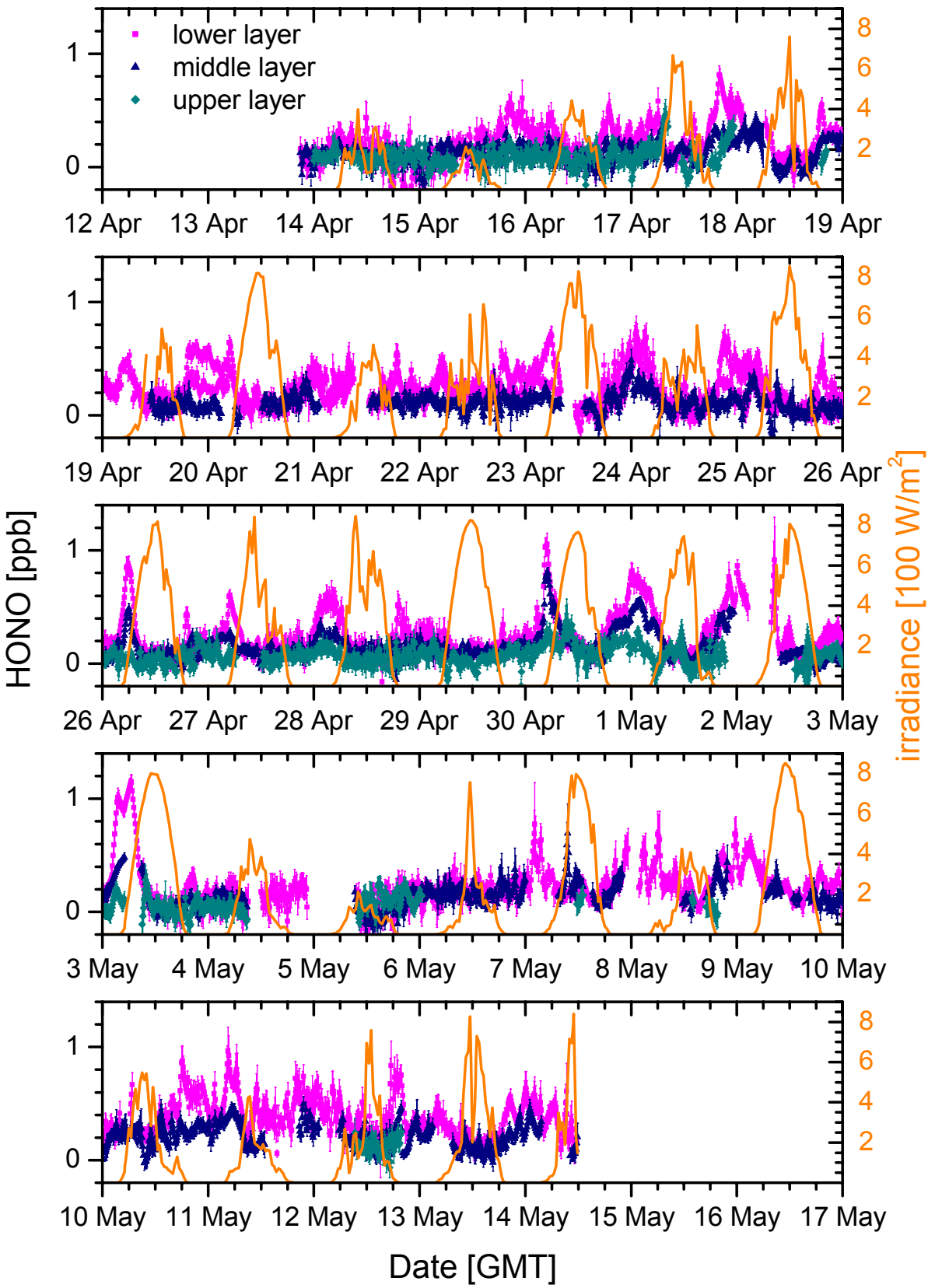

Figure 35: HONO time series evaluated by the three layer model within the same period as in Figure 34. The mean detection limits in the layers are plotted as lines and range between 0.09 and 0.22 ppb.

6.1.3 Time series of the ratio HONO/NO_2

Figure 37 shows the time series of the ratio HONO/NO_2 for the April/May 1999 period: the ratios range between 0 % up to 12 % in all three layers, with typical errors of 1% in the lower and middle layer and 1.8% in the upper layer. As already mentioned above, the HONO/NO_2 ratio shows a frequent correlation with radon activity, especially during the night. It is also obvious from Figure 37 that the errors of the ratios often prohibit an evaluation of the variation of the HONO/NO_2 ratio with height. Apart from using periods with low random errors of the fitting algorithm to estimate the vertical variation of the ratio, the evaluation of the data with respect to the mean ratios over longer periods can also provide a statistically significant result: Figure 36 shows the correlation of all HONO mixing ratios with the NO_2 mixing ratio measured during the April/May period.The HONO and NO_2 mixing ratios in the upper layer are generally smaller than the respective values in the lower layer.A linear fit to the HONO data depending on NO_2 yields a slope that decreases constantly from the lower to the upper layer. Apart from the large variations, the dependency of HONO on NO_2 is well-reproduced by the linear fit, indicating that HONO formation is indeed of first order in NO_2 and therefore proceeds primarily via R. 27. The ratio does not only depend on the height over ground, but also on the time of day. At night, typically higher HONO/NO_2 values are found than in daytime: a linear fit to the HONO values plotted against the corresponding NO_2 data (see Figure 36) yields at night a ratio of HONO/NO_2 = 2.46% and 1.97 % in the lowermost and uppermost layer, respectively. In daytime, the ratio is only found at 1.53 % in the lowermost and 1.08% in the uppermost layer. Interestingly, the difference of the ratios in the uppermost and lowermost layer is nearly constant: in the lowermost layer the ratio is about 0.5 % higher than in the upper layer at day and night.

It should be noted that, at a closer look,the diurnal variation is also visible in the time series of the ratio HONO/NO_2 plotted in Figure 37: typically, the ratio slowly increases between dawn and dusk. After dusk, the ratio decreases again, with a rate depending on solar radiation.

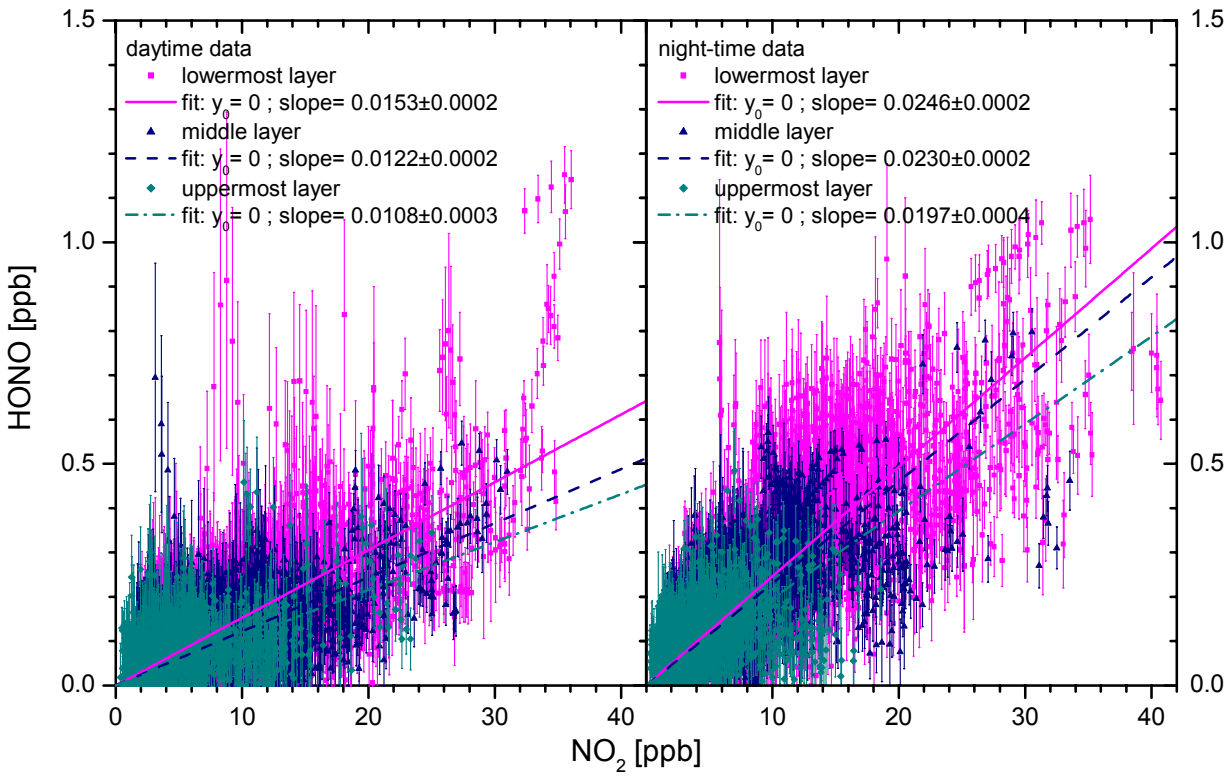

Figure 36: Correlation of HONO with NO_2 in the three layers for April/May 1999.

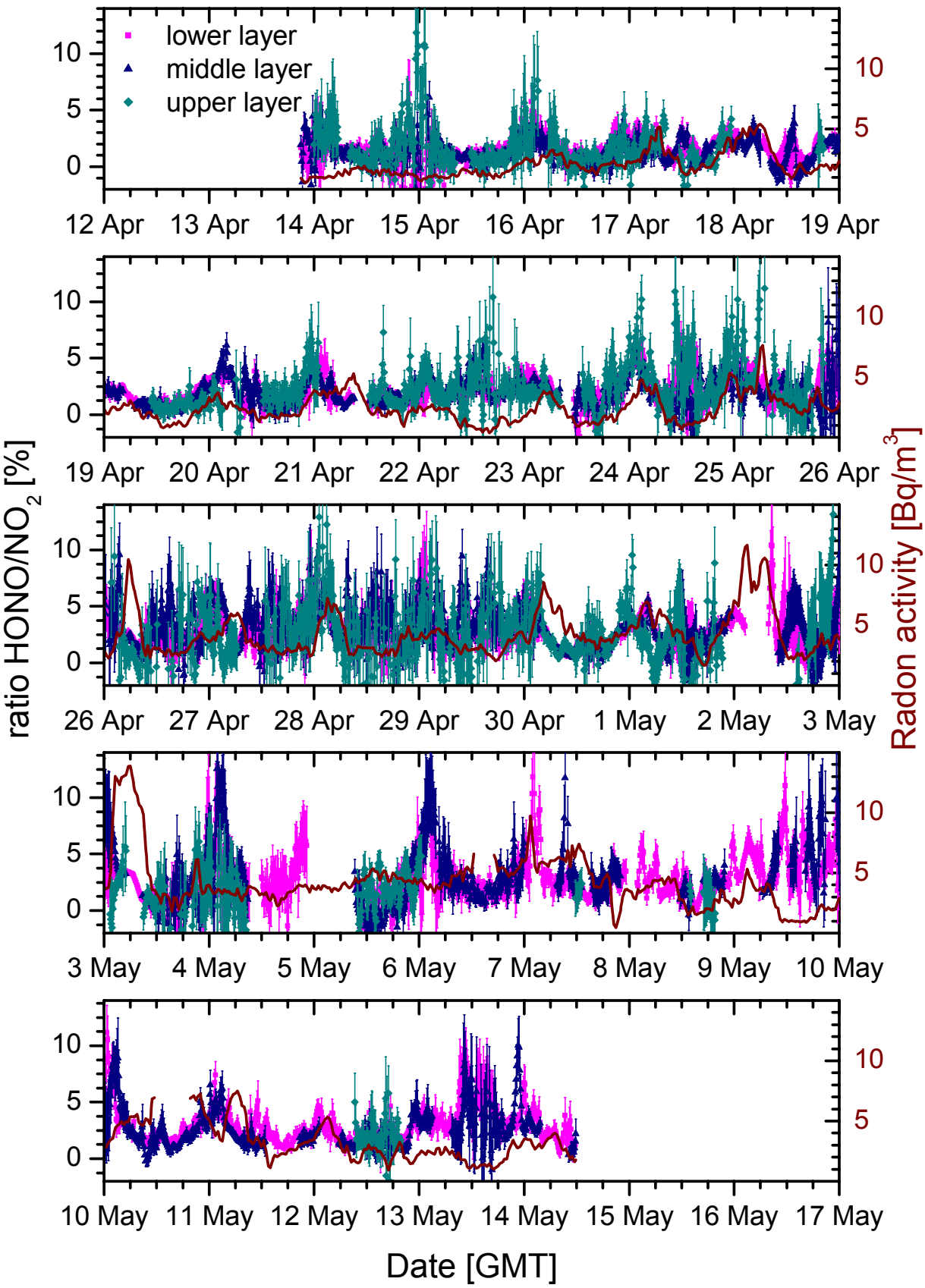

Figure 37: Time series of the ratio HONO/NO_2 in the three layers computed from the individual mixing ratios of NO_2 and HONO plotted in Figure 34 and Figure 35, respectively.

6.1.4 Vertical gradients of NO_2 and HONO

The evaluation of trace gas profile measurements with respect to the vertical gradients of the observed species is usually done with respect to the vertical fluxes J using the relation

$$\frac{dC}{dz} = \frac{J}{\kappa \cdot u^* \cdot z} \cdot \Theta\left(\frac{z}{L_{MO}}\right) \qquad \text{Equ. 12}$$

(see chapter 3.2 and references therein). However, no detailed meteorological data for the computation of the Monin-Obukhov length L_{MO} and the friction velocity u^* was available for the Heidelberg profile measurements. Thus, the evaluation of vertical fluxes would only be possible for assuming neutral stratification or typical values for L_{MO} and u^*.
Therefore, the analysis of the measurements is done with respect to concentration gradients and gradients in the trace gas ratio HONO / NO_2 to draw conclusions on source and sink processes of the observed trace gasses.

Definition of the relative gradient

To obtain a comparable measure for the decreasing or increasing mixing ratios of NO_2 and HONO, instead of the concentration gradient

$$\frac{dc}{dz} = \frac{c_i - c_{i-1}}{z_i - z_{i-1}} \qquad \text{Equ 52}$$

the relative gradient, normalised by the trace gas concentration in the lowermost layer

$$\left(\frac{dc}{dz}\right)_{rel} = \frac{dc}{dz} \cdot \frac{1}{c_1} = \frac{1}{dz} \cdot \left(\frac{c_i}{c_1} - 1\right) \qquad \text{Equ. 53}$$

can be used (with i = 2,3 for the middle and upper layer, respectively). Since the height intervals are constant for the whole measurement period, the factor $1/dz$ can be omitted. In consequence, the relative gradient defined as

$$\left(\frac{dc}{dz}\right)^{|}_{rel} = dc \cdot \frac{1}{c_1} = \frac{c_i}{c_1} - 1 \qquad (i = 2,3) \qquad \text{Equ. 54}$$

will be used to compare the gradients of NO_2 and HONO: negative values of the relative gradient indicate that the mixing ratio decreases with height over ground (which is the case for both NO_2 and HONO for almost the whole measurement period). The absolute value of the relative gradient indicates the "steepness" of the vertical trace gas profile: the larger abs($(dc/dz)_{rel}$), the larger the difference between the trace gas concentrations between the two respective layers.

Results form the relative gradient evaluation

Figure 38 shows the result of the gradient evaluation for NO_2 and HONO on 19/20 April 1999 (see Figure 33 for all data recorded on this day): the relative gradients of NO_2 and HONO between the middle and lower box (plotted in the lowermost panel) hardly differ significantly. However, in the period between 19:00 and 0:00, when the HONO concentration is at its first night-time maximum, the HONO gradient seems to be steeper than the NO_2 gradient. This finding is confirmed when looking at the relative gradient (c_3/c_1)-1 between the lowermost and the uppermost layer, which is plotted in the second panel from below. Throughout the night – when the HONO mixing ratios are well above the detection limits and guarantee small errors in the relative gradient – the HONO gradient is steeper than the NO_2 gradient.
Figure 39 depicts the relative gradient between the lowermost and uppermost layers for NO_2

and HONO for the whole April/May 1999 period and simultaneously the main problem of the gradient evaluation, especially for the HONO gradients: the large errors that mainly result from the random errors of the DOAS trace gas evaluation prohibit a clear distinction between the relative gradients of the different species. Thus, information on the formation pathway of HONO is seldom available with the same 10-minute time resolution as used for the evaluation of the trace gas measurements. However, most relative gradients for NO_2 and HONO range between 0 and –1, with the absolute value of the HONO gradient usually larger than for NO_2, as already concluded from the 24-hour period plotted in Figure 38.

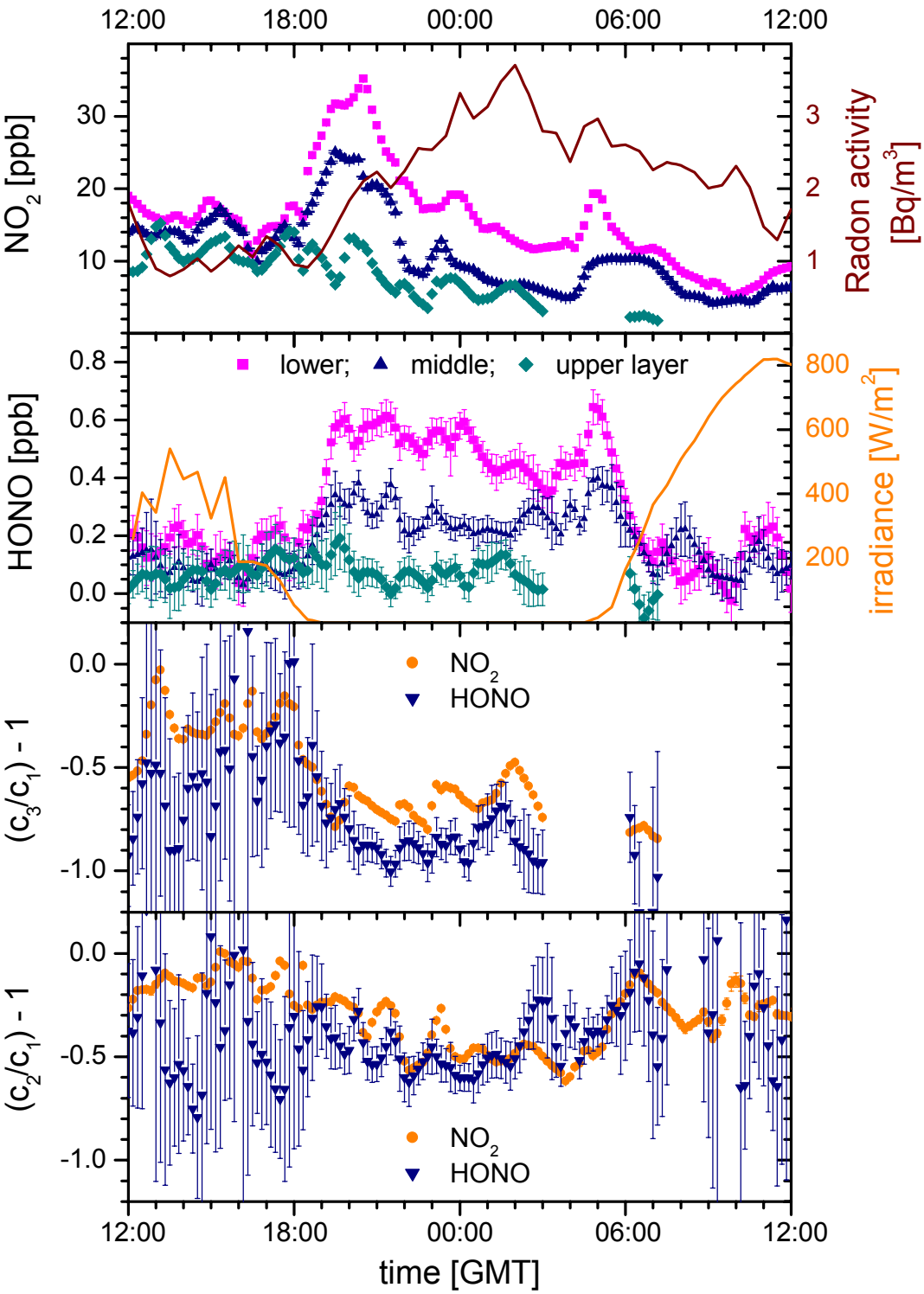

Figure 38: Vertical profiles and relative gradients (see Equ. 54) of NO_2 and HONO on 19/20 April 1999.

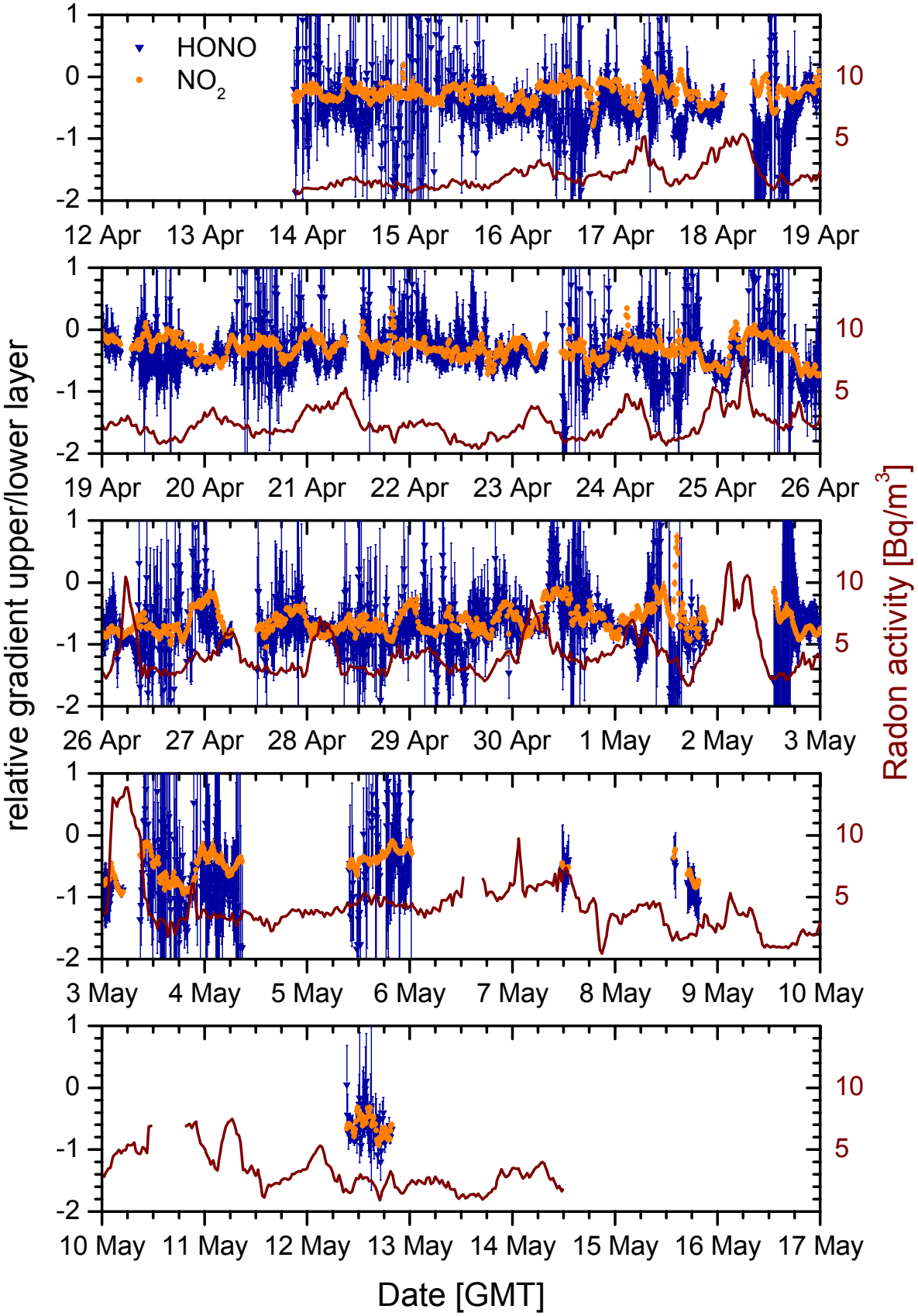

Figure 39: Vertical profiles of NO_2 and HONO as well as the Radon activity (full line) in the April/May 1999 period.

6.2 Evaluation of the monthly means

6.2.1 Statistical methods for data evaluation

The statistical evaluation of the measured data is applied to compensate the errors of the individual data points for the ratio NO_2 and the gradients of NO_2 and HONO. Additionally, the statistical evaluation is used to obtain mean values typical for a defined time period or meteorological situations. A useful method is the frequency analysis of all data measured within a defined period. Figure 40 illustrates this method for the relative gradients of NO_2 and HONO (upper two panels) and the ratio HONO/NO_2 in the three layers (lower panel): the total number of all data points found in a given interval is plotted against the interval mean. A suitable distribution function can be fitted to the resulting curve, to obtain the distribution mean and the standard deviation (or a comparable quantity).

To get an impression of the mean gradients that could be observed in the April/May 1999 period discussed above, the relative gradients both of NO_2 and HONO found between layers 2 and 1 as well as between layers 3 and 1 are plotted with their occurrence in Figure 40. The mean values μ of the Gauss distribution fitted to the measured data and their respective errors indicate that the absolute value of the HONO gradient is larger than the one of NO_2 for both $(c_2/c_1) - 1$ and $(c_3/c_1) - 1$. The ratio HONO versus NO_2 decreases almost constantly from the lower to the upper layer.

However, the standard deviations σ for the different Gauss fits are always larger than the differences of the distribution means. For the understanding of this observation, two effects have to be taken into consideration:

- The width of the distribution is linked to the statistical errors of the DOAS evaluation: consequently, the measured values differ from the real (and constant) value within the limits imposed by the errors of the DOAS evaluation.
- The "real" value, which is measured, is also subject to variations that are forced by atmospheric parameters. For example, the ambient HONO concentration is subject to variations forced by solar irradiation and atmospheric stability, which are significantly larger than the 1 σ errors of the DOAS evaluation.

Thus, for the data presented here, the distribution mean gives an average value for the relative gradients or ratios of HONO and NO_2 for all atmospheric conditions which occurred during the observation period of nearly five weeks. The standard deviation represents the interval in which the gradient or ratio will be found under most atmospheric conditions and not – as it will would? be the case in a purely statistical process – the 1σ deviation of the measured values from the average (or real) value.

The criteria for the significance of data obtained from the evaluation by a Gauss distribution are applied For a better understanding of the statistics, (e.g. [*Taylor*, 1990]). The confidence interval

$$\Delta U = \mu \pm \frac{Z \cdot \sigma}{\sqrt{n}} = \mu \pm \varepsilon \qquad \left(\text{with } \varepsilon = \frac{Z \cdot \sigma}{\sqrt{n}} \right) \qquad \text{Equ. 55}$$

is used for that purpose. Here, μ represents the distribution mean, Z is the probability factor depending on the desired level of confidence ([*Taylor*, 1990] defines Z = 3 for a confidence level of 99.74%) and n is the number of values of the distribution (ranging between 4171 and 2570 for the dataset discussed here). If σ exceeds ΔU, a value differs significantly from zero. To decide whether two distribution means differ significantly at a certain level of confidence, the mean value of one distribution is compared to the confidence interval of the other and vice versa. If both confidence intervals do not include the mean of the other distribution, the means differ significantly.

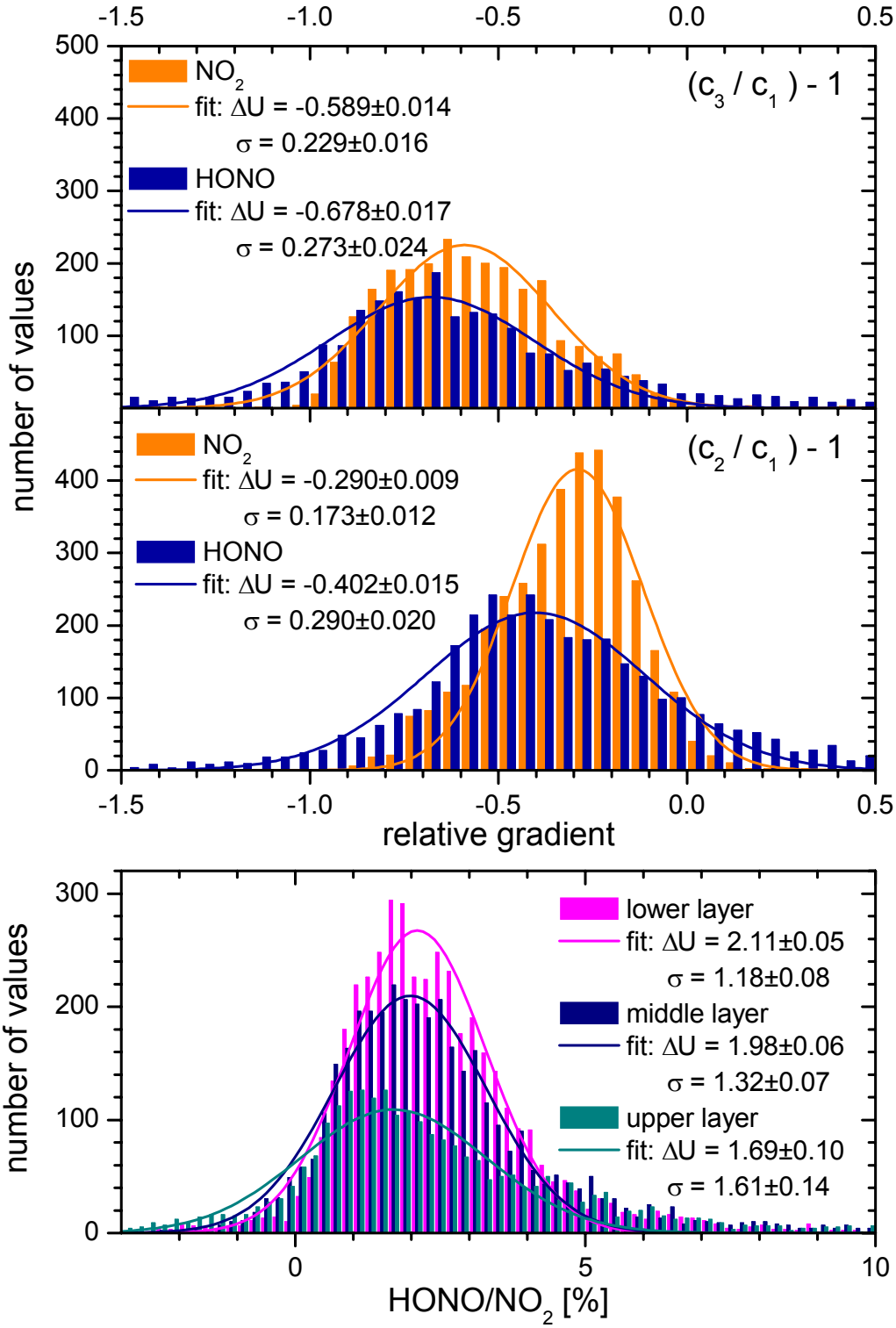

Figure 40: Comparison of the relative gradients of NO_2 and HONO obtained by the model for April / May 1999 . The probability distribution for the relative gradient is plotted, computed by using the approximately 4000 data points available. Gauss fits yield the mean gradients between layers 2 and 1 as well as between layers 3 and 1 (with negative values indicating concentrations decreasing with height). ΔU denotes the confidence interval defined by the mean μ and its error ε (with 2ε being the width of the confidence interval, see Equ. 55) at a 99.74 % level of confidence. σ labels the standard deviation (see text). The lowermost panel shows the probability for the ratio $HONO/NO_2$ in the three layers and the respective Gauss fits.

The statistical evaluation of the data plotted in Figure 40, using the criteria mentioned above, yields the relative gradients presented in Table 12. Comparing the mean gradients of NO_2 and HONO between the upper and lower layer and their respective confidence intervals, values of $\Delta U = -0.59 \pm 0.01$ and $\Delta U = -0.68 \pm 0.02$ are found for NO_2 and HONO, respectively. It becomes evident from Table 12 that both relative gradients $(c_3/c_1) - 1$ and $(c_2/c_1) - 1$ are significantly steeper for HONO than for NO_2. This proposition is still valid at a confidence level of 99.99 %. Therefore we can conclude that the HONO decrease with height is always sharper than the decrease of NO_2 for the atmospheric conditions found in Heidelberg. The standard deviations of the relative gradients $(c_3/c_1)-1$, however, are found at values of $\sigma = 0.23$ for NO_2 and $\sigma = 0.27$ for HONO. Thus, the variability of the atmospheric conditions within a 5-week period causes large variations in the NO_2 and HONO gradients.
The evaluation of the ratios $HONO/NO_2$ is also shown in Figure 40. The results of the Gauss fit are summarised in Table 13. The mean ratio in the lower layer is found at a value of $\Delta U = 2.11 \pm 0.05$ %, decreasing significantly to 1.98 ± 0.06 % in the middle layer and 1.69 ± 0.10 % in the upper layer. These findings further confirm the fact that HONO decreases more sharply with height than NO_2. Large variations of the ratio $HONO/NO_2$ caused by atmospheric conditions are also found here, indicated by the standard deviations of $\sigma = 1.18$ % in the lower layer to $\sigma = 1.6$ % in the upper layer.

Table 12: Overview of the relative gradients gained by the statistical evaluation of the April/Mai 1999 period of the long-term measurements in Heidelberg. Given are the number of data points n, the mean values μ and the standard deviations σ of the Gauss fit and the half-width of the confidence interval (computed at a confidence level of 99.74 %, i.e. for Z = 3) for the mean gradients of NO_2 and HONO, respectively.

		NO_2			HONO		
	n	μ	$\varepsilon = \frac{Z\sigma}{\sqrt{n}}$	σ	μ	$\varepsilon = \frac{Z\sigma}{\sqrt{n}}$	σ
c_2/c_1	3730	-0.290	0.009	0.173	-0.402	0.015	0.290
c_3/c_1	2550	-0.589	0.014	0.229	-0.678	0.017	0.273

Table 13: Overview of the ratios $HONO/NO_2$ for the three layers gained by the statistical evaluation of the April/Mai 1999 period. The half-width of the confidence interval is computed for a confidence level of 99.74 %.

Layer	n	μ [%]	$\varepsilon = \frac{Z\sigma}{\sqrt{n}}$ [%]	σ [%]
1	4171	2.11	0.05	1.18
2	3804	1.98	0.06	1.32
3	2570	1.69	0.10	1.61

NO_2 and HONO mixing ratios feature a strong diurnal variation that is not only forced by the changing emission rates of nitrogen oxides, but also by the effectiveness of vertical transport. Thus, a more detailed evaluation of the monthly means of the HONO/NO_2 ratio and the gradients of NO_2 and HONO is necessary, even for the discussion of the monthly means. That is why the statistical evaluation presented above for was repeated, but separately for all data recorded from 06:00 to 18:00 GMT and 18:00 to 06:00 GMT, respectively.
The resulting frequency analyses and Gauss fits for the ratios HONO/NO_2 are presented in Figure 41: obviously, the ratios show the same height dependency already reported for the analysis of the April/May 1999 data presented above. However (but not surprisingly), the ratio HONO/NO_2 is substantially smaller in daytime than at night for all three layers. In the lower layer, a daytime mean ratio of 1.6 % is found, which compares to 2.7 % at night. In the upper layer, the day/night difference is of the same order?: ratios of 1.1 % and 2.3 % are found by day and night, respectively. Figure 42 and Figure 43 show the result of the statistical analysis of the diurnal and nocturnal gradients evaluated for the April/May 1999 period, respectively. As for the ratios, the overall picture does not change, but the gradients of both, NO_2 and HONO, are steeper at night than by day. This effect is more pronounced for the relative NO_2 gradient between the lower and upper layer rising from an absolute value of 0.53 by day to 0.64 at night. The HONO gradient increases only from 0.64 in daytime to 0.70 at night. Chapter 6.2.5 deals with the detailed discussion of the monthly means of the gradients.

The evaluation technique discussed here was used in a total of 9 periods of the Heidelberg profile data, each comprising 4 to 5 weeks. The frequency analysis plots are shown in Annex A, including the Gauss distributions fitted to the measurement data and the resulting confidence intervals and standard deviations. The following sections present a detailed discussion of the seasonal trend of the means of NO_2, HONO, their ratio and the respective gradients.

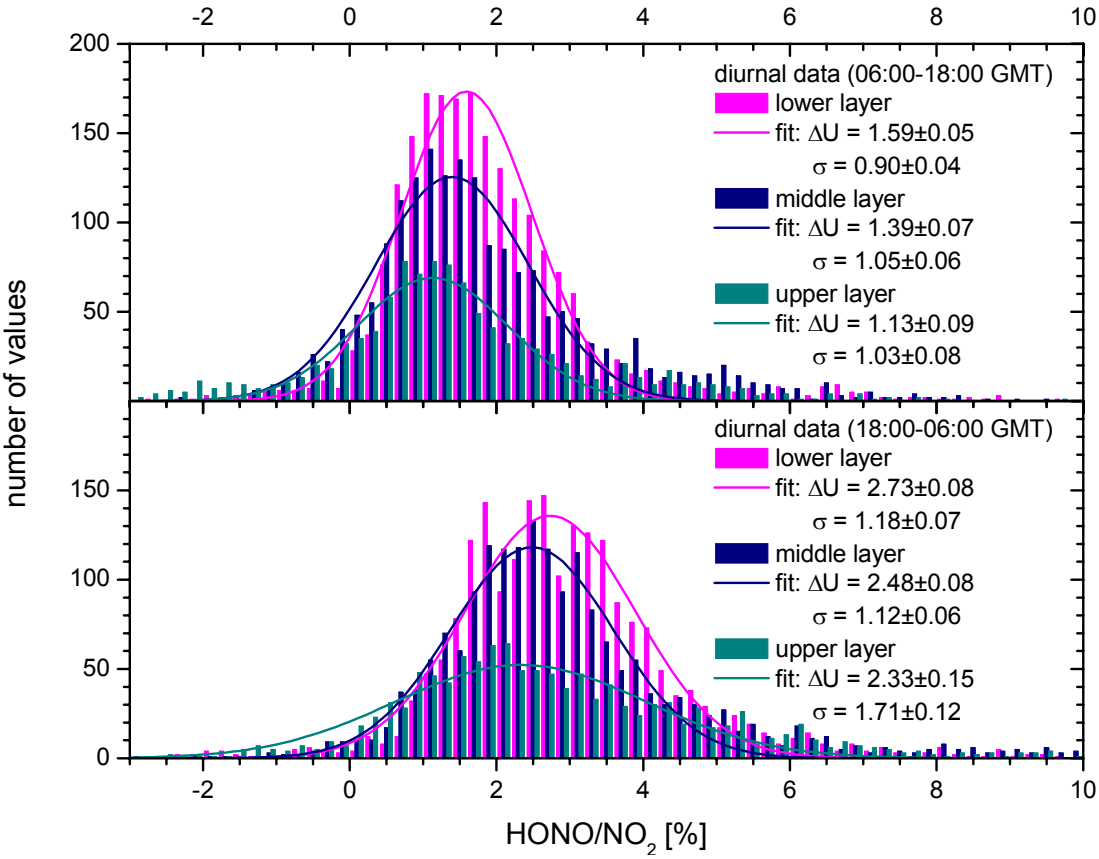

Figure 41: Comparison of the frequency analysis for the diurnal and nocturnal HONO/NO_2 ratios in the three layers and the respective Gauss fits.

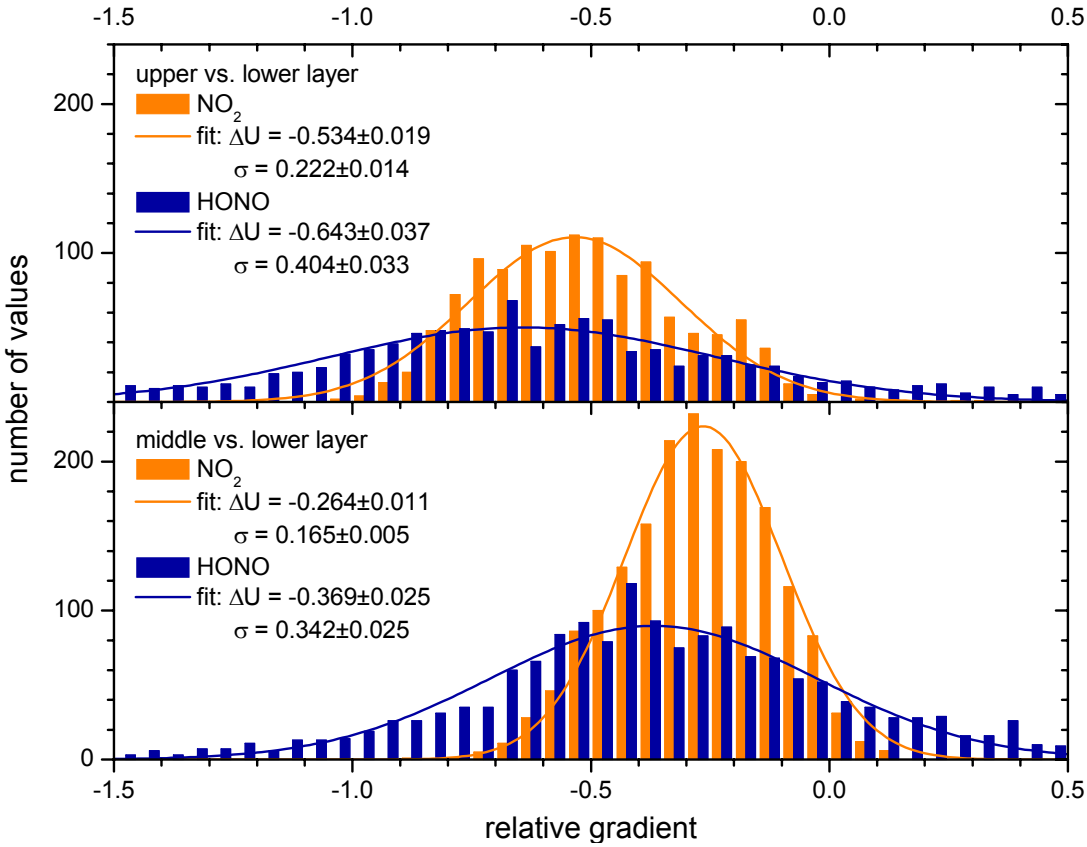

Figure 42: Comparison of the relative gradients of NO_2 and HONO for the daytime (06:00 to 18:00 GMT) data of the April / May 1999 period.

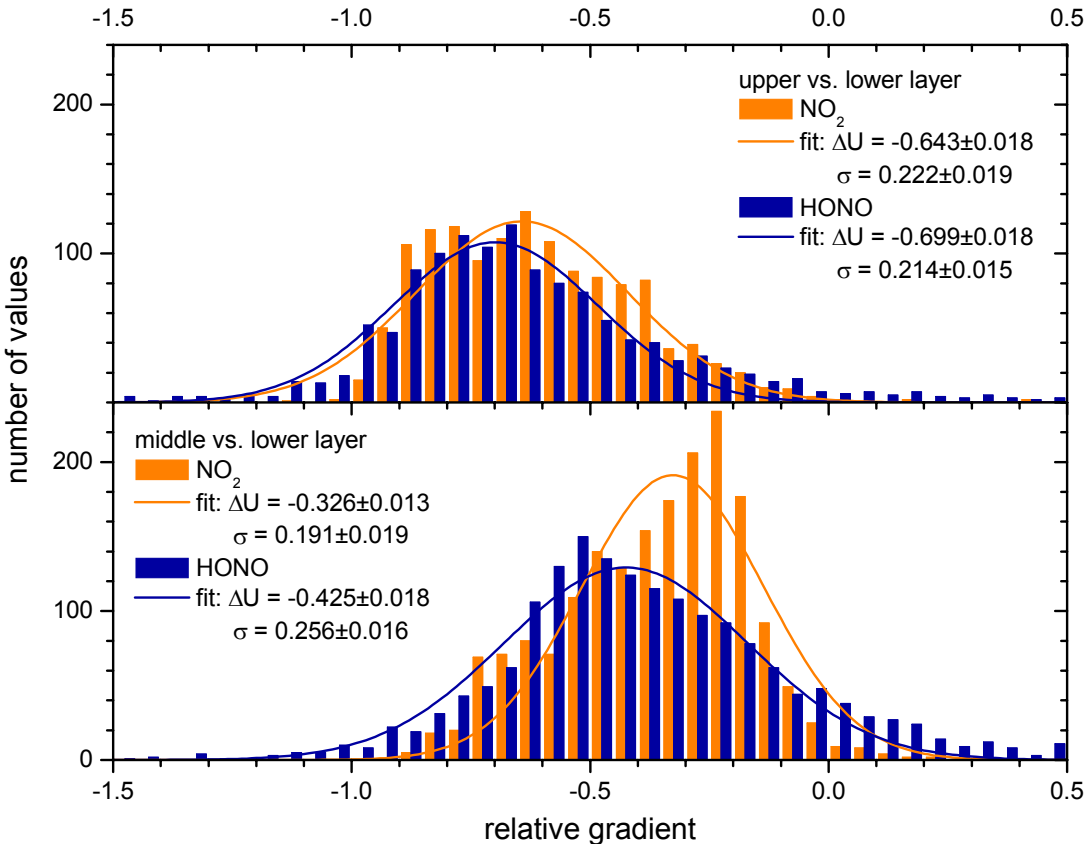

Figure 43: Comparison of the relative gradients of NO_2 and HONO for the night-time (18:00 to 06:00 GMT) data of the April / May 1999 period.

6.2.2 Seasonal trend of NO_2

The dependency of the monthly NO_2 means on solar irradiation is obvious in the seasonal trend of NO_2 plotted in Figure 44. For the diurnal data, an anti-correlation of solar irradiation and the NO_2 mean can easily be understood by the photochemical steady state system between NO, NO_2 and O_3, which is described by the Leighton ratio

$$\frac{[O_3]\cdot[NO_2]}{[NO]} = \frac{k_{O_3+NO}}{J_{NO_2}} \quad \text{or} \quad [NO_2] = \frac{[NO]}{J_{NO_2}} \cdot k_{O_3+NO} \cdot [O_3] \qquad \text{R. 4}$$

in the undisturbed case and

$$[NO_2] = \frac{[NO]}{J_{NO_2}} \cdot \left\{ k_{O_3+NO_2} \cdot [O_3] + k_{HO_2+NO_2} \cdot [HO_2] + \sum_{RO_2} k_{RO_2+NO} \cdot [RO_2] \right\} \qquad \text{R. 14}$$

in the presence of VOCs. In both cases, the NO_2 concentration is expected to be linearly anti-correlated to J_{NO2}, which is directly correlated to solar radiation (see e.g. [*Alicke*, 2000]). For the March 1999 to December 1999 period, the anti-correlation of NO_2 and solar irradiation is found in all three layers. It should be noted that the anti-correlation of NO_2 and irradiation is also caused by the time intervals chosen for the computation of the means: the diurnal mean is the average of all values between 06:00 and 18:00 GMT, the nocturnal mean is computed for all data recorded between 18:00 and 06:00. Obviously, in summer the diurnal (and also the nocturnal) NO_2 is exposed to irradiation for a larger fraction of the day than in winter. Despite this effect, fixed time intervals for the computation of the means were preferred to a timescale linked to the solar zenith angle, as the emission maxima of NO_2 were found to be strongly dependent on the time of day (see annex A).

In the winter months January and February, deviations from this anti-correlation are observed: comparing the daytime NO_2 means and irradiances of November and December 1999 to the corresponding values in the Jan/Feb 1999 and February 2000 periods, one would expect smaller NO_2 means in January and February, as the mean irradiation in these months is higher than in November and December. A possible cause for the higher NO_2 means observed in January and February might be less effective vertical transport in these months, as urban NO_2 concentrations are often found to be anti-correlated to the efficiency of vertical transport (see e.g. [*Febo et al.*, 1999]). A direct dependency of NO_2 on radon activity (i.e. vertical mixing) is not clearly indicated by Figure 44: especially in February 2000, one would expect a higher mean radon activity to explain the observed NO_2 concentrations. However, radon measurements were interrupted for nearly 2 weeks in February 2000. Thus the indicated radon mean might be not fully representative for the whole month. The mean nocturnal temperatures, which are also plotted in the lower panel, should also have an impact on the NO_2 concentrations: at low temperatures, heating causes increased NO_2 emissions, which might – in conjunction with less effective vertical transport – be an explanation for the high NO_2 concentrations observed in Jan/Feb 1999.

Other, more complex chemical and meteorological processes also have an impact on the diurnal variation of NO_2, but these will be discussed later.

The monthly NO_2 means in the three layers presented in Table 14 and Figure 44 further confirm findings that the NO_2 concentration always decreases with altitude: this is caused by the fact that most NO_x sources in the PBL are near the ground. A detailed discussion of the gradients will follow in chapter 6.2.5.

Table 14: Characteristic values for the NO_2 evaluation of the Heidelberg campaign.

NO_2	diurnal average [ppb]			nocturnal average [ppb]			maximum [ppb]		detection limit [ppb]	
layer	1	2	3	1	2	3	1	3	1	3
Jan/Feb 99	21.5	15.3	7.0	20.5	15.7	6.5	54.0	31.4	0.29	0.17
Mar/Apr 99	14.3	9.9	6.5	17.4	11.8	6.9	48.9	44.8	0.32	0.19
Apr/May 99	11.5	8.4	5.5	12.7	8.0	4.5	40.8	25.0	0.4	0.17
Aug 1999	10.3	7.8	3.6	10.7	6.6	3.3	48.6	18.3	0.37	0.19
Sep 1999	13.4	9.4	4.9	13.2	7.9	4.4	50.1	21.4	0.31	0.2
Oct 1999	16.1	12.3	7.0	14.5	11.8	8.2	39.6	36.2	0.36	0.16
Nov 1999	19.2	16.0	10.9	18.3	16.3	12.0	51.1	37.1	0.36	0.17
Dec 1999	18.7	14.4	8.2	15.7	12.9	6.0	49.7	31.8	0.43	0.19
Feb 1999	20.9	16.1	11.0	20.0	15.5	10.1	48.8	39.6	0.36	0.17

(1) average for all data points measured between 06:00 and 18:00 GMT
(2) average for all data points measured between 18:00 and 06:00 GMT

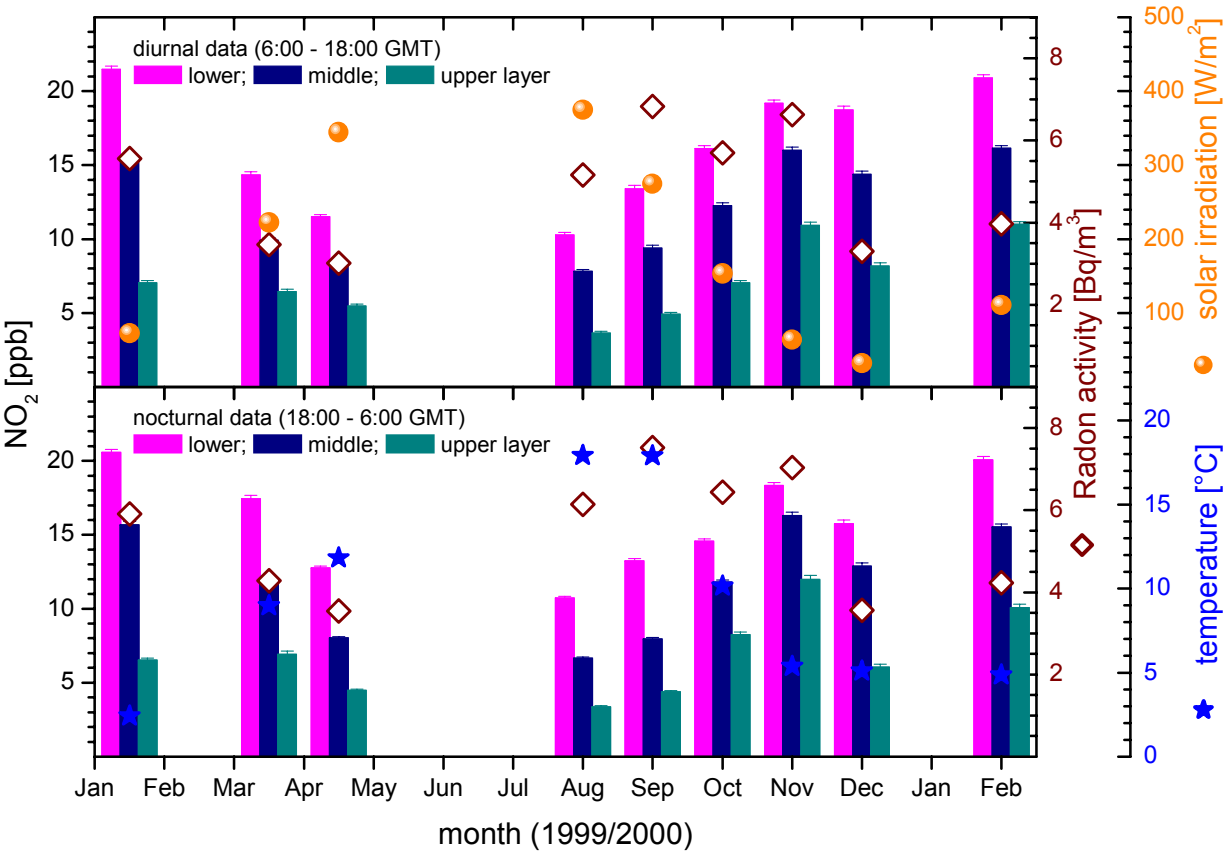

Figure 44: Seasonal trend of diurnal (upper panel) and nocturnal (lower panel) NO_2 compared to Radon activity.

6.2.3 Seasonal trend of HONO

Table 15 and Figure 45 present an overview on the diurnal and nocturnal monthly averages and the maximum mixing ratios of HONO measured in the respective periods. The mean and maximum HONO mixing ratios measured during the Heidelberg long-term campaign are listed in Table 15. These values compare well to other HONO measurements in a moderately polluted environment: most recently, a study by [*Reisinger*, 2000] at Christchurch, New Zealand, found maximum HONO mixing ratios up to 2.9 ppb at a corresponding NO_2 value of 33 ppb, while the bulk of the HONO data was below 1 ppb at night and 100 ppb during the day, respectively. [*Alicke*, 2000] reports a night-time HONO maximum of about 1.2 ppb, typical HONO values at night of 0.3-0.6 ppb and below 0.11 ppb by day at Pabstthum near Berlin/Germany during the BERLIOZ campaign. The HONO maximum coincided with a NO_2 mixing ratio of 20.5 pp, while typical NO_2 night-time data was about 3-6 ppb. Other measurements by [*Ackermann*, 2000; *Andres-Hernandez et al.*, 1996; *Harrison et al.*, 1996; *Notholt et al.*, 1992] show similar results.

Figure 45 clearly indicates that the diurnal average of HONO is strongly anti-correlated to solar radiation. This finding is expected, as HONO photolysis

$$HONO + h\nu \xrightarrow{300nm<\lambda<405nm} OH + NO \qquad \text{R. 21}$$

is linked directly to solar radiation in almost the same way as NO_2 photolysis. Thus, the diurnal means of HONO show nearly the same trend as the corresponding NO_2 values. However, some distinct differences are obvious: daytime HONO values in January and February are not increased in the same way as NO_2, while in December 1999, daytime HONO is much lower compared to the NO_2 mean measured in the same month. An explanation for this behaviour is not obvious from Figure 45, as not only solar radiation but also vertical transport should have the same effect on HONO and NO_2 (see e.g. [*Febo et al.*, 1996; *Lammel*, 1996]).

The nocturnal HONO means show a direct correlation to radon activity, which is much more pronounced than for NO_2, especially in the winter months. Interestingly, the highest HONO concentrations of 2.36 ppb at night were not measured in November 1999, where the highest mean (also for Radon) is found, but in January 1999 coinciding with extremely high Radon activities. Thus, the HONO mixing ratio in the lower layer is strongly forced by Radon activity, even more than the mixing ratio of NO_2. This is the first strong indication that HONO is formed predominantly near the ground: [*Febo et al.*, 1999] state that especially trace gasses emitted or formed near the ground feature a direct and strong correlation to radon activity.

The second indication for a dominant HONO ground source is the fact that the HONO mean decreases strongly with height in the whole measurement period. Especially in the uppermost layer, a nocturnal HONO “background” hardly exceeding monthly means of 0.1 ppb is found throughout the year. In daytime, the HONO gradient seems to be even more pronounced: in the upper layer, a mean of about 0.05 ppb is found. It should also be noted that the mean HONO mixing ratio in the upper layer shows only a weak seasonal cycle in day- and night-time, which contrasts with the strong seasonal variations in the lower and the middle layer.

The seasonal variation of the HONO gradient, which should yield further information on HONO source processes – especially when compared to the corresponding NO_2 gradients – will be discussed in chapter 6.2.5 below.

Table 15: Characteristic values for the HONO evaluation of the Heidelberg campaign.

HONO	diurnal(1) average [ppb]			nocturnal(2) average [ppb]			maximum [ppb]		detection limit [ppb]	
layer	1	2	3	1	2	3	1	3	1	3
Jan/Feb 99	0.40	0.21	0.06	0.51	0.31	0.11	2.36	0.47	0.15	0.09
Mar/Apr 99	0.15	0.07	0.04	0.36	0.23	0.12	1.17	0.78	0.17	0.1
Apr/May 99	0.19	0.12	0.07	0.34	0.20	0.11	1.15	0.49	0.21	0.09
Aug 1999	0.16	0.06	-0.04	0.28	0.11	0.00	1.61	0.61	0.21	0.11
Sep 1999	0.30	0.16	0.08	0.50	0.25	0.12	1.80	0.46	0.17	0.1
Oct 1999	0.39	0.19	0.06	0.50	0.27	0.11	2.10	0.58	0.2	0.09
Nov 1999	0.49	0.25	0.10	0.56	0.34	0.17	1.50	0.73	0.2	0.09
Dec 1999	0.31	0.16	0.07	0.34	0.20	0.10	1.82	0.54	0.21	0.1
Feb 1999	0.33	0.18	0.11	0.46	0.27	0.17	1.62	0.73	0.2	0.09

(1) average for all data points measured between 06:00 and 18:00 GMT
(2) average for all data points measured between 18:00 and 06:00 GMT

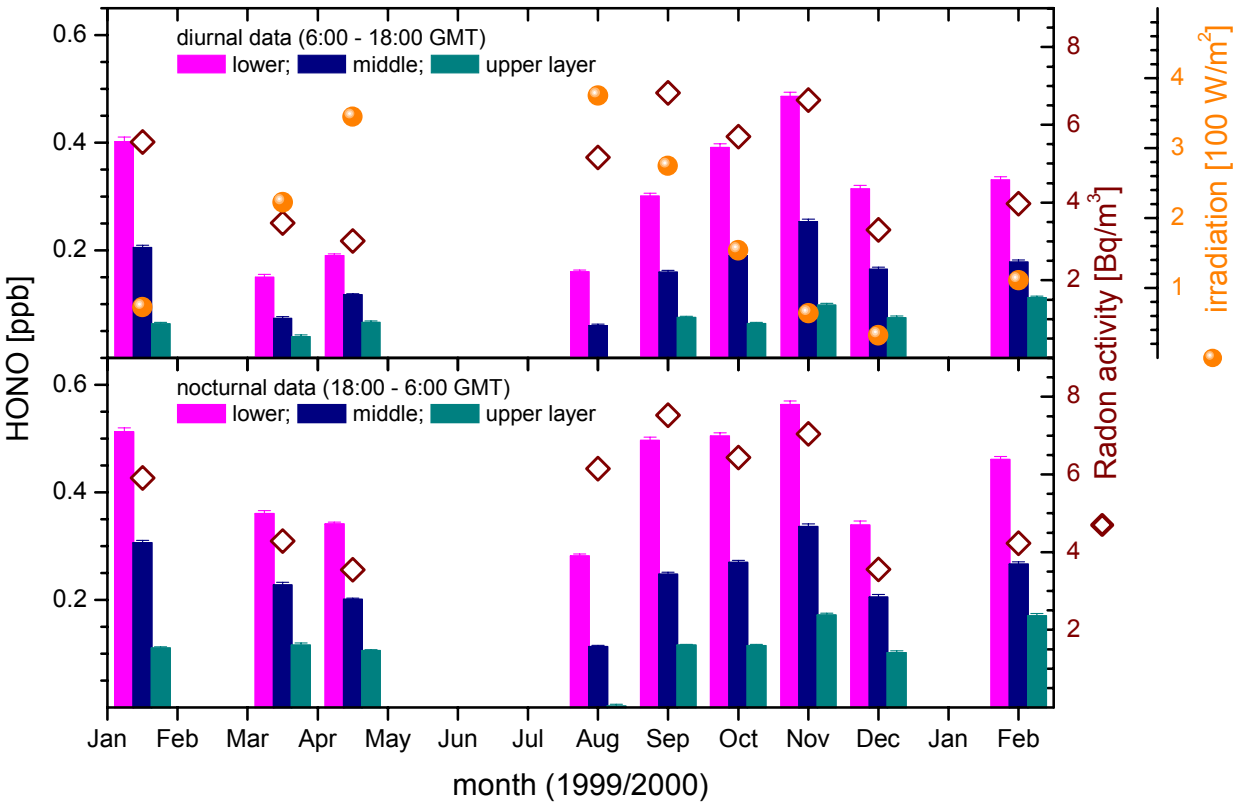

Figure 45: Seasonal trend of diurnal (upper panel) and nocturnal (lower panel) HONO in the three layers compared to Radon activity.

6.2.4 Seasonal trend of the HONO/NO_2 ratio

Comparing the time series of HONO and NO_2 plotted in Figure 35 and Figure 34, respectively, it is obvious that both species are strongly correlated. Figure 37 indicates that the ratio HONO/NO_2 is not constant, but varies with time and with height– which is the focus of this thesis – . The effects of solar radiation and radon activity (i.e. vertical transport) on the ratio HONO/NO_2, which were already reported in the general discussion (chapter 6.1.3), can also be seen in the seasonal trend presented in Table 16 and Figure 46.

Obviously, the ratio is smaller by day than at night: in the lower layer, the monthly means of daytime HONO/NO_2 range from 0.7 % in March/April 1999 to 2.3 % in November 1999, with a typical error of 0.06 %. The nocturnal ratios are found between 2.0 % in March/April 1999 and 3.3 % in October 1999. Earlier publications by [*Andres-Hernandez et al.*, 1996; *Appel et al.*, 1990; *Febo et al.*, 1996; *Harrison and Kitto*, 1994; *Harrison et al.*, 1996; *Notholt et al.*, 1992; *Sjödin*, 1988] report a wide range between 0.5 % and 5 % for the HONO/NO_2 ratio. Recent measurements by [*Reisinger*, 2000] found HONO/NO_2 at a mean (day- and night-time) value of (1.6±1.0) %, while [*Alicke*, 2000] reports a steady state after sunset that does not exceed HONO/NO_2 = 5 % in Milan, near Berlin. and in Nashville/USA. The mean nocturnal values presented here are expectedly smaller, as [*Alicke*, 2000] states that the steady state builds up in the course of the night to be fully established in the middle of the night. A detailed discussion of the diurnal cycle of HONO/NO_2 will follow in chapter 6.3.2.

The ratio always decreases with altitude, with the exception of the nocturnal HONO/NO_2 profile in December 1999 and both diurnal and nocturnal profiles in February 2000. In these cases, the ratios in the middle and upper boxes are within the confidence intervals of each other. But still, the differences between the lower and the upper layer are evident: by day, ratios between 0 % and 1.3 % are found in the uppermost layer while at night the ratios increase to 0.1 % and 2.5 % in August 1999 and September 1999, respectively. It is rather surprising that the maxima and minima of the monthly means of the upper layer are found in two successive months. However, the fact that the HONO/NO_2 ratio is near zero in August is mainly caused by the fact that HONO concentrations in this month were found to be extremely low in the uppermost layer (see previous chapter), while at the same time measurements on the upper light path were only possible for only 10 days (due to maintenance work on the Königsstuhl radio tower). Thus, the results of the statistical evaluation of the data obtained on the upper light path are questionable.

In literature, the ratio HONO/NO_2 has mostly been used to obtain information on the influx of aerosol surfaces. In the case that HONO is formed effectively on aerosol, the ratio of HONO versus NO_2 is expected to be linked to the surface area of the aerosols present within the observed air mass. Most recently, [*Reisinger*, 2000] states that highest HONO/NO_2 values coincide with the detection of an high aerosol surface area on the DOAS light path, while [*Alicke*, 2000] could not find any dependency of the ratio on aerosol concentration and surface are, even in heavily polluted Milan. However, [*Febo et al.*, 1996; *Febo et al.*, 1999; *Lammel*, 1996] strongly recommend to include the efficiency of vertical mixing in the evaluation of the HONO/NO_2 ratios, as vertical mixing could force a correlation of both compounds that is independent from atmospheric chemistry.

Comparing the monthly means of Radon activity and aerosol (PM10 dust) concentration to the means of HONO/NO_2 in Figure 46, the correlation to Radon activity is rather obvious, especially at night: high Radon activity indicating a shallow boundary layer or less effective vertical transport coincides with high ratios of HONO/NO_2 in the lower layer. A direct effect of aerosol on the ratio however, cannot be deduced directly from Figure 46.

Table 16: Characteristic values for the mean HONO/NO_2 ratios measured during the Heidelberg long-term campaign. All values are given in percent.

$\frac{HONO}{NO_2}$ [%]	lower layer		middle layer		upper layer	
	diurnal	nocturnal	diurnal	nocturnal	diurnal	nocturnal
Jan/Feb 99	1.37±0.04	2.24±0.06	1.09±0.04	1.96±0.05	0.98±0.11	1.79±0.11
Mar/Apr 99	0.69±0.06	2.00±0.07	0.53±0.07	1.66±0.07	0.24±0.09	1.63±0.14
Apr/May 99	1.59±0.05	2.73±0.08	1.39±0.07	2.48±0.08	1.13±0.09	2.33±0.15
Aug 1999	1.48±0.07	2.63±0.09	0.68±0.06	1.41±0.09	-0.19±0.18	0.05±0.27
Sep 1999	2.04±0.07	3.08±0.11	1.55±0.07	2.93±0.18	1.31±0.09	2.47±0.17
Oct 1999	2.17±0.07	3.29±0.10	1.31±0.05	2.25±0.09	0.75±0.07	1.28±0.08
Nov 1999	2.33±0.07	3.05±0.07	1.48±0.06	2.07±0.06	0.82±0.08	1.49±0.09
Dec 1999	1.44±0.05	1.96±0.07	0.99±0.05	1.51±0.06	0.83±0.07	1.51±0.14
Feb 1999	1.25±0.04	2.16±0.06	0.85±0.04	1.67±0.05	0.90±0.06	1.68±0.09

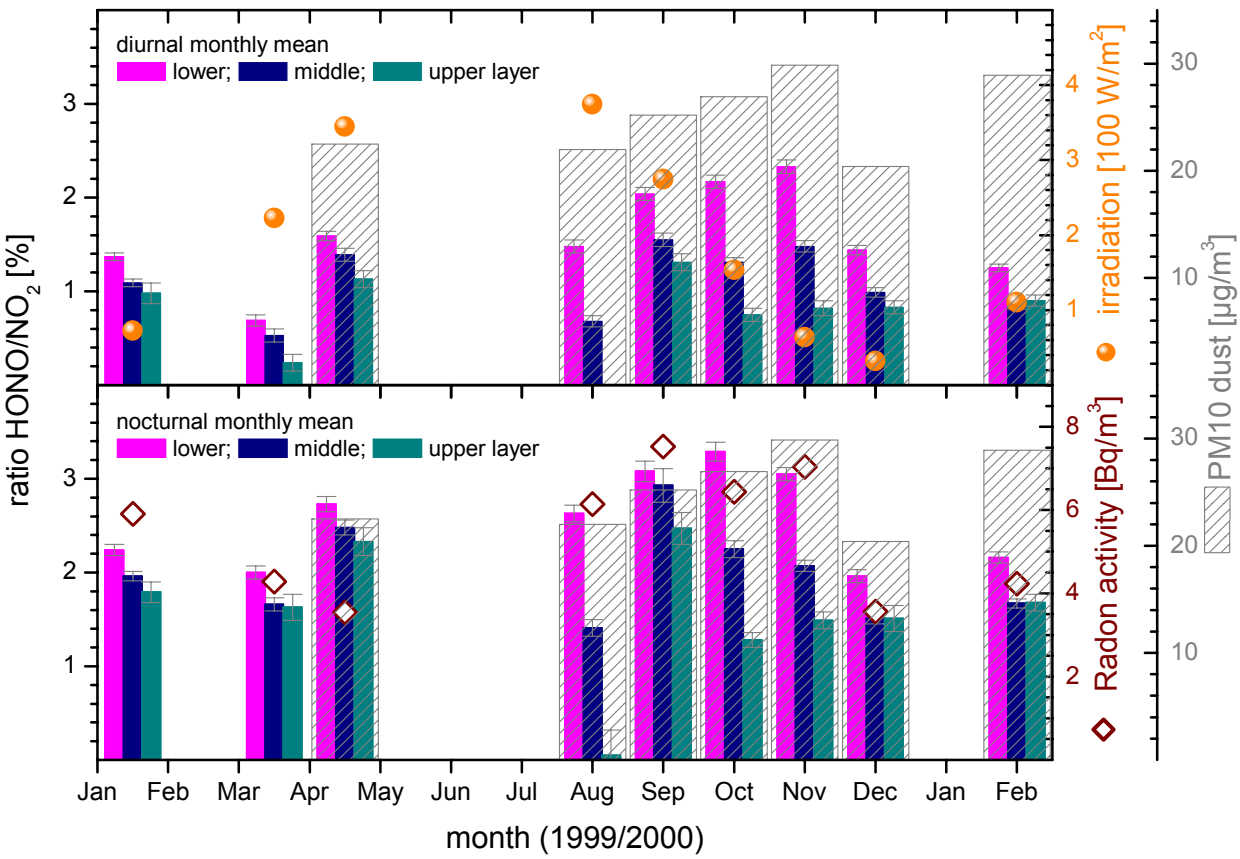

Figure 46: Seasonal trend of the of diurnal (upper panel) and the nocturnal (lower panel) HONO/NO_2 ratio in the three layers compared to Radon activity, solar irradiance and the PM10 aerosol fraction. Plotted are the means µ computed from a Gauss fit to the frequency distribution of the HONO/NO_2 ratios measured within the respective 5-week period.

Figure 47 can be used to further clarify the influx of aerosols on the efficiency of heterogeneous HONO formation: plotted are the mean HONO/NO_2 ratios in the three layers against the monthly means of PM10 dust concentration for the diurnal (06:00-18:00) and nocturnal (18:00-06:00 GMT) data. If the heterogeneous reaction

$$NO_{2(gas)} + NO_{2(gas)} + H_2O_{(liq)} \xrightarrow{surface} HONO_{(g)} + HNO_{3(g)} \qquad \text{R. 27}$$

on aerosol surfaces was be a major HONO source, a clear increase in the ratio HONO/NO_2 could be expected at increasing aerosol concentrations, not only in the lowermost layer (that includes huge ground surfaces), but also in the middle and upper layer: in the upper PBL aerosols provide the only surfaces for heterogeneous reactions. It is obvious from Figure 47 that no positive correlation between PM10 and HONO/NO_2 can be found in all three layers, neither by day nor at night. The mean Radon activity for the respective periods, however, indicates that the major effect forcing the ratio HONO/NO_2 is vertical mixing. Both Figure 46 and Figure 47 show that months featuring a more effectively mixed PBL also feature a ratio HONO/NO_2 that is generally smaller than in months with a less mixed atmosphere and therefore higher mean Radon activity.

It should be noted at this point that the dependency of the gradient on the ratio HONO/NO_2 is not directly linked to the vertical mixing. It is questionable, however, whether the vertical gradient of HONO/NO_2 can be expected to be steeper for less effective vertical mixing than for a well- mixed PBL: if both compounds are formed predominantly near the ground, only compound-specific sink processes at higher altitudes would change the ratio of the compounds. This question will be discussed in detail in chapter 6.2.6.

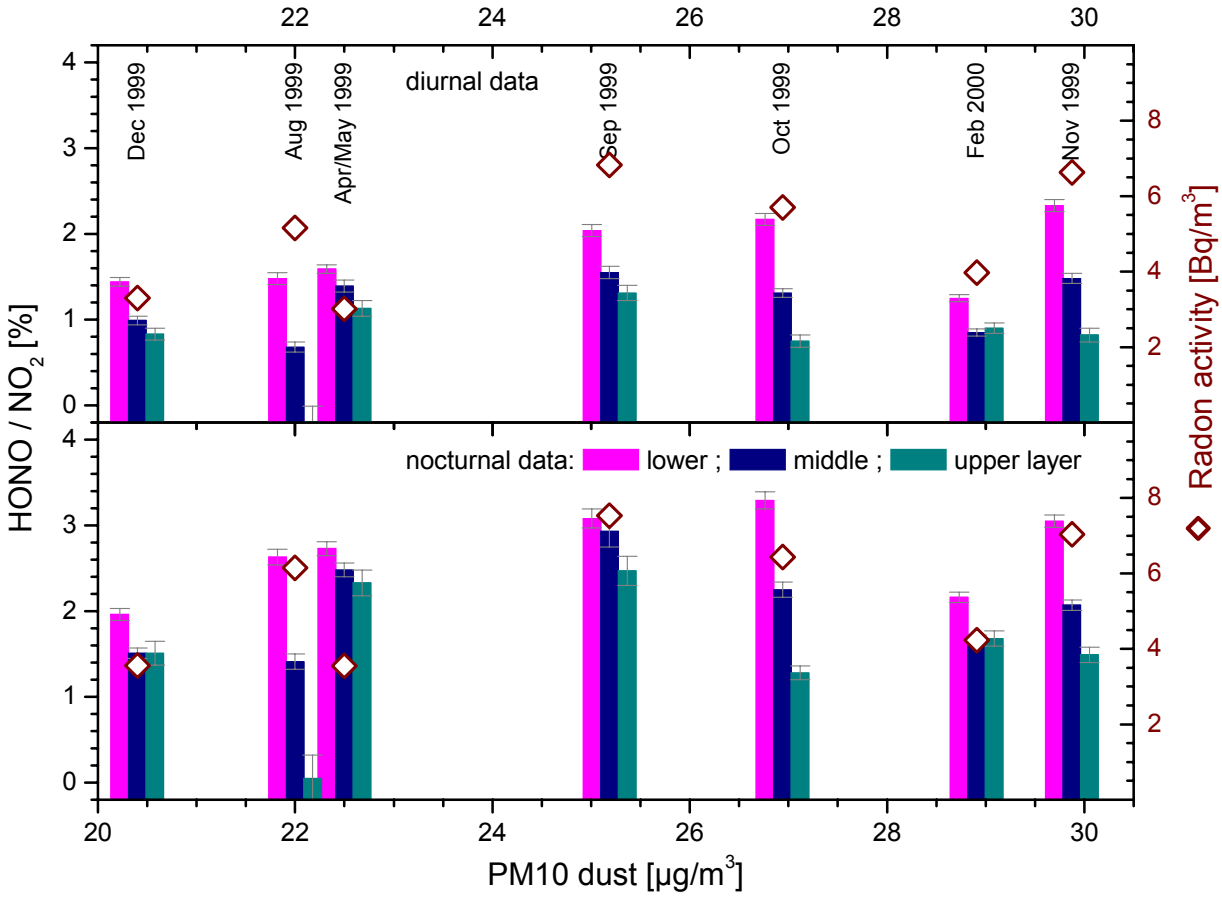

Figure 47: Correlation of the diurnal (upper panel) and nocturnal (lower panel) HONO/NO_2 ratio in the three layers to the PM10 dust fraction.

6.2.5 Seasonal trend of the gradients

Table 17 and Figure 48 present the seasonal variation of the NO_2 and HONO gradients between the middle and lower layer, while Table 18 and Figure 49 show the same for the gradients between the upper and lower layer. All mean gradients are obtained by the same statistical evaluation method as used on the HONO/NO_2 ratios and described in chapter 6.2.1 above.

The monthly means of the gradients are always steeper for HONO than for NO_2, both for the gradient between the upper and lower and between the middle and lower layer. A seasonal trend is only indicated for NO_2: in the summer months. The gradient seems to be generally steeper than in winter. The NO_2 nocturnal gradient is significantly larger than the diurnal gradient in the period from January to September, while from October to December, the diurnal gradient is larger.

For HONO however, no significant seasonal cycle is visible: the maximum gradients were detected in August for both $(c_3/c_1) - 1$ and $(c_2/c_1) - 1$. In the remaining period, variation of the diurnal and nocturnal gradients hardly exceeds the limits of the respective errors (which are defined by the confidence intervals computed from the statistical evaluation). Apart from the period from October to December, the difference between the diurnal and nocturnal gradients is not significant, as the confidence intervals overlap.

However, neither the gradients of NO_2 nor of HONO seem to depend on the monthly means of the atmospheric stability (again using Radon activity as an indicator) or PM10 dust. Mean wind speed and direction also show no effect on the gradients. A temperature dependency could not be detected.

This is rather unexpected: assuming that both species are formed primarily near the ground, the vertical mixing would force directly the dilution of the compounds into the volume of the PBL. Thus, the gradients of NO_2 and HONO should be correlated to Radon levels: in months with high mean Radon activity (i.e. less effective mean vertical mixing), also higher absolute values of all gradients should have been detected. Additionally, a clear day/night difference would have been expected, as vertical mixing is generally less effective during the night (due to more stable stratification and the lack of convection, see also chapter 3.3).

It should be noted in this context that the difference in the gradients of HONO and NO_2 indicated by the ratio

$$\frac{\left(dc/dz\right)_{rel}(HONO)}{\left(dc/dz\right)_{rel}(NO_2)} = \frac{\left(\left(c_i/c_1\right)-1\right)_{HONO}}{\left(\left(c_i/c_1\right)-1\right)_{NO_2}} \qquad (i = 2,3) \qquad \text{Equ. 56,}$$

which is plotted in Figure 50, has its maximum from October to December for both the diurnal and nocturnal monthly mean (the peak in the daytime gradient ratio in August 1999 is most likely due to poor statistics, see above). The difference between the gradients of the individual compounds is more pronounced for the gradients between the middle and lower layer, but also visible for the gradients between the upper and lower layer.

Explanations for the “irregular” seasonal behaviour are pure speculation at this point. The only positive indications of the monthly means computed for the gradients are the facts that the HONO gradient is steeper than the NO_2 gradient under all meteorological situations and that the gradients cannot be correlated to the aerosol concentration.

However, the discussion of the diurnal cycle of the gradients in chapter 6.3.2 will yield a more satisfying result that helps to understand the vertical mixing of both NO_2 and HONO.

Table 17: Monthly means for the gradients of NO_2 and HONO between the middle and lower layer measured during the Heidelberg long-term campaign.

$\frac{c_2}{c_1}-1$	diurnal		nocturnal	
	NO_2	HONO	NO_2	HONO
Jan/Feb 99	-0.247±0.008	-0.411±0.013	-0.245±0.009	-0.360±0.016
Mar/Apr 99	-0.213±0.011	-0.379±0.038	-0.309±0.019	-0.376±0.028
Apr/May 99	-0.264±0.011	-0.369±0.025	-0.326±0.013	-0.425±0.018
Aug 1999	-0.286±0.012	-0.674±0.028	-0.417±0.016	-0.625±0.020
Sep 1999	-0.292±0.014	-0.497±0.02	-0.372±0.023	-0.525±0.016
Oct 1999	-0.249±0.01	-0.529±0.014	-0.218±0.013	-0.478±0.013
Nov 1999	-0.164±0.011	-0.484±0.014	-0.143±0.013	-0.419±0.015
Dec 1999	-0.266±0.011	-0.510±0.021	-0.196±0.010	-0.433±0.022
Feb 1999	-0.232±0.009	-0.476±0.018	-0.234±0.01	-0.421±0.016

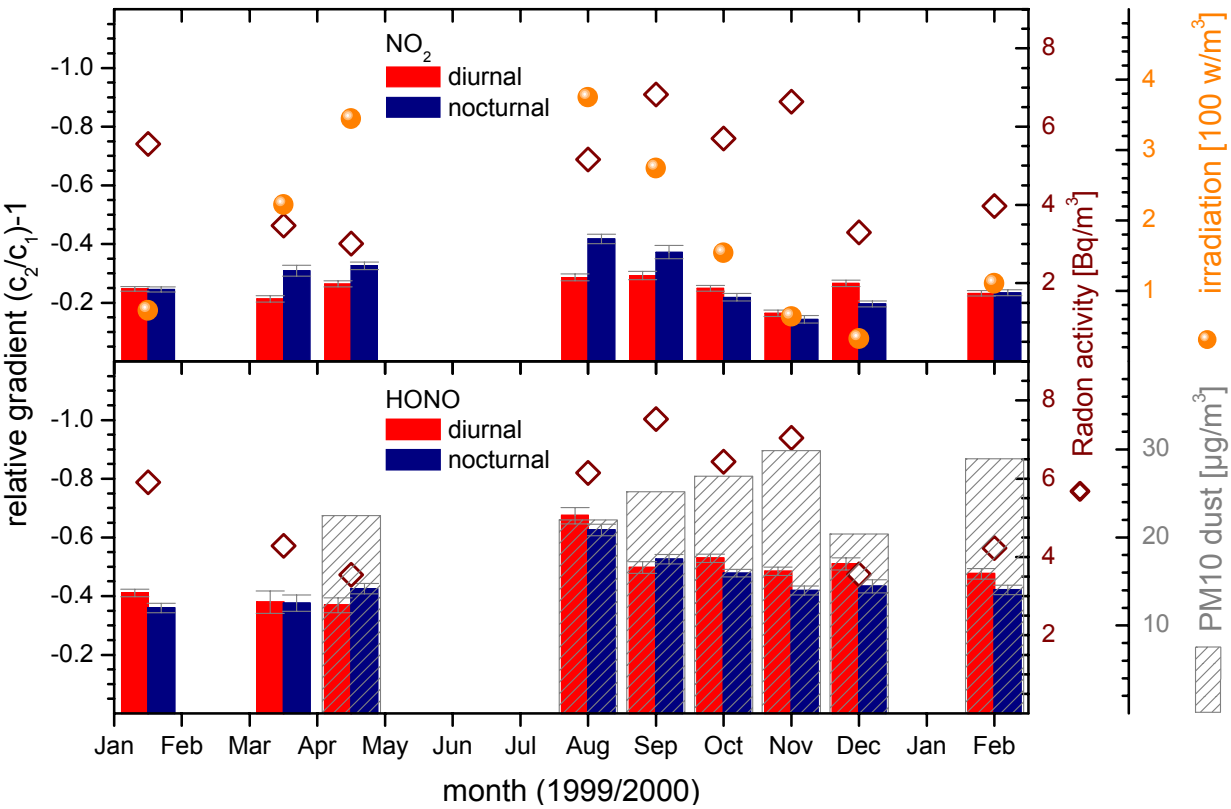

Figure 48: Seasonal trend of the relative gradients of NO_2 and HONO between the middle and lower layer compared to irradiation, Radon activity and aerosol (PM10) concentration.

Table 18: Monthly means for the gradients of NO_2 and HONO between the upper and lower layer measured during the Heidelberg long-term campaign.

$\frac{c_3}{c_1}-1$	diurnal		nocturnal	
	NO_2	HONO	NO_2	HONO
Jan/Feb 99	-0.555±0.017	-0.753±0.021	-0.613±0.020	-0.745±0.020
Mar/Apr 99	-0.451±0.021	-0.733±0.068	-0.674±0.021	-0.736±0.028
Apr/May 99	-0.534±0.019	-0.643±0.037	-0.643±0.018	-0.699±0.018
Aug 1999	-0.661±0.020	-1.07±0.055	-0.741±0.022	-0.989±0.038
Sep 1999	-0.601±0.017	-0.769±0.018	-0.704±0.019	-0.793±0.012
Oct 1999	-0.540±0.015	-0.824±0.015	-0.497±0.023	-0.770±0.016
Nov 1999	-0.472±0.024	-0.814±0.019	-0.411±0.030	-0.684±0.024
Dec 1999	-0.570±0.020	-0.758±0.023	-0.532±0.023	-0.675±0.031
Feb 1999	-0.493±0.018	-0.691±0.022	-0.558±0.021	-0.696±0.023

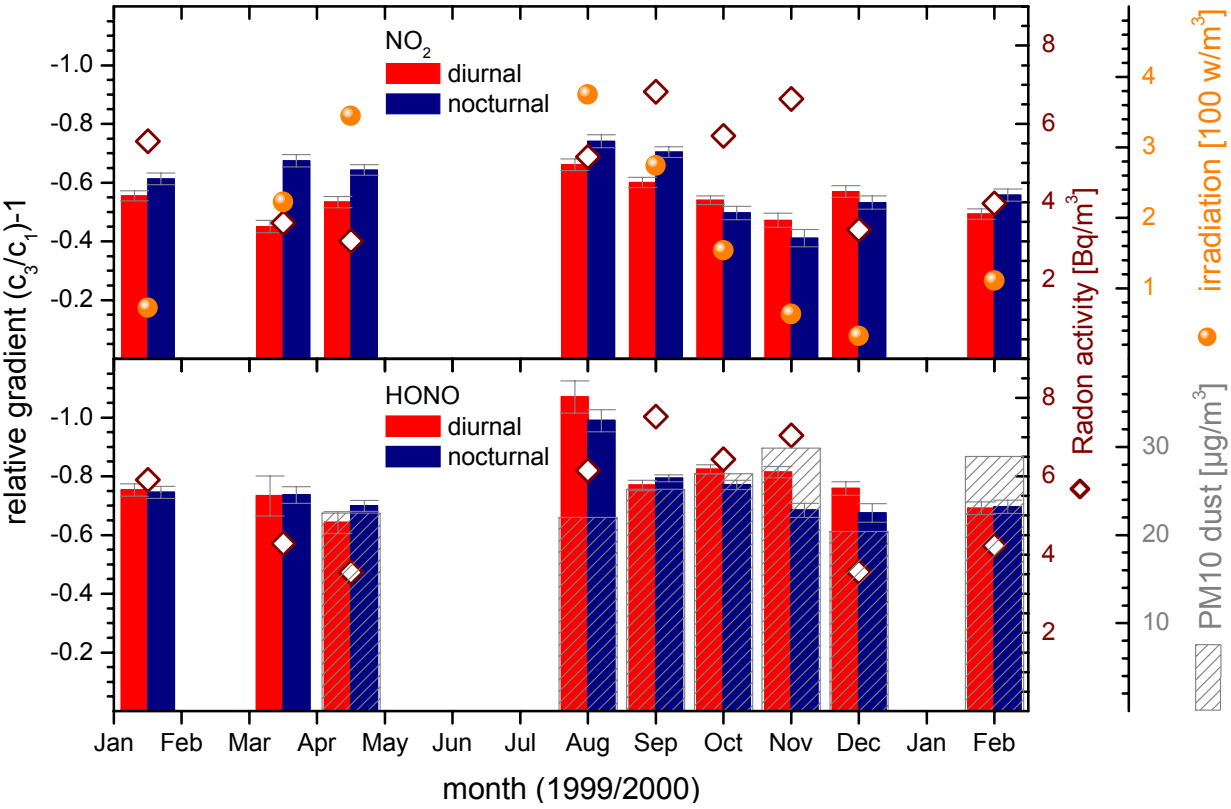

Figure 49: Seasonal trend of the relative gradients between the upper and lower layer for NO_2 and HONO compared to irradiation, Radon activity and aerosol (PM10) concentration.

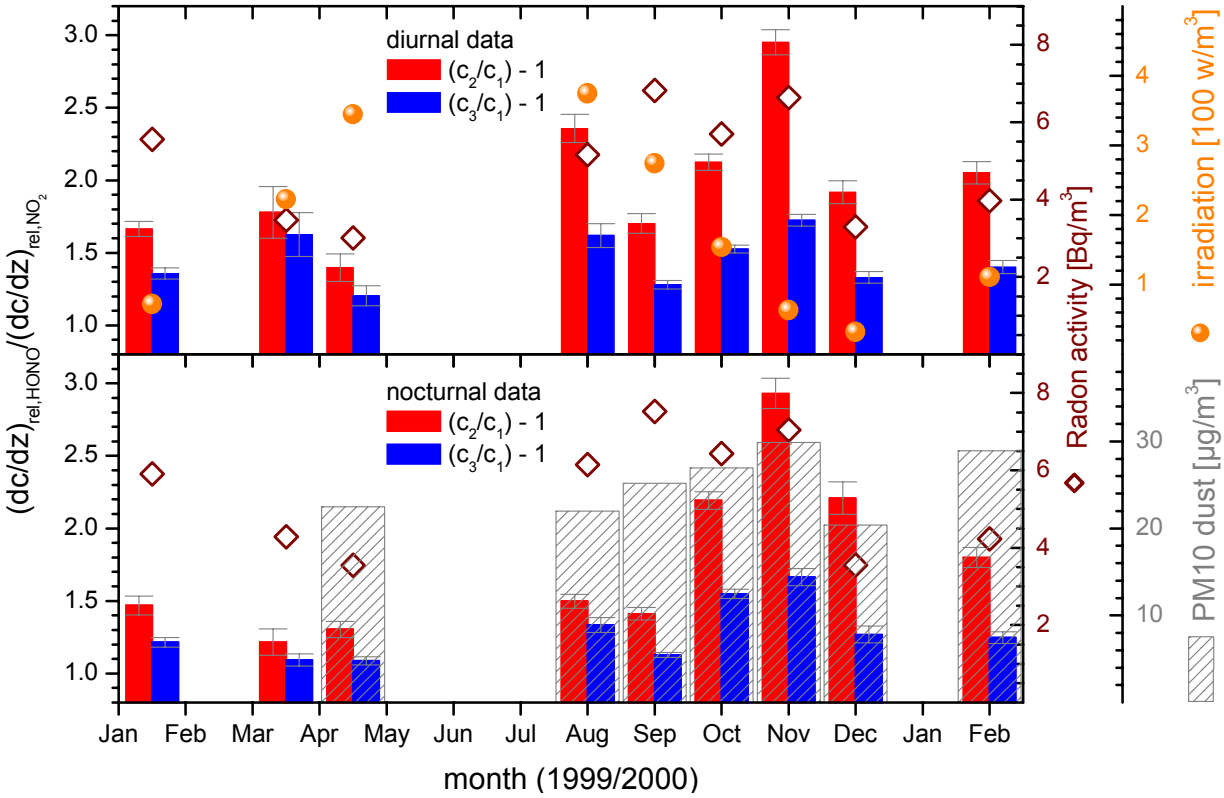

Figure 50: Seasonal trend of the ratio between the relative gradients of HONO and NO_2 compared to irradiation, Radon activity and aerosol (PM10) concentration.

6.2.6 Discussion of the results

For the thorough discussion of the monthly means presented in the chapters above, the general equation for atmospheric trace gasses (Equ. 23, defined in chapter 3.3.2) can be used. However, for the evaluation of the HONO vertical profiles, some initial assumptions must be made, which result from the current state of knowledge on atmospheric HONO chemistry discussed in chapter 2.3 (see also [*Febo et al.*, 1999; *Geyer and Trick*, 2002]):

- Direct HONO emissions from combustion processes are dependent on NO_2 emissions at a fraction of 0.8 ± 0.1 % [*Kurtenbach et al.*, 2001] ($\rightarrow \Phi_P(HONO) = 0.008 \cdot [NO_2]$).
- The mass flow of HONO originating from surfaces Φ_S is linked to the HONO density on these surfaces (see e.g. [*Febo et al.*, 1999]) and depends on the NO_2 mixing ratio. The correlation factor of $\Phi_S(HONO)$ to $[NO_2]$, however, is forced by many parameters (e.g. the surface type and roughness and possibly also the relative humidity) and has a possible temporal shift with respect to $[NO_2]$. Thus, a mathematical expression for this factor cannot be deduced at the moment.
- HONO production in the volume of the PBL is only possible on aerosol surfaces ($P_i \rightarrow P_{Part}$). The efficiency of aerosol surfaces for HONO formation however, is still unknown.
- HONO is most effectively removed by photolysis (R. 21: $L_j \rightarrow L_\lambda$), but deposition on the ground is not negligible ($\rightarrow L_S \neq 0$, see [*Stutz et al.*, 2001] and references therein). The HONO self reaction

$$2HONO \longrightarrow NO + NO_2 + H_2O \qquad \text{R. 56}$$

and second order loss reactions, which could be a sink during the transport of HONO to the upper boundary layer, are considered to be insignificant as a HONO sink in a medium polluted atmosphere: the rate constants for these reactions both for the homogeneous

[*Chan et al.*, 1976; *Mebel et al.*, 1998] and the heterogeneous [*Svensson et al.*, 1987; *TenBrink and Spoelstra*, 1998] pathways seem to be too slow to be significant (see also chapter 2.3.3). The same can be assumed for the reaction of HONO and HNO_3 [*Kaiser and Wu*, 1977b]. Laboratory measurements by [*Febo et al.*, 1999] clearly indicate that surfaces can enhance the efficiency of the HONO self reaction and reactions of adsorbed HONO with NO_2 in the gas phase by five orders of magnitude. It is questionable, however, if suitable surfaces are available in the middle and upper PBL. Thus, the equilibrium between the HONO removal by self-reaction as well as by HNO_3, and the source reactions R. 26 and R. 27 postulated by [*Trick*, 2000] can be considered to be effective only near the ground.

This results in the general atmospheric equation for HONO:

$$\frac{\partial HONO}{\partial t} = \frac{1}{h_{BL}}\left[\Phi_P + \Phi_S\right] - K(z)\cdot\frac{\partial HONO}{\partial z} + P_{Part} - L_\lambda - L_S + Adv \qquad \text{Equ. 57.}$$

Direct measurement data are available for the variation of HONO and NO_2 with time and height, while the combination of the PBL height h_{BL} and the vertical mixing coefficient $K(z)$ as well as HONO photolysis can be deduced from tracer measurements of Radon activity and global irradiance, respectively. The possible influx of a HONO volume source would be linked to the daily means of the PM10 fraction of aerosol. This implies that Equ. 57 can be used for a qualitative analysis of the major source and sink processes that contribute to the vertical profiles measured in Heidelberg, because exact information on vertical transport, boundary layer height and photolysis frequencies are not available.

The analysis of the seasonal trends of NO_2 and HONO, the ratio HONO/NO_2 and the gradients yields the following results for the contribution of the different terms of Equ. 57 to the temporal and vertical variation of HONO:

- Direct emissions of HONO (Φ_P) contribute significantly to the overall HONO budget, because the mean ratio HONO/NO_2 is always in the range of 0.7 to 3.3 %. This is in the same order of magnitude as the fraction of direct HONO emission per NO_2 of 0.8 % reported in literature.
- Surfaces near the ground form the most prominent HONO source by day and night. A major indication for this is the strong dependency of the temporal variation of HONO on Radon activity. Such a dependency is only expected if HONO is formed primarily at or near the ground (where Rn is emitted, see [*Febo et al.*, 1999])
  The comparison of the vertical profiles of HONO and NO_2 hints at the same assumption: the profiles of both compounds always decrease with altitude, but the mixing ratio of HONO is generally found to decrease faster with height than NO_2. Possible reasons for this will be discussed below.
- There is no indication that HONO is formed effectively on aerosol surfaces: the evaluation of the seasonal trend of the ratio HONO/NO_2 yields no correlation to the aerosol (PM10) load of the atmosphere. Thus, P_{Part} is likely to be negligible under the atmospheric conditions found in Heidelberg but cannot be ruled out completely.
- The seasonal trend of the diurnal HONO mean is anti-correlated to solar irradiance, indicating that daytime HONO is forced mainly by photolysis (as already expected from L_λ).
- The daytime HONO concentrations in the upper layer range from 0.05 to 0.10 ppb, which is more than expected at these altitudes.

Two terms of the general equation can not be quantified from the analysis of the seasonal trend, because no direct correlation to seasonal effects is expected: the influx of deposition and advection can only be discussed by the evaluation of the diurnal variation of HONO and NO_2, which will be the subject of chapter 6.3.2.

Other effects that are reported from the evaluation of the monthly means should be discussed in more detail:

- Assuming that both compounds are formed near the ground, it is not obvious that the gradient for HONO is always steeper than for NO_2.
- The mean HONO gradients are not found to correlate with Radon activity, as it would be expected: Equ. 24 clearly indicates that Radon activity should be linked to the vertical diffusion coefficient *K(z)* forcing the vertical distribution of atmospheric compounds emitted or formed near the ground.

The general atmospheric equation clearly indicates that only the different source and sink pathways (including chemical reactions an surface exchange processes) for HONO and NO_2 are responsible for the different vertical profiles of both compounds. So which reactions and surface processes can explain the vertical profiles of NO_2 and HONO?
Basically, there are three different options (or a combination of these) ways of explaining the different HONO and NO_2 vertical profiles:

1. With increasing height over ground, HONO sink processes become more effective than NO2 sink processes:
   In daytime, the most effective HONO volume sink is the photolysis to OH and NO. The photolysis frequency of HONO is estimated from the empirical relationship suggested by [*Kraus and Hofzumahaus*, 1998]:

   $$J_{HONO} = 0.189 \cdot J_{NO_2} + 8.433 \cdot 10^{-2} \cdot \left(J_{NO_2}\right)^2 \qquad \text{Equ. 58.}$$

   Thus, J_{HONO} is always smaller than the NO_2 photolysis frequency, which can be calculated by the simple relationship for the rate constant of the reaction

   $$NO_2 + h\nu \xrightarrow{O_2} NO + O_3 \qquad \text{R. 58}$$

   suggested by [*Schurath et al.*, 1983]:

   $$J_{\text{R. 58}} = 6.1\overline{6} \cdot 10^{-6} \frac{1}{\text{sec}} \cdot R_k \cdot \frac{m^3}{W} \qquad (R_k = \text{global irradiation [W/m}^3\text{]}) \qquad \text{R. 59.}$$

   Assuming a mean daytime solar irradiation of 500 W/m^2, this results in lifetimes of roughly 5.5 and 30 min for NO_2 and HONO, respectively. However, the mixing ratios of both compounds are governed by a photochemical state which is described by the enxtended Leighton ratio (R. 14, see chapter 2.1.2) in the case of NO_2 and by the steady state by HONO production reactions from R. 23, R. 26, R. 27 on the one hand and photolysis (R. 21) on the other hand. Thus, the comparison of the lifetimes is misleading, as it oversimplifies the problem. For a quantitative analysis, regional chemical transport models (CTM) and detailed information on reactive atmospheric compounds, such as OH and peroxy and hydroxy radicals formed from VOCs, would be needed (which is not available for the Heidelberg measurements). Additionally, the HONO daytime chemistry and its dependency on vertical transport is not fully understood (see chapter 7), which makes it difficult to simulate the sinks and sources of daytime HONO properly [*Vogel et al.*, 2002].
   At night, photolysis can be ruled out as a HONO sink. Other possible homogeneous and heterogeneous loss processes, such as the HONO self reaction and reactions of HONO with NO_2 and HNO_3, are too slow or not efficient in the middle and upper PBL due to the lack of suitable surfaces (see above). In contrast, NO_2 has known and effective sinks in the volume of the PBL, such as the reaction with NO_3 (see below).
   Thus, the steeper HONO gradients are most likely not caused by more effective volume sinks for HONO than for NO_2.

2. NO_2 has significant sources in the upper boundary layer, which force the ratio $HONO/NO_2$ to decrease with altitude. Here, multiple reaction cycles should be considered:
   Gas-phase reactions of NO with ozone, alkylperoxy and hydroperoxy radicals forming NO_2 such as

$$NO + O_3 \longrightarrow NO_2 + O_2 \qquad \text{R. 3}$$

$$NO + RO_2 \longrightarrow NO_2 + RO \qquad \text{R. 9}$$

$$NO + HO_2 \longrightarrow NO_2 + OH \qquad \text{R. 11}$$

   are possible in the entire volume of the PBL. O_3 is measured at mean mixing ratios exceeding 5 ppb at ground level throughout the year (see Annex A) and usually increases with altitude (see e.g. [*Baumbach and Vogt*, 1995]). RO_2 and HO_2 are formed via photochemical oxidation of VOCs (see chapter 2.1) by day, while the formation of both radicals at night is initiated by NO_3 [*Carslaw et al.*, 1997; *Geyer et al.*, 2000a; *Mihelcic et al.*, 1993; *Platt et al.*, 1990]. In this context, especially isoprene emissions by the forest on the hillside of the Königsstuhl (see chapter 5.1) should contribute significantly to the formation of peroxy radicals in the upper two layers (see [*Geyer*, 2000]). The remaining question is whether NO has a sufficient lifetime to allow its transport to the altitude range of the two upper boxes.
   At night, one can assume a mean O_3 mixing ratio of 25 ppb within the lower layer. The NO lifetime period versus O_3 resulting from

$$\frac{d[NO]}{dt} = -k_{R.3} \cdot [O_3][NO]$$

$$k_{R.\,3}(298K) = 1.8 \cdot 10^{-14}\ \mathrm{cm^3 molec^{-1} s^{-1}},\ [\textit{DeMore et al.}, 1997]$$

   is computed by

$$\tau = \frac{1}{k_{R.3} \cdot [O_3]} \qquad \text{R. 60.}$$

   Lifetimes of NO computed from R. 60 for typical day- and night-time mixing ratios of O_3 are presented in Table 19. A transfer time for trace gasses of about 12 min from 1 m above ground level to the top of the lower layer at 30 m is computed from the transfer resistances for a horizontal wind velocity of 3 m/s and neutral stratification (see Table 4). Comparing this transfer time with the values for the NO lifetimes, it is obvious that only small amounts on NO reach the middle layer. Thus, a significant NO_2 source from NO in the middle and upper layer is only likely for labile stratification or a highly convective PBL featuring short transfer times.
   Consequently, NO is also not available at higher altitudes for the oxidation by HO_x or RO_x radicals: both radicals are formed from VOCs emitted by trees on the hillside of the Königsstuhl and are therefore present in the two upper layers, while NO has no sources in that area.

   The photolysis of NO_3 at sunrise might be another NO_2 source in the upper PBL as the NO_3 maximum concentrations of about 300 ppt are found at altitudes of 300 – 500 m [*Friedeburg et al.*, 2001]. This process should therefore yield a burst of about 300 ppt of NO_2 at sunrise. Compared to maximum NO_2 values of about 8 ppb in the upper layer and up to 35 ppb in the lower layer, NO_2 production by NO_3 photolysis is negligible. However, the major role of NO_3 with respect to NO_2 is being a NO_2 sink, especially at higher altitudes in the presence of O_3 (see also [*Friedeburg et al.*, 2001]). NO_3 is formed from NO_2 and O_3 via

$$NO_2 + O_3 \longrightarrow NO_3 + O_2 \qquad \text{R. 61}$$

(see also chapter 6.3.2). Subsequently N_2O_5 can be formed by the equilibrium reaction of NO_3 with another NO_2 molecule:

$$NO_2 + NO_3 \xleftrightarrow{M} N_2O_5 \qquad \text{R. 17.}$$

This reaction represents only a NO_2 source in the upper PBL, if N_2O_5 is transported from the lower PBL and decays thermally in the upper PBL. Considering the NO_3 profiles mentioned above, it is not likely that significant amounts of N_2O_5 can be transported during the night from the lower to the upper layer to generate a net NO_2 source by thermal decay. Furthermore, thermal decay of N_2O_5 is not the only sink for this molecule: hydrolysis and subsequent dry or wet deposition play a significant role, too [*Alicke*, 2000]. So one can suggest that N_2O_5 can be neglected as a net source of NO_2 in the upper PBL, but that it represents – in conjunction with the reaction of NO_2 and O_3 – a net NO_2 sink.

3. HONO is formed predominantly on surfaces at or near the ground and is successively transported to higher altitudes: by day, the very effective HONO photolysis keeps the HONO mixing ratio at low values. Thus at nightfall, the upper PBL consists of air masses which feature only the daytime HONO concentrations. Simultaneously, HONO formed by heterogeneous source reactions near the ground can accumulate, as photolysis is no longer active. In the course of the night, HONO is then transported to the upper PBL by turbulence.
   Looking at the monthly means of HONO discussed in chapter 6.2.3, this explanation is likely, but cannot be confirmed quantitatively as the daytime and night-time monthly means include all data within the fixed 12-hour period from 06:00 to 18:00 GMT and from 18:00 to 06:00 GMT, respectively. For a quantitative analysis of this effect, a time resolution of at least an hour is required to distinguish between the HONO mixing ratio in bright sunshine (i.e. in the afternoon) and at night. This is of special importance in the lowermost layer, where the HONO mixing ratio increases from its daytime minimum of roughly 0.1 ppb to night-time values around 1 ppb within one or two hours at dusk and dawn. Therefore, the seasonal variation of the intensity and duration of solar irradiation within the 12-hour intervals used for the computation of the diurnal and nocturnal means partially masks the "real" day/night variation of HONO. A detailed analysis of the diurnal variation of HONO and its gradient will follow in chapter 6.3.2.

To summarise this discussion, it can be stated that in daytime the very effective HONO photolysis causes steeper gradients for HONO than for NO_2. At night, the most likely explanation for the steeper HONO gradients is a combination of effects 2 and 3: HONO is primarily formed on surfaces at or near the ground and then transported to higher altitudes. NO_2 is also formed near the ground, but has an additional daytime source in the volume of the PBL "weakening" the vertical gradient by day, while reactions of NO_2 forming N_2O_5 in the upper PBL cause a steeper NO_2 gradient at night.

Table 19: Lifetimes of NO for O_3 mixing ratios close to the ground typical for the measurements in Heidelberg.

time of day [GMT]	O_3 [ppb]	NO [ppb]	τ_{NO} [sec]	remarks
07:00	16.0	32.5	139	diurnal NO_x maximum
16:00	39.5	13.5	56.3	diurnal O_3 maximum
19:00	28.5	8.5	78.0	first night-time HONO peak
02:00	25.5	2.0	87.1	diurnal NO_x minimum

6.3 The “average day”

6.3.1 Computation of the hourly means

The hourly means of the measured time series provide the opportunity to evaluate the typical diurnal variation of the observed species, their ratio and their gradients. To obtain statistically significant results, the hourly means were computed from all data recorded during the same 5-week periods already used for the evaluation of the seasonal variation in the chapter above. The computation included the weighting of the individual data points by their reciprocal random measurement errors to suppress the distortion of the means by single data points featuring large deviations from the mean due to problems during data acquisition or within the DOAS evaluation. For the computation of the error-weighted means, one can assume that all data points measured in a 1-hour interval should fall on a straight line. The chi-square for a linear function is defined as

$$\chi^2(a,b) = \sum_{i=1}^{N} \left(\frac{y_i - a - b \cdot x_i}{\sigma_i^2} \right)^2 \qquad \text{Equ. 59}$$

with σ_i being the absolute errors of the single data points y_i recorded at the time x_i. N is the total number of data points recorded for one species in the 1-hour interval. As a common mean for all values of this species is desired, the slope b of the linear function should be zero:

$$\chi^2(a) = \sum_{i=1}^{N} \left(\frac{y_i - a}{\sigma_i^2} \right)^2 \qquad \text{Equ. 60.}$$

To obtain the mean value within the interval, chi-square is differentiated with respect to the intercept a of the linear function and successively set to zero:

$$\frac{\partial \chi^2(a)}{\partial a} = -2 \cdot \sum_{i=1}^{N} \frac{y_i - a}{\sigma_i^2} = 0 \qquad \text{Equ. 61.}$$

Solving this relation to obtain a yields the error-weighted mean

$$a = \sum_{i=1}^{N} \frac{y_i}{\sigma_i^2} \Bigg/ \sum_{i=1}^{N} \frac{1}{\sigma_i^2} \qquad \text{Equ. 62.}$$

The error of the hourly mean is computed by the Gauss method yielding

$$\Delta a = \left(\sum_{i=1}^{N} \frac{1}{\sigma_i^2} \right)^{-1/2} \qquad \text{Equ. 63.}$$

Equ. 62 and Equ. 63 were used to compute the 1-hour means for the time series of NO_2, HONO, the ratios and the gradients of both species within all nine evaluation periods. The results of this evaluation are displayed in Annex A and will be discussed in the following.

Figure 51 presents the diurnal variation of the hourly means of NO_2, HONO, the ratio HONO/NO_2 and the respective gradients measured by the LP-DOAS in April/May, with additional point measurement data obtained by the evaluation of the UMEG data.

It should be noted in this context that the mean diurnal cycles discussed in this section are averaged over all atmospheric conditions that occurred in the respective 5-week period. Consequently, these cycles only yield information about the typical day/night cycle of the observed species (chapter 6.3.2) and about the seasonal variations of the diurnal cycle (chapter 6.3.3). The impact of distinct periods featuring pronounced atmospheric stability or instability on the diurnal variations on the measured values will be discussed in chapter 6.4.

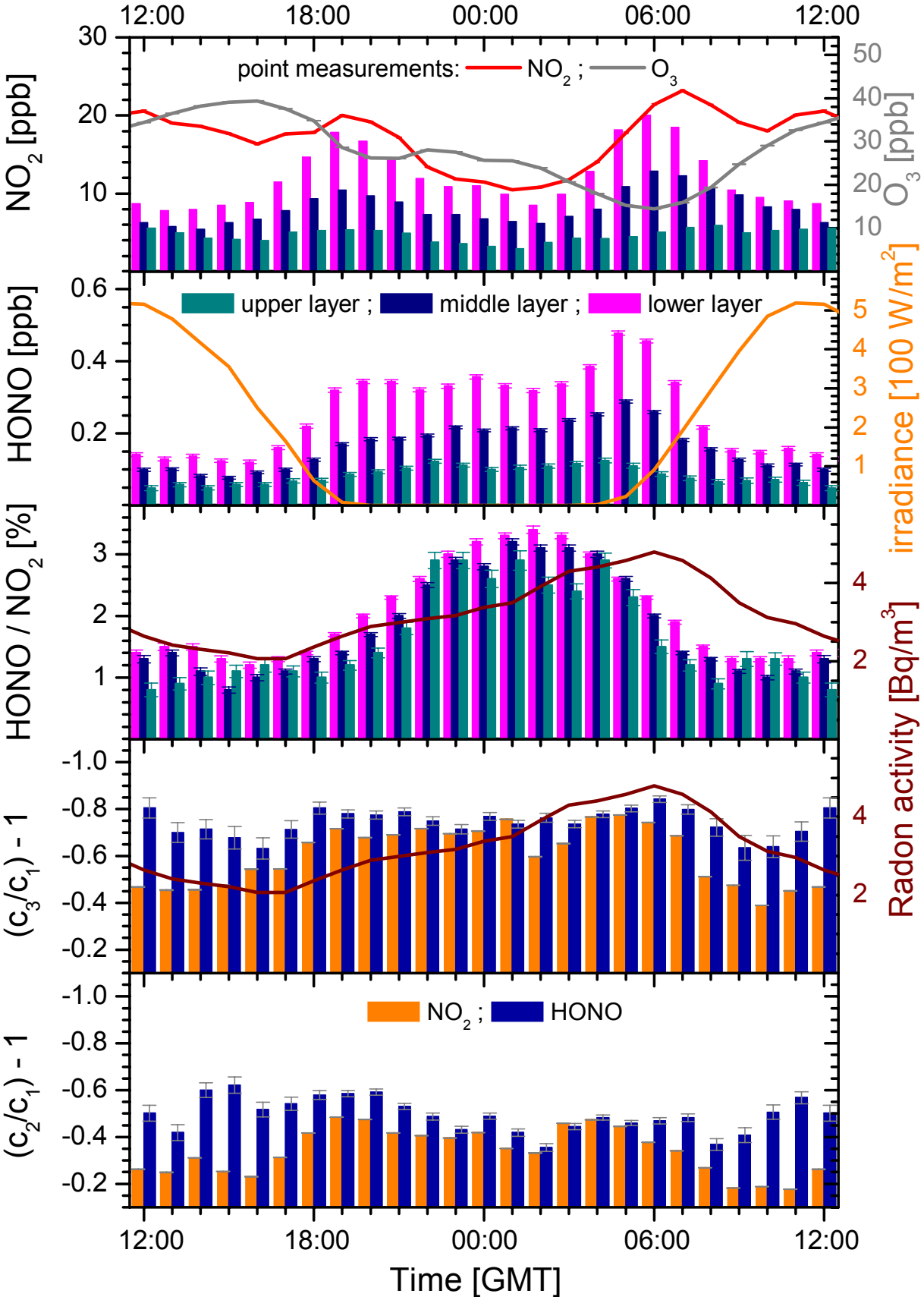

Figure 51: Hourly means of NO_2, HONO, the ratio HONO/NO_2 in the three layers and the gradients computed for the data of the April/May period plotted in Figure 34, Figure 35 and Figure 37, respectively.

6.3.2 Evaluation of the hourly means in April/May 1999

The evaluation of the hourly means will first focus on the April/May 1999 period already used for the general discussion of the measured time series in chapter 6.1. This 5-week period is characterised by intense atmospheric activity, indicated by the very low Radon activity measured throughout the day. Consequently, the mixing times within the PBL are rather short in this period when compared to periods featuring higher mean Radon activity such as August and September 1999. However, the pressure at ground level ranges in a relatively narrow band between 990 and 1006 mbar, which excludes pronounced high pressure and low pressure situations (i.e. fully-developed anticyclones and cyclones, respectively) but indicates unsettled weather conditions in the whole period.

Diurnal variation of NO_2

The mean diurnal variation of NO_2 shows again the strong influx of photochemistry, emission and – even in this period featuring only weak ground inversions in the morning – the efficiency of vertical transport:

Daytime NO_2 has its minimum around 14:00 GMT (that is 16:00 local time), with NO_2 mixing ratios ranging from around 8 ppb in the lowermost layer to about 4 ppb in the uppermost layer. In the afternoon, when the photochemical steady state of NO, NO_2 and O_3 favours NO_2 due to decreasing solar irradiation, the NO_2 mixing ratio slowly increases. The NO_2 maximum is recorded shortly after sunset at 19:00 GMT, which is at least delayed by 2 hours with respect to the evening rush hour. The mean evening peak values are 18, 10.5 and 5.5 ppb in the lower, middle and upper layer, respectively. The evening peak can also be seen in the time series of the UMEG point measurement recorded beside a major road near the IUP.

In the first half of the night, NO_2 decreases from the evening maximum to values of 8.5, 6.0 and 4.0 ppb in the lower, middle and upper layer, respectively. For the lowermost layer, the half-time of the reaction of NO_2 and O_3 (R. 20) is computed as

$$t_{1/2} = \frac{\ln(2)}{k_{R.20} \cdot [O_3]} = \frac{\ln(2)}{k_{R.20} \cdot 30\,\text{ppb}} = 11.6\,\text{h} \qquad \text{R. 62.}$$

This compares to a mean half-time of roughly 7 h measured in the April/May 1999 period in Heidelberg (see middle panel of Figure 52). Considering that NO_2 is also removed from the atmosphere by dry and wet deposition and surface reactions forming HONO (see chapter 0 and the paragraph on HONO formation below, respectively), the NO_2 decrease at night is quantitatively understood.

In the morning hours, the NO_2 mixing ratio increases again to maximum values of 20 and 13 ppb at 06:00 GMT in the lower and middle layer, respectively. Contrastingly, in the upper layer the maximum value in the morning of 6 ppb is found two hours later, at 08:00 GMT. The morning maximum in the two lower layers coincides with the rush hour in the morning and the diurnal maximum of Radon activity, which indicates an amplification of the NO_2 emission peak in the morning caused by coinciding ineffective vertical transport. The delayed peak in the upper layer is also most likely an effect caused by vertical mixing: one can assume an inversion height located at the centre of the middle layer for the ground inversion in the morning (which is a well-founded estimation, see chapter 6.4). When this inversion breaks up at 06:00, a neutral stratification is a good first order approximation for the transition from the stable stratification at night to a convective daytime PBL in the following 1-2 hours. Thus, the transfer resistances of the middle and upper layer for a mean wind speed of 3 m/s yields the transfer time of NO_2 to the upper limit of the uppermost layer:

$$t_{mix} = R_2 \cdot \tfrac{1}{2} h_2 + R_3 \cdot h_3 = 11.4\,\tfrac{\text{sec}}{m} \cdot 60\text{m} + 8.24\,\tfrac{\text{sec}}{m} \cdot 330\text{m} \approx 1\text{h}\,.$$

This result verifies the assumption that vertical transport from the lower to the upper layer causes the time delay between the respective NO_2 peaks in the morning. The evening peak does not show this time delay, as vertical mixing is more effective in the late afternoon and early evening: thus, the NO_x emitted in the evening rush hour is mixed to the upper layer in a shorter time.
The decreasing NO_2 mixing ratio in the morning hours until 14:00 GMT is explained by the photochemical steady state of NO, NO_2 and O_3 and the break-up of the ground inversion in the morning: as soon as the exchange of air masses within the inversion layer and above is possible, not only NO_2 is mixed to the middle and upper troposphere, but also O_3 present in the air masses above is mixed into the PBL and decomposes NO_2 yielding NO and O_2.
Interestingly, NO_2 has its diurnal minimum at 14:00 GMT only in the lower and middle layer, while the upper layer the shows a diurnal NO_2 minimum at 01:00 GMT.

It is obvious that the diurnal variability of NO_2 is significantly less pronounced with increasing layer height: in the lowermost layer, the delta(NO_2) = max(NO_2) - min(NO_2) is 12 ppb, decreasing to 8 ppb and 3 ppb in the middle and lower layer, respectively. This is expected, however, as the major NO_2 sources are located near to the ground and NO_2 is subsequently removed by (photo)chemistry and dilution into the volume of the PBL as well as by surface reactions and deposition on the ground.

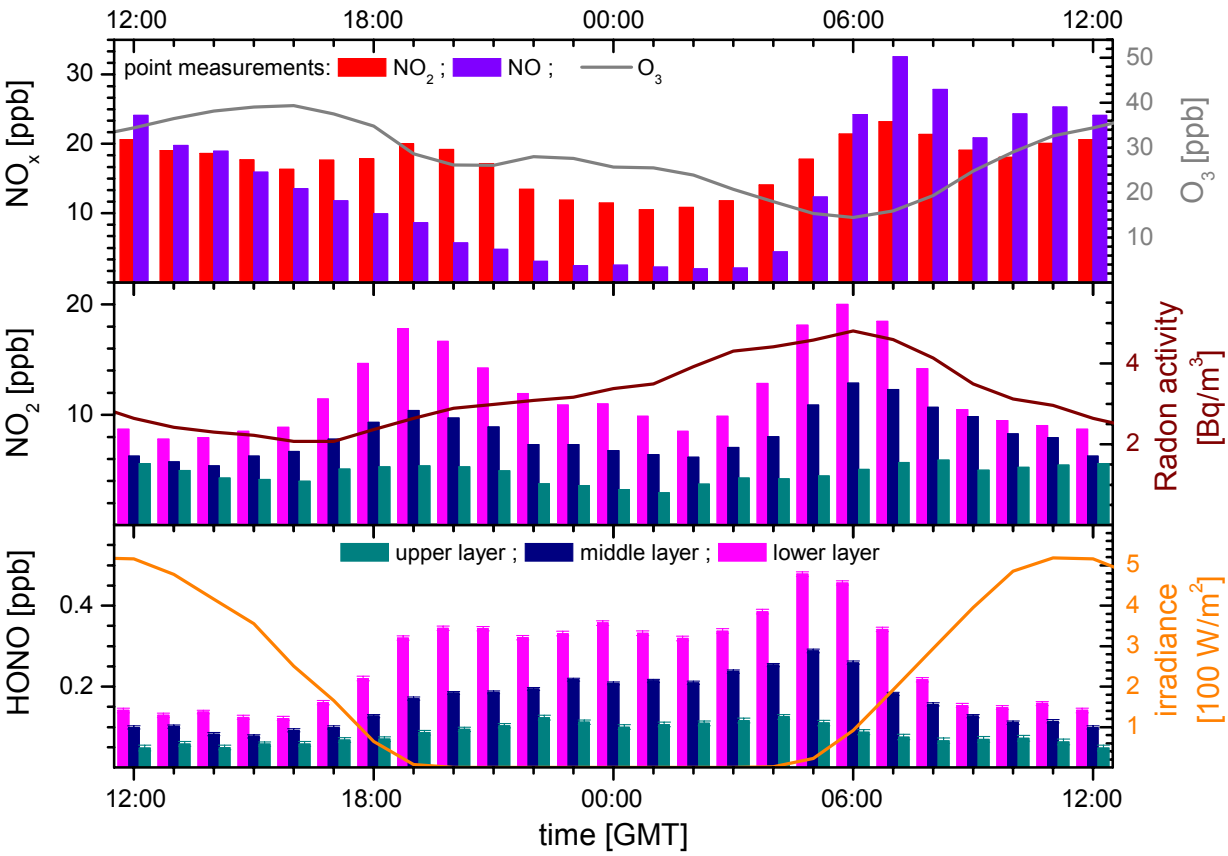

Figure 52: Hourly means of NO_2 and HONO measured by the LP-DOAS (lower two panels) and NO, NO_2 and O_3 measured at the UMEG site (uppermost panel) for the April/May 1999 period.

Diurnal variation of HONO

The hourly means of HONO in April/May 1999 also show the typical HONO time series (see Figure 52 and chapter 6.1.2): the diurnal minimum caused by photolysis is found in all three layers in the afternoon between 14:00-15:00 GMT. The minimum mean HONO concentrations are found at 0.13, 0.08 and 0.05 ppb in the lower, middle and upper layer, respectively. At about16:00 GMT, the HONO mixing ratio begins to increase in the lowermost and middle layer to reach a first night-time maximum of 0.34 and 0.18 ppb at 20:00 GMT, respectively. In the uppermost layer, the HONO increase in the evening is positively identified to start at 18:00 GMT and reaches its maximum of 0.12 ppb at 22:00 GMT.

At night between 22:00 and 03:00 GMT, the HONO concentrations in all three layers are more or less constant at levels comparable to the first maximum in the evening. Interestingly, a second HONO maximum in the lower layer at 00:00 GMT seems to be correlated with a short period of constant NO_2 levels between 22:30 and 00:30 GMT.

In the early morning, at increasing NO_2 and Radon levels, the mean HONO concentrations in the lowermost and middle layers indicate a second maximum at 05:00 GMT featuring mixing ratios of 0.48 and 0.29 ppb, respectively. A further increase of HONO is prevented by increasing solar irradiation, which forces the HONO mixing ratios in all three layers to decrease within the next 3 hours to the daytime levels mentioned above. The maximum of night-time HONO is found one hour earlier than the NO_2 maximum at 06:00 GMT, as HONO photolysis overcompensates the growing HONO production from the increasing NO_2 mixing ratios.

It is obvious that the HONO concentration also always decreases with altitude, indicating that the bulk of HONO is formed from NO_x near the ground. The fact that the early morning peak is evident in the lower and middle layer, but not in the upper layer, is most probably an effect of both vertical transport and chemistry: HONO formation becomes more effective in the morning as NO_2 levels increase and HONO is subsequently mixed within the ground inversion layer that extends well into the middle layer. But HONO is neither formed within nor transported into the upper layer so that HONO mixing ratios start to fall in this layer as soon as solar irradiation starts to rise.

HONO formation rate at night

Assuming that HONO formation proceeds heterogeneously on surfaces via reaction

$$2NO_2 + H_2O \xrightarrow{surface} HONO + HNO_3 \qquad \text{R. 27}$$

with the rate limiting step being not the reaction of two NO_2 molecules with H_2O on the surface, but transport processes to and from the surface (see chapter 2.3.2).
[*Alicke*, 2000] uses the relation

$$\overline{F_{HONO,night}} = \frac{[HONO](t_2) - [HONO](t_1)}{(t_2 - t_1) \cdot [NO_2]_{night}} \qquad \text{R. 63}$$

to compute the average night-time NO_2-to-HONO conversion rate (or formation rate *F*). HONO production is assumed here to be proportional to the mean NO_2 concentration, but does not depend on gas-phase water, as suggested by [*Kleffmann et al.*, 1998]. The mean NO_2 concentration is computed from all NO_2 values measured within the time interval $[t_1;t_2]$. When R. 63 is applied to the HONO increase between 16:00 and 20:00 GMT in the late afternoon, an HONO formation rate of

$$\overline{F_{HONO,night}} = 0.51 \pm 0.11\%_{\mathrm{HONO/NO_2}} \cdot \mathrm{h}^{-1}$$

is computed. This HONO formation rate is at least a factor of 2 smaller than the HONO formation rates found by [*Alicke*, 2000], ranging from 0.0097 to 0.021 (ppb HONO)/(h · ppb NO_2) at Nashville/USA and Pabstthum near Berlin/Germany, respectively.

It should be noted, however, that R. 63 yields only a first order estimate for the upper limit of the HONO formation rate: Figure 53 clearly indicates that the NO_2 mixing ratio roughly doubles in the period used for the computation of the HONO formation rate. Consequently, the assumption of a constant NO_2 concentration leads to an overestimation of the HONO formation rate. Additionally, increasing stratification stability at nightfall (see chapter 3.3) also causes a rise in the concentrations of all trace gasses, which are emitted or formed primarily at or near the ground. This leads to a further overestimation of the HONO formation rate. It is very likely that the increased HONO formation rates measured at Pabstthum by [*Alicke*, 2000] are partially caused by theemerging strong night-time ground inversions that often occurr at this site [*Alicke*, 2001; *Geyer*, 2001]: thick fog was regularly observed within the lowest 10 metres in the late night and early morning hours. Thus, a proper estimation of the HONO formation rate from LP-DOAS measurements is only possible if the vertical diffusion constant and the inversion layer height are known.

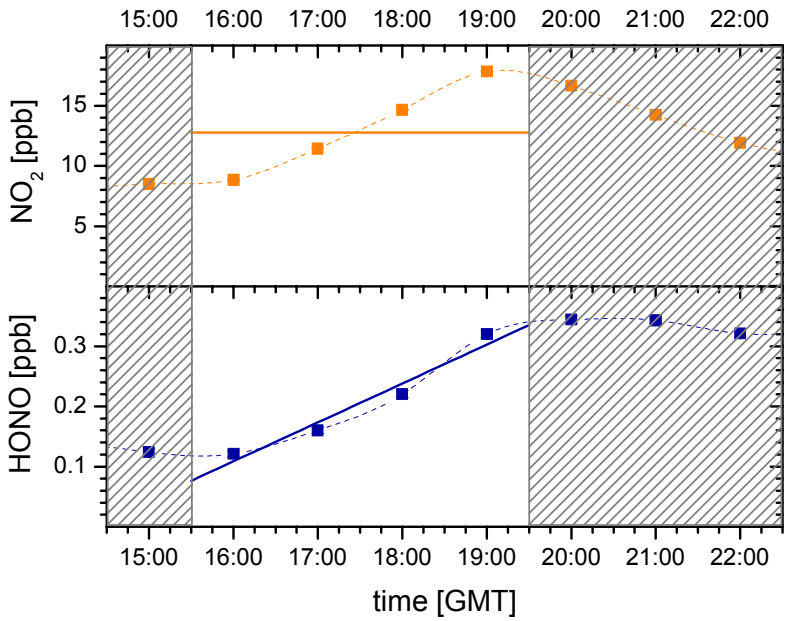

Figure 53: Late afternoon increase of the mean NO_2 and HONO concentrations in the April/May 1999 period. The clear area marks the data used for the computation of F_{HONO} by R. 63: the drawn lines indicate the mean NO_2 concentration (top panel) and the mean HONO increase (bottom panel).

Diurnal variation of the ratio HONO/NO_2

The diurnal variation of the ratio HONO/NO_2 – plotted for the April/May 1999 period in Figure 54 – is strongly influenced by solar radiation (see Figure 52): in daytime the ratio is found at typical values of 1.4 ± 0.1 % in the lowermost layer and at 1.0 ± 0.2 % in the uppermost layer. These values clearly exceed the direct HONO emission rate of 0.8 % deduced by [*Kurtenbach et al.*, 2001] from measurements in a road traffic tunnel. It is obvious, however, that in daytime the photochemical steady state of HONO depends on three processes: direct emission, heterogeneous formation and the photolysis of HONO as the dominating effect . Thus, without exact knowledge on the HONO photolysis frequency, a comparison of the contributions of direct emission and heterogeneous formation to the total HONO production is only possible at night.

Coinciding with the decline of solar irradiation to zero at 19:00, the ratio HONO/NO_2 begins to increase, beginning in the lowermost layer, and proceeding less steeply and with a time delay in the middle and upper layer. The maximum, which is clearly pronounced in the case

of the lower and middle layers, is reached at 02:00 GMT at values of 3.4 ± 0.05 % and 3.2 ± 0.05 %, respectively. In the upper layer the ratio varies strongly throughout the night, with a maximum value of 2.9 ± 0.13 % at 01:00 GMT. From the night-time data presented in Figure 54, the mean increase of $HONO/NO_2$ within the lowermost layer (indicated by the thin red line in the top panel of Figure 54) is computed by

$$\overline{F_{HONO/NO_2,night}} = \frac{\left[\frac{HONO}{NO_2}\right](t_2) - \left[\frac{HONO}{NO_2}\right](t_1)}{(t_2 - t_1)} = 0.31 \pm 0.01\ \%_{HONO/NO_2} \cdot h^{-1} \quad \text{R. 64.}$$

This rate is three times faster than measured by the laboratory experiments: [*Trick et al.*, 2002] reports a $k_{eff,HONO} = 6.0 \cdot 10^{-9}\ s^{-1} ppm^{-1} m$, yielding an increase in HONO with respect to NO_2 of 0.1 % h^{-1} for a flat tarmac surface in the laboratory. This effect is most likely caused by an increased surface-to-volume ratio in the real lower PBL (see also chapter 2.3.2). [*Trick et al.*, 2002] compute an increase of the HONO formation rate by a factor of 5 if the surface of the city is covered with houses of 40 m height by 50%. Thus, the HONO formation rate with respect to NO_2 is well within the values reported in literature. A remarkable observationin this context is that the relative formation rate of HONO computed from the increase of the ratio $HONO/NO_2$ is smaller than the HONO formation rate of 0.51 % h^{-1} computed from R. 63. This is most likely caused by the following effects:

- the time intervals used for the computation of both "relative HONO formation rates" are different (which is inevitable, as the increase in $HONO/NO_2$ is delayed with respect to the HONO increase in the evening);
- the HONO formation rate computed from R. 63 overestimates the HONO formation as the NO_2 mixing ratio constantly increases during the observed time interval;
- HONO sinks, such as deposition and the HONO self reaction are expected to influence the $HONO/NO_2$ ratio (despite processing rather slowly in the atmosphere, see chapters 2.3.3 and 6.2.6);
- Increasing atmospheric stability also has an influx of both formation rates (see chapter 6.4.1) and can hardly be corrected for due to the lack of information on the vertical transport parameters.

The values for the HONO formation rate computed from the $HONO/NO_2$ ratio will be used in the following, as the influx of HONO sinks can be assumed to be rather insignificant in the first part of the night. Additionally, the result of R. 64 features an error that is about a factor of ten smaller than for the formation rate computed from R. 63 (primarily due to better statistics).

The maxima of $HONO/NO_2$ coincide with the night-time minima of NO_2: with increasing NO_2 concentrations in the early morning, the ratio decreases, despite an increasing HONO concentration (for a comparison of all three time series, see Figure 51). The decline of the ratio $HONO/NO_2$ ends at 09:00 GMT, when the daytime mixing ratios are established reached again.

The shape of the diurnal variation of the ratio $HONO/NO_2$ observed here is typical for the whole 13-month measurement period since the major effects forcing the 24-hour cycle are the same throughout the year:

The increase of the ratio $HONO/NO_2$ at night is explained by two partially linked processes: First, sink reactions of NO_2 with O_3 and NO_3 in the gas phase cause decreasing NO_2 concentrations. Simultaneously, NO_2 is removed from the gas phase by deposition on (wet) surfaces. Second, the NO_2 adsorbed on wet surfaces is subsequently converted to HONO and HNO_3. While the latter mostly remains dissolved (see chapter 2.2), HONO is released partially into the gas phase.

The maximum $HONO/NO_2$ ratios exceeding 3 %, which are observed in the second half of the night, indicate that direct emission cannot solely explain the night-time HONO concentrations: the maximum ratio of $HONO/NO_2$ is at least 3 times larger than the values reported for direct emission. Additionally, in the course of the night, traffic and heating as the major NO_x sources become less, which also causes declining direct HONO emissions. Thus, the slow increase of the ratio in the course of the night indicates that HONO is primarily formed by heterogeneous conversion from NO_x on the ground and is subsequently released (and mixed, see below) into the PBL.
The decrease of the ratio in the early morning can be understood considering that the surface reactions producing HONO are too slow to keep the ratio $HONO/NO_2$ at a constant level when NO_2 increases rapidly (forced by increasing NO_x emissions and atmospheric stability, see above).
In daytime, the very effective HONO photolysis keeps the $HONO/NO_2$ ratio at the observed low values of 1 to 1.5 %.

It should be noted in this context that the maximum values of the ratio $HONO/NO_2$ in the lower layer clearly exceed the steady state ratio of 2.5 % postulated by [*Stutz et al.*, 2001] for the compensation point between HONO exhalation from the surfaces and HONO deposition on the surfaces. The fact that the maximum ratio correlates with the minimum of the NO_x emissions is of special importance, because [*Stutz et al.*, 2001] state that higher ratios observed during their experiments are mostly linked to increased NO_x emissions.
The cause for the higher ratios measured above Heidelberg might be linked to the different surface types below the light paths set up at each experiment: the studies by [*Stutz et al.*, 2001] were performed above a grass meadow in Milan/Italy while the experiments presented here took place over a mix of natural and artificial surfaces in the city of Heidelberg. The experiments performed by [*Trick et al.*, 2002] indicated that HONO formation is very likely more effective on artificial surfaces, which would consequently affect the steady state value of $HONO/NO_2$. But [*Trick et al.*, 2002] state that further experiments are required to understand and quantify the different effects contributing to this steady state.

For the discussion of the diurnal cycle of the vertical profile of the ratio $HONO/NO_2$, it is important to keep in mind that the April/May period is characterised by high atmospheric instability. Consequently, a well-mixed PBL is assumed during almost the whole period. Thus, the diurnal cycle of the $HONO/NO_2$ height profile is somehow atypical: the time series and absolute values of the ratios $HONO/NO_2$ are rather common in all three layers.
During most other periods, the evening increase of the ratio in the middle and upper layer is significantly less steep than in the lower layer, and also the absolute values of the ratio decrease more significantly with increasing height (see chapter 6.3.3 below and Annex A). However, a significant $HONO/NO_2$ decrease with height was also observed in April/May 1999, especially at night (see Figure 54). This observation indicates again that the surface area which is effective for HONO formation decreases with altitude.

Diurnal variation of the gradients

After the discussion of the seasonal variation of the gradients in chapters 6.2.5 and 6.2.6 one major question remains open: why do the diurnal and nocturnal monthly means of the gradients not depend on the mean Radon activities (i.e. atmospheric stability)?
The diurnal variation of the relative gradients shown in the lowermost and middle panels of Figure 54 can at least partly answer this question: a dependency of the NO_2 gradients on Radon activity is only observed in the morning hours between 02:00 and 09:00, when a ground inversion builds up and ceases again. The gradient (c_3/c_1)-1 of HONO shows a similar temporal variation during this period.
However, during the rest of the day, the gradient seems to be forced mainly by the diurnal variation of the sources and sinks of NO_2 and HONO. Especially, the variations of the NO_2

gradients (c_3/c_1)-1 and (c_2/c_1)-1 strongly resemble the variation of NO_2 in the lowermost layer: the local maxima of the absolute values of both relative gradients are found at 19:00 and 05:00 GMT For the morning maximum, the effect becomes more evident in periods with less intense vertical mixing (see chapter 6.4.1 below). Consequently, the coincidence of the morning maxima of the absolute NO_2 gradient and the Radon activity is only partially linked to atmospheric stability.

For the HONO gradients, the diurnal variation is less obvious, apart from a weak correlation of the HONO gradient (c_3/c_1)-1 with the HONO concentration in the lowermost layer: the local maxima at 18:00 and 06:00 GMT coincide closely with the diurnal HONO maxima. However, the HONO gradient (c_2/c_1)-1 shows a rather inconsistent diurnal variation, which still is significantly wider than the mean errors.

In summary, the diurnal variation of the gradients of NO_2 and HONO further confirms the thesis established in chapter 6.2.6 above: HONO – like NO_2 – is formed mainly at or near the ground and subsequently transported to the upper PBL:

- By day, the steeper gradients of HONO compared to NO_2 are explained by the rapid photolysis causing a HONO lifetime that is shorter or in the same order of magnitude as the transfer times to the upper layer. Contrastingly, NO_2 is in a photochemical steady state with NO and O_3 that also allows NO_2 production at higher altitudes of the PBL.
- The decreasing difference between the gradients of HONO and NO_2 at night is explained by the assumption that the NO_2 sources in the upper PBL cease while reactions forming N_2O_5 represent a NO_2 sink increasing with altitude. HONO still has its only sources near the ground and must be transported to higher altitudes. However, vertical transport is significantly less effective at night than by day. Thus, the absolute value of the HONO gradient does not change even if photolysis is not effective at night.

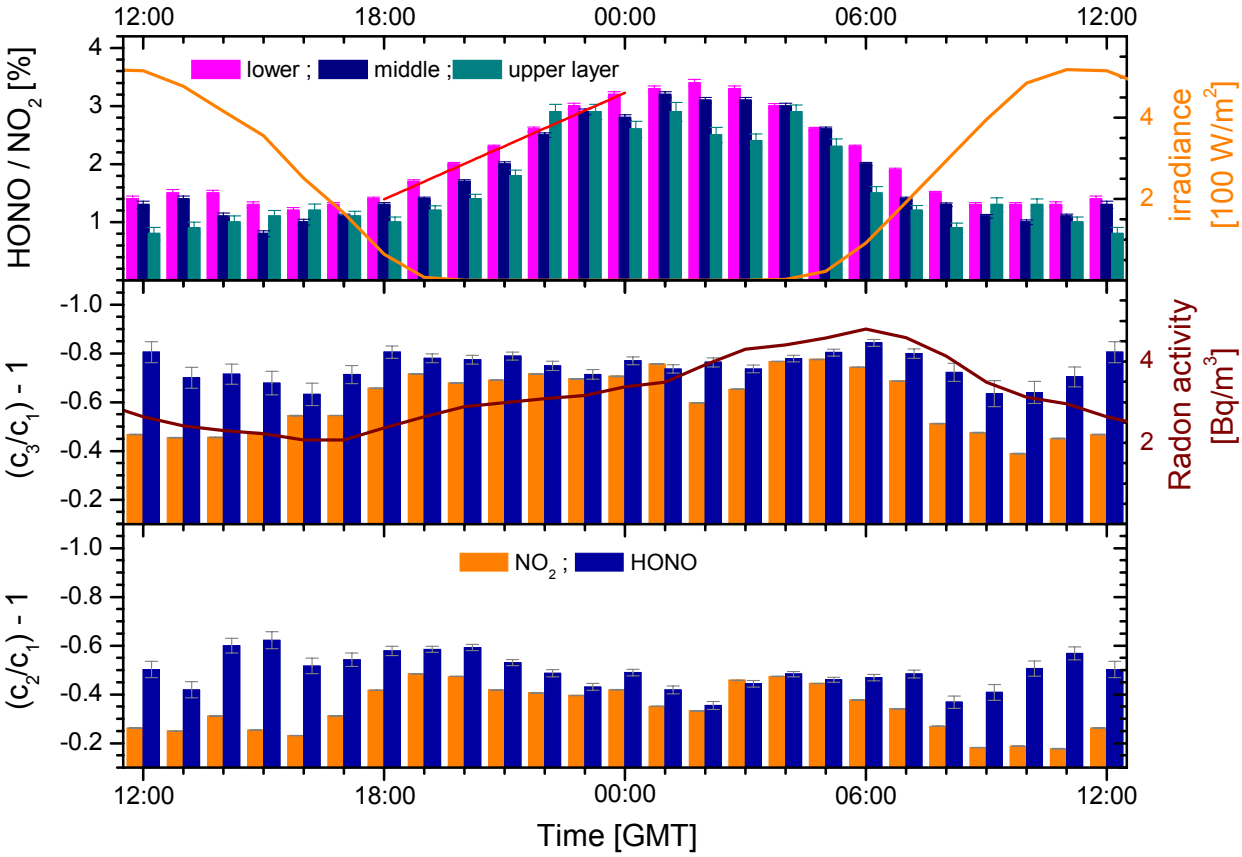

Figure 54: Hourly means of HONO/NO_2 and the relative gradients for NO_2 and HONO measured in April/May 1999. The thin red line in the top panel indicates the linear fit to the increase of HONO/NO_2 in the first half of the night.

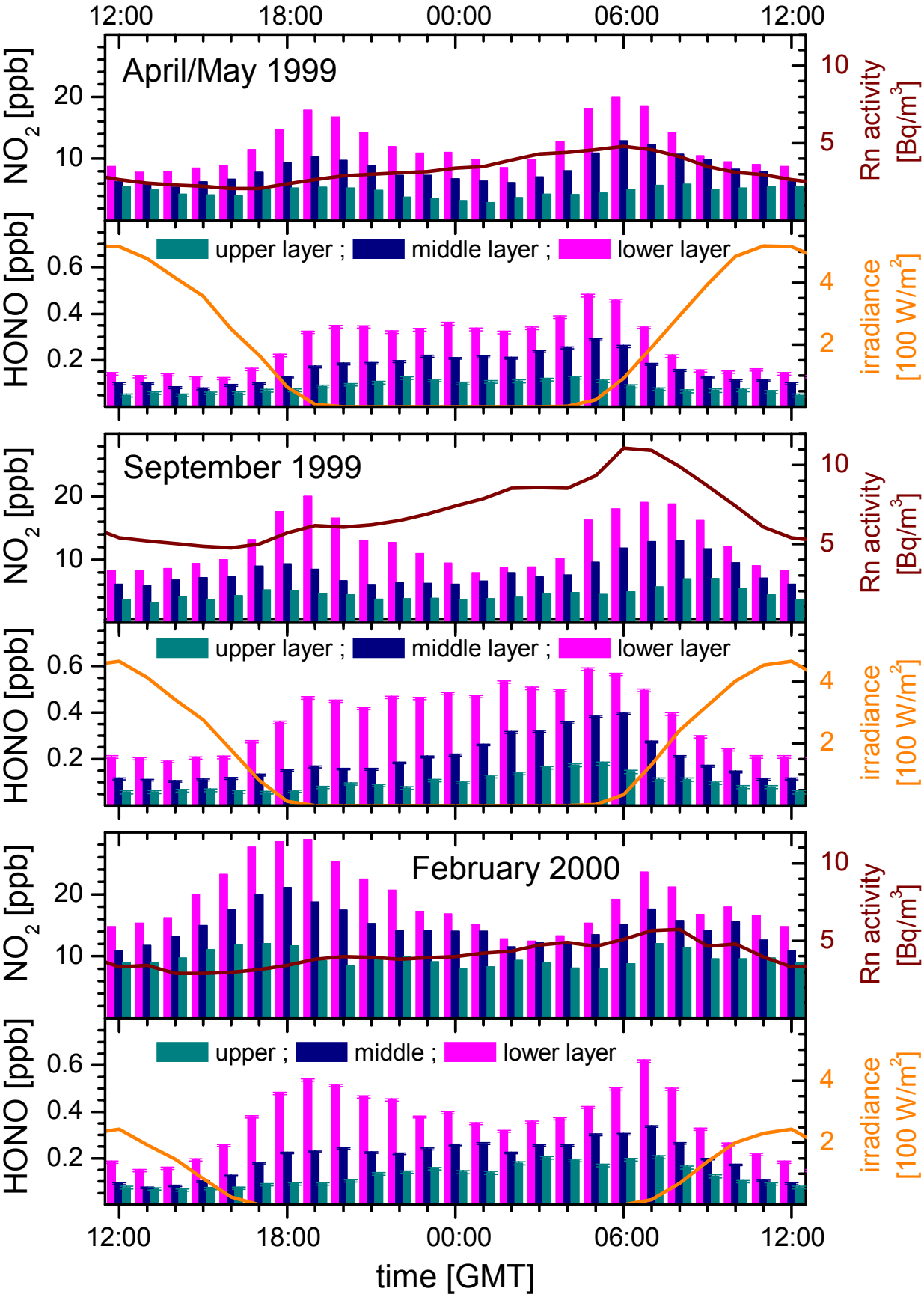

Figure 55: Seasonal variation of the hourly means of NO_2 and HONO exemplified by the diurnal time series of April/May 1999, September 1999 and February 2000.

6.3.3 Seasonal variation of the diurnal cycles

It is expected that the seasonal variation of the climatic conditions in the PBL also has an effect on the mean diurnal cycle of both compounds, their ratio and their gradients. So the variability of the mean diurnal cycles computed for the nine 5-week periods should yield further information on the dependence of the profiles on atmospheric parameters. Of special interest is the influx of stratification stability, because the vertical transport efficiency forces not only the gradients of NO_2 and HONO in the PBL, but also the accumulation of both compounds in the lowermost PBL, i.e. close to their sources.

For a first overview, three of the nine periods will be compared, each typical for atmospheric conditions found in the respective season:

1. The April/May 1999 period for spring, featuring effective mixing due to high atmospheric activity (see above).
2. The September 1999 period for summer with effective daytime mixing due to convection driven by intense solar irradiation and stable stratification at night due to temperature inversions forced by the cooling of the Earth's surface.
3. The February 2000 period as an example of the conditions found in the central European winter, with strong cyclones alternating with stable high-pressure situations featuring high atmospheric stability.

The mean diurnal cycles of NO_2, HONO, the ratio HONO/NO_2 and the gradients of both compounds for the these three and the remaining six periods are also presented in Annex A.

NO_2 and HONO

Figure 55 shows the mean diurnal variation of NO_2 and HONO in the spring, summer and winter periods. The most obvious distinction between the mean cycles of both NO_2 and HONO are the mean concentrations observed at night (see also Table 20).

Especially the NO_2 maximum at nightfall is found at much higher concentrations in winter (28.8 ppb) than in late summer (20.0 ppb) and spring (17.8 ppb). The NO_2 concentrations in the middle layer feature evening maxima of 21.1, 9.2 and 10.4 ppb in February, September and April/May, respectively, while in the upper layer evening maxima of 12.1, 5.1 and 5.4 ppb are found in the same periods. As the mean Radon activity at this time of day is highest in September and the highest mean wind speeds are found at 2.7 m/s in February, changing atmospheric stability can be ruled out as the reason for this effect.

The lower temperatures in winter, however, have an indirect effect on the higher NO_2 concentrations observed in February: NO_x emissions by heating in the city of Heidelberg feature a maximum in winter and therefore cause higher ambient NO_2 concentrations.

Additionally, the mean NO_2 mixing ratios observed at nightfall are directly linked to photochemistry and the intensity and duration of solar irradiance during a 24-hour period: in April/May, the hourly means of solar irradiation are not only the highest observed in all three periods discussed here, but also exceed zero for more than 14 hours, which is slightly more than in September and substantially more than in February. Consequently, the O_3 mixing ratios at nightfall are found to be lowest in February and highest in April/May. The same seasonal trend is observed for the sum of total VOC concentration (without Methane) measured by [*UMEG*, 1999; *UMEG*, 1999-2001] that is also strongly correlated to photochemistry (see [*Finlayson-Pitts and Pitts*, 2000]). Thus, the observed seasonal variation of the maximum NO_2 concentrations also seems to be linked to the photochemical steady state of NO_x, O_3 and VOCs described by R. 14, which would cause lower NO_2 concentrations in periods featuring higher solar irradiances.

Closely correlated to the evening NO_2 maximum is the first local HONO maximum in the course of the night, which also shows the maximum concentrations in all three layers in February : in the lowermost layer, HONO is found to rise to 0.54 ppb, while only 0.34 ppb are

observed in April/May at 19:00 GMT. This effect is also linked to photochemistry: in February. Solar irradiation ceases significantly earlier in the afternoon, resulting in an earlier increase of HONO concentration (see Figure 55). Additionally, the higher NO_2 concentrations in February avail HONO formation, yielding higher amounts of HONO in the lower layer. In the middle layer, the seasonal differences in the HONO mixing ratios are significantly smaller (0.22 ppb in February, 0.18 ppb in April/May and 0.17 ppb in September), although the NO_2 mixing ratio almost halves from February to April/May and September. This is a further indication that HONO is formed mainly near the ground. A closer correlation of HONO and NO_2 would be expected if a HONO source waspresent in the volume of the PBL. In the upper layer, HONO only builds up slowly in the course of the night. Thus a distinct local maximum cannot be identified in the evening.

Table 20: Mean trace gas concentrations and atmospheric stability parameters measured during the evening NO_2 maximum at 18:00/19:00 GMT.

	April/May 1999	September 1999	February 2000
NO_2 (lower layer) [ppb]	17.84 ± 0.01	20.0 ± 0.01	28.80 ± 0.01
NO_2 (middle layer) [ppb]	10.41 ± 0.01	9.29 ± 0.01	21.10 ± 0.01
NO_2 (upper layer) [ppb]	5.37 ± 0.01	5.1 ± 0.01	12.08 ± 0.01
HONO (lower layer) [ppb]	0.344 ± 0.006	0.463 ± 0.005	0.536 ± 0.005
HONO (middle layer) [ppb]	0.184 ± 0.004	0.166 ± 0.004	0.223 ± 0.003
HONO (upper layer) [ppb]	0.094 ± 0.006	0.077 ± 0.005	0.089 ± 0.005
O_3 [ppb]	28.64 ± 0.07	23.31 ± 0.07	7.11 ± 0.08
VOC [$\mu g/m^3$]	41.26 ± 0.04	65.0 ± 0.04	72.29 ± 0.04
Rn activity [Bq/m^3]	2.64 ± 0.08	6.16 ± 0.07	3.8 ± 0.1
wind speed [m/s]	1.5 ± 0.2	1.0 ± 0.2	2.8 ± 0.2

Table 21: Mean trace gas concentrations and atmospheric stability parameters measured during the night-time NO_2 minimum at 01:00/02:00 GMT.

	April/May 1999	September 1999	February 2000
NO_2 (lower layer) [ppb]	8.52 ± 0.01	7.93 ± 0.01	12.43 ± 0.01
NO_2 (middle layer) [ppb]	6.15 ± 0.01	6.08 ± 0.01	12.21 ± 0.01
NO_2 (upper layer) [ppb]	2.92 ± 0.01	3.66 ± 0.01	8.13 ± 0.01
HONO (lower layer) [ppb]	0.319 ± 0.006	0.469 ± 0.005	0.316 ± 0.005
HONO (middle layer) [ppb]	0.209 ± 0.004	0.217 ± 0.004	0.222 ± 0.003
HONO (upper layer) [ppb]	0.106 ± 0.006	0.099 ± 0.005	0.137 ± 0.006
O_3 [ppb]	25.5 ± 0.01	22.25 ± 0.07	13.39 ± 0.08
VOC [$\mu g/m^3$]	14.14 ± 0.04	18.74 ± 0.04	17.09 ± 0.05
Rn activity [Bq/m^3]	3.49 ± 0.07	7.86 ± 0.07	4.7 ± 0.1
wind speed [m/s]	1.6 ± 0.2	1.3 ± 0.2	3.3 ± 0.2

In the course of the night, NO_2 concentrations decrease in all heights and seasons. The minimum values at night are reached typically at 01:00/02:00 GMT. The reasons for this decrease (reactions with O_3, NO_3 and H_2O and subsequent deposition of HNO_3) are discussed in chapter 6.3.2. Table 21 compares the minimum NO_2 concentrations at night in the three periods: again, the highest values are found in February (at 12.4 ppb), while the mixing ratios in the other periods are roughly the same (7.9 to 8.5 ppb). The most marked differences are observed in the upper layer, with only 2.9 ppb in April, while in September and February 3.7 and 8.1 ppb are observed, respectively. Obviously, this effect is linked to the O_3 concentration in the upper layer: in April, photochemistry by day and more effective vertical mixing at night cause a higher flux of O_3 from the free troposphere to the upper PBL. Subsequently, NO_2 is titrated by O_3 according to the reaction cycle summarised in the modified Leighton Ratio (R. 14).

Contrastingly, the highest HONO concentrations in the lower layer are found in September, coinciding with the seasonal maximum of the indicators for atmospheric stability: at highest Radon activities and lowest wind speeds, HONO accumulation in the lowermost part of the PBL is most effective. In the upper two layers the differences in the HONO concentrations are less significant. The most notable fact is that, in February, the highest HONO mixing ratio in the uppermost layer and the highest wind speeds are observed simultaneously . The obvious dependency of HONO concentrations in the lowermost layer on the efficiency of vertical transport verifies again the assumption that the HONO sources are predominantly situated in the lower PBL (see [*Febo et al.*, 1999] and chapter 6.2 above).

At 05:00/06:00 GMT, just prior to sunrise, the second night-time NO_2 and HONO maximum is observed in the lowermost PBL. It is caused by the early-morning ground inversion coinciding with the first diurnal NO_x emission peak due to the rush-hour. The observed mean concentrations of NO_2 and HONO are listed in Table 22. Again, the highest NO_2 mixing ratios in all three layers are found in February (ranging from 23.6 ppb in the lowermost to 12.1 ppb in the uppermost layer), while the values in April/May and September are similar (20 to 19 ppb in the lowermost and 5.9 to 7.0 ppb in the uppermost layer).

The maximum HONO concentration in the lower layer is observed in February, which contrasts the findings at the night-time NO_2 minimum from above, where highest HONO concentrations are found in September, anti-correlated to the efficiency of vertical mixing. An explanation for this is easily found: as solar irradiation increases more slowly and approximately 2 hours later in February compared to September, HONO can build up for a longer time (with an additional thrust by the early morning NO_2 peak, which is also more pronounced in February), before being photolysed. Accordingly, the morning HONO maximum in February is observed 2 hours later than in September.

In the middle layer, however, the maximum HONO concentration at the end of the night is found in September and only one hour earlier than in February (see Figure 55). Additionally, the mean nocturnal time series of HONO in September shows a constant increase of HONO in the middle layer until photolysis starts in the morning. The same effect can be observed in the upper layer, but at a significantly lower amplitude. Contrastingly, in the other two periods HONO concentrations in the middle and upper layer are quite constant after the first increase in the late evening hours. An effective HONO volume source is rather unlikely, because the comparison of the aerosol concentrations in the three periods indicates no significant increase of aerosol in September. The stratification structure of the nocturnal PBL and vertical transport are more likely to be the reason for the constantly increasing HONO mixing ratios in the middle layer. As detailed meteorological information has not been available, this effect cannot be explained here conclusively , but HONO profile measurements supplemented by measurements of the 3D wind field on the same height scale should clarify this question.

The daytime NO_2 levels summarised in Table 23 show a constant decrease with altitude in all three layers while seasonal variation of the mixing ratios is anti-correlated to solar irradiation (see chapters 6.1.1, 6.2.2 and 6.3.2).
As the mean HONO concentrations during the day are below the detection limits on all three light paths, daytime HONO levels will be discussed separately in chapter 0 below. Nevertheless, the values presented in Table 23 are typical for daytime HONO at Heidelberg.

Table 22: Mean trace gas concentrations and atmospheric stability parameters measured during the early morning NO_2 maximum at 06:00/07:00 GMT.

	April/May 1999	September 1999	February 2000
NO_2 (lower layer) [ppb]	20.01 ± 0.01	19.03 ± 0.01	23.58 ± 0.01
NO_2 (middle layer) [ppb]	12.88 ± 0.01	12.87 ± 0.01	17.61 ± 0.01
NO_2 (upper layer) [ppb]	5.90 ± 0.01	6.96 ± 0.01	12.09 ± 0.01
HONO (lower layer) [ppb]	0.478 ± 0.01	0.586 ± 0.006	0.618 ± 0.005
HONO (middle layer) [ppb]	0.288 ± 0.01	0.396 ± 0.004	0.336 ± 0.003
HONO (upper layer) [ppb]	0.12 ± 0.01	0.180 ± 0.007	0.205 ± 0.007
O_3 [ppb]	14.5 ± 0.1	9.51 ± 0.07	7.78 ± 0.08
VOC [$\mu g/m^3$]	41.36 ± 0.04	56.40 ± 0.04	67.55 ± 0.04
Rn activity [Bq/m^3]	4.80 ± 0.07	11.06 ± 0.07	5.8 ± 0.1
wind speed [m/s]	1.4 ± 0.2	1.2 ± 0.2	3.2 ± 0.2

Table 23: Mean trace gas concentrations and atmospheric stability parameters measured during the daytime NO_2 minimum at 14:00 GMT.

	April/May 1999	September 1999	February 2000
NO_2 (lower layer) [ppb]	7.80 ± 0.09	8.26 ± 0.01	14.76 ± 0.01
NO_2 (middle layer) [ppb]	5.39 ± 0.07	5.88 ± 0.01	10.90 ± 0.01
NO_2 (upper layer) [ppb]	3.99 ± 0.01	3.19 ± 0.01	8.92 ± 0.01
HONO (lower layer) [ppb]	0.129 ± 0.005	0.208 ± 0.006	0.147 ± 0.005
HONO (middle layer) [ppb]	0.077 ± 0.004	0.109 ± 0.004	0.073 ± 0.003
HONO (upper layer) [ppb]	0.058 ± 0.005	0.058 ± 0.006	0.063 ± 0.005
O_3 [ppb]	38.2 ± 0.1	39.12 ± 0.09	18.83 ± 0.09
VOC [$\mu g/m^3$]	44.3 ± 0.04	39.55 ± 0.04	45.46 ± 0.05
Rn activity [Bq/m^3]	2.30 ± 0.08	5.39 ± 0.08	3.3 ± 0.1
wind speed [m/s]	2.3 ± 0.2	1.9 ± 0.2	4.3 ± 0.2

Ratio $HONO/NO_2$

The discussion of the diurnal cycles of NO_2 and HONO has yielded the result that atmospheric parameters influence both compounds in a specific way: consequently, the diurnal cycle of the ratio $HONO/NO_2$ is also expected to feature a seasonal variation. Figure 56 shows the mean diurnal variation of the ratio for the three exemplary periods. At first sight, there are three significant differences :

- The absolute value of the ratio that is reached in the course of the night is strongly depending on the measurement period: in the lower layer, the highest $HONO/NO_2$ ratios of 4.6±0.05 % are found in September, compared to 3.6±0.06 % and 2.9±0.03 % in April/May 1999 and February 2000, respectively.
- The shape of the diurnal cycles in the three layers vary with the season. Most notably, the steepest increase of the ratio $HONO/NO_2$ is found in September: in the lower layer, $HONO/NO_2$ increases by 0.39±0.01 % h^{-1} within the first 6 hours after sundown. This is comparable with 0.31±0.01 % h^{-1} and 0.27±0.02 % h^{-1} in April/May and February, respectively.
- The variation of the shape of the diurnal cycle is not common in all three layers: in all three periods, the increase of the ratio in the upper layers is less steep than in the lower layer (see also Table 24). The smallest differences between the three layers are found in April/May 1999, where the slope of the evening increase and the maxima in the three layers decrease only slightly with height. In September 1999, however, the slope of the evening increase of the ratios becomes significantly smaller with height: the difference between the slopes in the lower and middle layer is significantly larger than between the middle and upper layer. The third case is represented by February 2000: the ratios in the middle and upper layer show a common time series (slope and maxima/minima), while the values for the ratio in the lower layer are generally higher throughout the day. The slope observed in the first part of the night also decreases with height in this period: again. The difference between the slopes in the lower and middle layer is more marked than between the middle and upper layer.

Firstly, regarding the seasonal variations of the absolute $HONO/NO_2$ ratios , it is obvious from Figure 56 and Table 24 that the maximum values for the ratio $HONO/NO_2$ and the HONO formation rate are found in the September 1999 period, which features the highest Radon activity at night. Additionally, the maximum ratio at night is found some 2 hours prior to sunrise in all seasons and at all heights, coinciding with the night-time minimum of 12.4 ppb NO_2 in the PBL (see also chapter 6.3.2). At this time of day, the NO concentration in the PBL is only about 2.0 to 2.5 ppb.

Thus, the bulk of the HONO detected in the PBL must originate from heterogeneous surface reactions (see chapter 2.3) as direct HONO emission can only explain a maximum of 0.8 % in periods of significant NO_x emissions. However, the lowest diurnal concentrations of NO_2 and NO were observed in the period with the highest $HONO/NO_2$ ratio. Additionally, the ratio ceases significantly in the morning, when NO_x emissions reach their first diurnal maximum. Therefore, it is most likely that a smaller fraction of night-time HONO than the 0.8% per NO_x found by [*Kurtenbach et al.*, 2001] is emitted directly from combustion processes.

The fact that mean night-time $HONO/NO_2$ ratios significantly exceeding 3.0% are observed over five 5-week periods (from April/May 1999 to November 1999, see Annex A) raises another important question: [*Stutz et al.*, 2001] postulated a steady state between HONO formation and deposition on surfaces near the ground at a $HONO/NO_2$ ratio of 3.0 %. It is now rather obvious that this steady state is specific to the surface composition and the meteorological conditions found at the site of the measurements (Milan/Italy in April/May in this case). This reservation was also cautiously mentioned by [*Stutz et al.*, 2001] but should be

underlined here. With the current knowledge, it can only be stated that high atmospheric stability and low NO_x concentrations in the middle of the night (as observed in the September 1999 period) provide good conditions for high HONO concentrations and therefore high $HONO/NO_2$ ratios at night. Chapter 6.4 below deals with case studies that show specific situations favouring high $HONO/NO_2$ ratios.

The second important point is that the $HONO/NO_2$ ratio decreases with height under all atmospheric conditions and at all times. The largest differences between $HONO/NO_2$ in the lower and upper layer are found at night and for a stable stratification of the PBL. Inevitably, this observation confirms the thesis proposed in chapter 6.2.6 and reaffirmed in chapter 6.3.2: the surfaces most effective for HONO formation are located at or near the ground. Consequently, the slower increase of the ratio in the upper PBL at nightfall would be caused by vertical transport, whereas a volume source of HONO is only of second order . Unfortunately, no information on the vertical diffusion coefficient is available here to quantify a remaining volume production of HONO (e.g. on Aerosol surfaces or by gas-phase reactions), which cannot be ruled out completely by the evaluation presented here.

Vertical transport from the ground being the major source of HONO in the upper PBL would also explain the different shapes of the temporal variation of $HONO/NO_2$ in the upper layers: in a well-mixed nocturnal atmosphere (as found in April/May) the $HONO/NO_2$ ratio decreases only slowly with altitudewhereas a strongly stratified atmosphere (as observed in different shapes in September and February) causes steeper gradients on the ratio $HONO/NO_2$. This will be further exemplified by the case studies presented in chapter 6.4.

The time derivative of $HONO/NO_2$ in the first 6 hours after sundown, often used to compute the HONO formation rate (see chapter 6.3.2 and e.g. [*Alicke*, 2000; *Alicke et al.*, 2001a; *Alicke et al.*, 2001b; *Trick and Geyer*, 2002]) is also listed for the three periods in Table 24. Obviously, the formation rate in the lowermost layer is highest in September (at 0.39 % s^{-1}), coinciding with the highest atmospheric stability. In the April/May and February periods featuring more effective transport processes (indicated by lower a Rn activity and higher wind speeds), the HONO formation rates are substantially smaller (at about 0.30 % s^{-1}).
In the upper layer, the situation changes completely: $d(HONO/NO_2)/dt$ is highest in April/May 1999 and lowest in September 1999, while the value observed in February is only slightly higher than in September. Considering Radon activity and the wind speeds, it is obvious that these observations are also induced by atmospheric stability. Radon activity has its minimum in April/May and its maximum in September. Consequently, HONO is more effectively mixed into the upper PBL in April/May, causing a faster increase of $HONO/NO_2$ with time in the upper layer. The stable stratification in September prevents the transport of HONO to higher altitudes and induces a slower increase of $HONO/NO_2$. In February, however, the higher horizontal wind speeds and slightly higher Rn activity indicate a more efficient horizontal transport of HONO away from its sources in the city of Heidelberg. As the stratification of the PBL is still more stable as in April/May, the transport of HONO to the upper PBL is less efficient. So the $HONO/NO_2$ ratio in the upper layer shows a slightly faster increase than in September, but increases much slower than in April/May. These findings have two major consequences for the evaluation of HONO measurements in the PBL and the understanding of the source processes of HONO:

- The “real” formation rate of HONO cannot be deduced from atmospheric measurements without detailed data on the vertical and horizontal transport processes in the PBL.
- The assumption that the most effective HONO source reactions occur on surfaces near the ground and the major HONO source in the upper PBL is vertical transport from below is justified again.

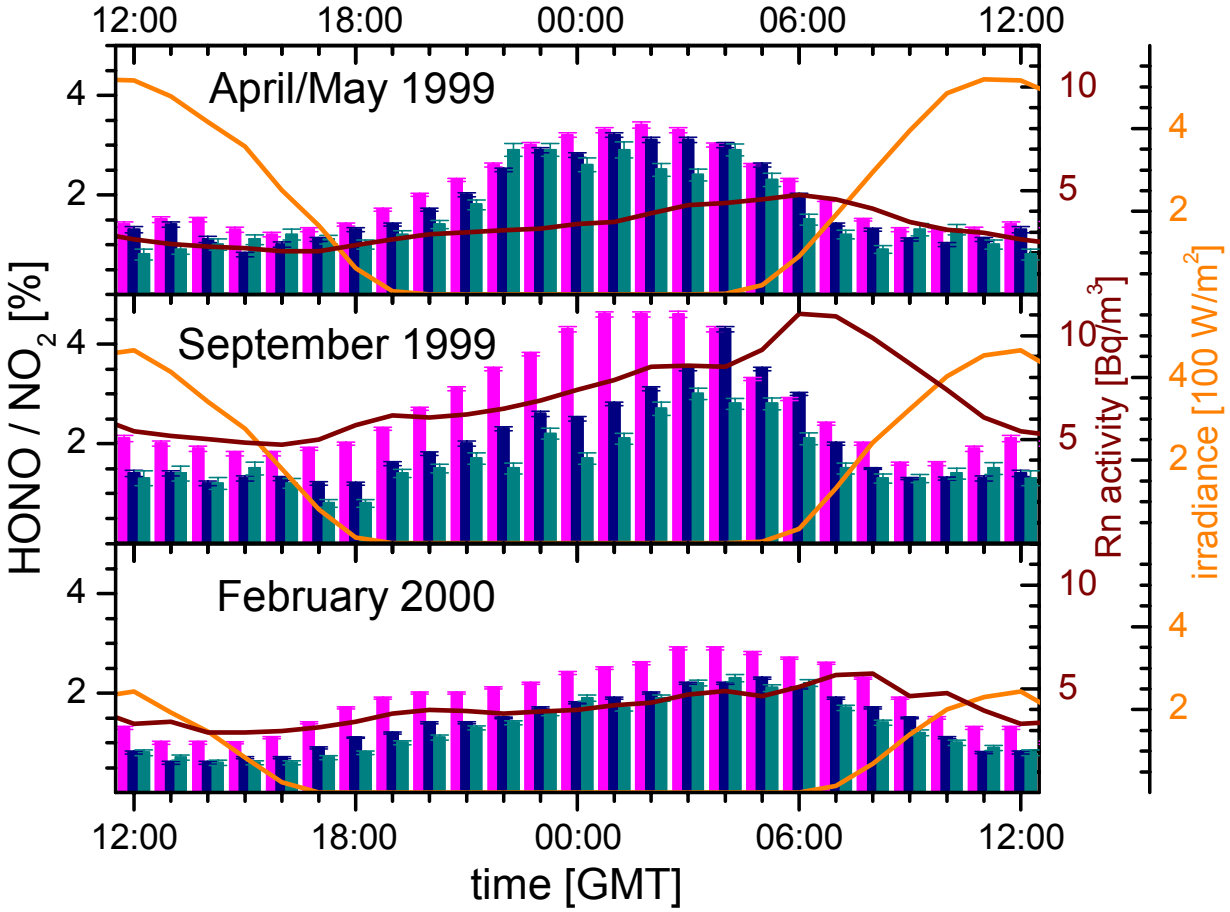

Figure 56: Seasonal variation of the hourly means of the ratio HONO/NO_2 exemplified by the diurnal time series of April/May 1999, September 1999 and February 2000.

Table 24: Maximum night-time HONO/NO_2 ratios and HONO formation rates in the first part of the night compared to the mean nocturnal Radon activity and wind speeds.

HONO/NO_2 [%]	April/May 1999	September 1999	February 2000
lower layer	3.6 ± 0.06	4.6 ± 0.05	2.9 ± 0.03
middle layer	3.2 ± 0.05	4.3 ± 0.05	2.3 ± 0.02
upper layer	3.0 ± 0.10	3.0 ± 0.11	2.3 ± 0.07
d(HONO/NO_2)/dt [% h^{-1}]			
lower layer	0.31 ± 0.01	0.39 ± 0.01	0.27 ± 0.02
middle layer	0.30 ± 0.05	0.20 ± 0.02	0.18 ± 0.02
upper layer	0.26 ± 0.05	0.11 ± 0.04	0.13 ± 0.02
Rn activity [Bq/m^3]	3.55 ± 0.04	7.53 ± 0.09	4.23 ± 0.08
wind speed [m/s]	1.54 ± 0.03	1.20 ± 0.02	3.23 ± 0.04

Gradients of NO_2 and HONO

Figure 57 shows the gradients of NO_2 and HONO. It is rather obvious that the main factor forcing the gradients is the temporal variation of the trace gas concentrations in the lower layer. The gradients (c_2/c_1)-1 and (c_3/c_1)-1 of both compounds feature maxima coinciding with the local maxima of the time series of the respective compound. This figure also shows that this trend is only partially amplified by increased atmospheric stability: the mean and absolute values of the gradients (c_3/c_1)-1 in April/May and September are quite similar (see Figure 57) for both compounds. But the effect of increased atmospheric stability in the gradients is still visible: the maximum in the absolute values of the gradients for HONO and NO_2 is found in September, while the maximum values of the NO_2 and HONO mixing ratios are observed in February. Additionally, the gradients (c_2/c_1)-1 show significant differences between April/May and September, especially in the first part of the night. These effects are most likely caused by the change of the stratification structure of the PBL (see Figure 8 in chapter 3.3.1). However, the lack of detailed information on the vertical diffusion constants and hence the height of the stable nocturnal layer (using Radon activity) prevents a quantitative analysis of the observed gradients.

The analysis of the seasonal variation of the gradients helps to understand the conclusion of chapter 6.2.5: the influx of atmospheric stability on the gradients used here is not consistent, but depends strongly on the time of day and the stratification structure of the PBL.

It can also be stated that the HONO gradients are steeper than the NO_2 gradients throughout the mean diurnal cycle derived from the hourly means. This reaffirms the results of the discussion of the diurnal cycle in the April/May period (chapter 6.3.2) and the diurnal and nocturnal means of the each period (see chapter 6.2.5).

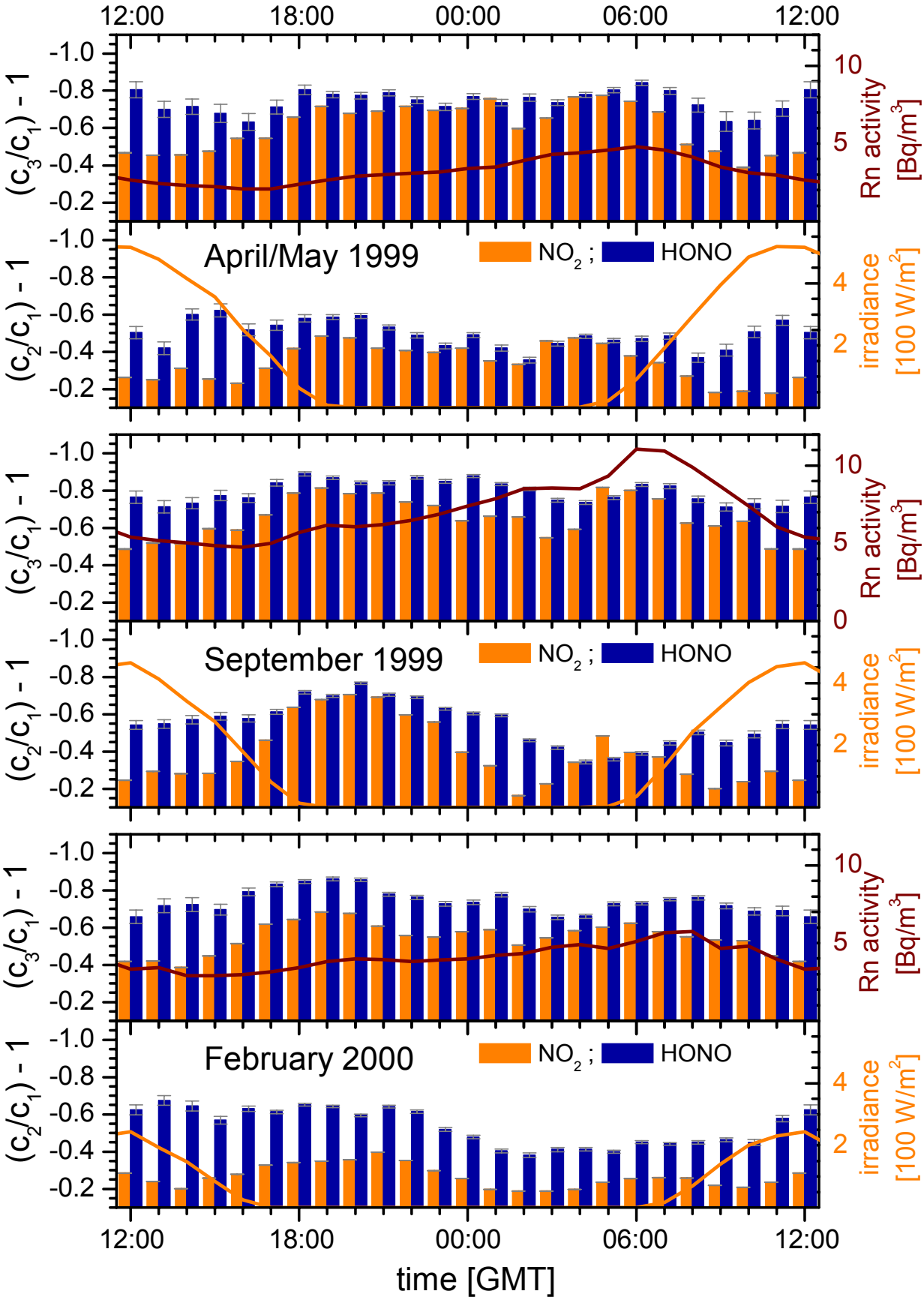

Figure 57: Seasonal variation of the hourly means of the NO_2 and HONO gradients exemplified by the diurnal time series of April/May 1999, September 1999 and February 2000.

6.4 Case studies

6.4.1 Mean dependency on the stratification stability of the PBL

As the discussion of the diurnal cycle of NO_2 and HONO, their ratio and gradients in the previous chapter has shown, the consideration of the meteorological situation is inevitable for a correct analysis of all time series obtained from the measurement. [*Febo et al.*, 1999] proposed a first order approach for the analysis of the impact of transport processes (horizontal and vertical) using the general atmospheric equation for HONO:

$$\frac{\partial HONO}{\partial t} = \frac{1}{h_{BL}}\left[\Phi_P + \Phi_S\right] - K(z)\cdot\frac{\partial HONO}{\partial z} + P_{Part} - L_\lambda - L_S + Adv \qquad \text{Equ. 57.}$$

It is obvious from Equ. 57 that a careful separation of high and low pressure situations can be used for a separate analysis of the impact of mixing processes and atmospheric chemistry on the measured time series of HONO (and other trace gasses) in the polluted PBL. If measurements of the 3D wind field are not available, other indicators for atmospheric activity can be used: atmospheric pressure (or its time derivative), horizontal wind speeds, the day/night temperature variance, solar irradiation and Radon activity. The following criteria are applied to separate periods of effective mixing (i.e. high atmospheric activity) from more stable periods:

Stable periods:

- high (or increasing) atmospheric pressure
- low wind speeds
- pronounced diurnal cycle of Radon indicating a definitively stable stratification at night and convective mixing by day (ideally coinciding with a pronounced diurnal cycle of the temperature indicating the same effects)
- pronounced diurnal profiles of all trace gasses emitted or formed at (or near) the ground
- similar shape of the diurnal cycles of all trace gasses featuring major sources near the ground and Radon activity
- in fall and winter, convective mixing by day ceases due to weaker solar irradiation, resulting in a (more or less) stable stratification of the PBL by day.

Unstable periods:

- low (or decreasing) atmospheric pressure
- high wind speeds
- reduced absolute values of radon coinciding with a less apparent diurnal radon cycle indicating effective vertical mixing
- less apparent diurnal cycles of all trace gasses and generally lower mixing ratios
- less apparent correlation of the diurnal cycles of the trace gasses and Radon
- reduced solar radiation (coinciding with a less apparent diurnal cycle of the temperature) indicating cloud cover

So, under stable conditions, the HONO time series can be expected to show a trend similar to the trend of Radon activity, if HONO is indeed formed primarily near the ground. If HONO has an additional significant source within the volume of the PBL, the diurnal cycles (and profiles) of HONO should feature less pronounced differences between stable and unstable periods. Especially the comparison to the diurnal cycle of the NO_2 mixing ratio and profiles can be useful in this context.

Additionally, the HONO formation rate can be approximated from the evening increase of HONO and the boundary layer height derived from Radon activity. In stable situations, the general equations of HONO and Radon simplify to:

$$\frac{\partial HONO}{\partial t} = \frac{1}{h_{BL}}\left[\Phi_P + \Phi_S\right] \qquad \text{Equ. 64}$$

$$\frac{\partial Rn}{\partial t} = \frac{1}{h_{BL}}\left[\Phi_{Rn}\right] \qquad \text{Equ. 65.}$$

Solving Equ. 65 with respect to h_{Bl}, Equ. 64 can be written as

$$\frac{\partial HONO}{\partial t} = \frac{\frac{\partial Rn}{\partial t}}{\left[\Phi_{Rn}\right]} \cdot \left[\Phi_P + \Phi_S\right] \qquad \text{Equ. 66.}$$

Thus, the "true" HONO production rate Φ_S can be derived from the Radon surface flux and the evening increase of HONO and Radon activity. The direct emission rate of HONO Φ_P can be approximated by the emission ratio HONO/NO_x = 0.8% published by [*Kurtenbach et al.*, 2001].

The criteria for the distinction of predominantly stable or labile stratification mentioned above were applied to the profile data measured in October 1999. In this period, a sequence of pronounced high and low pressure situations prevailed. Thus, two predominantly labile periods lasting 7 and 6 days each and 3 predominantly stable periods lasting 3 days each were extracted (see Figure 58). As all extracted data for the case studies were recorded within a 5-week period, major climatic changes can be excluded as a reason for changes in the diurnal mean profiles.

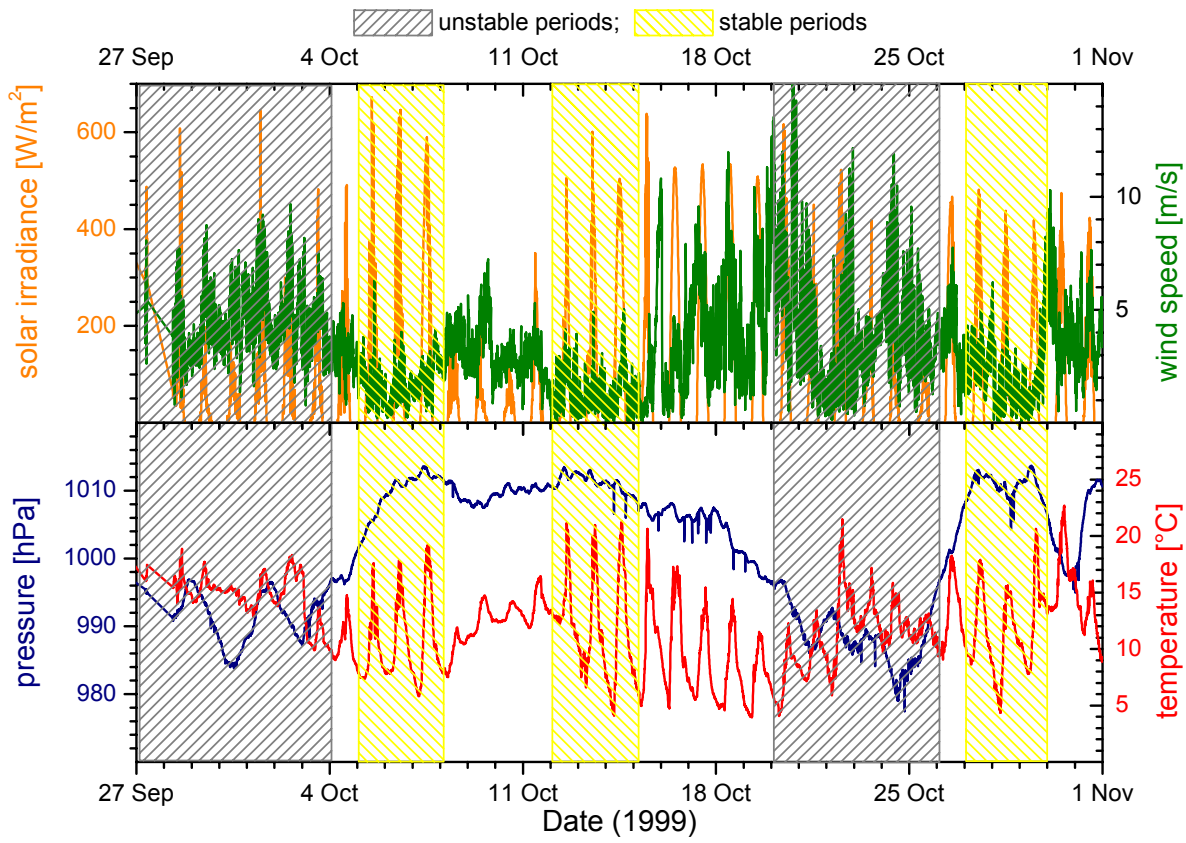

Figure 58: Meteorological data used as indicators for stable and unstable atmospheric situations in October 1999.

To obtain a statistically significant diurnal profile, the technique described in chapter 6.3.1 was applied to all data from the stable and instable periods to generate a "typical day" for both conditions. The results are shown in Figure 59 and Figure 60 for the stable and instable periods, respectively.

The difference between both atmospheric conditions is striking: the evening NO_2 concentrations in the lower layer rise from 20.6 ppb in the unstable periods by almost one third to 29.6 ppb under stable conditions (see Table 25 and Table 26). The evening and the morning peaks of HONO are more than two times higher under stable conditions (0.84 ppb) than under unstable conditions (evening 0.38 ppb / morning 0.40 ppb). This effect verifies both the propositions drawn from Equ. 57 above and the assumption that HONO is formed predominantly near the ground.

In stable situations, the NO_2 concentrations increase with increasing stability in the evening because NO_2 is formed from the steady state of NO, NO_2 and O_3 described by

$$\frac{[NO_2]}{[NO]} = \frac{1}{J_{(R.1)}} \cdot \left\{ k_{(R.3)} \cdot [O_3] + k_{(R.11)} \cdot [HO_2] + \sum_{RO_2} k_{(R.9)} \cdot [RO_2] \right\} \qquad \text{R. 14}$$

and accumulates in the stable PBL (the further time series of NO_2 in the course of the night has been discussed in chapter 6.3.2).

Consequently HONO can be formed by heterogeneous surface reactions of NO_2 and accumulates in the PBL. Decreasing NO_2 concentrations and night-time mixing cause almost constant HONO concentration in the lower layer and a slow HONO increase in the middle layer in the course of the night. In the same period, only a very slow increase of HONO can be observed in the upper layer. This effect can be understood considering that the night-time mixing in the lowermost urban PBL can be more effective than in the middle PBL due to heat fluxes and turbulence caused by urban heat sources and buildings [*Stull*, 1988].

Increasing solar irradiance and subsequent photolysis and convective mixing decrease the NO_2 and HONO concentrations in all three layers in the morning.

Under unstable conditions, NO_2 and HONO accumulation in the lower layer is not effective: horizontal and vertical mixing spread out both compounds. However, short periods of stability (indicated by the Radon activity increase at midnight) are correlated with increasing HONO concentrations in the lower layer. If significant amounts of HONO were be formed in the volume of the PBL, this effect would not be visible. But, HONO shows the same time series as NO_2 and Radon and must therefore also be formed primarily near to the ground.

It is obvious that the absolute value of the NO_2 morning peak, which rises by only 16% in the stable period, is less influenced by the mean diurnal stability. This effect is explained by the NO, O_3 and VOC concentration changes between the stable and unstable situations: early-morning O_3 concentrations in the stable PBL are significantly smaller than in the unstable periods, while NO concentrations are drastically increased in the stable PBL (see also Table 25 and Table 26). Thus, NO emitted in the morning into the stable PBL is significantly slower oxidised to NO_2, as insufficient O_3 for the fast[15] reaction

$$O_3 + NO \longrightarrow NO_2 + O_2 \qquad \text{R. 3}$$

is available. But still, NO can be oxidised by RO_x and HO_2 formed from VOCs (featuring a higher concentration in the stable atmosphere) and by the slower reaction of NO and O_2 [*Finlayson-Pitts and Pitts*, 2000]. Consequently, the NO_2 morning peak is less dependent on atmospheric stability, as one of the major formation pathways shuts down under stable conditions: most O_3 present in the PBL is already converted to O_2 and NO_2 by NO in the

[15] Rate constant $k_{R.3}(298K) = 1.8 \cdot 10^{-14}$ $cm^3 molec^{-1} s^{-1}$, [*DeMore et al.*, 1997]

evening (see R. 14) and increased stability prevents mixing of O_3 from the free troposphere to the lower PBL.

Table 25: Characteristic values of the hourly means for the stable periods in October 1999.

layer	lower	middle	upper
NO_2 [ppb] (morning peak)	22.85 ± 0.02	19.68 ± 0.02	10.99 ± 0.03
NO_2 [ppb] (evening peak)	29.58 ± 0.02	23.24 ± 0.01	15.61 ± 0.02
HONO [ppb] (morning peak)	0.834 ± 0.012	0.511 ± 0.013	0.164 ± 0.016
HONO [ppb] (evening peak)	0.839 ± 0.009	0.347 ± 0.006	0.094 ± 0.009
HONO/NO_2 [%] (maximum)	4.6 ± 0.06	3.4 ± 0.05	1.6 ± 0.25
d(HONO/NO_2)/dt [% h^{-1}]	0.25 ± 0.02	0.12 ± 0.02	0.09 ± 0.03
NO [ppb] (morning peak)	127.4 ± 0.3	-	-
O_3 [ppb] (NO morning peak)	0.91 ± 0.14	-	-
VOC [µg/m^3] (NO morn. peak)	112.2 ± 0.1	-	-
Rn activity [Bq/m^3] (max.)	13.22 ± 0.14	-	-
wind speed [m/s] (max.)	2.6 ± 0.3	-	-

Table 26: Characteristic values of the hourly means for the unstable periods in October 1999.

layer	lower	middle	upper
NO_2 [ppb] (morning peak)	19.68 ± 0.02	13.91 ± 0.011	6.59 ± 0.02
NO_2 [ppb] (evening peak)	20.55 ± 0.017	2.49 ± 14.20	9.73 ± 0.016
HONO [ppb] (morning peak)	0.406 ± 0.009	0.224 ± 0.006	0.130 ± 0.011
HONO [ppb] (evening peak)	0.382 ± 0.009	0.011 ± 0.161	0.118 ± 0.008
HONO/NO_2 [%] (maximum)	2.9 ± 0.06	2.4 ± 0.06	1.7 ± 0.12
d(HONO/NO_2)/dt [% h^{-1}]	0.18 ± 0.02	0.16 ± 0.02	0.08 ± 0.04
NO [ppb] (morning peak)	17.7 ± 0.3	-	-
O_3 [ppb] (NO morning peak)	13.34 ± 0.12	-	-
VOC [µg/m^3] (NO morn. peak)	45.2 ± 0.1	-	-
Rn activity [Bq/m^3] (max.)	6.58 ± 0.12	-	-
wind speed [m/s] (max.)	4.6 ± 0.3	-	-

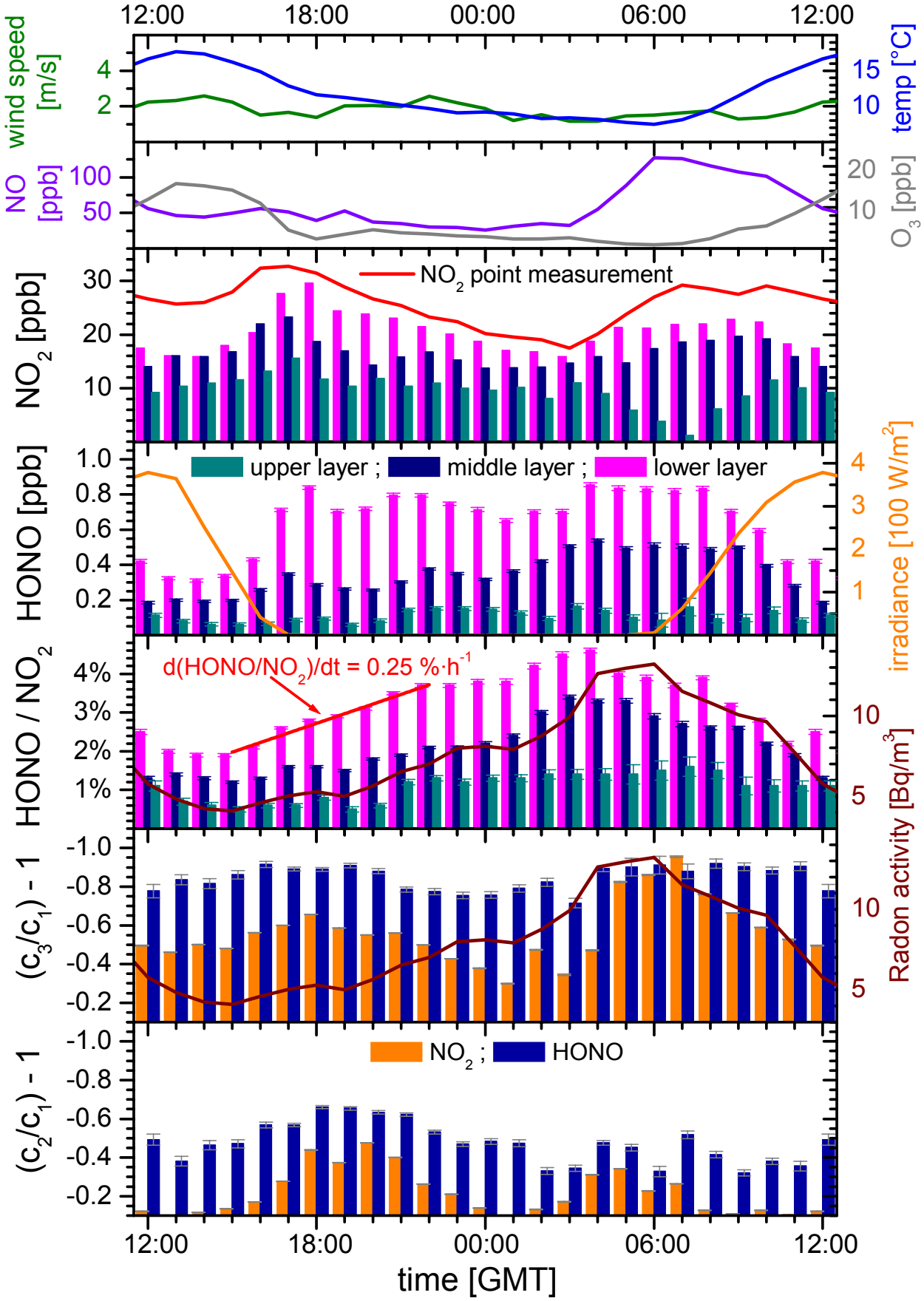

Figure 59: Hourly means of NO_2, HONO, the ratio HONO/NO_2 in the three layers and the gradients computed for the data measured during high-pressure periods in October 1999.

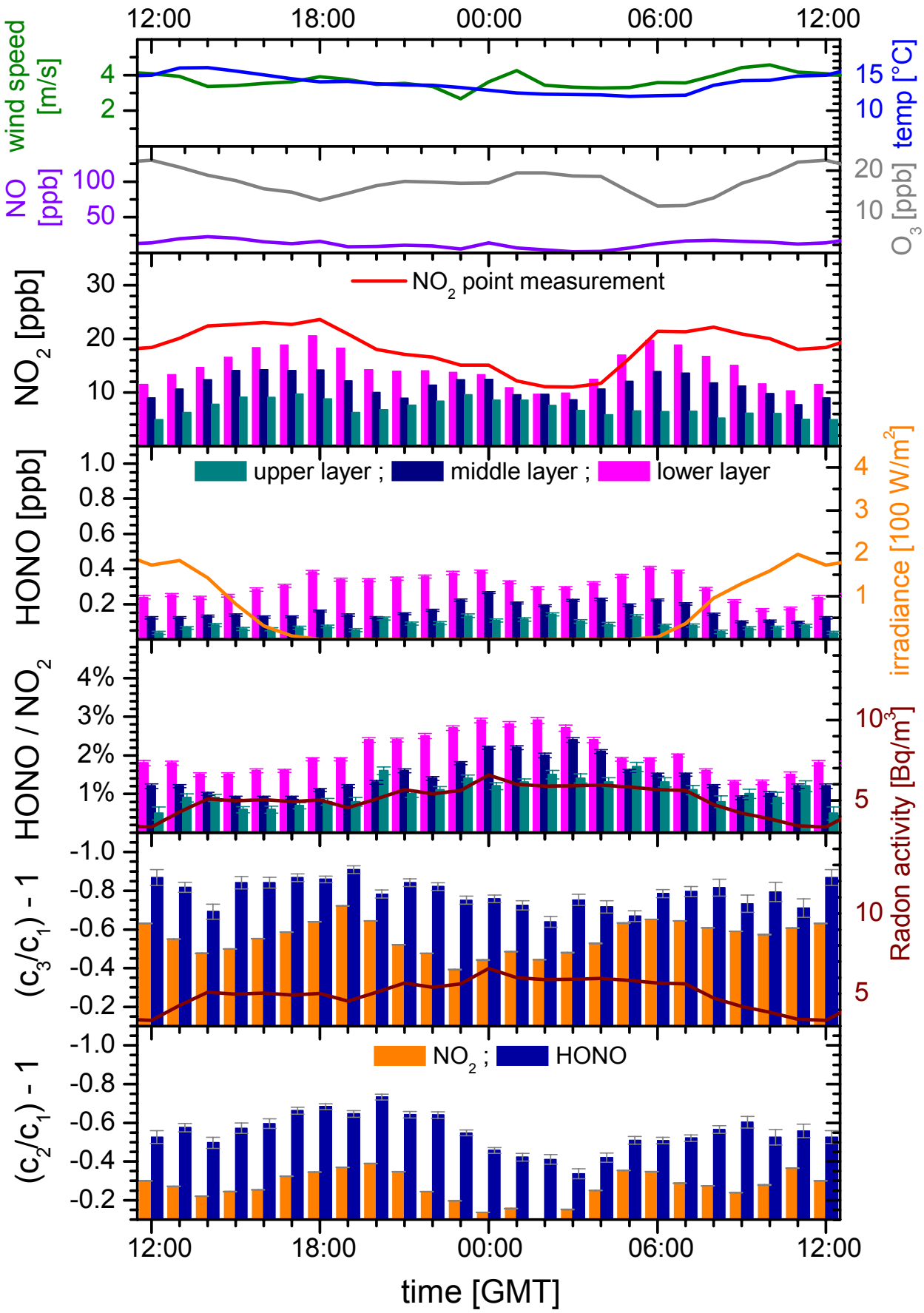

Figure 60: Hourly means of NO_2, HONO, the ratio HONO/NO_2 in the three layers and the gradients computed for the data measured during low-pressure periods in October 1999.

The comparison of the ratio $HONO/NO_2$ for stable and unstable conditions further verifies the existence of a ground-near HONO source.
In stable periods, the evening increase of the ratio is most effective in the in the lowermost layer with a time derivative of 0.25 % h^{-1}. In the middle and uppermost layer, the ratios are constantly smaller, and the increase is significantly slower as well: only 0.12 and 0.09 % h^{-1} are observed, respectively.
In unstable periods, the time derivative of $HONO/NO_2$ in the evening is observed at values of 0.18, 0.16 and 0.08 % h^{-1} in the lower, middle and upper layer, respectively. This effect is explained by more effective mixing. HONO formed at a constant rate (independently from atmospheric stability) near the ground is transported to higher altitudes much faster, causing a slower increase of $HONO/NO_2$ in the lower layer, but a faster increase in the middle layer. In the upper layer, the time derivatives of $HONO/NO_2$ for stable and unstable situations are equal within the error limits. The reason for this effect is not clear, as more effective mixing is expected to increase the $HONO/NO_2$ ratio in the upper layer, too. However, it might be correlated to the micrometeorological characteristics of the Neckar valley, which are not known by now.

For the stable PBL, a first order approximation for the HONO flux from the ground can be made: solving Equ. 66 yields:

$$\Phi_P + \Phi_S = \frac{\partial HONO}{\partial t} \cdot \frac{\Phi_{Rn}}{\frac{\partial Rn}{\partial t}} \qquad \text{Equ. 67.}$$

The mean evening increase of Radon for the stable period is computed from the data provided by [*Levin*, 1999-2001] as

$$\frac{\partial Rn}{\partial t} = 0.38 \pm 0.05 \text{ Bq} \cdot \text{m}^{-3} \cdot \text{h}^{-1} \ ,$$

while the Radon source strength can be approximated (see [*Levin et al.*, 2002]) as

$$\left[\Phi_{Rn}\right] = 55 \pm 5 \text{ Bq} \cdot \text{m}^{-2} \cdot \text{h}^{-1} .$$

The mean time derivative of HONO can be computed from the mean time derivative of the ratio $HONO/NO_2$ and the prevailing mean NO_2 concentration of 23.5 ppb in the evening hours. This yields

$$\Phi_P + \Phi_S = 5.92 \cdot 10^{13} \cdot \text{molec}_{\text{HONO}} \cdot \text{m}^{-2} \cdot \text{h}^{-1} \qquad \text{Equ. 68}$$

which compares well with data presented by [*Febo et al.*, 1999; *Geyer and Trick*, 2002] in the range of $(4 - 14) \cdot 10^{13}$ molec m^{-2} s^{-1}. It should be noted here that this HONO flux still includes direct emission of HONO by combustion processes.

As advection and vertical transport cannot be quantified for the unstable PBL, it is not possible to quantify the HONO production rate Φ_S under these conditions. Thus a comparison of the HONO production rates under stable and unstable conditions (which should be the same) is impossible.

6.4.2 Analysis of typical 24-hour periods

To sum up the evaluation of the long-term measurements at Heidelberg, three single 24-hour periods will be presented, each typical for distinct atmospheric conditions. The first example deals with a strongly stratified PBL featuring low wind speeds and a constant wind direction. The second 24-hour period discussed here exemplifies the change from a stable stratification in the first half of the night to an unstable PBL in the second half of the night, with wind speed continuously increasing. The third period illustrates a well-mixed PBL throughout the whole day, indicated by moderate wind speeds and low Radon activity.

Stable atmospheric conditions

Figure 61 presents the profile data recorded on 29/30 November 1999. The low wind speeds at a constant wind direction as well as the extremely high Radon activity clearly indicate that the stratification of PBL was extremely stable. The Radon activity plotted in Figure 117 and Figure 121 (see annex A) illustrates that the 24-hours discussed are embedded in a 3-day period featuring high stability.

This period illustrates and verifies two major findings of the statistical evaluation of the Heidelberg data ideally:

1. Increased atmospheric stability also increases the mixing ratios of all trace gasses in the lower PBL that are primarily formed or emitted near the ground.
   Consequently, the NO_2 and HONO concentrations measured in this period are comparably high. In the lowermost layer, NO_2 mixing ratios exceed 20 ppb throughout the day and reach a late evening maximum of 40 ppb, while HONO is found at mixing ratios of about 1 ppb for most of the night. Both concentrations are at the upper limit of the values typically found in Heidelberg. A comparison with the time series of NO_2, HONO and Radon activity for the whole measurement period (see annex A) shows clearly that similar concentrations of both trace gasses in the lower layer are always linked to high Radon activity indicating a momentary or episodic decrease of vertical mixing.
   An interesting feature of the period plotted in Figure 61 is that the NO_2 gradient changes its sign twice in the course of the night. In the late evening, the NO_2 variation with height shows the familiar pattern: highest concentrations in the lowermost layer, a small concentration decrease in the middle layer and significantly lower concentrations in the uppermost layer. After 22:00 GMT, the picture changes dramatically: now, the highest NO_2 concentrations are measured in the middle layer, while the concentrations in the lowermost and uppermost layer are rather similar (for a short period, the concentration in the lowermost layer drops even below the concentration in the uppermost layer).
   Horizontal transport processes that convey air masses loaded with a higher NO_2 mixing ratio into the middle layer are the most likely reason for this unusual effect. This assumption is justified no NO_x sources are expected in medium altitudes of the stable nocturnal boundary layer. Presumably, these polluted air masses had separated from the ground in daytime or in the evening at one of the industrial centres in the south and south-west of Heidelberg and were transported towards the cityin the course of the night.
2. HONO sources are located primarily near the ground. HONO formation on aerosols can be neglected as a HONO source, but not completely ruled out.
   The HONO time series in the three layers does not show an effect similar to the NO_2 time series discussed in the previous paragraph. On the contrary, the HONO concentrations always decrease with height, most obviously in the first half of the night. Additionally, the difference in the relative gradients of HONO and NO_2 is clearly visible in the lower two panels of Figure 61: the HONO gradient is always negative and constantly steeper than the NO_2 gradient throughout the full 24-hour interval.
   This behaviour /could be expected from the statistical evaluation and the predictions from

the general atmospheric equation for HONO (chapters 6.2.6 and 6.4.1). Obviously, HONO must be formed predominantly at surfaces near the ground. Otherwise, HONO concentration and the HONO/NO_2 ratio in the in the middle layer would be much higher at night, as NO_2 concentrations are at least as high as in the lowermost layer. Contrastingly, the ratio HONO/NO_2 is significantly smaller in the upper two layers than in the lower layer, where efficient surfaces for HONO formation are available (1 – 2 % compared to 2 – 4 %, respectively). For the increase in HONO concentration and the HONO/NO_2 ratio in the upper two layers in the course of the night three explanations are possible: first, weak vertical transport form the lower layer; second, horizontal transport of HONO by air masses that have separated? from the ground in the first part of the night (as for NO_2, see above); and, third, slow formation of HONO on aerosol surfaces available in the upper PBL. As neither detailed information on vertical and horizontal transport (including the small-scale effects in the Neckar valley) nor aerosol profiles with a time resolution comparable to the trace gas measurements are available, it is not possible to either quantify or to rule out the three different effects.
Interestingly, the sharp "drop" of the NO_2 concentration in the lower layer between 23:00 and 00:00 GMT is also visible in the HONO time series, but not in the ratio HONO/NO_2. This further justifies the thesis that this effect is caused by horizontal transport. Most probably, this transport phenomenon is restricted to the Neckar valley and could therefore not be detected by the meteorological instruments at the IUP, located some 500 meters off the valley (see Figure 15 in chapter 5.1).

Change from stable to unstable atmospheric conditions

The second 24-hour period of the Heidelberg data, recorded on the 23/24 October and plotted in Figure 62, exemplifies the change from a stable stratification to unstable conditions. Radon activity indicates that a strong ground inversion builds up in the evening of the 23 October, while the wind speeds for this periods are still below 3m/s.
In this period, the same pattern of the NO_2 and HONO time series as described in the last paragraph is observed: with increasing stability and decreasing solar irradiance, the NO_2 and HONO concentrations in the lower layer increase quickly, reaching maximum values of 30 ppb at 16:00 GMT and 1.0 ppb at 20:00 GMT, respectively. Interestingly, the maximum of the HONO concentration coincides with the Radon peak. As already discussed above, the HONO increase is only visible in the lower layer. The HONO concentrations in the upper two layers hardly change in this period, while the HONO/NO_2 ratio increases only slowly, presumably forced by the NO_2 decrease in these layers. The gradients also show the expected pattern, with steeper gradients for HONO than for NO_2.

In the second half of the night, however, the situation changes: Radon activity drops from 14 Bq/m^3 at 20:00 GMT to 4 Bq/m^3 at 08:00 GMT in the following morning, while the wind speed increases and shows – like the wind direction – distinct variations in the morning hours.

The resulting effect on the concentrations of both compounds is obvious. The NO_2 and HONO concentrations in the lower layer decrease constantly, and the usual morning peak of both compounds is hardly visible. The gradients of HONO and NO_2 are now almost equal and with decreasing Radon activity, the ratio HONO/NO_2 in the middle layer decreases fast to the same values found in the lower layers (the ratio in the upper layer features large errors because the NO_2 and HONO concentrations are almost zero).
The reason for these observations is easily found: efficient vertical mixing and horizontal transport dilute both compounds into the whole volume of the PBL. Thus, both compounds can not accumulate in the lower PBL as observed during the usual ground inversion in the morning.

Unstable atmospheric conditions

The effect of effective vertical and horizontal mixing of the PBL on the profiles of NO_2 and HONO can be studied ideally with the example of the 1^t/2 October 1999 plotted in Figure 63: the lowest wind speeds in this period were recorded at 3 m/s at night and exceeded 8 m/s by day, and the peak Radon activity reached only 4 Bq/m^3 in the morning hours.
Consequently, the maximum NO_2 concentrations at night were recorded at only 20 ppb, while HONO concentrations reached only 0.4 ppb. Both values are rather low when compared to the values observed under more stable atmospheric conditions (see above).
The HONO/NO_2 ratios in the three layers can hardly be distinguished, because the differences are in the range of the respective errors. The same observation is made for the relative gradients of HONO and NO_2 between the upper and lower layer. Only the relative gradients of NO_2 and HONO between the middle and lower layer show a significant deviation from each other: the HONO gradient is clearly steeper than the gradient of NO_2. A possible explanation for this finding has already been given in chapter 6.2.6: for very effective vertical mixing, NO has a lifetime that is sufficient to allow transport of significant amounts of NO to the middle layer, where it is oxidised by O_3 and forms NO_2. Thus NO_2 features a volume source in the middle PBL which is not available for HONO. This volume source generates a NO_2 relative gradient with a smaller absolute value than for HONO. In the upper layer, NO is not available any more, as the transfer times are larger than the typical life times. Thus the gradients of HONO and NO_2 are equal.

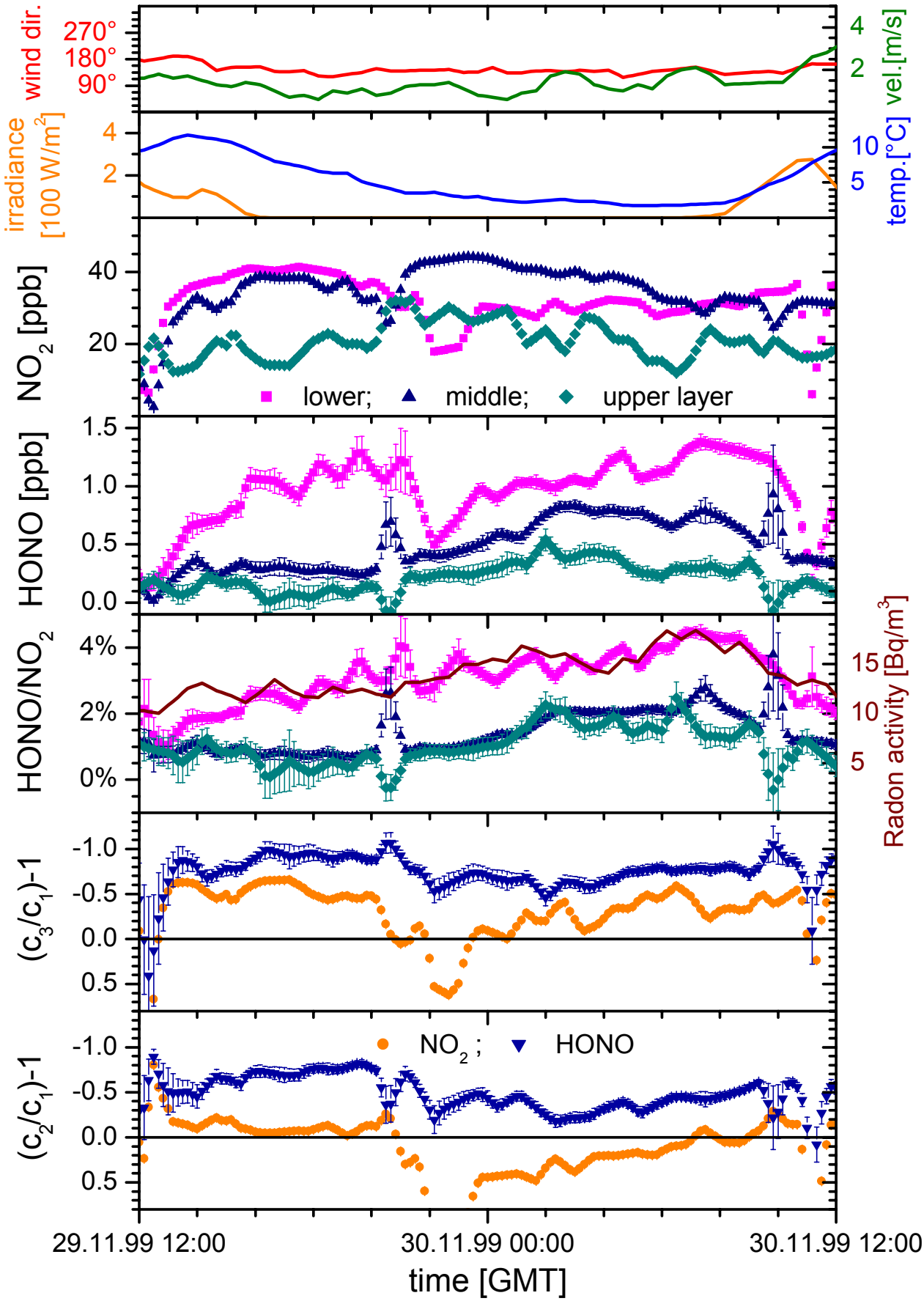

Figure 61: Profile data measured on 29/30 November 1999 in Heidelberg at the end of a high pressure period lasting 1 week.

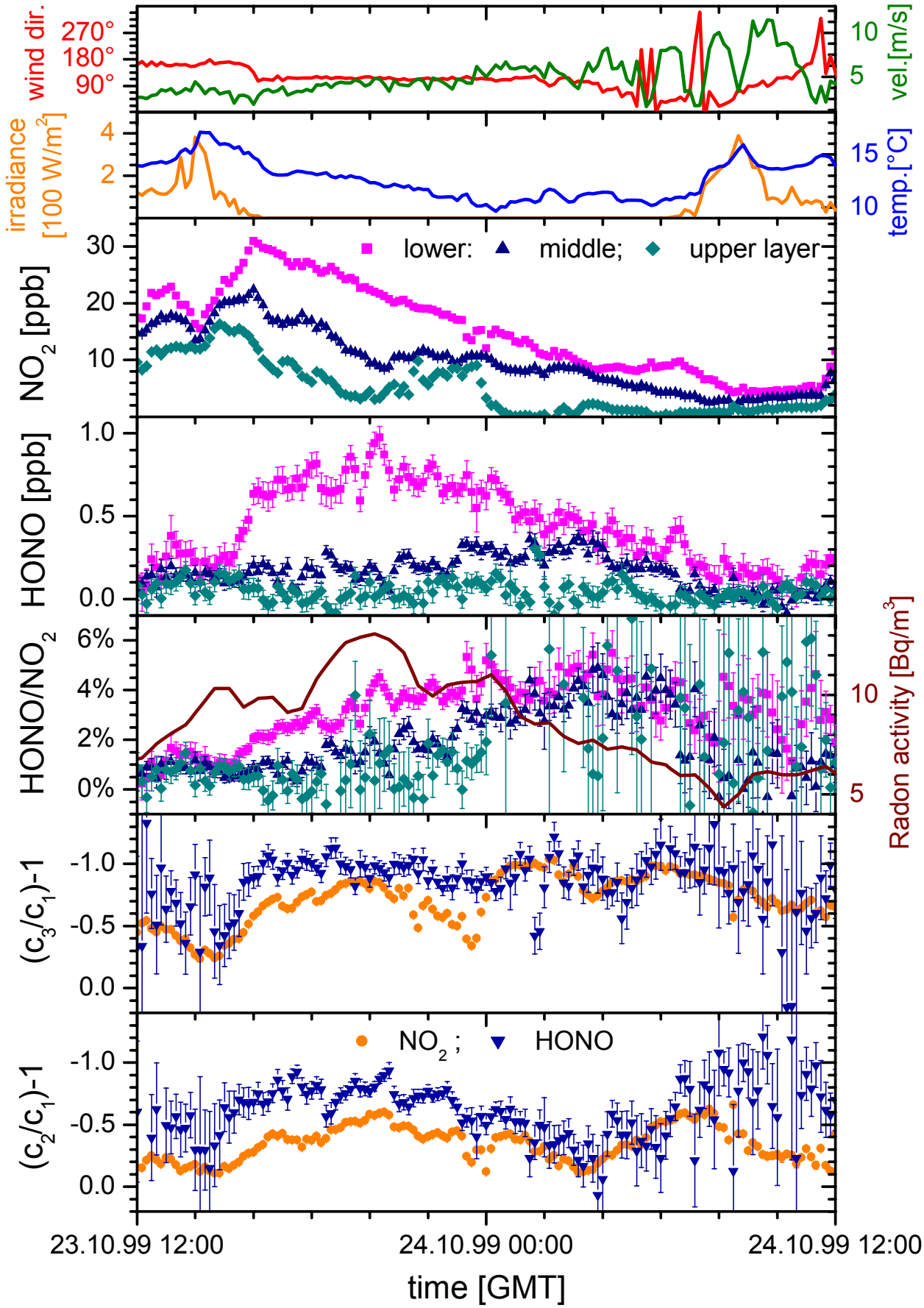

Figure 62: Profile data measured on 23/24 October 1999 in Heidelberg in the middle of a low pressure period lasting 1 week.

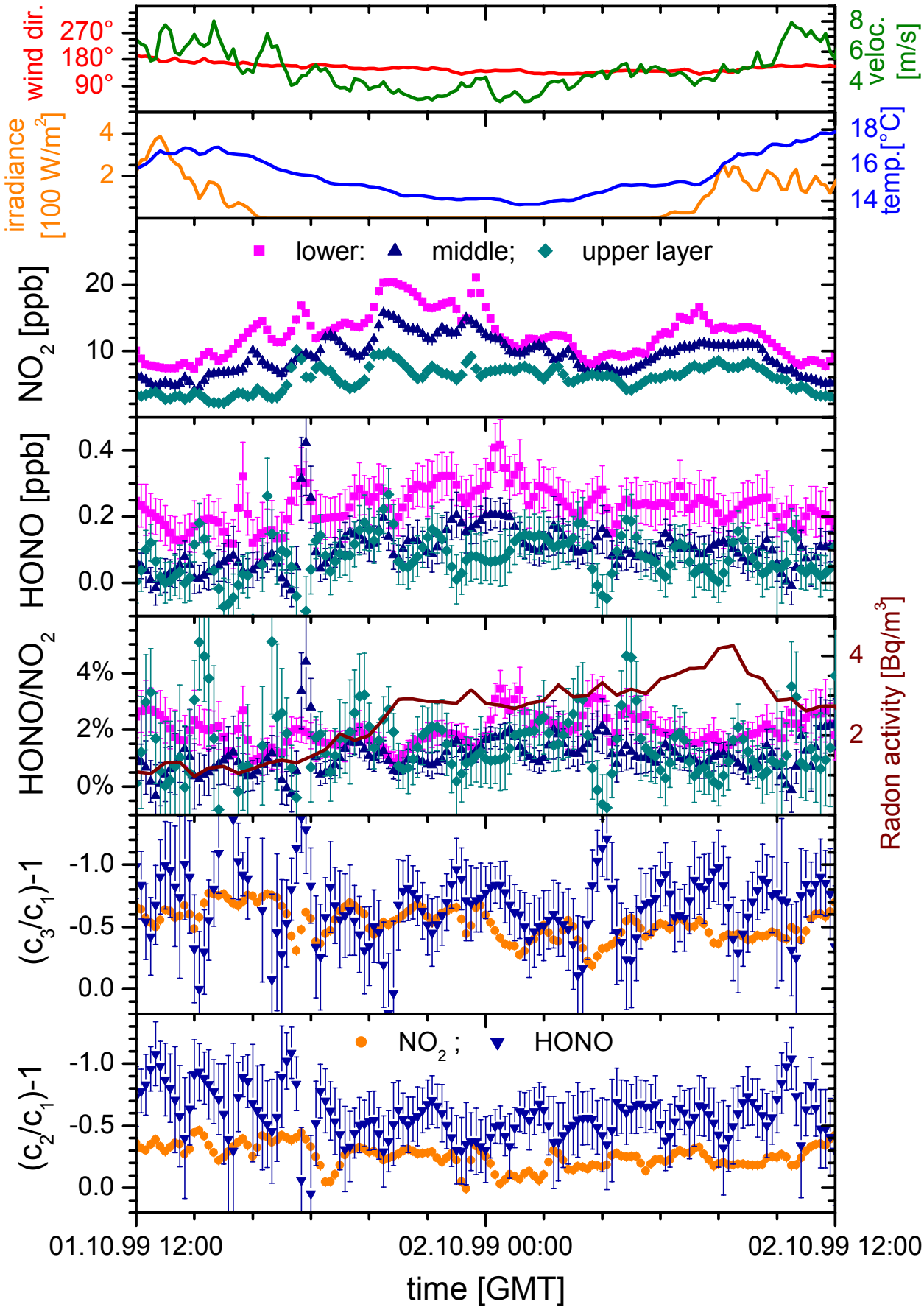

Figure 63: Profile data measured on 1/2 October 1999 in Heidelberg in the middle of a low pressure period lasting 1 week.

7 Daytime HONO chemistry

7.1 The photochemical steady state of HONO

An unexpected issue arose during the statistical evaluation of the Heidelberg profile data: the mixing ratio of HONO during daytime. It is obvious from the hourly means computed to obtain an "average day" for the statistical evaluation (see chapter 6.3.2), but also from the direct HONO measurement data (see Annex A) that daytime HONO is usually found below the detection limit, but almost constantly at values above zero. This finding is of particular interest in bright daylight, when HONO is subject to a photochemical steady state. The sources contributing to this steady state are the homogeneous and heterogeneous reactions:

$$NO + OH \longrightarrow HONO \qquad \text{R. 23}$$

$$2NO_2 + H_2O \xrightarrow{surface} HONO + HNO_3 \qquad \text{R. 27}$$

as well as direct HONO emission, quantified by [*Kurtenbach et al.*, 2001] as 0.8 % of the NO_x emissions. The major sinks are HONO photolysis and the reaction of HONO and OH:

$$HONO \xrightarrow{h\nu} NO + OH \qquad \text{R. 21}$$

$$HONO + OH \longrightarrow H_2O + NO_2 \qquad \text{R. 55.}$$

Thus, if HONO is present in bright daylight, it is strongly linked to OH chemistry. The first detailed study on the impact of HONO photolysis as a OH source was published by [*Alicke et al.*, 2001a; *Alicke et al.*, 2001b]. In both studies, HONO photolysis was accounted to be the source of up to one third of the total OH produced in the PBL in a 24-hour period. Of special importance is the fact that the bulk of OH formed from HONO is released into the atmosphere in the early morning hours, immediately after sunrise. At this time of day, other OH sources such as photolysis of O_3, VOCs, and HCHO are not effective. Consequently, the OH peak from HONO photolysis in the morning "ignites" diurnal photochemistry.
The studies of [*Alicke et al.*, 2001a; *Alicke et al.*, 2001b] could not detect daytime HONO in bright sunshine, but an upper limit for the daytime HONO mixing ratio of 120 ppt was computed from

$$[HONO] = \frac{[OH]\cdot[NO]\cdot k_{(R.23)} + P_{HONO,day}(NO_2)\cdot[NO_2] + E_{HONO}}{J_{HONO} + [OH]\cdot k_{(R.54)}} \qquad \text{R. 65}$$

for medium-polluted conditions in Milan/Italy, featuring 5.9 ppb of NO, 18.9 ppb of NO_2, a HONO photolysis rate of J_{HONO} = 0.00134 s^{-1} and an estimated OH concentration of $6\cdot10^6$ molec. cm^{-3} (E_{HONO} labels the direct emission of HONO).
Contrastingly???, the mean HONO concentrations in the afternoon measured at Heidelberg exceeded this value at substantially lower NO_2 concentrations of only 8-10 ppb. Extensive checks of the DOAS evaluation for a possible HONO offset or cross-sensitivities with other absorbers proved that less than 1 ppt of HONO found in the DOAS spectra can be attributed to these error sources (see chapter 5.3.2). Then, a more detailed evaluation of the daytime HONO concentrations was performed, which focused on representative HONO values for clear-sky, high-radiation situations.

7.2 Evaluation of HONO daytime concentrations at Heidelberg

The data of all nine 5-week periods were filtered for the data points measured between 10.00 and 14.00 GMT to obtain HONO daytime values for high solar radiation . A second filter excluded all HONO data recorded below a defined solar irradiance (from 200 W/m^2 in winter

to 500 W/m^2 in summer). For the remaining data contributions of night-time HONO, which is preserved until noon due to low solar radiation, can be excluded and the increase of HONO with decreasing solar radiation in the evening is not yet contributing. Thus, the filtered data are representative for the photochemical steady state concentration of HONO in the respective 5-week period.

To obtain statistically representative mean values, including the errors calculated from the 1 σ standard deviations, the same statistical analysis technique as for the calculation of the monthly means was applied (see chapter 6.2.1). As an example for the evaluation, Figure 64 shows the frequency analysis of the filtered HONO daytime concentrations for the April/May 1999 period and the statistical evaluation of this data. The evaluation results of the remaining periods are listed in Table 27, all figures illustrating the frequency analysis and the Gauss fits can also be found in Annex B.

The mean HONO daytime mixing ratios in the three layers for April/May 1999 range from 50 in the upper layer to 131 ppt in the lower layer (see Figure 64). It is obvious from the confidence intervals that the mean daytime values in the three layers differ not only significantly from zero, but also from each other. Table 27 compares the daytime mean concentrations and standard deviations of HONO for the three layers in all nine periods. The highest daytime HONO concentrations are found in winter, while the lowest values are found in August. Considering relation R. 21 for HONO photolysis, such an anti-correlation of solar irradiance and the HONO concentration is expected. The upper panel of Figure 65 visualises this relation: the mean daytime HONO concentration and the mean solar irradiation (both averaged between 10:00 and 14:00 GMT) are clearly anti-correlated in the seasonal cycle.

The extremely low values in the March/April 1999 period (which do not differ significantly from zero), however, do not fit in this scheme. Neither Radon activity (plotted in the lower panel of Figure 65), nor the mean wind speeds show a similar effect, thus atmospheric stability can be ruled out as a explanation. The standard deviations for daytime HONO concentrations, also plotted in the lower panel of Figure 65, also show no extraordinary values in March/April 1999, but are well in the range of the values calculated for the other periods. Sothis effect must be caused by an erroneous DOAS evaluation for HONO, most likely causing a negative offset for HONO in this period. However, the cross-sensitivity checks discussed in chapter 5.3.2 excluded a significant HONO offset caused by errors in the DOAS algorithm. This result should also be valid for March/April 1999, as the evaluation algorithm was not altered for the evaluation of the single periods (despite adaptations of the trace gas references to the hardly changing instrument parameters, see chapter 5.3.3). A comparison of the residuals (see Table 34) and mean lamp structures, however, shows that both fit parameters feature maximum values in this period. This indicates that problems with lamp correction within the DOAS evaluation (see chapter 5.3.2) are the most likely cause for the underestimation of HONO in the spectra recorded in March/April 1999.

Comparing HONO concentrations in the three layers, it is obvious from Figure 64 and Table 27 that a decrease of daytime HONO with height is observed in most periods of the long-term measurements. This finding is in agreement with the statistical and single-day evaluation of the data discussed in chapter 6. Consequently, the major daytime source of HONO is also located near the ground, as the daytime HONO gradients are always steeper than the NO_2 gradients (see chapters 6.2.5, 6.3 and 6.4).

In summary, it can be stated that in bright sunshine, the HONO concentrations in the lower layer constantly exceed 100 ppt throughout the year. Such high values were neither expected nor reported until recently, when DOAS measurements in Houston, U.S.A [*Stutz*, 2001], and Rome, Italy [*Geyer*, 2001], observed daytime HONO/NO_2 ratios which correspond with the measurements presented here. The next section will briefly deal with the effect of the HONO concentrations observed in Heidelberg on the oxidation capacity of the daytime PBL.

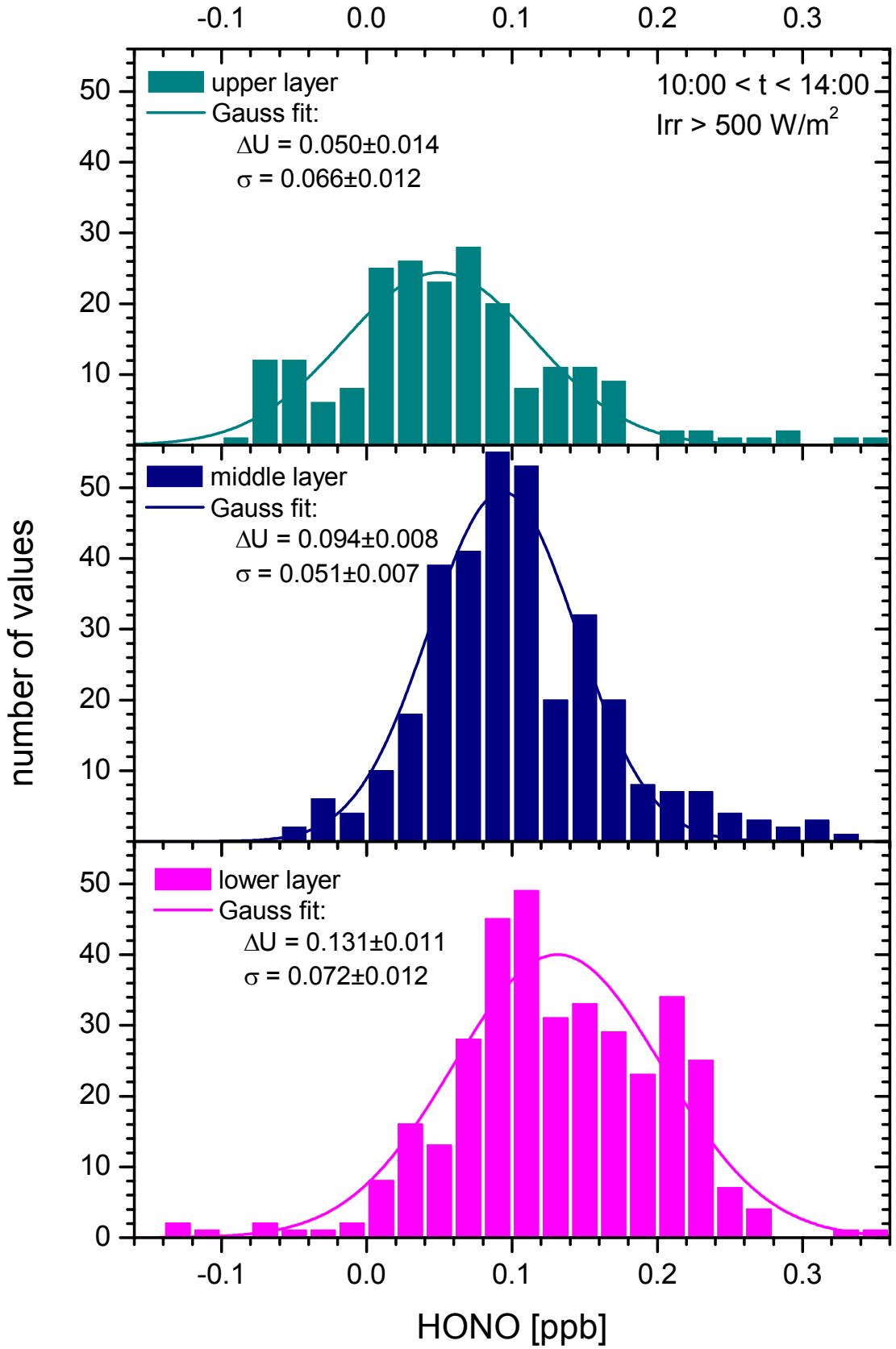

Figure 64: Statistics of HONO daytime values: shown here are all HONO values measured between 10:00 and 14:00 GMT at a solar radiance higher than 500 W/m^2 in the April/May 1999 period presented in Figure 35. A Gauss fit was used to compute the mean afternoon HONO concentrations. The mean NO_2 levels in the same time interval are about 8, 6 and 5 ppb in the lower, middle and upper layer, respectively,

Table 27: Mean HONO daytime values measured during the long-term vertical profiles campaign at Heidelberg (see also Annex B).

period	lower layer		middle layer		upper layer	
	mean [ppt]	sigma [ppt]	mean [ppt]	sigma [ppt]	mean [ppt]	sigma [ppt]
Jan/Feb 99	159 ± 17	76 ± 10	90 ± 12	51 ± 10	50 ± 12	46 ± 6
Mar/Apr 99	11 ± 13	59 ± 11	6 ± 12	49 ± 12	11 ± 20	60 ± 11
Apr/May 99	131 ± 11	72 ± 12	94 ± 8	51 ± 7	50 ± 14	66 ± 12
Aug 1999	96 ± 13	92 ± 13	19 ± 10	74 ± 6	-38 ± 14	65 ± 8
Sep 1999	187 ± 12	64 ± 12	97 ± 12	64 ± 6	46 ± 11	58 ± 7
Oct 1999	247 ± 18	74 ± 15	131 ± 12	55 ± 7	84 ± 10	42 ± 8
Nov 1999	227 ± 27	72 ± 17	119 ± 7	22 ± 6	47 ± 11	35 ± 11
Dec 1999	n/a	n/a	n/a	n/a	n/a	n/a
Feb 1999	169 ± 21	85 ± 26	99 ± 16	69 ± 13	105 ± 15	65 ± 14

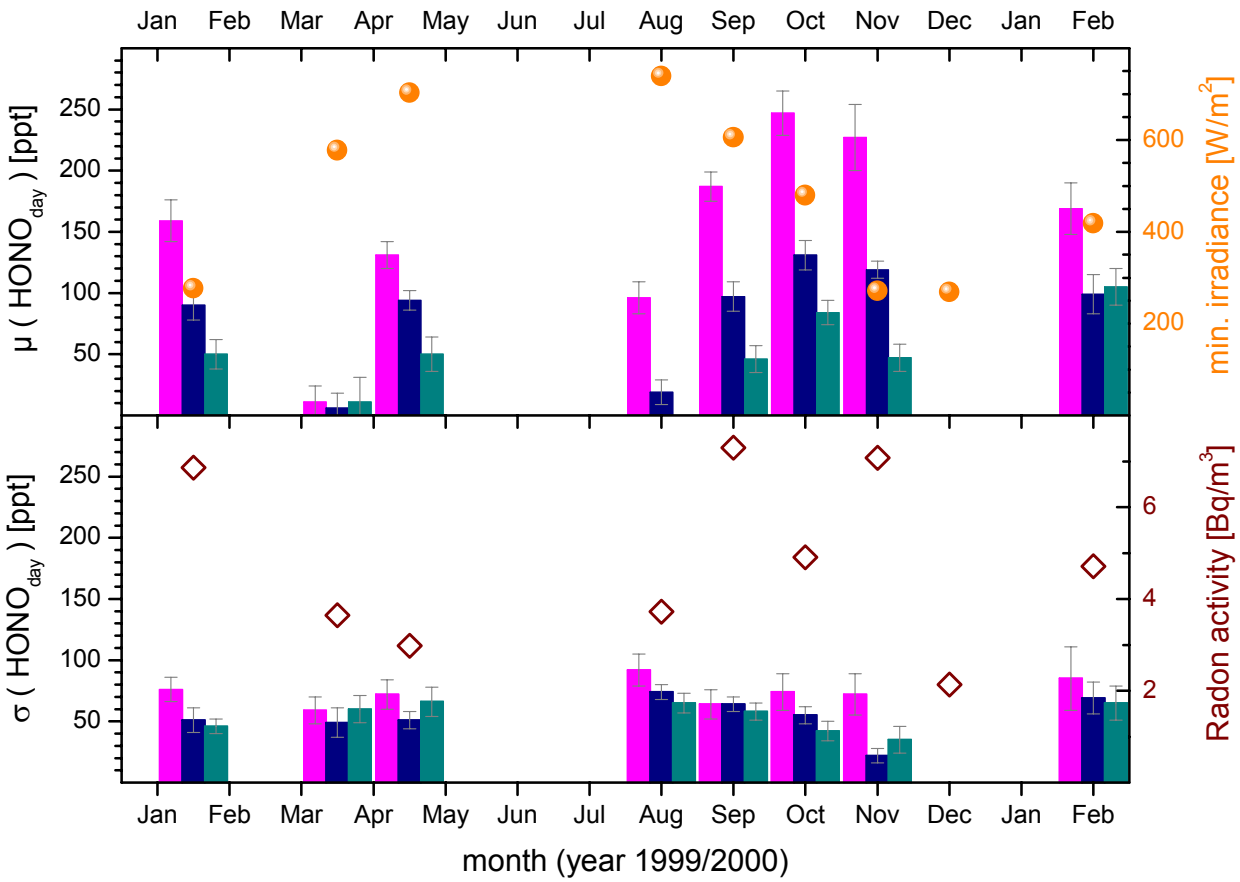

Figure 65: Daytime mean concentrations (upper panel) and standard deviations (lower panel) for HONO as measured in Heidelberg compared to the mean solar radiation and Radon activity in the respective periods.

7.3 Implications for OH chemistry

An interesting aspect of the daytime HONO mixing ratios is their contribution to the overall OH budget. Studies by [*Alicke et al.*, 2001a] yielded the result that up to 30 % of the total OH produced within a 24-hour period is formed by HONO photolysis. For the Heidelberg measurements, exact calculations are not possible, as detailed and consistent measurements of the ambient HCHO, O_3, VOC concentrations and the associated photolysis frequencies are not available.

7.3.1 Assessment of the net OH production by daytime HONO

For a first estimate of the OH production by HONO, however, a simple calculation can be done, following the approach by [*Alicke*, 2000]. In this case, the steady state concentration of HONO in daytime is only influenced by four processes: The major HONO sink is photolysis (R. 21), while the HONO sources are formation from NO and OH (R. 23), the heterogeneous reaction of NO_2 on wet surfaces (R. 27) and direct HONO emission. It is important in this context that HONO formed by R. 23 requires an OH radical. Consequently, reactions R. 23 and R. 21 form a zero-OH-cycle. Contrastingly, photolysis of HONO produced from the heterogeneous R. 27 and direct emission yields a net OH production as it is formed without participation of OH.

Therefore, the net OH production from HONO by day can be approximated from the relative HONO production rate in the evening computed in chapter 6.3.2:

$$\overline{F_{HONO/NO_2,night}} = 0.31 \pm 0.01\ \%_{\mathrm{HONO/NO_2}} \cdot \mathrm{h}^{-1} \qquad \text{R. 64}$$

as this production rate equals the net OH production in the photochemical steady state:

$$P_{OH}(HONO) = \overline{F_{HONO/NO_2,night}} \cdot \overline{[NO_2]} = (1.7 \pm 0.2) \cdot 10^5\ \mathrm{molec.cm^{-3}\ s^{-1}} \qquad \text{R. 66}$$

for a mean daytime NO_2 concentration of 8 ppb in April/May 1999. The total amount of OH produced by this source is computed from this production rate times the mean time of day, in which HONO photolysis is effective (here approximately 8 hours). This results in a total daytime OH production of $(4.9 \pm 0.6) \cdot 10^9$ molec cm^{-3}.

The OH production integrated over 24 hours can then be computed by adding the OH production from HONO formed at night and photolysed in the morning hours. For the April/May 1999 period in Heidelberg, the difference between the morning maximum and the daytime minimum of HONO is found at approximately (400 ± 50) ppt. This results in an additional OH yield of $(1.00 \pm 0.13) \cdot 10^{10}$ molec cm^{-3} from night-time HONO. Comparing this value to the OH production from steady-state HONO in daytime, it is obvious that the bulk of OH produced by HONO is released into the PBL in the morning hours, just after sunrise.

Thus the total net OH production integrated over a 24-hour period is approximately $(1.49 \pm 0.14) \cdot 10^{10}$ molec cm^{-3}. Data obtained during the BERLIOZ campaign can be used to compare this value to other OH sources in a medium-polluted boundary layer. For NO_2, HCHO and O_3 mixing ratios comparable to the conditions in Heidelberg, [*Alicke et al.*, 2001a] finds an OH production by O_3, HCHO, VOC+O_3 and NO_3 integrated over 24 hours as listed in Table 28. The comparison shows that HONO contributes only 7 % to the overall OH production with the photolysis of the night-time HONO yielding about 4.4 % of the overall 24-hour OH production.

Compared to the values obtained by [*Alicke*, 2000], the fraction of total OH produced from HONO computed here is significantly lower. The causes of this finding are a lower HONO production rate at night (used for the estimation of net OH production from HONO by day, see above) and significantly slighter differences between day- and night-time HONO: while

[*Alicke*, 2000] used a $\Delta HONO_{day/night}$ of about 1 ppb measured in distinct nights. Here the mean value computed from the monthly mean of the early morning HONO maximum was used.

As already mentioned above, this calculation can only be a first order estimate, as neither the photolysis frequency of HONO nor the concentrations and photolysis rates of other OH sources could be measured during the Heidelberg measurements. Recent measurements by [*Geyer and Trick*, 2002; *Trick and Geyer*, 2002] in Rome/Italy detected daytime HONO constantly above the detection limit at values between 100 and 200 ppt, even in bright sunshine.

The evaluation of these measurements (including photolysis rates and all other major OH sources) underline the finding that HONO is present at significant levels by day. However, first modelling results doubted the results of the simple model used by [*Alicke*, 2000] for the OH production from HONO: the simple model would yield an significant overestimation of the daytime OH levels. Further evaluation using a more sophisticated chemistry model is under way. Its results will be presented in a forthcoming PhD thesis by [*Trick and Geyer*, 2002].

Table 28: First order estimate of the OH production by different reactions integrated over 24 hours. The HONO values are computed using data of the Heidelberg measurements, while all other data have been provided by [*Alicke et al.*, 2001a].

species	OH production in 24 hours		total OH production
	[10^{10} molec cm^{-3}]	[ppb]	[%]
HONO	1.49 ± 0.14	0.596 ± 0.056	7
O_3	13.0 ± 1.4	5.2 ± 0.57	57
HCHO	4.63 ± 1.05	1.85 ± 0.42	20
VOC+O_3	2.93 ± 1.25	1.17 ± 0.5	13
NO_3	0.75 ± 0.38	0.3 ± 0.15	3

7.3.2 Comparison with a 3D Chemistry / Transport Model

The first order assessment of the OH-production from HONO in the daytime hours and the fraction of the total OH-production contributed by HONO can be compared to recent model results for the net OH-production from HONO published by [*Vogel et al.*, 2002].
These authors used the comprehensive numerical simulation model KAMM/DRAIS [*Vogel et al.*, 1995] including the aerosol model MADE [*Ackermann et al.*, 1998] to simulate the diurnal variations of the HONO profile in the lowermost 400 m of the atmosphere. The model also allows comparing the net OH production from the diurnal steady state described by R. 65 to the OH production from the reaction of excited oxygen-atoms $O(^1D)$ formed by ozone photolysis and water vapour.
Figure 66 shows the result of a simulation run for a typical summer day in the Rhine valley featuring NO, NO_2 and O_3 concentrations of below 0.5 ppb, 2.5 ppb and 100 ppb, respectively. Obviously, OH production from HONO reaches its maximum of 12.8 ppt min^{-1} (or $5.3 \cdot 10^6$ molec cm^{-3} s^{-1}) just after sunrise, while the daytime OH production from the steady state of HONO yields only 0.6 to 0.8 ppt min^{-1} (or 2.5 to $3.3 \cdot 10^5$ molec. cm^{-3} s^{-1}). The peak OH production rates from HONO in the morning as well as the OH production from the HONO steady state compare well with the findings by [*Alicke et al.*, 2001a]: these authors computed an early morning OH yield from HONO of $(5.3 \pm 1.1) \cdot 10^6$ molec cm^{-3} s^{-1} for comparable conditions during the BERLIOZ campaign near Berlin. Table 29 compares the afternoon production rates of OH from HONO derived by [*Alicke*, 2000] for measurements near Berlin and Milan, the simulation results obtained by [*Vogel et al.*, 2002] and the results from the Heidelberg measurements for this thesis. Obviously, all values fit together well .

It is also clearly visible from Figure 66 that in summer the bulk of the OH integrated over 24 hours is produced from O_3, while only a small fraction is formed fromby? HONO. If both curves computed by [*Vogel et al.*, 2002] are integrated over 24 hours, the net OH production from HONO yields approximately 40 % of the OH produced by Ozone photolysis and subsequent reaction with water vapour.

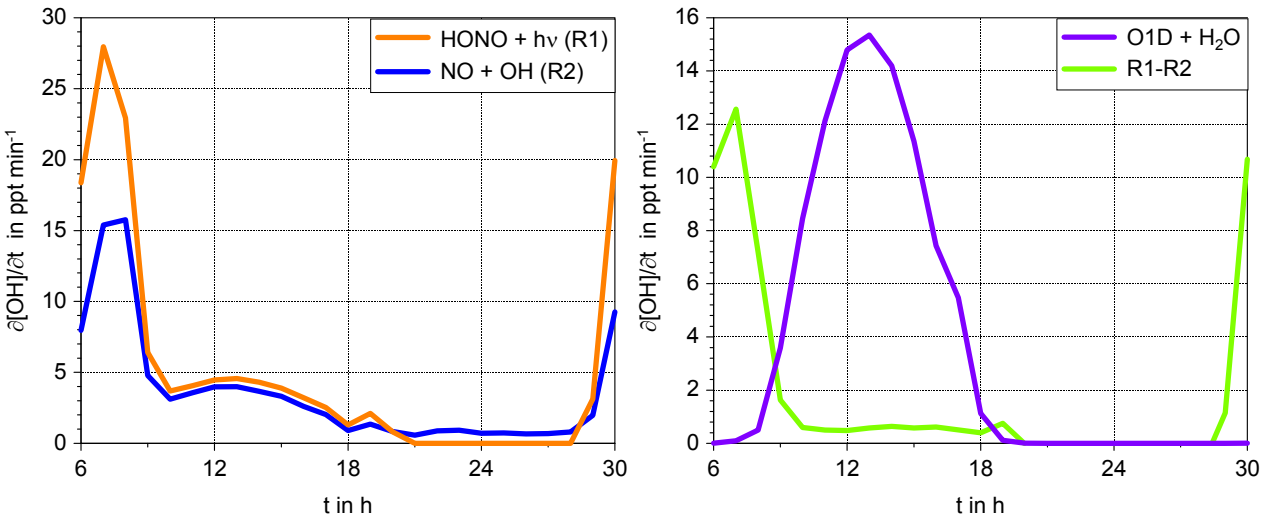

Figure 66: Left panel: Simulated daily cycles of HONO photolysis (R1) and homogeneous HONO production by OH and NO (R1);
Right panel: resulting net OH production from HONO by R1-R2 and from Ozone photolysis for a summer day [*Vogel et al.*, 2002].

In winter or in situations when OH formation from the photolysis of O_3 or HCHO is not as effective, the picture can change completely. The results of a second simulation run performed by [*Vogel et al.*, 2002] for a 24-hour period in October for typical trace gas concentrations in the Rhine valley of 15-20 ppb NO, 15-17 ppb NO_2 and 12 ppb O_3 in the afternoon are shown in Figure 67. In this case, the bulk of OH is formed by? HONO in the morning (by photolysis of approximately 0.6-0.7 ppb HONO at night), but OH production from the HONO steady state in the afternoon is still more effective than from O_3 photolysis. Integrated over 24 hours, up to 6 times more OH is formed by HONO than by O_3 in this case.

Measurements by [*Alicke*, 2000] in spring and summer verify the findings by [*Vogel et al.*, 2002]: in spring and summer, the OH production from HONO integrated over 24 hours yields only 31 % of the total OH formed from O_3, while for cloudy days in the same period, the OH yield from HONO is a factor 2.3 larger than from O_3.

For a detailed study and comparisons with model results of the Impact of HONO to the oxidation capacity of the polluted boundary layer, see the forthcoming publications by [*Geyer and Trick*, 2002; *Trick and Geyer*, 2002].

Table 29: Steady state HONO concentrations and resulting net OH production rates from HONO in the afternoon.

	HONO concentration [ppt]	OH production rate [10^5 molec. cm^{-3} s]
[*Alicke et al.*, 2001a], near Berlin, July	< 110	1 – 2
[*Alicke et al.*, 2001b], Milan, May	< 120	3 – 6
[*Vogel et al.*, 2002], simulated, summer	≈ 100	2.5 – 3.3
[*Vogel et al.*, 2002], simulated, October	≈ 200	1.6 – 2.1
this thesis, April/May	100 ± 13	1.7 ± 0.2
this thesis, October	250 ± 18	2.4 ± 0.2

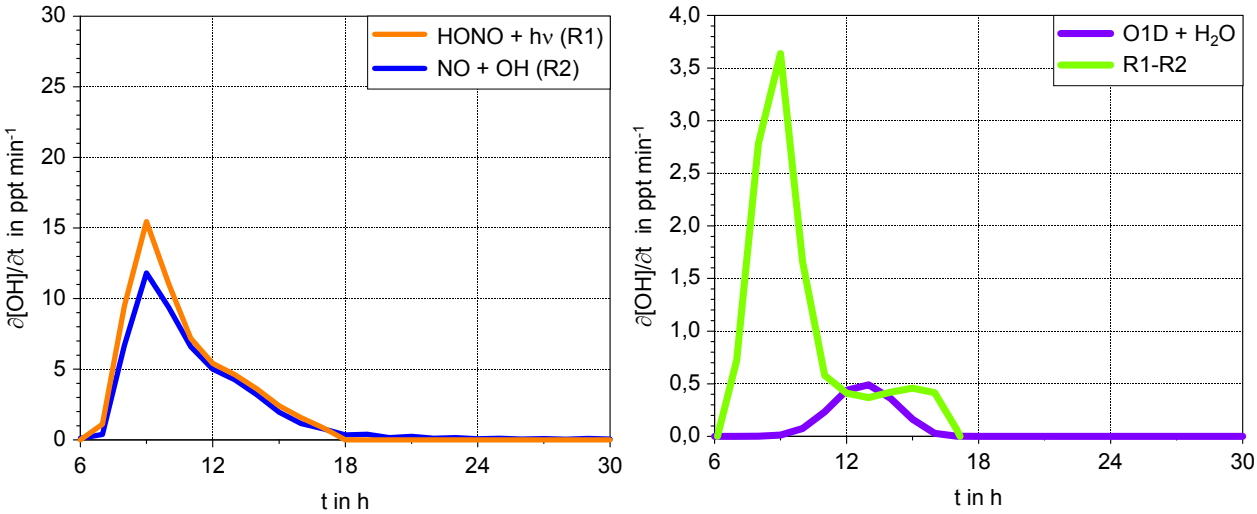

Figure 67: Same as Figure 66 but for a day in Mid-October [*Vogel et al.*, 2002].

8 Improved set-up for LP-DOAS with a tethered balloon

8.1 Motivation and technical challenges

The use of a tethered balloon as a platform for retro reflectors of a DOAS long path system is promising in various aspects. Measurements of vertical trace gas profiles with such a system are independent from the availability of masts, tall buildings or mountain sides for the reflector set-up. The vertical resolution does not depend on fixed heights chosen prior to the experiment, but can be adapted to atmospheric conditions in real-time (see Figure 68). To make use of these advantages, some technical challenges have to be mastered. Tethered balloons are influenced strongly by the wind in the boundary layer, which makes the retro reflectors move erratically in all three dimensions with velocities of some m/s and spin around the vertical axis with rates of up to 30 deg/s. The spinning of the balloon around the vertical axis and its wobbling movement do not directly depend on wind speed, but rather on turbulence generated by solar radiation and ground structures.

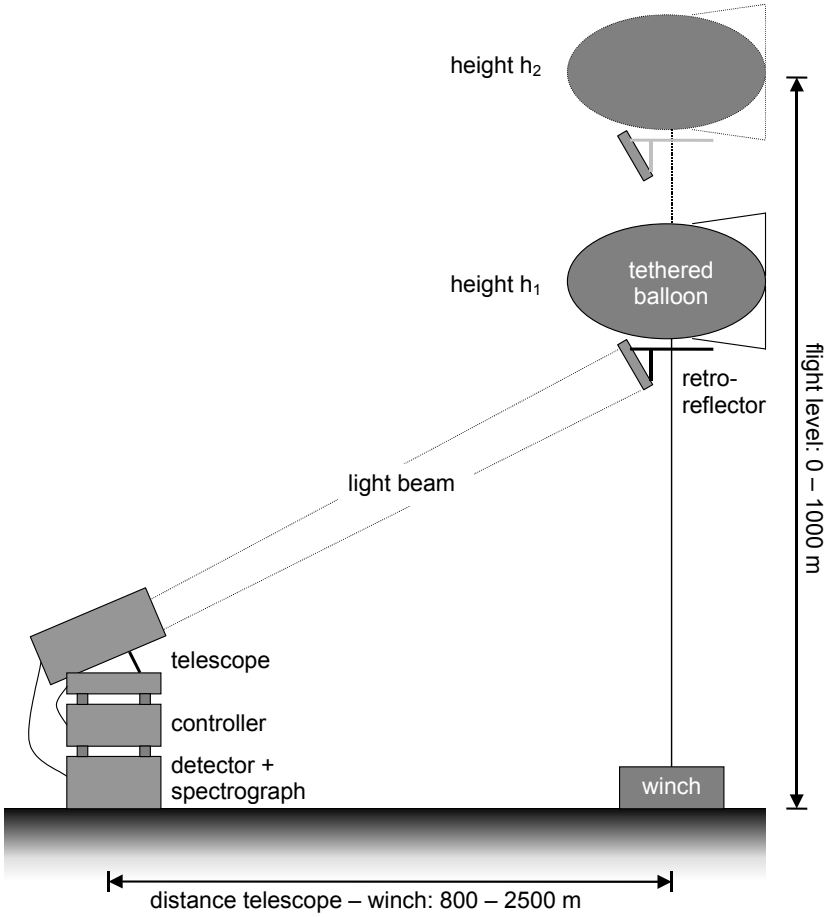

Figure 68: Set-up for DOAS measurements using a light path to a tethered balloon.

8.2 Characteristics and operation of the tethered balloon

The typical measurement set-up for a balloon-borne experiment consists of one or multiple in-situ monitoring instruments (e.g. ozone sondes, NO_x / SO_2 analysers, and / or meteorological sondes) attached below the balloon and then brought to altitudes ranging from just above ground level to 1000-1500 m (see e.g. [*Baumbach and Vogt*, 1995; *Eugster and Siegrist*, 2000; *Pötzsch*, 2001; *Pötzsch and Bächmann*, 2002] and references therein). Figure 69 and Figure 70 show balloons owned by the Institut für Meteorologie und Klimakunde (IMK) at the Forschungszentrum (FZ) Karlsruhe and the TU Darmstadt, respectively. Clearly visible in both pictures is the cigar-shape of the balloon,which helps – to stabilise the balloon together with the three fins at the tail: due to its shape, the balloon always faces in the direction of the mean wind. Both pictures show the balloons just prior to test flights performed at the Forschungszentrum Karlsruhe for LP-DOAS measurements in July 1999 and January 2001, respectively.

Specifications of tethered balloons used for atmospheric research

Different types of balloons are in use, depending on the so-called free lift[16] that is required to carry the measurement instrumentation to the desired altitude. Table 30 summarises the key data of balloons used for scientific research. The medium-sized balloon of the Technische Universität (TU) Darmstadt is ideally suited for the DOAS-application. Its free lift allows a payload of more than ten reflectors, while its size and handling characteristics allow balloon operations with a minimum of specialised personnel. Apart from the free lift of the balloon, there are also other important limitations for balloon operations:

- The balloon-rope-winch system is limited to wind speeds below 5 m/s and to dry weather conditions as both higher wind speeds and moisture can damage the balloon hull or the fasteners connecting the rope to the balloon.
  For mid-European weather conditions this strongly limits the use of such balloons, as wind speeds easily excel 5 m/s, especially at elevations of 50-100 m above ground level. To monitor the wind speeds and directions at elevations of 10, 25, 50, 75, 100, 150 and 200 m, the meteorological mast at the FZ Karlsruhe was used during the test flights preformed there. For wind speeds exceeding 4 m/s at 100 m, the balloon proved to be extremely unstable, especially in the lowermost 250 m. Thus, LP-DOAS measurements to reflectors fixed to the balloon required the absence of fronts, rain, low cloud cover and fog.
- German flight regulations impose further limitations to balloon operations: a range of sight above 8 km is required, and balloon flights are limited to 08:00 to 17:00 local time, but not before / after sunrise or sunset, respectively.
- The locations for balloon experiments are limited, as the balloon is not allowed to fly over railroad tracks, major roads and close to civil and military airports.

Consequently, balloon operations were only possible under stable high pressure conditions (see chapter 6.4.1). In the densely populated south-west of Germany, balloon flights are only allowed at selected places and limited to the daytime hours. But such experiments still provide the opportunity to measure daytime trace gas profiles in the undisturbed PBL.

Table 30: Specifications of different tethered balloons in use for atmospheric research. All balloons feature a signal-coloured PE hull and are cigar-shaped for better stability in the wind field of the PBL.

type	volume [m^3]	length [m]	diameter [m]	free lift [kg]	Notes (see below)
TS-1BR-1	3.25	4.9	1.1	1.6	1,2
TS-1BR-4	7.5	6.6	1.6	5	1,3
n/a	56	n/a	n/a	15	4

1 supplied by Atmospheric Instrument Research, Inc., Boulder, U.S.A
2 in use by the group of Dr. U. Corsmeier, Institut für Meteorologie und Klimaforschung, FZ Karlsruhe, Germany
3 used by the group of Prof. Bächmann, Institut für Anorganische Chemie, TU Darmstadt, Germany, now by the IUP Heidelberg
4 in use by the group of Prof. Baumbach, Institut für Verfahrenstechnik und Dampfkesselwesen, Universität Stuttgart, Germany

[16] The free lift characterises the maximum load the balloon can carry to its maximum ceiling, apart from the weight of the rope, which is also lifted by the balloon.

Figure 69: Balloon of the IMK, FZ Karlsruhe prior to its (final) flight. A small gondola for 3 retro reflectors is mounted below the balloon.

Figure 70: Balloon of the TU Darmstadt used for the measurements discussed in chapter 9. Visible below the balloon is the new gondola for 9 reflectors.

Movement of the balloon in the wind field of the PBL

The Ekman spiral forces changes in the mean wind speed and direction changes within the PBL (see chapter 3). Depending on the roughness of the ground , the changing mean wind direction implies a rotation of the cigar-shaped balloon within an angle range of 15° to 50° [*Roedel*, 1994] in the height interval between ground level and the balloon ceiling. Additionally, the mean wind speed forces horizontal drift of the balloon up to several 100 meters away from the location of the winch.

The mean wind speed is also of major importance for the stability of the balloon flight: Below 1 m/s, the balloon erratically turns around the vertical axis, as the air stream is not sufficient to stabilise the orientation of the balloon. So even light breezes can change the balloon orientation by an angle of several 10° , resulting in full 360° turns within timescales below several minutes. Mean wind speeds in the range of 1 to 4 m/s proved to be ideal for balloon-LP-DOAS measurements. Under such conditions, the balloon orientation is generally limited to an angle range of ± 50° with respect to the mean wind direction, while the drift of the balloon stays below 200 m from the winch location. Above 4 m/s, test flights rendered the experience that the drift movement was nearly in the same order as the balloon ceiling, which strongly influences the light path length. Additionally, wind shear – especially within the lowermost 50 m – causes strong flutter of the balloon, which inhibits the constant tracking of

the reflectors by the sending beam. At wind speeds exceeding 5 m/s, the operational limits of the balloon inhibit flights.
Turbulences can force the balloon into erratic flutter movements (in the order of 1-5 balloon lengths) in all 3 spatial directions and into rotation around its vertical axis. , wind shear turbulence is of major importance within the lowermost 50 to 100 m above ground, where the gradient of friction velocity is at its maximum (see also chapter 3). Convective turbulence generated by heat flux from the ground, limit the balloon stability in the height interval from 50-100 m up to the ceiling flight level of the balloon (especially during periods of high solar irradiation).
Buoyant lift generated by the vertical wind interacting with the body of the balloon generally has a positive effect on balloon stability. As buoyant lift and static buoyancy generated by the helium filling of the balloon add up, the balloon is less vulnerable to turbulence. However, if a wind blast hits the balloon and generates a huge amount of uplift and simultaneously induces a sudden horizontal drift, the collapse load of critical parts (e.g. the rope and its fasteners to the balloon) can be exceeded. This can lead to the total loss of the balloon and its payload. During the first experiment with the complete balloon-DOAS in July 1999, such an incident caused the balloon to fly away, when it was caught by a sudden wind blast at an altitude of about 5 metres above ground.

8.3 Reflector mounting for the balloon

8.3.1 Operating requirements for the reflector fixed to the balloon

The rotation of the balloon around its vertical axis cannot be compensated by a tracking mechanism on the ground. Thus, the gondola carrying the retro reflectors must feature a suitable device to guarantee that light sent to the reflectors by the DOAS telescope is returned despite changes in the orientation of the balloon. Basically, there are two possible ways of compensationg balloon rotation.
The first would be an active device that aligns the optical axis of the retro reflectors with the axis of the sending beam. Such devices are available, but usually require a power supply and weigh more than 5 kg (mainly to provide the required inertia). Therefore, an active correction device is not suitable for balloon operations, at least for the class of balloons used for the experiments presented here (see above).
The second option is to arrange a number of retro reflectors at different angles in a suitable mounting connected to the balloon. If the angle between the optical axis of each reflector (see below) is smaller than the effective reflection angle of a single reflector, an almost constant backscattered light intensity can be achieved: at last one reflector of the array is constantly effective for the light reflection. This option is more suitable for tethered balloon experiments, since a single reflector only has a typical weight of 360 g including the setting and 110 g for the quartz prism . Thus, a balloon featuring a free lift of 5000 g would be able to carry up to 13 reflectors with and up to 45 reflectors without the metal setting (using e.g. a common lightweight composite setting).

8.3.2 Optical parameters of the retro reflectors

General principle

The main feature of retro reflectors is that an incident parallel light beam (e.g. a laser) is reflected exactly to the same direction. This can be achieved by orienting three reflective planes perpendicularly to each other. There are two common types of reflectors using this principle by different means: triple-mirror reflectors forming a corner cube and triple-prism reflectors made of (quartz) glass. Figure 71 shows the optical path of incident and reflected

beam as well as the orientation change of the image compared to the original. The triple prism reflector shown in the graph is of the same type as the reflectors generally used for LP-DOAS. The dimensions of a reflector are h = 60 mm and H = 40 mm, using the labels given in Figure 71. It is obvious from this figure that the beam is reflected once by each of the three back planes, using total reflectance on the surfaces of the prism. The optical axis of such an reflector arrangement is defined as perpendicular to the entrance surface and passing the point of intersection of the three back surfaces. The accuracy of the alignment of the incident and reflected light beams depends on the quality of the retro reflector, especially on the angle accuracy between the perpendicular back planes. The mean divergence between incoming and reflected beam is less than two arc seconds for the reflectors in use at the IUP. The reflectors are made from quartz glass to improve the transmission in the near UV, but are not coated at the back planes for better reflectiveness.

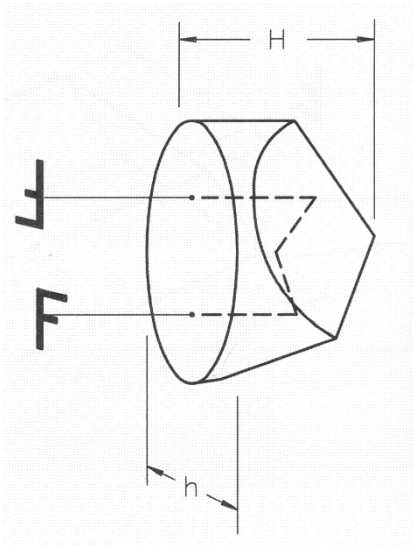

Figure 71: Optical path of the incident and reflected beam for a triple prism reflector. [*LINOS*, 2000]

It is important for the understanding of the principle of retro reflectors that the reflected beam is sent back in the same direction as the incident beam, but not on the same way (see also Figure 71). Therefore, the light transmitted by a pinpoint source to the reflector opening is sent back as a concentric circle with a diameter of two times the diameter of the reflector entrance opening h. The diameter of the image neither depends on the distance between light source and reflector nor on the number of reflectors mounted in the same plane [*Lösch*, 2001]. For the LP-DOAS application, this implies that the sending beam is not reflected back to exactly the same area on the main mirror of the telescope, but into an area that is extended by a minimal diameter of 2 h, but further increased by atmospheric turbulence, stray processes and diffraction [*Rudolf*, 1993]. Only the combination of these effects enables the receiving telescope to “see” the image of the lamp generated by the sending telescope and the reflectors.

Effective reflection angle

The fact that retro reflectors send the incident light back to the same direction makes the adjustment of the LP-DOAS system much easier, as the optical axis of the reflector (generally an array consisting of 7 to more than 100 single reflectors) only has to point in the general direction of the DOAS telescope. However, the effectiveness of the reflection still depends on the angle between the incident beam and the optical axis of the reflectors by two different effects: first, the entrance area “seen” by the sending telescope decreases with the cosine of the angle between incident beam and reflector axis. Second, total reflection on the back planes of the reflector is only achieved within an angle range defined by the refractive index of the reflector material and the surrounding air.

The dependency of the backscattered intensity from the angle between the optical axis of the incident beam and the reflector axis was investigated by [*Rityn*, 1967; *Schmieder*, 1967]. Figure 72 depicts the result of the measurements by [*Rityn*, 1967]: the fraction of the backscattered intensity decreases quickly from unity to 50 % at an angle of about 22° between the optical axes of the incident beam and the reflector. At angles exceeding 40°, the fraction of backscattered intensity is zero. Measurements presented by [*Lösch*, 2001], using a reflector array consisting of 59 retro reflectors, verify these results.

[*Rityn*, 1967] also studied the dependency of the reflected light intensity on the turning angle

of the reflector: Figure 73 shows that for uncoated triple prism reflectors, a much smaller fraction of the incident light is reflected, compared to a triple prism featuring a reflective coating. Therefore, coated prism reflectors would be ideal for balloon-LP-DOAS measurements, but were not available for the measurements presented here.

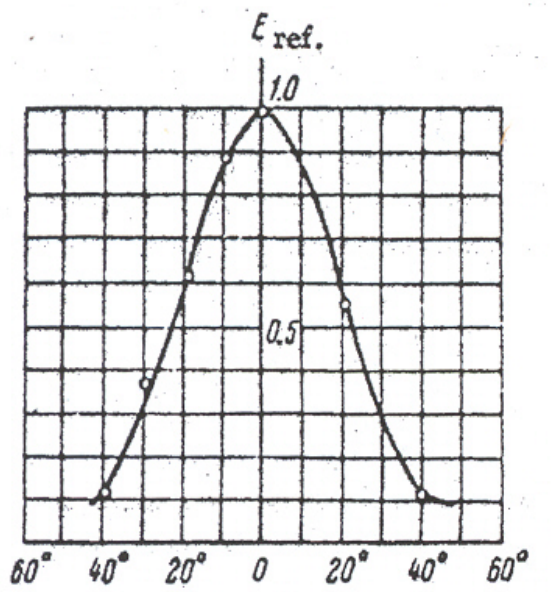

Figure 72: Relative intensity of the backscattered light in dependency from the angle between the optical axis of the incident beam and the reflector [*Rityn*, 1967].

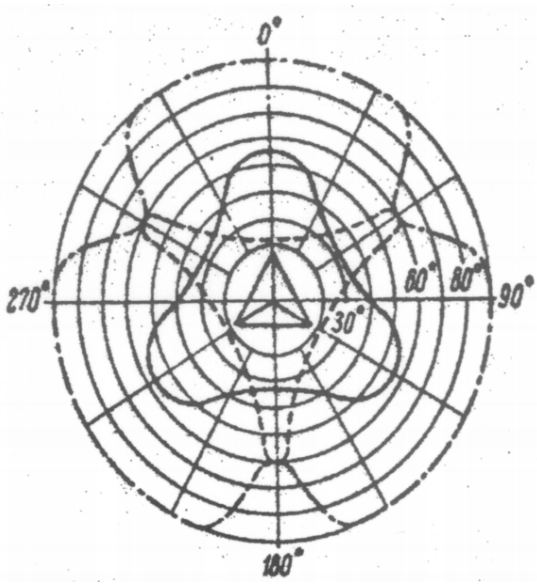

Figure 73: Dependency of the acceptance angle from the turning angle of the reflector [*Rityn*, 1967] (solid line: triple prism; dashed: triple prism with reflective coating; dash/dotted: triple mirror).

8.3.3 Design of the reflector gondola

A reflector mounting for the balloon was designed that fulfills he operation requirements for the reflector gondola established in chapter 8.3.1 and the retro reflector characteristics described in chapter 8.3.2, . The mounting consists of a trihedron (Figure 74) connected to the reflector gondola by a turning foot (Figure 75). The trihedron is fixed by wires about 1 m below the balloon, oriented along the roll axis. The turning foot allows to adjust the reflector gondola in the rough direction of the LP-DOAS telescope prior to the flight (360° around the vertical and about ±20° around the horizontal axis).

The gondola consists of two aluminium mounting plates, one above the other, the upper allowing the installation of 4 reflectors, the lower of 5 reflectors. The optical axes of the individual reflectors within each layer are angled at steps of 25° and the layers are oriented with an angle of 12.5° against each other. This results in an angle of 12.5° between the optical axes of the individual reflectors. Therefore, a backscattered signal which is constantly above 80 % of the maximum reflected intensity[17] can be achieved on an angle range of 125°.

To compensate the impact energy of at an uncontrolled landing (e.g. due to a leak or rupture in the balloon hull), two layers of polystyrene plates with a total thickness of 80 mm were fitted below the lower reflector layer (not shown in Figure 75).

The total weight of the gondola including 9 reflectors is about 4 kg, leaving about 1 kg of free lift as a buoyancy reserve that increases the flight stability of the balloon.

[17] Defined as 100% at an angle of 0° between the optical axis of a single reflector and the incident beam.

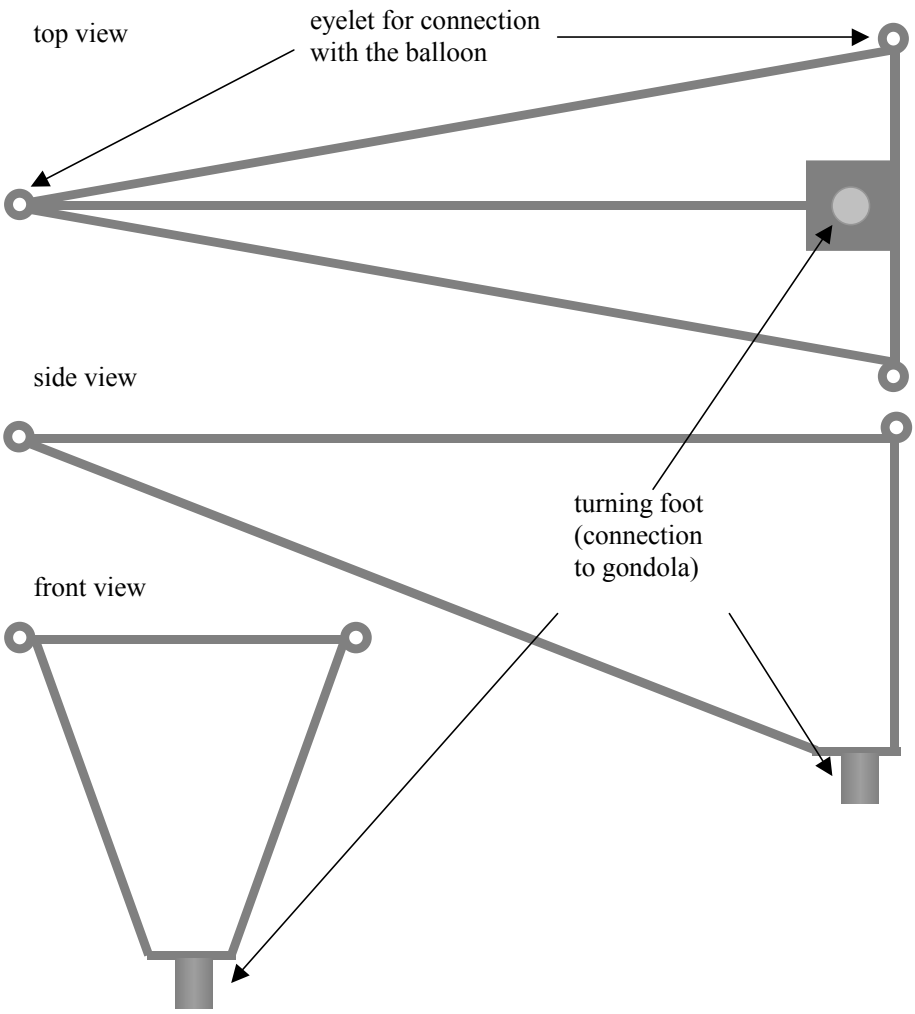

Figure 74: Sketch of the balloon trihedron carrying the reflector gondola.

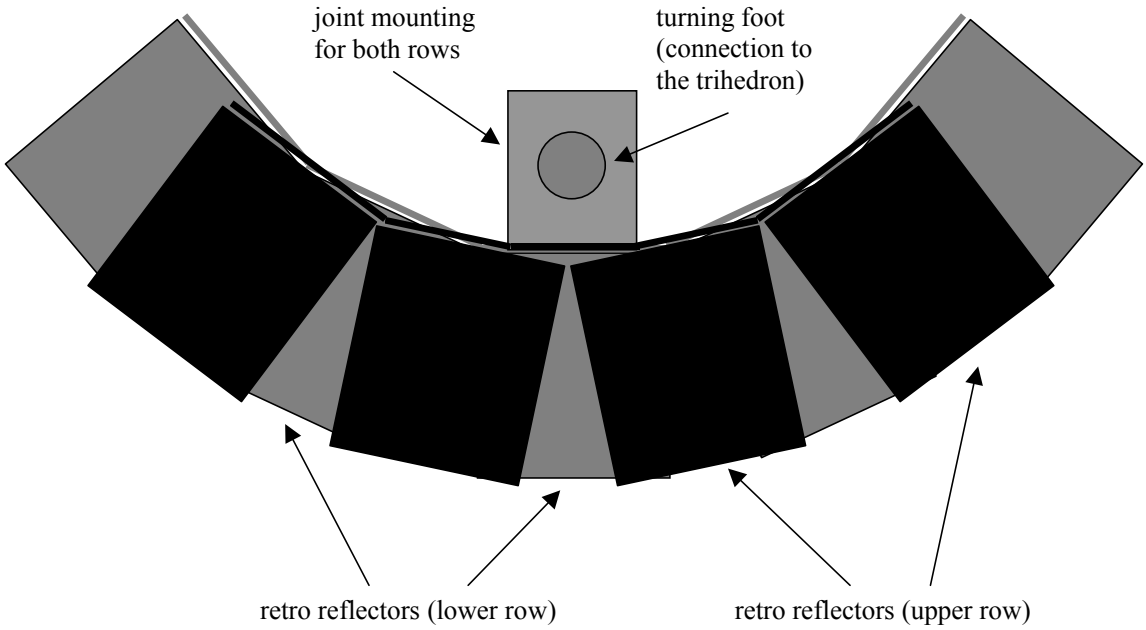

Figure 75: Sketch (top view) of the balloon gondola carrying 9 retro reflectors.

8.4 Modifications on the LP-DOAS telescope

The mechanics of a/the DOAS telescope must meet two main requirements for measurements to retro reflectors mounted on a tethered balloon:

- The actuation and kinematics of the telescope in both horizontal and vertical axis have to permit turn rates that are fast enough follow the movements of the balloon in the turbulent 3D wind field of the PBL.
- The kinematics of the telescope has to be be precise enough to keep the reflector in the field of view (FoV) of the receiving telescope collecting the light backscattered from the reflector despite the erratic flutter movements of the balloon discussed above. (Due to beam divergence – which is discussed in detail in 8.5.3 – the sending beam usually features a larger diameter at the reflectors than the FoV of the receiving telescope.)

As the telescope was specially designed to allow LP-DOAS measurements on multiple light paths (see chapter 5) from the very beginning, these requirements could easily be met: multi-path LP-DOAS measurements also require a high degree of angular precision of the telescope mechanics in both the horizontal and the vertical axis. Fast turn rates of the telescope are important for such measurements, too, as they guarantee a short time resolution by saving time during the change of light paths.

Specifications of the mechanics of the DOAS telescope

The telescope is actuated by stepper motors, which allow turn rates of the telescope of 6 mrad/s in both horizontal and vertical axis to match the requirements mentioned above. The precision of the horizontal movement exceeds 0.05 mrad. With the vertical motor, an adjustment precision of 0.03 mrad is achieved. For a typical distance of 1000 m between the telescope and the balloon winch, this makes it possible to follow a balloon moving at a maximum speed of 6 m/s, and a theoretical tracking precision of 50 mm in the horizontal and 30 mm in the vertical axis. As the operating conditions for the balloon require wind speeds below 5 m/s, the turn rates of the telescope are sufficient for LP-DOAS measurements to reflectors mounted on a tethered balloon.

Joystick control software

The control software for LP-DOAS uses relative or absolute (measured against a fixed “home position”) step numbers of the stepper motors actuating the telescope movements to direct the telescope into a pre-set position. The command sequence is typed in by keypad (for the DOS-based MFC [*Gomer et al.*, 1996]) and/or by menu and button commands (Windows-based DOASIS [*Kraus*, 2001]). For standard LP-DOAS measurements, for which light paths to a single or to multiple retro reflectors mounted at fixed positions are used, this practice is well suited, especially when it is automated via a command script (see chapter 5.2.4).
For balloon measurements, however, the position of the retro reflector is constantly changing and the movement pattern that is hardly predictable. Thus, a user-friendly control interface is required to allow a manual tracking of the reflectors mounted on the balloon by the DOAS telescope. Thus, the DOASIS control software was supplemented by a module allowing the steering of the DOAS telescope with a joystick. A calibration routine within the joystick module allows to adjust the precision and sensitivity of the joystick inputs and the stepper motor frequency and step width to the conditions required by the balloon movements.

Laser range finder

To measure balloon height and light path length, which are needed to obtain the mean trace gas concentrations on the light path, a laser range finder (LRF) was employed (LASRETAPE FG21-HA produced by Riegl GmbH, Austria). This LRF provides a maximum range of

10 km and is equipped with an inclination sensor, which makes it possible to compute the reflector height from distance and elevation angle (for full specifications see Table 31).
The laser range finder was attached to the LP-telescope by an adjustable mounting, allowing to line up the field of view of the LRF with the optical axis of the sending beam. A software package was developed that integrated all functions of the LRF to the DOASIS software. The results of the LRF measurements, i.e. distance to the reflector, height of the detector and horizontal distance to the reflector, are directly written to the spectrum data file. Thus, all information obtained from the LRF is available for later evaluation of the spectra.

Table 31: Specifications of the Riegl LASERTAPE FG21-HA [*Riegl*, 1998].

range finder	distance sensor mode	range finder mode
maximum range (retro reflector target)	5000 m	10 000 m
minimum distance to target	2 m	20 m
precision	±0.05 m	±0.5 m
range resolution	0.05 m	0.2 m
evaluation time	self-adapting (depending on signal intensity)	
inclination sensor		
angle range	+60° to –30°	
resolution	0.1°	

8.5 Modifications on the quartz fibre

First field experiments showed that it was possible to track the reflectors on the balloon continuously with the transmitted beam (diameter about 1.5 m in a distance of 1000 m) despite the flutter of the balloon. So a nearly constant backscattered signal was achieved. For the balloon-LP-DOAS application, however, the field of view and the diameter of the quartz fibre at the focus of the receiving telescope are also of major importance. If the standard quartz fibre with a diameter of 200 µm is connected to the receiving telescope, the resulting field of view has a diameter of 0.33 m at a distance of 1000 meters (see chapter 8.5.3). This is about a factor of 4.5 smaller than the transmitted beam. As the diameter of a single retro reflector measures 60 mm and the motors have a precision exceeding 50 mm at a similar distance, it was assumed prior to the first experiments that the continuous tracking of a densely packed cluster of 3-7 retro reflectors should be possible.
But first measurements, showed that the image of the reflectors in the plane of the fibre entrance was moving erratically with deviations from the centre position on a scale of three diameters of the standard quartz fibre. This was caused by small-scale flutter movements of the balloon due to turbulences. The frequent loss of signal caused by this effect resulted in a strongly changing light intensity at the end of the quartz fibre. Traditionally, the integration time for DOAS measurements is determined by a short “snap-shot” measurement of the received light intensity before the actual trace gas measurement (for which the mean light intensity is then assumed as a constant). Thus, a strongly and unpredictably changing intensity of the received light causes either a bad signal-to-noise ratio or numerous saturated channels within the measured spectra.
In order to increase the aperture and to compensate the variations of the received light intensity, a complex quartz fibre assembly was adopted, including an intensity meter controlling the integration time of the detector.

Optical parameters and test bed for the characterisation of quartz fibres

The major optical parameters of a quartz fibre are the light transmission efficiency and its numerical aperture (or acceptance angle), labelled transmission and NA in the following. The NA is usually defined by the maximum acceptance angle Θ (measured from the optical axis of the fibre) as:

$$NA = \sin\Theta \qquad \text{Equ. 69.}$$

To enable the quantitative characterisation of the optical properties of quartz fibres as well as the effect of the mode mixer on the light transmission of quartz fibres, a quartz fibre test bed was developed and installed within this project (see Figure 76). The test bed allowed to focus a light beam generated by a HeNe-laser or a halogen lamp to a quartz fibre. The NA of the incident beam as well as the angle α between the axes of the incident beam and the fibre can be varied to measure the optical characteristics (i.e. NA, transmission efficiency and beam profile) of the light transmitted by the fibre.

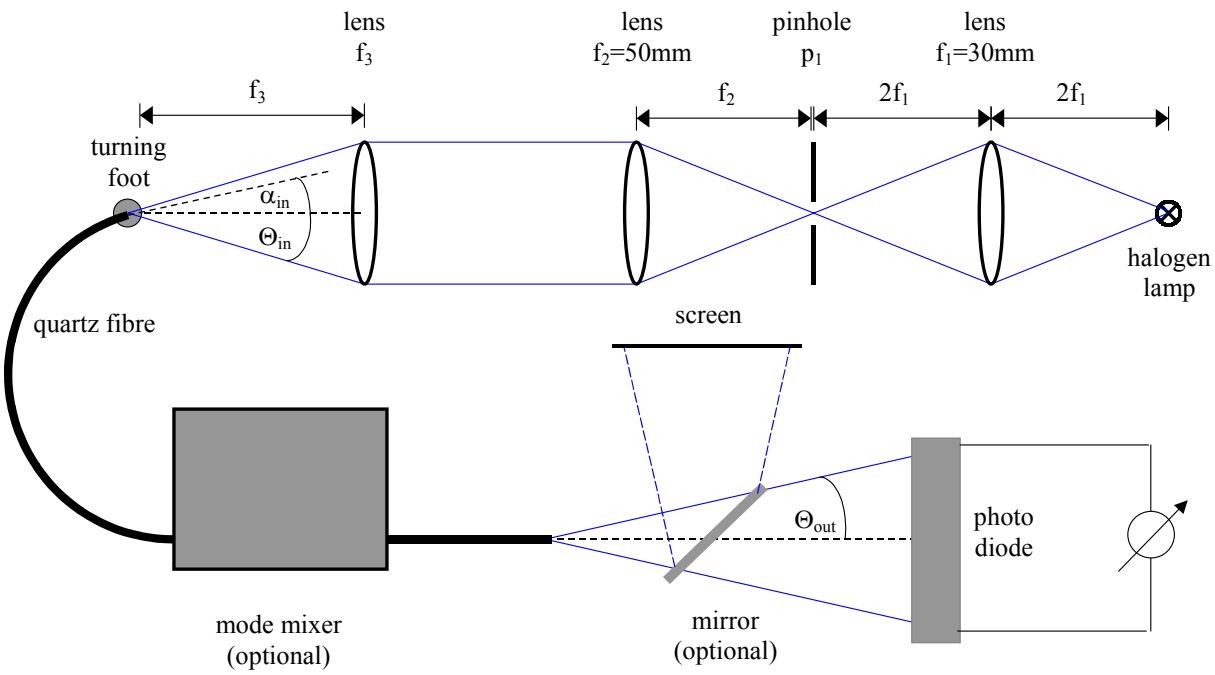

Figure 76: Schematic set-up of the quartz fibre test bed using a halogen lamp as the light source. The NA of the incident beam at the fibre entrance can be changed by varying the focal length of the lens f_3. Additionally, the quartz fibre entrance is mounted on a turning foot, which allows to change the angle α between the optical axis of the fibre and the optical axis of the incident beam. The photo diode is used to measure the transmitted light intensity. Alternatively, the transmitted light can be projected to a screen (using the optional mirror) to characterise the beam profile (NA and intensity distribution) of the transmitted light.
The set up using a HeNe-laser as the light source is similar, but features adaptations for the characteristics of the laser, i.e. another lens directly in front of the laser to widen the beam profile, a different focal length of the lens f_1 and a set of grey filters to protect the photo diode.

8.5.1 Standard quartz fibre

200 µm quartz fibres are used as the standard fibre type for LP-DOAS applications at the IUP for two reasons: their diameter allows a direct connection to the spectrograph (omitting the entrance slit) yielding an optimal spectral resolution for the DOAS evaluation. The numerical aperture of these fibres is optimised to the NA of the spectrograph (NA = 0.12) to minimise stray light and loss of light intensity. To obtain comparable values for the optical properties of the new fibre assembly, the standard 200 µm fibre will be characterised first (although the standard fibre proved to be unsuitable for the balloon-LP-DOAS measurements).

Set-up

The standard IUP fibre set-up consists of a quartz fibre AS UV..VIS 200/220/245 µm, with the three numbers denoting the outer diameters of the core, cladding and protective coating, respectively. Apart from the protective film on the fibre, an additional shielding of the fibre is provided by a PTFE tube, which covers most of the total fibre length of 3 m, leaving out only 0.5 m for the installation of the quartz fibre mode mixer (see [*Stutz and Platt*, 1997]). At one end of the fibre, a SMA-F plug is attached for the connection with the telescope, while at the other end a connector to the 3D-adjustable quartz fibre mount of the spectrograph is fixed. A schematic sketch of the fibre set-up can be found in Figure 77.

Figure 77: Schematic set-up of the standard quartz fibre used at the IUP .

Optical parameters

The transmission of the fibre type used for the standard fibres at a wavelength of 350 nm is given as 0.06 to 0.08 dB/m or I / I_0 = 98.6 %/m to 98.2 %/m by the manufacturer, depending on the individual fibre. The NA of the fibre is specified to NA = 0.12, requiring non-standard fibres (the standard being NA = 0.22).

The first series of measurements was performed to characterise the transmission of the quartz fibre in dependency on the numerical aperture of the incoming light using a pinhole $p_1$with a diameter of 200 µm. To obtain the I_0 values of the light transmitted into the fibre, a pinhole of 200 µm diameter was used instead of the fibre and the photodiode was located at a distance of 20 mm behind this pinhole. The focal length of the lens f_3 was changed to adjust the NA of the incident beam to the desired value.

The result of the basic transmission measurements is shown in the upper panel of Figure 78: without the mode mixer, the transmission reaches its maximum of about 95 % at NA = 0.07, while with the mode mixer a maximum of about 82 % is achieved at the same NA. The transmission without mode mixer compares well to the theoretical value of 95.3% for the 3 m fibre. However, the maximum transmission is not found for incident light featuring the NA specified for the fibre, but at a significantly smaller NA. Usually, only light radiating to the fibre at a NA exceeding the NA of the fibre cannot be transmitted to the fibre exit. Repeated measurements, verified this unusual finding. The lower panel of the same figure illustrates how the NA of the transmitted light depends on the NA of the incident beam: for the fibre without a mode mixer, the transmitted NA never drops below NA = 0.10, increasing slowly to a maximum of about NA = 0.112 at an incident NA of 0.233. For the same fibre with the mode mixer, the shape of the curve looks quite similar, but is shifted to a minimum transmitted NA of roughly 0.145 for an incident NA below 0.10 and a maximum transmitted NA of 0.155.

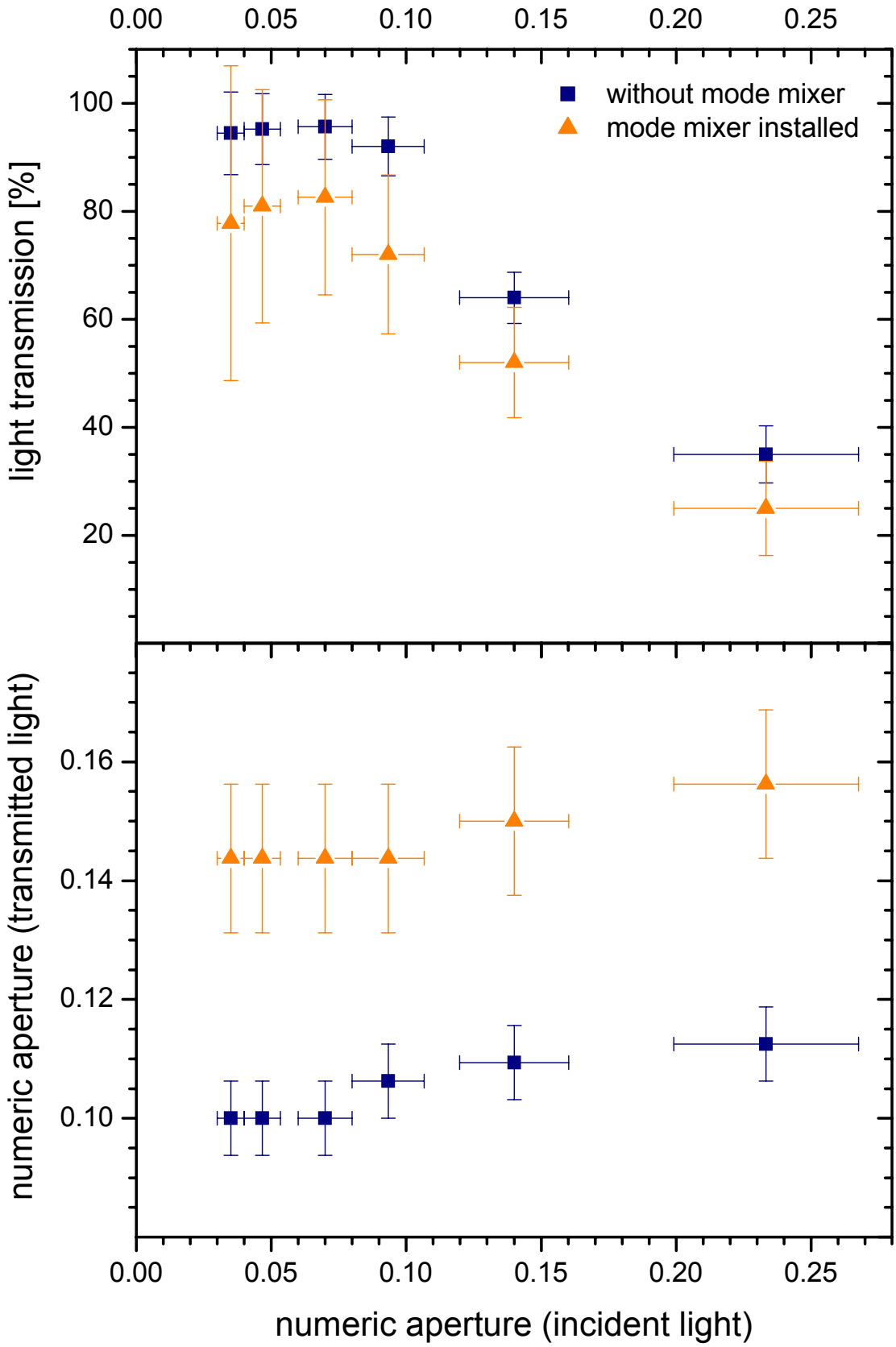

Figure 78: Effect of the mode mixer and different numerical apertures of the incident beam on the NA of the transmitted light and the transmission efficiency of the 200 µm standard fibre.

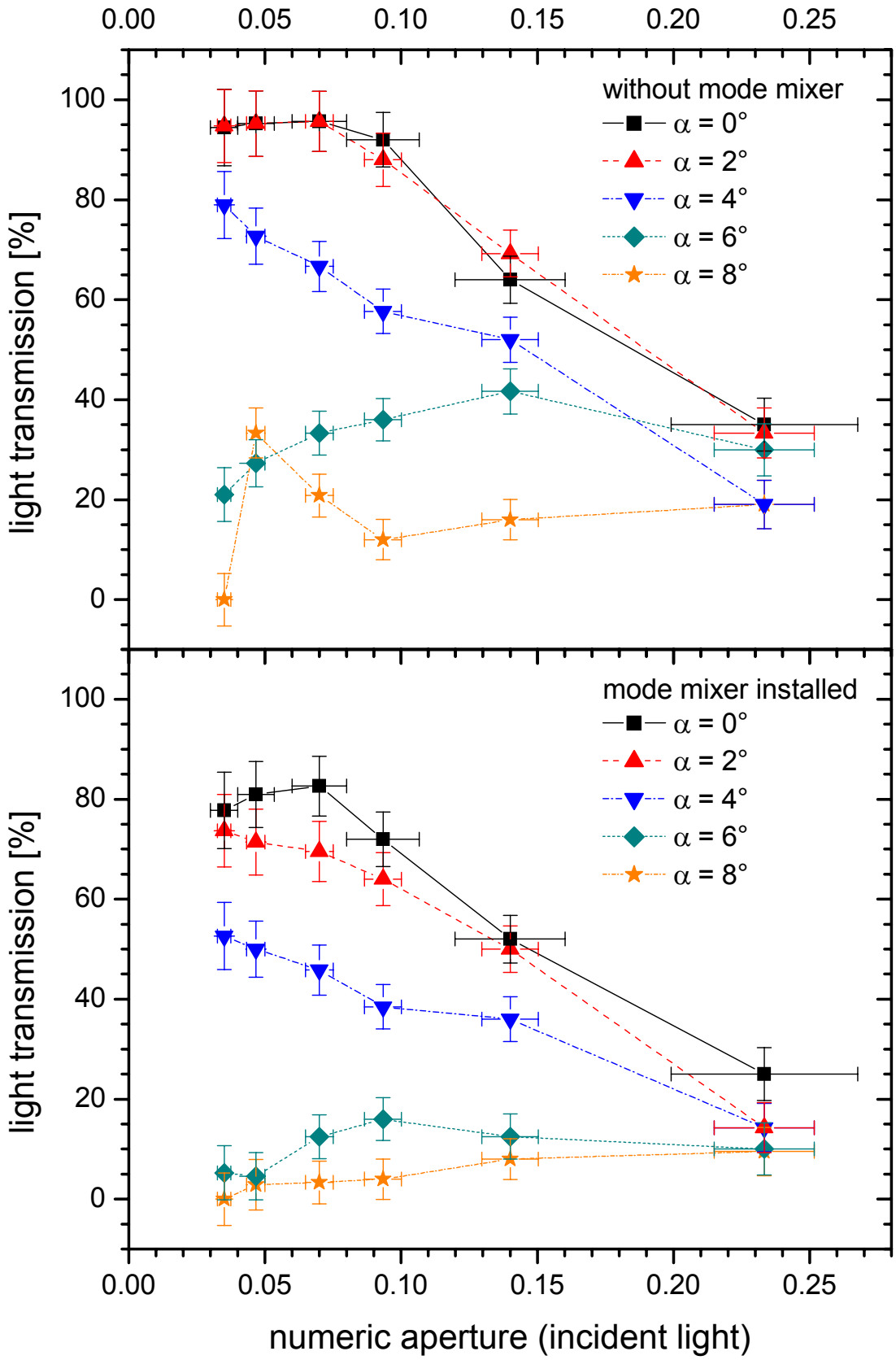

Figure 79: Effect of the mode mixer and different orientations of the incident beam with respect to the optical axis of the fibre on the light transmitted by the 200 µm standard fibre.

Figure 79 shows the variation of the transmission efficiency depending on the NA of the incident beam and the angle α between the optical axes of the incident beam and the quartz fibre aperture. As expected, the transmission efficiency decreases with increasing α for the fibre with and without mode mixer. The installation of the mode mixer again causes a decrease of the transmission efficiency, while removing all intensity variations from the transmitted beam up to α = 6°, and still compensates most structures at α = 8°. This is sufficient for LP-DOAS measurements: for a well-aligned instrument a maximum value of α = 1° is not exceeded.
In summary, it can be stated that no relation was foundbetween the incident NA and the NA of the transmitted light, contradicting naïve expectations. The mode mixer, however, showed the desired effect of removing all structures (i.e. concentric circles of varying light intensity, see [*Stutz and Platt*, 1997]) from the transmitted beam. As expected, the mode mixer caused a loss of total transmitted light intensity due to physical stress applied to the fibre.

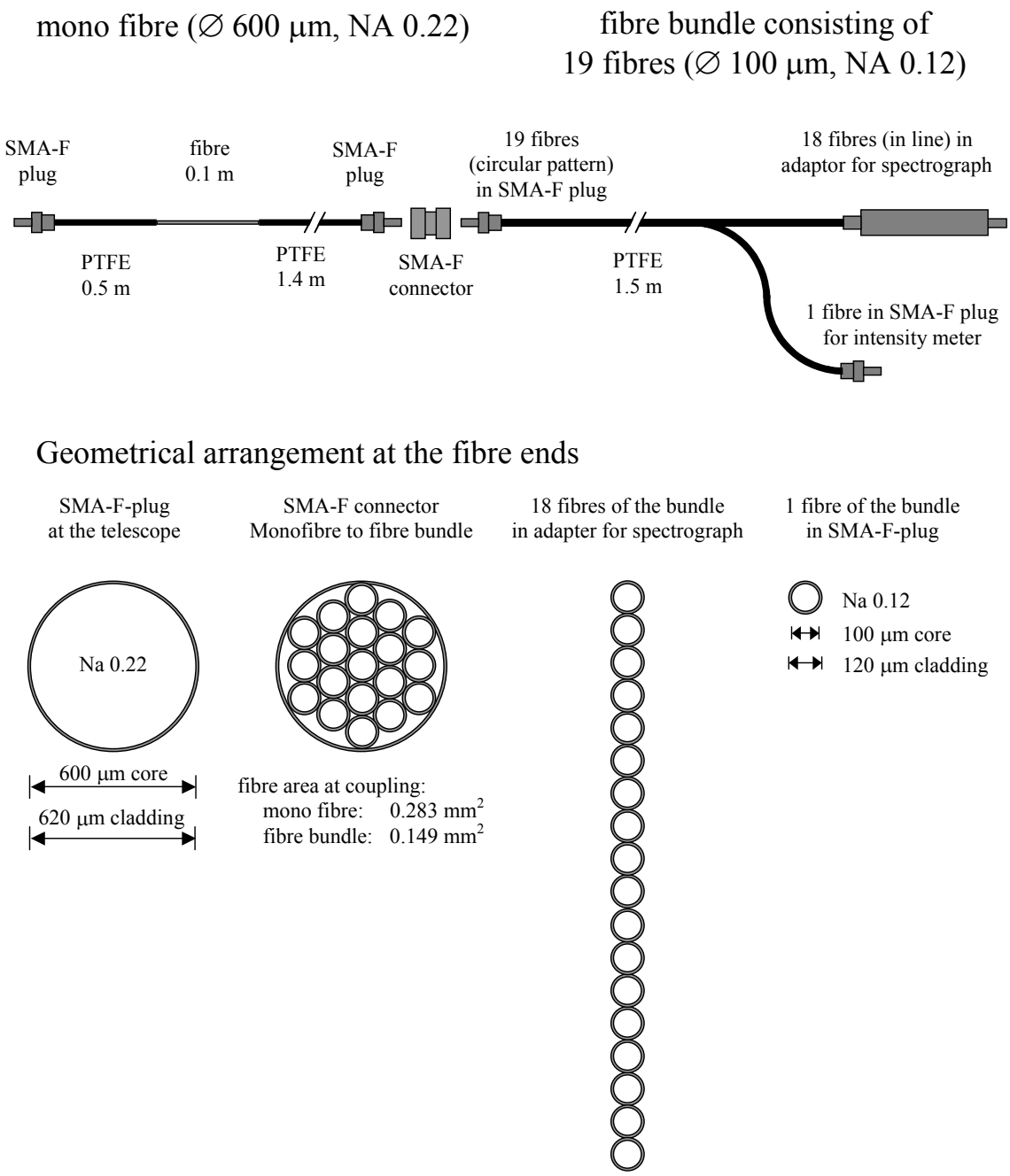

Figure 80: Set-up of the quartz fibre assembly for the balloon-measurements.

8.5.2 Optical parameters of the improved quartz fibre assembly

Numerical aperture of the 600 µm mono fibre

The 600 µm fibre was not available at reasonable prices with a numerical aperture of 0.12, which would be adapted to the NA of both receiving telescope and the spectrograph. Thus a fibre featuring NA = 0.22 was chosen, which is the minimum NA commonly available for such fibres. Thus, the effect of the fibre-specific NA on the NA of the light transmitted had to be studied: using the fibre test bed in a procedure similar to that used for the 200 µm fibre presented above, laser light of different incident numerical apertures was focused on the fibre. Figure 81 shows the result of the measurements performed with and without mode mixer: an almost linear increase of the transmitted NA with increasing incident NA can be observed. For small incident NAs however, the transmitted light features a larger NA than the incident NA, an effect that diminishes for incident NAs exceeding 0.22 (which is the maximum NA specified for the fibre). The installation of the mode mixer accentuates this effect: the NA of the transmitted light is increased again, especially for small incident NAs.
The reason for the NA increase of the light transmitted by the 600 µm mono fibre exceeding the specified NA is most probably the bending of the quartz fibre when installed on the LP-DOAS instrument or on the fibre test bed. In both cases, the fibre is bent to (or below) its minimum bending radius of 40 cm. The physical stress applied to the fibre by bending it to such small radii has almost the same effect as the mode mixer, which also induces physical stress by bending and squeezing the fibre, and thus increases the NA of the transmitted light for virtually all incident NAs.
Incident light featuring NA = 0.12 (i.e. light sent to the fibre by the receiving telescope) yields transmitted light of NA ≈ 0.17. Implications of the increased NA of the transmitted light for the light throughput of the fibre assembly will be discussed below.

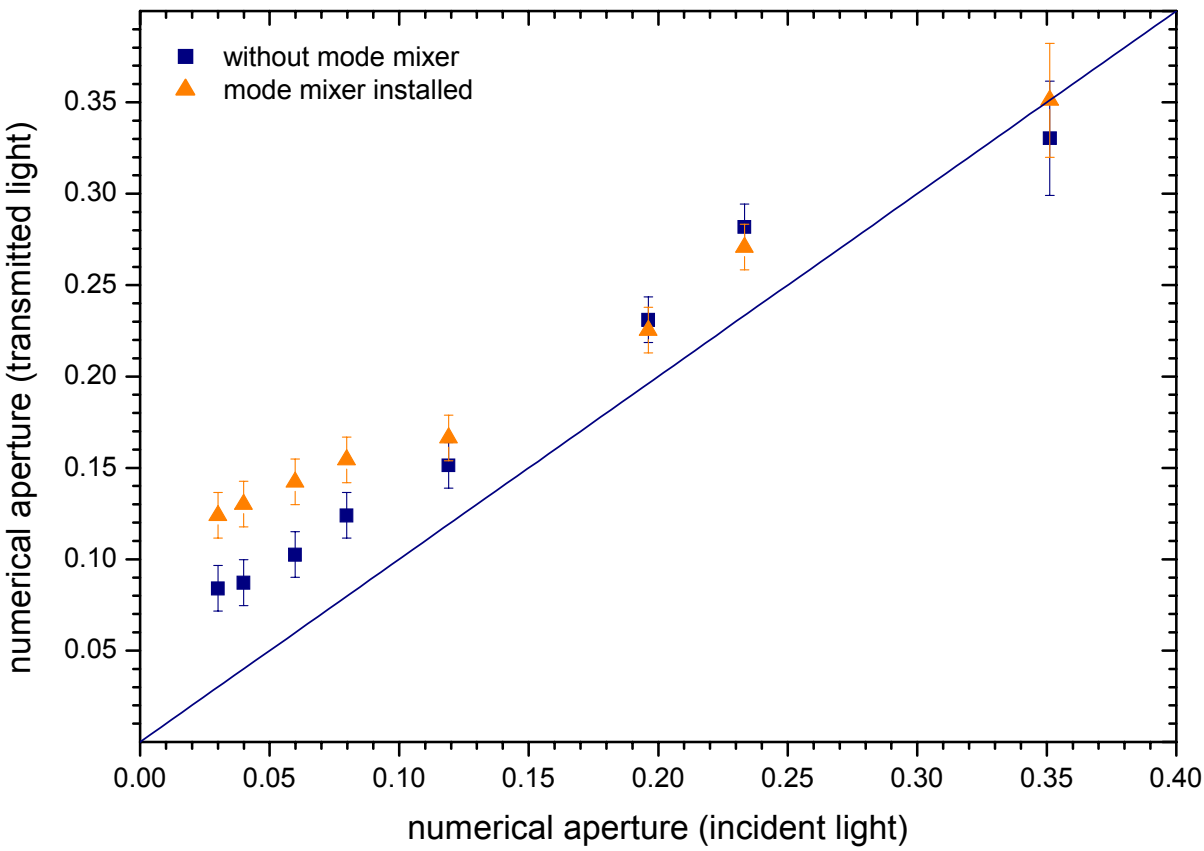

Figure 81: Effect of the incident NA to the NA of the light transmitted by the 600 µm mono fibre (NA = 0.22) with and without mode mixer installed.

Numerical aperture of the fibre bundle

For the fibre bundle, quartz fibres with a NA of 0.12 were used, adapted to the NA of the spectrograph. Transmitting light of a higher NA into the spectrograph would not yield any advantages, but would only increase stray light in the spectrograph and therefore increase the noise level of the spectra recorded. The light loss at the connection of the 600 µm mono fibre and the fibre bundle due to the different NAs will be discussed below.

Figure 82 quantifies the variation of the NA of the light transmitted by the fibre bundle depending on the NA of the incident light. Obviously, the transmitted light always exceeds the specified maximum NA of 0.12 for the fibre, even at much smaller incident NAs. The clear linearity of the transmitted NA observed for the 600 µm fibre could not be reproduced here. The transmitted NA remains at around 0.15 for incident NAs below ≈ 0.15 and increases to another plateau at 0.18-0.19 for incident NAs exceeding 0.25.

Most probably, the desired NA of 0.12 is not achieved by this fibre. A NA of 0.15 is more likely for this example. As no mode mixer is installed and the fibre is not bent below its minimum radius (which is smaller than 5 cm), the increase of the measured NA with respect to the specified NA cannot be caused by physical stress. Possibly, the refractive indices of the core and cladding show variations depending on the fibre charge, caused by impurities of the material used for the fibres.

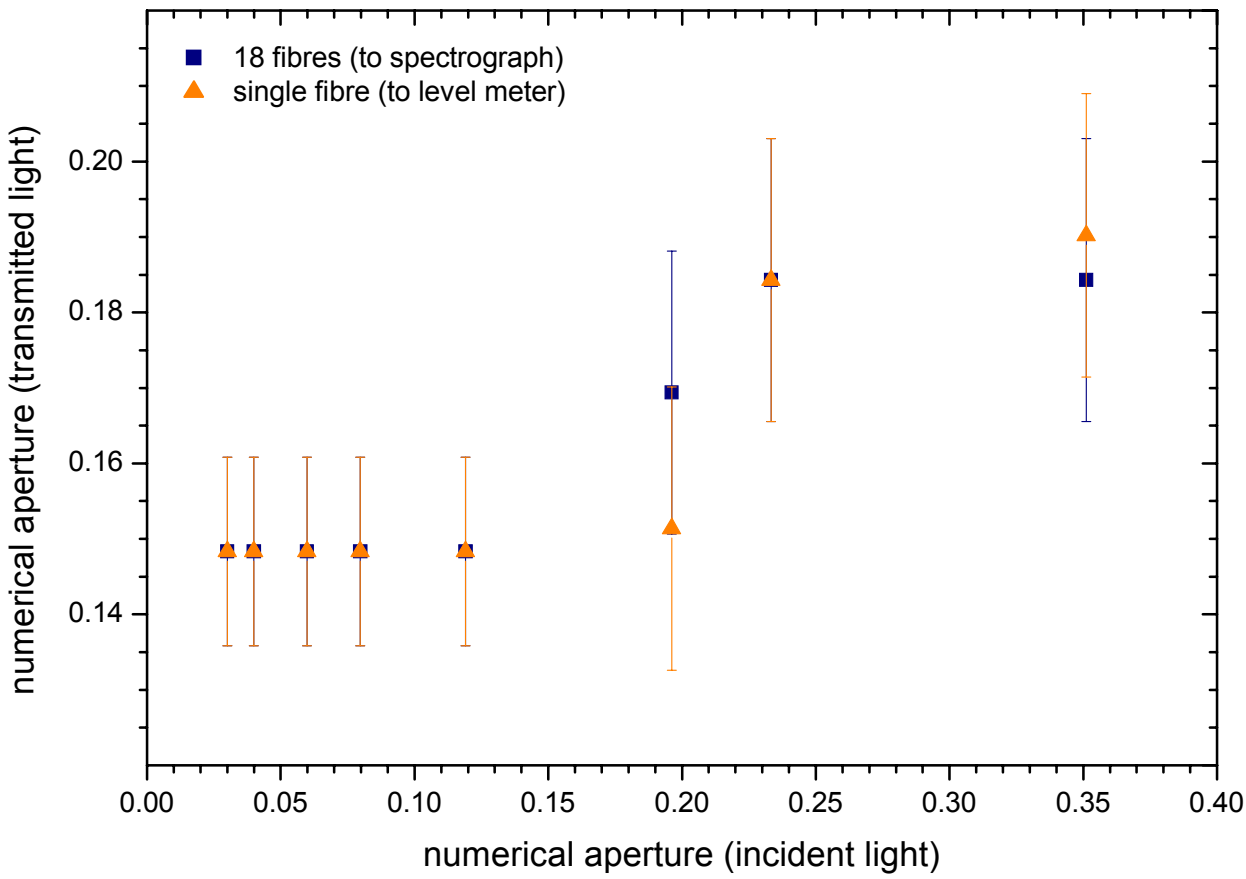

Figure 82: Effect of the incident NA on the NA of the light transmitted by the fibre bundle (NA = 0.12) to the spectrograph and the light level meter.

Transmission efficiencies of the fibre assembly

The transmission efficiency of the fibre bundle is not only affected by the transmission of the 600 µm mono fibre and the 100 µm fibres of the bundle, but also by light losses at the connection between the mono fibre and the bundle. A test series was performed on the quartz fibre test bed to determine the transmission efficiencies of the fibre assembly and its components : the laser light transmitted through a 600 µm pinhole at an incident NA of 0.14 was used as the reference intensity against which the intensities transmitted by the fibre assembly and its components were measured.

Table 32 presents the results of these measurements: it is obvious, that the 600 µm mono fibre causes no light losses when transmitting the laser light, neither without nor with the mode mixer installed. The 18 fibres of the fibre bundle connected to the spectrograph however, showed a transmission efficiency of only 60 %. Comparing the entrance area effective for transmission (i.e. the aperture of the 18 100 µm fibres leading to the spectrograph) with the illuminated area (featuring a diameter of 600 µm), a fraction of 50 % is expected. Thus, the transmission efficiency of the single fibres should be nearly 100 %, and the efficiency of the fibre bundle is at least as good as expected by the area ratio. The fact that a larger fraction as expected is transmitted, cannot be fully explained by measurement errors, so possibly a fraction of light projected at the fibre cladding is refracted into the core and also transmitted to the spectrograph.

It is also obvious from Table 32 that the different numerical apertures of the mono fibre and the fibre bundle cause light losses at the connection of both fibres: when coupled together, the transmission of the total fibre assembly decreases to 42 %, which is significantly smaller than the product of the transmissions of the two components (which should be 60 %). Thus, a transmission efficiency of 71% is found for the fibre coupling.

As already discussed above, the difference in the numerical apertures of the light exiting the mono fibre (NA = 0.17 at an incident NA of 0.12) and the light accepted by the single fibres of the bundle (NA = 0.15) should cause an effective loss in the light throughput of the total fibre assembly. A simple calculation using the numerical apertures of the mono fibre and the fibre bundle yields the result that the fibre bundle only accepts a fraction of 77 % of the total light transmitted by the mono fibre.

An additional loss of intensity at the fibre coupling is expected due to total reflection on the surfaces of the fibres coupled to each other: even if the coupling is very tight (in this case realised by the SMA-to-SMA-coupling), a thin layer of air will still remain between the fibres, generating two interface planes on which a part of the incident light will be reflected. The reflectance of the surfaces depends on the refractive indices of the media on each side of the interface, which are $n_{air} = 1.000272$ and $n_{quartz\ glass} = 1.46008$. This yields a transmission efficiency at each surface of

$$T = 1 - \left(\frac{n_{quartz} - n_{air}}{n_{quartz} - n_{air}} \right)^2 = 96.5\% \qquad \text{Equ. 70}$$

and a total transmission due to reflections and the NA difference of 71.7% at the fibre coupling. Assuming an NA error of ± 0.1, this result is surprisingly consistent with the measurement.

Figure 83 shows an overview of the transmission efficiencies of the standard fibre, the 600 µm mono fibre and the fibre assembly (all with a mode mixer installed): Surprisingly, the 600 µm fibre is much more effective for light transmission than the 200 µm standard fibre. This effect might partly be caused by the mode mixer, which seems to have a much stronger effect on the light transmission of the fibres with a smaller diameter: although the transmission of the 200 µm fibre is reduced from 80-85 % to 60-65% when the mode mixer is

installed (see Figure 79), the transmission of the 600 µm fibre is hardly reduced by the mode mixer. Figure 79 indicates a second explanation for the smaller transmission efficiencies: the transmission of the standard fibre is strongly dependent on the NA of the incident light beam. The maximum transmission is encountered at an NA = 0.7, which is almost half of the NA = 0.12 specified for the fibre. All tests presented in Figure 83 were performed with an NA = 0.12, meaning that even if the 600 µm fibre featured the same effect, it would be not that significant, as the incident NA is almost half of the specified NA = 0.22 of the fibre. The transmission efficiency of the total fibre bundle is at the expected values of about 45 % (see above).
All fibres show the expected decrease of the transmission efficiency when the diameter of the bright spot at the fibre aperture decreases. In fact, a much sharper decrease is was? expected (from the ratio of the illuminated area and the fibre aperture). However, the inhomogeneous intensity profile of the incident laser beam – which shows a strong maximum in the beam centre – partially compensates this effect.

Table 32: Transmission efficiencies of the fibre assembly and its components

600 µm mono fibre		fibre bundle		complete fibre assembly	
w/o mode mixer	with mode mixer	spectrograph	level meter	spectrograph	level meter
(100 ± 3) %	(105 ± 3) %	(60 ± 3) %	(3.3 ± 3) %	(42.5 ± 3) %	(2.2 ± 3) %

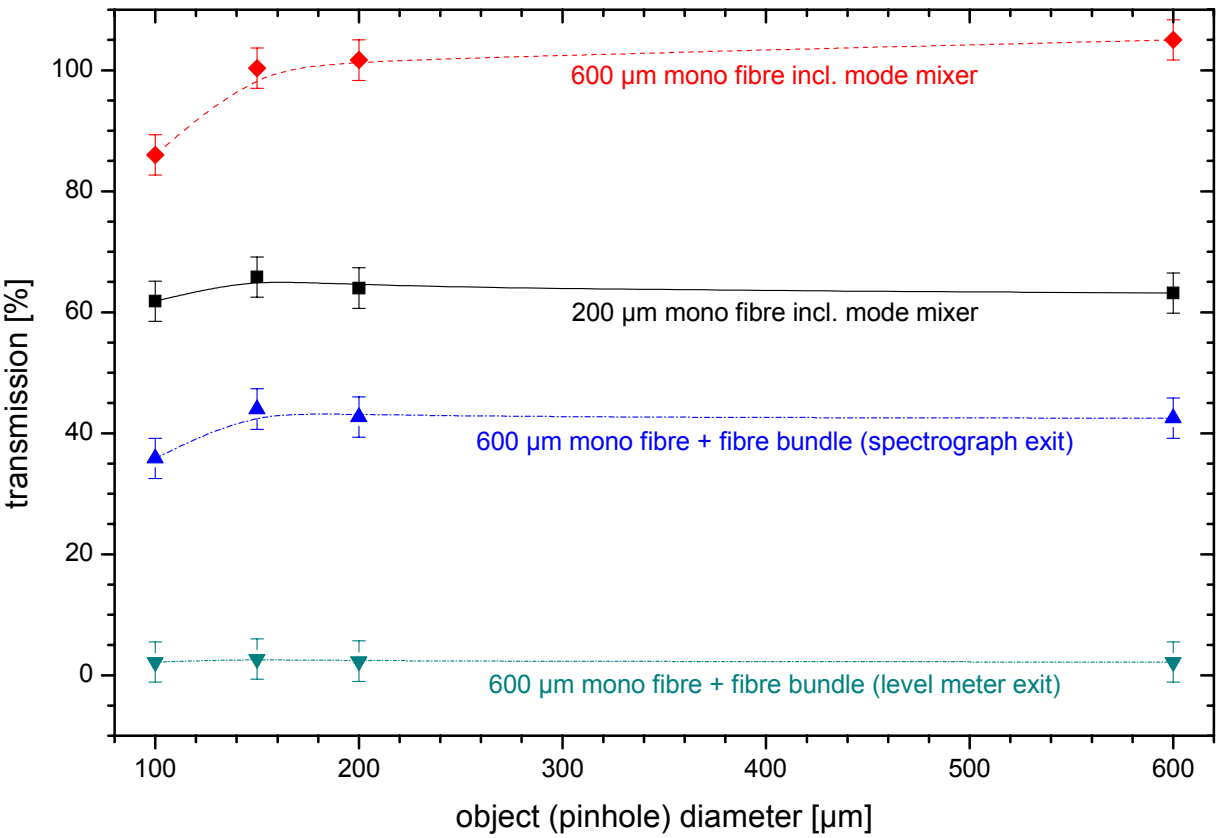

Figure 83: Comparison of the transmission efficiencies of the 200 µm standard fibre and the 600 µm fibre assembly, depending on the diameter of the "bright spot" projected to the fibre entrance. The transmission for the fibre assembly and its components is normalised on the intensity measured behind a 600 µm pinhole replacing the fibre, while for the 200 µm fibre a pinhole with a diameter of 200 µm was used.

8.5.3 Enhancement of the field of view

The main reason for the development of the quartz fibre assembly was to improve the field of view (FoV) of the receiving telescope. A straightforward calculation for the diameter of the FoV can be made by using the relation

$$D_{FoV} = \frac{d_{fibre}}{f_{telescope}} \cdot L_{reflectors} \qquad \text{Equ. 71}$$

with D_{FoV} designating the diameter of the field of view in a distance $L_{reflectors}$ from the telescope with a focal length of $f_{telescope}$ and a quartz fibre with a diameter d_{fibre}. Thus, the use of a 600 µm mono fibre in the focus of the receiving telescope instead of the standard 200 µm fibre (see chapter 5.2) should yield an increase of the FoV by a factor of three.

To study the effects of the enhanced FoV on light throughput of the instrument and stray light in the spectra, measurements were made using an array of 7 retro reflectors set up on the steeple of the St. Raphael church in Heidelberg-Neuenheim. The LP-DOAS instrument was situated at the IUP, with a distance from the reflectors of 869 m. The interpretation of these measurements, however, is only possible if the optical properties of the telescope, the reflectors and the optical effects on the light path through the atmosphere are properly understood. [*Kah*, 1998; *Rudolf*, 1993; *Stutz*, 1996] have discussed the LP-DOAS optics in detail, so here only a brief summary of the dominant effects will be given.

The diameter of the beam D_{Beam} generated by the transmitting telescope at the steeple is computed from the finite size of the lamp arc:

$$D_{Beam} = \frac{d_{Arc}}{f_{telescope}} \cdot L_{Retro} \qquad \text{Equ. 72.}$$

Here, D_{Beam} is the beam diameter in a distance L_{Retro} from the telescope, d_{Arc} the diameter of the hot spot[18] of the Xe-lamp and $f_{Telescope}$ the focal length of the telescope. The intensity profile of the real light beam, however, cannot be described by a simple box function, which neglects scattering and refraction processes in the atmosphere. To consider such effects, [*Kah*, 1998] assumes a Gauss beam profile with a standard deviation σ_{Beam} being directly dependent on the geometrical diameter of the beam computed by Equ. 72:

$$\sigma_{Beam} = \frac{D_{Beam}}{\sqrt{8 \cdot \ln(2)}} \qquad \text{Equ. 73.}$$

Thus, the size and intensity distribution of the lamp image generated by the transmitting telescope at the reflectors can be simulated. The typical "hot spot" diameter for the Osram XBO 500 lamps used for the test measurements is 0.6 mm. This results in a beam diameter at the reflectors characterised by $\sigma_{Beam} = 387.5$ mm. As the diameter of the reflector array measures 200 mm, the reflector area is fully illuminated by the sending beam.

A similar computation can be used to compute the diameter of the reflector image, which is reproduced by the receiving telescope at the fibre entrance . But the specific optical properties of corner cube retro reflectors have to be taken into account: the diffraction of the light by the front opening of the reflectors can be neglected over short distances [*Rudolf*, 1993], but the effects of the reflection of the beam on the three back surfaces have to be considered. Small deviations from the 90° angle between the reflecting surfaces are known to widen the reflected beam [*Rityn*, 1967]. The reflectors also cause an offset between the incident and reflected beam that is parallel to the beam axis [*Rudolf*, 1993; *Stutz*, 1996]. As the effects of the reflectors and atmospheric scattering and refraction add up, the reflector image is larger

[18] Defined by the half-width of the intensity plotted against the position within the lamp arc [*Hermes*, 1999].

than computed by the simple geometrical relationship used in Equ. 72. An accurate analytical solution of the problem is hard to achieve, but measurements show that for the optical set-up used here, the reflector image is enlarged by a factor of two. The diameter of the reflector image in the plane can therefore be computed as

$$d_{Image} = 2 \cdot \frac{D_{Retro}}{L_{Retro}} \cdot f_{telescope} \qquad \text{Equ. 74,}$$

yielding a bright spot diameter of 0.276 mm. Thus, the full reflector image fits only in the aperture of the 600 µm fibre assembly, but not into the 200 µm mono fibre for an ideally aligned system.

To simulate a moving reflector and to study the effects of the different FoV of both fibres , the telescope was turned around one axis by small angles and the changing light intensity received by the detector was monitored. Figure 84 shows the result of the measurements to the St. Raphael steeple in Heidelberg. This figuredemonstrates that the 200 µm fibre has a much smaller field of view than the 600 µm fibre assembly. It also becomes clear that two major effects contribute to the received light intensity when using the 600 µm fibre: for small deviations from the optimal orientation of the telescope and reflectors, the Gauss intensity distribution at the reflectors determines the received intensity. Here, the fibre still "sees" the total the reflector image. At angles deviating more than 1' form the centre, the overlap of the reflector image and the fibre aperture at the focus of the receiving telescope is the dominating effect. This is also the dominating effect for the 200 µm fibre at angles exceeding 0.2'.

Both effects were simulated to obtain the theoretical curves plotted in Figure 84: the intensity distribution of the beam transmitted to the reflectors is computed by the Gauss distribution featuring the standard deviation deduced from Equ. 73. The reflected light intensity, which is transmitted to the detector by the fibre, is computed by the area of the retro image and its overlap with the fibre opening at the focal plane of the receiving telescope. For the simulation, the following labels are used:

- I_T: light intensity transmitted to the spectrograph
- I_R: light intensity received by the telescope from the reflectors
- r_R: diameter of reflector image (assumed as circular)
- r_F: radius of the fibre opening
- α: turning angle of the telescope
- a: distance between the centres of the retro image and the fibre opening, defined as $a = f_{Telescope} \cdot \tan\alpha$

In dependency from a, the problem is divided into three different cases:

1. The retro image fits completely into the fibre:

$$|a| \le |r_F - r_R| \quad \Rightarrow \quad \begin{array}{lll} a) & r_F > r_R & I_T(\alpha) = I_R(\alpha) \\ b) & r_F < r_R & I_T(\alpha) = \left(\frac{r_F}{r_R}\right)^2 I_R(\alpha) \end{array} \qquad \text{Equ. 75.}$$

   If the radius of the retro image is smaller than the fibre radius, the whole intensity received by the telescope is transmitted to the spectrograph. If the image radius is larger, the transmitted intensity scales with the ratio of the radii to the power of two.

2. Retro image and fibre opening overlap only partially:

$$|r_F - r_R| < |a| < r_F + r_R \quad \Rightarrow \quad I_T(\alpha) = \frac{S_F + S_R}{\pi \cdot r_{F,R}^2} \cdot I_R(\alpha) \qquad \text{Equ. 76.}$$

Here, S_F and S_R designate the circle segments of the fibre opening and the retro image, which contribute to the overlapping area. They are computed by

$$S_{F,R} = \frac{r_{F,R}^2}{2} \cdot \left(\frac{2\pi\beta_{F,R}}{180°} - \sin(2\beta_{F,R}) \right) \qquad \text{Equ. 77}$$

$$\text{with} \quad \beta_R = \arccos\left(\frac{r_F^2 - r_R^2 + a^2}{2 \cdot r_F \cdot |a|} \right); \quad \beta_F = \arccos\left(\frac{r_R^2 - r_F^2 + a^2}{2 \cdot r_R \cdot |a|} \right)$$

and divided by the area of the fibre ($r_F < r_R$) or of the retro image ($r_F > r_R$) to obtain the normalised value. As in case 1, the intensity transmitted to the spectrograph is additionally dependent on the intensity reflected from the reflectors at a telescope angle α.

3. The retro image is located completely off the fibre opening, thus no light is transmitted to the spectrograph:

$$|a| \geq r_F + r_R \qquad \Rightarrow \qquad I_T = 0 \qquad \text{Equ. 78.}$$

As Figure 84 shows, the simulation yields an agreement with the measurements: the signal transmitted to the reflectors and received by the detector is perfectly reproduced for both fibres. The simulation also shows that the FoV of the fibre assembly (denoted by the lines for the effective reflector area) is indeed three times larger than the FoV of the standard fibre. However, the figure also shows that a further increase of the fibre diameter and corresponding FoV would be pointless: at angles exceeding 2', the light intensity of the transmitted beam at the reflectors is only half of the original value due to the Gauss profile of the transmitted beam. A further widening of the FoV would therefore require an enlargement of the transmitted beam diameter, which is only possible when the transmitting telescope is ill-aligned on purpose. However, a net loss of intensity per area would be the consequence of this ill-alignment, which is proportional to the squared radius of the beam diameter. Thus, the advantage of a wider transmitted beam is compensated by strongly increased integration times.

Thus, the 600 µm fibre assembly shows a significant and very useful enhancement of the field of view which is well suited for the optics of the HMT-DOAS telescope.

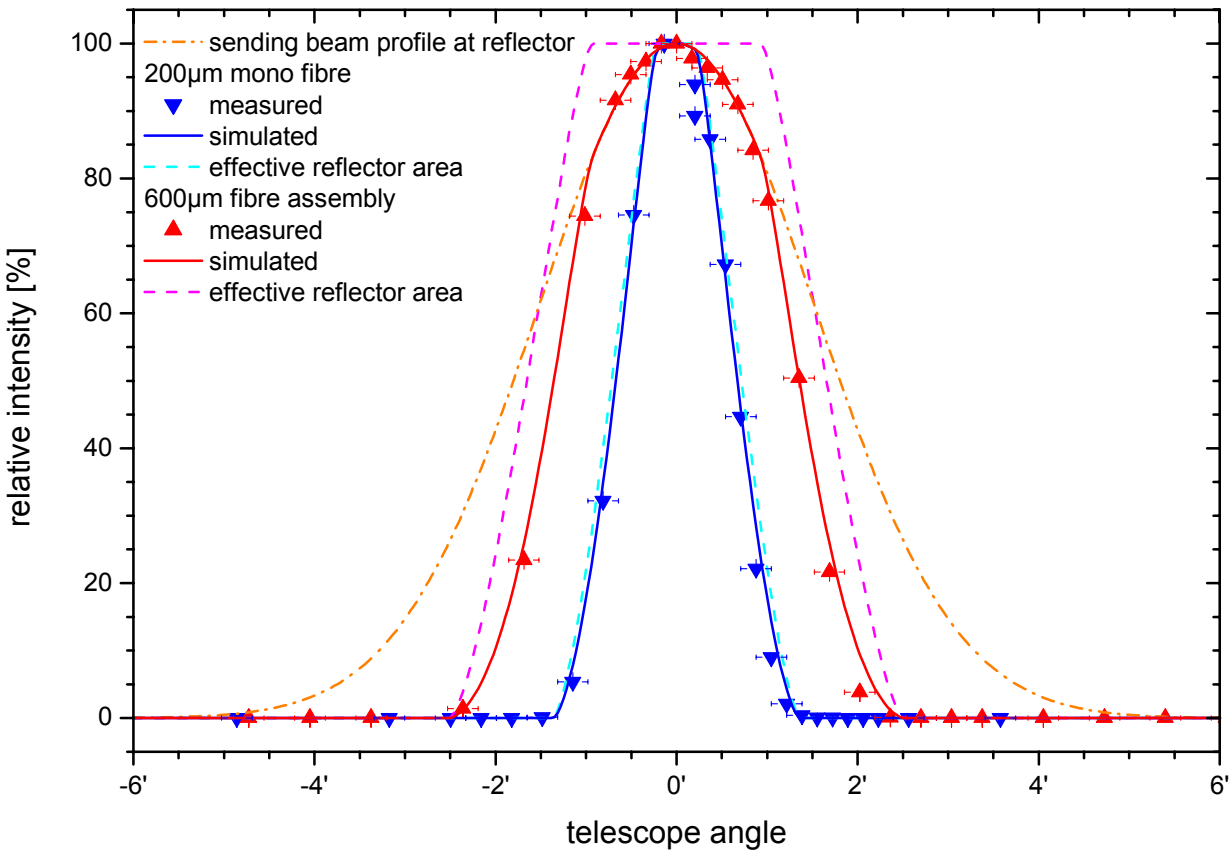

Figure 84: Measurements of the light intensity received by the detector through the different quartz fibres. All values are given as relative intensities normalised by the maximum intensity at an angle of 0'. The triangles designate the measured values; lines symbolise the results of the simulation. The curves for the effective reflector area show the percentage of the total reflector area within the FoV of the receiving telescope.

Comparison of the light yield

The spectra that were used to characterise the FoV of both fibres can also be evaluated with respect to the light throughput of both fibres. To obtain comparable values, the mean intensities of the individual spectra were normalised twice: first to the mean intensity recorded within a second, while the second step normalised all average intensities to the maximum intensity per second recorded within the whole set of spectra (comprising the spectra measured with both fibres). Here, the maximum intensity per second was recorded with the fibre assembly and the telescope ideally adjusted in the orientation of the reflector ($\approx 17 \cdot 10^4$ counts/sec on an total light path length of 1740 m).

Figure 85 shows the result of the evaluation: as expected, the 600 µm fibre assembly yields higher count rates, since the reflector image is completely within the aperture of this fibre. But the relative intensity recorded is smaller than computed by the simulation, which uses the same FoV and the transmitted light intensity at the reflector as above. Additionally, the result computed by Equ. 75 to Equ. 78 (shown in Figure 84) is multiplied by the ratio of the fibre aperture divided by the area of the reflector image, to take into account that only a fraction of the intensity sent back by the reflector could be transmitted to the detector. Consistently, the simulated intensity rate transmitted by the fibres is computed by:

$$I_{T,Norm} = \frac{A_{fibre}}{A_{reflector\ image}} \cdot \frac{I_T}{I_{T,\max}}$$ for the standard 200 µm fibre Equ. 79a

$$I_{T,Norm} = \frac{I_T}{I_{T,\max}}$$ for the 600 µm fibre assembly Equ. 79b.

It was not possible to perform the measurements with two – apart from the quartz fibre – identical LP-DOAS systems simultaneously, as only one instrument was available. Thus, the measurements for the mono fibre and the fibre assembly were done successively with a time lapse exceeding one hour. This leads to the assumption that the difference in the count rates is mainly caused by changes in the visibility of the atmosphere.
It should be noted that an increase of the light throughput by using the fibre assembly can only be achieved when the effective area can be increased at the same time, or if the reflector area is already larger as the FoV of the mono fibre (which is the case for the experiment discussed above). For all other measurement set-ups featuring an aperture larger than the reflector image, the fibre assembly induces a net loss of count rate to achieve an increased aperture (see chapter 8.5.3).

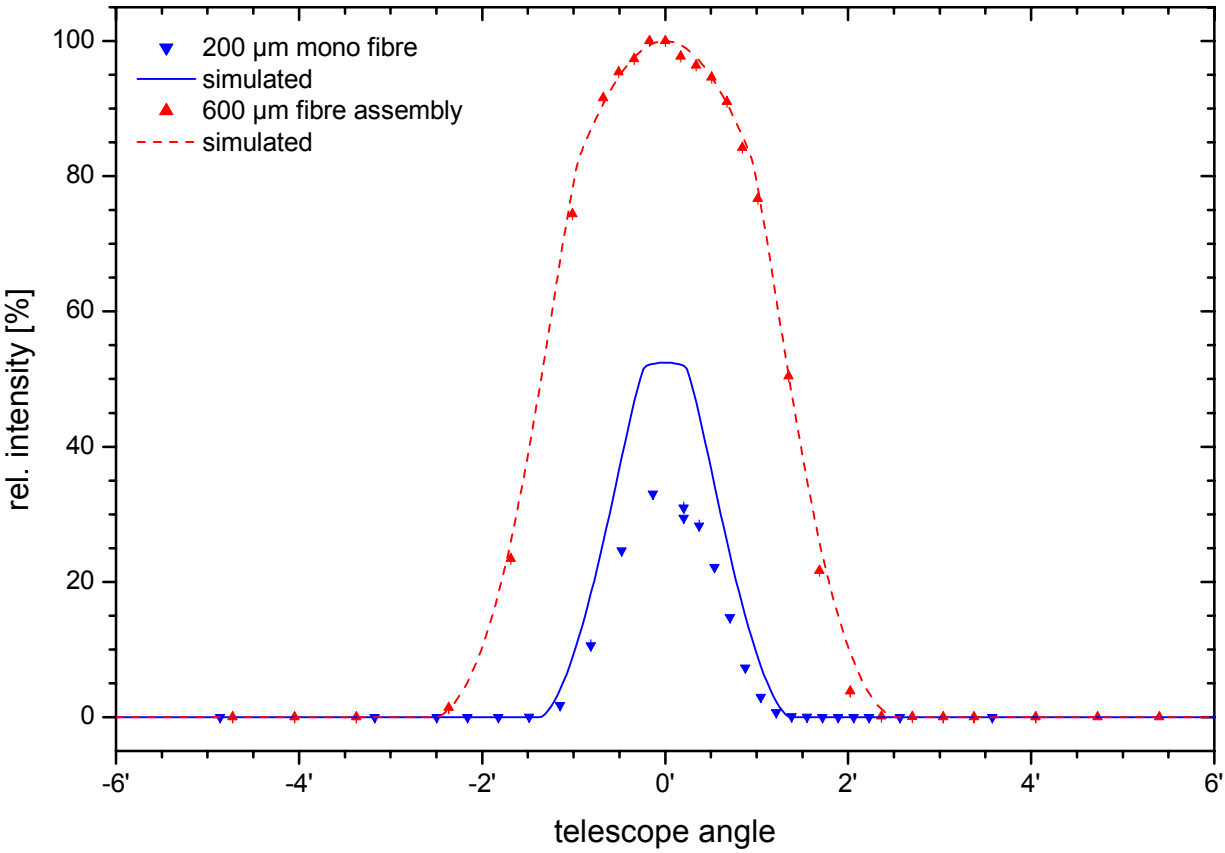

Figure 85: Comparison of the intensities transmitted to the detector by the 200 µm moo fibre and the 600 µm fibre assembly. The intensities are plotted in dependence on the angle between the telescope orientation and the reflectors (located at the centre of the FoV at an angle of 0°).

Stray light evaluation

The stray light level in the measured spectra generated by sunlight scattered into the receiving telescope contributes directly to the error of the spectral evaluation of the measurements (see chapter 4.3). As the 600 µm fibre assembly features a larger aperture, an increase of solar stray light transmitted to the detector is expected. To quantify the amount of additional stray light collected by the fibre bundle, the set of spectra already evaluated for the FoV tests are used. The effect of increased stray light on the spectral evaluation can be described by two criteria: the light intensity detected in the background spectra and the errors and residuals of the trace gas evaluation.

Background intensity

At the telescope position with a maximum angle to the reflector, the intensity received by the detector is completely due to solar stray light, as the reflector is not within the FoV. As an example, Figure 86 shows the background spectra recorded for the FoV evaluation at an angle exceeding 6' versus the orientation to the reflector. The upper panel of this figure gives an impression of the shape of the spectral structure of the background (note the different y-axis scales for the two spectra). Obviously, the structure does not change in shape. However, the lower panel of the same graph shows an increase in the average intensity transmitted by the fibre assembly, caused by the larger aperture.

This increase in the stray light level can be easily compensated for: a background spectrum is subtracted from the spectrum recorded for trace gas evaluation. If both spectra are recorded within a small period, the stray light correction proved to be very effective (see chapter 5.3.1).

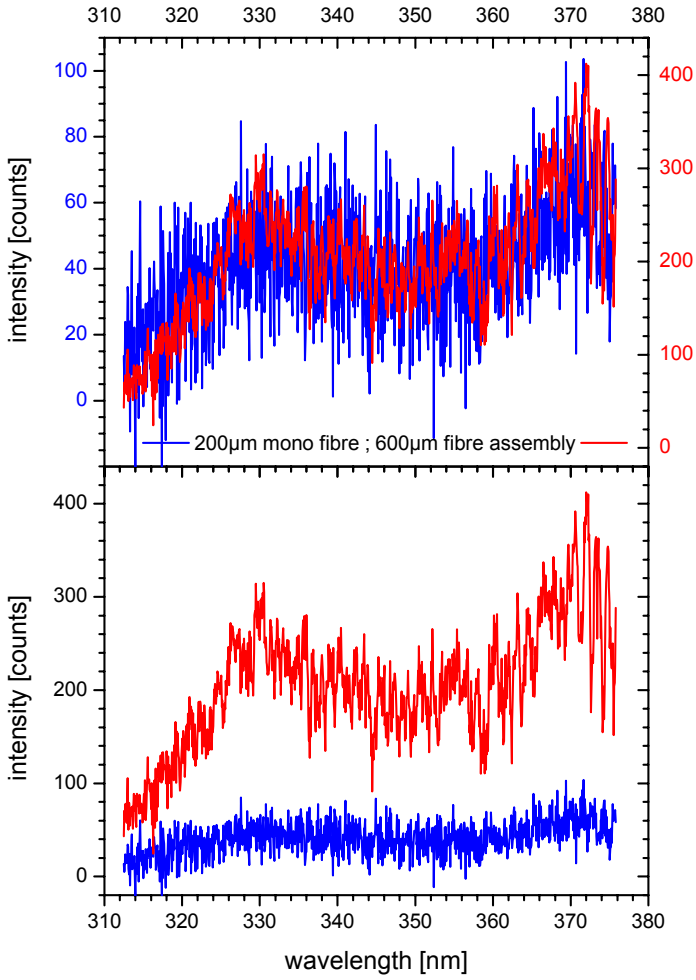

Figure 86: Comparison of the background spectra transmitted to the detector by the 200 µm moo fibre and the 600 µm fibre assembly.

Errors of the trace gas evaluation

Both fibre types were used during a measurement campaign performed with the HMT-DOAS instrument near Rome, Italy in May/June 2001 (within the framework of the NITROCAT project founded by the EU, see forthcoming publications). The measurements of NO_2, HONO, HCHO and O_3 mixing ratios on a single light path with a (return) length of approx. 10.5 km lasted four weeks. The fibre assembly was used for two and a half weeks of this campaign, while the mono fibre was used for the remaining ten days [*Geyer*, 2001; *Trick*, 2001]. This dataset provided the opportunity to compare the results of the trace gas evaluation

of approximately 1500 and 3000 spectra recorded at a wide variety of atmospheric conditions using the 600 µm fibre assembly and the 200 µm standard fibre, respectively. Apart from a significant loss of light transmission and therefore time resolution when using the fibre assembly (see above), no consistent effect of the fibre type on the residuals or measurement errors of the trace gas evaluation could be found: Table 33 indicates that the NO_2 and HONO evaluation in the spectral range from 346 to 367 nm yielded better results for spectra recorded with the mono fibre while the HCHO and O_3 evaluation in the spectral range from 342 to 332 nm showed better results for spectra recorded with the fibre assembly. However, most mean values for residuals and detection limits do not differ significantly from each other when the respective errors are considered.

As a summary for the comparison of the standard fibre and the new-designed fibre assembly, it can be stated that:

- The fibre assembly increases the FoV of the receiving telescope by a factor of 3.
- The light transmission of the fibre assembly is only ≈ 65 % of the standard mono fibre.

Consequently, for balloon-LP-DOAS experiments and for measurements on short light paths (where the full FoV of the fibre can be covered with reflectors), the 600 µm fibre assembly has huge advantages, whereas the 200 µm standard fibre is better suited for measurements on light paths exceeding a length of 4 km (i.e. a distance telescope – reflector of 2 km).

Table 33: Comparison of the results of the spectral evaluation of the Rome-Montelibretti data (provided by [*Geyer*, 2001; *Trick*, 2001]) recorded with both fibre types.

NO_2/HONO evaluation	fibre assembly	mono fibre
number of spectra	1435	2963
residual [‰]	1.92 ± 0.05	1.81 ± 0.01
mean NO_2 detection limit [ppb]	0.196 ± 0.008	0.162 ± 0.001
mean HONO detection limit [ppb]	0.086 ± 0.001	0.083 ± 0.002
O_3/HCHO evaluation	fibre assembly	mono fibre
number of spectra	1581	2973
residual [‰]	1.46 ± 0.02	1.56 ± 0.01
mean HCHO detection limit [ppb]	0.242 ± 0.006	0.246 ± 0.003
mean O_3 detection limit [ppb]	1.53 ± 0.04	1.75 ± 0.05

8.5.4 Light level meter

As mentioned above, the traditional "snap-shot" technique to deduce the integration time is not suitable for LP-DOAS measurements using reflectors mounted on a tethered balloon. The fibre assembly makes it possible to use a fraction of the light that is transmitted to the detector by the receiving telescope to control the signal level of the PDA: the 19th fibre of the fibre bundle is – unlike the other 18 – not connected to the spectrograph, but to a light level meter. The main optical components of this device are a filter, adapted to the spectral range recorded by the PDA, and photo diode which detects the light intensity transmitted through fibre and filter. The read-out electronics mainly consists of a trans-impedance-amplifier that transforms the photo current into a voltage, which is connected to the ADC (analogue-digital-converter) of the DOAS-controller. Here, the signal of the light level meter can be read out by the DOASIS software controlling the measurement process. If a scan is started by the automatic measurement routine or manually by the operator, an add-on module of DOASIS integrates over the signal transmitted to the level meter until a pre-set value is exceeded. This triggers the read-out of the PDA spectrumautomatically , either to transmit it to the computer or to enable the next scan of a multi-scan measurement, which is added up in the controller.
Thus, the signal level of the PDA is controlled independently from time, but dependently on the integrated light intensity intercepted by the telescope. So a constant signal-to-noise ratio for all spectra can be obtained and light intensity variations at the fibre exit due to a loss of signal generated by sudden balloon movements can be absorbed.

Linearity and spectral characteristics of the light level meter

As over-saturation – even of single channels – of the spectrum recorded by the PDA drastically worsens the quality of the spectral evaluation and a sufficient signal-to-noise ratio should be sustained, the level meter should ideally feature a response signal which is linear to the PDA saturation level.
To check whether the linearity of the level meter was achieved, the fibre assembly connected to spectrograph/detector unit and light level meter (without a band pass filter installed), was illuminated by a halogen lamp. The light intensity transmitted to the fibre could be varied by grey filters installed in the light path. Measurements were performed at all intensities and at 4 different centre wavelengths of the 40 nm spectral window recorded by the PDA. The light level meter was used to measure the spectra at a desired maximum saturation level of 90 % (or approx. $5.9 \cdot 10^4$) counts for a single channel. Figure 87 shows the result of these measurements: for a centre wavelength of 550 nm, an almost constant signal level of the PDA is achieved, with integration times nearly exponentially rising with decreasing light intensity at the fibre entrance. For wavelengths nearer to the UV range, however, the linearity could no longer be guaranteed: at 340 nm, the PDA signal level decreases with the initial light intensity, despite the level meter substantially increases the integration time. Even the use of a UG 5 band pass filter directly in front of the level meter diode to exclude light of the spectral and near-IR ranges does not improve the non-linearity. However, if the read-out trigger level for the intensity meter is set correctly, an almost constant PDA saturation level of 70-80% could be achieved in the 360 nm wavelength range used for the first balloon experiments (see below). For these measurements, the light level meter proved to be as indispensable as the fibre assembly with its increased aperture.

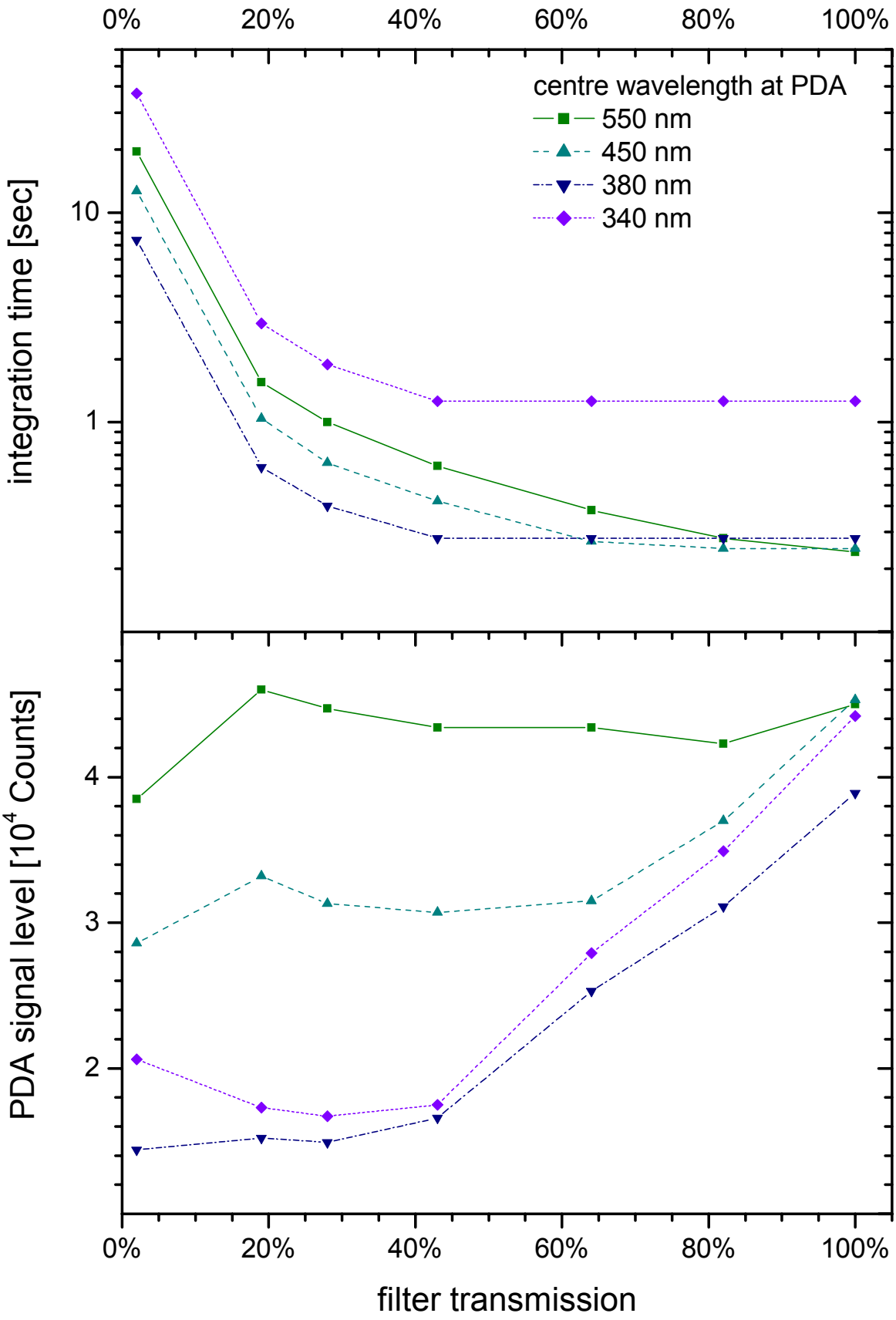

Figure 87: Integration time and linearity of the obtained signal level with the light level meter controlling the integration time at different light source intensities (generated by different quartz glass grey filters).

9 First measurements with the balloon-LP-DOAS

The HMT-DOAS system which features all improvements listed in chapter 8 above was tested in a measurement campaign at the Forschungszentrum Karlsruhe, Germany from January to March 2001. The objective of this campaign was to demonstrate that manually controlled DOAS profile measurements using a tethered balloon as a retro reflector platform are possible. Only measurements of NO_2 vertical profiles were planned, as the maximum light path lengths within the perimeter of the FZK were limited to 1800 to 2000 metres. NO_2 measurements were considered to be a "low-risk" possibility as daytime concentrations range typically between 10 and 40 ppb in the PBL and the differential cross section allows detection limits well below 1 ppb for such light path lengths.

9.1 Location and instrumental set-up

For the measurements at the FZK, the HMT-DOAS instrument was set up in an laboratory on the 6th floor of the main building of the Institut für Meteorologie und Klimakunde (IMK, Institute for Meteorology and Climatology). At a distance of 870 m from the DOAS telescope, the balloon winch was set up at the so-called "balloon meadow" (see Figure 88). The balloon of the Darmstadt group (for details see chapter 8.2) was used, carrying the gondola for 9 reflectors (see chapter 8.3). The flight level of the balloon ranged from 70 to 340 m, limited at the lower end by buildings looming in the light path, and at the upper end by the length of the kite wire used as the tether cable.
The meteorological tower of the FZK, located some 50 m south from the balloon meadow, is equipped with a wide set of instrumentation that provided all meteorological data presented below, namely temperature, wind direction and speed.

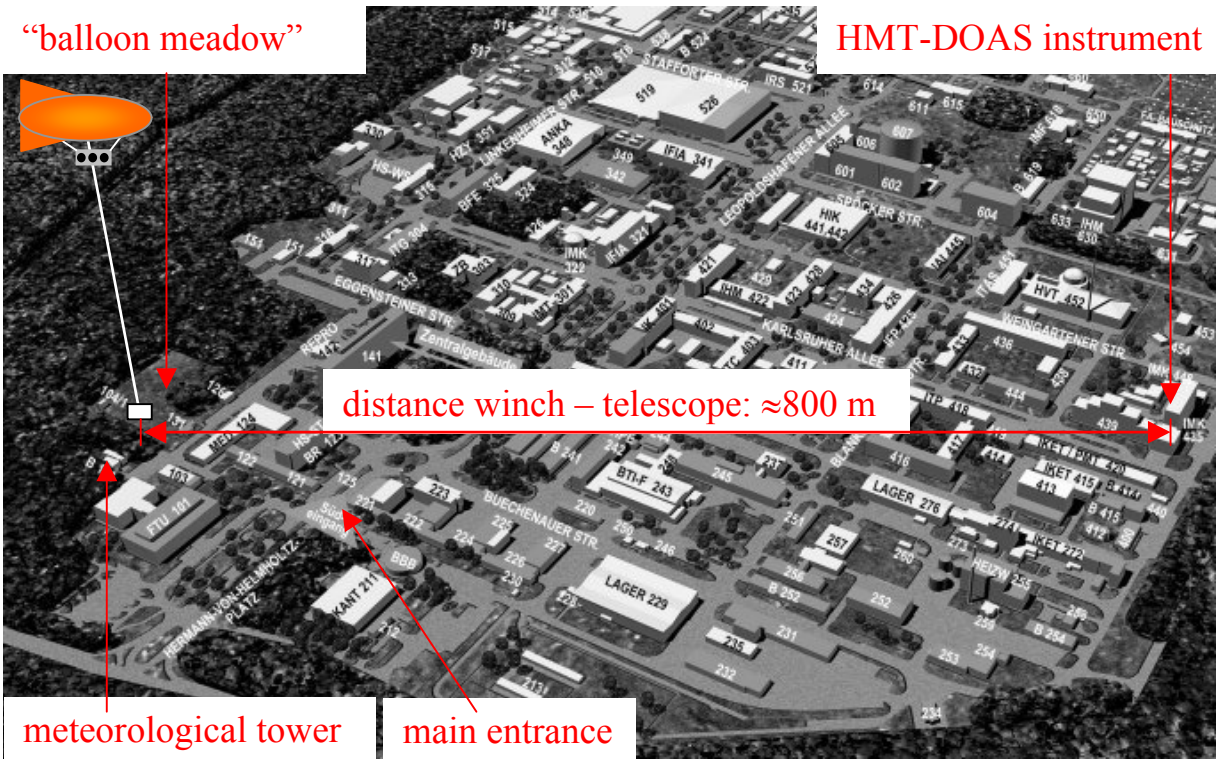

Figure 88: Area map of the FZK including the set-up for the balloon-LP-DOAS measurements.

9.2 Measurements

The first flights were performed on 17 January 2001, one in the morning and one in the afternoon. A stable high pressure system caused very calm atmospheric conditions that were ideal for the first experiments with the balloon-LP-DOAS instrument. The mean wind speeds in the height interval between ground level and 200 m were found to be in the range of 1-2 m/s throughout the day, which is extremely low for Central European conditions. Surface temperatures were well below 0°C in the morning and hardly exceeding the freezing point in the afternoon. Combined with the weak solar irradiation in January – despite clear sky – this guaranteed only a weak convection in the PBL. Thus, total atmospheric turbulence was very weak, which guaranteed a very stable flight behaviour of the balloon.

The flights lasted 60 – 90 minutes each and 8 - 9 measurements were taken at each ascent and descent. During each measurement, the balloon was kept at a constant tether cable length and consequently at a relatively stable horizontal and vertical position. The reflector was kept within the FoV of the receiving telescope by joystick control: under the atmospheric conditions described above, it was possible to achieve a nearly constant signal level at the PDA, rarely "missing" the picture of the reflectors at the fibre entrance. The mean integration time for the spectra recorded at each flight level was 32 seconds, the spectra consisting of 3 to 5 single scans (multi-scan measurements were not possible at that time due to software limitations). After each series of measurements to the reflector, a background spectrum (off-direction from the reflector) and a lamp spectrum (using the shortcut system) were recorded. Summarising all spectra of a flight level and correcting the sum by the background spectrum generated the measurement spectrum, which was evaluated for the trace gas absorptions. Software problems prohibited a precise correction of the background: the integration time controlled by the light level meter was not correctly saved to the spectrum file. Thus the achieved signal-to-noise ratio was only ≈ 450:1, yielding higher (about a factor of 2) residuals and detection limits (see chapter 5.3). Thus, only the NO_2 mixing ratios could be evaluated by the DOAS fitting algorithm, the quality of the spectra being not good enough to measure HONO, HCHO and O_3 at the same time. At the noise level present in the measured spectra, the ambient concentrations of HONO were too low to be detected, while the differential cross sections of HCHO and O_3 in the chosen spectral range were too small to yield significant results.

For each single spectrum, light path length and balloon height were measured by the laser range finder controlled by the DOASIS software. The height data obtained from the LRF were used to compute balloon flight levels, while the mean concentrations at the respective height interval were deduced from the evaluation algorithm presented in chapter 4.4.1.

The software integration, mainly of the light level meter, caused the main problems during the measurements: the inability to save the integration time controlled by the level meter and to trigger multiple scans directly from the DOASIS software hampered the measurement and evaluation process. However, immediately after the measurements and the evaluation of the obtained data presented in chapter below 9.3 were completed, the main software problems were corrected for. Further experiments at the FZK were prevented by the weather conditions, which did not allow additional flights within the given limits for balloon operations.

As the system proved to be well-suited for operation in the framework of larger field campaigns, further measurements with a LP-DOAS system using retro reflectors mounted at a tethered balloon are intended. Ideally, such measurements should be performed in conjunction with traditional active LP-DOAS instruments, preferably at a location with more predictable and more stable wind conditions.

9.3 Results

Morning flight

The morning flight was performed starting with the ascent at 9:20 local time, reaching a maximum ceiling of 345 m at 10:20 and being back on the ground at 11:10. The main goal of this flight was to check all newly-designed components of the instrument and to gain some experience with the joystick-tracking of the reflectors fixed to the balloon. Thus, the ascend and descent took nearly an hour each, yielding more an overall picture of the NO_2 gradient than a snap-shot of the actual gradient as measured in Heidelberg.

However, the potential temperature plotted for the ascent and descent of the balloon in Figure 89 and Figure 90, respectively, shows that the stratification of the PBL was stable, featuring a ground inversion at the period during which the flight took place. The wind direction plotted in the same figures shows the turning of the main wind direction due to the Ekman spiral, while the wind speed is constant with values of 1-1.5 m/s in the height interval covered by the meteorological tower. The NO_2 profiles – generated by the simple multi layer model described in chapter 4.4.1 – for the ascent and descent of the balloon are plotted in the far right panels of Figure 89 and Figure 90, respectively. Even when the huge error bars, especially for the uppermost data points, are taken into account for the discussion of the profiles, some conclusions are obvious: the NO_2 mixing ratios observed are relatively high, compared to measurements in Heidelberg under similar conditions. Values of 30-40 ppb could be measured in the whole height interval. Additionally, the gradient seems not to be as pronounced as observed in Heidelberg, where a distinct decrease of the NO_2 mixing ratio with increasing height could be observed under virtually all conditions.

The relatively constant NO_2 mixing ratio in the whole height interval and the stable stratification measured at the same time indicates that the NO_2 observed during the morning flight was not produced in the area of the measurements – otherwise a strongly negative gradient would have been expected – but has been transported to the measurement site by horizontal advection. The mean wind direction, which changed from east near the ground to south in the geostrophic wind field, indicated that the air masses are mainly transported to the FZK site from the moderately polluted city of Karlsruhe and the Autobahn connecting Karlsruhe and Frankfurt.

Afternoon flight

At the second flight in the afternoon, the ascent of the balloon to a maximum ceiling of 338 m lasted from 12:50 to 13:20, and the descent back to ground level was completed at 14:00. This time the measurement procedures were well-tried, so the ascend and descent took only half an hour each, yielding a much more precise picture of the actual gradient. The meteorological conditions changed mainly in terms of stratification stability in the boundary layer: the gradient of the potential temperature now decreases with altitude, indicating a moderately labile stratification. But atmospheric turbulence did still not influence the flight behaviour of the balloon negatively.

Figure 91 and Figure 92 show the results of the afternoon flight: the NO_2 mixing ratios are still at relatively high levels of about 35 ppb within the whole height interval. The gradient observed was about 4 ppb, which is again very small compared to the Heidelberg measurements.

It can be concluded that the NO_2 mixing ratios in the boundary layer were almost constant for the whole day. Thus, the NO_2 mixing ratio above the FZK is mainly influenced by advection, while no strong sources of NO_2 are expected nearby.

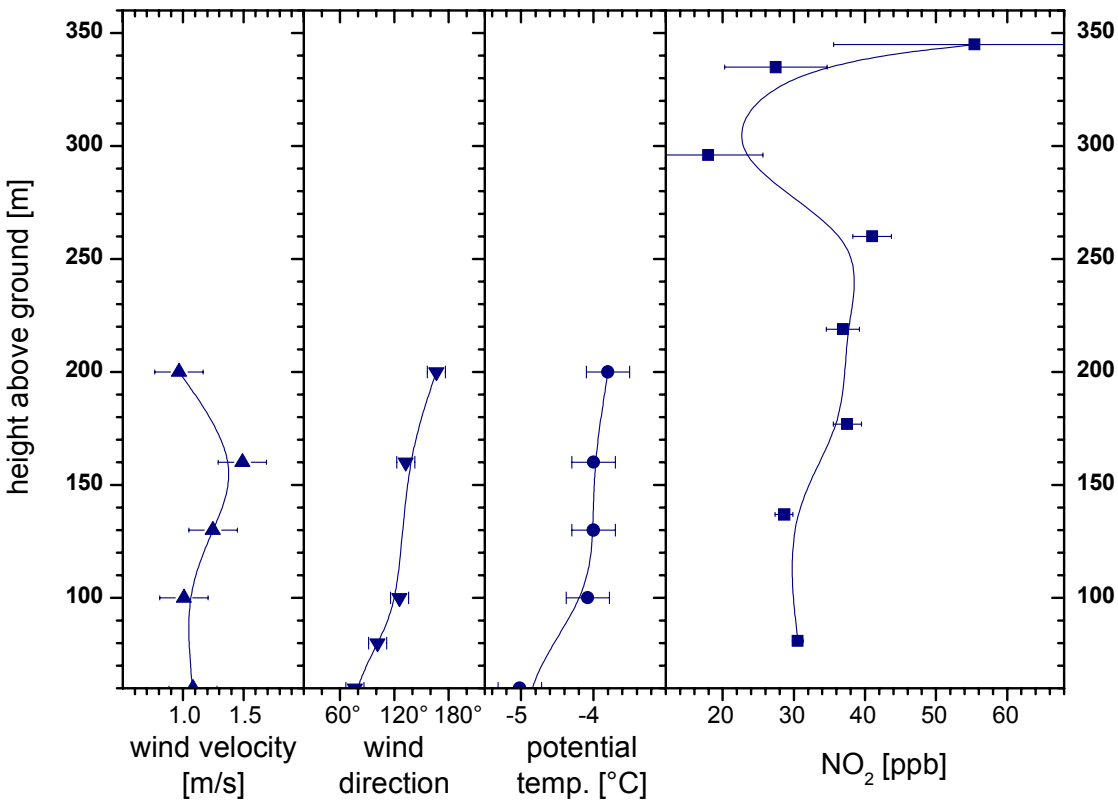

Figure 89: Profile measured during the ascent of the balloon during the morning flight with additional meteorological data measured on the mast.

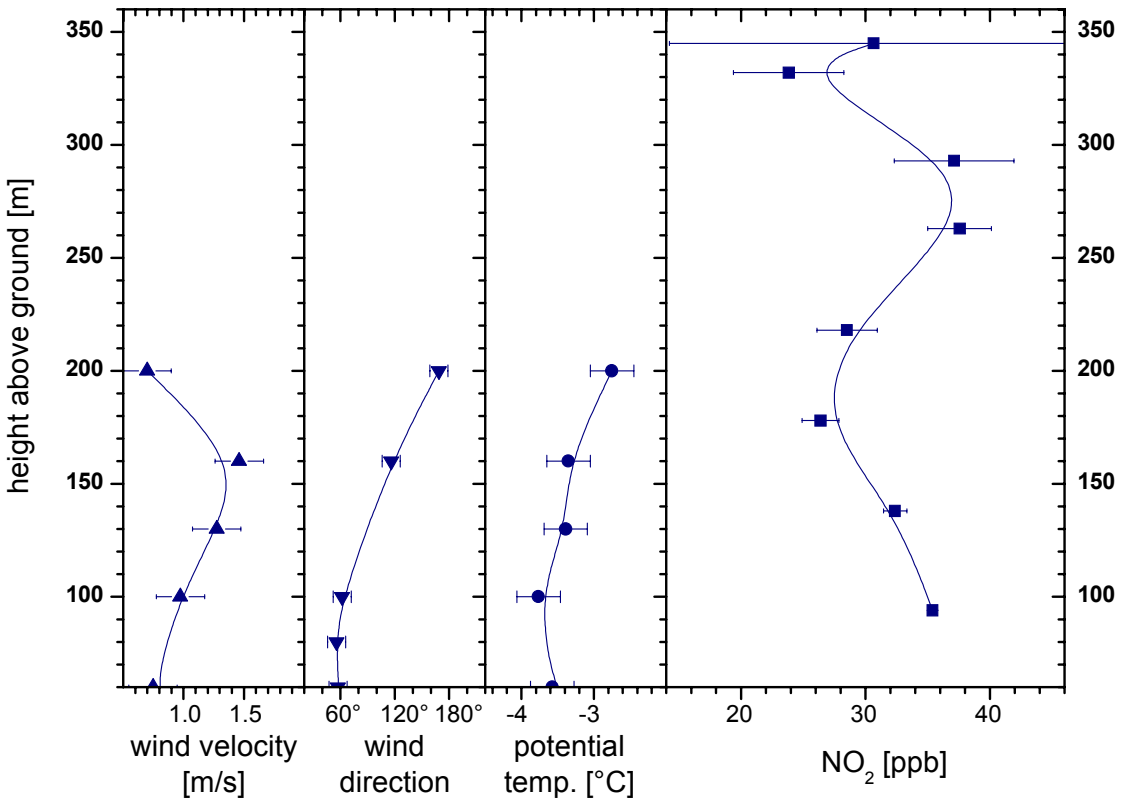

Figure 90: Profile measured during the descent of the balloon during the morning flight with additional meteorological data measured on the mast.

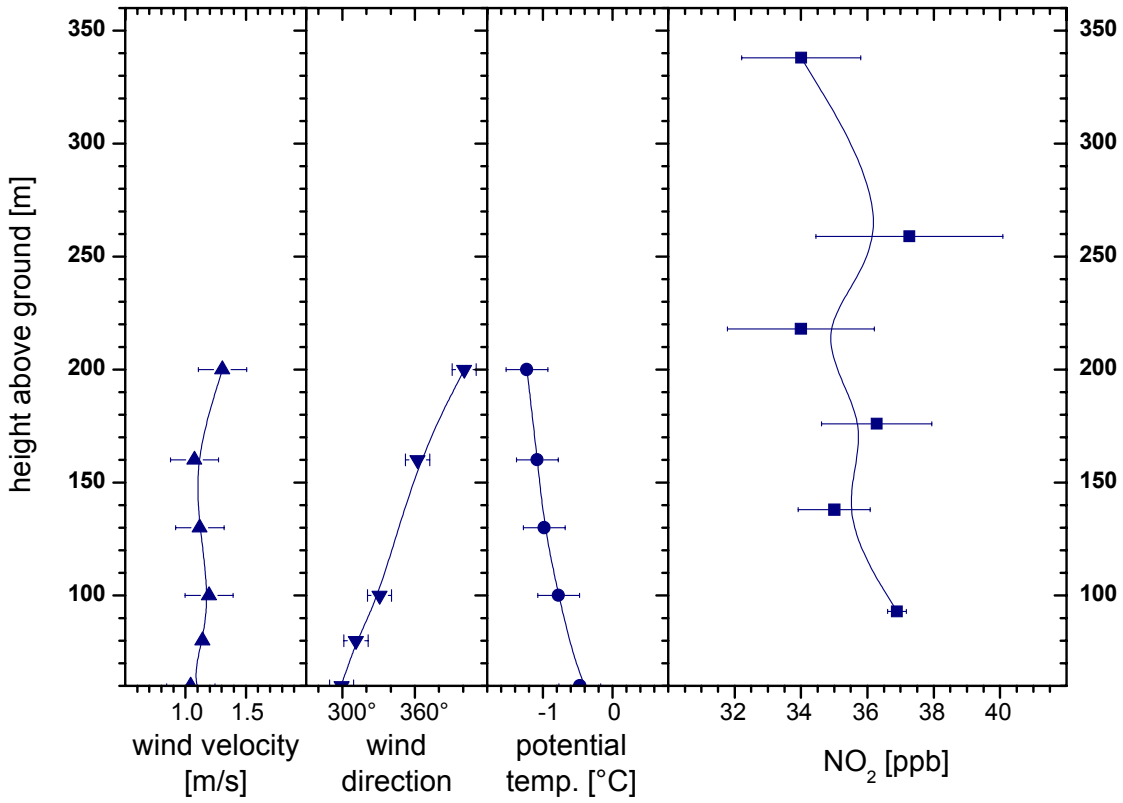

Figure 91: Profile measured during the ascent of the balloon during the afternoon flight with additional meteorological data measured on the mast.

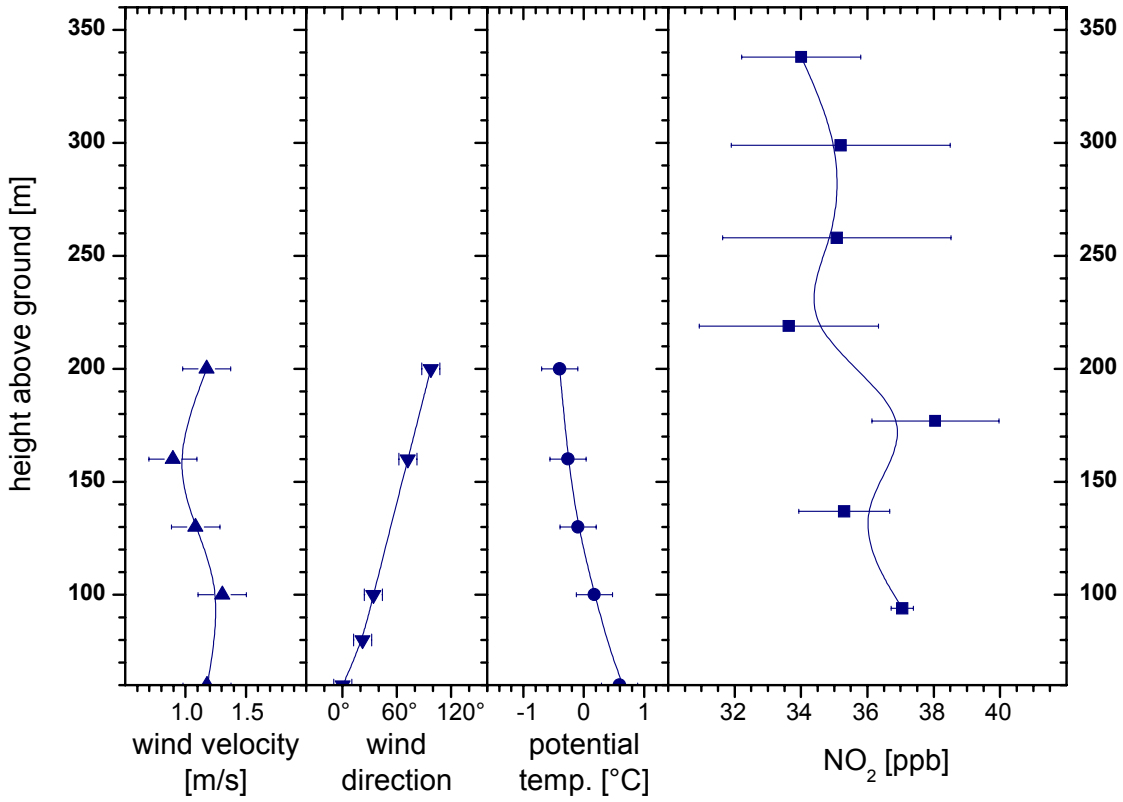

Figure 92: Profile measured during the descent of the balloon during the afternoon flight with additional meteorological data measured on the mast.

10 Conclusion and Outlook

The main subject of this thesis are measurements of vertical trace gas profiles, especially of nitrous acid (HONO) and NO_2, in the lower Planetary Boundary Layer (PBL). The measurement and analysis of such data is of major importance for the understanding of source and sink processes of anthropogenic (but also of natural) atmospheric compounds. It also helps to differentiate transport mechanisms and chemical processes that both force the concentration and the time series of all trace gasses in the PBL, a task that can hardly be accomplished with traditional point measurements.

However, the measurements and evaluation of vertical profiles for a single species can generally not provide enough information to understand its genesis and fate in the atmosphere. Especially, if one is interested in the source processes of a specific compound, data on the most prominent precursor(s) measured within the same air mass and on the same time scale are needed as well.

The active long path differential optical absorption spectroscopy (LP-DOAS) provides an excellent and proven tool for remote sensing measurements of multiple atmospheric compounds in the lower PBL. The standard application of LP-DOAS are measurements on a light path extending between a transmitter/receiver unit (the DOAS system) and a retro reflector array. The DOAS system contains the light source, the optics to transmit/receive the light beam to/from the reflectors, as well as the spectrograph and detector unit for signal analysis. Thus, the total absorption path length path is twice the distance between the DOAS and the reflectors. In most cases, the light path is more or less parallel to the ground. First vertical profile measurements using this technique were published twenty years ago, but until recently no routine profile measurements were performed with an LP-DOAS instrument, mainly due to the immense operating expenses of the quite complex systems in scientific use. Additionally, such measurements are limited to fixed height resolutions, using reflectors set up on a hillside or fixed to a mast at predefined heights. Such a set-up often lacks the flexibility needed to adapt the measurements to changing atmospheric situations in the course of the experiment.

This thesis presents a number of firsts in both the technical and the scientific aspects of vertical profile measurements. The field of application of the LP-DOAS technique has been enhanced for the long-term measurement of vertical profiles. The profiles of NO_2 and HONO obtained in the measurements at Heidelberg provide the first data set covering a full seasonal cycle of the HONO vertical profile in the lower PBL at a high time resolution. Additionally, major hardware and software improvements on the instrument used for the long-term measurements have allowed the first-ever DOAS measurements on a flexible light path to reflectors attached to a balloon.

The main aim of the long-term measurements was the scientific research of HONO source processes, while the focus during the establishment of the balloon LP-DOAS was more on the technical side. So the assessment of the achieved results will be performed separately in the following two sections.

Long-term vertical profile measurements in Heidelberg

The prototype of the semi-commercial HMT-DOAS[19] instrument, as it was available at the beginning of the work presented here, lacked the reliability and signal quality essential for routine long-term measurements on multiple light paths. Development work on the mechanical and optical components of the system has cured these problems. The kinematics of the telescope have been improved to allow a more precise alignment of the light beam

[19] Developed in cooperation with Hoffmann Meßtechnik (HMT), Rauenberg, Germany.

generated by the light source and the transmitting telescope with the reflectors. This is of major importance for the light throughput and, hence, the signal quality of the system. The switching between different reflector positions is eased by the fast tuning rates of the telescope around its horizontal and vertical axes. Thus, measurements on multiple light paths, which are required for vertical profiles, can be performed with a time resolution below 20 minutes.
Another major improvement of the telescope is the installation of a newly designed lamp shortcut system which allows the direct recording of lamp spectra. These spectra make it possible to correct the spectral structures of the lamp in the atmospheric spectra measured with the instrument precisely.

The sophisticated evaluation algorithm, including the correction of most instrument-related spectral structures, allows the evaluation of NO_2 and HONO spectra on a constant signal-to-noise level. This guarantees detection limits not achieved before with this instrument: for HONO, a mean detection limit of 90 ppt was achieved routinely on the upper light path (with a length of 8.4 km). The evaluation algorithm also ensures constantly low detection limits, even if the quality of the spectra decreased due to wear and tear of the optical components. Sensibility tests of the HONO evaluation assured that the measured HONO concentrations were not falsified by a possible offset generated by erroneous reference spectra. The low detection limits and the reliability of the evaluation algorithm proved to be of special importance for the evaluation of the daytime HONO concentrations in bright sunshine.

The long-term (13-month) campaign in Heidelberg, during which vertical profiles of NO_2 and HONO were measured, demonstrated the reliability of the HMT-DOAS instrument and the evaluation procedure. Both trace gasses were observed to feature concentrations that decrease with increasing altitude under virtually all atmospheric conditions. It was also found that the vertical gradient of HONO is always steeper than the NO_2 gradient.
The evaluation of the seasonal trend of NO_2, HONO, the ratio HONO/NO_2 and the associated relative gradients yielded the result that high HONO concentrations are primarily found at night, especially at high ambient NO_2 levels correlated with periods of high atmospheric stability. However, a distinct correlation to the aerosol concentration was not observed.
The subsequent analysis of the diurnal variations of HONO and NO_2 showed that the correlation of the time series of both compounds in the lowermost PBL does not only depend on chemistry, but is also strongly affected by stratification stability. In a stably stratified PBL featuring ineffective vertical mixing, both compounds accumulate very effectively: a HONO formation rate of ≈ 0.25 %(HONO/NO_2) h^{-1} was observed in the lower PBL. In the middle and upper PBL, however, the formation rates under stable conditions are substantially smaller: only ≈ 0.10 %(HONO/NO_2) h^{-1} are formed in or transported to these layers under such conditions. For unstable periods featuring a more effective horizontal and vertical mixing, the HONO formation rates (that include formation by chemical reactions, direct emissions and advection from the sources) are not only significantly smaller, but also less differentiated with height. This observation coincides with the fact that the HONO/NO_2 ratio, which always decreases with height, shows a much larger absolute gradient under conditions with less effective vertical mixing. These observations could also be exemplified in case studies dealing with 24-hour periods featuring stable and unstable conditions.
These findings give further strong indication that the formation of nitrous acid proceeds primarily via heterogeneous reactions on surfaces at or near the ground. This includes all surfaces present in the lower PBL, such as soil (asphalt, concrete, vegetation) and buildings or other structures. It can also be concluded that aerosol surfaces in the middle and upper PBL are only of minor importance for the formation of HONO.
However, the measurements and the evaluation presented here still have two major shortcomings. First, a quantification of the impact of chemistry and transport processes to the observed NO_2 and HONO have not been not possible, since detailed meteorological

information, especially on the 3D wind field has not been available. Second, it has not been possible to quantify the surfaces present in the upper two layers of the model. Neither have measurement data of the total aerosol surface area in the middle and upper PBL been available, nor has a precise evaluation of the effective area of the ground surface present in the middle and upper layers (since the mountain side of the Königsstuhl extended into both layers) been possible.

As a consequence of the results of this study, further HONO profile measurements should be performed on large masts/towers or to reflectors fixed at a balloon to overcome the problem generated by the ground surfaces present higher altitudes (i.e. mountain slopes). Additionally, extensive measurements of the most important meteorological parameters (3D wind speed and direction, temperature) as well as aerosol profiles should complement the trace gas measurements. Such information would not only allow a detailed analysis of the measured data, but also a comparison with modelled vertical profiles.

During the Heidelberg measurements, daytime HONO mixing ratios exceeding 100 ppt were observed regularly, even in bright sunshine. These values are substantially higher than previously reported and require a rethinking of the importance of HONO for the oxidation capacity of the polluted atmosphere. Detailed studies on this subject will be published in an oncoming PhD thesis [*Trick*, 2002].

Balloon-LP-DOAS

The adaptation of the LP-DOAS instrument for measurements to a set of reflectors fixed to a tethered balloon required the development and the integration of additional hardware and software.

The precision and speed of the telescope kinematics installed to the improved HMT-DOAS system proved to be sufficient for the tracking of the reflectors with the transmitted light beam. Yet the small-scale movement of the retro reflectors due to boundary layer turbulence raised the main problems during the development phase.

A major re-design of the quartz fibre connected to the receiving telescope was carried out to widen the field of view of the instrument. Additionally, a light level meter that assured a constant signal-to-noise ratio of the spectra was included in the quartz fibre assembly. The fibre assembly was extensively evaluated to study its characteristics, including the light transmission efficiency, and the realised field of view. The measured and simulated characteristics were found to be in perfect agreement. The increased stray light level (caused by the widened field of view) of the fibre assembly did not affect the quality of the obtained trace gas data.

With the improved LP-DOAS instrument, measurements of NO_2 vertical profiles were performed during a campaign at the Forschungszentrum (FZ) Karlsruhe. These experiments were the first ever application of the LP-DOAS technique using light paths to moving reflectors on a balloon.

The development of an automatic tracking system for routine measurements with the DOAS-balloon system was postponed because the major difficulties concerning the constant signal intensity at the spectrometer entrance had to be solved first. However, the adoption of an automatic tracking system is still under consideration, as it would ease the in-flight operation of the DOAS-balloon system even if it does not help to reduce the number of operating personnel, mainly required during launch and recovery of the balloon. The DOAS-balloon system will be used in the framework of larger field campaigns. Its application is mainly restricted by the limits for balloon operations in terms of weather conditions and flight regulations.

Literature

Ackermann, I.J., H. Hass, M. Memmesheimer, A. Ebel, F.S. Binkowski, and U. Shamar, Model Aerosol Dynamics Model for Europe: development and first applications, *Atmos. Environ.*, *32* (17), 1998.

Ackermann, R., Auswirkungen von Kraftfahrzeugemissionen in der urbanen Atmosphäre, PhD thesis, University of Heidelberg, Heidelberg, 2000.

Ahmed, M., C.J. Apps, C. Buewnel, I. Hillier, C. Hughes, N. Watt, and J.C. Whitehead, Absorption of NxOy-based molecules onlarge water clausters: an experimental and theoretical approach, *J. Phys. Chem.*, *A* (101), 1254 - 1259, 1997.

Albritton, D.L., A.L. Schmeltekopf, and R.N. Zare, An introduction to the least-squares fitting of spectroscopic data, in *Molecular Spectroscopy: Modern Research*, edited by R.K. Narahari, and M.W. Weldon, Acadamic, Orlando, Florida, 1976.

Alicke, B., The role of nitrous acid in the boundary layer, Dissertation thesis, Universität Heidelberg, Heidelberg, 2000.

Alicke, B., personal communication, 2001.

Alicke, B., A. Geyer, A. Hofzumahaus, F. Holland, S. Konrad, H.W. Pätz, J. Schäfer, J. Stutz, A. Volz-Thomas, and U. Platt, OH formation by HONO photolysis during the BERLIOZ campaign, *submitted to J. Geophys. Res.*, 2001a.

Alicke, B., U. Platt, and J. Stutz, Impact of nitrous acid photolysis on the total hydroxyl radical budget during the LOOP/PIPAPO study in Milan, *accepted for publ. by J. Geophys. Res.*, 2001b.

Ammann, M., M. Kalberer, D.T. Jost, L. Tobler, E. Rossler, D. Piguet, H.W. Gaggeler, and U. Baltensperger, Heterogeneous production of nitrous acid on soot in polluted air masses, *Nature*, *395* (6698), 157-160, 1998.

Andres-Hernandez, M.D., J. Notholt, J. Hjorth, and O. Schrems, A DOAS Study On the Origin of Nitrous Acid At Urban and Non-Urban Sites, *Atmospheric Environment*, *30* (2), 175-180, 1996.

Appel, B.R., A.M. Winer, Y. Tokiwa, and H.W. Biermann, Comparison of Atmospheric Nitrous Acid Measurements By Annular Denuder and Differential Optical Absorption Systems, *Atmospheric Environment Part a-General Topics*, *24* (3), 611-616, 1990.

Atkinson, R., A.M. Winer, and j. J. N. Pitts, Estimation of night time N2O5 concentrations from ambient NO2 and NO3 radical concentrations and the role of N2O5 in night time chemistry, *Atmos. Environ.*, *20*, 331 - 339, 1986.

Aumont, B., S. Madronich, M. Ammann, M. Kalberer, U. Baltensperger, D. Hauglustaine, and F. Brocheton, On the NO2 soot reaction in the atmosphere, *Journal of Geophysical Research*, *104* (D1), 1729-36, 1999.

Barney, W.S., and B.J. Finlayson-Pitts, Enhancement of N2O4 on porous glass at room temperature: A key intermediate in the heterogeneous hydrolysis of NO2?, *Journal of Physical Chemistry a*, *104* (2), 171 - 175, 2000.

Baumbach, G., and U. Vogt, A Tethered Balloon Measurement System for the Determination of the Spatial and Temporal Distribution of Air Pollutants like O_3, NO_2, VOC, Particles and Meteorological Parameters, *EUROTRAC Newsletter*, *16* (95), p. 23-29, 1995.

Berges, M.G.M., R.M. Hofffman, D. Scharffe, and P.J. Crutzen, Nitrous oxide emissions from motor vehicles in tunnels and their global extrapolation, *JGR*, *98*, 18527 - 18531, 1993.

Bevington, P.R., *Data reduction and error analysis for the physical sciences*, New York, 1969.

Bösch, H., Studies of the Stratospheric Nitrogen and Iodine Chemistry by Balloon-Borne DOAS Measurements and Model Calculations, Universität Heidelberg, Heidelberg, 2001.

Brauer, M., P.B. Ryan, H.H. Suh, P. Koutrakis, J.D. Spengler, N.P. Leslie, and I.H. Billick, Measurements of Nitrous Acid Inside 2 Research Houses, *Environmental Science & Technology*, *24* (10), 1521-1527, 1990.

Businger, J., Evaluation of the accuracy with which dry deposition can be measured with current micrometeorological techniques, *J. Clim. Appl. Met.*, *25*, 1100-1124, 1986.

Calvert, J.G., G. Yarwood, and A.M. Dunker, An Evaluation of the Mechanism of Nitrous Acid Formation in the Urban Atmosphere, *Research On Chemical Intermediates*, *20* (3-5), 463-502, 1994.

Carroll, M.A., and A.M. Thompson, NOx in the non-urban troposphere, in *Progress and Problems in Atmospheric Chemistry*, edited by J.R. Baker, pp. Chapter 7, World Scientific, Singapore, 1995.

Carslaw, N., L. Carpenter, J.M.C. Plane, B.J. Allan, R.A. Burgess, and K.C. Clemitshaw, Simultaneous observations of nitrate and peroxy radicals in the marine boundary layer, *JGR*, *102*, 18917 - 18933, 1997.

Chan, W.H., R.J. Nordstrom, J.G. Calvert, and J.H. Shaw, Kinetic study of HONO formation and decay reactions in gaseous mixtures of HONO, NO, NO_2, H_2O, and N_2, *Environ. Sci. Technol.*, *10*, 674-682, 1976.

Chapman, s., A Theory of Upper-Atmospheric Ozone, *Memoirs of the Royal Meteorological Society*, *Vol. III* (26), 1930.

Cheung, J.L., Q.Q. Li, J. Boniface, Q. Shi, P. Davidovits, D.R. Worsnop, J.T. Jayne, and C.E. Kolb, Heterogeneous interactions of NO2 with aqueous surface, *J. Phys. Chem. A*, *104*, 2655 - 2662, 2000.

Cox, R.A., The photolysis of gaseous nitrous acid, *J. Photochem.*, *3*, 175-188, 1974.

Crutzen, P.J., The influence of nitrogen oxides on the atmospheric ozone content, *Q. J. Roy. Meteorol. Soc.*, *96*, 320-325, 1970.

Crutzen, P.J., and P.H. Zimmermann, The changing photochemistry of the troposphere, *Tellus*, *43 AB*, 136 - 151, 1991.

Czerny, M., and A. Turner, *Z. Phys.*, *61*, 792, 1930.

DeMore, W.B., S.P. Sander, D.M. Golder, R.F. Hampson, M.J. Kurylo, C.J. Howard, A.R. Ravishankara, C.E. Kolb, and M.J. Molina, Chemical kinetics and photochemical data for use in stratospheric modeling, Jet Propulsion Laboratory, NASA National Aeronautics and Space Administration, Pasadena, California, 1997.

Dentener, F.J., and P.J. Crutzen, Reaction of N_2O_5 on tropospheric aerosols: impact on the global distributions of NO_x O_3 and OH, *J. Geophys. Res.*, *98*, 7149-7163, 1993.

EPA, National air pollutant emission trends 1990 - 1996, U.S. Environmental Protection Agency, 1997.

Eugster, W., and F. Siegrist, The influence of nocturnal CO_2 advection on CO_2 flux measurements, *Basic Appl. Ecol.*, *1*, 177-188, 2000.

Farman, J.C., B.G. Gardiner, and J.D. Shanklin, Large losses of total ozone in antarctica reveal seasonal CLO_x / NO_x interaction, *Nature*, *315*, 207-210, 1985.

Febo, A., and C. Perrino, Prediction and Experimental Evidence For High Air Concentration of Nitrous Acid in Indoor Environments, *Atmospheric Environment Part a-General Topics*, *25* (5-6), 1055-1061, 1991.

Febo, A., and C. Perrino, Measurement of High Concentration of Nitrous Acid Inside Automobiles, *Atmospheric Environment*, *29* (3), 345-351, 1995.

Febo, A., C. Perrino, and I. Allegrini, Measurement of Nitrous Acid in Milan, Italy, by DOAS and Diffusion Denuders, *Atmos. Env.*, *30* (21), 3599 - 3609, 1996.

Febo, A., C. Perrino, P. Bruno, and C. Mazziotti, FORMONA final report to the European Commission, Consiglio Nationale delle Ricerche, Rome, 1999.

Febo, A., C. Perrino, and M. Cortiello, A Denuder Technique For the Measurement of Nitrous Acid in Urban Atmospheres, *Atmospheric Environment Part a-General Topics*, *27* (11), 1721-1728, 1993.

Ferlemann, F., Ballongestützte messung atmosphärischer Spurengase mit differentieller optischer Absorptionsspektroskopie, PhD thesis, Universität Heidelberg, Heidelberg, 1998.

Fine, D.H., N-Nitroso compounds in the environment, *Adv. Environ. Sci. Technol.*, *10*, 39 - 123, 1980.

Finlayson-Pitts, B.J., and J.N. Pitts, *Chemistry of the upper and lower atmosphere : theory, experiments and applications*, xxii, 969 pp., Academic Press, San Diego, Calif. ; London, 2000.

Flatoy, F., and O. Hov, NOx from lightning and the calculated chemical composition of the free troposphere, *Journal of Geophysical Research*, *102* (D17), 21373-81, 1997.

Friedeburg, C.v., T. Wagner, A. Geyer, N. Kaiser, B. Vogel, H. Vogel, and U. Platt, Derivation of tropospheric NO_3 profiles using off-axis DOAS measurements during sunrise and comparison with simulations, *Journal of Geophysical Research*, *revised*, 2001.

Gerecke, A., A. Thielmann, L. Gutzwiller, and M.J. Rossi, The chemical kinetics of HONO formation resulting from heterogeneous interaction of NO2 with flame soot, *Geophysical Research Letters*, *25* (13), 2453-2456, 1998.

Geyer, A., Konzentrationsbestimmung des Nitratradikals und atmosphärischer Kohlenwasserstoffe mittels eines DOAS-Vielfachreflexionssystems in Heidelberg, Universität Heidelberg, Heidelberg, 1997.

Geyer, A., The role of the nitrate radical in the boundary layer, PhD thesis, Universität Heidelberg, Heidelberg, 2000.

Geyer, A., personal communication, 2001.

Geyer, A., B. Alicke, A. Hofzumahaus, F. Holland, S. Konrad, T. Klüpfel, H.-W. Pätz, D. Perner, A. Volz-Thomas, and U. Platt, Nighttime production of peroxy and hydroxyl radicals during the BERLIOZ campaign. Observations and modelling studies., *JGR*, 2000a.

Geyer, A., B. Alicke, S. Konrad, T. Schmitz, J. Stutz, and U. Platt, Chemistry and oxidation capacity of the nitrate radical in the continental boundary layer near Berlin, *JGR*, *submitted*, 2000b.

Geyer, A., B. Alicke, D. Mihelcic, J. Stutz, and U. Platt, Comparison of tropospheric NO_3 radical measurements by differential optical absorption spectroscopy and matrix isolation electron spin resonance, *Journal of Geophysical Research-Atmospheres*, *104* (D21), 26097-26105, 1999.

Geyer, A., and S. Trick, personal communication, 2002.

Gomer, T., T. Brauers, F. Heintz, J. Stutz, and U. Platt, MFC Manual, University of Heidelberg, Heidelberg, 1996.

Goodman, A.L., G.M. Underwood, and V.H. Grassian, Heterogeneous reaction of NO_2: Characterization of gas-phase and adsorbed products from the reaction, 2 NO_2 (g)+H_2O(a)-> HONO(g)+NO_3(a) on hydrated silica particles, *Journal of Physical Chemistry a*, *103* (36), 7217-7223, 1999.

Götz, F.W.P., Ergebnisse der kosmischen Physik, *Gerlands Beiträge zur Geophysik*, *Supplementbd. 1*, 180, 1931.

Hagen-Smit, A.J., E.F. Darley, M. Zaitlin, H. Hull, and W. Noble, Investigation on Injury of Plants from Air Pollution in the Los Angeles Area, *Plant Physiol.*, *27*, 18-34, 1952.

Hammeed, S., and J. Dignon, Global emissions of nitrogen and sulfur oxides in fossile fuel combustion, *J. Air Waste Manage. Assoc.*, *42*, 159 - 163, 1992.

Hanst, P.L., Air pollution measurement by fourier transform spectroscopy, *Appl. Opt.*, *17*, 1360-1366, 1978.

Harder, J.W., J.W. Brault, P.V. Johnston, and G.H. Mount, Temperature Dependent NO2 Cross Section at high Spectral Resolution, *J. Geophys. Res.*, *102* (D3), 3861 - 3879, 1997.

Harris, G.W., W.P.L. Carter, A.M. Winer, J.N. Pitts, U. Platt, and D. Perner, Observations of nitrous acid in the Los Angeles atmosphere and implications for the predictions of ozone-precursor relationships, *Environ. Sci. Technol.*, *16*, 414-419, 1982.

Harrison, R.M., and A.M.N. Kitto, Evidence For a Surface Source of Atmospheric Nitrous Acid, *Atmospheric Environment*, *28* (6), 1089-1094, 1994.

Harrison, R.M., and J.D. Peak, Measurements of concentration gradients of HNO2 and HNO3 over a semi-natural ecosystem: Discussion, *Atmospheric Environment*, *31* (17), 2891-2892, 1997.

Harrison, R.M., J.D. Peak, and G.M. Collins, Tropospheric Cycle of Nitrous Acid, *Journal of Geophysical Research-Atmospheres*, *101* (D9), 14429-14439, 1996.

Hausmann, M., U. Brandenburger, T. Brauers, and H.-P. Dorn, Simple Monte Carlo methods to estimate the spectra evaluation error in DOAS, *Applied optics*, *38* (3), 462-475, 1999.

Hermans, C., A.C. Vandaele, M. Carleer, S. Fally, R. Colin, A. Jenouvier, B. Coquart, and M.-F. Merienne, Absorption cross-sections of atmospheric Constituents: NO_2, O_2, and H_2O, *Environ. Sci. & Pollut. Res*, *6* (3), 151-158, 1999.

Hermes, T., Lichtquellen und Optik für die Differentielle Optische Absorptionsspektroskopie, Diploma thesis, University of Heidelberg, Heidelberg, 1999.

Holland, F., A. Hofzumahaus, and J. Schäfer, Measurements of OH and HO2 Radical concentrations during BERLIOZ by Laser Induced Fluorescence Spectroscopy, *submitted to J. Geophys. Res.*, 2000.

Hönninger, G., MAXDOAS: First application for boundary layer bromine oxide studies and comparison with LP-DOAS, PhD Thesis thesis, Universität Heidelberg, Heidelberg, 2001.

Howard, C.J., Kinetics of the Reaction of HO2 with NO2, *J. Chem. Phys.*, *67*, 5258-5263, 1977.

Hulst, H.C.v.d., *Light scattering by small particles*, Wiley, New York, 1957.

Jacobi, W., and K. André, The vertical distribution of radon 222, radon 220 and their decay products in the Atmosphere, *J. Geophys. Res.*, *63* (13), 3799-3814, 1963.

Jenkin, M.I., R.A. Cox, and D.J. Williams, Laboratory studies of the kinetics of formation of nitrous acid from the thermal reaction of nitrogen dioxide and water vapour, *Atmos. Environ.*, *22*, 487-498, 1988.

Johnston, H.S., Reduction of stratospheric ozone by nitrogen oxide catalysts from supersonic transportation exhaust, *Science*, *173*, 517-522, 1971.

Junkermann, W., and T. Ibusuki, FTIR Spectroscopic Measurements of Surface Bond Products of Nitrogen Oxides On Aerosol Surfaces - Implications For Heterogeneous Hno2 Production, *Atmospheric Environment Part a-General Topics*, *26* (17), 3099-3103, 1992.

Kah, O., Spektroskopische Langzeitmessung von NO_2, SO_2, O_3, HCHO und HONO in Heidelberg, Diploma thesis, Universität Heidelberg, Heidelberg, 1998.

Kaiser, E.W., and C.H. Wu, A kinetic study of the gas phase formation and decomposition reactions of nitrous acid, *J. Phys. Chem.*, *81*, 1701-1706, 1977a.

Kaiser, E.W., and C.H. Wu, Measurement of the rate constant of the reaction of nitrous acid with nitric acid, *J. Phys. Chem.*, *81*, 187-190, 1977b.

Kalberer, M., M. Ammann, F. Arens, H.W. Gaggeler, and U. Baltensperger, Heterogeneous formation of nitrous acid (HONO) on soot aerosol particles, *Journal of Geophysical Research-Atmospheres*, *104* (D11), 13825-13832, 1999.

Kessler, C., Gasfoermige salpetrige Saeure (HNO2) in der belasteten Atmosphaere, PhD thesis, University of Cologne, Cologne, 1984.

Kessler, C., and U. Platt, Nitrous acid in polluted air masses - Sources and formation pathways, in *Physio-chemical behaviour of atmosperic pollutants*, edited by B. Versino, and G. Angeletti, D. Reidel, Varese, Italia, 1984.

Keyser, L.F., S.B. Moore, and M.-T. Leu, Surface reaction and pore diffusion in flow tube reactors, *J. of Phys. Chem.*, *95*, 5496 - 5502, 1991.

Killus, J.P., and G.Z. Whitten, Behavior of trace NOx species in the nighttime urban atmosphere, *J. Geophys. Res.*, *90*, 2430-2432, 1985.

Kirchstetter, T.W., R.A. Harley, and D. Littlejohn, Measurement of Nitrous Acid in Motor Vehicle Exhaust, *Environmental Science & Technology*, *30* (9), 2843 - 2849, 1996.

Kleffmann, Heterogene Umwandlung von Stickoxiden an sauren Oberflächen, PhD thesis, University of Wuppertal, Wuppertal, 1998.

Kleffmann, J., K.H. Becker, and P. Wiesen, Heterogeneous NO_2 conversion processes on acid surfaces: possible atmospheric implications, *Atmos. Environm.*, *32*, 2721 - 2729, 1998.

Kleffmann, J., R. Kurtenbach, and P. Wiesen, Surface catalysed conversion of NO_2into HONO and N_2O: a new source of atmospheric N_2O?, in *Impact of Emissions from aircraft and Spacecraft upon the Atmosphere*, pp. 146-157, Porz-Wahnheide, Cologne, Germany, 1994.

Knoll, P., R. Singer, and W. Kiefer, Improving spectroscopic techniques by a scanning multichannel method, *Apl. Spectr.*, *44*, 776 - 782, 1990.

Kraus, A., and A. Hofzumahaus, Field measurements of atmospheric photolysis frequencies for O-3, NO2, HCHO, CH3CHO, H2O2, and HONO by UV spectroradiometry, *Journal of Atmospheric Chemistry*, *31* (1-2), 161-180, 1998.

Kraus, S., DOASIS, Institut für Umweltphysik, Universität Heidelberg, Heidelberg, 2001.

Kurtenbach, R., K.H. Becker, J.A.G. Gomes, J. Kleffmann, J.C. Lörzer, M. Spittler, P. Wiesen, R. Ackermann, A. Geyer, and U. Platt, Investigations of emissions and

heterogeneous formation of HONO in a road traffic tunnel, *Atmospheric Environment*, *35*, 3385-3394, 2001.

Lammel, G., A Doas Study On the Origin of Nitrous Acid At Urban and Non-Urban Sites - Comment, *Atmospheric Environment*, *30* (23), 4101-4103, 1996.

Lammel, G., and J.N. Cape, Nitrous acid and nitrite in the atmosphere, *Chemical Society Reviews*, *25* (5), 361+, 1996.

Lammel, G., and D. Perner, The atmospheric aerosol as a source of nitrous acid in the polluted atmosphere, *J. Aerosol Sci.*, *19*, 1199-1202, 1988.

Lee, J.H., and I.N. Tang, Accommodation coefficient of gaseous NO2 on water surfaces, *Atmos. Environ.*, *22*, 1147 -1151, 1988.

Leighton, P.A., Photochemistry of air pollution, *Academic Press, New York*, 1961.

Lenner, M., Nitrogen dioxide in exhaust from motor vehicles, *Atmos. Environ.*, *27*, 1673 - 1690, 1987.

Levenberg, K., A method for the solution of certain non-linear problems in least squares, *Quart. Appl. Math*, *2*, 164 - 168, 1944.

Levin, I., personal communication, 1999-2001.

Levin, I., M. Born, M. Cuntz, U. Langendörfer, S. Mantsch, T. Naegler, M. Schmidt, A. Varlagin, S. Verclas, and D. Wagenbach, Observations of atmospheric variability and soil exhalation rate of Radon-222 at Russian forest site: Technical approach and deployment for boundary layer sites, *submitted to Tellus*, *54B*, 2002.

Levy, H., J.D. Mahlman, and W.J. Moxim, A stratospheric source of reactive nitrogen in the unpolluted troposphere, *Geophys. Res. Let.*, *7*, 441 - 444, 1980.

LINOS, *Katalog*, LINOS Photonics GmbH, Göttingen, 2000.

Logan, J.A., Nitrogen Oxides in the troposphere: global and regional budgets, *J. Geophys. Res.*, *88* (C15), 10785 - 10807, 1983.

Logan, J.I., M.J. Prather, S.C. Wofsy, and M.B. McElroy, Tropospheric Chemistry: A Global Perspective, *JGR*, *86* (C8), 7210 - 7254, 1981.

Longfellow, C.A., T. Imamura, A.R. Ravishankara, and D.R. Hanson, HONO solubility and heterogeneous reactivity on sulfuric acid surfaces, *Journal of Physical Chemistry a*, *102* (19), 3323-3332, 1998.

Lösch, J., Bestimmung von NO_2- und SO_2- Emissionen von Kraftfahrzeugen mittels DOAS-Tomographie, Diploma thesis, Universität Heidelberg, Heidelberg, 2001.

Marquardt, D.W., An algorithm for least squares estimation of non-linear parameters, *J. Soc. Indust. Appl. Math.*, *11*, 431 - 441, 1963.

Mebel, A.M., M.C. Lin, and C.F. Melius, Rate constant of the HONO+HONO->H_2O+NO+NO_2 reaction from ab initio MO and TST calculations, *Journal of Physical Chemistry a*, *102* (10), 1803-1807, 1998.

Meller, R., and G.K. Moortgat, Temperature dependence of the absorption cross sections of formaldehyde between 223 and 323 K in the wavelength range 225 - 375 nm, *JGR*, *201* (D6), 7089 - 7101, 2000.

Mentel, T.F., D. Bleilebens, and A. Wahner, A study of nitrogen oxide oxidation in a large reaction chamber- The fate of NO_2, N_2O_5, HNO_3 and O_3 at different humidities, *Atmos. Environ.*, *30*, 4007-4020, 1996.

Mertes, S., and A. Wahner, Uptake of nitrogen dioxide and nitrous acid on aqueous surfaces, *J. Phys. Chem.*, *99*, 14000 - 14006, 1995.

Middleton, J.T., J.B.K. jr., and H.W. Schwalm, Injury to herbaceous plants by smog or air pollution, *U.S.D.A. Plant Dis. Rep.*, *34*, 245 - 252, 1950.

Mihelcic, D., D. Klemp, P. Musgen, H.W. Patz, and A. Volz-Thomas, Simultaneous Measurements of Peroxy and Nitrate Radicals At Schauinsland, *Journal of Atmospheric Chemistry*, *16* (4), 313-335, 1993.

Mößner, M., Vertikalprofilmessungen mittels differentieller optischer Absorptionsspektroskopie, Diploma thesis, Universität Heidelberg, Heidelberg, 1999.

Müller, J.-F., Geographical distribution and seasonal variation of surface emissions and deposition velocities of atmospheric trace gases, *JGR*, *97*, 3787 - 3804, 1992.

Nash, T., Nitrous acid in the atmosphere and laboratory experiments on its photolysis, *Tellus*, *26*, 175-179, 1974.

Nazaroff, W.W., Radon transport from soil to air, *Rewiews of Geophysics*, *30*, 137-160, 1992.

Neftel, A., A. Blatter, R. Hesterberg, and T. Staffelbach, Measurements of Concentration Gradients of HNO2 and HNO3 Over a Semi-Natural Ecosystem, *Atmospheric Environment*, *30* (17), 3017-3025, 1996.

Nguyen, M.T., R. Sumathi, D. Sengupta, and J. Peeters, Theoretical analysis of reactions related to the HNO2 energy surface: OH+NO and H+NO2, *Chemical Physics*, *230* (1), 1-11, 1998.

Nielsen, T., K. Plinegaard, A.H. Egelov, K. Granby, P. Hummelshoj, N.O. Jensen, and H. Skov, Atmospheric nitrogen compounds: occurence, composition and deposition, *Sci. Total. Environ.*, *189/190*, 459-465, 1996.

Notholt, J., J. Hjorth, and F. Raes, Long Path Field Measurements of Aerosol Parameters and Trace Gas Concentrations - Formation of Nitrous Acid During Foggy Periods, *Journal of Aerosol Science*, *22* (S1), S411-S414, 1991.

Notholt, J., J. Hjorth, and F. Raes, Formation of HNO2 on aerosol surfaces during foggy periods in the presence of NO and NO2, *Atmos. Environ.*, *26A*, 211-217, 1992.

Pagsberg, P., E. Bjergbakke, E. Ratajczak, and A. Sillesen, Kinetics of the gas phase reaction OH+NO(+M)->HONO(+M) and the determination of the UV absorption cross sections of HONO, *Chemical Physics Letters*, *272* (5-6), 383-390, 1997.

Parrish, D.D., M. Trainer, E.J. Williams, D.W. Fahey, G. Hübler, C.S. Eubank, S.C. Liu, P.C. Murphy, D.L. Albritton, and F.C. Fehsenfeld, Measurements of the NOx-O3 photostationary sate at niwot ridge, Colorado, *JGR*, *91*, 5361 - 5370, 1986.

Perner, D., *HNO_2 in urban atmospheres and its photochemical significance*, 159-173 pp., UBA, 1980.

Perner, D., D.H. Ehhalt, H.W. Paetz, U. Platt, E.P. Roeth, and A. Volz, OH radicals in the lower troposphere, *Geophys. Res. Lett.*, *3*, 466 - 468, 1976.

Perner, D., C. Kessler, and U. Platt, HNO_2, NO_2 and NO measurements in automobile engine exhaust by optical absorption, 1985.

Perner, D., and U. Platt, Detection of nitrous acid in the atmosphere by differential optical absorption, *Geophys. Res. Lett.*, *6*, 917-920, 1979.

Pitts, J.N., H.W. Biermann, A.M. Winer, and E.C. Tuazon, Spectroscopic identification and measurement of gaseous nitrous acid in dilute auto exhaust, *Atmos. Environ.*, *18*, 847-854, 1984a.

Pitts, J.N., E. Sanhueza, R. Atkinson, W.P.L. Carter, A.M. Winer, G.W. Harris, and C.N. Plum, An investigation of the dark formation of nitrous acid in environmental chambers, *Int. J. Chem. Kinet.*, *XVI*, 919-939, 1984b.

Pitts, J.N.j., H.W. Biermann, R. Atkinson, and A.M. Winer, Atmospheric implications of simultaneous nighttime measurements of NO3 radicals and HONO, *Geophys. Res. Let.*, *11*, 557 - 560, 1984c.

Pitts, J.N.j., D. Grosjean, K.v. Cauwenberghe, J.P. Schmid, and D.R. Fitz, Photooxidation of aliphatic amines under sumulated atmospheric conditions: Formation of nitrosamines, nitramines, amides and photochemical oxidant, *Env. Science & Technology*, *12* (8), 946 - 953, 1978.

Platt, U., Dry deposition of SO_2, *Atmos. Environ.*, *12*, 363 - 367, 1978.

Platt, U., *The origin of nitrous and nitric acid in the atmosphere*, 299-319 pp., Springer Verlag, 1986.

Platt, U., Differential Optical Absorption Spectroscopy (DOAS), in *Monitoring by Spectroscopic Techniques*, M. W. Sigrist, J. Wiley, New York, 1994.

Platt, U., G. Lebras, G. Poulet, J.P. Burrows, and G. Moortgat, Peroxy Radicals From Night-Time Reaction of NO3 With Organic Compounds, *Nature*, *348* (6297), 147-149, 1990.

Platt, U., and D. Perner, Direct measurements of atmospheric CH_2O, HNO_2, O_3, NO_2, and SO_2 by differential optical absorption in the near UV, *J. Geophys. Res.*, *85*, 7453-7458, 1980.

Platt, U., D. Perner, G.W. Harris, A.M. Winer, and J.N. Pitts, Observations of nitrous acid in an urban atmosphere by differential optical absorption, *Nature*, *285*, 312-314, 1980.

Platt, U., D. Perner, and H.W. Pätz, Simultaneous measurements of atmospheric CH_2O, O_3 and NO_2 by differential optical absorption, *J. Geophys. Res.*, *84*, 6329 - 6335, 1979.

Pötzsch, S., Entwicklung von miniaturisierten Verfahren zur Analyse von Carbonsäuren in unterschiedlichen atmosphärischen Phasen, PhD thesis, Technische Universität Darmstadt, Darmstadt, 2001.

Pötzsch, S., and K. Bächmann, Determination of Formic and Acetic Acid in Ambient Air Using a Microdenuder Sampling Technique and Subsequent Analysis by Capillary Electrophoresis, *Environmental Science and Pollution research*, *submitted*, 2002.

Price, C., J. Penner, and M. Prather, NOx from lightning. 1. Global distribution based on lightning physics, *Journal of Geophysical Research*, *102* (D5), 5929-41, 1997a.

Price, C., J. Penner, and M. Prather, NOx from lightning. 2. Constraints from the global atmospheric electric circuit, *Journal of Geophysical Research*, *102* (D5), 5943-51, 1997b.

Regener, E., and V. Regener, *Physikalische Zeitschriften*, *35*, 788, 1935.

Reisinger, A.R., Observations of HNO_2 in the polluted winter atmosphere: possible heterogeneous production on aerosols, *Atmospheric Environment*, *34*, 3864-3874, 2000.

Riegl, *Bedienungshandbuch Entfernungsmessgerät LASERTAPE FG21-HA*, Riegl GmbH, Horn, Austria, 1998.

Rityn, N.E., Optics of corner cube reflectors, *Opt. Tech.*, *34*, 198-201, 1967.

Roedel, W., *Physik unserer Umwelt: Die Atmosphäre*, Springer Verlag, Berlin Heidelberg New York, 1994.

Rondon, A., and E. Sanhueza, High HONO atmospheric concentrations during vegetation burning in the tropical savannah, *Tellus*, *41B*, 474-477, 1988.

Rudolf, T., Beschreibung und Charakterisierung einerLang-Pfad-DOAS-Apparatur und eine Analyse des Auswerteverfahrens, Diplomarbeit thesis, Universität Heidelberg, Heidelberg, 1993.

Russell, A.G., D.A. Winner, R.A. Herley, K.F. McCue, and G.R. Cass, Mathematical moedlling and control of the dry deposition flux of nitrogen-containing air pollutants, *Environ. Sci. Technol.*, *27*, 2772-2782, 1993.

Sakamaki, F., S. Hatakeyama, and H. Akimoto, Formation of nitrous acid and nitric oxide in the heterogeneous dark reaction of nitrogen dioxide and water vapor in a smog chamber, *Int. J. Chem. Kinet.*, *XV*, 1013-1029, 1983.

Schmieder, R.W., Operator Formulation of Plane Mirror Systems, *Applied Optics*, *6* (3), 537-544, 1967.

Schurath, U., personal communication, 2000.

Schurath, U., K. Heinrich, H. Lippmann, and W. Wendler, Untersuchungen zur Entwicklung eines chemischen Reaktionsmodells atmosphärischer Spurengas-Umsetzungen (Teil I), pp. Forschungsbericht 81-10402 511/02, Umweltforschungsplan des BMI, Luftreinhaltung, 1983.

Schwartz, S.E., and W. White, *Kinetics of the reactive dissolution of the nitrogen oxides and oxyacides in aqueous solution*, Brookhaven Nat. Lab., 1981.

Seinfeld, J.H., and S.N. Pandis, *Atmospheric chemistry and physics: From air pollution to climate change*, John Wiley & Sons Inc., New York Chichester Weinheim Brisbane Singapore Toronto, 1998.

Sjödin, A., Studies of the diurnal variation of nitrous acid in urban air, *Environ. Sci. Technol.*, *22*, 1086-1089, 1988.

Sjödin, A., and M. Ferm, Measurements of nitrous acid in an urban area, *Atmos. Environ.*, *19*, 985-992, 1985.

Spindler, G., E. Brüggemann, and H. Herrmann, Nitrous acid concentration measurements and estimation of dry deposition over grassland in Eastern Germany, *to be submitted*, 2000.

Stockwell, W.R., and J. Calvert, The mechanism of NO3 and HONO formation in the nighttime chemistry of the urban atmosphere, *J. Geophys. Res.*, *88*, 6673-6682, 1983.

Streit, N., E. Weingartner, S. Nyeki, A.S.H. Prevot, U. Baltensperger, R.v. Dingenen, J.-P. Putaud, A. Even, H.t. Brink, A. Blatter, A. Neftel, and H.W. Gäggler, Secondary aerosol characterization during summer smog events, *submitted to JGR*, 2000.

Stuhl, F., and H. Niki, Flash Photochemical Study of the Reaction OH + NO + M Using Resonance Fluorescent Detection of OH, *J. Chem. Phys.*, *57* (9), 3677 - 3679, 1972.

Stull, R.B., *An introduction to boundary layer meteorology*, Kluwer Academic Publishers, Dordrecht Boston London, 1988.

Stutz, J., Charakterisierung von Photodiodenzeilen zur Messung stratosphärischer Spurenstoffe, Diplima thesis, University of Heidelberg, Heidelberg, 1991.

Stutz, J., Messung der Konzentration troposphärischer Spurenstoffe mittels Differentieller Optischer Absorptionspektroskopie: Eine neue Generation von Geräten und Algorithmen, PhD thesis, Universität Heidelberg, Heidelberg, 1996.

Stutz, J., personal communication, 2001.

Stutz, J., B. Alicke, and A. Neftel, Nitrous acid formation in the urban atmosphere: Gradient measurements of NO_2 and HONO over grass in Milan, Italy, *J. Geophys. Res.*, *accepted for publ.*, 2001.

Stutz, J., E.S. Kim, U. Platt, P. Bruno, C. Perrino, and A. Febo, UV-visible absorption cross section of nitrous acid, *J. Geophys. Res.*, *105* (D11), 14585 - 14592, 2000.

Stutz, J., and U. Platt, Problems in using diode arrays for open path DOAS measurements of atmospheric species, in *Proc. EOS/SPIE Symp.*, pp. 329 - 340, Optical Methods in the Atmospheric Chemistry, Berlin, 1992.

Stutz, J., and U. Platt, Numerical analysis and estimation of the statistical error of differential optical absorption spectroscopy measurements with least-squares methods, *Applied Optics*, *35* (30), 6041-53, 1996.

Stutz, J., and U. Platt, Improving long-path differential optical absorption spectroscopy with a quartz-fiber mode mixer, *Applied Optics*, *36* (6), 1105-15, 1997.

Svensson, R., E. Ljungström, and O. Lindqvist, Kinetics of the reaction between nitrogen dioxide and water vapour, *Atmos. Environ.*, *21*, 1529-1539, 1987.

Taylor, J.K., *Statistical techniques for data analysis*, Lewis Publishers, 1990.

TenBrink, H.M., and H. Spoelstra, The dark decay of HONO in environmental (SMOG) chambers, *Atmospheric Environment*, *32* (2), 247-251, 1998.

Trick, S., Das Bildungspotential salpetriger Säure (HONO) an städtischen Oberflächen, diploma thesis, Heidelberg, Heidelberg, 2000.

Trick, S., personal communication, 2001.

Trick, S., , Institut für Umweltphysik, 2002.

Trick, S., and A. Geyer, personal communication, 2002.

Trick, S., A. Geyer, A. Alicke, and U. Platt, Effective HONO formation potential on asphalt streets, *in preparation*, 2002.

Tyndall, G.S., J.J. Orlando, and J.G. Calvert, Upper Limit For the Rate Coefficient For the Reaction HO2+NO2->HONO+O2, *Environmental Science & Technology*, *29* (1), 202-206, 1995.

UMEG, Jahresbericht 1999, pp. 1-119, Gesellschaft für Umweltmessungen und Umwelterhebungen mbH, Karlsruhe, 1999.

UMEG, personal communication, 1999-2001.

Veitel, H., Messung atmosphärischer Photonenweglängen für verschiedene meteorologische Situationen, Diploma thesis, Univerität Heidelberg, Heidelberg, 1997.

Vogel, B., F. Fiedler, and H. Vogel, Influence of topography and biogenic volatile organinc compound emissions in the state of Baden-Württemberg on ozone concentrations during episodes of high air temperatures, *J. Geophys. Res.*, *100* (D11), 22907-22928, 1995.

Vogel, B., H. Vogel, J. Kleffmann, and R. Kurtenbach, Quantification of the sources of HONO in the planetary boundary layer by numerical simulations, in *Eurotrac Symposium*, Garmisch-Partenkirchen, 2002.

Voigt, S., J. Orphal, K. Bogumil, and J.P. Burrows, The temperature dependence (203-293 K) of the absorption cross sections of O_3 in the 230-850 nm region measured by Fourier-transform spectroscopy, *J. Photochem and Photobiol. A*, *143*, 1-9, 2001a.

Voigt, S., J. Orphal, and J.P. Burrows, High-resolution reference data by UV-Visible Fourier-transform spectroscopy: Absorption cross sections of NO_2 in the 250-800 nm range at atmospheric temperatures (223-293 K) and pressures (100-1000 mbar), *in preparation for J. Photochem and Photobiol. A*, 2001b.

Volkamer, R., Absorption von Sauerstoff im Herzberg I System und Anwendung auf Aromatenmessungen am European Photo Reaktor (EUPHORE), Diploma thesis, Universität Heidelberg, Heidelberg, 1996.

Wayne, L.G., and D.M. Yost, *J. Chem. Phys.*, *19*, 41, 1951.

Westenberg, A.A., and N. DeHaas, Rate measurements on OH + NO +M and OH + NO2 +M, *J. Chem. Phys.*, *57* (12), 5375 - 5378, 1972.

White, J.U., Long Optical Paths of Large Aperture, *J. Opt. Soc. Am.*, *Vol. 32*, 1942.

White, J.U., Very Long Optical Paths in Air, *J. Opt Soc. Am.*, *66* (5), 1976.

Wild, J., D. Kley, A. Rockel, P. Rockel, and H.J. Segschneider, Emission of NO from several higher plant species, *JGR*, *102*, 5919 - 5927, 1997.

Winer, A.M., and H.W. Biermann, *Measurements of nitrous acid, nitrate radicals, formaldehyde and nitrogen dioxide for the Southern California Air Quality Study by differential optical absorption spectroscopy : final report*, 1 v. (various pagings) pp., Statewide Air Pollution Research Center University of California, Riverside, Calif., 1989.

Winer, A.M., and H.W. Biermann, Long Pathlength Differential Optical Absorption Spectroscopy (Doas) Measurements of Gaseous Hono, NO2 and HCHO in the California South Coast Air Basin, *Research On Chemical Intermediates*, *20* (3-5), 423-445, 1994.

Zabarnick, S., Kinetics of the Reaction OH+NO+M->HONO+M as a Function of Temperature and Pressure in the Presence of Argon, SF6, and N2 Bath Gas, *Chemical Physics*, *171* (1-2), 265-273, 1993.

Annex A: Heidelberg long-term profile data

Table 34: Mean detection limits and residuals for the trace gas evaluation with respect to NO_2 HONO and HCHO on the three light paths of the Heidelberg long-term measurements.

period		detection limits [ppb]									residual [‰]		
		NO_2			HONO			HCHO					
light path		1	2	3	1	2	3	1	2	3	1	2	3
Jan/Feb 1999	16.01.-23.02.1999	0.29	0.20	0.17	0.15	0.10	0.09	1.5	1.0	0.9	1.85	1.74	1.97
Mar/Apr 1999	16.03.-17.04.1999	0.32	0.22	0.19	0.17	0.12	0.10	1.7	1.2	1.0	2.51	1.79	2.58
Apr/May 1999	13.04.-14.05.1999	0.40	0.25	0.17	0.21	0.14	0.09	2.1	1.3	0.93	1.94	2.39	1.72
August 1999	30.07.-31.08.1999	0.37	0.24	0.19	0.21	0.13	0.11	2.0	1.3	1.2	2.07	1.93	2.23
September 1999	01.-30.09.1999	0.31	0.23	0.2	0.17	0.13	0.10	1.6	1.2	1.0	1.67	1.74	2.01
October 1999	01.-31.10.1999	0.36	0.22	0.16	0.20	0.12	0.09	1.8	1.2	0.8	1.93	1.71	1.65
November 1999	01.-31.11.1999	0.36	0.22	0.17	0.20	0.12	0.09	1.9	1.2	0.9	1.89	1.68	1.79
December 1999	01.29.12.1999	0.43	0.26	0.19	0.21	0.13	0.10	2.1	1.3	0.9	2.06	1.79	1.82
February 2000	03.-28.02.2000	0.36	0.22	0.17	0.20	0.12	0.09	1.9	1.2	0.9	1.59	1.55	1.62

January / February 1999

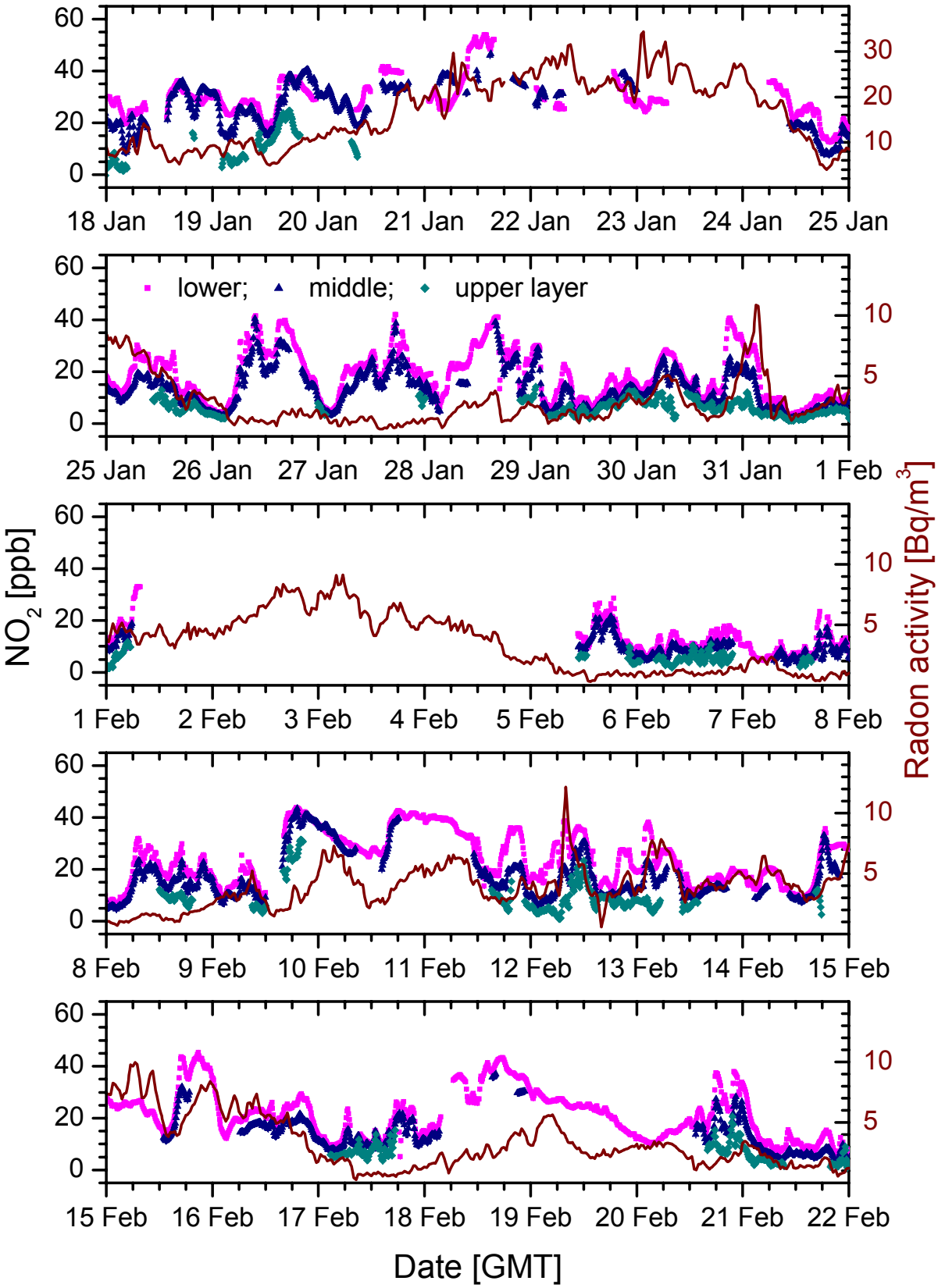

Figure 93: Time series of the NO_2 profiles in January / February 1999

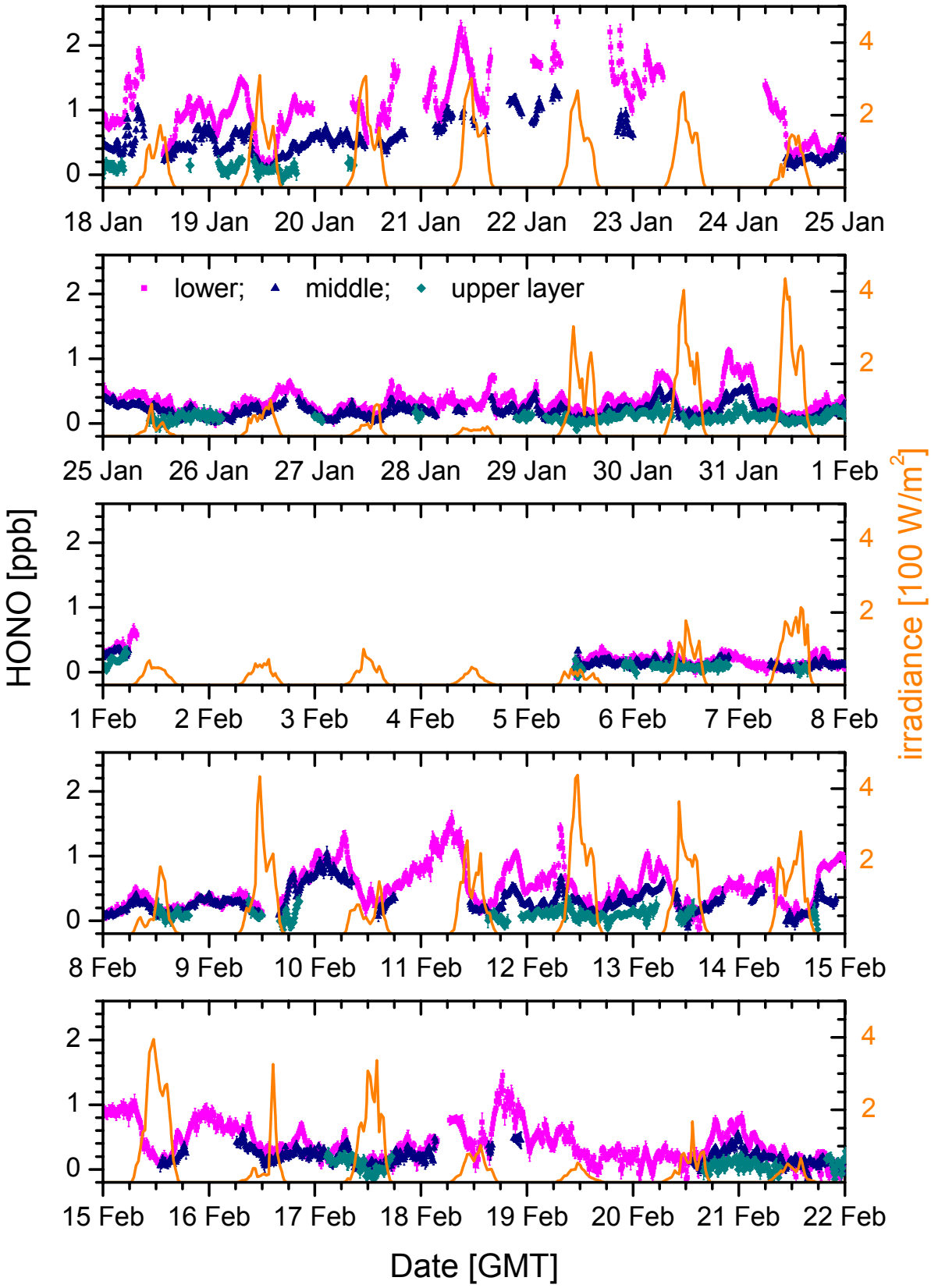

Figure 94: Time series of the HONO profiles in January / February 1999

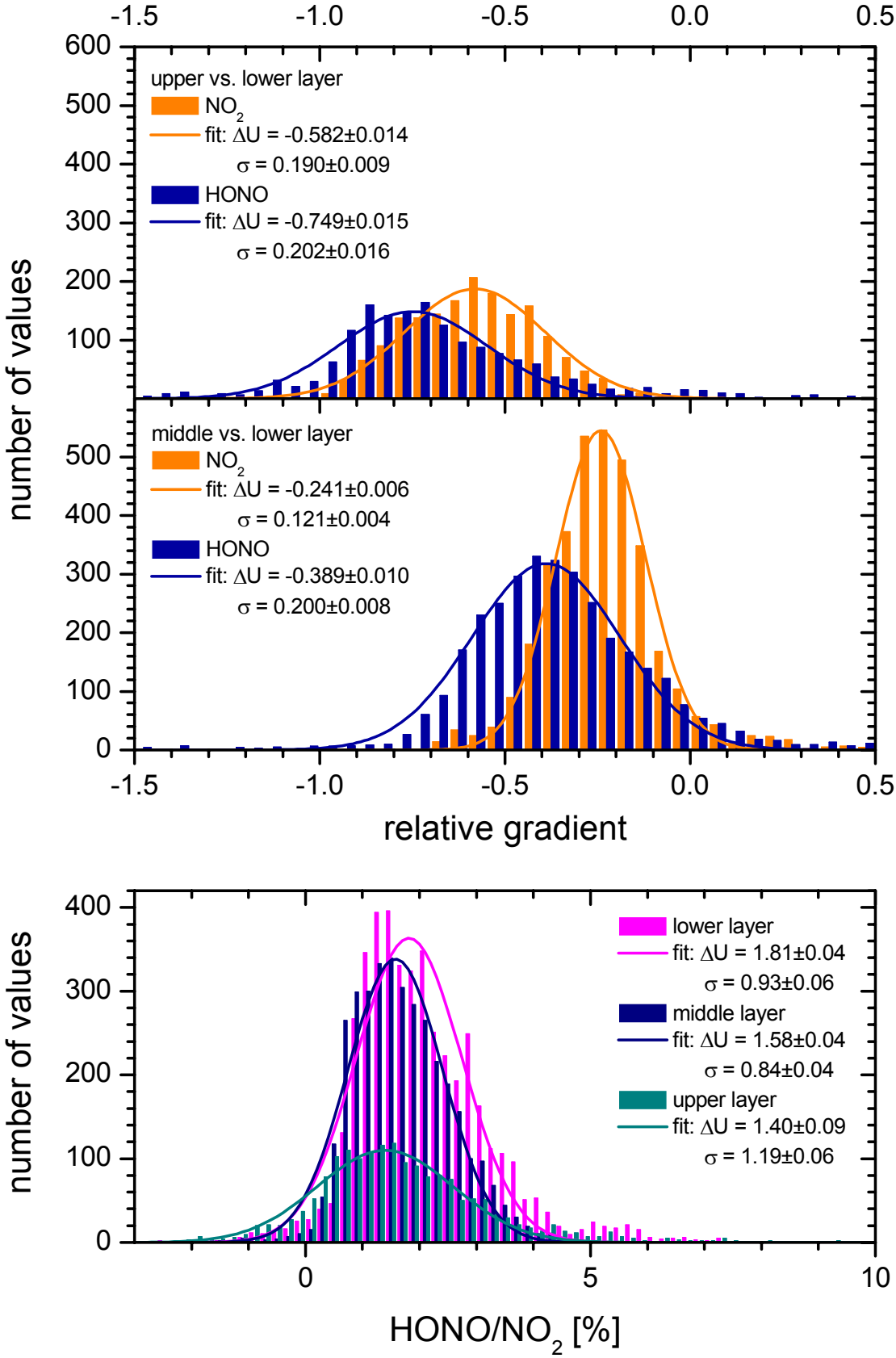

Figure 95: Frequency analysis of the relative gradients and HONO/NO_2 ratios in January / February 1999

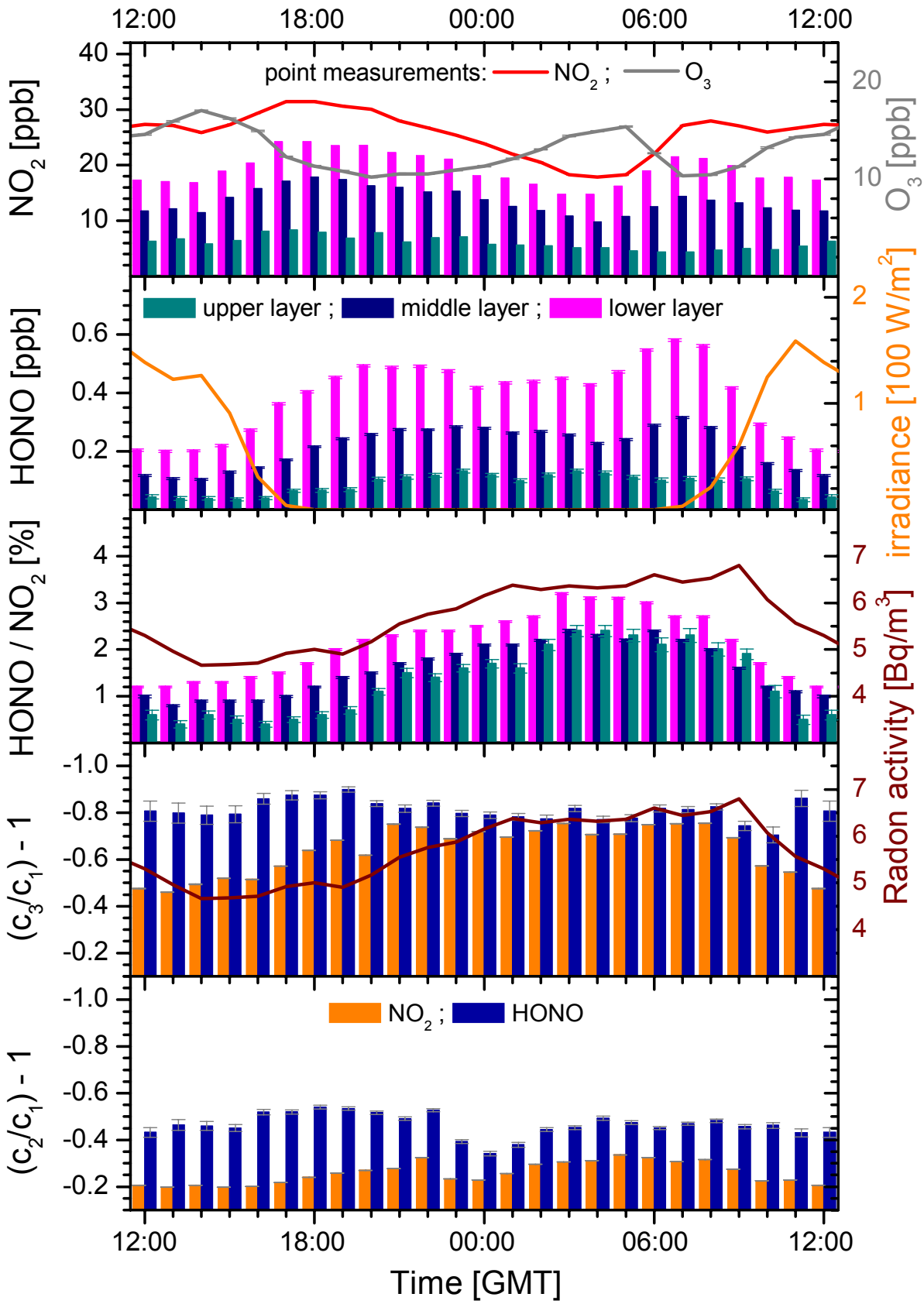

Figure 96: Hourly means of the NO_2 and HONO time series, the HONO/NO_2 ratios and the gradients in January / February 1999

March / April 1999

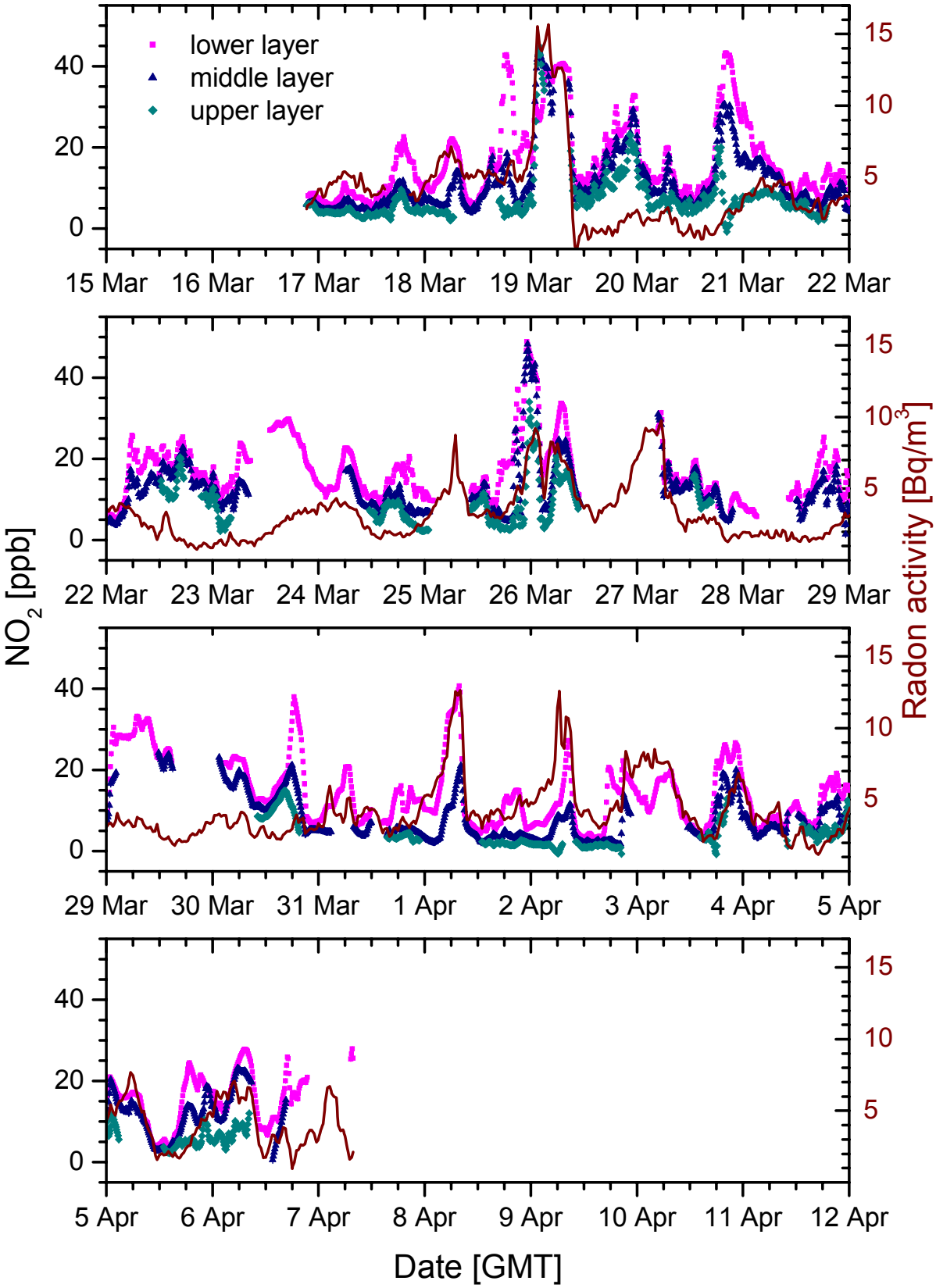

Figure 97: Time series of the NO_2 profiles in March / April 1999

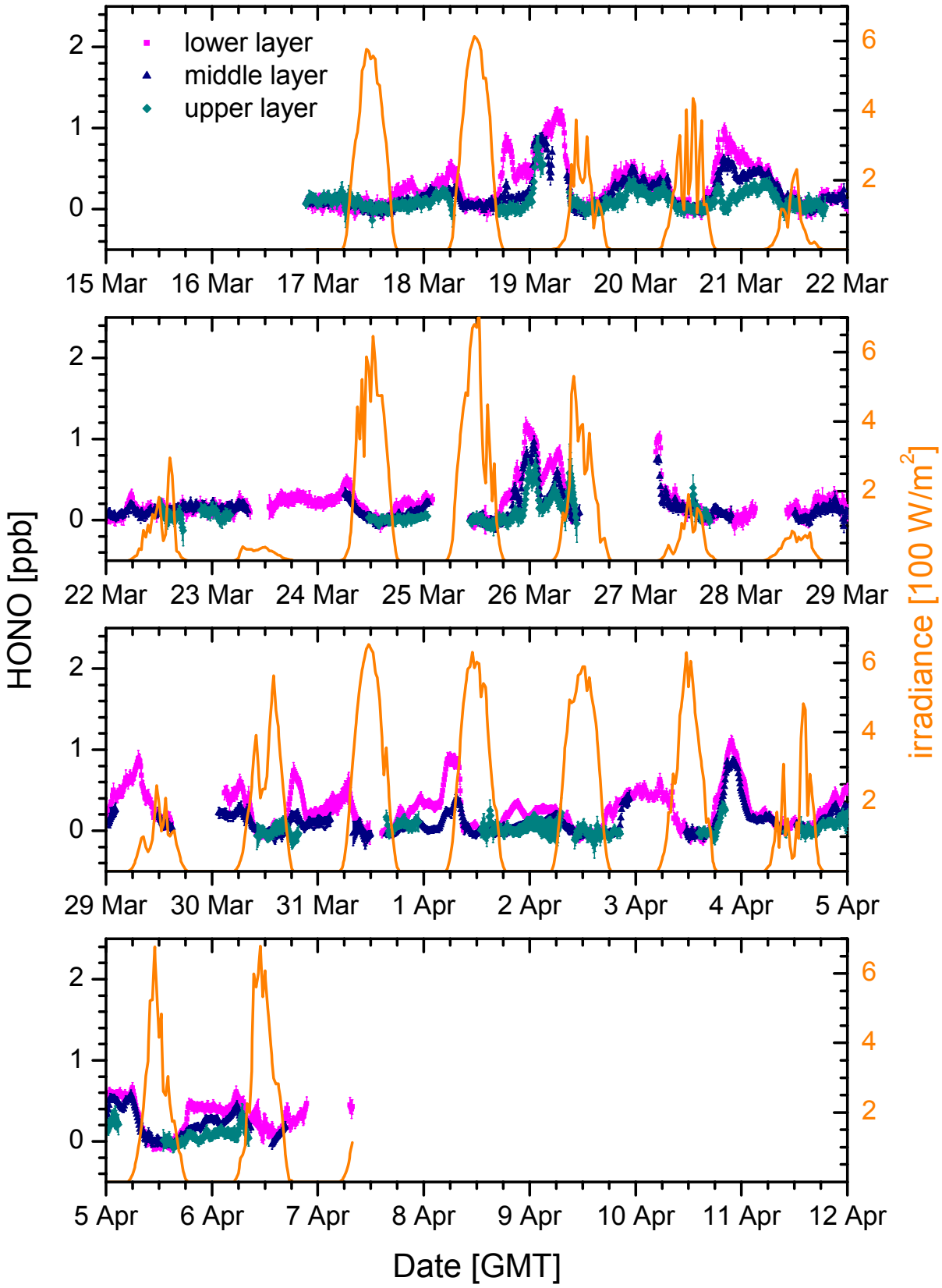

Figure 98: Time series of the HONO profiles in March / April 1999

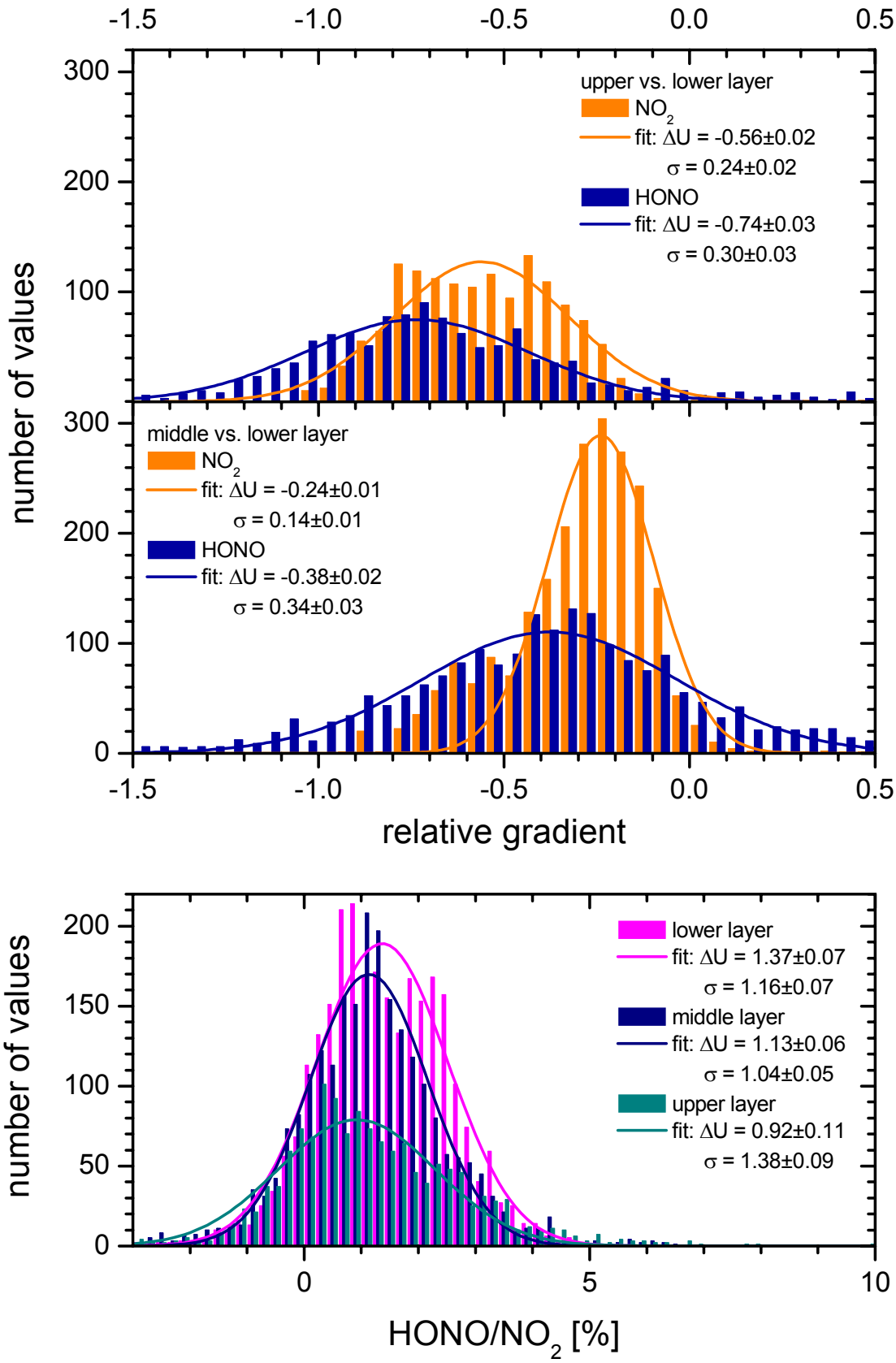

Figure 99: Frequency analysis of the relative gradients and HONO/NO_2 ratios in March / April 1999

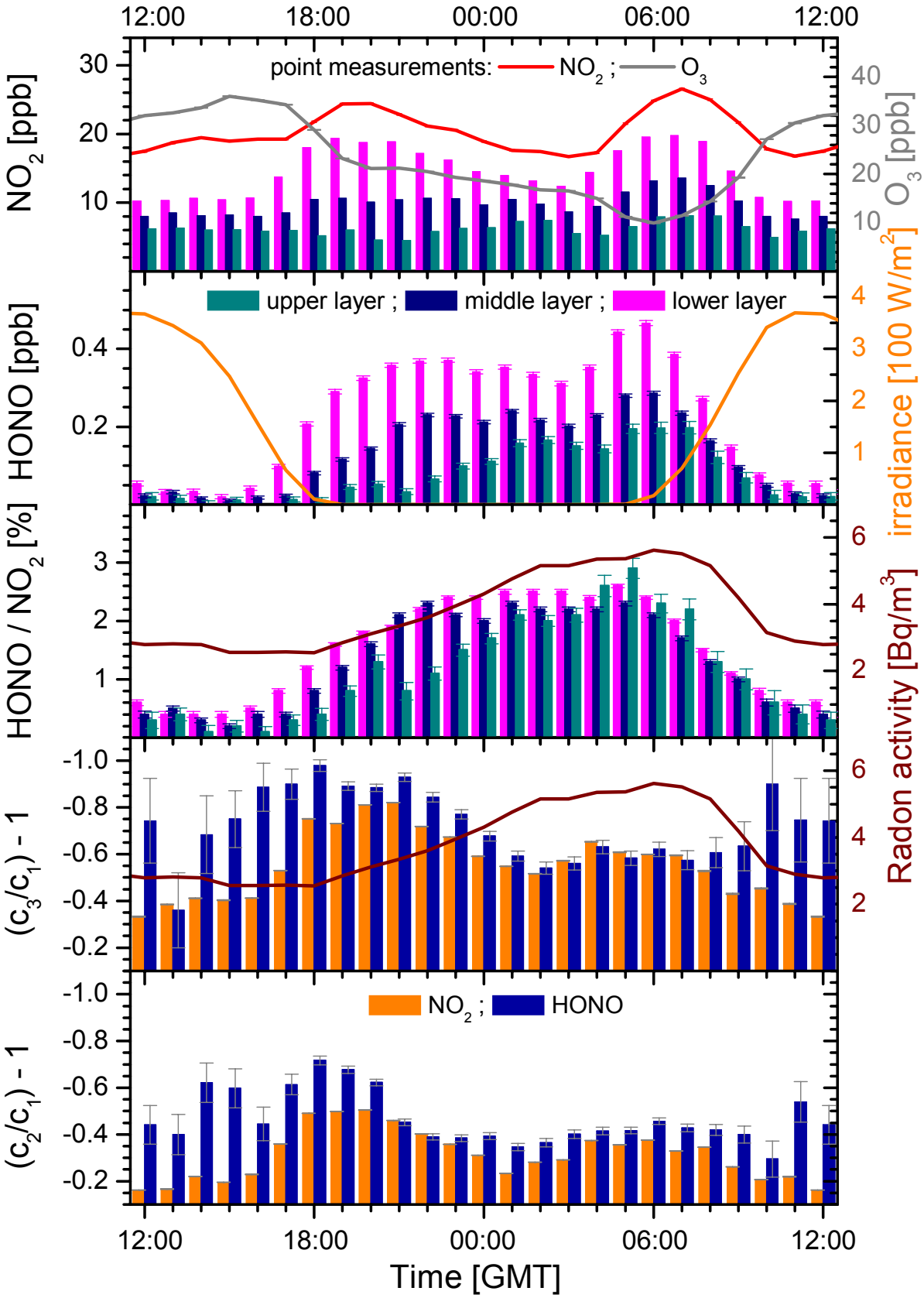

Figure 100: Hourly means of the NO_2 and HONO time series, the HONO/NO_2 ratios and the gradients in March / April 1999

April / May 1999

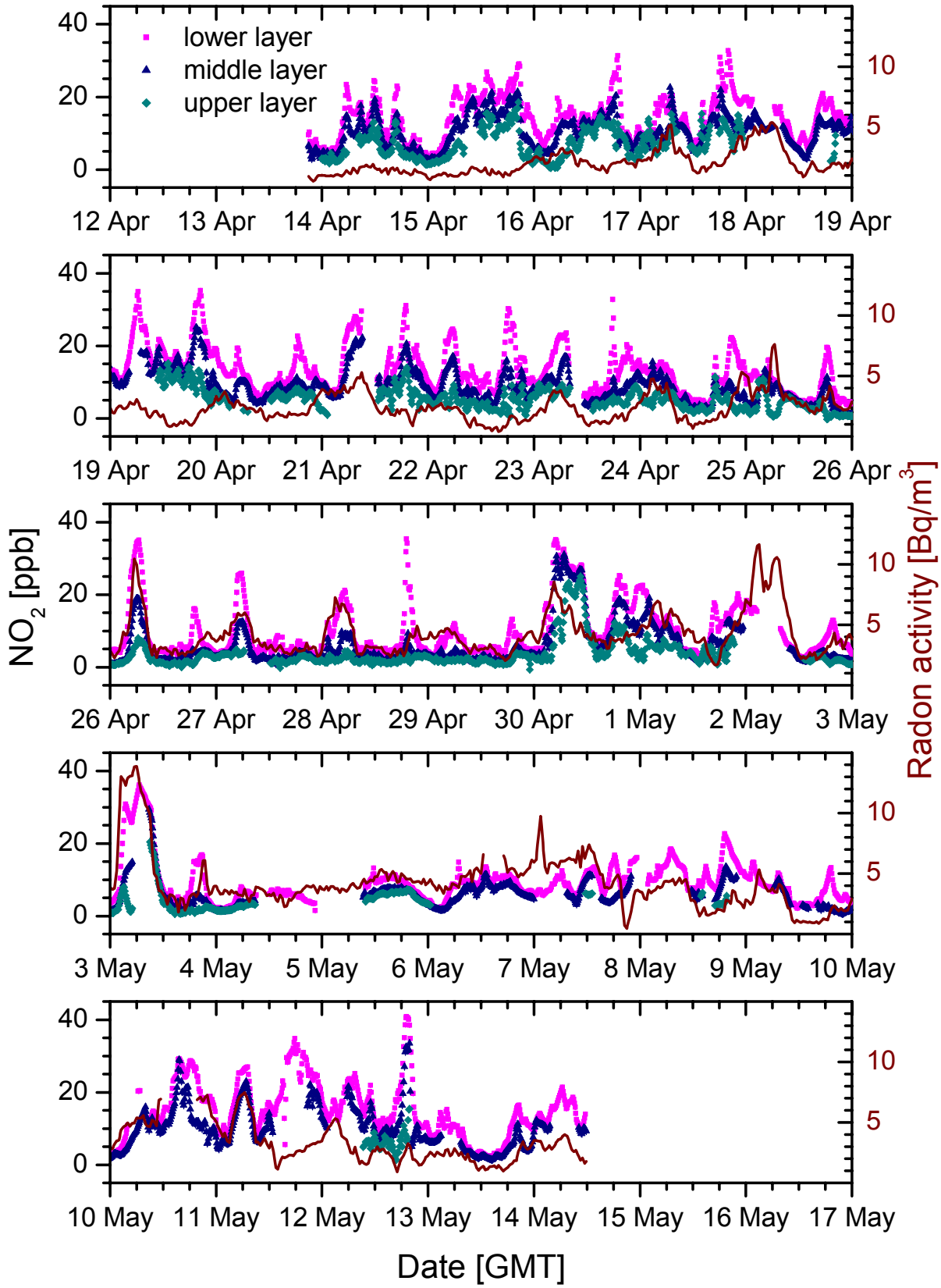

Figure 101: Time series of the NO_2 profiles in April / May 1999

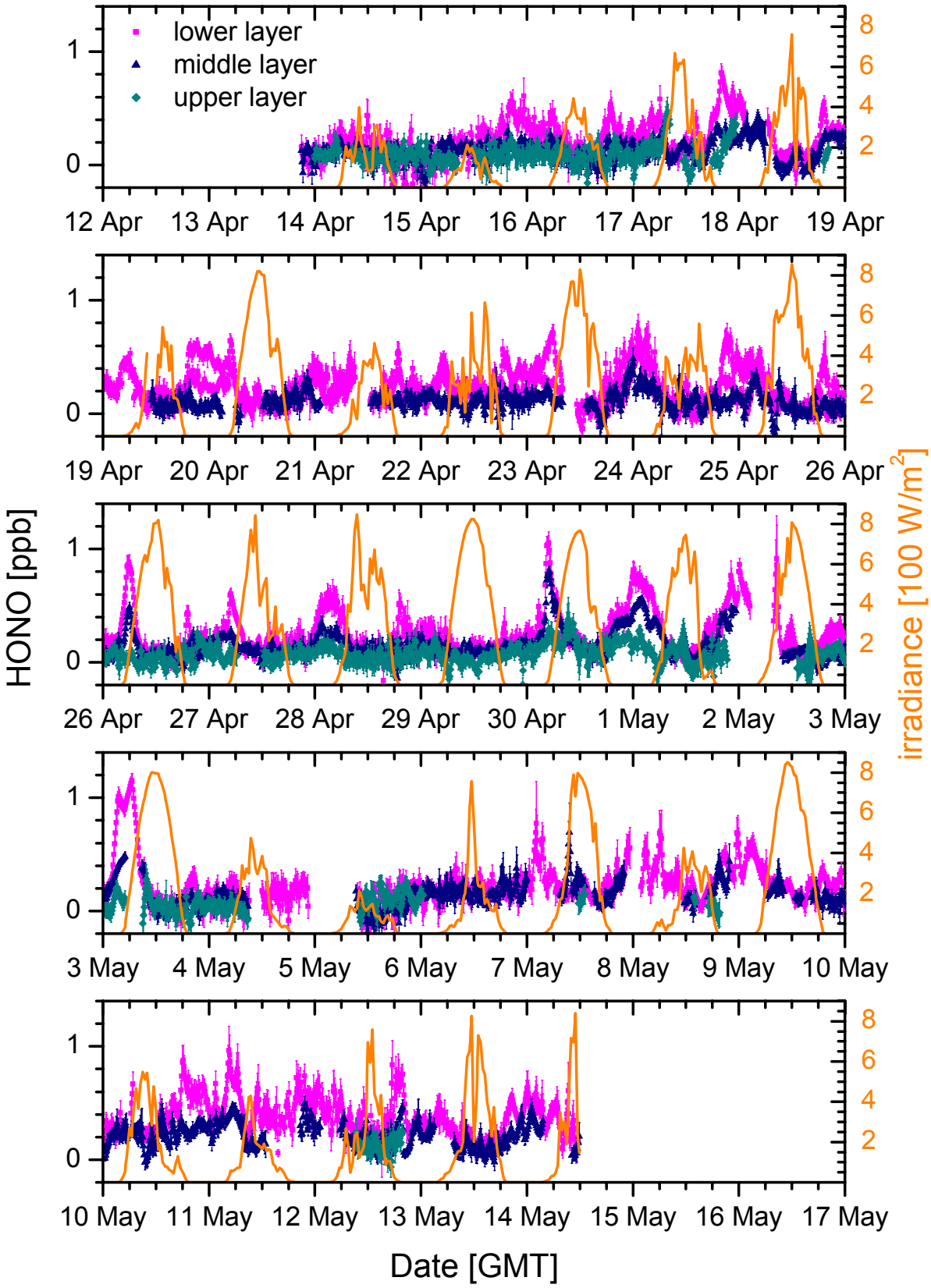

Figure 102: Time series of the HONO profiles in April / May 1999

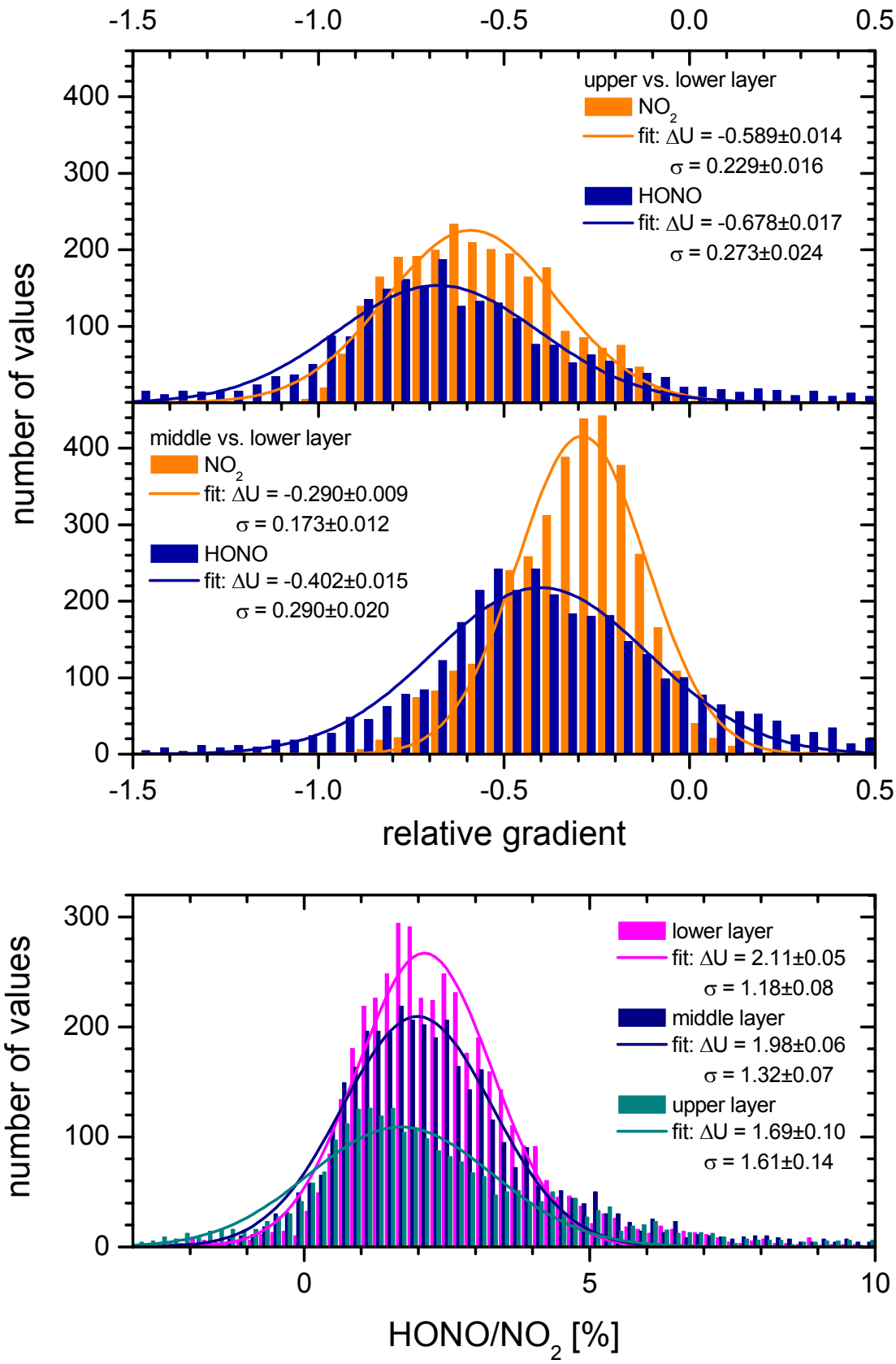

Figure 103: Frequency analysis of the relative gradients and HONO/NO_2 ratios in April / May 1999

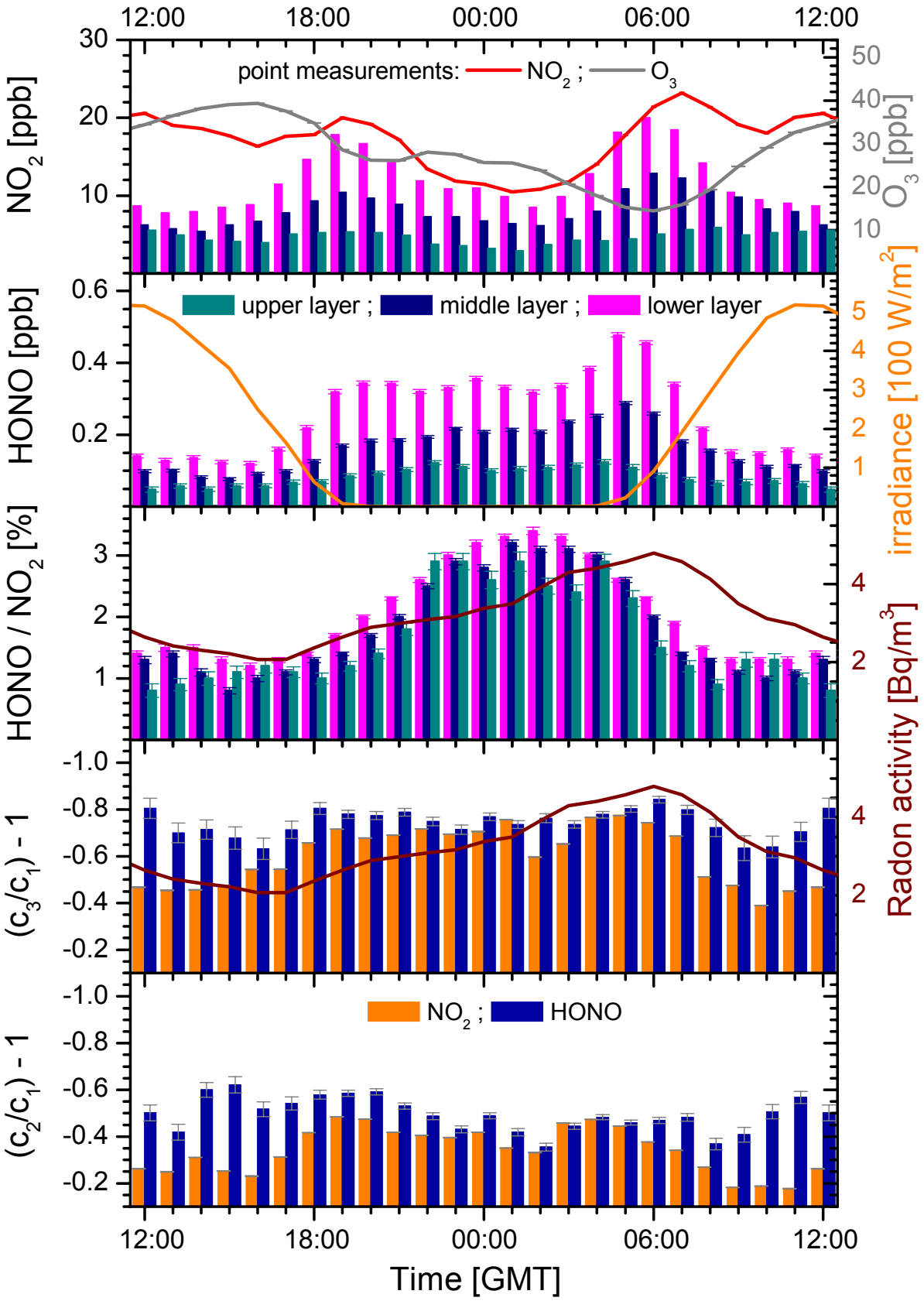

Figure 104: Hourly means of the NO_2 and HONO time series, the HONO/NO_2 ratios and the gradients in April / May 1999

August 1999

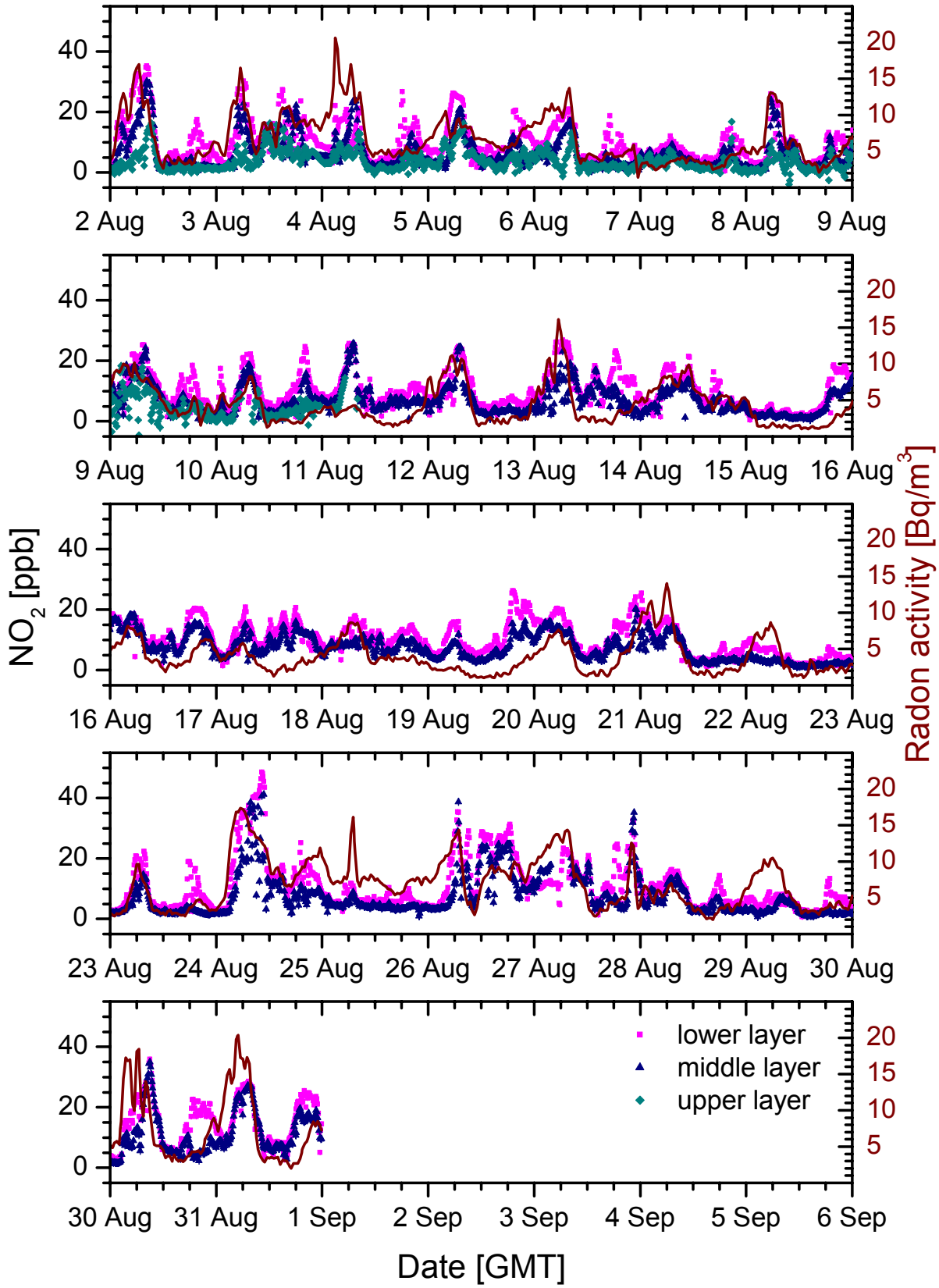

Figure 105: Time series of the NO_2 profiles in August 1999

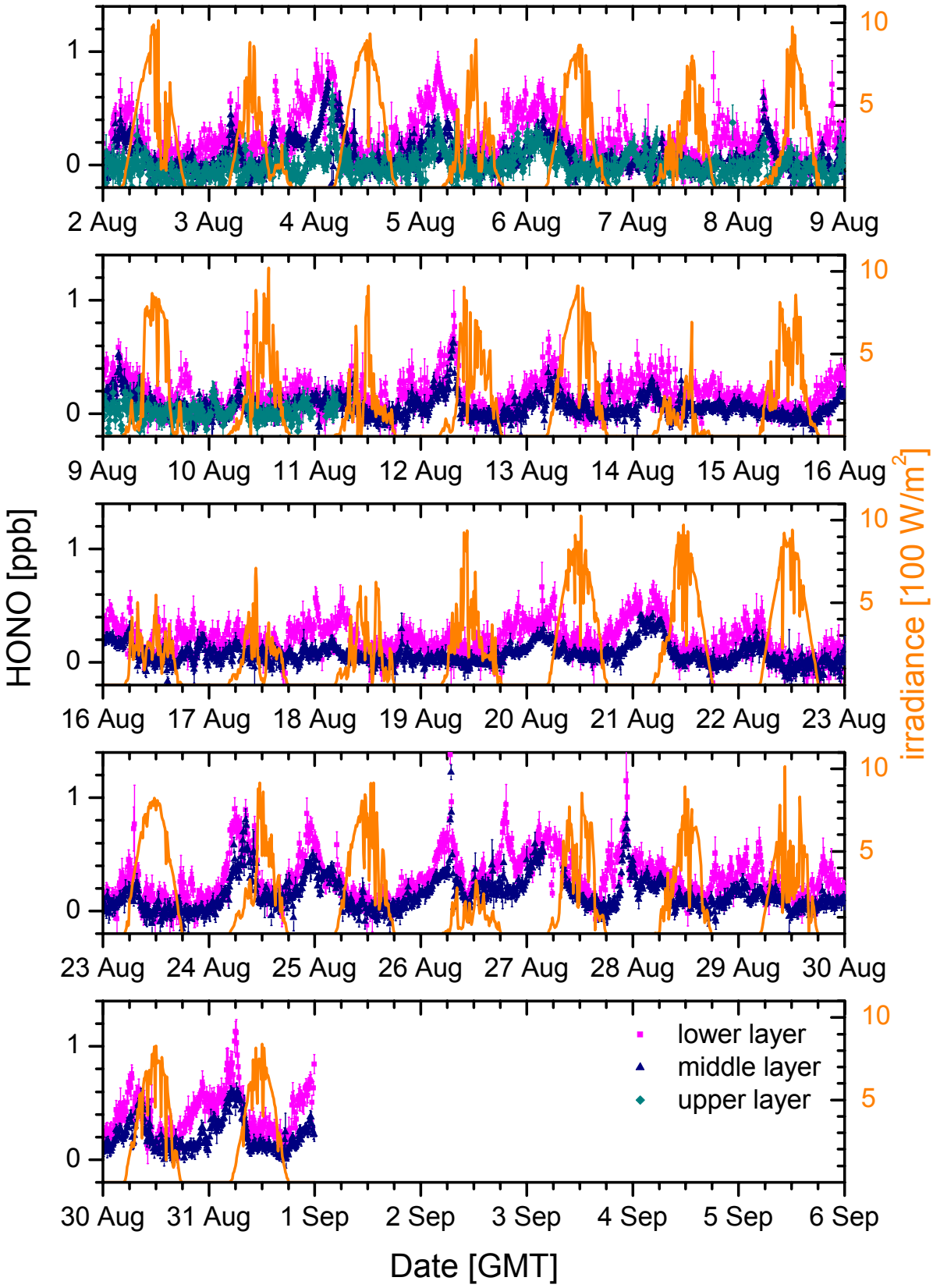

Figure 106: Time series of the HONO profiles in August 1999

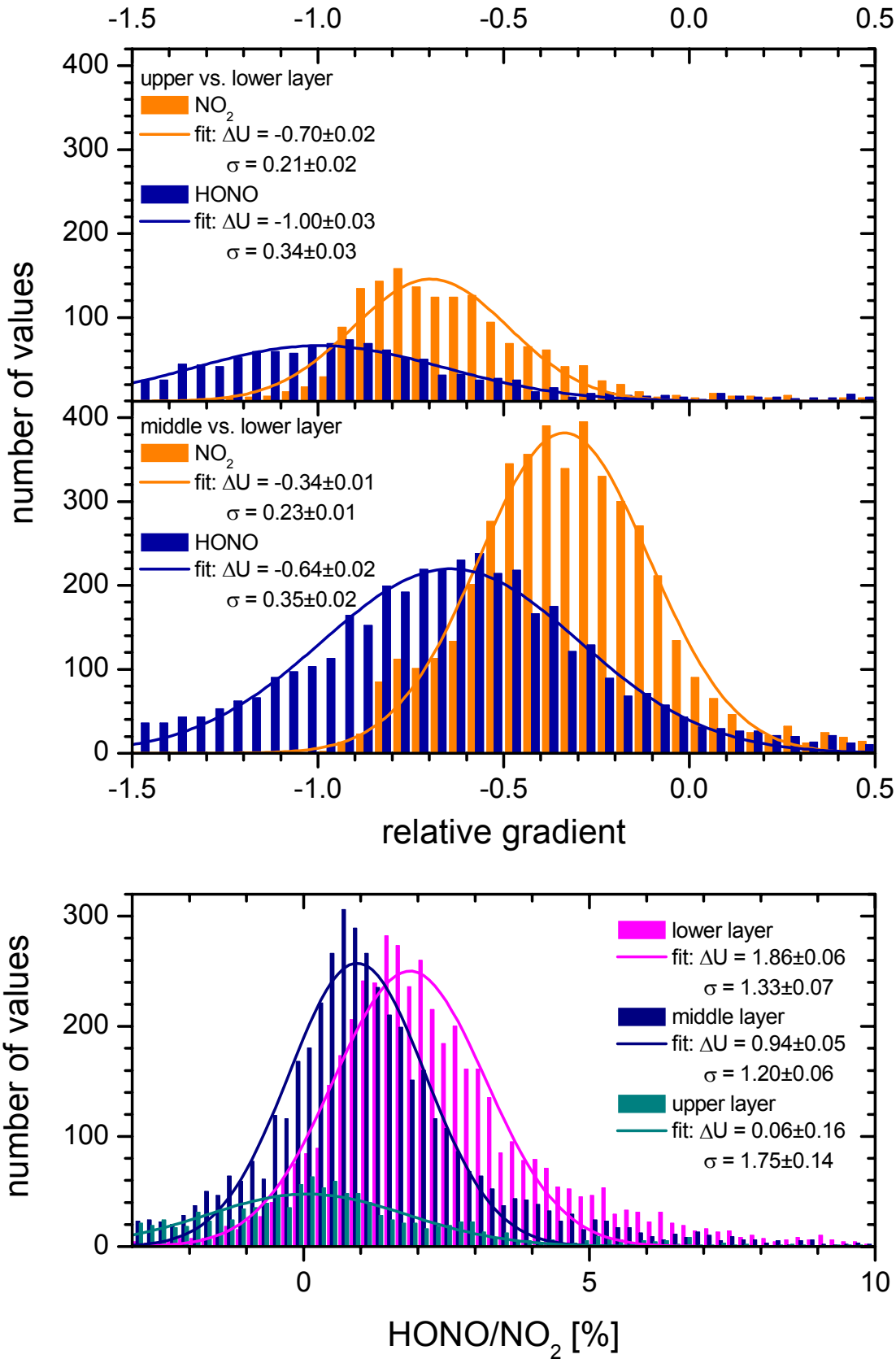

Figure 107: Frequency analysis of the relative gradients and HONO/NO_2 ratios in August 1999

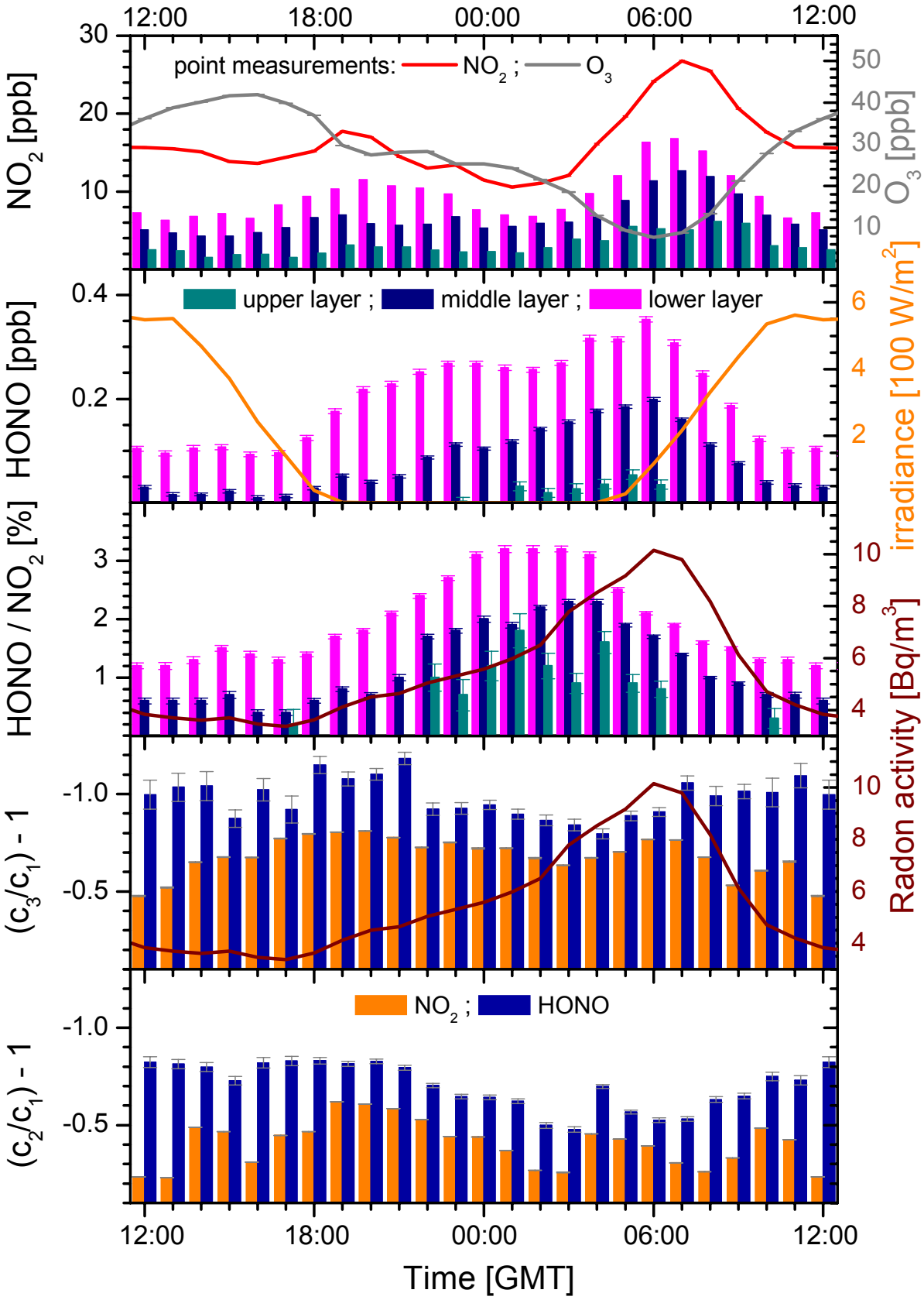

Figure 108: Hourly means of the NO_2 and HONO time series, the HONO/NO_2 ratios and the gradients in August 1999

September 1999

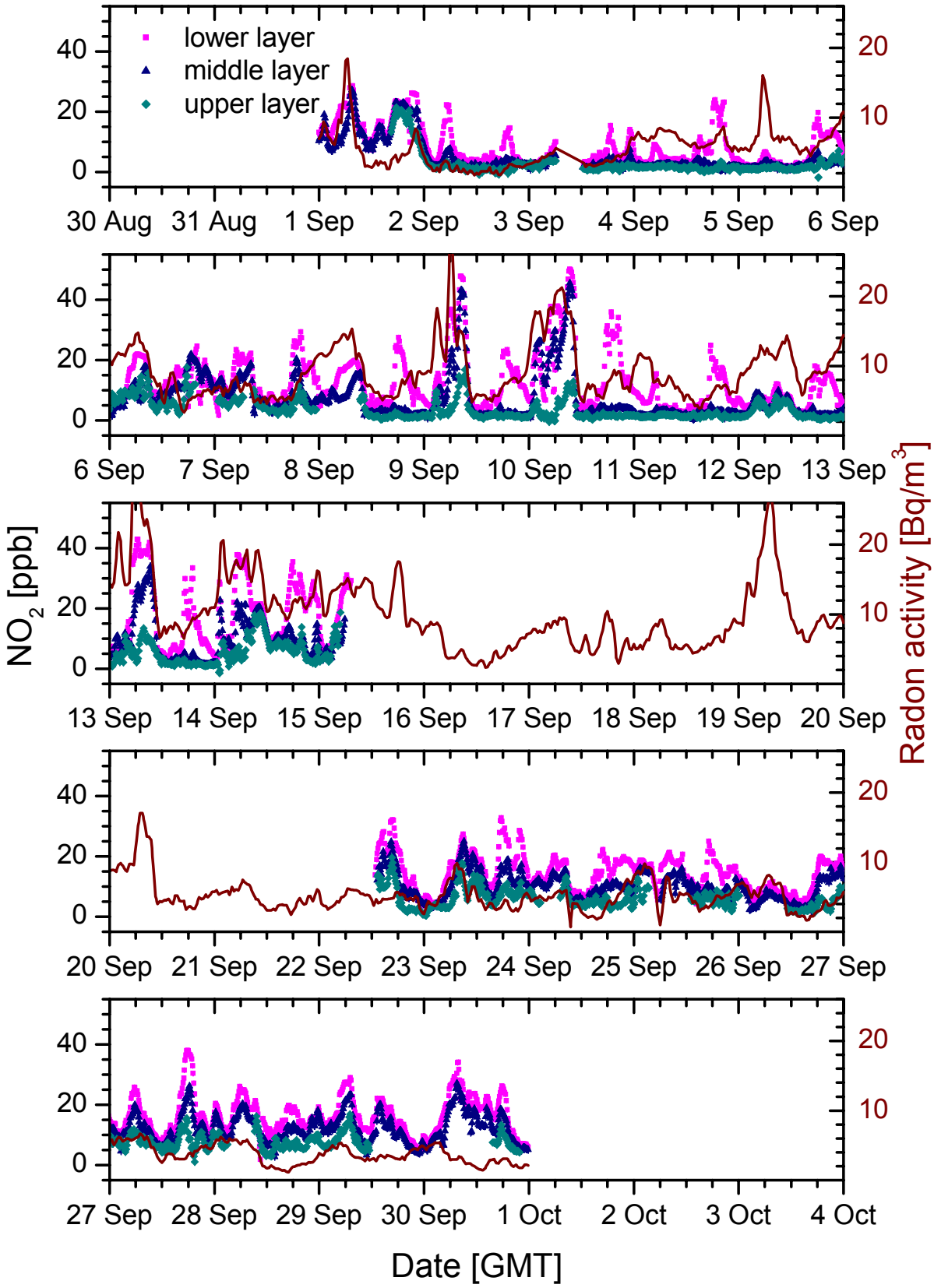

Figure 109: Time series of the NO_2 profiles in September 1999

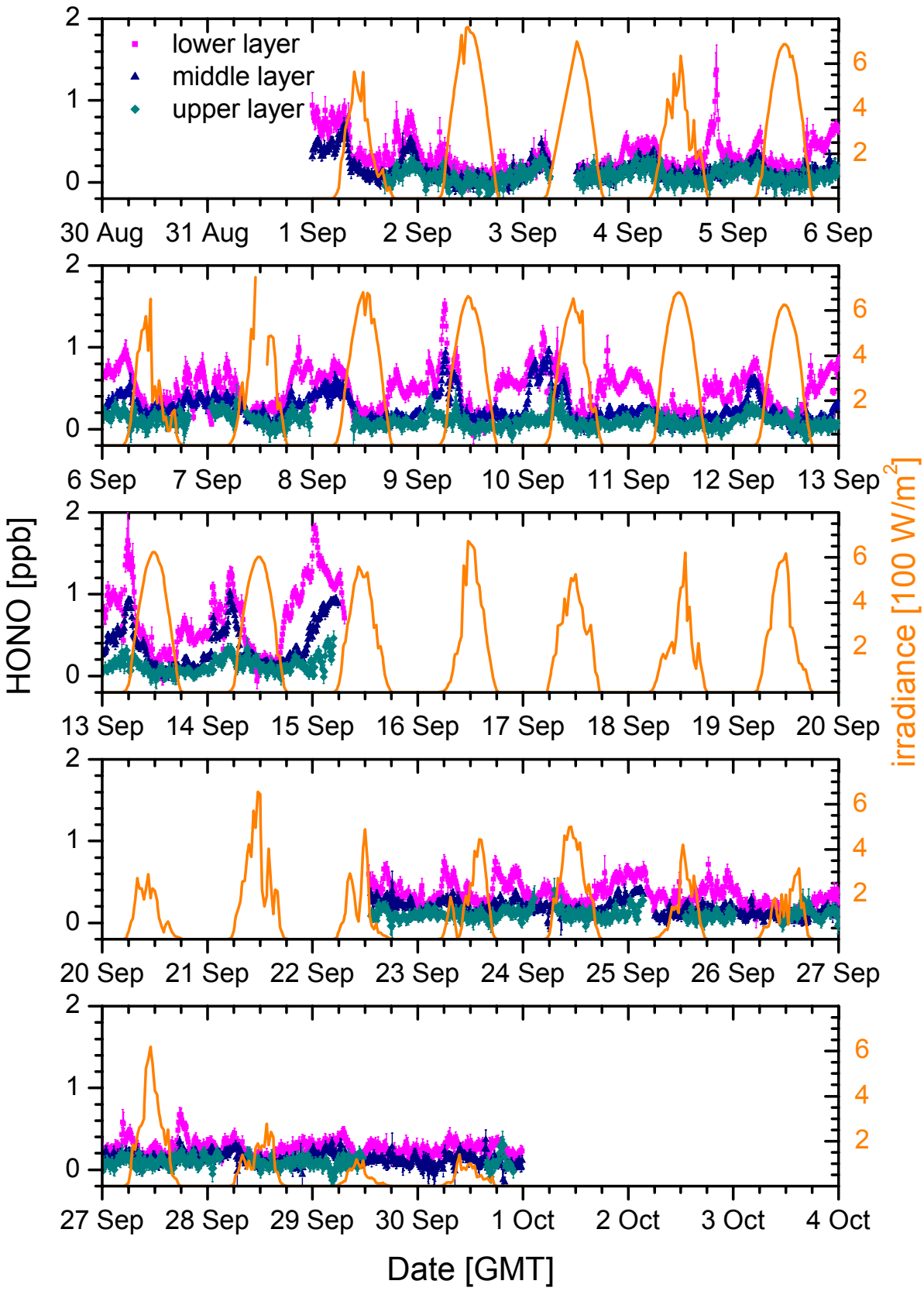

Figure 110: Time series of the HONO profiles in September 1999

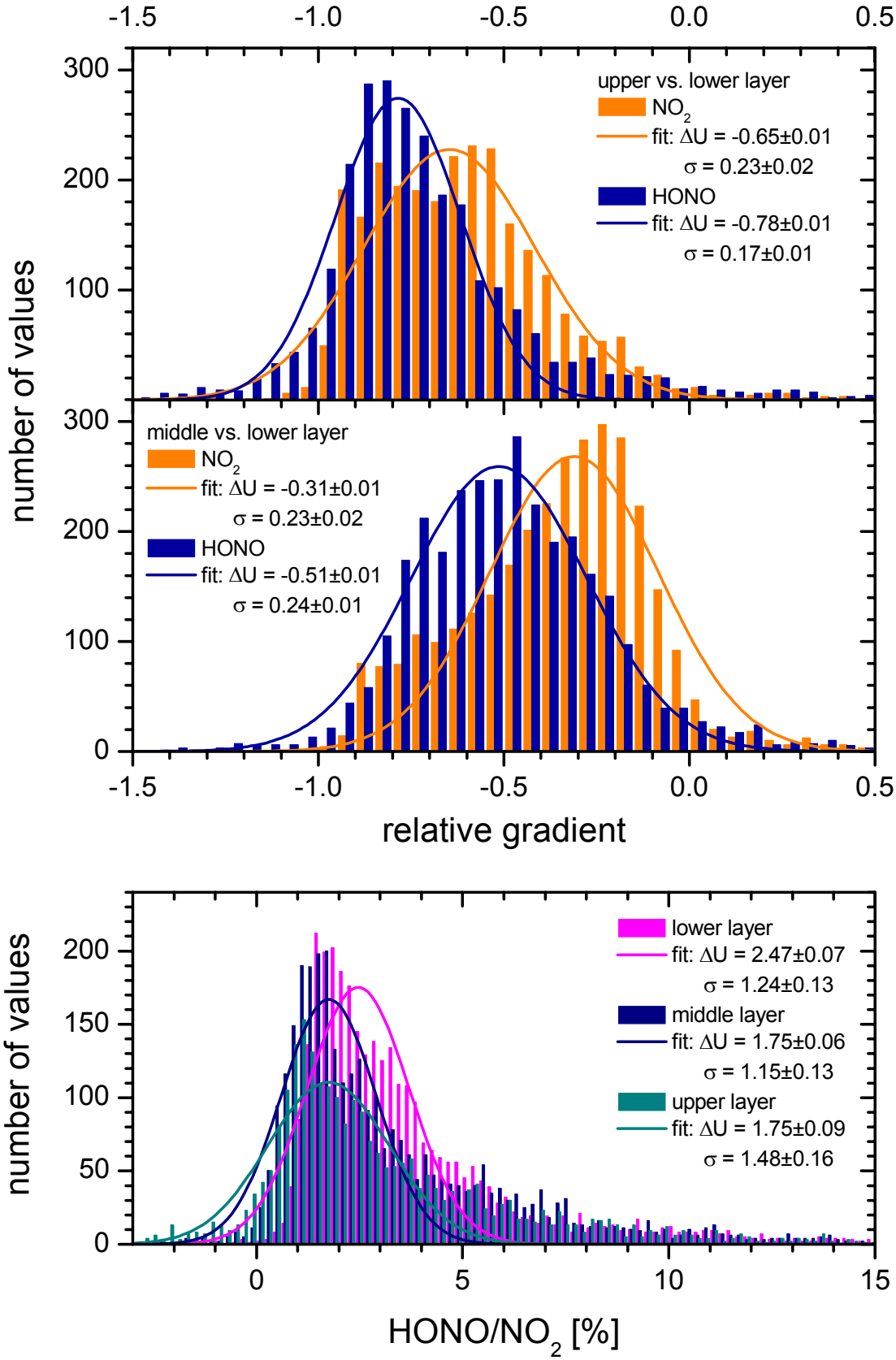

Figure 111: Frequency analysis of the relative gradients and HONO/NO_2 ratios in September 1999

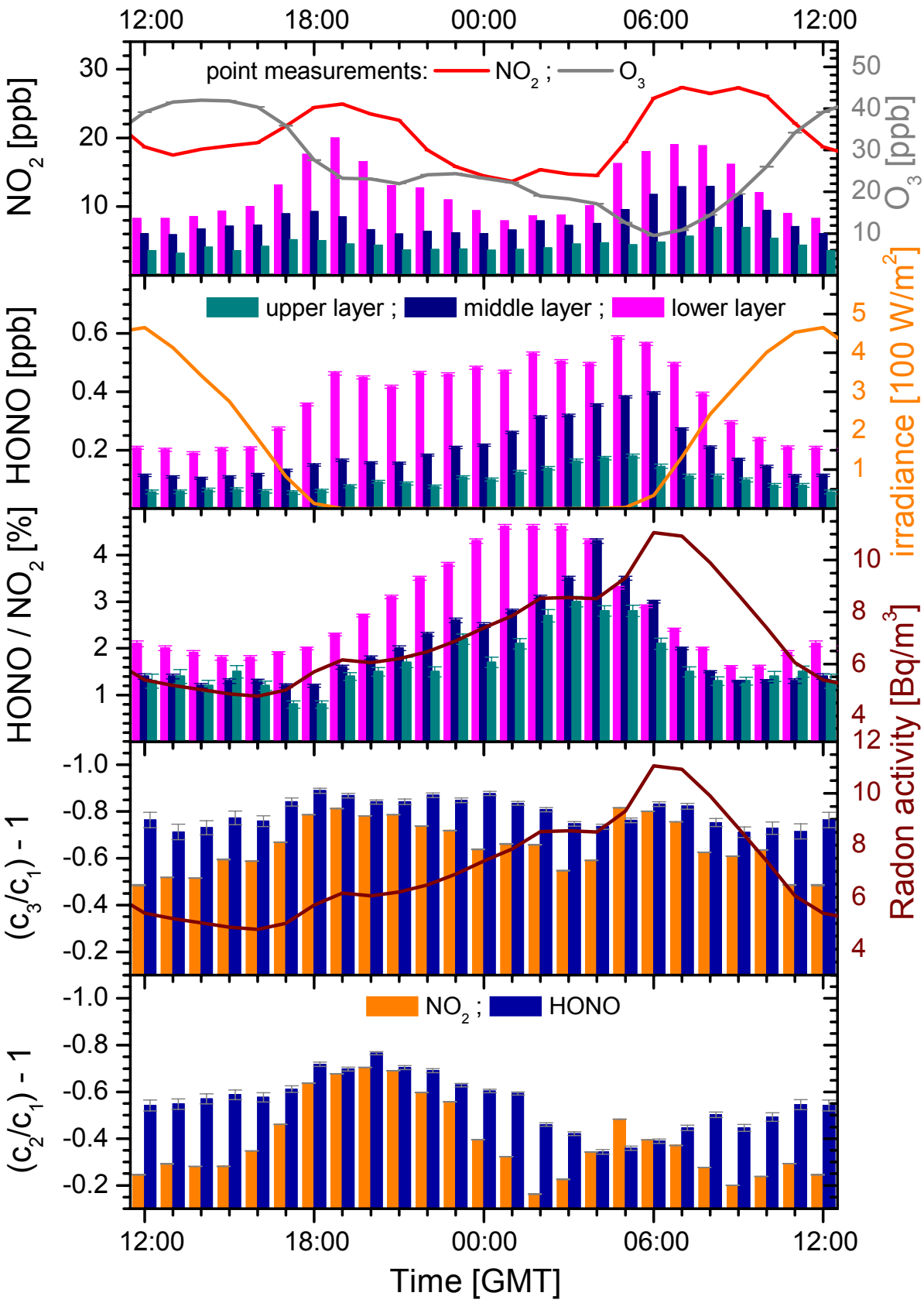

Figure 112: Hourly means of the NO_2 and HONO time series, the HONO/NO_2 ratios and the gradients in September 1999

October 1999

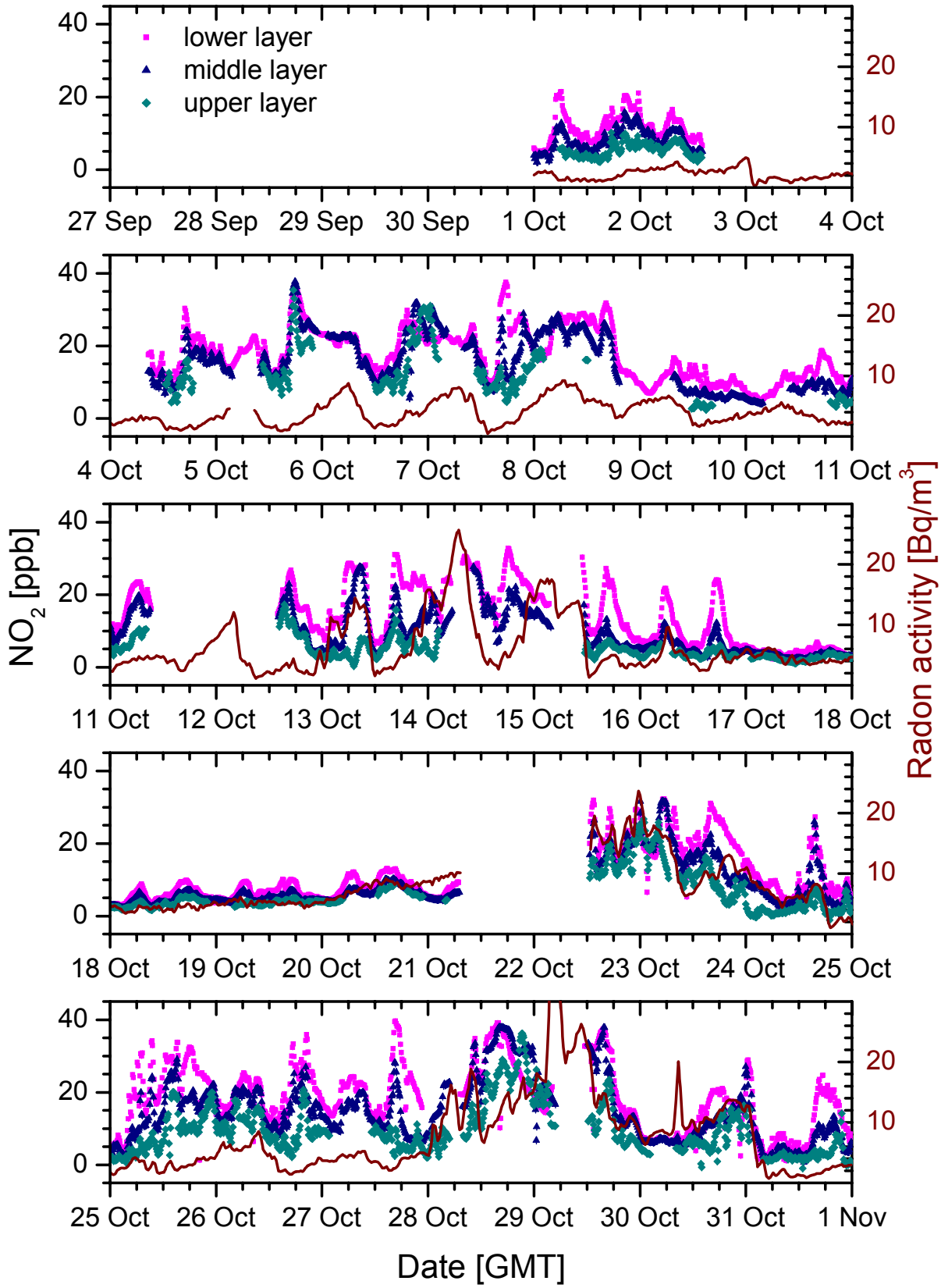

Figure 113: Time series of the NO_2 profiles in October 1999

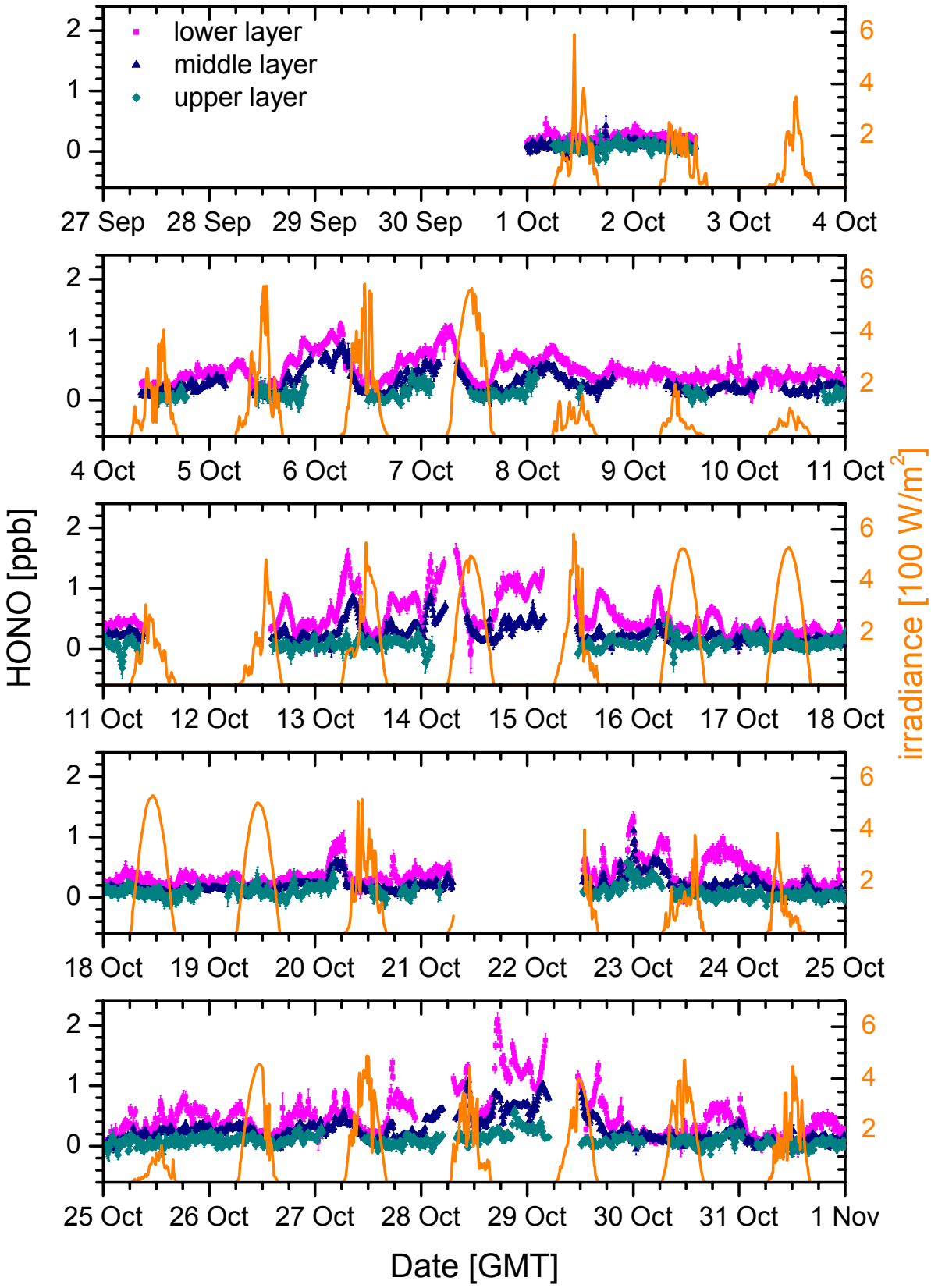

Figure 114: Time series of the HONO profiles in October 1999

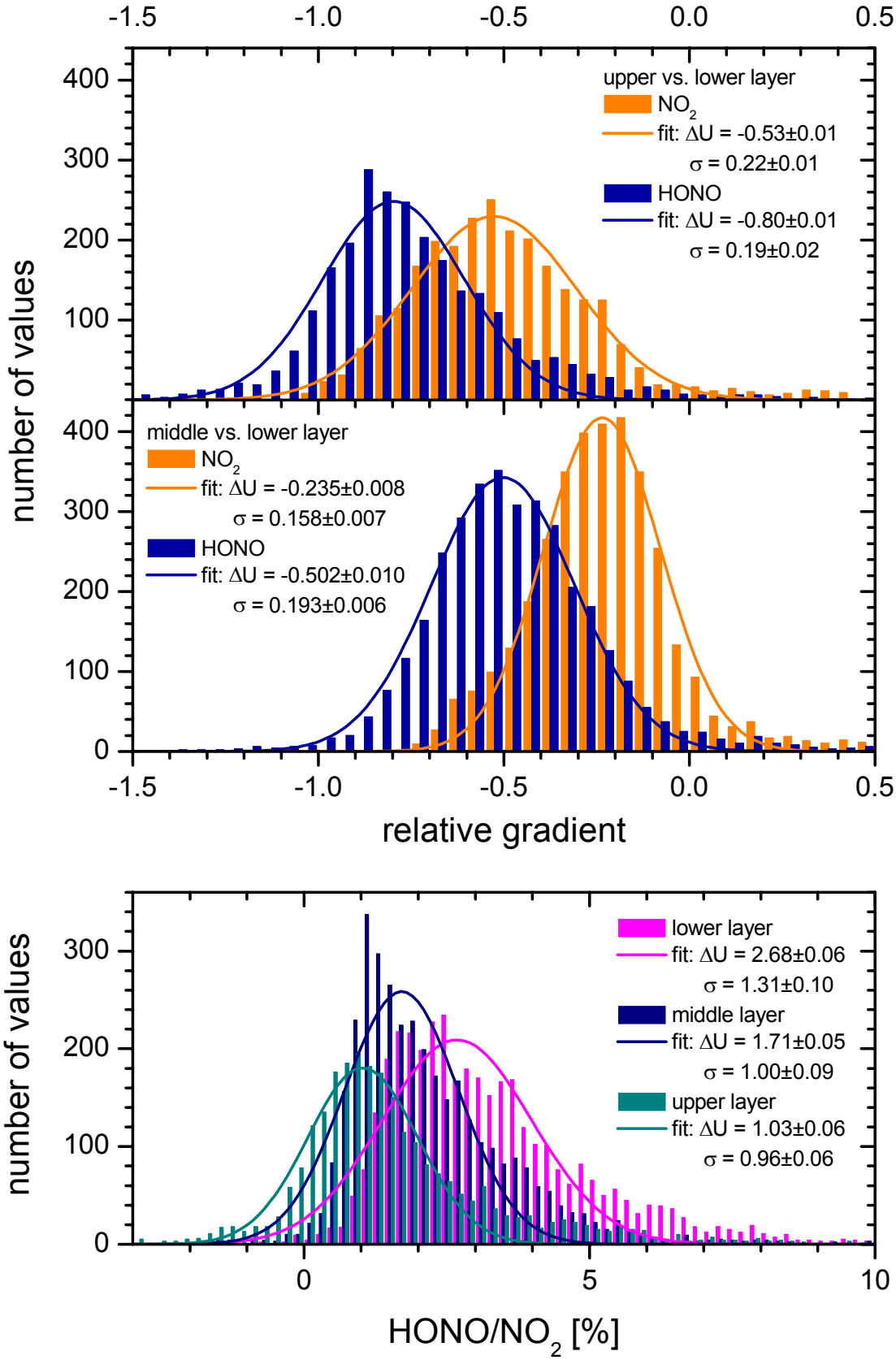

Figure 115: Frequency analysis of the relative gradients and HONO/NO_2 ratios in October 1999

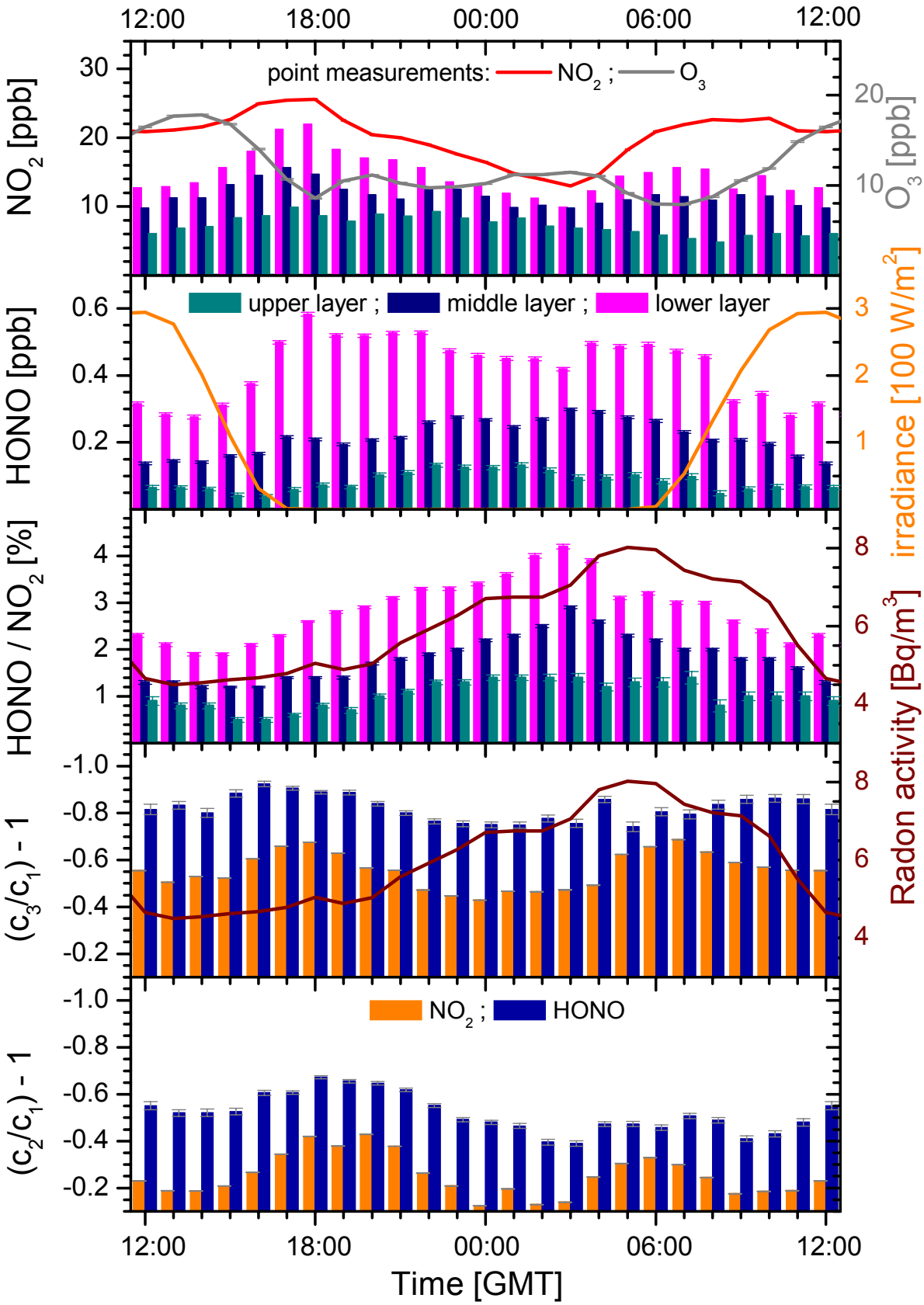

Figure 116: Hourly means of the NO_2 and HONO time series, the HONO/NO_2 ratios and the gradients in October 1999

November 1999

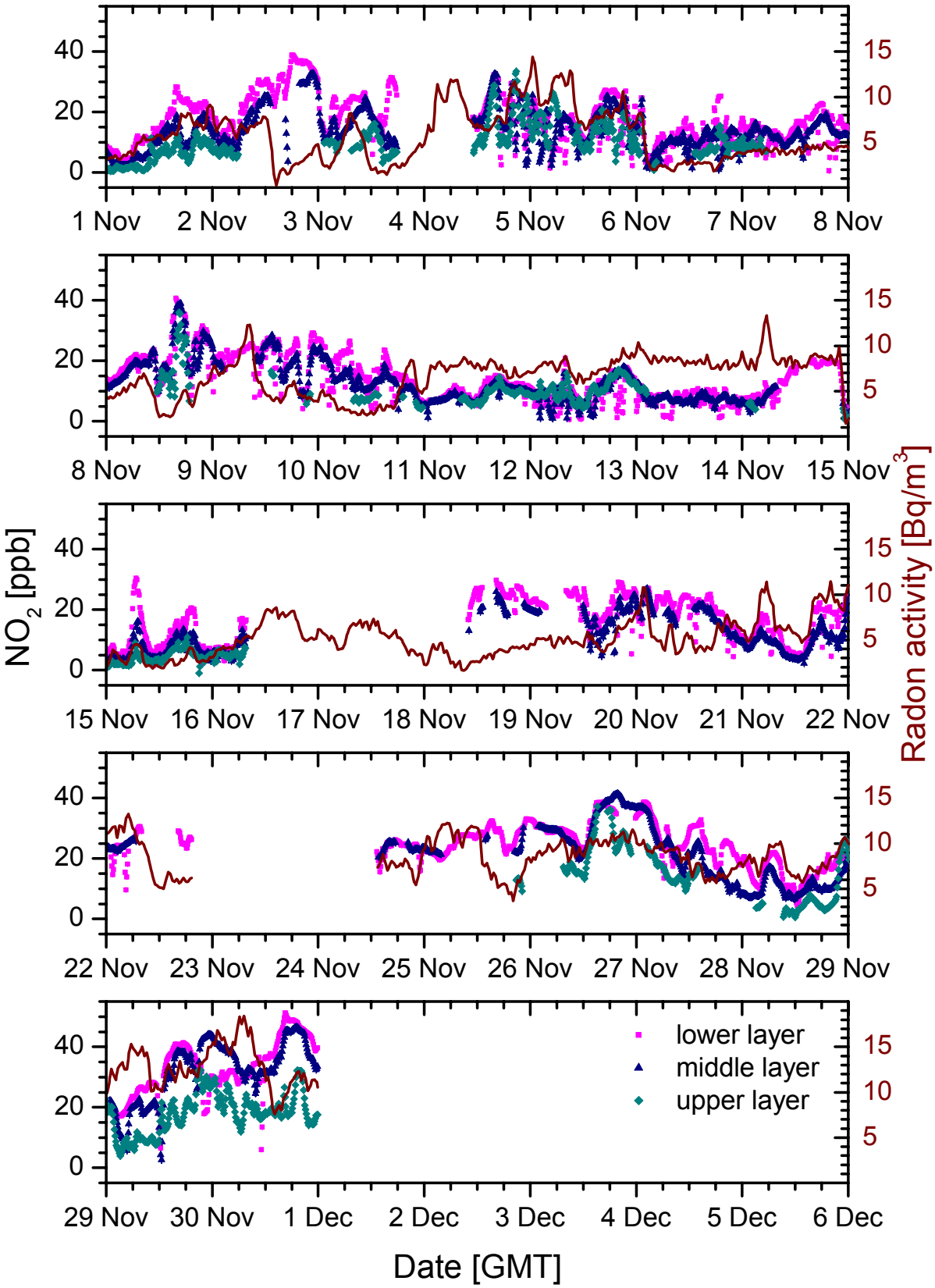

Figure 117: Time series of the NO_2 profiles in November 1999

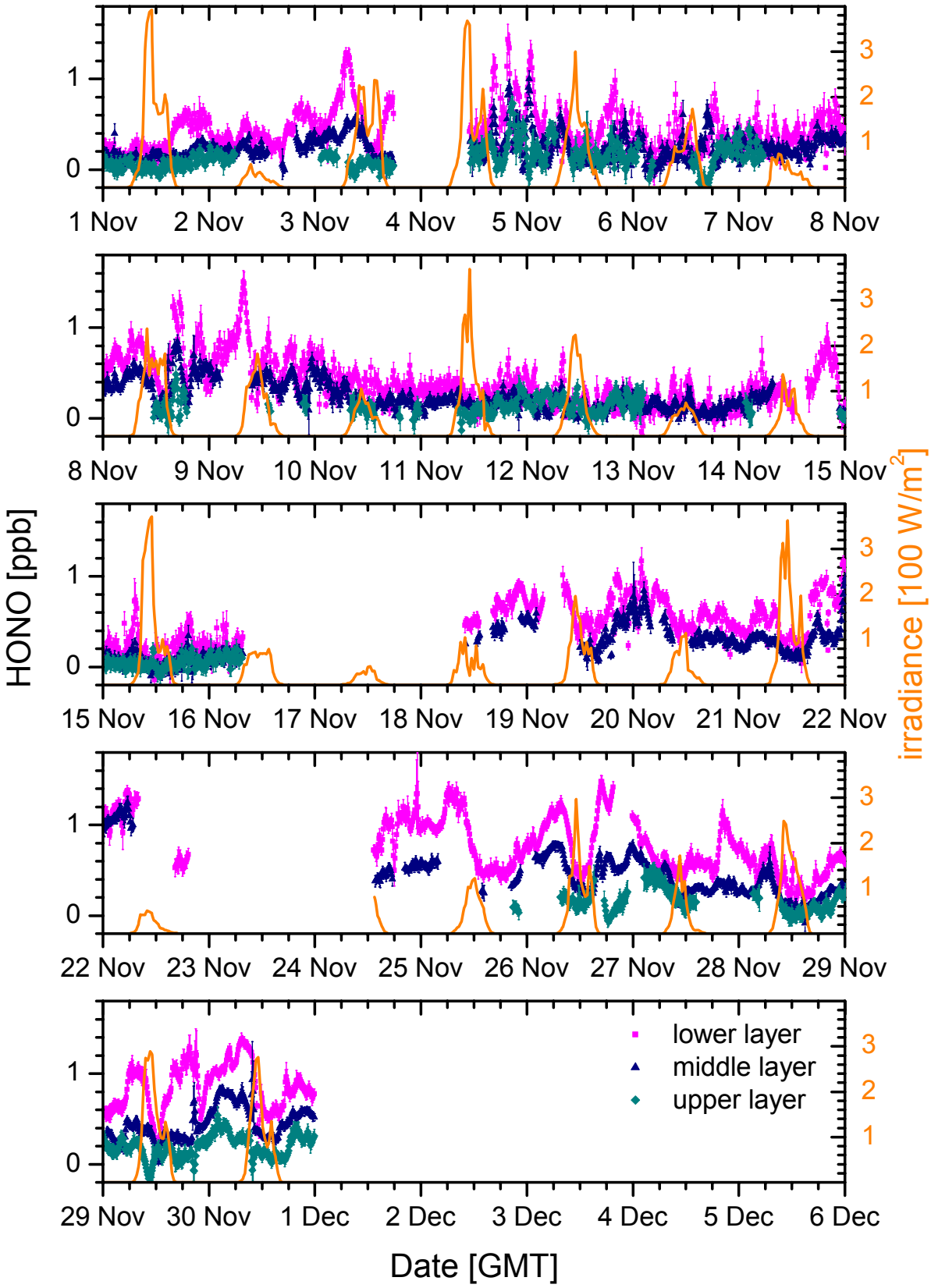

Figure 118: Time series of the HONO profiles in November 1999

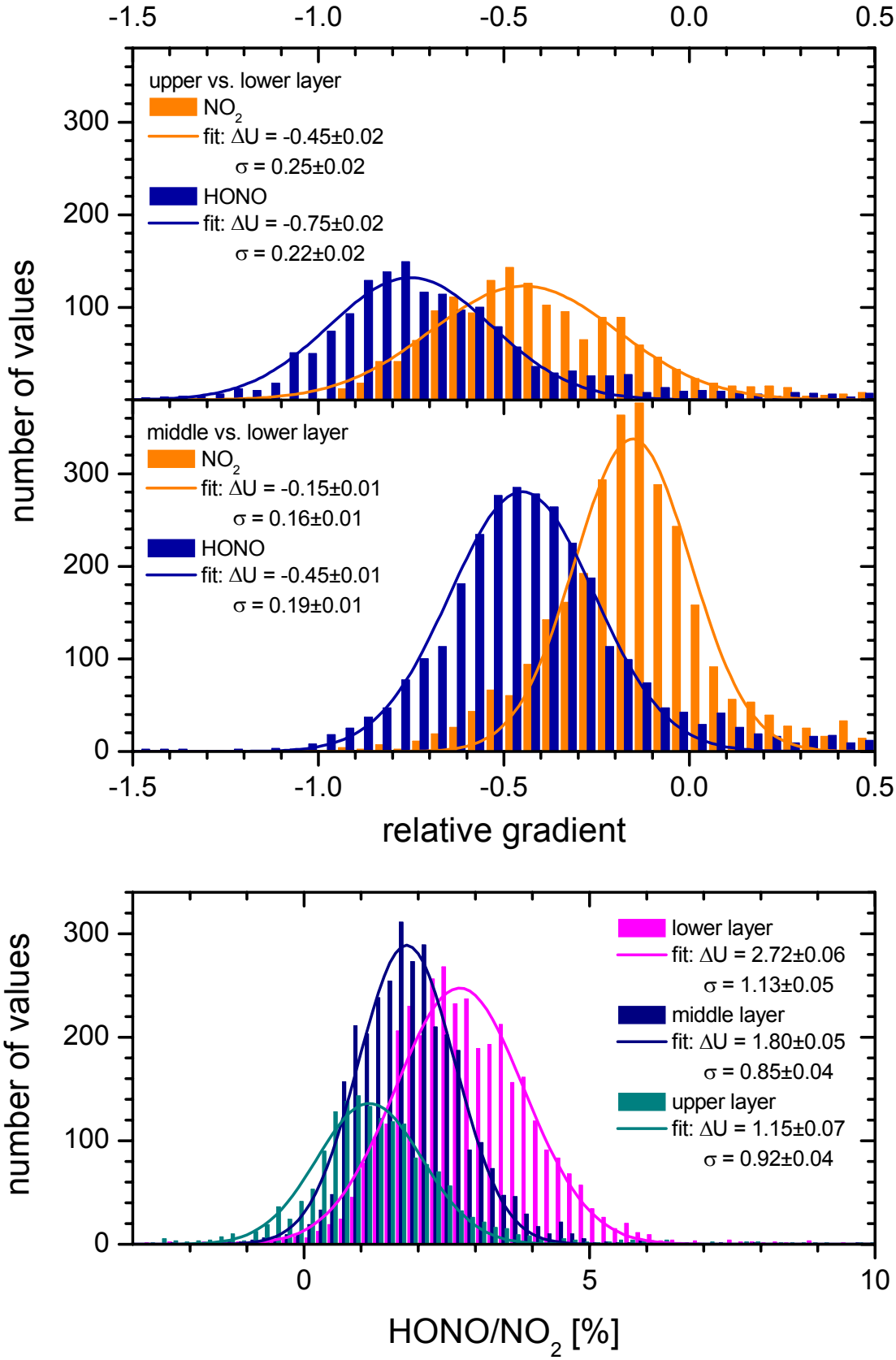

Figure 119: Frequency analysis of the relative gradients and HONO/NO_2 ratios in November 1999

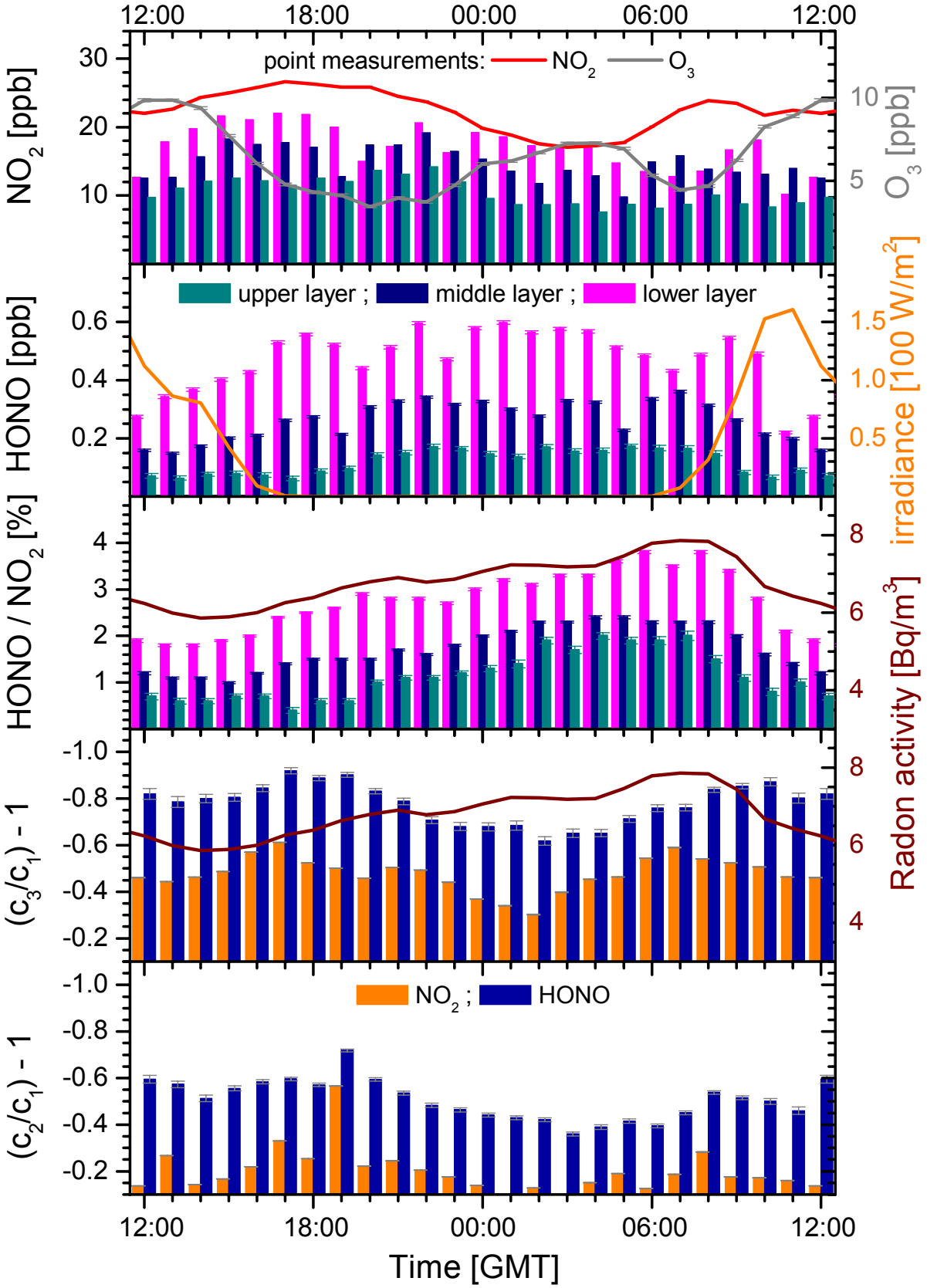

Figure 120: Hourly means of the NO_2 and HONO time series, the HONO/NO_2 ratios and the gradients in November 1999

December 1999

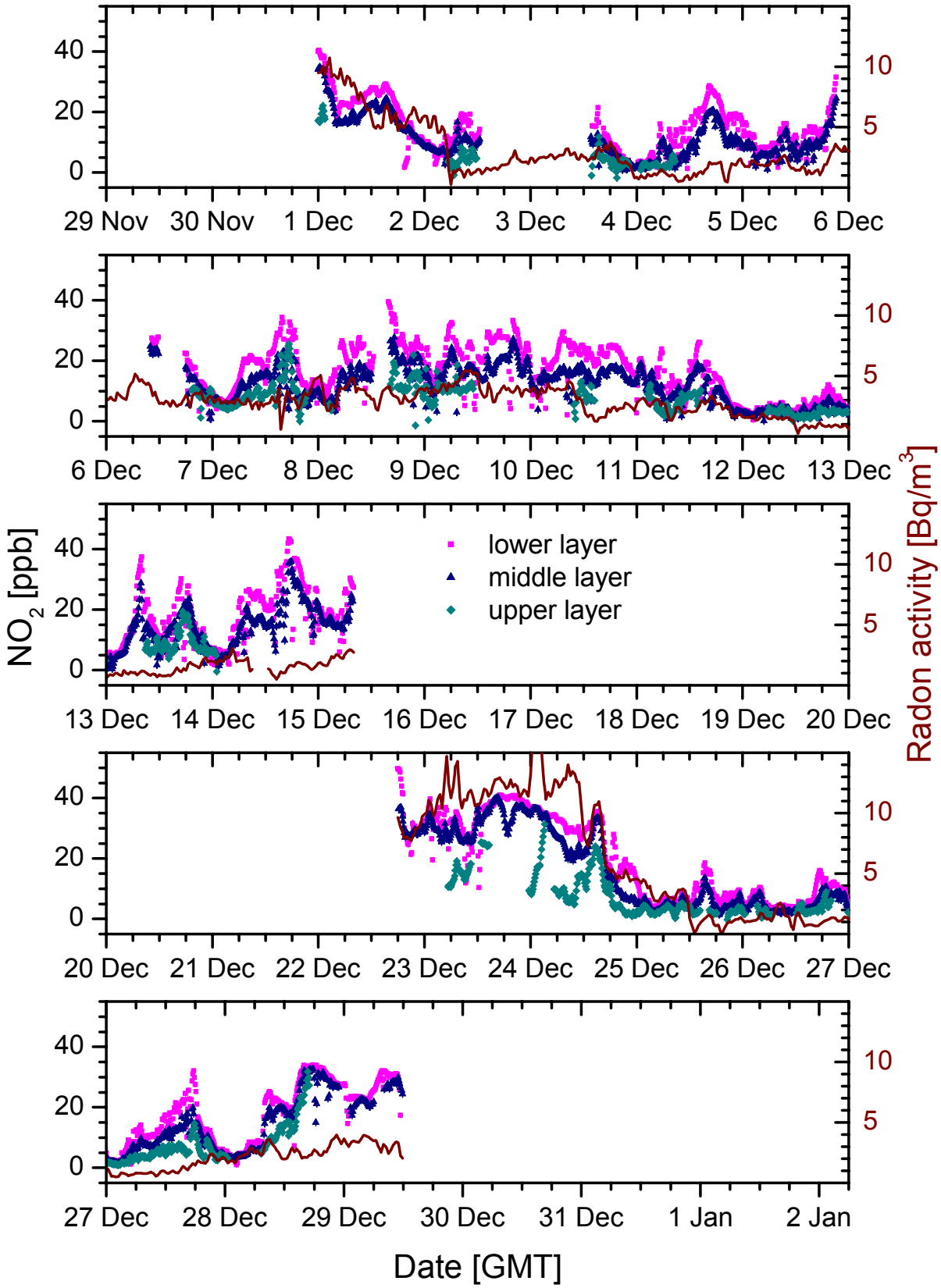

Figure 121: Time series of the NO_2 profiles in December 1999

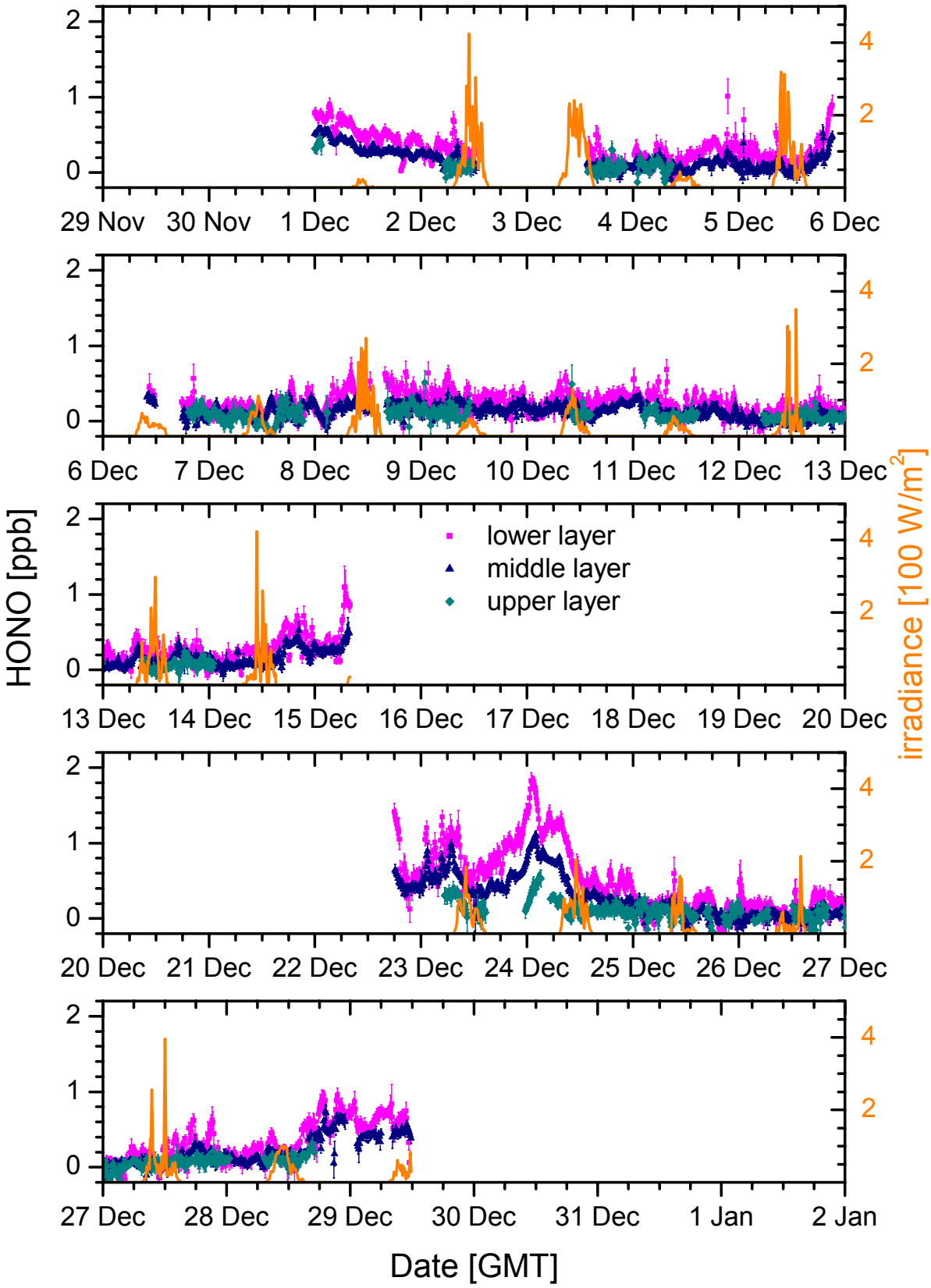

Figure 122: Time series of the HONO profiles in December 1999

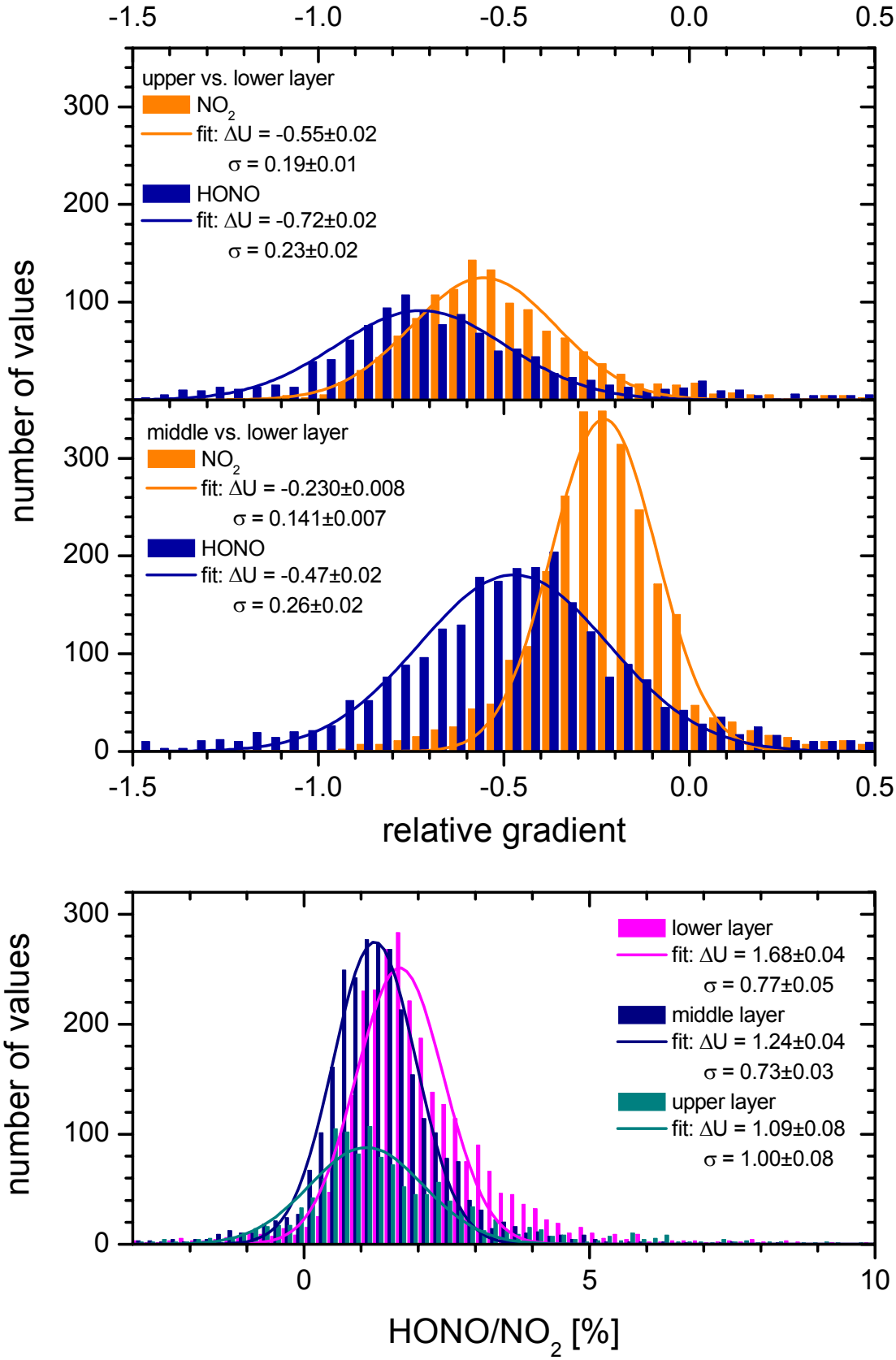

Figure 123: Frequency analysis of the relative gradients and HONO/NO_2 ratios in December 1999

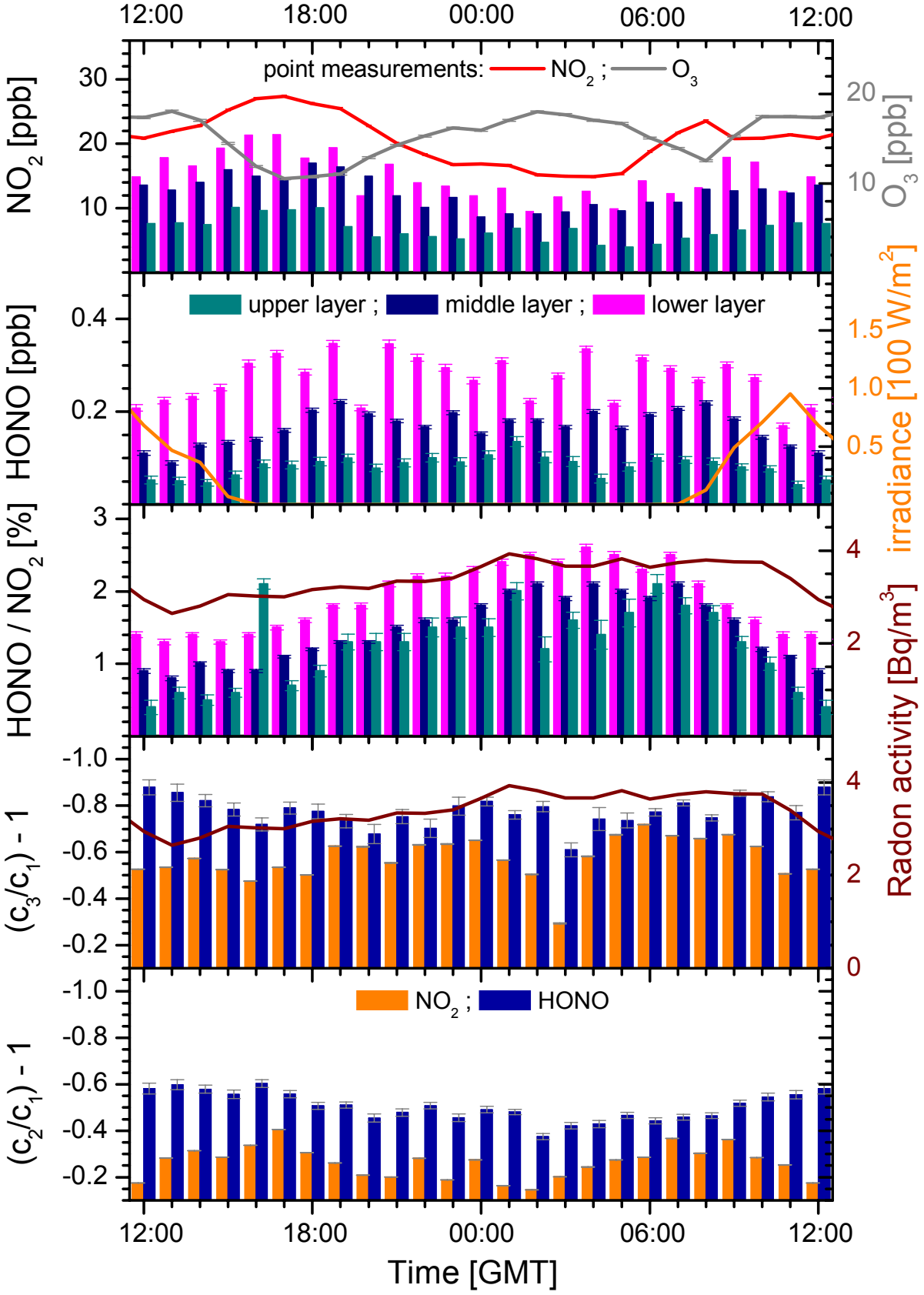

Figure 124: Hourly means of the NO_2 and HONO time series, the HONO/NO_2 ratios and the gradients in December 1999

February 2000

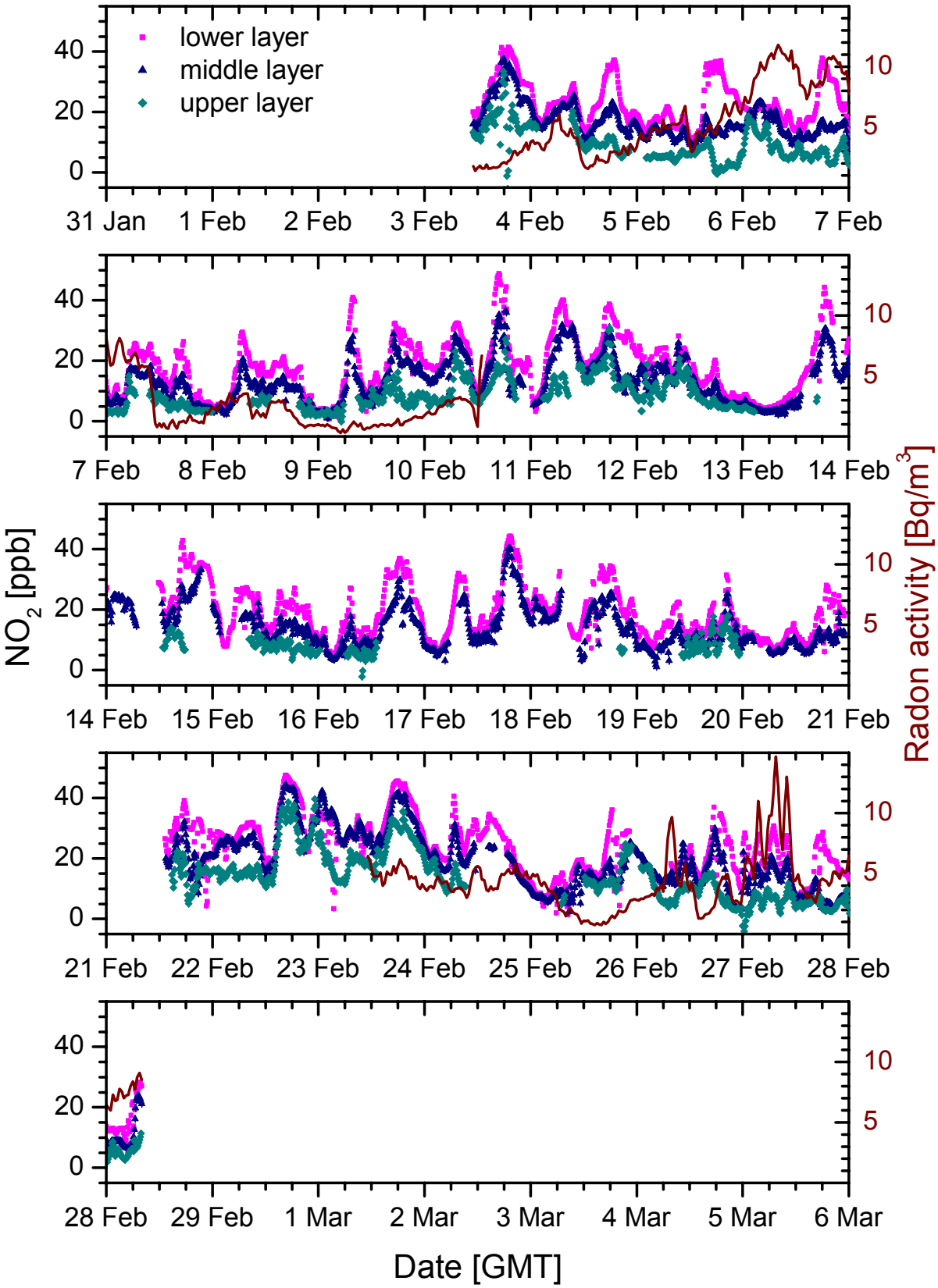

Figure 125: Time series of the NO_2 profiles in February 2000

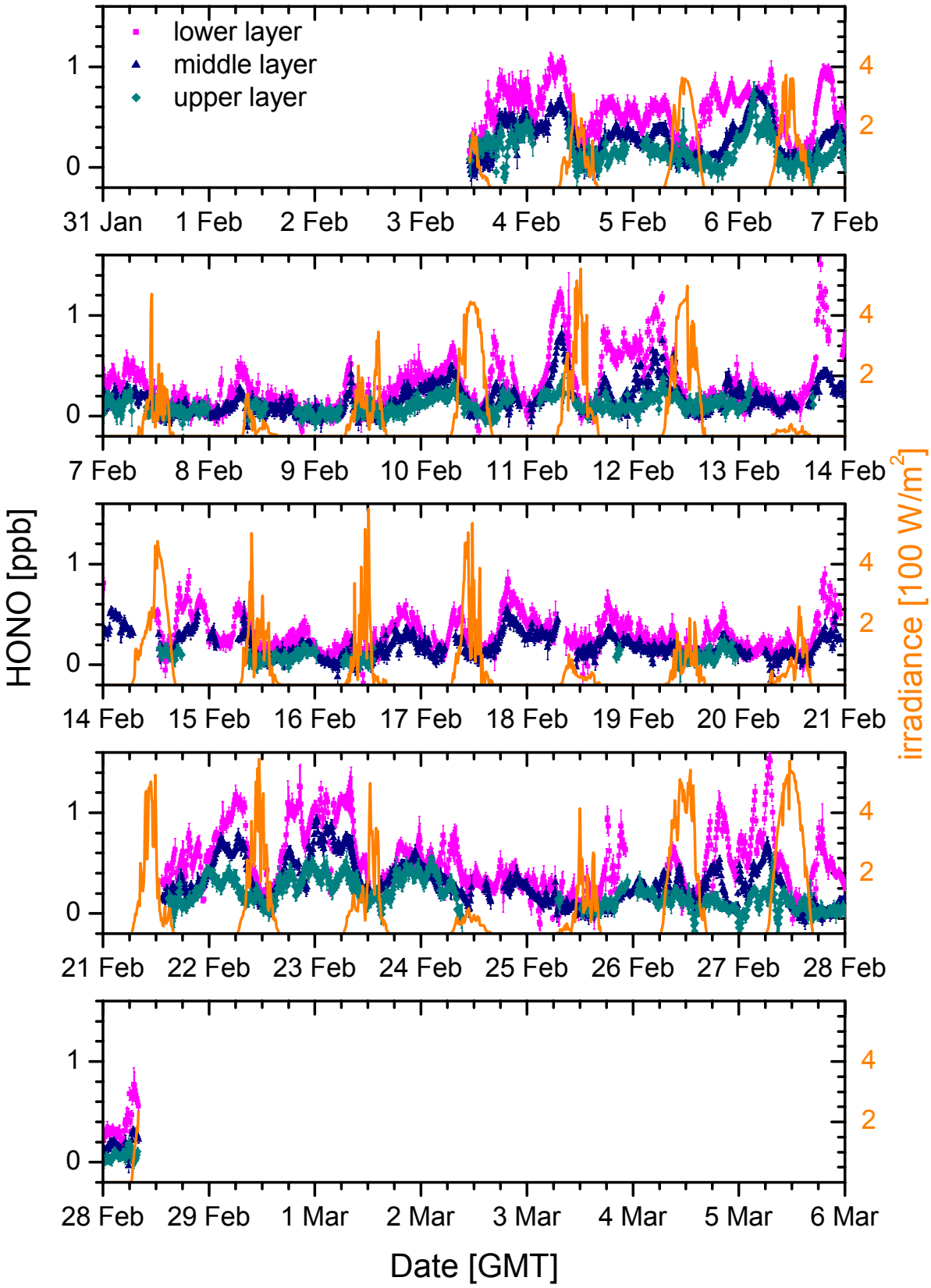

Figure 126: Time series of the HONO profiles in February 2000

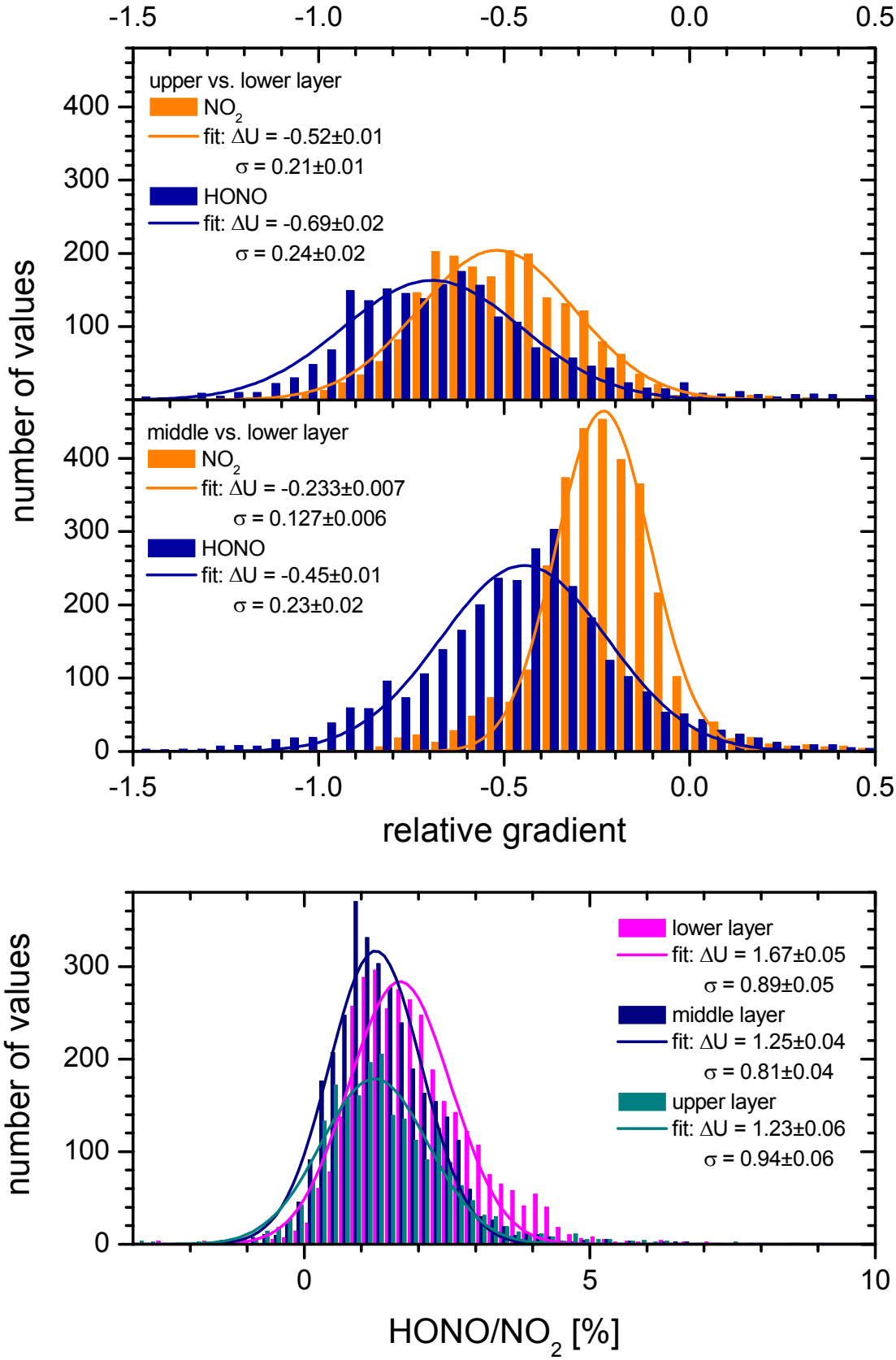

Figure 127: Frequency analysis of the relative gradients and HONO/NO_2 ratios in February 2000

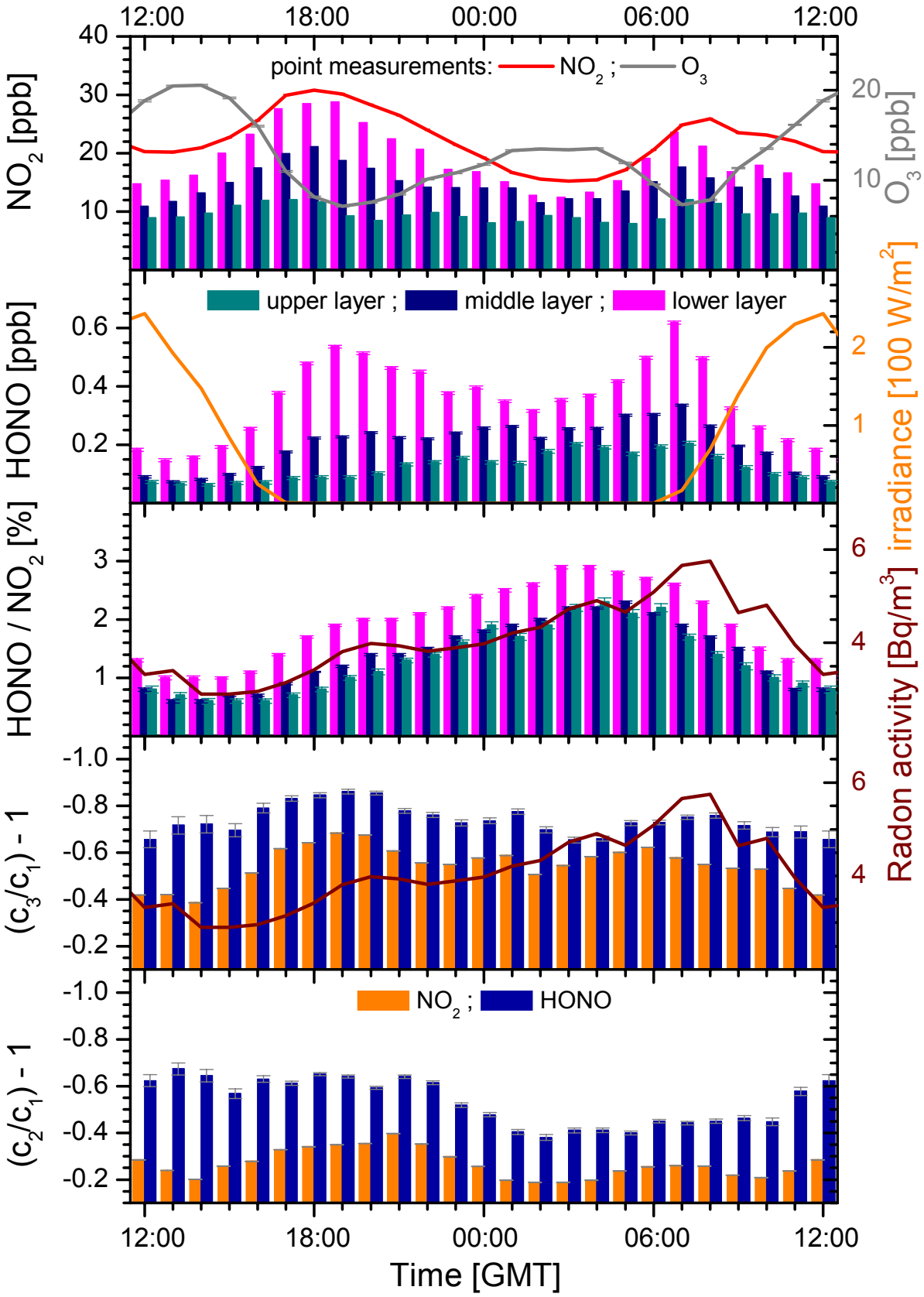

Figure 128: Hourly means of the NO_2 and HONO time series, the HONO/NO_2 ratios and the gradients in February 2000

Annex B: HONO daytime concentrations at Heidelberg

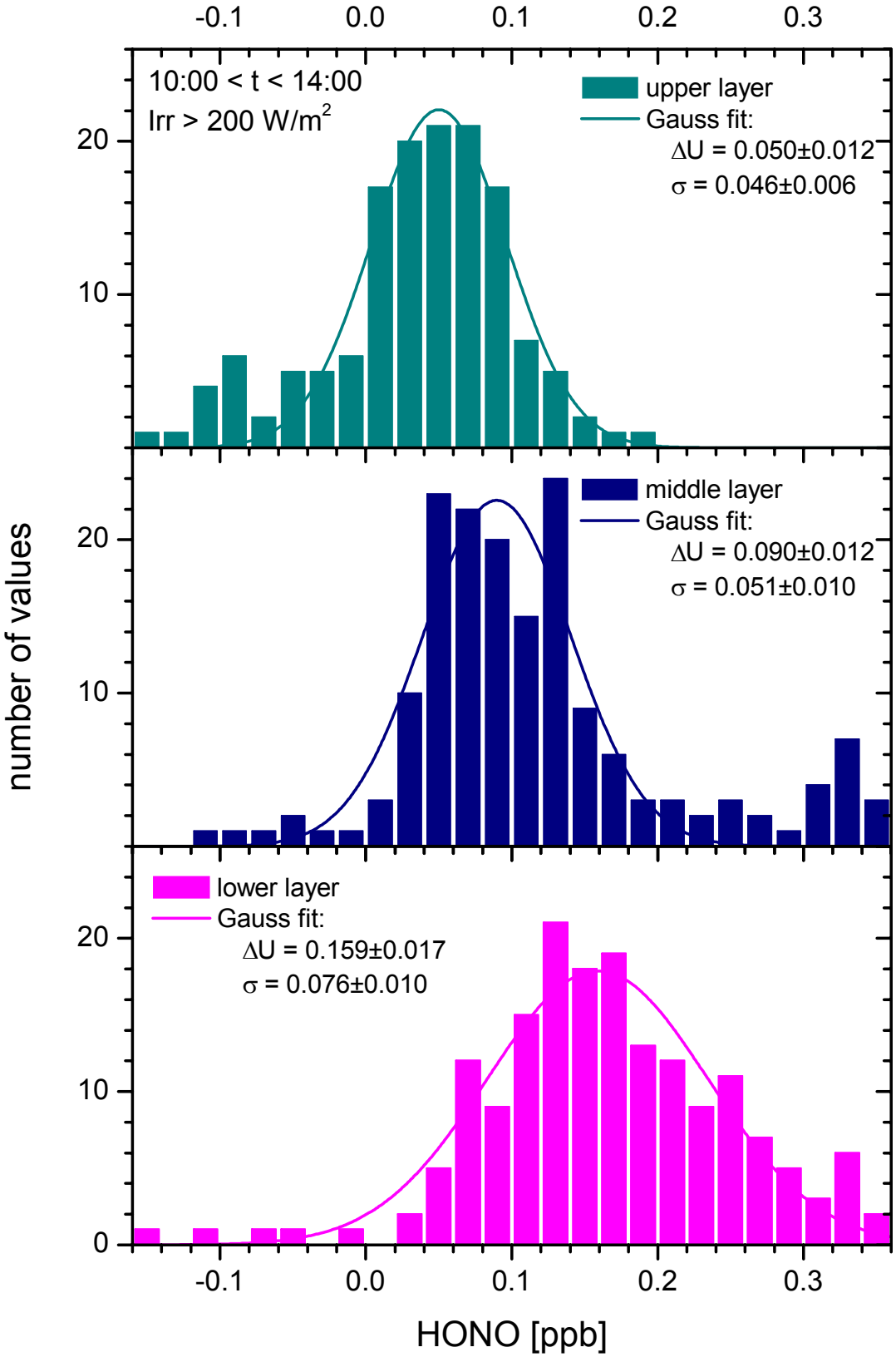

Figure 129: Frequency analysis of the daytime HONO mixing ratios in January/February 1999

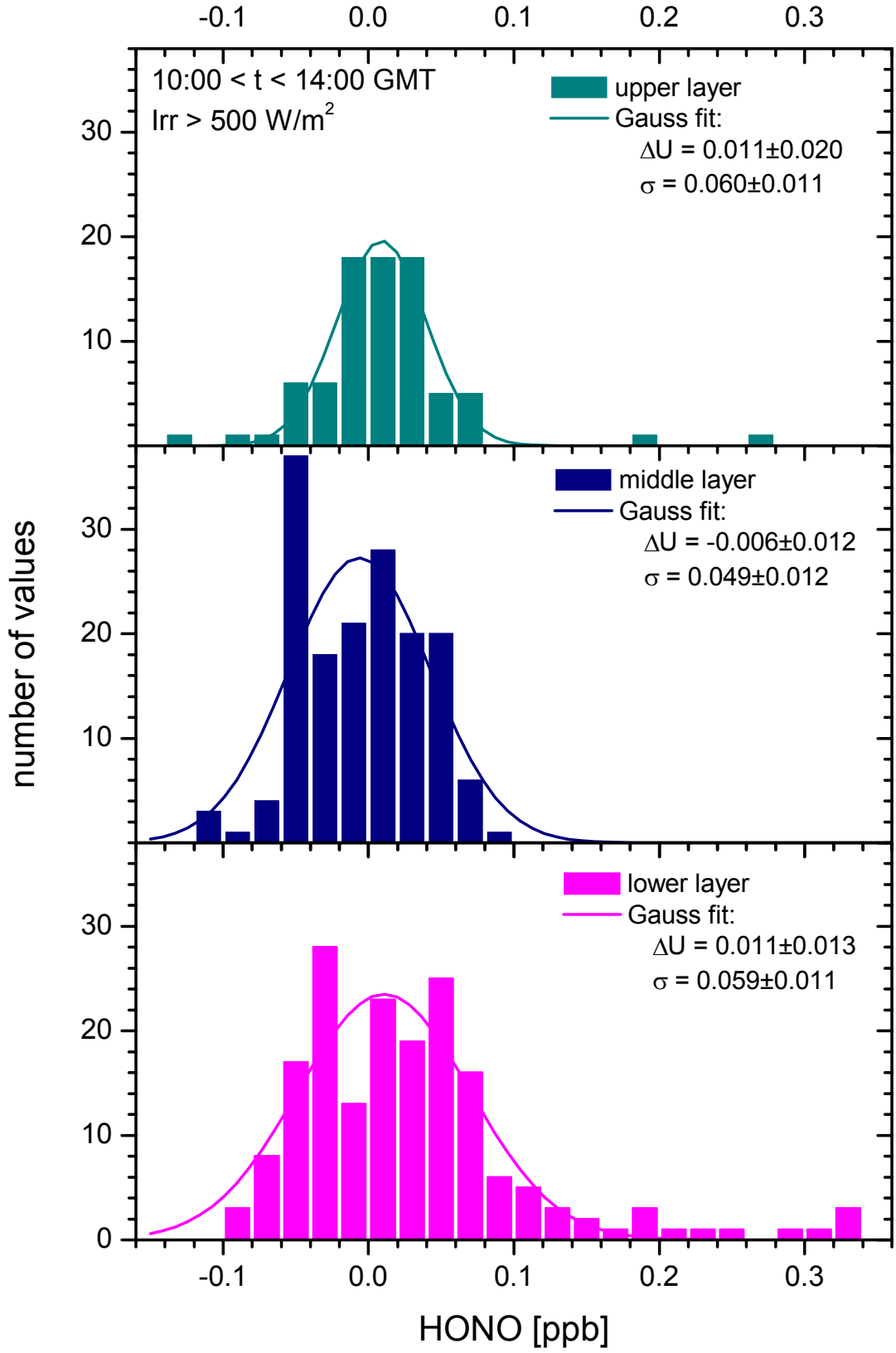

Figure 130: Frequency analysis of the daytime HONO mixing ratios in March/April 1999

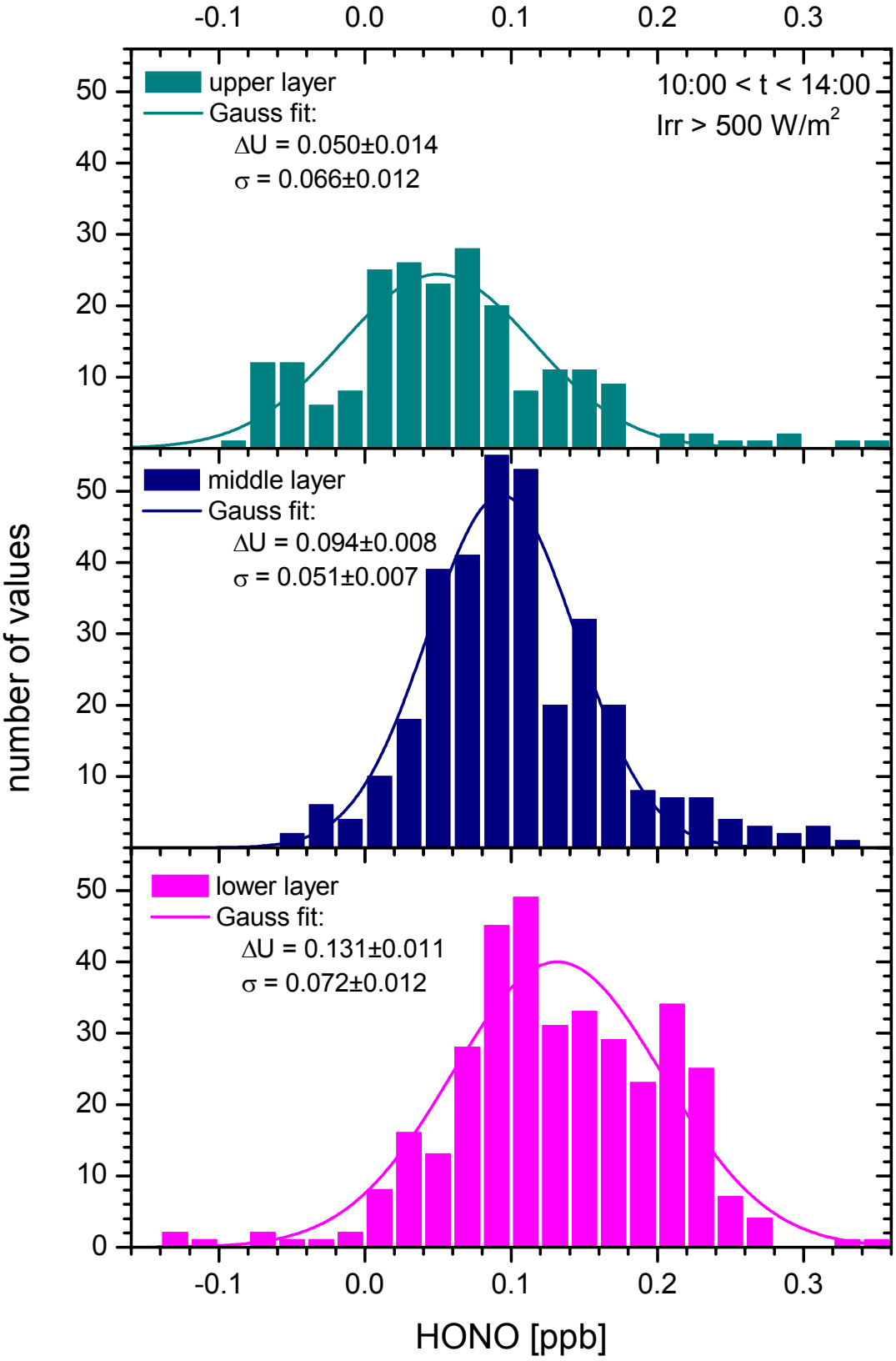

Figure 131: Frequency analysis of the daytime HONO mixing ratios in April/May 1999

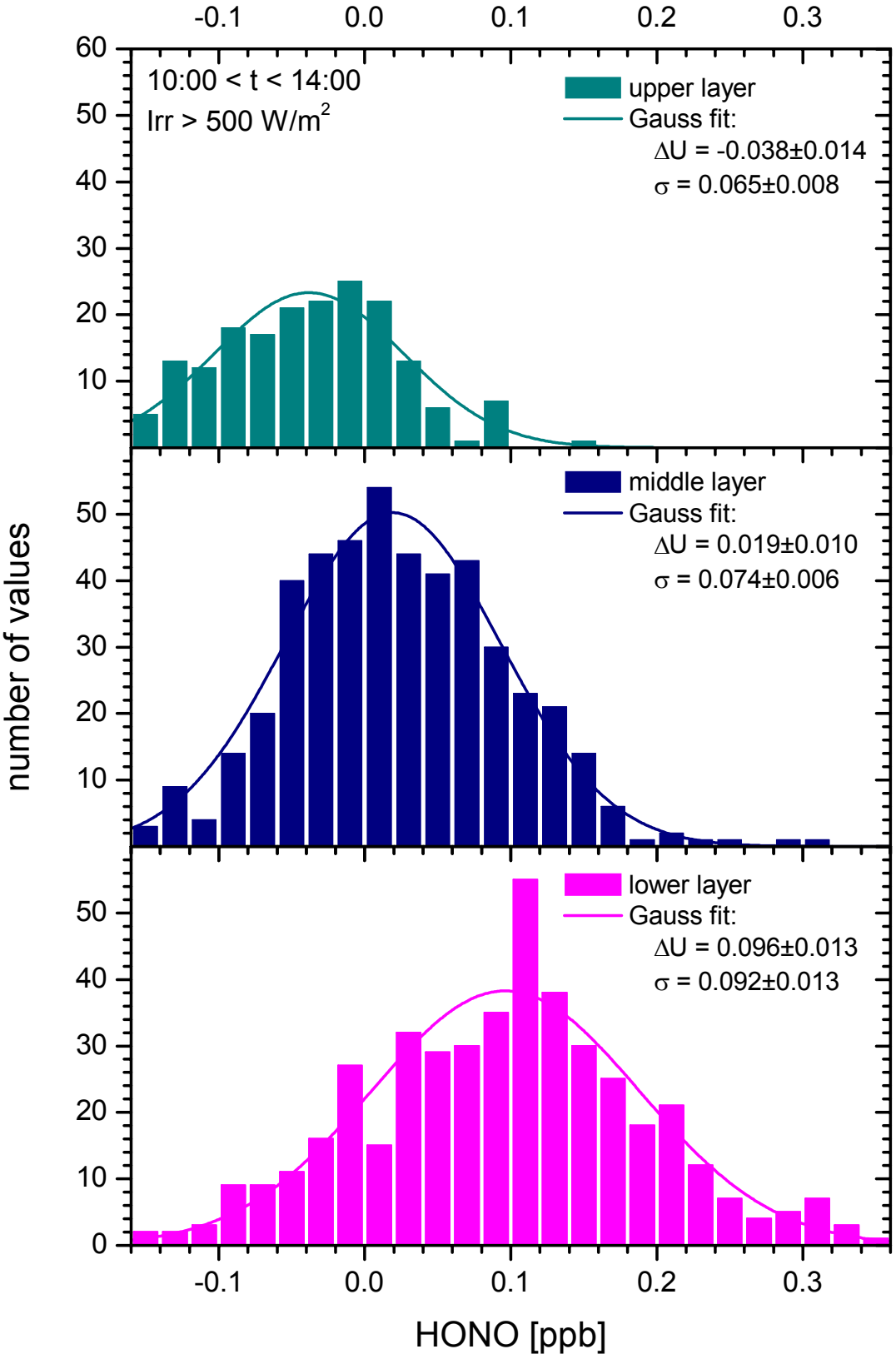

Figure 132: Frequency analysis of the daytime HONO mixing ratios in August 1999

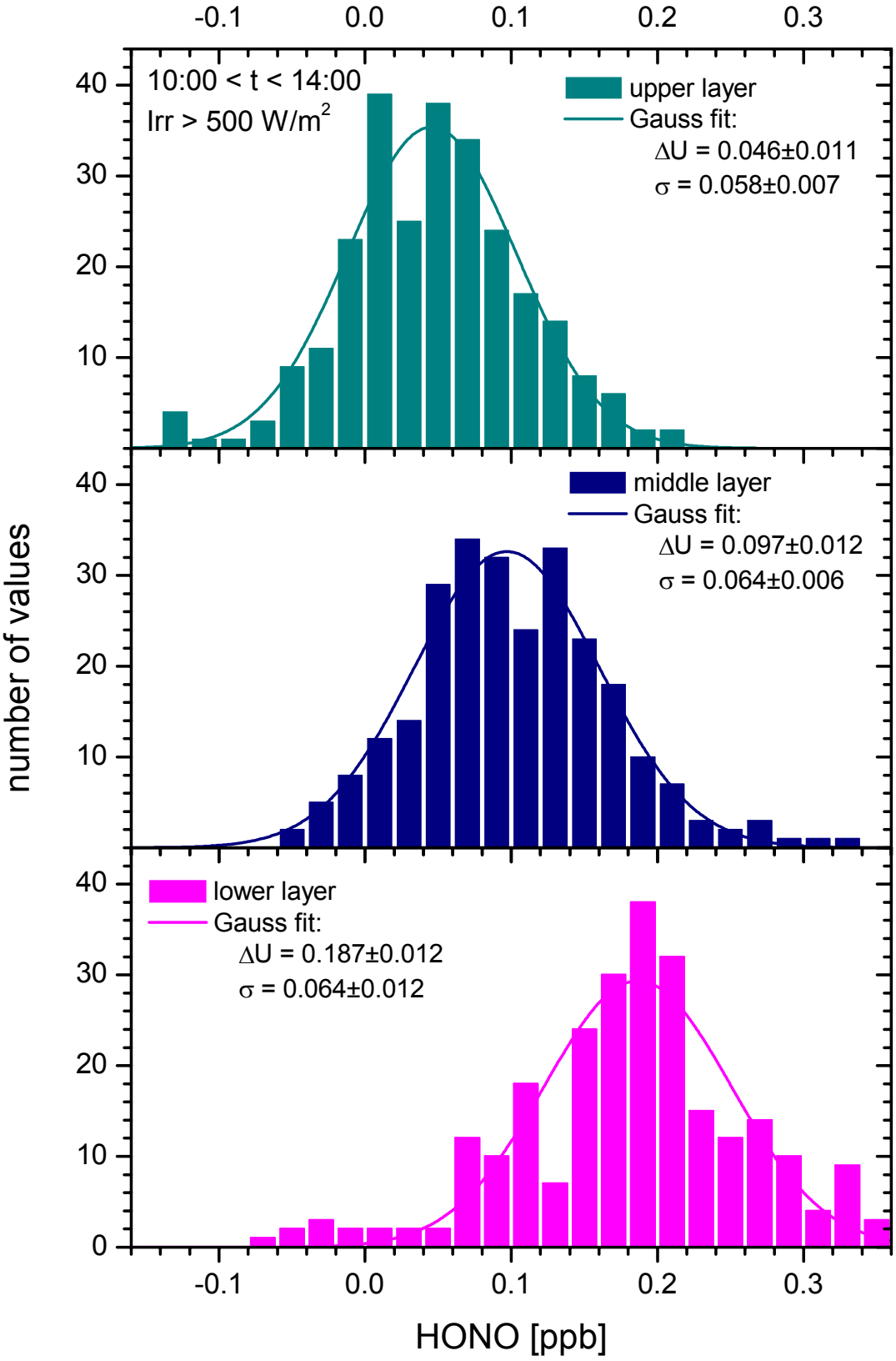

Figure 133: Frequency analysis of the daytime HONO mixing ratios in September 1999

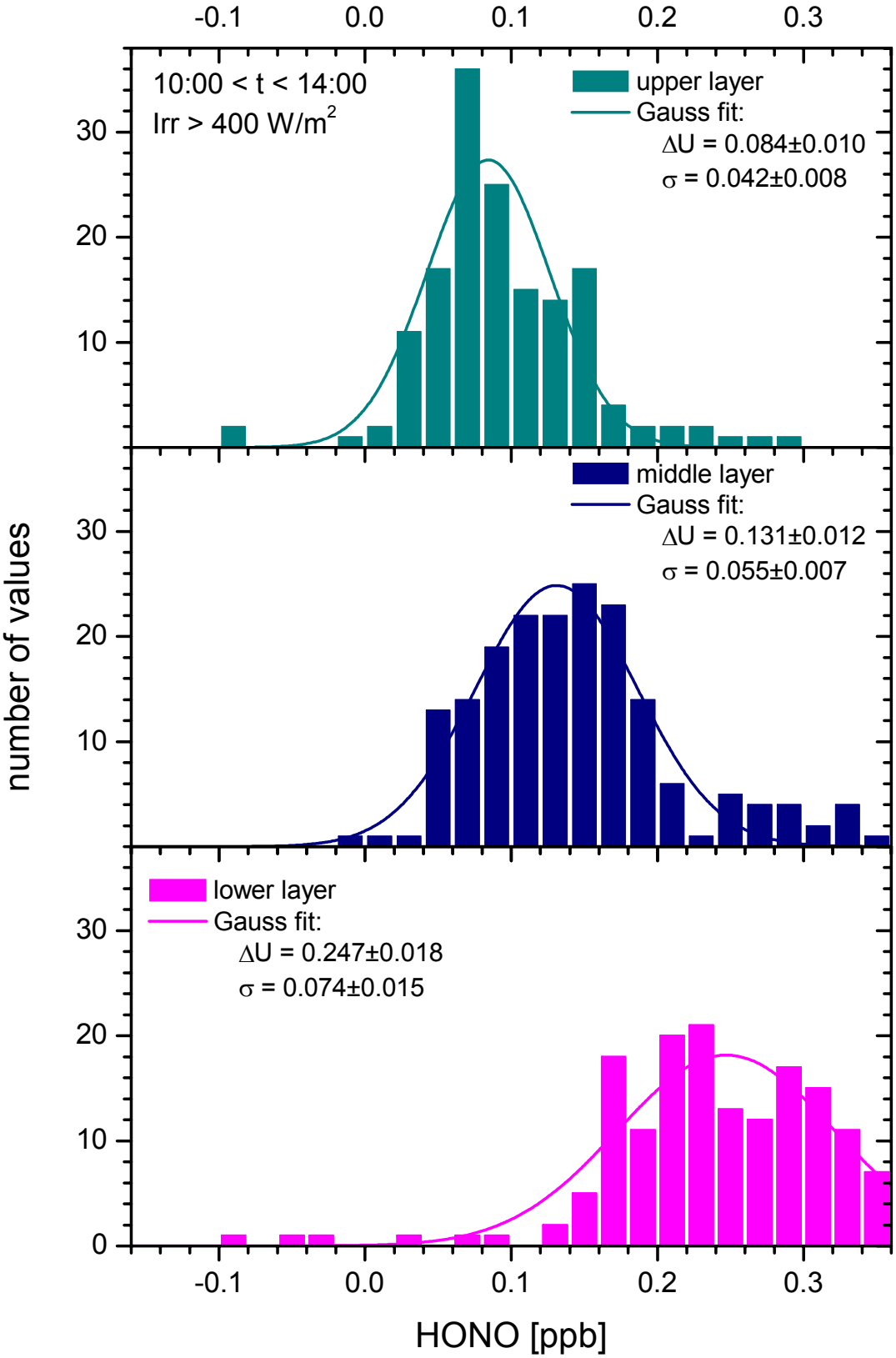

Figure 134: Frequency analysis of the daytime HONO mixing ratios in October 1999

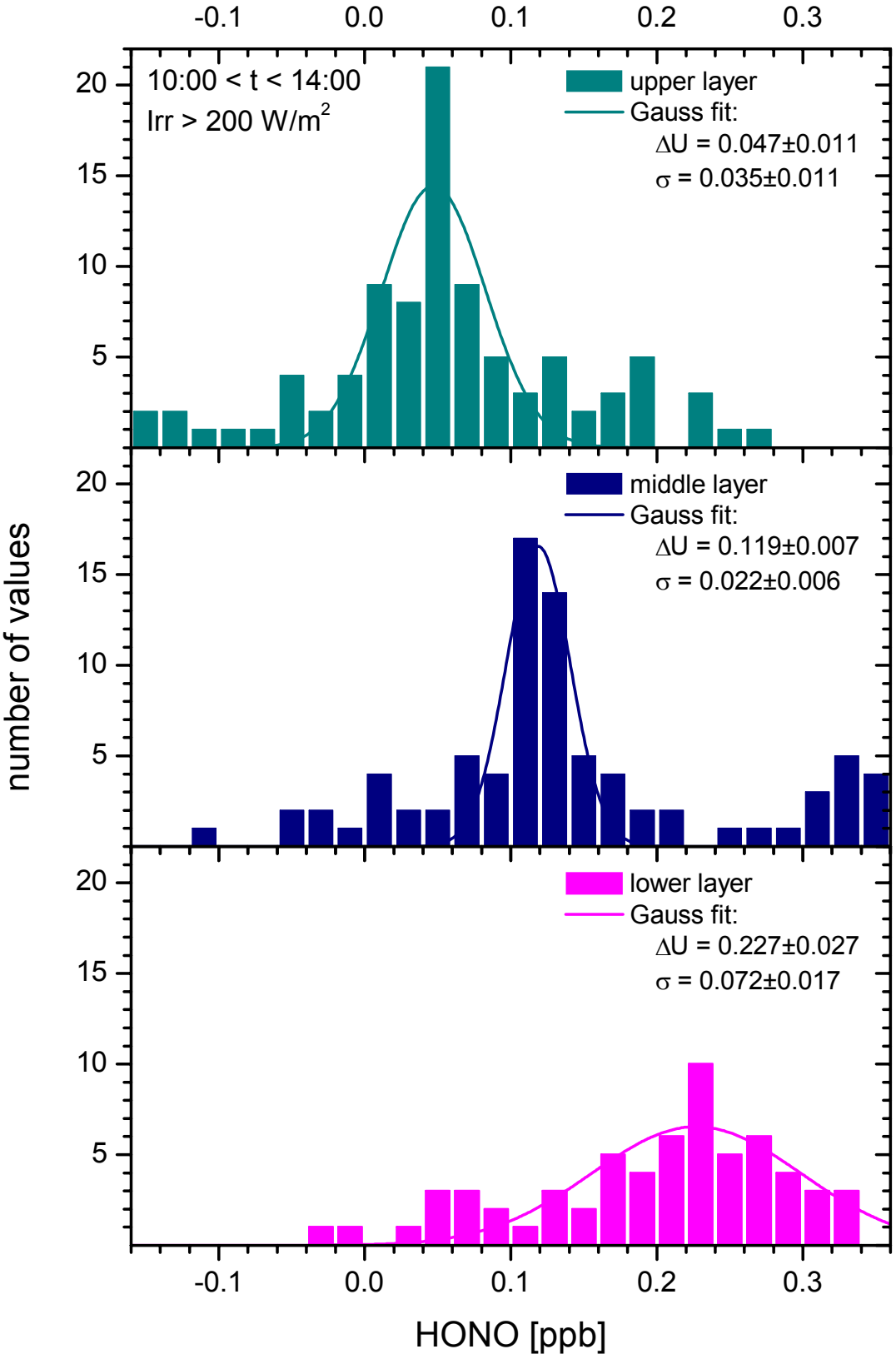

Figure 135: Frequency analysis of the daytime HONO mixing ratios in November 1999

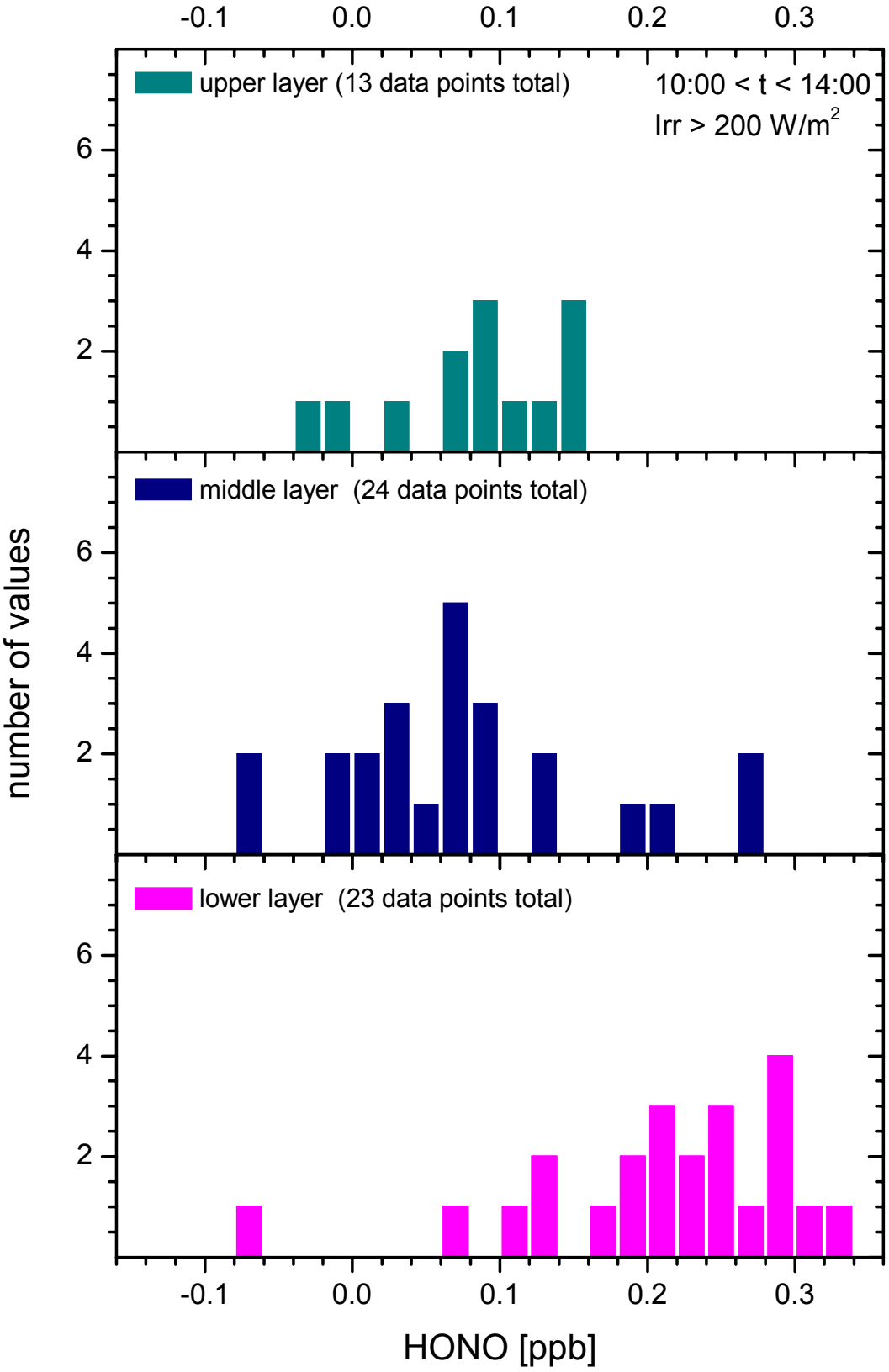

Figure 136: Frequency analysis of the daytime HONO mixing ratios in December 1999

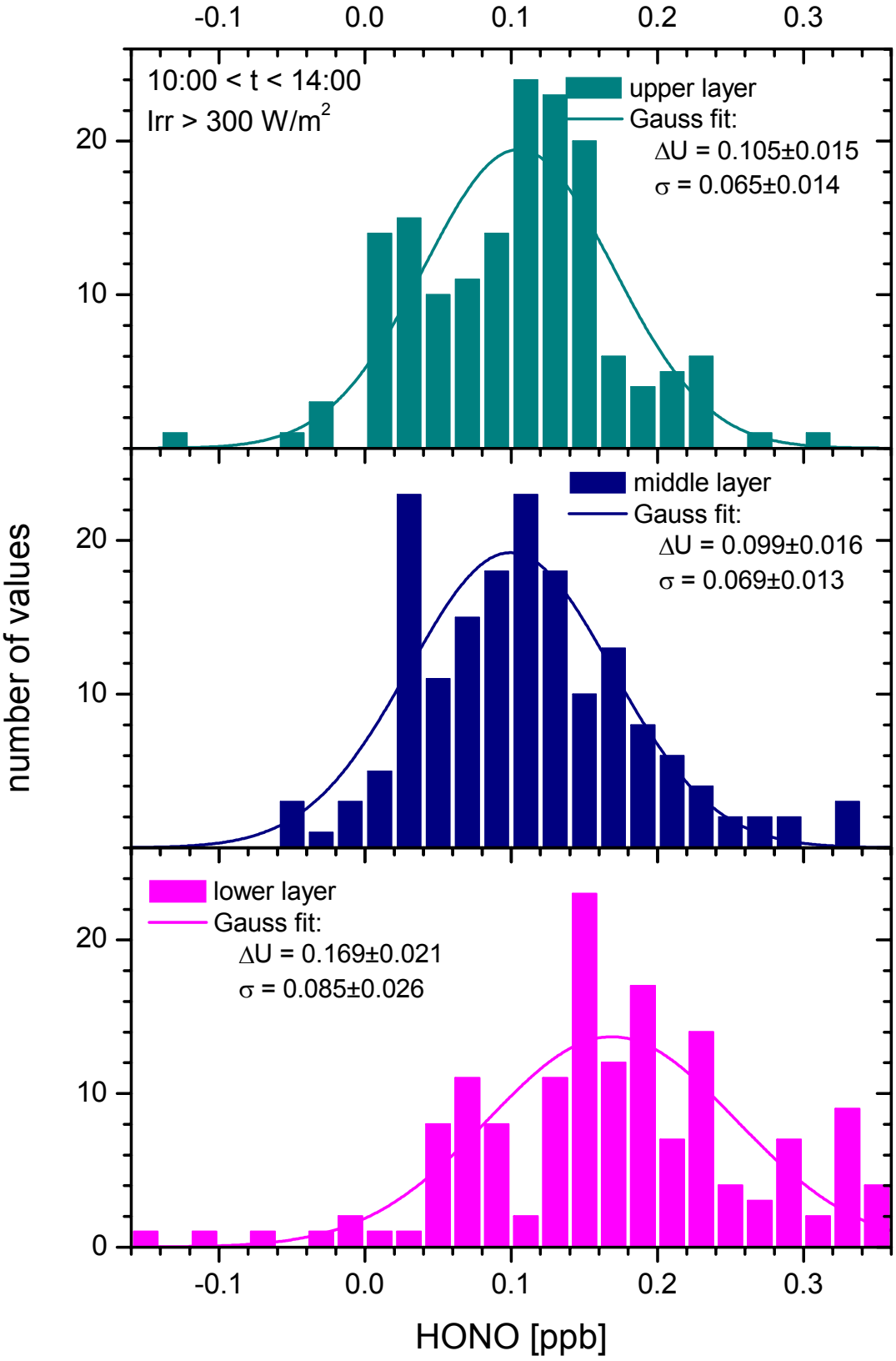

Figure 137: Frequency analysis of the daytime HONO mixing ratios in February 2000

Acknowledgements

I would like to thank all the people who helped me while I was doing my doctorate. Many of them, like Andrea and my parents, gave me strength and courage, even if they thought that I was working on strange and bewildering things (sometimes I had to agree with them…). Others, like my dear colleagues at the Institut für Umweltphysik, especially the guys of the "Troposphere Group", gave valuable advice on scientific matters, but also made work – especially the coffee breaks – a lot more relaxed. Finally, it was a pleasure to work with other scientists from all over Europe, who provided me with (sometimes practical) help, new ideas and fair comments.
Last but not least thanks to all my colleagues from Berlin, Darmstadt, Karlsruhe, Wuppertal, Lausanne, Rome and from elsewhere, who helped me during this thesis, but remain unmentioned here.

Mein herzlichster Dank gilt Andrea, deren Unterstützung und Wärme mich während der gesamten Promotion begleitet haben. Du hast großen Anteil daran, dass ich nach der schwierigen Anfangsphase neuen Mut und Kraft geschöpft habe und diese Arbeit letztlich erfolgreich zu Ende bringen konnte. Zu guter Letzt hat Deine geduldige Englisch-Korrekturabeit wesentlich zur Lesbarkeit ("Nicht schon wieder however!") der Dissertation beigetragen und für den grammatikalischen Feinschliff ("defining oder non-defining?") gesorgt.

Dank auch an meine Mutter („Ich versteh´s!") und meinen Vater („Aha..."), die mir durch ihre Unterstützung das Physikstudium ermöglichten und mir jederzeit Rückhalt gegeben haben.

Meinem Doktorvater U. Platt danke ich für die Möglichkeit, in seiner Gruppe zu arbeiten, sowie für die interessanten – und fordernden – Diskussionen, die meiner Arbeit neue Impulse gaben.

Dank auch an Herrn Schurath für die regelmäßigen „HONO - Diskussionen" im Rahmen verschiedener Projekte, sowie für die Begutachtung meiner – zugegeben etwas umfangreichen – Arbeit.

Vielen Dank an Herrn Roedel, der mit seiner interessanten und hervorragend präsentierten Vorlesung mein Interesse an der Atmosphärenphysik geweckt hat.

Den Kollegen in der Umweltphysik, speziell der „HÖNÖ – Fraktion" Andreas, Björn, Mirko und Sebastian danke ich für zahlreiche Diskussionen, Hilfe bei den Messkampagnen und der Korrektur verschiedener Pamphlete...
Außerdem natürlich den Rest der „Plattmaten", speziell Gerd, Jutta, Kai-Uwe, Kai, Nicole, den Olivers, Ralf und Udo, für die gute Zusammenarbeit und eine Menge Spaß neben und bei der Arbeit.

Ingeborg Levin danke ich für die Überlassung der Heidelberger Radon-Daten, die wesentlich zum Verständnis der hier gemessenen Vertikalprofile beigetragen haben.

Der IUP-Werkstatt für die hervorragende Erledigung auch ausgefallenster Arbeitsaufträge (möglichst bis gestern) sowie für die Möglichkeit zu lernen, wie man anständig mit den Händen arbeitet...

Der Firma Hoffmann Messtechnik, besonders A. Hoffmann, für die Zusammenarbeit bei der Weiterentwicklung des HMT-DOAS, sowie für die Schulung meiner analytischen Fähigkeiten und meiner Argumentations- und Überzeugungskraft.

Der Gruppe von Uli Corsmeier am IMK für unverzichtbare Hilfe bei der Durchführung mehrerer Ballonkampagnen am FZ Karlsruhe, sowie für die zeitweise Überlassung des Fesselballon – Systems (falls der kleine Ballon von jemandem im Schwarzwald oder den Vogesen entdeckt wird, sagt Bescheid). Besonderer Dank gilt Stefan Kraus für die Hilfe und Einweisung mit dem Ballon – System.

Der Gruppe von Herrn Bächmann, speziell Sven Pötzsch, am Institut für Anorganische Chemie, TU Darmstadt für die Überlassung ihrer Ballon-Ausrüstung.

Der Deutschen Bundesstiftung Umwelt für die Förderung dieser Arbeit im Rahmen des Großverbundes “Atmosphärische Diagnostik”, Förderkennzeichen 12637.